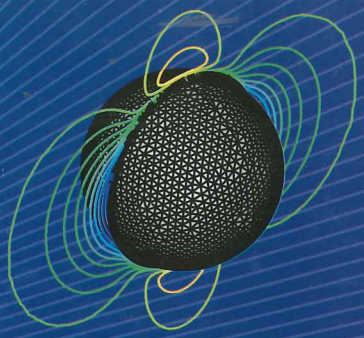

First International Conference on

COMPUTATIONAL METHODS FOR THERMAL PROBLEMS

September
8-10, 2009
Napoli, Italy

Giannini
Editore

THERMACOMP2009

1ST INTERNATIONAL CONFERENCE ON COMPUTATIONAL METHODS FOR THERMAL PROBLEMS

SEPTEMBER 8-10, 2009, NAPLES, ITALY

EDITED BY:

NICOLA MASSAROTTI
DIPARTIMENTO PER LE TECNOLOGIE
UNIVERSITÀ DEGLI STUDI DI NAPOLI "PARTHENOPE"
NAPOLI, ITALY

PERUMAL NITHIARASU
CIVIL AND COMPUTATIONAL ENGINEERING CENTRE
SCHOOL OF ENGINEERING, SWANSEA UNIVERSITY
SWANSEA, UNITED KINGDOM

WITH THE SUPPORT OF:

ALESSANDRO MAURO, UNIVERSITÀ DEGLI STUDI DI NAPOLI "PARTHENOPE"

1st International Conference on Computational Methods for Thermal Problems, 2009, Napoli, Italy

First Edition, September 2009

ISBN-13: 978-88-7431-459-1

Editore: Giannini Editore
Via Cisterna dell'Olio 6/b, 80134 Napoli
www.gianninispa.it

PREFACE

It is our pleasure to welcome all participants of the *First International Conference on Computational Methods for Thermal Problems* (THERMACOMP2009) to Napoli. Computational and mathematical methods have had a profound impact on the understanding and advancement of engineering science and technology over the last few decades. Though there are many conferences in the area of computational methods serving the community, a focused conference in the area of computational methods for thermal problems has been long overdue. The conference aims to convene a diverse scientific audience of mathematicians, physicists and computational scientists that have a communal interest in modelling thermal problems. It is encouraging to learn that this conference represents an interdisciplinary forum of scientists with expertise ranging from heat conduction, convection and radiation to CFD and micro and nano heat transfer. We hope that the interaction between scientists during the conference leads to new topics of research and new collaborations.

THERMACOMP2009 consists of three plenary lectures, six keynote lectures, four organized mini-symposia and nine standard sessions. We are grateful to all invited speakers for accepting our invitation.

We thank THERMACOMP2009 sponsors, supporters, mini-symposium organizers, executive**,** advisory and local committee members for their support.

Nicola Massarotti
Università degli Studi di Napoli "Parthenope"
Italy

Perumal Nithiarasu
Swansea University
United Kingdom

SPONSORS

UNIVERSITÀ DEGLI STUDI DI NAPOLI
"PARTHENOPE"

AVL - ADVANCED SIMULATION TECHNOLOGIES

QI S.R.L.

SUPPORTING ORGANIZATIONS

REGIONE CAMPANIA

DIPARTIMENTO PER LE TECNOLOGIE

UNIVERSITÁ DEGLI STUDI DI CASSINO

UNIVERSITÁ DEGLI STUDI DI NAPOLI "FEDERICO II"

SECONDA UNIVERSITÁ DEGLI STUDI DI NAPOLI

SWANSEA UNIVERSITY

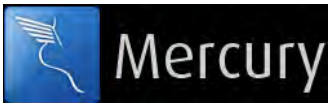

COMMITTEES

HONORARY CHAIR
Professor R.W. Lewis, Swansea University, UK

CO-CHAIRS
N. Massarotti, University of Naples “Parthenope”, Italy
P. Nithiarasu, Swansea University, UK

INTERNATIONAL EXECUTIVE COMMITTEE
F. Arinç, Middle East Technical University, Turkey
A. Carotenuto, University of Naples "Parthenope", Italy
G. Comini, University of Udine, Italy
G. de Vahl Davis, University of New South Wales, Australia
Y. Jaluria, Rutgers, The State University of New Jersey, USA
O. Manca, Second University of Naples, Italy
C. Meola, University of Naples Federico II, Italy
V. Naso, University of Naples Federico II, Italy
E. Oñate, Universitat Politècnica de Cataluña, Spain
B. Sunden, Lund University, Sweden
K. Vafai, University of California, Riverside, USA

INTERNATIONAL ADVISORY COMMITTEE
N. Bianco, University of Naples Federico II, Italy
G. Biswas, Indian Institute of Technology Kanpur, India
S. Chang, National University of Singapore, Singapore
R. Codina, Universitat Politècnica de Catalunya, Spain
R.M. Cotta, Universidade Federal do Rio de Janeiro, Brazil
D. Drikakis, Cranfield University, UK
D. Gethin, Swansea University, UK
D. Givoli, Technion - Israel Institute of Technology, Israel
Y. Joshi, Georgia Institute of Technology, USA
X. Li, Dalian University of Technology, China
R. Lohner, George Mason University, USA
W. Malalasekera, Loughborough University, UK
A.G. Malan, Council for Scientific and Industrial Research, South Africa
J.C. Mandal, Indian Institute of Technology Bombay, India
S. Nardini, Second University of Naples, Italy
C. Nonino, University of Udine, Italy
D. Poulikakos, ETH Zurich, Switzerland
D.A.S. Rees, University of Bath, UK
J. Reese, University of Strathclyde, UK
B. Sarler, University of Nova Gorica, Slovenia
K.N. Seetharamu, PES Institute of Technology, India
P. Tucker, University of Cambridge, UK
V.R. Voller, University of Minnesota, USA

LOCAL ORGANISING COMMITTEE
A. Andreozzi, University of Naples Federico II
F. Arpino, University of Cassino
M. Costa, Istituto Motori, CNR
A. Mauro, University of Naples “Parthenope”
L. Vanoli, University of Naples “Parthenope”

CONTENTS

PARALLEL SESSIONS

NUMERICAL METHODS

CONDUCTION, CONVECTION AND RADIATION

COUPLED PROBLEMS

CHEMICAL PROCESSES AND HEAT TRANSFER

HEAT EXCHANGERS AND FUEL CELLS

NUMERICAL METHODS IN ENERGY CONVERSION SYSTEMS

MICRO- AND NANO- HEAT TRANSPORT

HEAT AND MASS TRANSFER IN POROUS MEDIA

BOILING AND CONDENSATION

PLENARY LECTURES

First International Conference on Computational Methods for Thermal Problems
ThermaComp2009, September 8-10, 2009, Napoli, Italy
N.Massarotti and P.Nithiarasu (Eds.)

ROLE OF EXPERIMENTS IN THE ACCURATE NUMERICAL SIMULATION OF THERMAL PROCESSES

Yogesh Jaluria
Board of Governors Professor
Mechanical and Aerospace Engineering Department
Rutgers University, Piscataway, NJ, USA
jaluria@jove.rutgers.edu

ABSTRACT

Experimental results play a crucial role in the validation of mathematical and numerical models for a variety of basic and applied thermal transport problems. They are also used to establish the accuracy and predictability of numerical simulation, particularly for complex transport processes that arise in practical thermal systems. Material properties that are crucial to any accurate simulation are also obtained experimentally. In addition, there are many important processes where the boundary conditions are not well defined, or limited information is available on the imposed conditions. This makes an accurate numerical simulation of the problem difficult and, in several cases, virtually impossible. However, experimental work can be used, along with the numerical solution of an inverse problem, in some cases to provide the appropriate boundary conditions to allow the simulation of the system to be carried out and to obtain realistic and accurate results. Finally, there are many problems in which numerical simulation is particularly suitable over given parametric ranges, while experimentation is more appropriate over other regions, as defined by the governing parameters and operating conditions. In such cases, a concurrent numerical and experimental approach may be used to solve the problem more accurately and efficiently. The role and importance of experimental data in the accurate numerical simulation of a variety of fundamental and practical problems is discussed in this paper. The basic considerations that arise in these approaches are outlined and a few circumstances, where a coupling of the experimentation with the simulation is appropriate, are discussed. It is shown that experimental data are valuable in solving complex practical problems that involve thermal transport processes and are often critical for obtaining accurate, valid, physically realistic and dependable numerical results.

Key Words: *Simulation, Experimentation, Validation, Accuracy, Thermal Processes*

1. INTRODUCTION

Numerical simulation of fundamental and practical problems, that involve convective heat transfer, is widely used to understand the underlying phenomena and to design, control and optimize thermal systems. Simulation involves mathematical modeling, which gives rise to the governing equations and the relevant boundary conditions, numerical modeling, which results in the discretized form of these equations, and the implementation of the model on a computer to obtain numerical results at a finite number of locations. Numerical modeling and simulation are extensively used because of the limited applicability of analytical methods, particularly for practical applications, which are generally quite complicated, and the expense and time involved in experimental methods [Jaluria, 2008]. However, the model is usually validated by the use of analytical and experimental results, if available. Experimental

results are also valuable for physical insight and basic understanding. However, besides validation and physical insight, experiments are needed in a wide range of problems to initiate and proceed with the numerical simulation, to obtain greater convenience, accuracy or efficiency in the solution, or to provide necessary inputs for accurate results. This paper focuses on circumstances where the simulation is strongly dependent or driven by the experimental data.

Of particular interest in this review paper are the following aspects:

- Material Characteristics and Properties
- Validation
- Experimentally Obtained Boundary Conditions
- Solution of Inverse Problems with Experimental Inputs
- Concurrent Simulation and Experimentation

All these aspects are important for accurate, efficient, and convenient numerical simulation of practical convection heat transfer problems. The basic considerations involved in each are presented in this paper, along with examples from areas such as materials processing and cooling of electronic equipment to illustrate the approaches. Experimentation is needed to provide the material properties needed for the simulation, as well as data for validation of the mathematical and numerical models. In many problems, experimental results are needed to quantify the boundary conditions. In some cases, experiments can be obtained only over a limited region or domain and an inverse problem has to be solved to obtain the relevant conditions. Finally, there are circumstances where experimentation is more convenient, accurate and efficient than numerical simulation, whereas the latter may be more appropriate in other circumstances. Then, a combination of experimentation and numerical simulation can be used concurrently to solve the problem most efficiently and accurately. All these aspects are considered in detail in this paper.

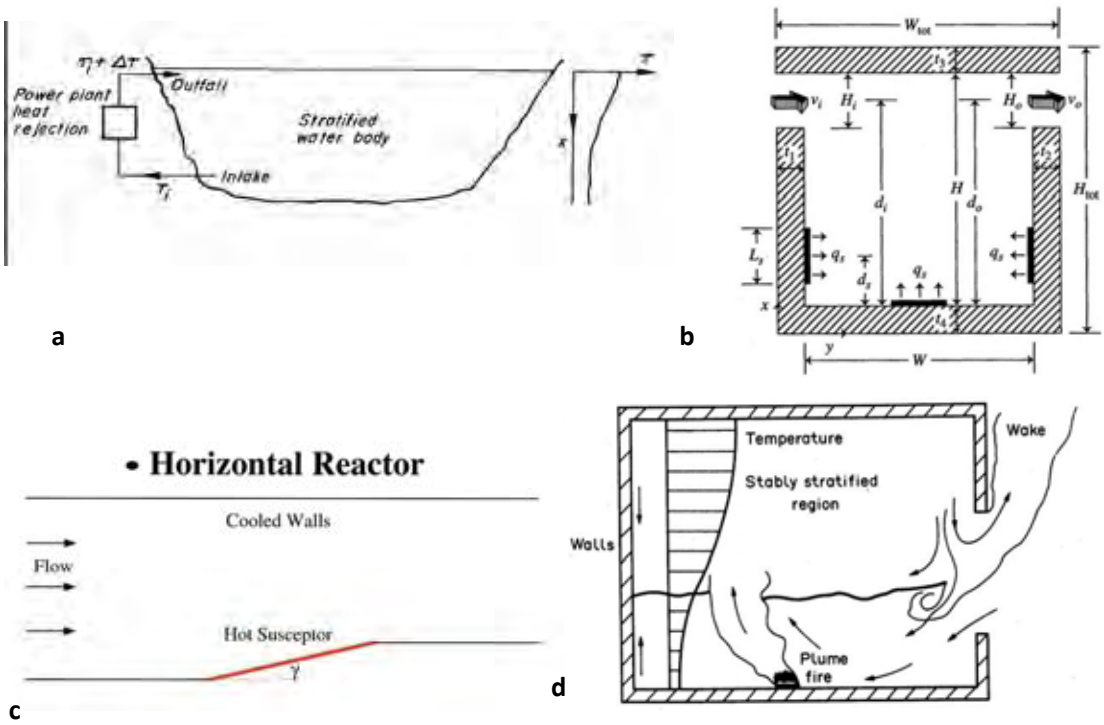

FIGURE 1. Examples of practical convective heat transfer problems: (a) Heat rejection from a power plant; (b) Cooling of an electronic system; (c) Chemical Vapor Deposition (CVD) reactor; (d) Fire in an enclosed region

Figure 1 shows some common convective heat transfer problems in which numerical simulation has been used to provide the inputs for design and for understanding the basic processes involved. The systems shown include heat rejection from the condensers of a power plant to a water body such as a lake, an electronic system consisting of three isolated heat sources, representing electronic devices, in an enclosure with forced flow driven by a fan, a horizontal chemical vapor deposition (CVD) reactor in which chemical reactions result in the deposition of a thin film on the hot susceptor, and a room with a fire showing the stratified hot upper layer generated in the room due to the fire plume and flow exchange through an opening. Because of complexities such as turbulent flow, combined heat and mass transfer, chemical reactions, complicated geometry, variable material properties, buoyancy effects, and combined transport mechanisms, numerical simulation is needed to model the flow and the heat transfer in such thermal processes and systems.

2. MATHEMATICAL AND NUMERICAL MODELING

Mathematical modeling is one of the most critical elements in the characterization, control, design and optimization of thermal systems. Practical processes and systems are generally very complicated and must be simplified through idealizations and approximations to make the problem solvable. Once the mathematical model is obtained, resulting in the governing equations and boundary conditions, numerical modeling and simulation are used to obtain results that can be used to characterize the process and provide inputs for design and optimization.

As an example, consider the schematic diagram in Figure 2, which shows the system for the polymer coating of an optical fiber after it is drawn in a furnace. The fiber is coated with a jacketing material for protection against abrasion, to reduce stress induced microbending losses, and for increased strength. Generally, curable acrylates, are used and the wet coating is cured by ultra-violet radiation as it passes through the curing station after the coating applicator. The basic

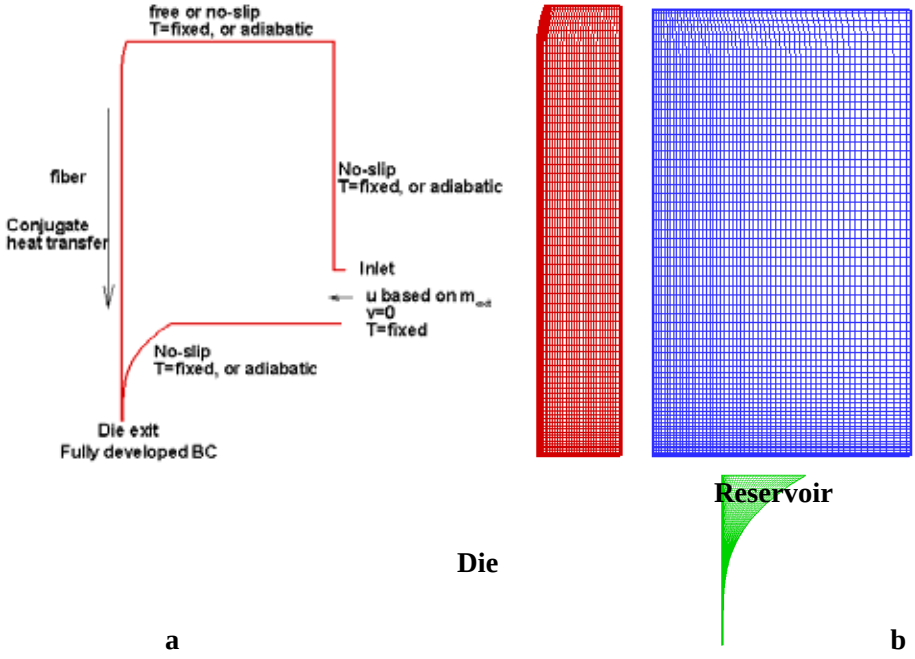

FIGURE 2. (a) Optical fiber coating system; (b) Grid for numerical simulation

coating process involves drawing the fiber through a reservoir of coating fluid from where it is passed through a die that may be used to control the thickness and the concentricity of the coating layer. Viscous shear due to the moving fiber results in a circulatory fluid motion within the fluid. A

balance between surface tension, viscous, gravitational, and pressure forces results in an upstream meniscus at the cup entrance. Similarly, an exit mensistus arises at the bottom of the applicator. This process is considered in some detail later.

If the boundary conditions are well defined, as shown in Fig. 2(a), the flow and heat transfer in the coating applicator and the die can be investigated numerically. The governing equations are:

Continuity Equation:

$$\frac{1}{r}\frac{\partial}{\partial r}(\rho v r) + \frac{\partial(\rho v)}{\partial z} = 0 \tag{1}$$

Momentum Equation in r-Direction:

$$\begin{aligned}&\frac{\partial \rho u}{\partial t} + \frac{1}{r}\frac{\partial}{\partial r}(r\rho u^2) + \frac{\partial}{\partial z}(\rho v u) = -\frac{\partial p}{\partial r} + \frac{1}{r}\frac{\partial}{\partial r}(\quad r\frac{\partial u}{\partial r}) + \frac{\partial}{\partial z}(\quad \frac{\partial u}{\partial z})\\ &+\frac{1}{r}\frac{\partial}{\partial r}(\quad r\frac{\partial u}{\partial r}) + \frac{\partial}{\partial z}(\quad \frac{\partial v}{\partial r}) - 2\quad \frac{u}{r^2} + \rho g r\end{aligned} \tag{2}$$

Momentum Equation in z-Direction:

$$\begin{aligned}&\frac{\partial \rho v}{\partial t} + \frac{1}{r}\frac{\partial}{\partial r}(r\rho u v) + \frac{\partial}{\partial z}(\rho v^2) = -\frac{\partial p}{\partial z} + \frac{1}{r}\frac{\partial}{\partial r}(\quad r\frac{\partial v}{\partial r}) + \frac{\partial}{\partial z}(\quad \frac{\partial v}{\partial z})\\ &+\frac{1}{r}\frac{\partial}{\partial r}(\quad r\frac{\partial u}{\partial r}) + \frac{\partial}{\partial z}(\quad \frac{\partial v}{\partial z}) + \rho g z\end{aligned} \tag{3}$$

Energy Equation:

$$\begin{aligned}&\frac{1}{r}\frac{\partial}{\partial r}(r\rho c_p u T) + \frac{\partial}{\partial z}(\rho c_p v T) = \frac{1}{r}\frac{\partial}{\partial r}(Rr\frac{\partial T}{\partial r}) + \frac{\partial}{\partial z}(R\frac{\partial T}{\partial z}) + q''' +\\ &\quad = 2[(\frac{\partial u}{\partial r})^2 + (\frac{u}{r})^2 + (\frac{\partial v}{\partial z})^2] + (\frac{\partial u}{\partial z} + \frac{\partial v}{\partial r})^2\end{aligned} \tag{4}$$

A wide variety of numerical methods, such as the SIMPLER algorithm developed by Patankar (1980), are available for the solution of these equations. Figure 2(b) shows the discretization of the computational domain. Three distinct regions are indicated. The first one is close to the fiber, which is around 125 m in diameter, the second is a larger far-field region approximating the reservoir, where an external pressure and inflow may be imposed, and the third one approximates the exit die. A free surface is assumed at the top and no-slip conditions are employed elsewhere. Clearly, the problem may be solved to obtain the temperature and flow fields, from which the coating layer thickness, stability and uniformity may be studied.

Similarly, in the case of a single-screw extruder, as shown in Fig. 3, the problem is complicated by the rotating screw and the complex geometry of the channel. Then, the coordinate system may be fixed to the rotating screw and the channel approximated as a wide channel, so that a two-dimensional flow may be assumed. The channels are straightened out mathematically, ignoring the effects of curvature. Then the complicated flow in the extruder is replaced by a pressure and shear driven channel flow, with shear arising due to the barrel moving at the pitch angle over a stationary screw. This is similar to the shear and pressure driven channel flow available in the literature. Therefore, this approximation substantially simplifies the mathematical/numerical model and has been used extensively to obtain the

velocity, temperature and pressure distributions in the extruder, from which the torque needed, pressure at the die inlet, and other engineering quantities of interest in the process can be determined [Karwe and Jaluria, 1990; Jaluria, 1996].

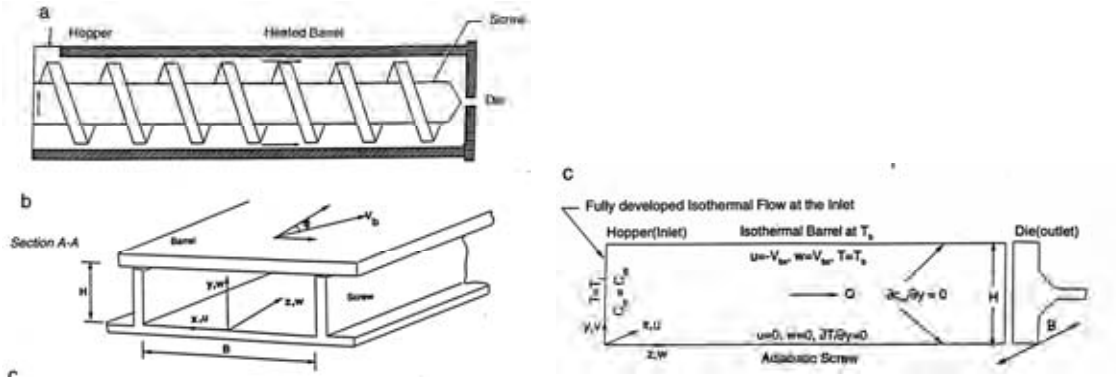

FIGURE 3. Single-screw polymer extruder; (a) Schematic of the system; (b) Mathematical modeling; (c) Resulting channel flow and coordinate system

3. MATERIAL CHARACTERISTICS AND PROPERTIES

Material properties are crucial to the accuracy of any numerical simulation. However, accurate property data are often not available and one has to base the simulation on the information available. Frequently, these data are available at conditions that may be different from those for the actual process, and thus severely limit the usefulness of the simulation. For instance, the manufacture of optical fibers employs the heating of a specially fabricated silica glass preform in a cylindrical furnace above its softening point T_{melt} of around 1900K and pulling it into a fiber through a neck-down region [Paek, 1999]. The neck-down profile depends strongly upon the drawing conditions, as well as on the physical properties of silica glass, which are strong functions of the temperature T. They also vary with the composition, the main effect being on the radiation properties. The variation in the viscosity is the most critical one for the flow, since it varies quite dramatically with temperature. An equation based on the curve fit of available data for kinematic viscosity is written for silica, in S.I. units, as

$$= 4545.45 \exp [\ 32\ (\textbf{Errore.-}\ 1)\ ] \qquad (5)$$

indicating the strong, exponential, variation of with temperature. The radiative source term q''' in the energy equation is non-zero for the glass preform/fiber because glass emits and absorbs energy. The variation of the absorption coefficient with wavelength has been measured for certain compositions and glasses, as shown in Fig. 4(a). However, such data are often at room temperature, whereas the process itself is at much higher temperatures. Also, data may not be available for the particular glass or composition that is being simulated. Still, such data are extremely valuable and are used in the simulation, often approximating the continuous variation as bands with constant absorption over each band. A two- or three-band absorption coefficient distribution can be effectively used, as shown in Fig. 4(b). Then, methods such as the zonal model and the discrete ordinates method can be successfully used to model the radiative transport [Yin and Jaluria, 1997]. Other more accurate methods have also been used, though the major constraint has been the availability of accurate radiative property data.

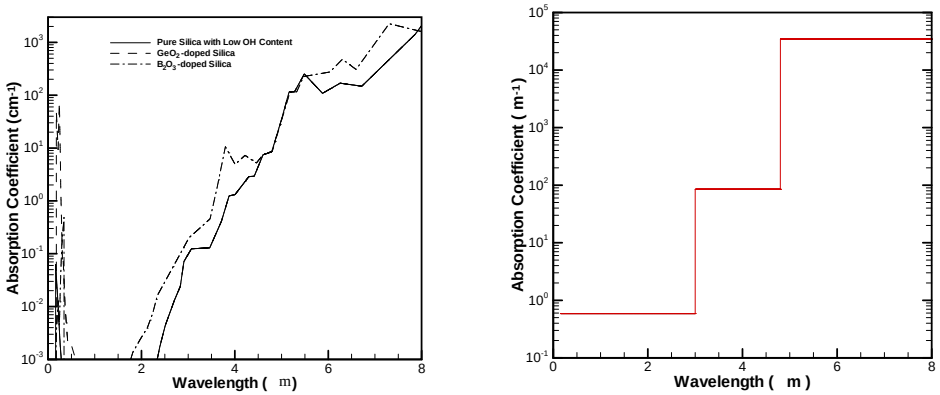

a **b**

FIGURE 4. (a) Measured absorption coefficient for silica glass; (b) Three-band model based on experimental data

Similarly, the transport processes in polymer processing or coating involve large material property changes. Since the properties may vary with temperature and species concentration, the flow is coupled with the heat and mass transfer problem. However, most materials are also non-Newtonian and the viscosity varies with the shear rate and thus with the flow, making the problem even more complicated. The fluid viscosity is often taken as

$$= \ _{o}(\dot{}, \ / \dot{}, \ _{o})^{n-1} \exp(b /T) \qquad (6)$$

where $\dot{}$, is the total strain rate, b the temperature coefficient of viscosity, subscript o indicates reference conditions and n is the power-law index of the fluid. The extruded material is thus treated as a Generalized Newtonian fluid [Tadmor and Gogos, 1979]. For food materials, the rheological model becomes even more involved because of the dependence on the moisture concentration C. The changes in the chemical structure can also be included as a factor in these equations if experimental data are available. Other constitutive relations for viscosity can easily be employed instead, depending on the material.

4. VALIDATION

An extremely important consideration in the modeling and simulation of thermal processes and systems is that of validation because of the simplifications used to treat various complexities. It is necessary to ensure that the numerical code performs satisfactorily and that the model is an accurate representation of the physical problem. Unless the models are satisfactorily validated and the accuracy of the numerical predictions established, the simulation cannot form the basis for design and optimization. A consideration of the physical behavior of the results obtained is used to ensure that the results and trends are physically reasonable. Comparisons with available analytical and numerical results, particularly benchmark solutions, can then be used for validation of the mathematical and numerical models, see, for instance, Roache (1998) and de Vahl Davis and Leonardi (2001). Comparisons with experimental results are obviously desirable. Experimental data may be available in some cases and, in others, data may be available on similar, though simpler, systems. These may be used for comparisons with numerical results. However, experimental data are often not available and it may become necessary to develop an experimental arrangement for providing inputs for validation. Though this is not a trivial exercise, it could be crucial to establish the validity of the models used, particularly for complex systems on which no other reliable information is available.

Figure 5 shows the comparisons between numerical results and experimental data on a natural lake, such as the one used for heat rejection in Fig. 1(a). A one-dimensional model is used, with approximations on mixing due to buoyancy [Moore and Jaluria, 1972]. The comparisons are shown for the yearly temperature cycle of the lake, indicating stable stratification in the summer and fully mixed conditions in the winter. Comparisons are also shown for the predicted and measured temperature profiles in the lake. It is interesting to note that, despite substantial complexities in the transport phenomena in the natural lake and the simplicity of the model, the numerical and experimental results show fairly good agreement. This is quite typical for a variety of practical processes, where the overall features are not very sensitive to the model. However, the local velocity and temperature fluctuations and distributions may be quite sensitive and could be used to select the most accurate model.

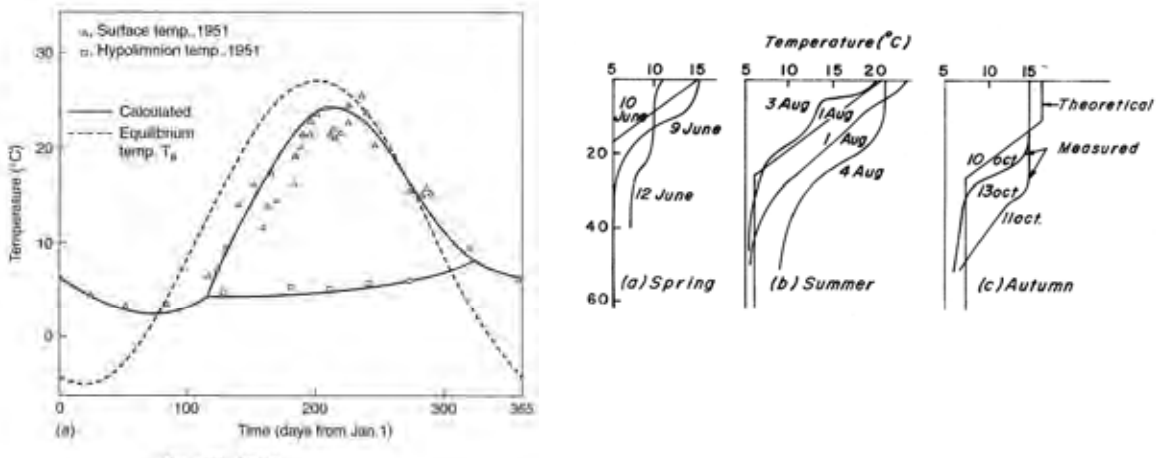

FIGURE 5. Predicted yearly temperature cycle of a natural lake and calculated temperature profiles at various times during the year, along with experimental data

Similarly, experiments have been carried to validate models for twin-screw extrusion, particularly the transport in the intermeshing region between the two rotating screws. Since the basic phenomena are not very well understood, an experimental system consisting of rotating cylinders was developed and the characteristics of the flow and the basic features of the mixing process in the intermeshing, or mixing, region were investigated [Sastrohartono et al., 1990]. Experimentally and

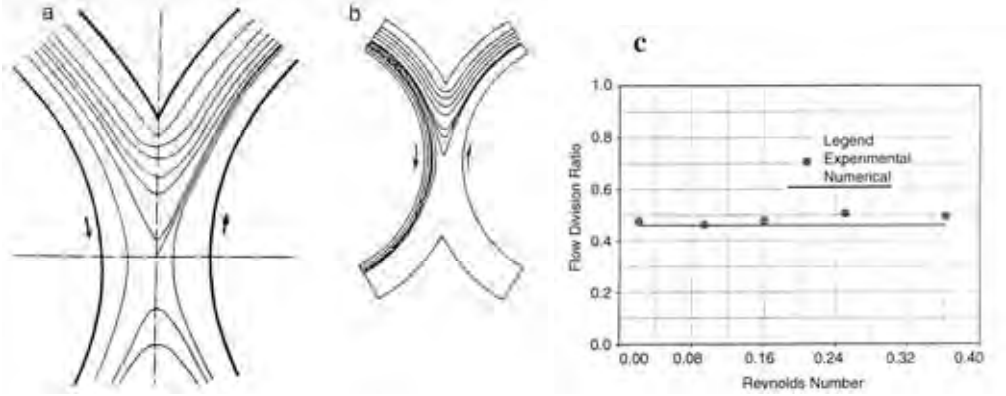

FIGURE 6. Streamlines in the region between two rotating cylinders for CMC solution at 16 rpm. (a) Experimental results; (b) Numerical predictions for flow entering the region over one cylinder; (c) Comparison of flow division ratio x_f obtained from experimental and numerical results

numerically obtained streamlines in the region between two rotating cylinders, approximating a twin-screw, are shown, indicating good agreement. Some of the fluid flowing adjacent to the left cylinder continues to flow along its surface, while the remaining fluid flows over to the other cylinder. A flow division ratio x_f, defined as the fraction of the mass flow that crosses over from one channel to the other, is taken as a measure of mixing and is determined by using the dividing streamline that separates the two fluid streams. A comparison between experimental and numerical results is shown, indicating good agreement at the typically small Reynolds numbers encountered in extruders. A small difference, between numerical and experimental results, arises as Reynolds numbers increase beyond 1.0, because of significant inertia effects, which were neglected in the mathematical model. For more detailed comparisons, velocity and temperature distributions have been obtained using more elaborate experimental systems and compared with the numerical results [Jaluria, 2003].

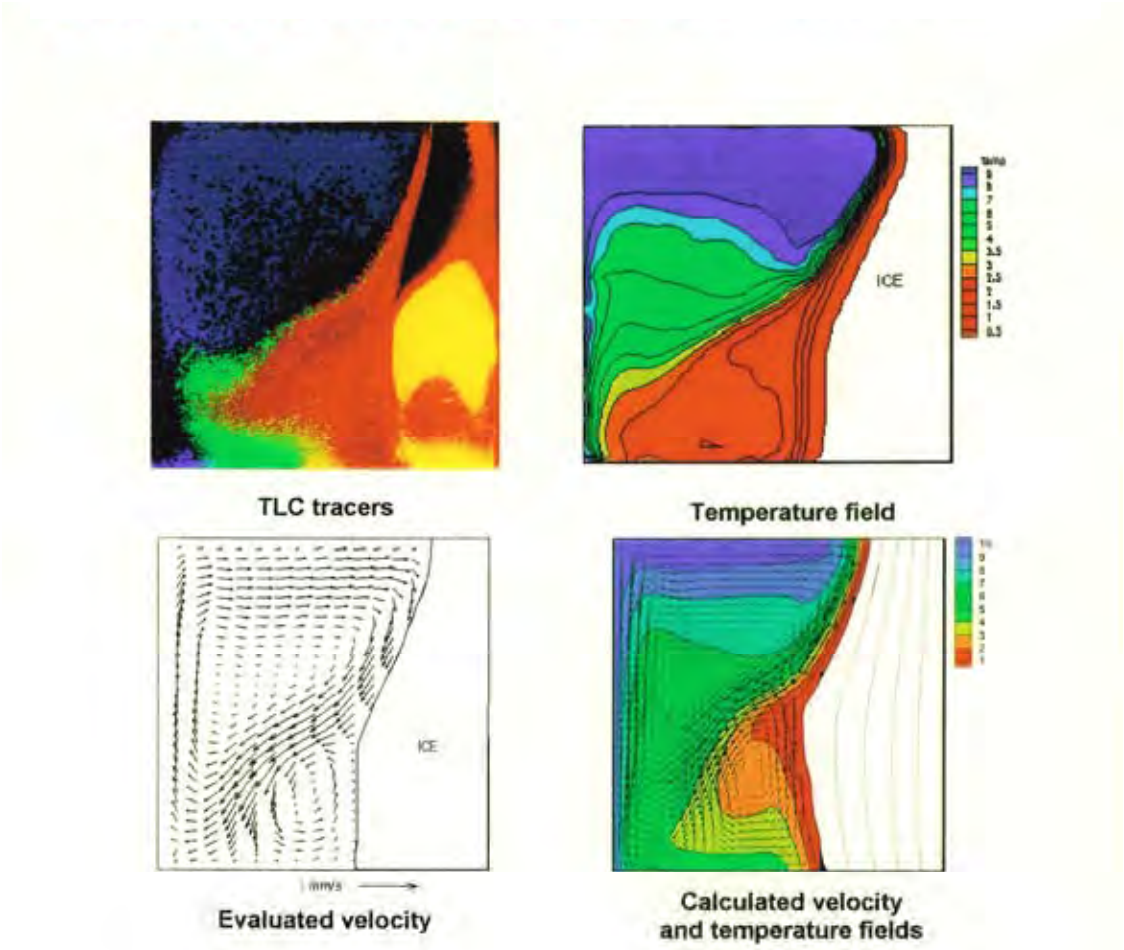

FIGURE 7. Experimental and numerical results for water solidification driven by convection and conduction, with conjugate transport in the mold

Figure 7 shows the numerical and experimental results for solidification of water in an enclosed region using the enthalpy-porosity model. The coupled conduction, or conjugate transport, in the walls of the mold is an important consideration in these problems. The effect of the imposed conditions at the outer surface of the mold on the solidification process can be obtained by solving this conjugate problem, which yields the temperature distribution in the mold as well as that in the solid and the liquid. Banaszek et al. [1999] carried out numerical simulations and appropriately designed experiments to demonstrate the importance of conduction in the wall, as shown in Fig. 7. Velocity and temperature fields are shown, along with the ice-water interface. The streamlines

indicate the effect of thermal buoyancy which causes the interface between the solid and the liquid to bend, rather than remain parallel to the vertical boundaries. The amount of material solified increases with time. The recirculation in the liquid is clearly seen. The numerical results are found to agree quite well with experimental results. Such numerical and experimental studies can be used to determine the movement of the solidification front with time and thus monitor the generation of voids and other defects in the casting. Experimental studies have been relatively few because of the complexity of the process [Viskanta, 1988]. Detailed accurate experimental results are needed to critically evaluate the various models employed for simulation, as well as to provide information on the characteristics of the interface for the development of microscale models.

5. EXPERIMENTALLY OBTAINED BOUNDARY CONDITIONS

In basic and practical problems that involve convective heat transfer, it is important to model the boundary conditions correctly and accurately since the accuracy and validity of the simulation are strongly affected by the transport mechanisms at the boundaries. However, the shape and location of the boundary itself are not known in some cases, such as the neck-down profile in optical fiber drawing, mentioned earlier. This is an unknown free-surface resulting from the various forces acting on the fiber, as is also the case for other free-surface flows, such as those with a meniscus. Even if the boundary is well known, the conditions at the surface may involve a coupled, much more complex problem. In such cases, the boundary conditions are obtained from a separate experiment in order to simplify the problem, or to provide inputs that are not readily available from analysis.

An example of a situation where experimentally obtained boundary conditions are frequently used to solve the problem is shown in Fig. 8. The conduction problem within the rectangular two-dimensional region can easily be solved by numerical simulation if the boundary conditions are given as convective with specified ambient temperature T_f and heat transfer coefficient h, as shown in Fig. 8(a). Here, h is obtained from available empirical correlations based on separate experiments on similar geometries. Such correlations are widely available and used for a fairly diverse set of problems of interest to the industry. If the heat transfer coefficient h is not given, the problem involves combined domains and a conjugate problem, as shown in Fig. 8(b), which is substantially more complicated (Jaluria and Torrance, 2003]. The temperature gradient at the surface in Fig. 8(b) can be used to yield the heat transfer coefficient h, if needed.

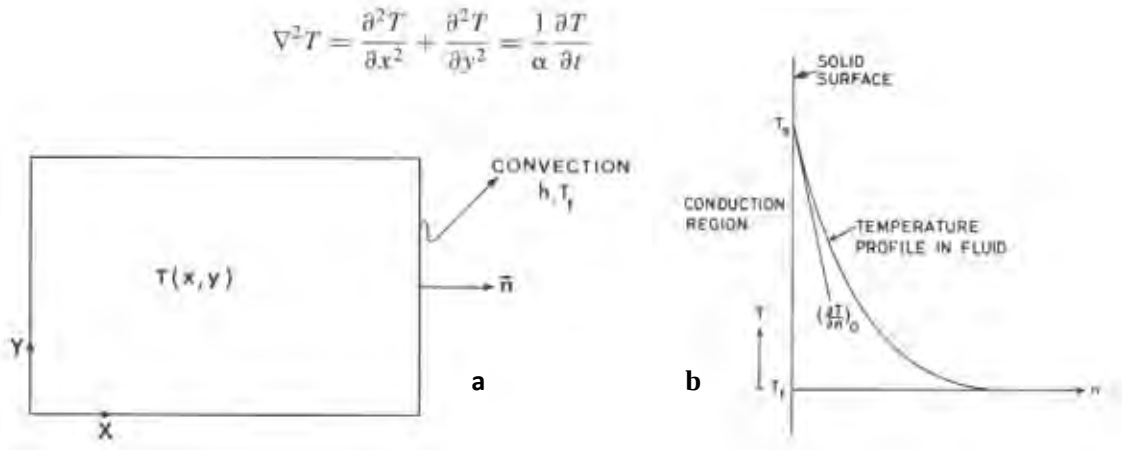

FIGURE 8. (a) Conduction problem with specified convective heat transfer coefficient h at the boundaries; (b) Conjugate conduction-convection problem

The nature and stability of the upper meniscus in the fiber coating process, shown in Fig. 2, have been studied in detail because the moving fiber can entrap air bubbles, resulting in a deterioration of the coating. This process is strongly affected by the stability and consequent breakdown of the meniscus. The problem is very complicated because it involves a dynamic contact angle, with the

fiber moving at speeds as high as 20 m/s through the air and then plunging into the liquid, with air being replaced by the liquid in the boundary layer. It is a difficult problem to model analytically or numerically. However, the shape and dimensions of the meniscus are needed to solve for the flow and convective heat transfer in the coating applicator.

Thus, this is a circumstance where experimentally obtained boundary conditions are needed for the numerical simulation to be carried out. Frequently, the shape of the meniscus is prescribed on the basis of experimental data and axisymmetric transport is assumed. The typical height of the meniscus varies from around 10 m to 100 m. The dynamic meniscus in pressurized and unpressurized fiber coating applicators has been studied experimentally by several investigators (Blyler and DiMarcello, 1980, Quere, 1999). Figure 9(a) shows the typical experimental results obtained by Abraham and Polymeropoulos (1999) and Ravinutala and Polymeropoulos (2002), in terms of images of the meniscus formed with the fiber moving into a pressurized applicator. They found that the effect of the imposed pressure is to flatten the meniscus and to increase the slope of the liquid-air interface near the fiber compared to that for an unpressurized meniscus. They also studied unpressurized applicators and obtained the meniscus for a wide range of fiber speeds and fluids.

Typical numerical results obtained with a meniscus specified on the basis of these experiments are shown in Fig. 9 (b) from Yoo and Jaluria (2007). The computed velocity field in the applicator is shown, along with the flow near the meniscus. Even though the flow near the meniscus was found to change substantially with a change in the meniscus shape and dimensions, the flow far away was found to remain largely unaffected. A nanosecond double pulse laser source was also used to map and probe the flow field in the applicator, particularly in the vicinity of the moving 125 m fiber, using particle image velocimetry. Good comparisons between the experimental and numerical results were ontained, lending strong support to the model.

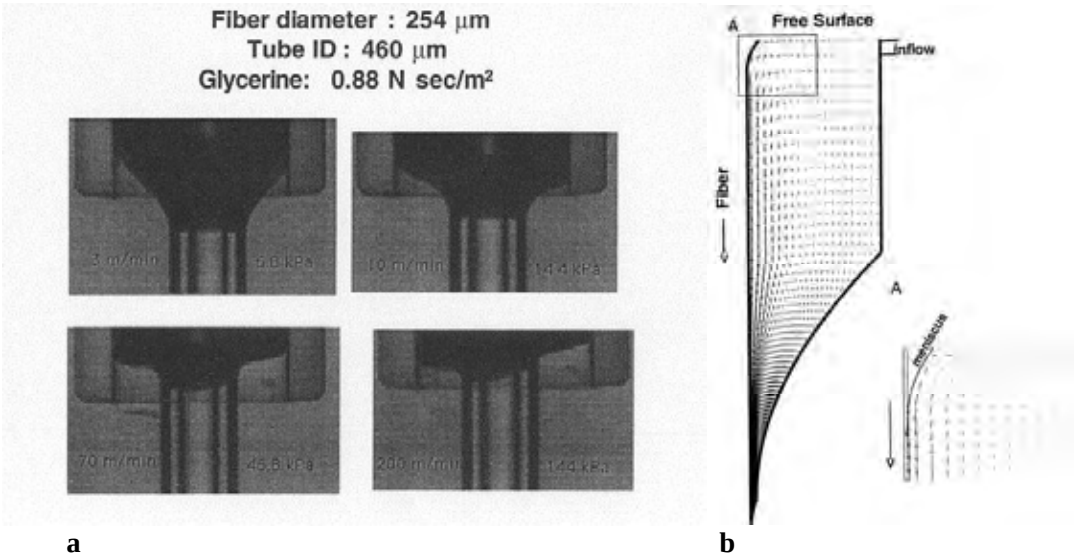

FIGURE 9. (a) Upper meniscus in optical fiber coating at different imposed pressures in the applicator; (b) Numerical results with a specified upper meniscus

Similarly, for optical fiber drawing in a furnace, several investigators assumed the neck-down profile on the basis of experimental data. This substantially simplified the analysis and, if experimental data are available for given ranges of the operating conditions, a specified neck-down

profile can be used to reduce the complexity of the problem and make it amenable to simulation with modest resources and effort [Roy Choudhury and Jaluria, 1998].

As another example of a practical problem where the boundary conditions are not known and experimental data are employed to define the conditions, consider the flow in a channel with isolated, protruding, heat sources, as shown in Fig. 10(a). The appropriate thermal boundary conditions at the walls are not known. Conjugate conditions exist at the boundary between the cooling fluid and the walls. Boundary conditions are also needed at the openings through which the fluid enters or leaves the system. The geometry can be complicated due to the positioning of the sources and the flow configuration. The governing mass, momentum and energy conservation equations for a two-dimensional laminar natural convection flow, with constant thermophysical properties and with Boussinesq approximations, can be written in the following dimensionless form as:

$$\frac{\partial U}{\partial X}+\frac{\partial V}{\partial Y}=0 \tag{7}$$

$$\frac{\partial U}{\partial}+\frac{\partial (U^2)}{\partial X}+\frac{\partial (UV)}{\partial Y}=-\frac{\partial P}{\partial X}+Pr\left(\frac{\partial^2 U}{\partial X^2}+\frac{\partial^2 V}{\partial Y^2}\right) \tag{8}$$

$$\frac{\partial V}{\partial}+\frac{\partial (UV)}{\partial X}+\frac{\partial (V^2)}{\partial Y}=-\frac{\partial P}{\partial Y}+Pr\left(\frac{\partial^2 U}{\partial X^2}+\frac{\partial^2 V}{\partial Y^2}\right)+GrPr\Theta \tag{9}$$

$$\frac{\partial \Theta}{\partial}+\frac{\partial (U\Theta)}{\partial X}+\frac{\partial (V\Theta)}{\partial Y}=\frac{\partial^2 \Theta}{\partial X}+\frac{\partial^2 U}{\partial Y^2} \tag{10}$$

where the dimensionless variables are defined as:

$$X=\frac{x}{h};\qquad Y=\frac{y}{h};\qquad U=u\frac{h}{};\qquad V=v\frac{h}{};$$

$$=t\frac{}{h^2};\qquad \Theta=\frac{T-T_0}{T_s-T_0};\qquad P=(p-p_0)\frac{h^2}{P^{\ 2}}; \tag{11}$$

$$Gr=\frac{g\ \ .h^3(T_s-T_0)}{^2};\qquad Pr=\ \text{—}\ ;\qquad =-\frac{1}{P}\left(\frac{P-P_0}{T-T_0}\right) \tag{12}$$

Figure 10(b) shows a comparison between the computed temperature distributions for the two-dimensional natural convection flow due to two sources located in the channel. The experimental study used the Filtered Rayleigh Scattering (FRS) technique to obtain the temperature profiles above the thermal sources, as shown in Fig. 10(a). However, the experimental study employed a channel open on all sides and the walls were unheated. The separation between the walls was much less than the width and length of the channel. The challenge was to simulate this experiment to obtain similar trends in the predictions (Icoz and Jaluria, 2005a) . The numerical results are compared with the FRS measurements in Fig. 10(b) for the region above the two sources, indicating good agreement. It is found that adiabatic conditions approximate the experiment much better than isothermal conditions. However, the actual boundary conditions involve conjugate transport. Developed flow conditions were assumed at the openings and this seemed to be a satisfactory approximation. Thus, even such a simplified model is able to capture the complexity of the experiment, which can, in turn, be used to obtain the appropriate boundary conditions.

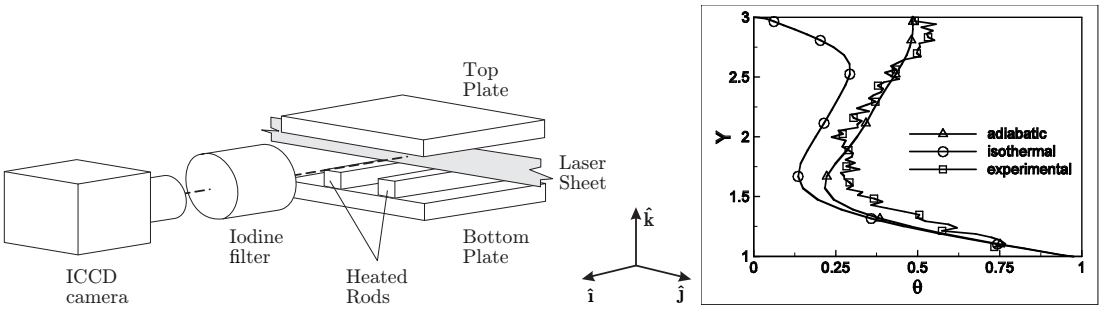

a **b**

FIGURE 10. (a) Experimental system for isolated protruding heat sources in a channel with openings; (b) Comparisons between numerical predictions and experiments for different boundary conditions

6. SOLUTION OF INVERSE PROBLEMS WITH EXPERIMENTAL INPUTS

There are circumstances where experiment data can be obtained over only a limited region because of access, time or other limitations. Strong constraints are thus placed on the experimental data that can be obtained through techniques such as laser and infrared diagnostics. Examples of such systems are combustors, furnaces, and reactors, where only a limited access to the convective domain is available. In such cases, numerical modeling and experimentation may be used together to solve an inverse problem in order to define and quantify the boundary conditions and then proceed to the numerical simulation of the complete problem. Thus, detailed quantitative information on the flow, temperature and other quantities, which is needed in order to optimize the system as well as to control the process, is obtained through the numerical solution of an inverse problem with selective experimental inputs.

An important example of such limited access is the optical fiber drawing furnace, shown in Fig. 11. This high-temperature furnace typically has an infrared sensor to monitor the temperature of the heating element at only one location and to use its output for control [Issa et al., 1996, Paek, 1999]. The boundary conditions, particularly the thermal conditions, are not very well known. The temperature distribution at the wall is the result of the heat transfer mechanisms, particularly radiation, operating in the furnace and is not a known input to the numerical model. The temperature distribution affects the material properties, as well as the transport processes. It is thus a critical variable in the calculation of the glass flow, which then yields the characteristics of the fiber. The energy input to the heating element is known, along with the geometry and material characteristics. But the resulting wall temperature distribution is not easily obtained and is thus largely an unknown parameter. In such cases, the limited data that can be obtained by experiment is used in conjunction with numerical modeling to solve an inverse problem to determine the wall temperature distribution.

Issa et al. (1996) obtained temperature measurements at the centerline of a rod placed at the axis of the furnace. An experimental procedure involving mounting rods of different materials and diameters axially within the furnace cavity was employed for this purpose. Each rod was instrumented with thermocouples inserted through an axial hole along the centerline. The temperature measurements were used along with a numerical model for the flow and heat transfer in the furnace in order to obtain the furnace wall temperature profile. This is an inverse problem since the centerline temperature in the rod is known whereas the furnace thermal conditions are not known. Then, they solved this inverse problem numerically to determine the wall temperature distribution that yielded the temperature measurements obtained in the graphite rod. An optimization technique was used to ensure

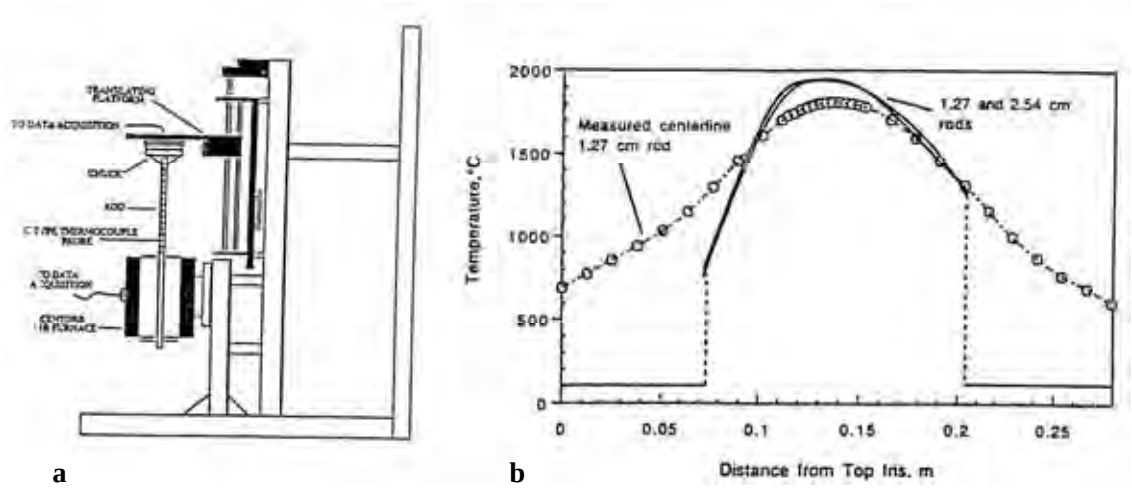

FIGURE 11. (a) Experimental system to measure the centreline temperature of graphite rods placed at the axis of the fiber draw furnace; (b) Measured and calculated centreline temperatures in the graphite rods, along with the predicted furnace wall temperature distribution

that the result of the inverse calculation was essentially unique. The results obtained using graphite rods suggest that the furnace temperature is not significantly affected by rod size, over the desired range of 0.5 – 2.0 cm. A study of the flow and thermal transport associated with the draw furnace require accurate knowledge of the furnace wall temperature distribution. Figure 11(b) shows the computed temperature distribution along the graphite heating element. The dashed lines represent the water cooled portion of the furnace wall. The convergence of the optimization method used for deriving the heating element temperature distribution is demonstrated by the agreement between the predicted and measured rod temperatures. The computed maximum element temperatures were in good agreement with the furnace sensor temperature at the hot zone centerline, lending support to the model for the transport processes in the furnace. Similar results were obtained for the other furnace temperatures and for other materials, including silica glass.

This approach was used for another practical system, the single-screw polymer extruder, shown in Fig. 12. The system consists of a rotating screw and a heated/cooled barrel, as described earlier. The temperature at the inner surfact of the barrel is critical in the computation of the flow, heat transfer, pressure and material changes in the extruder. However, the system involves a complicated, multi-region, conjugate problem, without well-known conditions at the outer surface. Access to the barrel wall is limited in practical systems because of the expense and complex geometry. Therefore, the approach outlined above may be used effectively. Limited experimental temperature data at the barrel wall and at the exit of the extruder may be used along with numerical simulation of the flow in the extruder to solve an inverse problem to determine the barrel tempeature distribution accurately and uniquely. This temperature distribution is then taken as an input to the computational model to calculte the conditions within the extruder, as shown in Fig. 12(b) in terms of the calculated isotherms. Substantial work has been done on this problem as well [Jaluria, 1996] and only a brief description is given here.

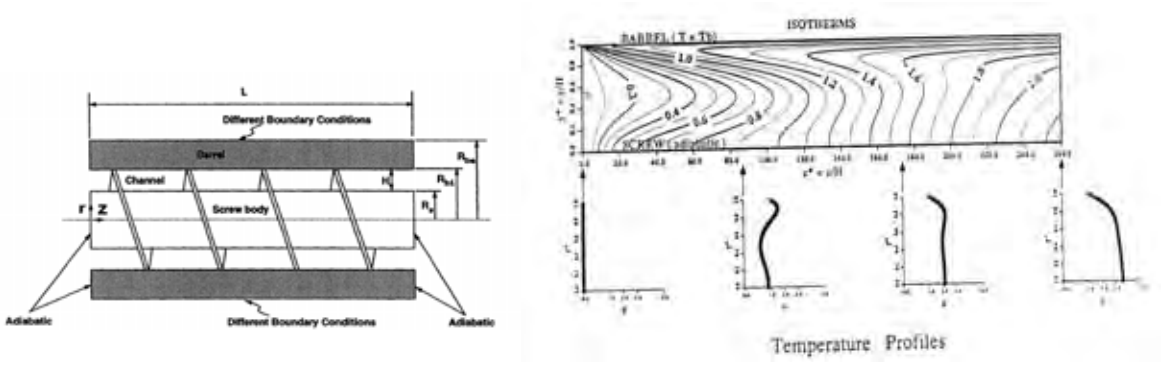

FIGURE 12. (a) Single-screw extruder system, showing conjugate transport in the barrel; (b) Calculated temperature field in the extruder channel

The preceding consideration can be further employed to develop Dynamic Data Driven Applications Systems (DDDAS), which is an innovative approach to engineering research based upon the synergistic interaction between experiment and simulation. There are two different implementations of DDDAS: Open Loop and Closed Loop. In Open Loop, experimental data is streamed into the simulation (or vice-versa) to achieve greater accuracy, detail and/or robustness. An example is real time streaming of meteorological measurements into weather simulations. In Closed Loop, experiment and simulation interact in an iterative manner, i.e., the experiment guides the simulation and the simulation in turn guides the experiment (Darema, 2004; Mandel et al., 2004). The DDDAS approach has been widely applied in engineering and science. Knight et al. (2002) and Zhao et al. (2007) applied the DDDAS concept to engineering design with the development of the Data Driven Design Optimization Methodology (DDDOM). This approach synergizes experiment and simulation in a manner, which exploits the advantages, and recognizes the limitations, of each approach, as discussed in the next section. This effort focuses on the assessment of fluid-thermal systems that are characterized by two major limitations, namely, (1) the experimental measurements are limited to diagnostics in restricted regions of the flow, as seen above, and (2) there is incomplete ***a priori*** specification of the boundary conditions for the flow simulation, as also discussed earlier. The approach is founded on the Closed Loop DDDAS concept wherein the experiment directs the simulation and vice-versa. The method approximates the unknown boundary conditions for the simulations by minimizing the error in the prediction of the measured data and identifies needed subsequent experimental measurements to reduce the error. The result is a complete assessment of the fluid-thermal system. Neither the experiments alone, nor any simulation based on the ***a priori*** boundary conditions, can provide a complete assessment of the fluid-thermal system. However, the synergism of experiment and simulation based upon the DDDAS concept yields a complete assessment of the fluid-thermal system (Knight et al., 2006, Ma et al., 2006).

To further discuss this methodology, let us consider a jet in cross-flow, as shown in Fig. 13(a). This flow is important in the evaluation of environmental effects of thermal and material discharges into the environment. If limited data taken downstream can be used to determine the location and conditions at the inlet, it would allow the determination of polluting source as well as the impact on the environment. In many cases, information on the source is not known, though information downstream can be obtained. This circumstance can be simplified in terms of a rectangular jet injected perpendicular to an incompressible air flow, as shown in Fig. 13(b). The inflow is an equilibrium laminar boundary layer in air defined by the specified free stream conditions, velocity U_∞ and temperature T_∞. The jet is defined by the jet average velocity U_j and temperature T_j. The computational domain is shown. For the simulations, the free stream conditions are assumed to be known. By analogy to the optical fiber drawing furnace, the jet average velocity U_j and temperature T_j are assumed unknown. The objective is then the determination of the jet average velocity U_j and temperature T_j based upon a Closed Loop DDDAS methodology.

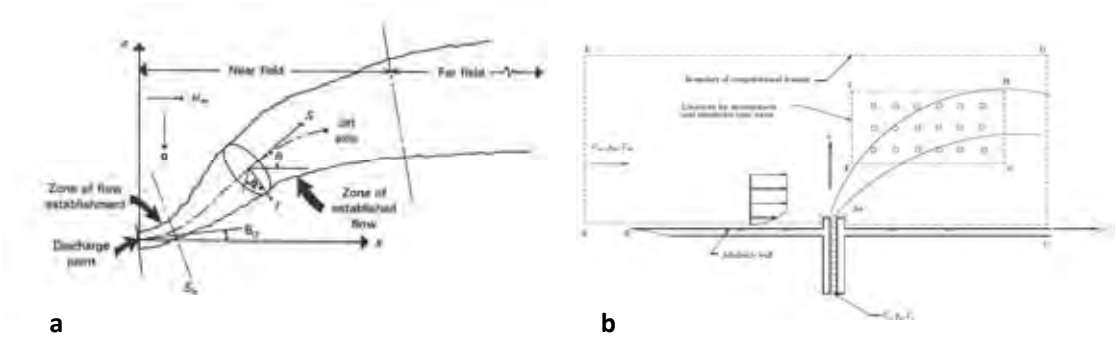

FIGURE 13. (a) Buoyant jet due to thermal or material discharge in a crossflow; (b) Arrangement to predict discharge conditions from downstream measurements

The experiments were performed in a low speed wind tunnel, with a test section of 0.7 m x 0.7 m in cross-section and a length of 2 m. The maximum velocity in the test section is 30 m/sec and is measured using a traversing pitot tube and wall pressure taps. The wind tunnel velocity is controlled using LabView. A two-dimensional slot jet protrudes from a flat plate with the jet centerline at a distance of 188 mm from the leading edge of the plate. The flat plate has a sharp leading edge and is raised 50 mm above the wind tunnel floor to avoid the tunnel floor boundary layer. The jet slot width is 3.2 mm and the spanwise depth is 545 mm. The jet fences protrude 8.8 mm above the flat plate and each fence is 6.4 mm wide in the *x*-direction. A diode laser system is used to measure the time-varying absorbance across the flow field in the spanwise direction at selected locations. A 761nm Vertical Cavity Surface Emitting Laser (VCSEL) is placed in a temperature controlled housing (ILX Lightwave 4412). The output wavelength is modulated by the injection current (ILX Lightwave Diode Laser Controller, LDC-3714B). Since the flow field is unsteady (as shown by the CFD simulations) at a fundamental frequency of approximately 20 Hz with higher order harmonics, the diode laser system was scanned at 400Hz. The experimental temperature was measured using both the laser absorbance method and by a thermocouple. Additional details are presented by Ma et al. (2006).

A validation study was performed to assess the accuracy of the simulations by comparison with experiment. The difference between the computed and measured mean temperature was found to vary from 0.2% to 10.5%. The variation between the laser and thermocouple measurements ranges from 2.4% to 10.8%. It is noted, however, that the thermocouple measures the temperature at a single point, whereas the laser absorbance is an integrated instantaneous measurement of the temperature over the span of the wind tunnel. Small instantaneous variations of the flow field in the spanwise direction will therefore cause a difference between the laser absorbance and thermocouple measurements. Moreover, the simulations are time-accurate two-dimensional, and therefore do not take into account possible small three-dimensional effects. We may conservatively conclude that the simulation is capable of prediction of the experimental mean temperature within 10 K.

The Closed Loop DDDAS methodology was applied to determine the unknown jet velocity U_j and jet temperature difference $\Delta T_j = T_j - T_\infty$, as shown in Fig. 14. First, six locations were selected and the predictions from the simulations were used to build the Response Surface Model. Next, the experiment was performed with the jet velocity U_j and temperature T_j selected by the experimentalists but not communicated to the person performing the Closed Loop DDDAS Method. The experimental mean temperature at the six selected locations was provided to the Response Surface Model. The predictions of U_j and ΔT_j based upon the Response Surface Model were found to be 7 ± 1 m/s and 117 ± 3 K. The uncertainty of ± 1 m/s in the predicted value of U_j is attributable to the uncertainty in the experimental U_∞ (i.e., $U_\infty = 4.0 \pm 0.5$ m/s). The uncertainty in the predicted value of ΔT_j is the standard deviation of the best fit to the Response Surface Model over the range of possible number of locations used to minimize the mean square error E. In Step No. 2, the Response Surface Models were used to select four additional locations. The second

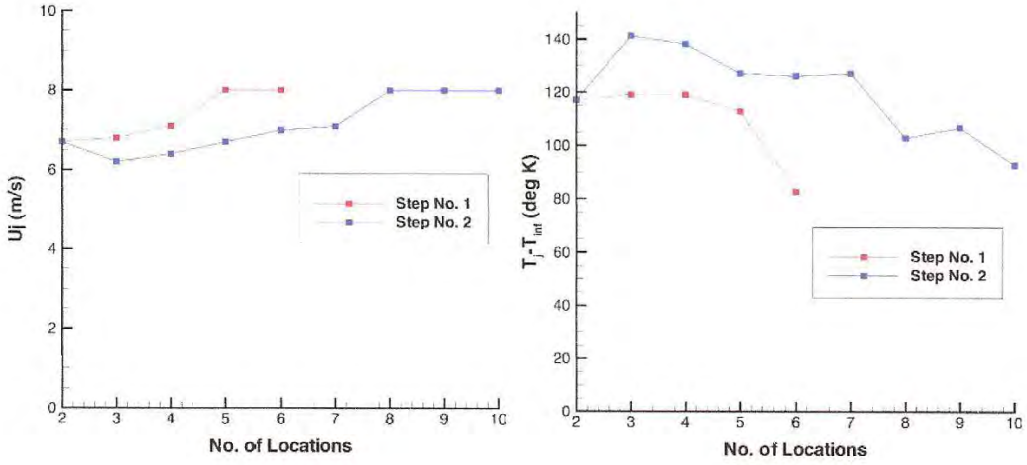

FIGURE 14. Results from applying the Dynamic Data Driven Applications Systems methodology to the flow circumstance of Fig. 13 (b)

experiment was performed and the mean temperature at the four additional locations was provided to the Response Surface Model. The predictions of U_j and ΔT_j based upon the Response Surface Model were 7 ± 1 m/s and 129 ± 9 K. Thereafter, the experimental values of U_j and ΔT_j were announced. The experimental values were U_j = 7.97 m/s and $\Delta T_j = 107 \pm 5$ deg K. Thus, the Closed Loop DDDAS methodology predicted the jet velocity U_j within the experimental uncertainty associated with U_∞ but over predicted ΔT_j by 9% in the first step and by 21% in the second step. The over prediction of 9% in the first step is comparable to the validated accuracy of the two-dimensional simulations compared to the experiment.

Thus, the Dynamic Data Driven Application Systems (DDDAS) method can be employed for assessing fluid-thermal systems wherein the complete boundary conditions are not known ***a priori***. A simple example of the temperature and velocity for a jet in cross flow is given here, but the approach can be extended to more complicated problems. Current effort is being directed at such problems, for example, the determination of the location and energy input of a fire in an extensive or enclosed region. Bu measuring temperatures at the door or at a wall, the methodology can be used to predict the location and conditions of the source, thus impacting on fire safety, prediction and control.

7. CONCURRENT SIMULATION AND EXPERIMENTATION

In the solution of practical convection problems, it is often found that numerical simulation is particularly suitable over a certain domain, whereas experimentation is more appropriate and accurate over other domains. Then, the two could be used ***concurrently*** to obtain a more efficient approach to solving the problem. This is particularly valuable in system design and optimization.

Conventional engineering design and optimization are based on sequential use of computer simulation and experiment, with the experiments generally being used for validation or for providing selective inputs, as discussed earlier. However, the conventional methods fail to use the advantages of using experiment and simulation concurrently in real time. Numerical simulation can easily accommodate changes in geometry, dimensions and material, whereas experiments can more conveniently study variations in the operating conditions such as flow rate, imposed pressure and heat input. Also, laminar and stable flows can be simulated conveniently and accurately, whereas transitional and turbulent flows are often more accurately investigated experimentally. By using concurrent numerical simulation and experimentation, the entire domain of interest can be studied for system design and optimization efficiently and accurately. This is the main motivation for this approach.

Consider the simple physical system shown in Figure 15, consisting of multiple isolated heat sources, which approximate electronic components, located in a horizontal channel in a two-dimensional configuration (Incropera, 1988, Sathe and Sammakia, 1998). A square vortex promoter of side h_p is also shown in the figure to induce oscillatory flow and thus enhance heat transfer. The height and width of the sources are h and w, respectively. The heat sources are separated by distance d. The thickness of the bottom plate is B. The problem involves removing the energy dissipated by these components by the flow of air or a liquid. The flow conditions are defined by Re and Gr, both being based on the channel height. The fluid is represented by its properties, particularly the Prandtl number Pr. Variables include the inlet fluid velocity, heat input to the components, channel dimensions, coolant, location and orientation of the heat sources. Typical design objectives are maximizing the heat removal rate from the components and minimizing the pressure drop. The temperature and pressure drop have to be kept below some allowable limits, T_{wo}, ΔP_o. Numerical and experimental methods are to be used concurrently to study a wide range of design variables and operating conditions. The overall inputs required for the design and optimization of

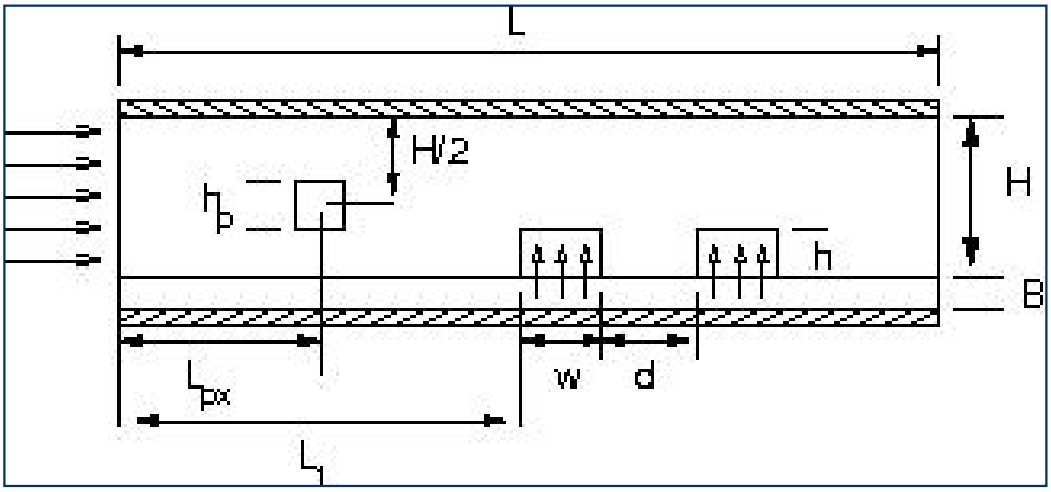

FIGURE 15. Two heating elements, simulating electronic components, in a channel with a uniform forced flow at the inlet and a vortex promoter

the system are obtained using numerical simulation for low flow rates and heat inputs and experimental systems for larger values. The switch from simulation to experiment is determined based on the critical values of Re and Gr values for transition to turbulence (Icoz and Jaluria, 2005b). Two experimental setups have been used in this study, one for air and the other for liquid cooling. The experiments for air are performed for Re = 1000 – 5200. A similar arrangement is used for water. The liquid cooling experiments are performed to study the free and mixed convective heat transfer characteristics of two flush mounted discrete heat sources. The Reynolds number based on the channel height is varied in the range from 2800 to 5800.

Numerical simulation can be used very satisfactorily for low Re and Gr. The governing non-dimensional differential equations for laminar mixed convection flow, with constant thermophysical properties can be written in the following form:

$$\nabla.\vec{V} = 0 \tag{13}$$

$$\frac{\partial \vec{V}}{\partial} + \vec{V}.\nabla\vec{V} = -\nabla P + \frac{1}{\mathrm{Re}}\nabla^2\vec{V} - \frac{Gr}{\mathrm{Re}^2}\Theta\vec{g} \tag{14}$$

$$\frac{\partial \epsilon}{\partial} + \vec{V}.\nabla\Theta = \frac{1}{\mathrm{Re}\,\mathrm{Pr}}\nabla^2\Theta \tag{15}$$

Conduction equation within the bottom plate (substrate):

$$\frac{\partial \epsilon}{\partial} = \frac{1}{\mathrm{Re}\,\mathrm{Pr}}\nabla^2\Theta \tag{16}$$

where the dimensionless variables are defined as:

$$X = \frac{x}{H}; \qquad Y = \frac{y}{H}; \qquad U = \frac{u}{U_m}; \quad V = \frac{v}{U_m}; \tag{17}$$

$$= t\frac{U_m}{H}; \qquad \Theta = \frac{T - T_0}{T_s - T_0}; \qquad P = \frac{p - p_0}{\rho U_m{}^2}; \tag{18}$$

$$Gr = \frac{g\ .h^3(T_s - T_0)}{2}; \ Pr = —; \quad = -\frac{1}{\rho}\left(\frac{P - P_0}{T - T_0}\right) \tag{19}$$

The boundary conditions implemented here involve fully developed axial and zero vertical velocity at the inlet at ambient temperature, fully developed flow conditions at the exit, no-slip conditions and adiabatic surface assumption at top and bottom walls.

To validate the code the computed results are compared to the results obtained by Kim et al. (1992, 1998) for forced convection in a channel problem with Re = 750. The local Nusselt number along the first heat source surface was plotted and two results showed very good agreement, validating the present results (Icoz et al., 2006).

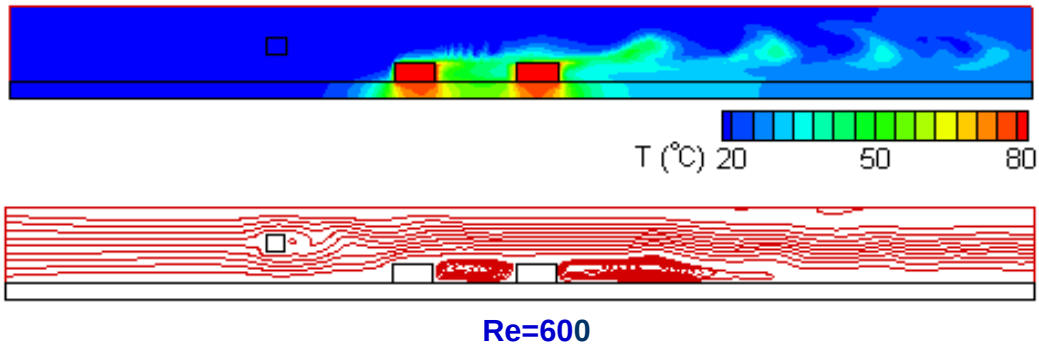

FIGURE 16. Flow and thermal fields due to a vortex promoter and isolated thermal sources in a channel with forced flow

The temperature and velocity distributions, the heat removal rates and pressure drop are then calculated for laminar flows, as well as the beginning of oscillatory flow. Experiments are used for translational and turbulent flows. The first part of the simulation results deals with the determination of the critical flow conditions up to which numerical simulation can be used satisfactorily. The Gr value, which is set at 7.2×10^5, is constant for all computations because the heat sources are treated as isothermal elements, at a temperature of 60°C above ambient, and the channel height, which is kept constant throughout the study, is chosen as the characteristic length for nondimensional parameters, such as Re and Gr. The critical Re value is determined by observing the transient change in Nu values as a function of time for different Re values. The

transient results reveal that the onset of unsteady flow starts at around Re = 1500. Similarly, other geometries and conditions were investigated.

The basic approach outlined here was used for liquid cooling and also for enhanced heat transfer with the use of a vortex promoter in the channel (Icoz and Jaluria, 2006). Typical results are shown in Fig. 16. The increase in the heat transfer due to the presence of a passive vortex promoter in the channel flow was determined and concurrent simulation and experimentation was used to obtain the heat transfer and pressure results, as shown in Fig. 17. This figure shows the heat transfer rates Q_1 and Q_2 for the two sources (Q_1 being for the source closer to the inlet) obtained from numerical simulation at low Re and from experiment at large Re. There is fairly good agreement between the two in the overlapping region, though there is uncertainty in the experimental data, as indicated here. These results were used to generate the response curves, from which optimal conditions were obtained. The shape of the promoter was also taken as a parameter, along with the channel height and source geometry. The operating conditions were also varied. Other optimization strategies were also used, but the input data needed for all these were obtained by concurrent simulation and experimentation. For additional results and further details, see Knight et al. (2002), Icoz and Jaluria (2006) and Zhao et al. (2007).

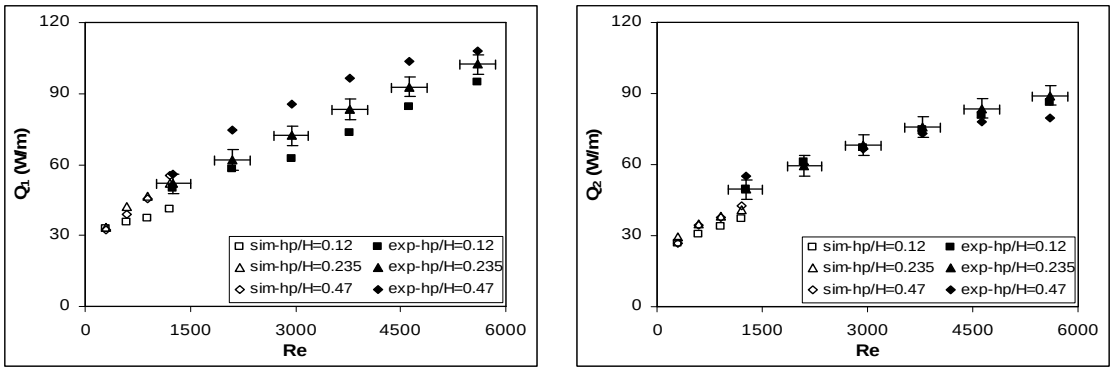

FIGURE 17. Computed and measured (shown with uncertainty) heat transfer rates as functions of Re from (a) first heat source, and (b) second heat source, for flow in a channel with a vortex

Similar results were obtained for the sources in the channel without the promoter, as shown in Fig. 18, which included results on Q_1 and on Δp. There is greater uncertainty in the experimental data for the pressure, as compared to that for the heat transfer rate. But there is reasonable agreement between the experimental and numerical results. Also, the two approaches are used concurrently to cover the entire domain. Similarly, parameters like geometry, dimensions and materials were varied in the search for the optimal design. Again, response surfaces were obtained and optimal conditions were determined. Figure 19 shows the variation of a composite objective function, which includes both the source temperature and the pressure drop, so that the minimum in the objective function is sought for the optimum.

This is really a multi-objective function problem and has to be handled by considering the two objective functions separately. But this simple approach of combining the objectives into a single function similifies the problem. The weighted sums method, [Deb 2002], may also be employed in the form of:

$$F = \sum W_i F_i(x_1, x_2, x_3) \tag{20}$$

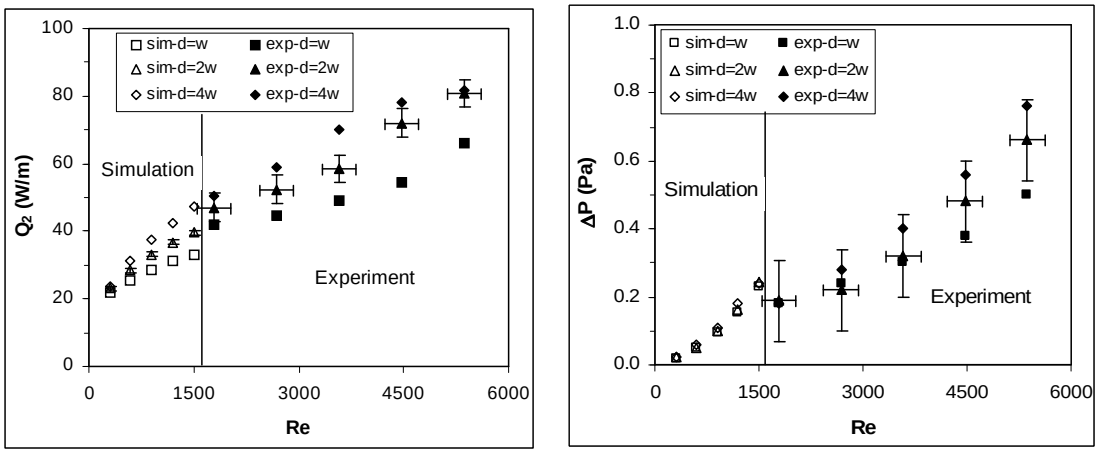

FIGURE 18. Computed and measured heat transfer rate from the first heat source and pressure drop as functions of Re and geometry, for flow in a channel without a vortex promoter

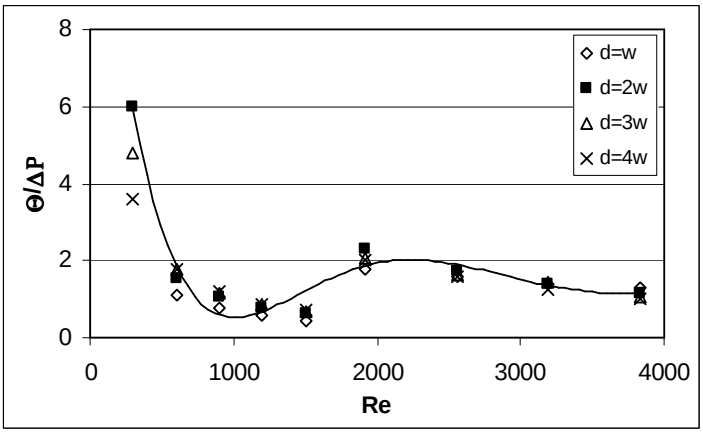

FIGURE 19. Optimization of the system with two isolated heat sources in a channel with forced flow, using a composite objective function

where W_i ($\in[0,1]$) is the weight of the i-th objective function, and $\sum W_i = 1$. The global optimal points and the value of the objective function for various weights were obtained. It was found that as the weight of the pressure drop is decreased to $W_1/2$ the optimal point is at the maximum values of the design variables. This is because the maximum heat transfer rates are obtained at the same point, and making ΔP less important by setting its weight a smaller value shifts the optimal point to the maximum values of the design variables. However, as the importance of ΔP increases, the optimal values of the design variables get smaller. When W_3 is set $2\times W_1$ and $3\times W_1$ the optimal value of Re drops to 2855 and 1450, respectively. The optimal heat source height is found to be either h/H=0.35 or 0.15 depending on the relative importance of the individual objective functions. If maximizing the heat transfer rates is the primary design objective, the optimal h/H is found to be 0.35. If minimizing the pressure drop is more important than the heat transfer rate, h/H is found to be 0.15. The optimal values of Re and d for a given of h/H, when the performance of individual

heat sources is of interest, were also obtained. The results reveal that the optimal Re value does not change significantly with h/H. For the objective function of maximizing $\overline{Q_1} - \Delta\overline{P}$, Re falls in the range of 3000 to 3400, and for the objective function of $\overline{Q_2} - \Delta\overline{P}$, it varies between 1900 and 2200. Similar results arise for liquid cooling. A comparison of cooling capabilities of natural convection of air and de-ionized water was performed. Results show that the heat transfer coefficient for water is around 19 times greater than that for air. The maximum heat transfer coefficient attained when d = 3.5w is found to be 18W/m^2.K for air and 350W/m^2.K for water.

Therefore, it is shown that numerical simulation and experimentation can be used concurrently to yield an efficient approach to cover the entire operational domain and thus provide inputs needed for understanding the operation of the system, as well as for design and optimization. Though only a few simple circumstances are discussed here, the approach was used for more complicated circumstances such as the design of extruder systems, particularly dies, supersonic aircraft inlet and the system for polymer injection treatment of osteoporosis in human orthopedic systems.

8. CONCLUSIONS

Experimentation is needed in a wide range of basic and applied convective heat transfer problems in order to provide the inputs needed for accurately defining the boundary conditions, simplifying the modelling and obtaining results over regions where simulation is inaccurate, inconvenient or inefficient. In addition, experimental data are needed for material properties and for the validation of the models used. The accuracy of the numerical results depends strongly on the material properties. This paper presents various circumstances where the numerical simulation may be efficiently combined with experimentation, and indeed driven by experimental data, to obtain accurate, valid and realistic numerical predictions. Several examples of such problems are given and the difficulties with specifying the boundary conditions as well as with simulating the entire domain for design and optimization are outlined. Approaches for using experimental data driven simulation in such cases are discussed and results are presented for some simple and complex problems. It is shown that such approaches are critical to an accurate numerical simulation in many cases of practical interest. The basic methodology is presented and the present status as well as the needed future work is discussed. The review paper thus focuses on the role played by experimentation in an accurate numerical simulation of thermal processes and systems.

9. ACKNOWLEDGEMENTS

The author acknowledges the support of the National Science Foundation, through several grants, for much of the work reported here. The support from Corning, Inc., for donated fiber coating equipment and optical fiber, is also acknowledged. The author also acknowledges the interactions with Professors D. Knight, T. Rossmann and C. Polymeropoulos, and the work done by several students, as referenced here, that made it possible to present this review.

10. REFERENCES

[1] A. Abraham and C.E. Polymeropoulos, Dynamic menisci on moving fibers, *Proc. 48th Int. Wire Cable Sym.*, Atlantic City, NJ, 1999.

[2] J. Banaszek, Y. Jaluria, T.A. Kowalewski, and M. Rebow, Semi-implicit FEM analysis of natural convection in freezing water, *Numerical Heat Transfer*, 36, 449-472, 1999.

[3] L.L. Blyler and F.V. DiMarcello, Fiber drawing, coating and jacketing, *Proc. IEEE,* 68, 1194-1198, 1980.

[4] F. Darema, Dynamic data driven application systems: A new paradigm for application simulations and measurements, in *Fourth International Conference on Computational Science*, Springer-Verlag, Berlin, 662-669, 2004.

[5] K. Deb, *Multi-Objective Optimization Using Evolutionary Algorithms*, John Wiley & Sons, New York NY, 2002.

[6] G. De Vahl Davis and E. Leonardi, Eds., *Advances in Computational Heat Transfer II*, Begell House Pub., New York, NY, 2001.

[7] T. Icoz and Y. Jaluria, Numerical simulation of boundary conditions and the onset of instability in natural convection due to protruding thermal sources in an open rectangular channel, *Numerical Heat Transfer*, 48, pp. 831-847, 2005a.

[8] T. Icoz and Y. Jaluria, Design of cooling systems for electronic equipment using both experimental and numerical inputs, *ASME J. Elec. Packaging*, 126, pp. 465-471, 2005b.

[9] T. Icoz and Y. Jaluria, Design optimization of size and geometry of vortex promoter in a two-dimensional channel, *ASME J. Heat Transfer*, 128, pp. 1081-1092, 2006.

[10] T. Icoz, N. Verma and Y. Jaluria, Design of air and liquid cooling systems for electronic components using concurrent simulation and experiment, *ASME J. Elect. Pkg.*, 128, 466-478, 2006.

[11] F.P. Incropera, Convection heat transfer in electronic equipment cooling, *ASME Journal of Heat Transfer*, 110, pp. 1097–1111, 1988.

[12] J. Issa, Z. Yin, C.E. Polymeropoulos, and Y. Jaluria, Temperature distribution in an optical fiber draw tower furnace, *Journal of Materials Processing and Manufacturing Science*, 4, 221-232, 1996.

[13] Y. Jaluria, Heat and mass transfer in the extrusion of non-newtonian materials, *Adv. Heat Transfer*, 28, 145-230, 1996.

[14] Y. Jaluria, Thermal processing of materials: From basic research to engineering, *ASME J. Heat Transfer*, 125, pp. 957-979, 2003.

[15] Y. Jaluria, *Design and Optimization of Thermal Systems,* Second Edition, CRC Press, Boca Raton, FL, 2008.

[16] Y. Jaluria and K.E. Torrance, *Computational Heat Transfer*, Second Edition, Taylor & Francis Pub. Co., New York, 2003..

[17] M.V. Karwe and Y. Jaluria, Numerical simulation of fluid flow and heat transfer in a single-screw extruder for non-newtonian fluids, *Numerical Heat Transfer*, 17, 167-190, 1990.

[18] S.Y. Kim, H.J. Sung and J.M. Hyun, Mixed convection from multiple-layered boards with cross-streamwise periodic boundary conditions, *Int. Journal of Heat and Mass Transfer*, 35, 2941-2952, 1992.

[19] S.Y. Kim, B.H. Kang and Y. Jaluria, Thermal interaction between isolated heated electronic components in pulsating channel flow, *Numerical Heat Transfer, Part A*, 34, 1-21, 1998.

[20] D. Knight, G. Elliott, Y. Jaluria, N. Langrana, and K. Rasheed, Automated optimal design using concurrent integrated experiment and simulation, *AIAA* Paper No. 2002-5636, 2002.

[21] D. Knight, T. Rossman and Y. Jaluria, Evaluation of fluid-thermal systems by dynamic data driven application systems, *International Conference on Computational Science (ICCS06)*, 2006.

[22] Q. Ma, Y. Luo, T. Rossman, D. Knight, and Y. Jaluria, Measurements for DDDAS: Flow field reconstruction using experimental and numerical data, *AIAA Aerodynamic Measurement Technology and Ground Testing Conference*, 2006.

[23] J. Mandel, M. Chen, L. Franca, C. Johns, A. Pulhalskii, J. Coen, C. Douglas, R. Kremens, A. Vodacek, and W. Zhao, A note on dynamic data driven wildfire modeling, in *Fourth International Conference on Computational Science*, Springer-Verlag, Berlin, 725-731, 2004.

[24] F.K. Moore and Y. Jaluria, Thermal effects of power plants on lakes, *ASME J. Heat Transfer*, 94, 163-168, 1972.

[25] U.C. Paek, Free drawing and polymer coating of silica glass optical fibers, A*SME Journal of Heat transfer*, 121, 774-788, 1999.

[26] S.V. Patankar, *Numerical Heat Transfer and Fluid Flow*, Taylor and Francis, New York, 1980.

[27] D. Quere, Fluid coating on a fiber, *Ann. Rev. Fluid Mech.*, 31, 347-384, 1999.

[28] S. Ravinutala and C.E. Polymeropoulos, Entrance meniscus in a pressurized optical fiber coating applicator, *Int. J. Exp. Heat Transfer Fluid Mech.*, 26, 573-580, 2002.

[29] P.J. Roache, *Verification and Validation in Computational Science and Engineering*, Hermosa Publishers, Albuquerque, New Mexico, 1998.

[30] S. Roy Choudhury and Y. Jaluria, Practical aspects in the drawing of an optical fiber, *Journal of Materials Research*, 13, 483-493, 1998.

[31] S. Sathe and B. Sammakia, A review of recent developments in some practical aspects of air-cooled electronic packages, ASME *J. Heat Transfer*, 120, 830-839, 1998.

[32] T. Sastrohartono, M. Esseghir, T.H. Kwon and V. Sernas, Numerical and experimental studies of the flow in the nip region of a partially intermeshing co-rotating twin screw extruder, *Polymer Engg. Sci.*, 30, 1382-1398, 1990.

[33] Z. Tadmor and C. Gogos, *Principles of Polymer Processing*, Wiley, New York, 1979.

[34] R. Viskanta, Heat transfer during melting and solidification of metals, *ASME J. Heat Transfer*, 110, 1205-1219, 1988.

[35] Z. Yin and Y. Jaluria, Zonal method to model radiative transport in an optical fiber drawing furnace, *ASME J. Heat Transfer*, 119, 597-603, 1997.

[36] S.Y. Yoo and Y. Jaluria, Fluid flow and heat transfer in an optical fiber coating process, *Int. J. Heat Mass Transfer*, 50, 1176-1185, 2007.

[37] H. Zhao, T. Icoz, Y. Jaluria, and D. Knight, Application of data driven design optimization methodology to a multi-objective design optimization problem, *J. Engg. Design*, 18, 343-359, 2007.

First International Conference on Computational Methods for Thermal Problems
ThermaComp2009, September 8-10, 2009, Napoli, Italy
N.Massarotti and P.Nithiarasu (Eds.)

THE PARTICLE FINITE ELEMENT METHOD IN THERMAL PROBLEMS

Sergio Idelsohn
ICREA Research Professor at CIMNE, UPC, Barcelona, Spain, sergio@cimne.upc.edu

Eugenio Oñate
Professor at CIMNE, UPC, Barcelona, Spain

Julio Marti and Riccardo Rossi
Researchers at CIMNE, UPC, Barcelona, Spain

ABSTRACT

In this presentation, new computational procedures for analysis of thermal problems like the melting and flame spread of polymers under fire conditions is presented. The method, termed Particle Finite Element Method (PFEM) [1-3], combines concepts from particle-based techniques with those of the standard Finite Element Method (FEM).

Key Words: *Fluid- Combustible Interactions, Finite Elements, Particles Methods, Thermoplastic.*

1. INTRODUCTION

Thermoplastic objects, including mattresses, upholstered furniture, and moulded objects such as electronic housings and automobile parts, respond to fire by melting and dripping onto the surface below. The flow of material affects heat and mass transport within the object, and the accumulating melt pool below the object extends the flaming zone and increases the overall rate of heat release. If the fire from the object and the pool fire interact, the intensity of the fire is enhanced even further.

Computer modelling and simulation of the melting flow and flame spread of thermoplastics is extremely complex involving fluid flow, heat transfer, material degradation, flame chemistry, surface tension, and complex material properties. In addition, the drastic changes in shape pose a severe challenge to traditional modelling methods. Attempts to model melt flow of polymeric material in fire using the volume of fluid (VOF) method have encountered difficulties with numerical instabilities and excessive runtimes.

In this presentation the Particle Finite Element Method (PFEM) will be used to solve melting and flame spread of polymers under fire conditions. The key feature of the PFEM is the use of an updated Lagrangian description to model the motion of nodes (particles) in the thermoplastic material. Nodes are viewed as material points which can freely move and even separate from the main analysis domain representing, for instance, the effect of melting and dripping of polymer particles. A mesh connects the nodes defining the discretized domain where the governing equations are solved as in the standard FEM. An incremental iterative scheme for the solution of the non linear transient coupled thermal-flow problem including mass loss of mass by gasification is used.

Examples of the possibilities of the PFEM for the modelling and simulation of different thermal problems like the melting and flame spread of polymers under different fire conditions are shown.

2. BASIC STEP OF THE PFEM

In the PFEM the analysis domain is modelled with an updated Lagrangian formulation. The analysis domain can include solid and fluid sub domains. As an example we can model one or several thermoplastic objects and the surrounding air as forming part of the analysis domain. All variables in the fluid and solid domains are assumed to be known in the current configuration at time t. The new set of variables in all domains is sought for in the next configuration at time t + delta t. The finite element method (FEM) is used to solve the continuum equations in all the domains. Hence a mesh discretizing these domains must be generated in order to solve the governing equations for both the fluid and solid problems in the standard FEM fashion. To do this, the nodes discretizing the analysis domain are treated as material particles whose motion is tracked during the transient solution. This is useful to model the separation of particles from a solid domain, such as in the dripping of melt particles in a thermoplastic object, and to follow their subsequent motion as individual particles with a known density, an initial acceleration and velocity, and subject to gravity forces. Every node is a material point and hence is characterized by the density of the polymer material. The mass of a given domain is obtained by integrating the density at the different material points over the domain. The quality of the numerical solution depends on the discretization chosen as in the standard FEM. Adaptive mesh refinement techniques can be used to improve the solution in zones where large motions of the fluid or the structure occur.

In this paper we will consider the analysis domain to be formed of polymer material and the surrounding hot air as a part of the analysis domain. Melted drips of the polymer material separating from the main body of the heated object will be treated as imbibed in the air domain.

3. ACCOUNTING FOR GASIFICATION EFFECTS

The effect of gasification can be introduced by adding a (nonlinear) energy loss term in the energy equation. This term represents the energy that migrates from the system to the gas due to the evaporation (gasification) of a part of the material during the heating process.

Once the temperature field is known, the volume variation is fixed at every point of the mesh. This allows defining a continuum distribution of the volumetric variation over the whole polymer domain. The computed mass loss has to be included in the fluid problem to ensure that the volume variation of the sample is correctly modelled. The concept is thus to solve the momentum equations prescribing as a constraint the local volume variation.

From a practical point of view this implies adding the gasification heat flux into the boundary term vector and adding the volumetric deformation rate into the stabilized mass balance equation.

4. RESULTS

In a first example the PFEM is used to simulate an experiment performed at NIST (National Institute for Standard and Technology, USA) in which a slab of polymeric material is mounted vertically and exposed to uniform radiant heating on one face. Degradation of the polymer decreases its viscosity by several orders of magnitude and produces fuel gases. Polymer melt is captured by a pan below the sample.

A schematic of the apparatus used in the experiments is the following: A rectangular polymeric sample of dimensions 10 cm high by 10 cm wide by 5 cm thick is mounted upright and exposed to uniform heating on one face from a radiant cone heater placed on its side. The sample is insulated on its lateral and rear faces. The melt flows down the heated face of the sample and drips onto a surface below. A load cell monitors the mass of polymer remaining in the sample, and a laboratory balance measures the mass of polymer falling onto the catch surface. The relationship used in the model is an empirical viscosity-temperature curve that implicitly accounts for molecular weight changes.

An initial spacing of 2.0 mm between nodes results in a finite element model of 1537 nodes and 2818 elements, while a spacing of 1,4 mm results in 3098 nodes and 5832 elements. No nodes are added during the course of the run.

The addition of a catch pan to capture the dripping polymer melt tests the ability of the PFEM model to recover mass when a particle or set of particles reaches the catch surface.

For this problem, heat flux was only applied to free surfaces above the midpoint between the catch pan and the base of the sample. However, every free surface is subject to radiation and convective heat was studied for three heat flux level of 20, 30 and 40 kW/m2 losses. To keep the melt fluid, the catch pan was set to a temperature of 250 degrees. The thickness of the sample is reduced to 2.5 cm to achieve results more quickly.

Figure 1 shows snapshots of the time evolution of the melt flow into the catch pan using the finer grid and a heat flux level of 20 kW/m2.

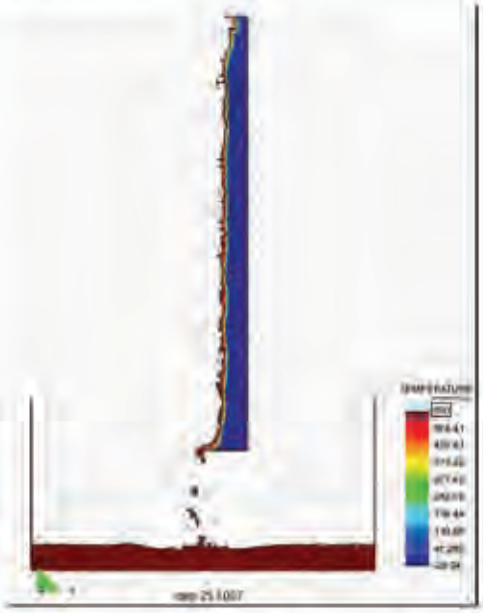

FIGURE 1. Evolution of the melt flow into the catch pan at t = 700s

Directly below the base of the sample where the melt is dripping, the temperature of the melt is higher. On the catch pan away from this point, the top of the melt has cooled to a temperature below the 600 K of the catch pan surface. The melt spreads to either side from the point at which the dripping melt contacts the catch pan.

The total mass reflects a conservation of mass within 5%. Note that because of the way nodes are eliminated and recreated at surfaces in the PFEM, the total mass at times may exceeds 100% of the

initial mass. This error can be reduced by increasing the number of particles (nodes), as in the standard FEM.

In a second example the total fluid-combustible interaction problem is solved to analyse the burning of a chair. Initially the fire starts on the upper part of the seat. Due to the convective air effect, the flame spread to the back of the chair and finally the entire chair is burned. Figure 2 represents the temperature distribution a two different time steps.

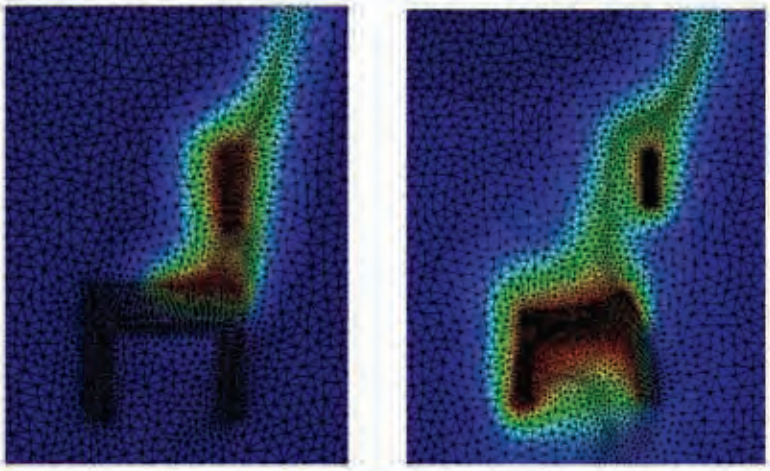

FIGURE 2. Evolution of the temperature during the burning of a chair

REFERENCES

[1] S. R. Idelsohn, E. Oñate and F. Del Pin. " The Particle Finite Element Method: a powerful tool to solve incompressible flows with free-surfaces and breaking waves" *International Journal for Numerical Methods in Engineering.* Vol.61, Number 7, pp 964-984, 2004.

[2] S. R. Idelsohn and E. Oñate "To mesh or not to mesh. That is the question...". *Computer Methods in Applied Mechanics and Engineering,* Volume 195, Issues 37-40, pp 4681-4696, 2006.

[3] S. R. Idelsohn, M. Mier-Torrecilla, and E. Oñate. "Multi-fluid flows with the Particle Finite Element Method", *Comput. Methods Appl. Mech. Engrg.* 198, pp: 2750–2767, 2009.

First International Conference on Computational Methods for Thermal Problems
ThermaComp2009, September 8-10, 2009, Naples, Italy
N.Massarotti and P.Nithiarasu (Eds.)

FINITE ELEMENT TECHNIQUES FOR THERMAL/FLUID PROBLEMS

David K. Gartling
Engineering Sciences Center
Sandia National Laboratories
Albuquerque, New Mexico USA
dkgartl@sandia.gov

Roy E. Hogan
Engineering Sciences Center
Sandia National Laboratories
Albuquerque, New Mexico USA
rehogan@sandia.gov

ABSTRACT

A variety of finite element capabilities are described for simulations of general problems in thermal and fluid transport.

Key Words: *Finite element, computational heat transfer, computational fluid dynamics, coupled problems.*

1. INTRODUCTION

The Finite Element Method (FEM) is often the method of choice when considering the development of general simulation capabilities for the fluid and thermal sciences. The primary reasons for this choice of numerical method are usually cited in terms of: a) the advantages of using a weak or variational form of the boundary value problem, b) the simplicity of local approximations of variables in terms of simple functions, c) the geometric generality engendered by unstructured, heterogeneous meshes and d) the ease of boundary condition and interface specification. The basic Finite Element methodology is now reasonably mature for fluid and thermal applications having been extensively applied and refined for numerous problem areas. Though improvements are still being made in stabilization techniques, matrix solution methods and approaches for representing physical behavior (*e.g.* turbulence, rheologically complex materials and multiphase materials), the method is an essential part of modern engineering practice. However, a basic solution method is not sufficient for the demanding applications found in many current engineering and scientific studies. A wide spectrum of modeling and simulation capabilities must be available to extend and compliment the basic FEM resolution of the bounday value problems of interest. Some of these capabilities are outlined and demonstrated in the following sections. All of these capabilities will make use of the fundamental properties of the FEM, especially the last feature regarding boundary and interface conditions. The techniques to be decribed have all been implemented and used for thermal conduction/radiation problems; some of the techniques have also been extended to nonisothermal flows.

2. MULTIPHYSICS AND CONJUGATE PROBLEMS

Multiple physical phenomena required in a simulation may be treated by either of two approaches: the coupling of single physics codes via data exchange or the implementation of multiple PDE's in a monolithic code. Both methods are usually required to handle a complete spectrum of problems. Conjugate

problems are generally solved most effectively using a single code. In considering thermal transport problems it has been found useful to allow the optional definition of one or more additional diffusion or advection-diffusion equations that are solved fully coupled with the energy equation. With this capability, a number of multiphysics problems are immediately accessible such as thermoelectric, mass transfer and simple porous flow problems. The presence of a second PDE also provides the infastructure for time harmonic thermal problems and a stochastic description of thermal conduction. Specialized equations, such as descriptions of chemically reactive materials, are also important to have available in a general thermal transport simulation. In the fluid mechanics area, additional advection-diffusion equations may again be used for mass transfer and extent of reaction descriptions. Though not strictly an additional equation, the ability to redefine or optionally add terms to the standard nonisothermal, Navier Stokes system allows Darcy-Brinkman porous flows to be considered. Conjugate problems involving porous and clear fluid regions can then be addressed as can certain types of solidification problems with embedded mushy zones [1,2].

For more complex multiphysics applications, multiple single physics codes must be utilized. For many problems involving thermal transport, the energy equation sets the time scale for the coupled problem. This suggests that the thermal code will be the driver or master process in the simulation. A particularly useful coupling implementation allows the thermal code to control the overall simulation process and request data updates (solutions) from the subordinate simulation processes when needed. When all codes are finite element based, data transfer is simplified, even for dissimilar meshes. This type of process has been implemented in parallel where memory-to-memory transfers were used to transfer relevant data between codes. Both thermal and fluid codes were coupled to one or two external codes that considered the solid mechanics and electromagnetic response of the problem.

As an example of a three-code, coupled thermal/mechanical/electrical simulation, the resistance weld problem shown in Figure 1 is considered [3]. The tapered cylinder is subject to a short duration, time dependent current flow that produces Joule heating in the part. The cylinders are also subject to an axial force that causes a plastic strain in the material and the large deformation at the joint.

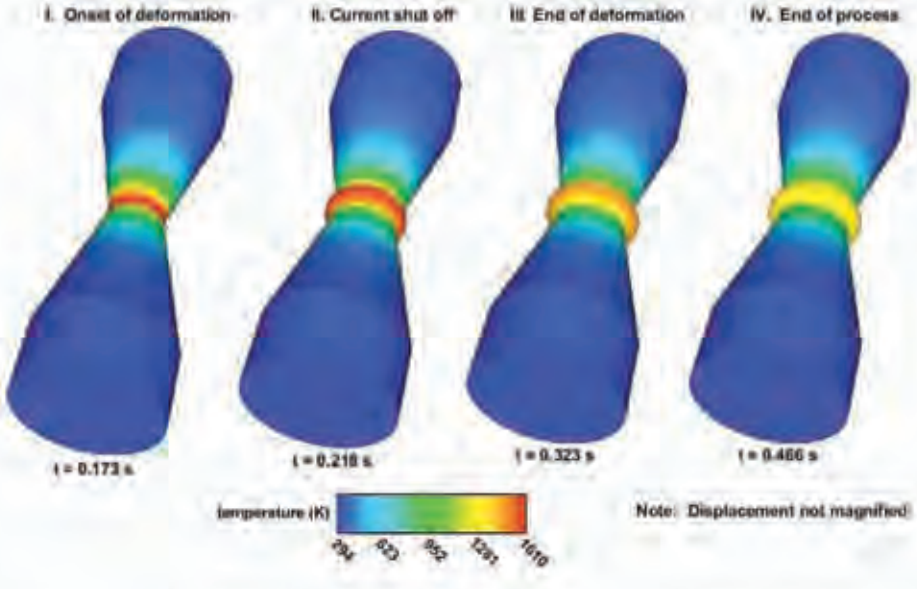

FIGURE 1. Temperature histories for resistance weld

3. MATERIAL MOTION

Simulations involving the relative motion of rigid or deforming bodies require a variety of computational techniques. The type of method depends on the transport process and the range of material motions; multiple techniques may be required in a single simulation and must be computationally compatible. Thermal diffusion problems with a Lagrangian description will typically require a general

contact detection and boundary condition implementation that considers dynamic surface interactions between noncontiguous meshes. The implementation of this capability demands an efficient and robust point-in-element search procedure that scales effectively in a parallel environment. When deformation is important, similar contact procedures are required though the kinematics are updated from an external source. In concert with arbitrary contact, partially exposed element surfaces and boundary condition applications must be considered. For some prescribed motions or surface interactions, multipoint constraint methods may be required. This type of constraint is also applicable to merging of static, noncontiguous meshes and sliding mesh methods for Arbitrary Lagrangian Eulerian (ALE) descriptions in fluid-thermal transport [4].

Shown in Figures 2 and 3 is an example of a dynamic contact problem where the kinematics of the body are specified. A single diamond compact drag bit is specified to execute a circular path on a slab of rock. A simple friction model is used to generate heat in the cutter while the contact condition provides a heat transfer path to the slab. The drag bit is convectively cooled on the exterior by (unmodeled) drilling fluid; some bit geometries also have an interior cooling chamber. More complex kinematics can account for bit bounce on the rough rock surface and the intermittent cooling of the cutting surface. Bit bounce obviously requires a change in the boundary condition at the drag bit and slab interface. Subsequent transfer of the temperature history in the cutter to a solid mechanics code allows the stress state and fatigue life of the cutter head to be estimated.

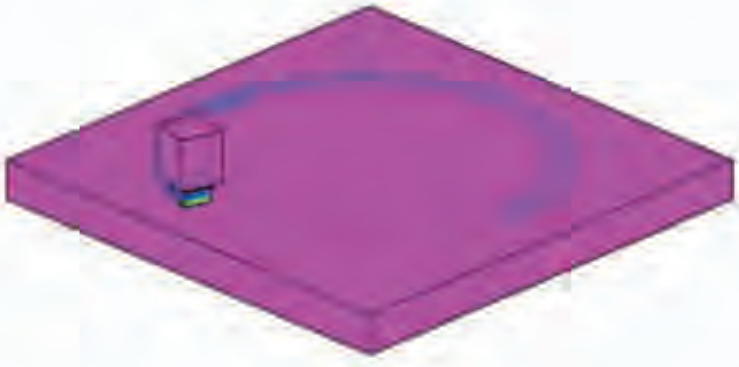

FIGURE 2. Drag bit moving on a slab, dynamic contact boundary condition

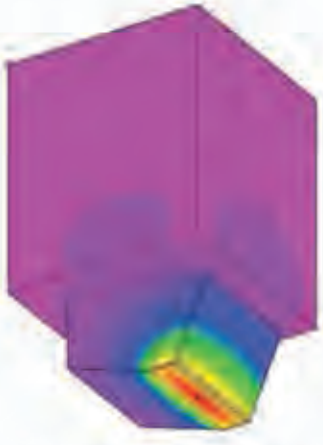

FIGURE 3. Temperature field in drag bit

Deforming mesh methods are useful for simulating relatively small changes in surface geometry as may be found in ablation problems. This again requires the availability of additional PDE's to describe the

elastic "solid mechanics" motion of the mesh. Material addition and deletion for thermal problems is conveniently simulated using an element birth/death algorithm. When elements are added or removed from the simulation the inheritance of boundary conditions must be taken into account.

4. MISCELLANEOUS METHODS

Specialty finite elements have proven extremely useful in complex and high fidelity simulations. Bar and shell elements compliment continuum elements in thermal problems and permit complex structures to be effectively modeled. Pipe elements for flow problems allow continuum flow regions to be realistically coupled to overall fluid systems such as might occur in building HVAC models. Bulk node or zero dimensional elements have proven valuable in thermal problems to represent fluid regions where fluid motion is not deemed important but an overall energy representation is required.

Despite the steadily increasing ability to perform more complex and larger thermal and fluid simulations, there is a significant need for reduced order models. The engineering design community, in particular, requires very rapid simulation of complex systems such that control systems may be designed and evaluated. Model reduction is another capability that is increasingly required from general finite element codes.

5. CONCLUSIONS

The finite element method lends itself to great generality in terms of modeling and simulation capabilities. Most of these techniques rely heavily on the basics of the finite element methodolgy and the element-by-element building block nature of the method.

REFERENCES

[1] D. K. Gartling, C. E. Hickox and R. C. Givler, Simulation of coupled viscous and porous flow problems, *International Journal of Computational Fluid Dynamics*, 7, 23-48, 1996.

[2] D. K. Gartling and P. A. Sackinger, Finite element simulation of vacuum arc remelting, *International Journal for Numerical Metods in Fluids*, 24, 1271-1289, 1997.

[3] A. R. Ortega, J. W. Foulk, M. L. Chiesa and D. K. Gartling, Development of validated resistance weld modeling tools, *Proc.6th ASME-JSME Thermal Engineering Joint Conference*, TED-AJ03-156, Maui, Hawaii, 2003.

[4] D. K. Gartling, Multipoint constraint methods for moving body and non-contiguous mesh simulations, *International Journal for Numerical Metods in Fluids*, 47, 471-489, 2005.

KEYNOTE LECTURES

First International Conference on Computational Methods for Thermal Problems
ThermaComp2009, September 8-10, 2009, Naples, Italy
N.Massarotti and P.Nithiarasu (Eds.)

DYNAMIC SUBSCALES IN THE FINITE ELEMENT APPROXIMATION OF THERMALLY COUPLED INCOMPRESSIBLE FLOWS

Ramon Codina
Universitat Politècnica de Catalunya (UPC), ramon.codina@upc.edu

Javier Principe
International Center for Numerical Methods in Engineering (CIMNE), principe@cimne.upc.edu

Matías Ávila
International Center for Numerical Methods in Engineering (CIMNE), matiasavila@hotmail.com

ABSTRACT

In this work we propose a variational multiscale finite element approximation for the incompressible Navier-Stokes equations using the Boussinesq approximation to model thermal coupling. The main feature of the formulation in contrast to other stabilized methods is that we consider the subscales as transient and orthogonal to the finite element space. These subscales are solution of a differential equation in time that needs to be integrated. Likewise, we keep the effect of the subscales both in the nonlinear convective terms of the momentum and temperature equations and, if required, in the thermal coupling term of the momentum equation. Apart from presenting the main properties of the formulation, we also discuss some computational aspects such as the linearization strategy or the way to integrate in time the equation for the subscales. This strategy allows us to approach the problem of dealing with thermal turbulence from a strictly numerical point of view and discuss important issues, such as the relationship between the turbulent mechanical dissipation and the turbulent thermal dissipation, that is to say, what could be called the turbulent Prandtl number.

Key Words: *Thermally coupled flows, variational scale splitting, dynamic subscales*

1. PROBLEM STATEMENT

Let $\Omega \subset \mathbb{R}^d$, with $d = 2, 3$, be the computational domain in which the flow takes place during the time interval $[0, T]$, and let Γ be its boundary. The initial and boundary value problem to be considered consists in finding a velocity field $\boldsymbol{u}$, a pressure p and a temperature ϑ such that

$$\begin{aligned} \partial_t \boldsymbol{u} + \boldsymbol{u} \cdot \nabla \boldsymbol{u} - \nu \Delta \boldsymbol{u} + \nabla p + \alpha \boldsymbol{g} \vartheta = \boldsymbol{f} + \alpha \boldsymbol{g} \vartheta_0 \quad & \text{in } \Omega,\ t \in (0,T), \\ \nabla \cdot \boldsymbol{u} = 0 \quad & \text{in } \Omega,\ t \in (0,T), \\ \partial_t \vartheta + \boldsymbol{u} \cdot \nabla \vartheta - \kappa \Delta \vartheta = Q \quad & \text{in } \Omega,\ t \in (0,T), \end{aligned}$$

together with appropriate initial and boundary conditions. In these equations, ν is the kinematic viscosity, κ the thermal diffusivity, α the thermal expansion coefficient, $\boldsymbol{f}$ the external body forces, ϑ_0 the reference temperature, $\boldsymbol{g}$ the gravity acceleration vector, Q the heat source and $\boldsymbol{u}^0$ and ϑ^0 the initial conditions for velocity and temperature, respectively.

2. SCALE SPLITTING

Let us consider a finite element partition $\{\Omega_e\}$, $e = 1, ..., n_{\rm e}$, of the computational domain Ω, from which we can construct finite element spaces for the velocity, pressure and temperature in the usual

manner. We will assume that they are all built from continuous piecewise polynomials of the same degree k.

The basic idea of the multiscale approach we will follow [1] is to split the continuous unknowns as

$$\boldsymbol{u} = \boldsymbol{u}_h + \tilde{\boldsymbol{u}}, \tag{1}$$

$$p = p_h + \tilde{p}, \tag{2}$$

$$\vartheta = \vartheta_h + \tilde{\vartheta}, \tag{3}$$

where the components with subscript h belong to the corresponding finite element spaces. The components with a tilde belong to any space such that its direct sum with the finite element space yields the functional space where the unknown is sought. For the moment, we leave it undefined. These additional components are what we will call *subscales*. Each particular variational multiscale method will depend on the way the subscales are approximated. However, our main focus in this work is *not* how to choose the space of subscales (in our case for velocity, pressure and temperature), but to explain the consequences *of considering these subscales time dependent*, and therefore requiring to be integrated in time. Likewise, we will keep the previous decomposition (1)-(3) in *all the terms of the variational equations of the problem*. The only approximation we will make for the moment is to assume that the subscales vanish on the interelement boundaries, $\partial\Omega_e$. This happens for example if one assumes that their Fourier modes correspond to high wave numbers, as it is explained in [2].

From the previous splitting two sets of equations can be obtained. The first is the projection the original equations onto the finite element spaces of velocity, pressure and temperature. On the other hand, the equations for the subscales are obtained by projecting onto their corresponding spaces, that is, by taking the test function $\tilde{\boldsymbol{v}}$ in the space of subscales instead of in the finite element space. If P' denotes the projection onto any of the subscale spaces (for velocity, pressure or temperature), these equations are

$$P'[\partial_t\tilde{\boldsymbol{u}} + (\boldsymbol{u}_h + \tilde{\boldsymbol{u}})\cdot\nabla\tilde{\boldsymbol{u}} - \nu\Delta\tilde{\boldsymbol{u}} + \nabla\tilde{p} + \alpha\boldsymbol{g}\tilde{\vartheta}] = P'(\boldsymbol{R}_u) \tag{4}$$

$$P'(\nabla\cdot\tilde{\boldsymbol{u}}) = P'(R_p) \tag{5}$$

$$P'[\partial_t\tilde{\vartheta} + (\boldsymbol{u}_h + \tilde{\boldsymbol{u}})\cdot\nabla\tilde{\vartheta} - \kappa\Delta\tilde{\vartheta}] = P'(R_\vartheta), \tag{6}$$

where

$$\begin{aligned}
\boldsymbol{R}_u &= \boldsymbol{f} + \alpha\boldsymbol{g}\vartheta_0 - [\partial_t\boldsymbol{u}_h + (\boldsymbol{u}_h + \tilde{\boldsymbol{u}})\cdot\nabla\boldsymbol{u}_h - \nu\Delta_h\boldsymbol{u}_h + \nabla p_h + \alpha\boldsymbol{g}\vartheta_h] \\
R_p &= -\nabla\cdot\boldsymbol{u}_h \\
R_\vartheta &= Q - [\partial_t\vartheta_h + (\boldsymbol{u}_h + \tilde{\boldsymbol{u}})\cdot\nabla\vartheta_h - \kappa\Delta_h\vartheta_h],
\end{aligned}$$

are the residuals of the finite element unknowns in the momentum, continuity and heat equation, respectively. Equations (4)-(6) need to be solved within each element and, as we have assumed, considering homogeneous velocity and temperature Dirichlet boundary conditions.

It is not our purpose here to discuss how to approximate (4)-(5) which, in fact, is the essence of the different stabilized finite element methods that can be found in the literature. We will adopt a simple approximation that can be found, for example, in [2] and references therein. Our main concern, as in the reference just mentioned, is *to keep the time dependence of the subscales, as well their nonlinear effects*. When their time derivative is neglected, we will call them *quasi-static*, whereas otherwise we will call them *dynamic*.

Using the same arguments as in [2], now extended to thermally coupled flows, we propose to compute the subscales *within each element* of the finite element partition as solution to

$$\partial_t\tilde{\boldsymbol{u}} + \frac{1}{\tau_1}\tilde{\boldsymbol{u}} = P'(\boldsymbol{R}_u), \tag{7}$$

$$\frac{1}{\tau_2}\tilde{p} = P'(R_p + \tau_1\partial_t R_p), \tag{8}$$

$$\partial_t\tilde{\vartheta} + \frac{1}{\tau_3}\tilde{\vartheta} = P'(R_\vartheta), \tag{9}$$

where the *stabilization* parameters τ_1, τ_2 and τ_3 are computed as

$$\tau_1 = \left(c_1 \frac{\nu}{h^2} + c_2 \frac{|\boldsymbol{u}_h + \tilde{\boldsymbol{u}}|}{h} \right)^{-1}, \tag{10}$$

$$\tau_2 = \frac{h^2}{c_1 \tau_1} = \nu + \frac{c_2}{c_1} h |\boldsymbol{u}_h + \tilde{\boldsymbol{u}}|, \tag{11}$$

$$\tau_3 = \left(c_1 \frac{\kappa}{h^2} + c_2 \frac{|\boldsymbol{u}_h + \tilde{\boldsymbol{u}}|}{h} \right)^{-1}, \tag{12}$$

where h is the element size and c_1 and c_2 are algorithmic constants (we have adopted $c_1 = 4$ and $c_2 = 2$ in the numerical experiments).

3. MAIN PROPERTIES OF THE FORMULATION

The first and most important point to be considered is the effect of considering the subscales dynamic, and therefore to deal with their time variation. Some of these properties are:

- The effect of the time integration is now clear. Certainly, the effective stabilization parameters have to be modified (as it is done for example in [3, 4]), but when the steady-state is reached the subscale $\tilde{\boldsymbol{u}}$ that is obtained satisfies

  $$\left(\frac{1}{\beta \delta t} + \frac{1}{\tau_1} \right) \tilde{\boldsymbol{u}} = \frac{1}{\beta \delta t} \tilde{\boldsymbol{u}} + \boldsymbol{R}_u,$$

  from where

  $$\tilde{\boldsymbol{u}} = \tau_1 \boldsymbol{R}_u,$$

  so that the usual expression employed for stationary problems is recovered.
- From the point of view of the algebraic solver, the factor $\left(\frac{1}{\beta \delta t} + \frac{1}{\tau_1} \right)^{-1}$ instead of τ_1 is crucial for the conditioning of the system matrix, since both for $\delta t \to 0$ and for $\delta t \to \infty$ the matrix contribution of the stabilization terms is dominated by the contribution from the Galerkin terms. If τ_1 is used as stabilization factor, when $\delta t \to 0$ (and thus the leading terms are those coming from the discretization of the time derivative) both the Galerkin and stabilizing terms could lead to matrix terms of the same order and the condition number of the matrix of the Galerkin method could be deteriorated.
- It is clear that space discretization (understood as scale splitting) and time discretization commute, that is *time discretization + stabilization (scale splitting) = stabilization (scale splitting) + time discretization*.
- Numerical experiments show that the temporal time integration is significantly improved:
  - Oscillations originated by initial transients are eliminated.
  - The numerical dissipation is minimized.

  For the numerical results that demonstrate this fact we refer to [5]. This is also observed in the numerical experiments of Section 4.
- The numerical analysis shows optimal stability without any restriction between τ_1 and δt. Contrary to classical stabilized methods, anisotropic space-time discretizations are allowed [6]. See [5] for a stability analysis of the linearized Navier-Stokes equations and [7] for a complete stability and convergence analysis for the Stokes problem.
- It can be shown that the formulation presented implies *global momentum conservation*, and also *global energy conservation*. The proof of the first fact can be found in [5], whereas the proof of the second follows similar arguments.

Another very important issue of the formulation presented in the possibility to model turbulent flows. The term $\langle \tilde{\boldsymbol{u}}^{n+\beta}, \tilde{\boldsymbol{u}}^{n+\beta} \cdot \nabla \boldsymbol{v}_h \rangle = \langle \nabla \boldsymbol{v}_h, \tilde{\boldsymbol{u}}^{n+\beta} \otimes \tilde{\boldsymbol{u}}^{n+\beta} \rangle$ can be understood as the contribution from *the residual stress tensor* or the *subgrid scale tensor* of an LES approach. Therefore, we may expect that, in some sense, *modeling $\tilde{\boldsymbol{u}}^{n+\beta}$ implies to model the subgrid scale tensor*. The question is how good this model will be. The numerical models proposed here yield two possibilities, but many others can be devised.

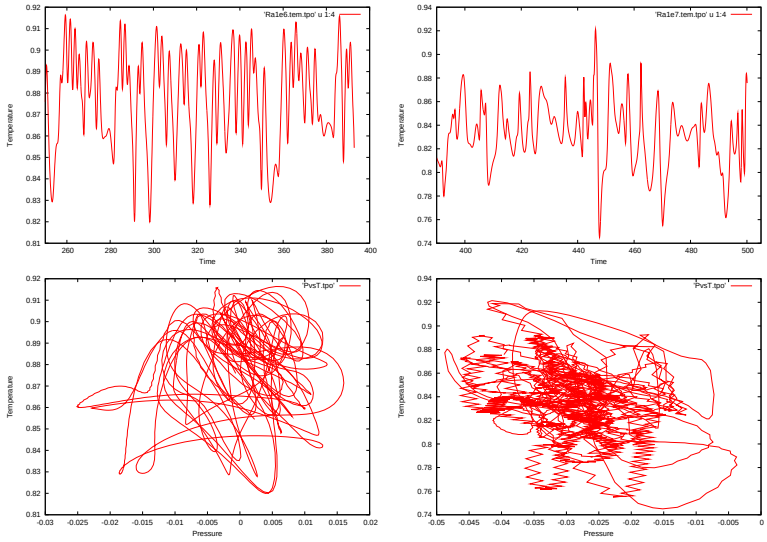

FIGURE 1. Temperature evolution and p-ϑ limit cycle for the 8:1 cavity. Left: $\mathrm{Ra} = 10^6$, right: $\mathrm{Ra} = 10^7$

Related to the why turbulence is modeled, the numerical formulation proposed has an inherent turbulent Prandtl number. In other words, it is not necessary to specify which is the amount of turbulent thermal dissipation, but emanates directly from the formulation.

4. EXAMPLE

As an example of application of the formulation presented, we have modeled the flow in a differentially heated cavity with aspect ratio 8. The data of the problem can be found in [8]. The interest of this problem in that it displays transition to chaos as the Rayleigh number is increased.

In Fig. 1 the temperature evolution and the p-ϑ limit cycles are shown for $\mathrm{Ra} = 10^6$ and $\mathrm{Ra} = 10^7$. In the second case, the flow is fully chaotic. For $\mathrm{Ra} = 10^6$ good results are obtained even if the dynamic behavior of the subscales is neglected, that is to say, quasi-static subscales are used (see Fig. 1 left). However, for $\mathrm{Ra} = 10^6$ there are some oscillations in the pressure when using quasi-static subscales (see Fig. 1 right) that are removed when dynamic subscales are used (not shown).

REFERENCES

[1] T.J.R. Hughes, G.R. Feijóo, L. Mazzei, and J.B. Quincy. The variational multiscale method–a paradigm for computational mechanics. *Computer Methods in Applied Mechanics and Engineering*, 166:3–24, 1998.

[2] R. Codina. Stabilized finite element approximation of transient incompressible flows using orthogonal subscales. *Computer Methods in Applied Mechanics and Engineering*, 191:4295–4321, 2002.

[3] F. Shakib and T.J.R. Hughes. A new finite element formulation for computational fluid dynamics: IX. Fourier analysis of space-time Galerkin/least-squares algorithms. *Computer Methods in Applied Mechanics and Engineering*, 87:35–58, 1991.

[4] T. Tezduyar and S. Sathe. Stabilization parameters in SUPG and PSPG formulations. *Journal of Computational and Applied Mechanics*, 4:71–88, 2003.

[5] R. Codina, J. Principe, O. Guasch, and S. Badia. Time dependent subscales in the stabilized finite element approximation of incompressible flow problems. *Computer Methods in Applied Mechanics and Engineering*, 196:2413–2430, 2007.

[6] P.B. Bochev, M.D. Gunzburger, and R.B. Lehoucq. On stabilized finite element methods for the Stokes problem in the small time-step limit. *International Journal for Numerical Methods in Fluids*, 53:573–597, 2007.

[7] S. Badia and R. Codina. On a multiscale approach to the transient Stokes problem. Transient subscales and anisotropic space-time discretization. *Applied Mathematics and Computation*, 207:415–433, 2009.

[8] M.A. Christon, P.M. Gresho, and S.B. Sutton. Computational predictability of natural convection flows in enclosures. *International Journal for Numerical Methods in Fluids*, 40:953–980, 2002.

First International Conference on Computational Methods for Thermal Problems
ThermaComp2009, September 8-10, 2009, Naples, Italy
N.Massarotti and P.Nithiarasu (Eds.)

Multi-scale computational modelling of flow and heat transfer

Dimitris Drikakis[1] and **Nikolaos Asproulis**
[1]Invited Author
Fluid Mechanics & Computational Science Group,
Department of Aerospace Sciences,
Cranfield University, United Kingdom
d.drikakis@cranfield.ac.uk

ABSTRACT

Over the past decade micro and nanofluidics have emerged as vital tools in the ongoing drive towards the development of nano-scale analysis and manufacturing systems. Understanding of the flow and heat transfer phenomena involved at micro/nano scales is essential in order to speed up the industrial nanotechnology processes. The key challenge of the numerical modelling of micro/nano flows is associated with the inherently multi-scale nature of the phenomena and the absence of a computational unified approach that can circumvent the associated accuracy and efficiency problems. This paper concerns investigation of different approaches for applying macroscopic boundary conditions to a molecular system. A number of simulations has been performed for both gas and liquid systems under various velocity and temperature conditions. The results indicated that the selection of the most suitable approach is not a trivial task and is highly associated with the nature of the fluid flow problem.

Key Words: *Multiscale modelling, hybrid atomistic-continuum, heat transfer, micro/nanofluid dynamics.*

1. INTRODUCTION

In recent years, numerical modelling of fluid flow inside micro and nanochannels has drawn the attention of the scientific community primarily due to its potential to shed light on the micro/nano multi-scale physics and assist with the design of micro and nano fluidic devices.

The traditional continuum models neglect the microscopic mechanisms of the phenomena involved at nano scales and, therefore, in cases where the macroscopic constitutive relations or boundary conditions are no longer applicable, models such as molecular dynamics (MD) have to be employed. The Achilles heel of the molecular simulations is their high computational cost that restricts their applications to nanoscale systems and time scales below microseconds [1]. To circumvent the implications arising from the disparity of scales, both spatial and temporal, multiscale frameworks and specifically hybrid atomistic-continuum methods have been developed [2–5]. The accuracy and efficiency of the above computational frameworks are based on the successful data exchange between the continuum and atomistic domains. The most challenging task is to impose macroscopic boundary condition on a molecular simulation.The main difficulty is that the microscopic description is associated with more degrees of freedom compared to the macroscopic one.

In this paper, the two main approaches for applying continuum information to a molecular simulation are presented and applied to various scenarios aiming to broaden our understanding of continuum-atomistic interface.

2. METHODOLOGY

Two techniques are discussed here with respect to the boundary continuum transfer (BCT): (i) rescaling and (ii) velocity distribution functions.

2.1. **Rescaling Techniques.** Suppose that the continuum conditions are applied into a constrained region R_{con}, then the average velocity of particles inside this region should be equal to the continuum one $\boldsymbol{u}_{con}$

$$\frac{1}{M_{total}^{constrain}} \sum_{i \in R_{con}} m_i \boldsymbol{u_i} = \boldsymbol{u_{con}}. \tag{1}$$

where $M_{total}^{constrain} = \sum m_i,\ i \in R_{con}$ is the total mass of particles inside the region. Apart from the velocity constraints, the normal pressure calculated from the continuum solver has to be applied in order to ensure that the microscopic simulations are consistent to the macroscopic description. The application of the normal pressure also prevents the particles from escaping the molecular region. Application of a continuum pressure P_{con} to the microscopic system is implemented by transferring an equivalent amount of momentum F_{ps} given by

$$F_{ps} = P_{con} \cdot A \cdot \Delta t, \tag{2}$$

where A is the area of the constrained region normal to the direction of the applied pressure and Δt is the time step of the microscopic simulation. A velocity reversing scheme is employed, where the momentum is transferred by reversing the particles' velocity components in the direction of the applied pressure. For example, reversing the velocity component $u_{i,a}$ of one atom in the direction a will introduce a momentum $2m_i u_{i,a}$ in the corresponding direction. The scheme starts by reversing the velocities of the outermost atoms that are about to escape from the molecular region until the desired momentum is introduced.

The macroscopic temperature is applied to the microscopic system through an energy transfer scheme [5]. The energy transfer is performed independently for each dimension and is achieved through scaling of the velocity vectors of the atoms as follows

$$\boldsymbol{u_i^{new}} = \boldsymbol{u_i} \cdot f + \boldsymbol{c}. \tag{3}$$

f represents a scaling factor calculated for each dimension $a = \{x, y, z\}$ as

$$f_a = \left(1 + \frac{E_{T_a}^{con}}{E_{k,int_a}}\right), \tag{4}$$

where E_{k,int_a} is the internal kinetic energy of the atoms in the constrained region and $E_{T_a}^{con}$ is the target energy of the constrained atoms. The internal kinetic energy is given by

$$E_{k,int_a} = \sum_{i \in R_{con}} \frac{1}{2} m_i \left(u_{i_a} - \overline{u}_a\right)^2, \tag{5}$$

where $\overline{u}_a$ is the mean velocity component of the constrained particles in the direction a, which is calculated by $\overline{u}_a = \frac{1}{M_{total}^{constrain}} \sum m_i u_{i_a},\ i \in R_{con}$. The target energy imposed by the applied continuum temperature is given by

$$E_{T_a}^{con} = \frac{1}{3} \cdot \left(\frac{dof}{2} \cdot k_B \cdot T^{con}\right), \tag{6}$$

where $dof = (system's\ dimensions) \cdot (particles'\ number)$ is the number of the degrees of freedom. The factor $\boldsymbol{c}$ is given by

$$c_a = \overline{u}_a \cdot (1 - f_a) \tag{7}$$

and ensures that zero momentum is transferred along with the energy.

2.2. **Techniques based on velocity distribution functions.** The second BCT method utilises velocity distribution functions. For the scope of this study the atomistic velocities are periodically sampled either from the Maxwell-Boltzmann or the Chapman-Enskog distribution. The Maxwell-Boltzmann velocity distribution defines the probability of the one-dimensional velocity component of an atom being in a specific range, based on the temperature T and the atom mass m_i. For the Maxwell-Boltzmann distribution, the probability density $f(\boldsymbol{C})$ of the thermal velocity $\boldsymbol{C} = \boldsymbol{u}/\left(2k_B T/m_i\right)^{1/2}$ is given by

$$f(\boldsymbol{C}) = \frac{1}{\pi^{3/2}} exp\left(-\boldsymbol{C}\right), \tag{8}$$

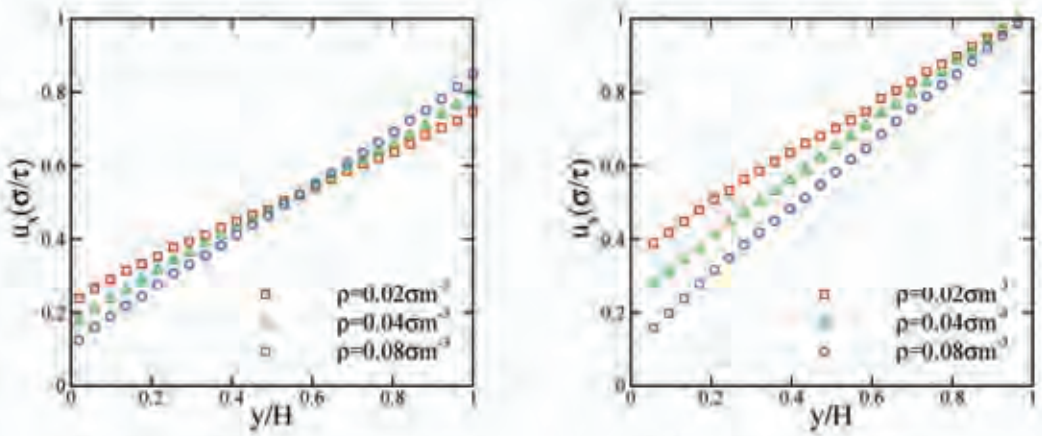

(a) Maxwell-Boltzmann based BCT method

(b) Chapman-Enskog-based BCT method

Figure 1: Velocity profiles obtained with Maxwell-Boltzmann and Chapman-Enskog distributions, respectively, for different gas densities.

where k_B denotes the Boltzmann's constant

Away from equilibrium the Chapman-Enskog distribution is utilised for sampling the atomistic velocities. The aforementioned distribution has been used primarily in hybrid simulations of dilute gases see [7, 8]. The Chapman-Enskog distribution is a perturbed Maxwell-Boltzmann distribution [9] with probability density given by

$$f(\boldsymbol{C}) = \Gamma(\boldsymbol{C})\,\pi^{-3/2} exp\left(-\boldsymbol{C}^2\right), \tag{9}$$

$\Gamma(\boldsymbol{C})$ is the perturbation term

$$\begin{aligned}\Gamma(\boldsymbol{C}) \;=\; & 1 + (q_x u_x + q_y u_y + q_z u_z)\left(\frac{2}{5}\boldsymbol{C}^2 - 1\right) - \\ & 2\left(\tau_{x,y} C_x C_y + \tau_{x,z} C_x C_z + \tau_{y,z} C_y C_z\right) - \tau_{x,x}\left(C_x^2 - C_z^2\right) - \\ & \tau_{y,y}\left(C_y^2 - C_z^2\right),\end{aligned} \tag{10}$$

where q_a and $\tau_{a,b}$, $a, b = x, y, z$ denote the dimensionless heat flux and stress tensor, respectively.

3. Results

The size of the molecular domain for the gas flow simulations is 200σ in the x and z directions, and 120σ in the y direction. The molecular domain is divided into two sub-domains; the first one is the flow region, where $y < 100\sigma$, and the second one is the BCT region, with $100\sigma < y < 120\sigma$. At the bottom of the molecular domain a stochastic thermal wall is imposed. Stochastic thermal walls have been extensively used in the literature for gas flow simulations, e.g., [10, 11]. The first test case includes simulations, where BCT is performed through a Maxwell-Boltzmann distribution. The simulations have been performed for different values of the gas density with continuum constrains $u_{x-con} = 1.0\ \sigma/\tau$ and $T_{con} = 1.0\ \epsilon/k_B$ and wall temperature $T_{wall} = 1.0\ \epsilon/k_B$. Three values of density were simulated $\rho = 0.02\ m\sigma^{-3}$, $\rho = 0.04\ m\sigma^{-3}$ and $\rho = 0.08\ m\sigma^{-3}$ resulting in the generation of 10240, 20000 and 40316 particles respectively. The time step used for the MD simulations is $\Delta t_{MD} = 0.001\tau$, each simulation has been run for $8 \cdot 10^6$ time steps and the calculated quantities have been averaged over $2 \cdot 10^6$ time steps.

For the second test case the rescaling based technique and the one based on the Chapman-Enkog's distribution are utilised for gas flow simulations in the same domain as used in the above gas simulations, with density $\rho = 0.05\ m\sigma^{-3}$, continuum constrains $u_{x-con} = 1.0\ \sigma/\tau$ and $T_{con} = 1.0\ \epsilon/k_B$ and wall temperature $T_{wall} = 1.0\ \epsilon/k_B$. In the performed simulations, 25, 168 particles have been generated;

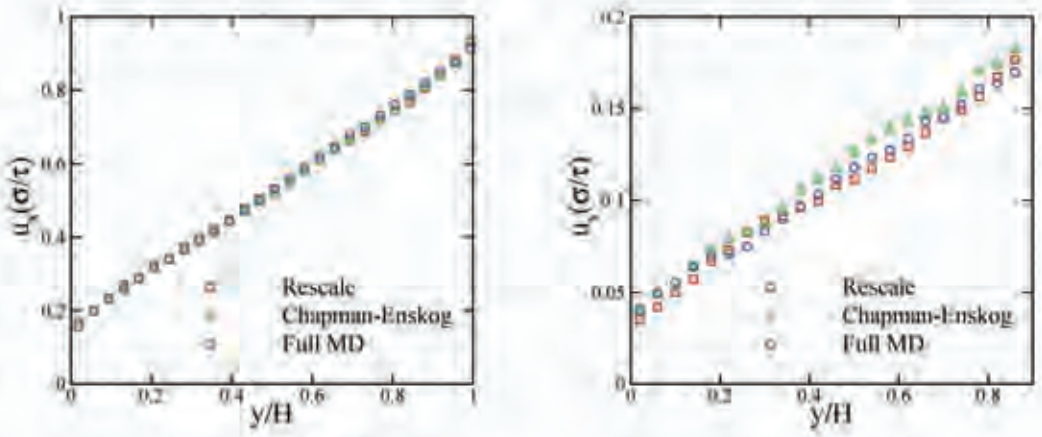

(a) $u_{x-con} = 1\,\sigma/\tau$ (b) $u_{x-con} = 0.2\,\sigma/\tau$

Figure 2: Velocity profiles for gas with $\rho = 0.05\,m \cdot \sigma^{-3}$ obtained from the rescaling BCT method; the BCT method based on the Chapman-Enskog distribution; and the full MD simulation.

the MD time step is $\Delta t_{MD} = 0.001\tau$; each simulation has been run for $8 \cdot 10^6$ time steps; and the calculated quantities have been averaged over $2 \cdot 10^6$ time steps.

The above results show that the selection of an appropriate BCT method is not a trivial issue. It depends on the specific simulated problem and a number of other parameters such as the accuracy requirements and the available resources. The main advantage of the rescaling method is its generic nature and broad applicability. However, it is less computationally efficient compared to the velocity distribution function method.

References

[1] N. Asproulis and D. Drikakis. Nanoscale materials modelling using neural networks. *J. Comput. Theo. Nano Sci.*, 6(3):514–518, 2009.

[2] S.T. O'connell and P.A. Thompson. Molecular dynamics-continuum hybrid computations: A tool for studying complex fluid flows. *Phys. Rev. E*, 52(6):R5792–R5795, 1995.

[3] R. Delgado-Buscalioni and P.V. Coveney. Continuum-particle hybrid coupling for mass, momentum and energy transfers. *Phys. Rev. E*, 67:046704, 2003.

[4] M. Kalweit and D. Drikakis. Multiscale methods for micro/nano flows and materials. *J. Comput. Theo. Nano Sci.*, 5(9):1923–1938, 2008.

[5] M Kalweit and D Drikakis. Coupling strategies for hybrid molecularcontinuum simulation methods. *Proceedings of the I MECH E Part C Journal of Mechanical Engineering Science*, 222:797–806(10), 2008.

[6] N.R. Bimalendu. *Fundamentals of Classical and Statistical Thermodynamics*. John Wiley, West Sussex, England, 2002.

[7] T. E. Schwartzentruber, L. C. Scalabrin, and I. D. Boyd. Hybrid particle-continuum simulations of nonequilibrium hypersonic blunt-body flowfields. *J. Therm. and Heat Tran.*, 22(1):29–37, 2008.

[8] H. S. Wijesinghe and N. G. Hadjiconstantinou. A hybrid atomistic-continuum formulation for unsteady, viscous, incompressible flows. *CMES*, 5(6):515–526, 2004.

[9] A. L. Garcia and B. J. Alder. Generation of the chapman-enskog distribution. *J. Comput. Phys.*, 140(1):66–70, 1998.

[10] D. K. Bhattacharya and G. C. Lie. Nonequilibrium gas flow in the transition regime: A molecular-dynamics study. *Phys. Rev. A*, 43(2):761–767, 1991.

[11] J. L. Xu and Z. Q. Zhou. Molecular dynamics simulation of liquid argon flow at platinum surfaces. *Heat and Mass Tran.*, 40(11):859–869, 2004.

First International Conference on Computational Methods for Thermal Problems
ThermaComp2009, Septem r 8-10, 2009, Napoli, Italy
N.Massarotti and P.Nithiarasu (Eds.)

Reduced Order Thermal Modeling of Data Centers via Proper Orthogonal Decomposition-A Review

Emad Samadiani and Yogendra Joshi

G.W. Woodruff School of Mechanical Engineering,
Georgia Institute of Technology, Atlanta, Georgia 30332, U.S.A.
samadiani@gatech.edu ; yogendra.joshi@me.gatech.edu

1. Thermal Management of Data Centers

Data centers are computing infrastructure facilities that house arrays of electronic racks containing data processing and storage equipment, whose temperature must be maintained within allowable limits as it dissipates power. A common approach currently used for thermal management of air cooled data centers consists of computer room air conditioning (CRAC or AC) units that deliver cold air to the racks arranged in alternate cold/hot aisles through perforated tiles placed over an under-floor plenum.

The power consumption of data center facilities can be in the range of tens of MW, with an additional 30% or more needed for powering the cooling systems. Energy-efficient design of the cooling systems is essential for containing operating costs, and promoting sustainability. Through better design and preventing over-provisioning, it should be possible to reduce energy consumption by the cooling systems. Predicting the flow and specially temperature fields inside data centers in terms of the involved design parameters is necessary for an energy efficient and reliable cooling system design.

2. CFD/HT Modeling of Data Centers

Generally, the air flow inside data centers is turbulent. Also, buoyancy effects can usually be neglected. The Reynolds-averaged Navier-Stokes equations (RANS) are commonly used to simulate the turbulent mean flow in air-cooled data centers, by modeling the effect of turbulence on the mean flow as a spatially dependent effective viscosity. Also, the mean energy equation with effective thermal conductivity can be used to compute the temperature field.

Several researchers have simulated the air flow and temperature fields in data centers. Optimization and design incorporating different parameters involved in these systems have also been performed. Computational Fluid Dynamics/Heat Transfer (CFD/HT) is usually used to predict the air velocity and temperature fields inside the data center. Numerical thermal modeling has been used for geometrical optimization of plenum depth, facility ceiling height and cold aisle spacing for a single set of CRAC flow rates and uniform rack flow and power dissipation. Researchers have either modeled individual racks as black-boxes with prescribed flow rate and temperature rise, or with fixed flow rate and uniform heat generation. A procedure

to model individual servers within each rack was developed in [1]. The multi-scale nature of data centers needs to be considered in the numerical modeling. The multi-scale model of a representative data center in [1, 2] consists of ~1,500,000 grid cells and needs more than 2400 iterations to obtain a converged solution. This model took about 8 hours to converge on a 2.8 GHz Xeon with 2 GB memory [1]. In light of this, a comprehensive CFD/HT multi-scale model of operational data centers, which may contain thousands of racks, seems infeasible due to limits on available computing. A compact or low-dimensional model which could run much faster, while including the influence of all important scale parameters with sufficient fidelity is essential.

3. Low-Dimensional Modeling Approaches

Meta-modeling techniques can be used to extract the dominant characteristics of a system, trading a degree of accuracy for much greater computational speed. Approaches such as linear response surfaces using Design of Experiments (DOE), krieging, multivariate adaptive regression splines, and other more advanced interpolation approaches offer approximations to generate a surrogate model of the system response in terms of the design variables.

On the other hand, reduced order modeling of turbulent thermal/fluid systems can be done through flow structure identification. The process of taking a model based either on detailed numerical simulations or full-field experimental measurements from a large number of degrees of freedom (DOF) to one involving significantly fewer DOF is termed model reduction. An approach to develop reduced order models of turbulent flows is based on the observation that many such flows are characterized by characteristic recurrent forms that are collectively called coherent structures. These are energetically dominant in many flows. So, it should be possible to build a relatively realistic, low-dimensional model of the flow by keeping only the dominant coherent structures, and simulating the effect of the smaller, less energetic, apparently incoherent part of the flow in some way [3].

Flow structure identification techniques can be used to capture the coherent structures of turbulent flows, using a time dependent data set obtained after refining some numerical or experimental velocity data. Eulerian or Lagrangian approaches can be used for physical description of the coherent structures.

Appropriate averaging procedures and corresponding transport equations are needed to compute the evolution of the coherent structures in turbulent flows. The fundamental principle in generating low dimensional turbulence modeling based on the coherent structures is to find a representative set of modes or bases to project the governing equations onto, reducing the solution procedure to finding the appropriate weight coefficients that combine the modes into the desired approximate solution. All classical methods in turbulence rely on the Fourier representation. But, turbulent motions are nonseparable in the Fourier representation. Wavelet transform-based techniques are alternative tools to identify the coherent/incoherent structures, and model and compute turbulent flows. The most useful property of the wavelet transform is its ability to detect and accurately measure the strength of individual singularities in a signal. So, wavelet-

based techniques can be used to separately model the coherent and incoherent flow components, something that Fourier based models cannot do.

In addition to the Fourier and wavelet based techniques, the Proper Orthogonal Decomposition (POD) can also be used to accomplish low dimensional turbulence modeling. The POD, also known as the Karhunen-Loeve decomposition, is a statistical technique and has several properties that make it well suited for turbulent flows. First, it has been shown experimentally that low-dimensional models using POD can well address the role of coherent structures in turbulence generation [3]. Secondly, it captures more of the dominant dynamics for a given number of modes than any other linear decomposition [3]. Finally, the empirical determination of the basis functions makes this method ideal for nonlinear problems.

4. Low-dimensional Modeling of Data Centers

Aside from CFD/HT, Simulation methods based on some heuristic approaches have also been explored to predict the air temperature at discrete points, such as server inlets/outlets, for a new heat load distribution among the data center racks or servers. Recent work on reduced order thermal modeling of data centers using POD has extended the capabilities of the POD technique [4-6]. These extensions and representative results from [4-6] are briefly reviewed in the following.

Samadiani and Joshi [4] have presented an approach to handle the challenges of multi-parameter reduced order thermal modeling in complex multi-scale convective systems. The approach is centered on the integration of three constructs: a) POD, b) Galerkin projection, and c) energy balance/heat flux matching. It is applicable to systems where the temperature field at selected scales or components drives the thermal design decision. The energy equation is solved only at these dominant components via system POD modes and Galerkin projection to obtain a more accurate zoomed prediction at these components, instead of the entire domain. The effects of the phenomena at other scales are modeled through simple energy balance equations and known heat flux and temperature matching, as well as appropriate matching conditions at the component interfaces. Unlike the previous studies on data center rapid modeling, the POD based modeling is a deterministic approach which can predict the temperature at the whole data center domain in terms of multiple design variables. Also, a novel feature, compared with the previous POD related studies, is the use of POD modes and Galerkin projection with special treatment of boundary conditions for solving the governing turbulent convection equation in a complex multi-scale system. The method has been applied to a representative data center cell with 5 design variables. It is shown that the average error at the rack inlets for different test cases is less than 1 ^{o}C, while the maximum local error is ~2.5 ^{o}C for some small regions [4]. Also, the mean error, the standard deviation, and the Euclidean L2 norm of the POD temperature error at all 114,000 points of the rack scale for 15 test cases have been shown in [4]. The mean error varies from 0.35 ^{o}C to 2.29 ^{o}C, while the average error is 1.36 ^{o}C, and the average standard deviation 1.12 ^{o}C. Also, the error norm changes from 1.8% to 10.1%, while the average is 6.2% [4]. These values confirm that the presented POD method is accurate enough at the rack scale for design purposes.

Regarding the computational efficiency of the technique, the POD-based algorithm [4] generates the temperature field for a new test case with different CRAC velocity and rack heat loads in 12 minutes, while the CFD/HT simulation takes ~2 hours for the same test case on the same computing platform (a high end desktop computer). Also, the most time-consuming part of the method, integrating the velocity terms in the Galerkin projection over the domain, can be done once for all observed CRAC velocities, if the method is to be used for many simulations. It takes ~38 minutes to calculate these terms. After that, the algorithm is ready to obtain the POD temperature field for each new test case in only 4 seconds [4].

Samadiani and Joshi in [5] have presented a simpler POD based method to generate a reduced order thermal modeling of complex systems such as air cooled data centers. In this method, the algebraic equations to be solved for POD coefficients are obtained simply through energy balance equations, heat flux matching, and/or surface temperature matching for all convective components of the complex system. The method application for a data center cell shows that the average error at the rack inlets for different test cases is less than 1.5 ^{o}C, while the maximum local error is ~2.5 ^{o}C for some small regions. Also, the temperature prediction error at all 431,120 points representing the entire data center cell have been studied for six test cases in [5]. The mean error for the six test cases varies from 0.63 ^{o}C or 2.4% to 2.13 ^{o}C or 8.4%. The average of the mean absolute and relative error for all cases is 1.24 ^{o}C and 4.9%, while the average standard deviation is 1.46 ^{o}C. These values confirm that the presented POD method is accurate enough for the entire data center cell. Regarding the computational efficiency, it takes only ~48 seconds to obtain the POD temperature field by the method in [5], which is ~150 times faster than the full field CFD/HT simulation.

Each of the two POD based methods explained above has its own pros and cons. Unlike the POD based method in [4], the presented method in [5] does not need fluid flow modeling and is accurate throughout the entire domain. Also, the method in [5] is much simpler and its application is easier for reduced order thermal modeling of operational data centers, where the observation data are gathered experimentally and thermal sensors are deployed at the inlet/outlet of the servers.

As a deficiency, the number of available algebraic equations to be solved for the POD coefficients in the presented method in [5] is limited by the number of convective components and available thermal information for the components in the system. This brings a limitation to the method whose effect on the results for the data center cell is studied in [5]. It is concluded that the method can be used as a reliable and rapid predictor to obtain a new temperature field throughout the system, unless the number of components or available thermal information in the form of equations at the component boundaries is very close to or less than the number of dominant modes. This would not typically cause a problem in thermal model reduction of operational data centers with several housed servers if enough numbers of servers have thermal sensors at their inlet/outlet.

On the other hand, the POD technique based on Galerkin projection in [4] does not have any limitation regarding the number of components, since using Galerkin projection to obtain the algebraic equations results in *m* distinct algebraic equations for each component, if *m* POD modes are used.

5. Conclusions

While most of the studies in the literature on rapid thermal modeling of data centers are based on heuristic approaches, two recently developed POD based reduced order thermal modeling methods for data centers are reviewed and compared. POD based techniques have shown great approximation for multi-parameter thermal modeling of data centers. It is believed that wavelet based techniques due to the their ability to separate between coherent and incoherent structures- something that POD cannot do- can be considered as new promising tools for reduced order thermal modeling of complex electronic systems such as data centers.

References

1. J. Rambo and Y. Joshi, Multi-Scale Modeling of High Power Density Data Centers, Proc. ASME InterPACK03, Kauai, Hawaii, ASME, InterPack2003-35297, 2003.
2. J. Rambo and Y. Joshi, Thermal Modeling of Technology Infrastructure Facilities: A Case Study of Data Centers, in W.J. Minkowycz, E.M. Sparrow, and J.Y. Murthy (eds.), The Handbook of Numerical Heat Transfer, pp. 821-850, Taylor and Francis, New York, 2006.
3. P. Holmes, J.L. Lumley, and G. Berkooz, Turbulence, Coherent Structures, Dynamical Systems and Symmetry, Cambridge University Press., Great Britain, 1996.
4. E. Samadiani and Y. Joshi, Multi-Parameter Model Reduction in Multi-Scale Convective Systems, International Journal of Heat and Mass Transfer, under review, 2009.
5. E. Samadiani and Y. Joshi, Proper Orthogonal Decomposition for Reduced Order Thermal Modeling of Air Cooled Data Centers, ASME Journal of Heat Transfer, under review, 2009.
6. E. Samadiani, Y. Joshi, H. Hamann, M.K. Iyengar, S. Kamalsy, and J. Lacey, Reduced Order Thermal Modeling of Data Centers via Distributed Sensor Data, Proc. ASME InterPACK '09, San Francisco, CA, 2009.

First International Conference on Computational Methods for Thermal Problems
ThermaComp2009, September 8-10, 2009, Naples, Italy
N.Massarotti and P.Nithiarasu (Eds.)

Effective Modelling of Multi-Phase Heat and Mass Transfer Systems

A. G. Malan
Council for Scientific and Industrial Research (CSIR), Brummeria, Pretoria, South Africa, 0001,
email: amalan@csir.co.za

ABSTRACT

The effective modelling of heat and mass transfer in strongly coupled multi-phase systems has presented a challenge in computational mechanics for the last decade. This work considers problems which range from non-linear heat conduction to single and multi-species porous systems. A set of volume-averaged local thermal-disequilibium governing equations are employed to describe the general case. Special attention is given to account for conductive, convective, radiative and phase change effects within the domain as well as at boundaries. All non-linear variations in phenomenological coefficients are fully and accurately accounted for. Enhanced hybrid-unstructured compact edge-based finite volume technology is developed for spatial discretized and a generalized artificial-compressibility pressure-projection methodology employed for solution purposes. The latter is both efficient and completely matrix free. For the purpose of reducing computational time while preserving the matrix-free nature of the technology we develop two methodologies viz. distributed memory parallelization and a preconditioned Generalised Minimal Residual (GMRES) algorithm. The METIS library is used for balanced domain decomposition and super linear speed-up demonstrated. A semi-analytical Newton-linearization methodology is constructed for the GMRES technique and preconditioning effected via Lower-Upper Symmetric Gauss-Seidel (LU-SGS). Reductions in CPU-time of 30 to 1000 are demonstrated. The developed technology is employed to model systems ranging from non-hygroscopic to hygroscopic porous materials with and without phase change. Commendable accuracy is demonstrated in all cases.

Key Words: *Multi-Phase Heat and Mass Transfer, porous systems, matrix-free, high performance computing.*

1. INTRODUCTION

Computational mechanics has advanced to the point where a need exists for a generic tool which allows for the routine, fast and accurate modelling of heat and mass transfer in strongly coupled multi-phase systems. These may range from heat transfer dominated, to strongly coupled multi-phase flow in porous or particulate systems. Examples found in industry range from drying of particulate materials and heat and mass transfer through packed pebble beds, to heat transfer in high pressure aerospace turbine blades.

The equations that govern heat and mass transport in multi-phase systems are perplexingly intricate, highly non-linear and strongly coupled [1, 2, 3, 4, 5, 6, 7, 8, 9]. Main stream formulations are either mechanistic (classical) [10, 11] to mathematically formal (Luikov [12] and Whitaker [13]), the latter being mathematically more rigorous at the cost of abstraction and complexity. We propose the use of a generalised set of volume averaged governing equations, and such that systems ranging from multi-phase porous to non-linear heat conduction may be described in an effective manner.

The favourable characteristics of both structured and unstructured [14, 15] grid generation methods should is adopted by meshing different regions of a particular spatial domain with the most suitable type, i.e. structured or unstructured. The result is an unstructured-hybrid mesh. In the interest of computational and programming efficiency, the chosen spatial discretisation algorithm should be naturally applicable to any part of an unstructured-hybrid mesh. This is achieved by employing a purely

edge-based compact [16, 17] discretisation methodology, which holds the additional advantage of being computationally considerably more efficient than element-based approaches [18].

An efficient and accurate unstructured-hybrid spatial discertisation algorithm is to be complemented with a suitably memory-efficient, fast and robust solution algorithm whih are naturally suited to distributed parallel computing. Matrix-free schemes offer such an alternative. Two approaches are adopted viz. (a) a fusion of the Pressure-projection and existing artificial-compressibility technologies due to recent work by Nithiarasu [19] for convection dominated systems, and (b) a preconditioned *Generalised Minimal Residual* (GMRES) algorithm for non-linear diffusion dominated problems [20].

The developed technology is validated via application to a number of non-linear problems. These range from diffusion dominated systems such as non-linear hear conduction and multi-phase heat and mass transfer in drying particulate materials, to combined convective-conductive-radiative heat transfer in heterogeneous porous materials. Accuracy is assessed by comparing predicted results with experimental data and found to be in excellent agreement. Solution speed-ups on account of preconditioned GMRES solution or parallel computing is documented.

2. GOVERNING EQUATIONS

The heat and mass transfer systems under consideration contains from one to four species, of which up to three are mobile (three phase flow) viz. liquid, vapor and pure gas. A generalised type continuum model is employed which is embodies the aforementioned [8, 9, 20], and may be written in a generalised axi-symmetric/cartesian co-ordinate system as:

$$\frac{\partial \mathbf{W}}{\partial t} + \frac{\partial \mathbf{F}^j}{\partial x_j} - \frac{\partial \mathbf{G}^j}{\partial x_j} + r\varepsilon \frac{\partial \mathbf{H}}{\partial x_j} = \mathbf{S} \tag{1}$$

where **W**, **F**, **G**, **H** respectively denote the primitive variables being solved for, convective, diffusive and pressure fluxes. Further, **S** denotes the source term and t and x_j are time and cartesian co-ordinate in direction j. Finally, ε is porosity and r denotes radius in the case of axi-symmetric analyses or else unity. The equations may be specialized for the physics being dealt with via the volume averaged phenomenological coefficients. These are typically obtained from experimental data.

3. SPATIAL DISCRETIZATION AND SOLUTION PROCEDURE

An unstructured vertex-centred edge-based finite volume algorithm is employed for spatial discretisation purposes as it is naturally applicable to any part of an unstructured-hybrid mesh. The aforementioned algorithm further exhibits a number of computational advantages as compared to other methods. An edge-based data structure is computationally more efficient than element-based approaches [21], while the vertex-centred variant of the finite volume scheme is superior to cell-centred counterparts in terms of memory usage, as pointed out by Zhao and Zang [18].

For the purpose of solving the governing equations, two solution procedures are employed viz. for convection dominated problems a pressure-projection artificial-compressibility methodology [19], and in the case of non-linear diffusion dominated problems a preconditioned GMRES methodology [20]. Both of these procedures are matrix free and well suited to parallel computing.

Due to the fully matrix-free nature of the numerical method at solver sub-iteration level, data reference is local (nodes only see neighbouring nodes, with some exceptions) which means that computation can be very efficiently parallelized. The mesh is divided into separate domains by applying the METIS library [22] to its connectivity graph, and then the solver is run on each domain with information being communicated between the nodes where they join. Linear speed-up is achieved on distributed memory machines with up to 120 cores.

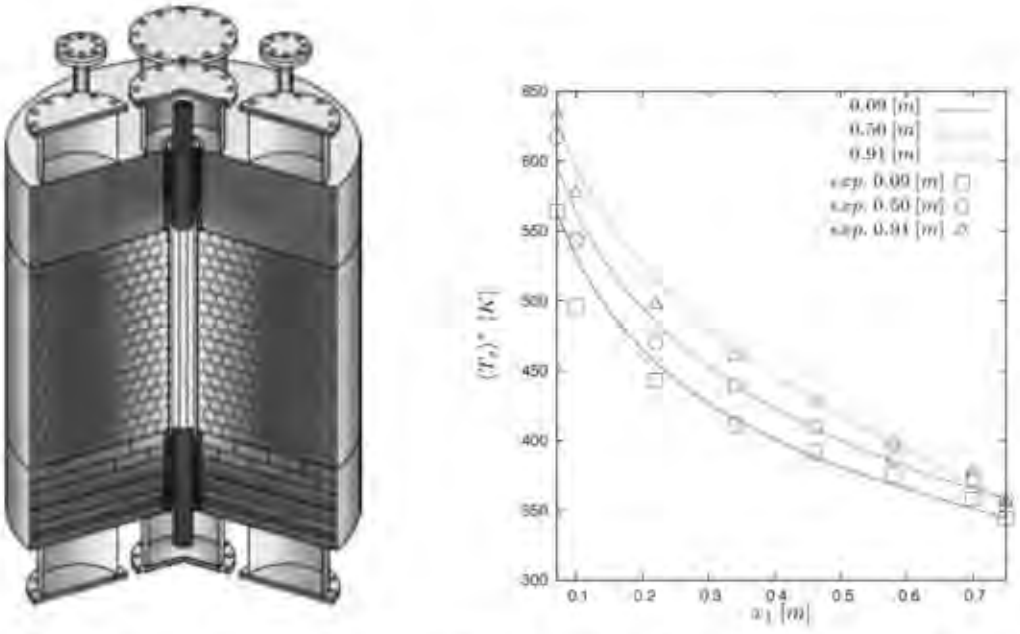

FIGURE 1. Schematic diagram of the SANA test setup (left) with central heating element [23] and predicted pebble temperature distribution compared to experimental (exp.) measurements at three different heights.(right).

4. RESULTS

The developed numerical technology is validated by application to a number benchmark test-problems viz. non-linear heat conduction, heat and mass transfer in particulate materials with phase change, and combined convective-conductive-radiative heat transfer in heterogeneous porous materials with thermally active fluid and solid phases. For the purpose of the latter case we consider the SANA test setup at the Jülich Research Center [23]. The setup, which is shown schematically in Figure 1, consists of a cylindrical vessel filled with randomly packed graphite spheres. The working fluid considered in this work was helium. The heat input to the system is via a centrally placed electrical heater. The predicted pebble temperature distribution at three different heights is compared to measurements [23] in Figure 1. As shown in the figure a commendable modelling accuracy was achieved, with the maximum and average errors of 12% and 3% respectively.

5. CONCLUSIONS

The work dealt with the effective modelling of heat and mass transfer in strongly coupled multi-phase systems. A set of volume-averaged local thermal-disequilibium governing equations were employed to describe the general case. All non-linear variations in phenomenological coefficients are fully and accurately accounted for. An enhanced hybrid-unstructured compact edge-based finite volume technology is developed for spatial discretized an artificial-compressibility pressure-projection methodology employed for the solution of convection dominated problems. The developed technology is validated and commendable accuracy is demonstrated in all cases.

REFERENCES

[1] R. W. Lewis, K. Morgan, and H. R. Thomas. A non-linear analysis of shrinkage stresses in porous materials. In *Proceedings of the 1st International Conference on Numerical Methods in Thermal Problems*, pages 515–526, Swansea, 1979.

[2] M. Fortes and M. R. Okos. A non-equilibrium thermodynamics approach to transport phenomena in capillary porous media. In *Proceedings of the 1st International Symposium on Drying*, McGill University, Montreal, Canada, 1978.

[3] W. J. Ferguson, R. W. Lewis, and L. Tomosy. Finite element analysis of freeze-drying of a coffee sample. *Computer Methods in Applied Mechanics and Engineering*, 108(3-4):341–352, 1993.

[4] K. Vafai and C. L. Tien. Boundary and inertia effects on flow and heat transfer in porous media. *International Journal for Heat and Mass Transfer*, 24:195–203, 1981.

[5] J. A. M. Kuipers, K. J. van Duin, F. P. H. van Beckum, and W. P. M. van Swaaij. A numerical model of gas-fluidised beds. *Chemical Engineering Science*, 47(8):1913–1924, 1992.

[6] P. Nithiarasu, K. N. Seetharamu, and T. Sundararajan. Natural convection heat transfer in a fluid saturated variable porosity medium. *International Journal for Heat and Mass Transfer*, 40(16): 3955–3967, 1997.

[7] N. Massarotti, P. Nithiarasu, and A. Carotenuto. Microscopic and macroscopic approach for natural convection in enclosures filled with fluid saturated porous medium. *International Journal of Numerical Methods for Heat and Fluid Flow*, 13(7):862–886, 2003.

[8] R. W. Lewis and A. G. Malan. Continuum thermodynamic modeling of drying capillary particulate materials via an edge-based algorithm. *Computer Methods in Applied Mechanics and Engineering*, 194(18-20):2043–2057, 2005.

[9] C. Visser, A. G. Malan, and J. P. Meyer. An artificial compressibility algorithm for modelling natural convection in saturated packed pebble beds: A heterogeneous approach. *International Journal for Numerical Methods in Engineering*, 75:1214–1237, 2008.

[10] J. R. Philip and D. A. de Vries. Moisture movement in porous materials under temperature gradients. *Transactions of the American Geophysics Union*, 38(2):222–232, 1957.

[11] V. Prasad, G. Lauriat, and N. Kladias. Non-darcy natural convection in a vertical porous cavity. In *Heat and Mass Transfer in Porous Media*., pages 293–314. Elsevier, 1992.

[12] A. V. Luikov. Heat and mass transfer in capillary-porous bodies. *International Journal for Heat and Mass Transfer*, 9:139–152, 1966.

[13] S. Whitaker. *Advances in Heat Transfer - Coupled Transport Phenomena in Multi-phase Systems: A Theory of Drying*, volume 31. Academic Press, New York, 1998.

[14] L. Sbarbella and M. Imregun. An efficient discretization of viscous fluxes on unstructured mixed-element grids. *Communications in Numerical Methods in Engineering*, 16:839–849, 2000.

[15] A. Khawaja and Y. Kallinderis. Hybrid grid generation for turbomachinery and aerospace applications. *International Journal for Numerical Methods in Engineering*, 49(1-2):145–166, 2000.

[16] P. I. Crumpton, P. Moinier, and M. B. Giles. An unstructured algorithm for high Reynolds number flows on highly stretched meshes. *Numerical Methods in Laminar and Turbulent Flow (ed. C. Taylor and J. T. Cross)*, pages 561–572, 1997.

[17] A. G. Malan and R. W. Lewis. Modeling coupled heat and mass transfer in drying non-hygroscopic capillary particulate materials. *Communications in Numerical Methods in Engineering*, 19(9): 669–677, 2003.

[18] Y. Zhao and B. Zhang. A high-order characteristics upwind FV method for incompressible flow and heat transfer simulation on unstructured grids. *International Journal of Numerical Methods in Engineering*, 37:3323–3341, 1994.

[19] P. Nithiarasu. An efficient artificial compressibility (ac) scheme based on the characteristic based split (cbs) method for incompressible flow. *International Journal for Numerical Methods in Engineering*, 56(13):1815–1845, 2003.

[20] A. G. Malan, J. P. Meyer, and R. W. Lewis. Modelling non-linear heat conduction via a fast matrix-free implicit unstructured-hybrid algorithm. *Computer Methods in Applied Mechanics and Engineering*, 196(45-48):4495–4504, 2007.

[21] H. Luo, J. D. Baum, and R. Löhner. Edge-based finite-element scheme for the Euler equations. *AIAA*, 32(6):1183–1190, 1994.

[22] G. Karypis and V. Kumar. A fast and high quality multilevel scheme for partitioning irregular graphs.

[23] H. F. Niessen and B. Stöcker. *Data Sets of SANA Experiment: 1994-1996*. JUEL-3409, Forschungszentrum Jülich, 1997.

First International Conference on Computational Methods for Thermal Problems
ThermaComp2009, September 8-10, 2009, Napoli, Italy
N.Massarotti and P.Nithiarasu (Eds.)

SIMULATION OF COMPACT HEAT EXCHANGER PERFORMANCE

Bengt Sunden
Lund University, Department of Energy Sciences, Heat Transfer, P.O. Box 118, SE-221 00 Lund, Sweden, bengt.sunden@energy.lth.se

ABSTRACT

This extended abstract briefly presents some methods to determine the performance of compact heat exchangers. Engineering methods for the rating, sizing and design of heat exchangers as well as methods based on computational fluid dynamics methods are concerned. Results are presented to highlight the opportunities and limitations of the considered methods.

Key Words: *Compact Heat Exchangers, CFD, Engineering Approaches, Correlations.*

1. INTRODUCTION

To calculate or estimate the performance of compact heat exchangers some different methods are possible. One method is to adopt an engineering approach based on overall data and such approaches are generally described in textbooks or handbooks in heat transfer, [1-3]. Conveniently rating and sizing issues can be handled. Another method is to adopt so-called computational fluid dynamics approaches (CFD) which also allow detailed analysis of basic transport processes within a heat exchanger. The principles of CFD might be found in [4, 5]. This paper describes these computational procedures for compact heat exchangers. Constraints, problems, difficulties and limitations are outlined. In the full paper some examples are presented to demonstrate the methods and the results are interpreted. It is found that computational heat transfer methods of various kind and complexity are useful tools if carefully handled. What approach being recommended depends on the overall purpose of the calculations, i.e., related to what kind of results being of interest.

2. ENGINEERING APPROACHES

2.1 The LMTD Method for Analysis of Heat Exchangers

In the thermal analysis of heat exchangers the total heat transfer rate $\dot{Q}$ [W] is of primary interest. To get started, the overall heat transfer coefficient U is assumed to be constant in the whole heat exchanger (average value). The heat transfer rate is then written

$$\dot{Q} = UA \cdot \Delta t_{\mathrm{m}} \tag{1}$$

where A is the heat transferring area and Δt_{m} a proper average of the temperature difference between the hot and cold fluids. Now one has to find an expression for Δt_{m} so that eq. (14) is valid. In general the logarithmic mean temperature difference (LMTD) for a counter flow heat exchanger is applied. For heat exchangers not operating in counter flow, correction factors are introduced. The overall heat transfer coefficient (U) is found from available empirical correlations for the heat transfer coefficients on the hot and cold sides, respectively.

2.2 The - NTU Method for Analysis of Heat Exchangers

In the analysis of the performance of a certain heat exchanger the amount of heat being transferred, outlet temperatures of the fluids and the pressure drops are of most interest. At the design and sizing stage of a heat exchanger, the heat transferring area and other dimensions are determined in such a way that a prescribed heat flow can be transferred and that the pressure drops are within permitted limits.

If the inlet and outlet temperatures of the hot and cold fluids are given, the *LMTD* – method is quite suitable. In other cases the so-called - *NTU* method is more appropriate.

The efficiency or effectiveness is defined as

$$= \frac{\text{real heat transfer rate}}{\text{maximum possible heat transfer rate}} = \frac{\dot{Q}}{\dot{Q}_{max}} \tag{2}$$

NTU, the number of transfer units is defined as

$$NTU = \frac{UA}{C_{min}} \tag{3}$$

Relations between and NTU are available for some heat exchanger configurations in textbooks.

3. CFD – HEAT TRANSFER AND FLUID FLOW ANALYSIS

As the flow pattern is important for the convective heat transfer process both the flow and thermal fields have to be considered as research and development for improvement are attempted. In heat exchanger applications many duct configurations are employed. Enhancement of heat transfer on one or both sides of the heat exchanger is attempted for to reduce the size of the equipment for a given duty, increase the capacity of an existing apparatus, or decrease the approach temperature difference. Common enhancement techniques are offset strip fins, wavy fins, tube inserts and vortex generators. Also the duct walls might be corrugated or wavy. As measurement procedures become quite difficult and it is a formidable task to obtain whole field information particularly for complex and narrow geometries it would be ideal if some form of computer simulations could be carried out. Computational Fluid Dynamics, CFD, is nowadays an established name for a technique to model fluid flow and heat transfer (and other transport phenomena as well) using computer simulations. The rapid growth of powerful computer resources and the development of general purpose CFD software packages have created a tool for simulation of industrial thermal problems. Nevertheless several shortcomings still exist but progress is continuously achieved. The CFD tool can be applied to simulate the flow and temperature fields, the pressure drop and heat duty. The temperature fields can be used to calculate heat transfer coefficients which can be applicable in structural analysis of the equipment. Then some evaluation versus the design specifications can be made. If needed an iterative process can be performed and the geometry data can be changed and the simulations be repeated until satisfactory results have been achieved. The fluid-structure coupling (becoming more and more important) is of a sequential type allowing various codes to be applied. However, recently development of CFD methods to directly couple the solid-fluid and thermal analyses has been promoted, [8]. Nowadays computational tools are able to handle geometries of any arbitrary shape. The geometry has to be represented by a computational mesh consisting of a large number of cells

or control volumes. All equations are solved in all these control volumes according to the conservation equations describing the transport phenomena (momentum, heat, mass). Special mesh generating software produces meshes based on CAD (computer-aided-design)-data representing the three-dimensional geometry. Such mesh generators enable convenient adaptation of the mesh to modifications in the CAD-data. The accuracy and resolution of the results obtained depend on the number and distribution of the control volumes, convection-diffusion schemes being applied and how the turbulence is modeled.

The results from the simulations can be visualized as vector plots for flow velocities, contour plots for scalar quantities like pressure, temperature etc. Many CFD packages have visualization tools and can also be linked to such independent tools. Animations are also possible and such opportunities are particularly useful for unsteady or transient problems. Figure 1 shows a plot of the flow and thermal fields (including local Nusselt numbers) for a ribbed duct. The ribs are used to enhance the heat transfer.

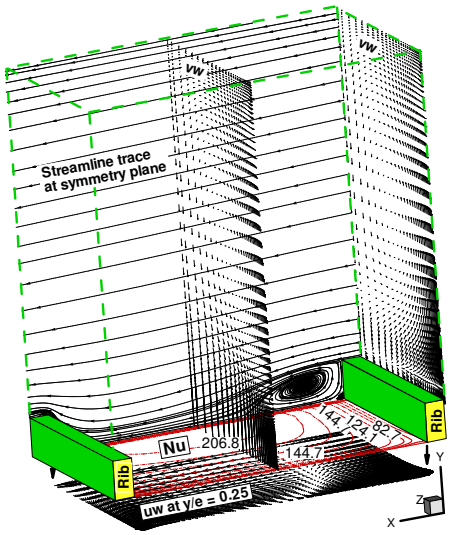

Figure 1. Flow and thermal fields for a ribbed duct.

CFD is particularly useful in the initial design steps reducing the number of testing of prototypes and providing a good insight in the transport phenomena occurring in the heat exchanger. Also heat exchanger optimization is important for process intensification and here also CFD can be a helpful tool. Failure investigation is another opportunity. For severe situations where very high pressure prevails, very hot or cold or toxic fluids are involved, quick results are needed, accurate CFD tools would be ideal.

CFD can be applied to heat exchangers in different ways. One way is to model the entire heat exchanger or the heat transferring surface. This can be done by using large scale or relatively coarse computational meshes or by applying a local averaging or porous medium approach. For the latter case volume porosities, surface permeabilities as well as flow and thermal resistances have to be introduced. The porous medium approach was first introduced by Patankar and Spalding [9] for shell-and-tube heat exchangers and has later been followed up by many others and not only for shell-and-tube heat exchangers.

Another way is to identify modules or group of modules which repeat themselves in a periodic or cyclic manner in the main flow direction. This will enable accurate calculations for the modules but the entire heat exchanger including manifolds and distribution areas are not included. The idea of streamwise periodic flow and heat transfer was introduced by Patankar et al. [10] and has been successfully followed up by many investigators.

Nowadays, there are a number of software packages available and CFD codes are introduced to various extent in industries. To be successful in application of CFD methods for engineering tasks it is required that experience and understanding exist for the physics of transport phenomena and fundamentals of numerical algorithms and turbulence modeling. Without these it is unlikely that the user will benefit extensively from the available commercial codes. Awarenesses of shortcomings and limitations are also important for successful application.

4. CONCLUSIONS

It is found that computational heat transfer methods of various kind, complexity etc. are useful tools if carefully handled. However, there are several constraints, difficulties and limitations to be aware of.

REFERENCES

[1] R.K. Shah and D. Sekulic, *Fundamentals of Heat Exchanger Design*, J. Wiley & Sons, New York, 2003.

[2] B. Sunden, Heat transfer and heat exchangers, *Kirk-Othmer Encyclopedia in Chemical Technology*, J. Wiley & Sons, New York, 2007.

[3] F.P. Incropera nd D.P. DeWitt, *Fundamentals of Heat and Mass Transfer*, 4th ed., J. Wiley & Sons, New York, 1996.

[4] H.K. Versteeg and W. Malalasekera, *An Introduction to Computational Fluid Dynamics, the Finite Volume Method*, 2nd ed., Pearson-Prentice Hall, New York, 2007.

[5] J.H. Ferziger and M. Peric, *Computational methods for fluid dynamics*, Springer-Verlag, Berlin, 1996.

[6] B. Sunden, Computational fluid dynamics in research and design of heat exchangers, *Heat Transfer Engineering*, Vol. 28, no 11, 898-910, 2007.

[7] B. Sunden, Computational heat transfer in heat exchangers, *Heat Transfer Engineering*, Vol. 28, no 11, 895-897, 2007.

[8] D.B. Spalding, Extending the boundaries of heat transfer, *James P. Hartnett Lecture, 13th Int. Heat Transfer Conference*, Sydney, Australia, 2006.

[9] S.V. Patankar and D.B.Spalding, A calculation procedure for transient and steady state behavior of shell-and-tube heat exchangers, In *Heat Exchanger Design Theory Source Book*, eds. N.H. Afgan and E.U. Schlunder, McGraw-Hill, New York, 1974.

[10] S.V. Patankar, C.H. Liu and E.M. Sparrow, Fully developed flow and heat transfer in ducts having streamwise-periodic variations of cross-sectional area, *ASME J. Heat Transfer*, Vol. 99, 180-186, 1977.

First International Conference on Computational Methods for Thermal Problems
ThermaComp2009, September 8-10, 2009, Napoli, Italy
N.Massarotti and P.Nithiarasu (Eds.)

THE APPLICATION OF NUMERICAL HEAT TRANSFER METHODS IN GEOLOGICAL SYSTEMS: NOVEL MOVING BOUNDARIES AND ANOMALOUS DIFFUSION

Vaughn R. Voller
Department of Civil Engineering, University of Minnesota, Minneapolis, MN 55455,
volle001@umn.edu

ABSTRACT

The objective of this paper is to highlight recent advances in modeling and understanding geological systems through the adoption and development of key concepts from the field of numerical heat transfer. The work reported was carried out in close collaboration with my student Jorge Lorenzo-Trueba and colleagues Chris Paola, Department of Geology and Geophysics, University of Minnesota and John Swenson, Department of Geology, University of Minnesota-Duluth. This work was supported by the STC program of the National Science Foundation via the National Center for Earth-surface Dynamics under the agreement Number EAR-0120914.

Key Words: *Heat Transfer, Geo-morphology Moving Boundaries, Anomalous Diffusion.*

1. INTRODUCTION

The governing equation for sediment transport and deposition, in a one-dimensional cross section of the landscape, is the Exner equation [1]

$$\frac{\partial h}{\partial t} = \frac{\partial}{\partial x}(q) - \qquad (1)$$

where h is the height of the land surface above a datum(sea-level), is the porosity of the deposit, is a subsidence/uplift rate, and q is a unit sediment flux (area/time). The sediment is moved and deposited across the land surface by water flows. Through a momentum balance, coupled to basic sediment transport laws, it is possible to show, for a variety of field and laboratory scenarios [2], that the sediment flux can be reasonably modeled by the diffusion law

$$q = - \frac{\partial h}{\partial x} \qquad (2)$$

where $= f(x)$ is the diffusivity. When the law in (2) is applicable, (1) essentially reduces to the Fourier heat conduction equation with a source term. In this way, a range of interesting and critical geomorphology problems can be molded using the tools and methods of numerical heat transfer. This not only provides a rich area of application for these tools but also leads to the derivations of problems and models that contain unique features and signatures not usually associated with traditional heat transfer problems. In this paper this aspect is illustrated via two examples.

2. EXAMPLES OF GEOLOGICAL PROBLEMS WITH HEAT TRANSFER ELEMENTS

In its simplest form the first example involves the filing of sediment, at a constant flux, into a body of water with a variable base bedrock topology. As time advances a sediment “wedge” is developed that advances into the body of water. The elements of this problem are illustrates in Figure 1.

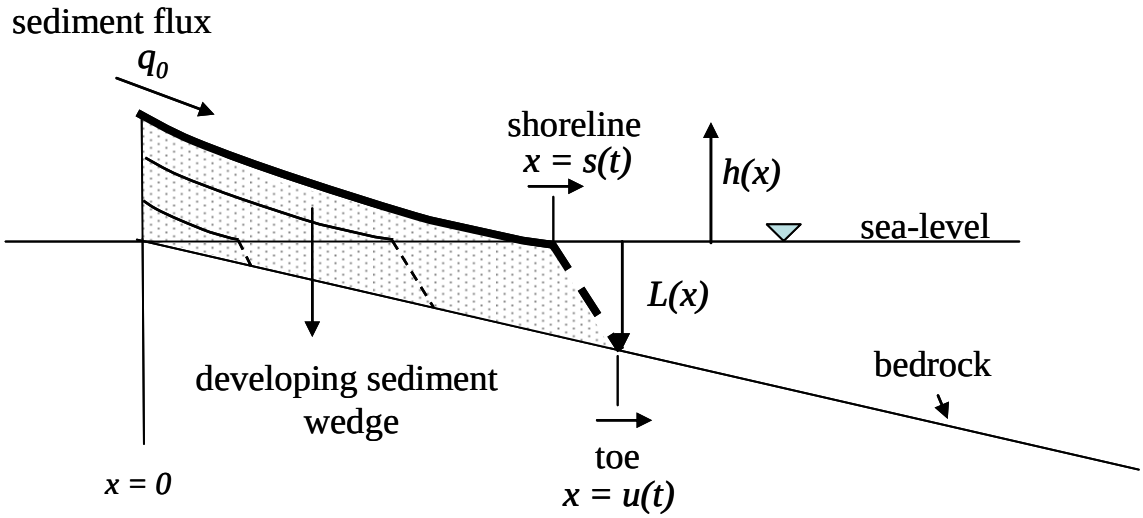

FIGURE 1. Schematic of sediment wedge advancing into a body of water with variable topology.

At time $t = 0$ a constant sediment flux q_0 is introduced into the system at $x = 0$. This flux deposits into the ocean to form sediment wedge with subaerial (fluvial) and submarine portions. As time increase the shoreline, $s(t)$—the wedge vertex marking the transition between the subaerial and submarine sediment—advances into the ocean. At the same time, the height of sediment at the origin increases from its initial value of $h(0) = 0$. If submarine sediment transport processes are assumed to maintain a constant slope for the submerged front of the sediment wedge (dashed line in Figure 1) and subsidence is neglected, the problem of tracking the advance of the shoreline can be stated as follows. Sediment transport and deposition in the subaerial fraction of the domain is described by

$$\frac{\partial h}{\partial t} = \frac{\partial}{\partial x}\left(\frac{\partial h}{\partial x} \right), \qquad 0 \le x \le s(t) \tag{3}$$

with boundary conditions $\partial h/\partial x = -q_0$ at $x = 0$ and $h = 0$ at $x = s(t)$. An additional condition resulting from the mass balance of sediment at the shoreline $s(t)$ is [3]

$$-\frac{\partial h}{\partial x} = (u - s)\frac{ds}{dt} \tag{4}$$

Equations (3) and (4) can be seen to have an immediate connection to the classic one-phase Stefan melting problem. As such the extensive numerical heat transfer tools (enthalpy, deforming mesh, coordinated transformation, level set, heat balance integral, etc.,) can be used to arrive at methods to track the advance of the shoreline $x = s(t)$. Recognise, however, that the condition (4) represents a unique modification over the standard Stefan condition. In the standard condition the latent heat term L is a constant. In the sediment wedge problem however $L = (u - s)$, i.e., it is a *function of position*. In fact, if subsidence/sea-level rise was also included in the model the latent heat term would be a function of both *space and time*. This condition, along with other geological considerations, leads to fascinating behaviours such as (i) the appearance of multiple moving boundaries where vertices of the sediment wedge can move both seaward and landward [2], and (ii) boundaries that can reverse in direction [3]. A range of experimentally validated analytical and numerical solutions [2-4] have been developed for this general moving boundary problem. An example of a case with multiple moving boundaries is illustrated in figure 2. This figure shows predictions for a fixed grid enthalpy like solution for a two-dimensional version of the problem in

Figure 1. In this solution two moving fronts need to be tracked, the shoreline advancing out into the ocean and the landward moving alluvial/bedrock transition, the line where sediment begins to deposit on the bed-rock. As described in [3] the phenomenon of boundary reversal occurs when subsidence is important. In this situation, an ever increases amount of sediment needs to be provided to maintain the system. This eventually results in a starving of sediment supplied to the shore that can only be fed by a reversal of the shoreline movement.

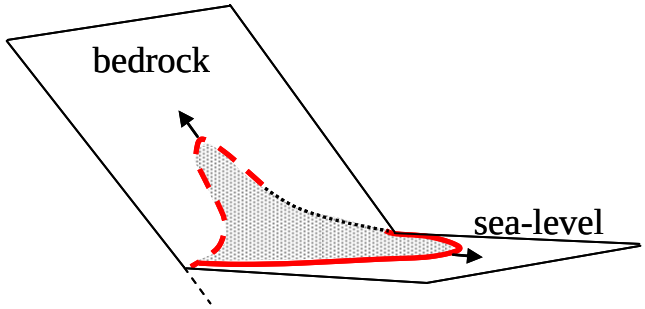

FIGURE 2. Subaerial fraction of an ocean delta forming on constant sloping bedrock: Note two moving fronts; (i) an advance of the delta shoreline to the right (solid line) and (ii) the repositioning of the alluvial bedrock transition up the bedrock slope (dashed line) to the left.

The second example of an interesting numerical heat transfer application in geomorphology relates to anomalous diffusion. Up to this point, all the examples presented assume the sediment transport is via diffusion, i.e., the sediment flux is proportional to the local slope of the landscape, $\partial h / \partial x$ (h-height of landscape above a datum). There are good arguments, however, that suggest, in some cases, that sediment transport is via anomalous diffusion where, for example, the flux is related to a fractional slope $\partial^{\alpha} h / \partial x^{\alpha}$, $0 < \alpha < 1$. Such diffusion forms are not readily amenable to basic numerical heat transfer methodologies. One approach, however, is to use a Monte Carlo simulation. Typical Monte Carlo heat transfer simulations are based on the random-walk analogy with heat diffusion. In application, the steps in the random walk are chosen from a normal distribution with decaying vanishing tails. This Monte Carlo approach can be extended to the anomalous diffusion by selecting the steps from random walks from an alternative PDF (associated with the fraction α) which has decaying but non-vanishing "thick" tails—representing the non-local behavior of the diffusion. Figure 3 shows recent simulations [5] using this Monte Carlo approach to predict the fluvial surface shape for a steady-state diffusion transport problem.

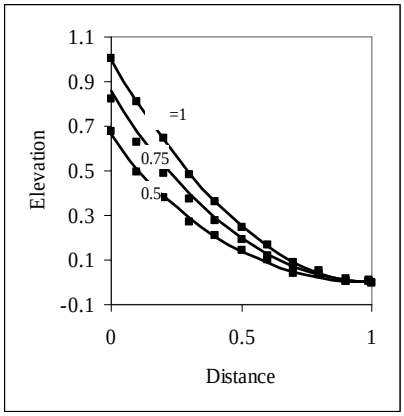

FIGURE 3. Fluvial profiles solution of steady-state fractional diffusion equation, solid lines analytical solution, points Monte Carlo Solution.

4. CONCLUSIONS

Thos short paper has illustrated two current problems in the modelling and understanding of geomorphology systems that can be readily resolved using the techniques and methods of numerical heat transfer. In many ways the problems are just reveal the “tip of the iceberg” in terms of the research opportunities to apply numerical heat transfer techniques to problems in geomorphology.

REFERENCES

[1] C. Paola, and V.R.Voller, A generalized Exner equation for sediment mass balance, *J. Geophys. Res.,* 110, F04014, doi:10.1029/2004JF000274, 2005.

[2] J. Lorenzo Trueba, V. R. Voller, T. Muto, W. Kim, C. Paola, and J. B. Swenson, A similarity solution for a dual moving boundary problem associated with a coastal-plain depositional system, *J. Fluid Mechanics*, 628, 427-443, 2009.

[3] J.B. Swenson, V.R. Voller, C. Paola, G. Parker, and J. G. Marr, Fluvio-deltaic sedimentation: A generalized Stefan problem, *Eur. J. Appl. Math.* 11, 433-452, 2000.

[4] V.R. Voller, J.B. Swenson, W. Kim, and C. Paola, An enthalpy method for moving boundary problems on the earths surface, *Int. J. Heat and Fluid Flow* 16, 641-654, 2006.

[5] V.R. Voller, and C. Paola, Can anomalous diffusion describe depositional fluvial profiles? *J. Geophys. Res.,* In Review, 2009.

MINI-SYMPOSIA

First International Conference on Computational Methods for Thermal Problems
ThermaComp2009, September 8-10, 2009, Napoli, Italy
N.Massarotti and P.Nithiarasu (Eds.)

NUMERICAL ANALYSIS OF CONVECTIVE HEAT TRANSFER ENHANCEMENT IN HELICAL TUBES

Sara Rainieri*, Fabio Bozzoli, Linda Schiavi and Giorgio Pagliarini
Department of Industrial Engineering, University of Parma
V.le Usberti 181/A 43100 Parma - Italy.
*e-mail: sara.rainieri@unipr.it

ABSTRACT

The convective heat transfer in helical tubes is numerically investigated with the aim of evaluating the enhancement effect associated to the swirl flow regime. The effect of the geometrical parameters, and of the Swirl and Reynolds numbers as well, on both the thermal and the velocity boundary layer and then on the Nusselt number is analysed in order to provide heat transfer correlations capable of predicting the thermal performance of the geometry.

Key Words: *Enhanced Heat Transfer, Convective Heat Transfer, Swirl Flow, Helical Tubes.*

1. INTRODUCTION

Regarding to forced internal flow in single-phase systems, a widely used passive heat transfer enhancement technique is based on wall corrugations which are expected to act on the boundary layer by producing significant benefits to the local heat transfer coefficient. A method which has revealed particularly attractive consists in helical repeated corrugations which are performed by cold working on a thin metal wall. These surface roughnesses produce a single or multiple helical profile which may result in a good heat transfer enhancement without severe pressure drop and fouling factor penalties.

Most of the available data about this type of tubes deal with turbulent forced flow of single-phase Newtonian fluids, see, for instance, [1,2]. In these conditions, a significant heat transfer augmentation (up to 300 percent increase over the smooth tube) is reported. It is widely accepted in literature (see for instance [3]) that the augmentation mechanism related to wall corrugation is due to several reasons, among which the augmentation of the heat transfer surface, the periodic disruption of the boundary layer, that forms on the heat exchange surface, by increasing the temperature gradient at the wall, the induced secondary flows which promote the mixing in the boundary layer and the onset of instabilities in the flow which lead to an early transition to the turbulent flow.

From the analysis of the literature data on heat transfer enhancement in forced convection inside channels, it appears evident that the most important effect is related to the macroscopic mixing of the fluid, activated by the destabilization of the flow which leads to the transitional/turbulent regime. Consequently, when the flow is characterized by very low Reynolds numbers, like in highly viscous fluids, the surface corrugation is expected not to produce significant benefits to the energy transfer [4], since the onset of instabilities in the flow are prevented in these conditions. Therefore it can be concluded that the local disturbance due to the wall corrugation is accompanied by a significant heat transfer enhancement only if the transition flow regime is achieved.

The majority of the literature on passive techniques of heat transfer enhancement based on wall corrugation relies on experimental investigations. The results are then presented in terms of correlations which are of certain usefulness in the design of the heat transfer apparatuses but which are often not exhaustive for understanding the mechanisms responsible for the intensification of the heat transfer coefficient. Either the numerical or the analytical approach, when available, may

provide a better deal of insight into the flow structure. The detailed mapping of the flow velocity and temperature distributions allows to understand the connection between the overall heat transfer performance and the changes induced in the flow pattern by the shape of the surface, thus providing the necessary guidelines in order to optimize the heat exchanger's design. The numerical approach has been widely used to investigate the heat transfer in periodic wavy passages with various profiles, (see for instance [5,6,7,8]). This approach enables to correlate the wall geometry to the onset of flow instabilities which are responsible of the departure from the laminar regime. In relation to the transition, a heat transfer enhancement effect, which is explained as a consequence of the enhanced mixing between the core fluid and the fluid near the walls which periodically happens in the oscillatory and then unsteady quasi-chaotic regime, is reported.

When the flow conditions are such that the critical Reynolds number cannot be reached, because for instance of the strong effect of viscous forces as it may happen in the flow of fluid foods, the passive enhancing techniques which act on the hydrodynamic and thermal boundary layer by optimizing the fluid velocity and temperature profiles appear a suitable solution. In fact it is well-known [9,10] that the devices which are able to disturb the axial flow, by inducing tangential velocity components, bring positive effects to the heat transfer by locally increasing the heat transfer coefficient. These solutions, which generally produce a swirl flow regime, have been extensively considered in applied research for heat exchanger applications. Twisted tape, wire coil inserts or guided vane swirl generators belong to this category of passive enhancement techniques and they are widely used in applications dealing with the laminar flow of highly viscous liquids.

An alternative technique to obtain a swirl-type flow and thus modifications in the boundary layer able to intensify the convective heat transfer coefficient, is based on the curvature of the tube's wall [13]. This effect is for instance achieved by coiling the tube helically. The main factor affecting the flow pattern, and therefore the heat transfer performance of the geometry, is the swirl intensity, generally quantified by means of the Swirl number [11], defined as the ratio of the angular momentum flux to the axial momentum flux at a given cross-section. The Swirl number can be computed on a given cross section only if the velocity distribution is known. This can be hardly reconstructed by means of experimental measurements, and therefore, in the practical engineering approach, the Swirl number is often replaced by a design Swirl number, defined as the ratio of maximum (or average) tangential velocity to a maximum (or average) axial velocity ([12]). In fact, several empirical correlations are available for estimating the heat transfer performance in swirl flow conditions where the Nusselt number is expressed as a function of a design Swirl number and of the Reynolds number as well. In this contest, the analytical or numerical analysis appears as a powerful tool for understanding in detail how the curvature of the surface may affect the velocity and temperature boundary layers and therefore the heat transfer performance of the geometry. The numerical approach is here adopted to investigate the effect of the swirl flow regime on the heat transfer performance of a promising geometry [13] obtained by protruding a circular section helicoidally, that is by rototranslating a circular section eccentric with respect to the rotation axis.

2. GEOMETRY AND SOLUTION PROCEDURE

A module of a representative helical tube, completed by the definition of the important geometrical parameters, is reported in figure 1. The governing equations, that is the continuity, the momentum and the energy equations are here integrated numerically in time under the assumption of incompressible Newtonian and constant properties fluid and of periodically fully developed laminar flow both for what concerns the hydrodynamic and thermal problem. The numerical integration of this system of partial differential equations is performed within Comsol 3.5a© environment under the assumption of uniform heat flux density applied to the wall, that is by assuming the Neumann boundary condition for the thermal problem.

3. RESULTS

Five helical geometries characterized by a dimensionless eccentricity e/D equal to $\sqrt{2}/5$ and dimensionless helix pitch P/D equal to 4,5,6,7 and 8 have been here investigated in Reynolds number range 100÷600 for a Newtonian fluid having a unitary Prandtl number. The corresponding flow show a stable behaviour in the whole Reynolds number range investigated, thus confirming the effect of turbulence suppression of the wall curvature, as reported in [14]. Es expected, the resulting velocity distribution (reported with regards to the azimuthal component in figure 2) confirms the onset of a continuous swirl flow as a consequence of the torsion of the trajectories which the fluid particle are forced to follow. Moreover the secondary centrifugally induced pressure gradient forces the fluid in the core region to be swept outward and the fluid near the wall to be driven toward the core region. Therefore by increasing the Reynolds number the velocity profile departs from the parabolic shape, as shown by the data reported in figure 3, thus inducing two local maxima close to the wall. The Swirl number, reported in figure 4, increases with the Reynolds number by assuming a constant value depending, for a given helix eccentricity, on the dimensionless helix pitch. The Nusselt number, averaged over a module of the helical tube, is reported versus the Reynolds number divided by the dimensionless helix pitch in figure 5. As expected, the heat transfer performance of the helical tube, as a consequence of the increased velocity gradient near the wall, is enhanced in comparison to the straight tube for which the value of 48/11 holds for the asymptotic Nusselt number in the fully developed laminar flow regime. Helical enhanced tubes show then interesting heat transfer performances and they suggest convenient applications also for highly viscous fluids which are often treated under the laminar flow regime.

Acknowledgements: The financial support by MIUR (grant 2007) is gratefully acknowledged.

4. REFERENCES

[1] Withers J.G. Heat Transfer Eng 1980, 2, 43-50.

[2] Marto P.J.; Reilly R.J.; Fenner J.H. In Advances in Enhanced heat Transfer; Editor Chenoweth M.; Kaellis J.; Michel J.; Shenkman S.M.; ASME: New York, 1979.

[3] Garimella S.; Chandrachood V.; Christensen R.N.; Richards D.E. ASHRAE Transaction 1988, 94 (2), 1119-1131.

[4] Rainieri S.; Pagliarini G., Int J Heat Technol 1997, 15, 69-75.

[5] Wang G.; Vanka S.P. Int J Heat Mass Tran 1995, 38 (17), 3219-3230.

[6] Ničeno B. ; Nobile E. Heat Fluid Flow 2001,22, 156-167.

[7] Comini G.; Nonino C.; Savino S. Int. J Numer Methods Heat 2002, 12 (6),735-755.

[8] Rainieri S.; Bozzoli F.; Pagliarini G. Proc of 4th ICCHMT 2005, Paris-Cachan, France Paper No. 495.

[9] Berger S.A.; Talbot L. Ann Rev Fluid Mech 1983, 15, 461-512.

[10] Naphon P.; Wongwises S. Renew Sust Energ Rev 2006,10, 463-490.

[11] Ward-Smith A.J. Internal fluid flow: The fluid dynamics of flow in pipes and ducts, Clarendon Press: Oxford, 1980.

[12] Martemianov S.; Okulov V.L. Int J Heat Mass Tran 2004, 47, 2379-2393.

[13] Rainieri S. And Pagliarini G. Heat Transfer in Fluid Food Processing, in Progress in Food Engineering Research and Development. p. 131-173, Nova Science Publishers, Inc., New York, 2008.

[14] Hüttl T.J.; Friedrich R. Int J Heat Fluid Fl 2000, 21, 345-353.

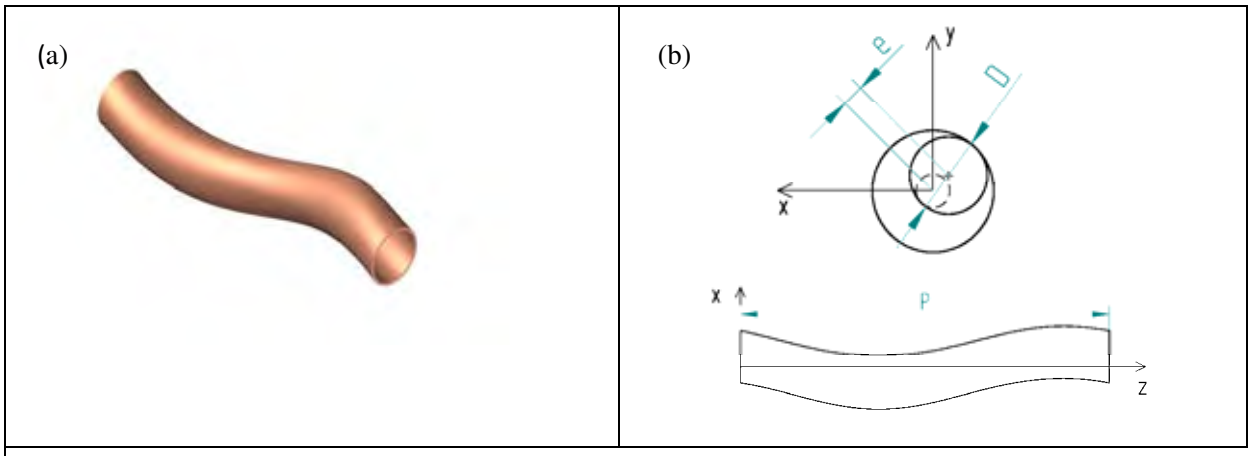

FIGURE 1. A module of the helical tube under test (a) and geometrical characterization (b).

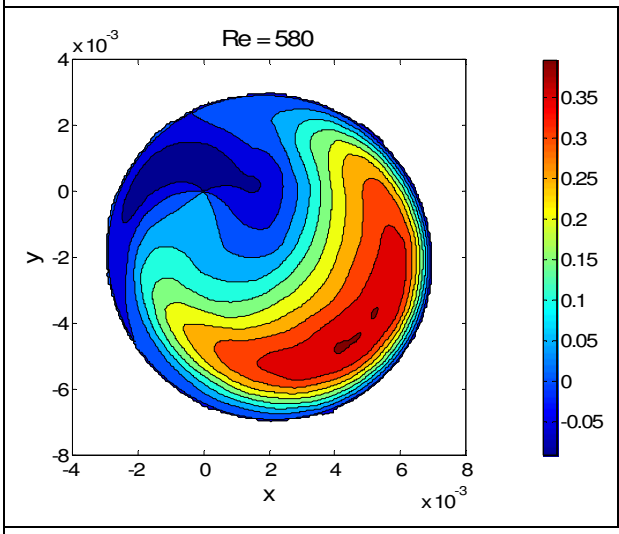

FIGURE 2. Distribution of the azimuthal velocity for Re=580.

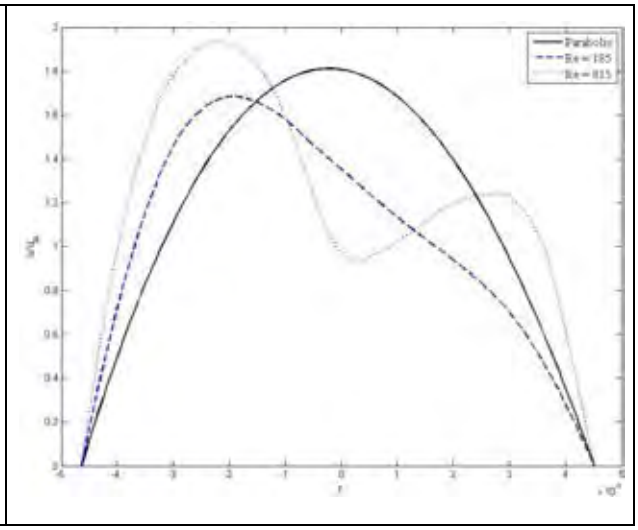

FIGURE 3. Dimensionless axial velocity distribution for different Re.

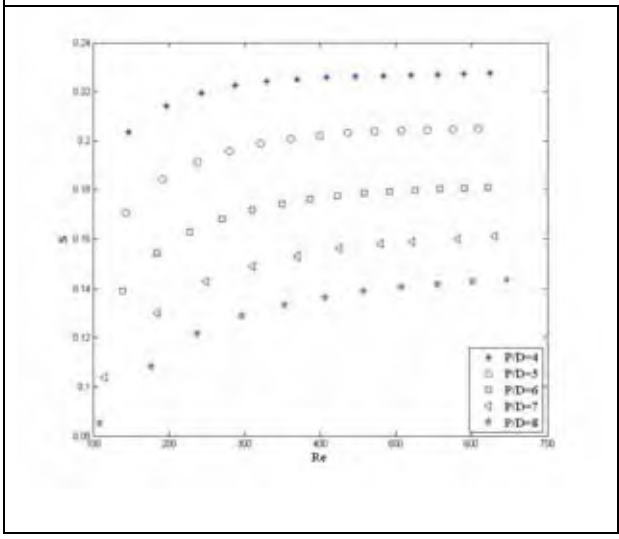

FIGURE 4. Swirl number for the helical tubes under test.

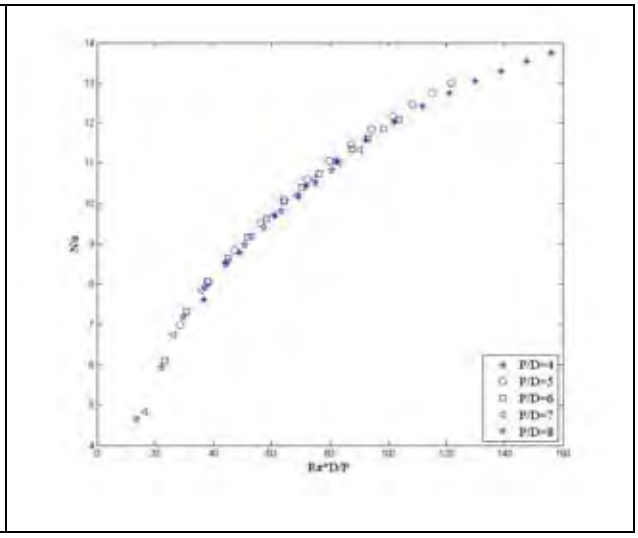

FIGURE 5. Average Nusselt number for the helical tubes under test.

First International Conference on Computational Methods for Thermal Problems
ThermaComp2009, September 8-10, 2009, Napoli, Italy
N.Massarotti and P.Nithiarasu (Eds.)

COUPLED CONDUCTION AND CONVECTION IN FIN ARRAYS FOR ELECTRONIC COOLING

Stefano Savino
Department of Energy Technologies, University of Udine,
Via delle Scienze 208, 33100 Udine, Italy, stefano.savino@uniud.it

Gianni Comini
Department of Energy Technologies, University of Udine,
Via delle Scienze 208, 33100 Udine, Italy, gianni.comini@uniud.it

ABSTRACT

A numerical analysis of conjugate heat transfer in a typical finned heat sink used for electronic cooling is carried out. The uniform thermal load, applied on the unfinned face of the base plate, is redistributed through conduction in the solid and concentrated toward the fin roots. The effect of such a redistribution is investigated for various base plate thicknesses and for different Reynolds numbers in the laminar regime. Most previous literature references for the same type of analysis rely on reduced computational domains with simplified boundary conditions of constant temperature or constant heat flux. In this work, such reduced models are compared with the fully conjugate heat transfer solutions and it is shown that, for common high conductive solid materials, the most appropriate simplified boundary condition is a Dirichlet boundary on the temperature.

Key Words: *electronic cooling, fin arrays, conjugate heat conduction and convection, numerical analysis, uniform heat flux boundary condition.*

1. INTRODUCTION

Typical heat sinks used for electronic cooling consist of an array of longitudinal fins attached to a common solid plate [1], as shown in figure 1a. The fins are relatively thick, being characterized by a ratio $_f / _b$ between the fin and the plate thickness of the order of 1. A fluid, very often air, flows through the channels formed by adjacent fins and the thermal load, applied on the unfinned face of the plate, is dissipated first through conduction in the solid and then through convection in the fluid. Thus, even if a uniform heat flux is applied, the conduction redistributes the heat flow lines leading to higher heat fluxes through the fin roots [2].

The numerical investigations of heat sinks have almost invariably disregarded the coupled conduction-convection problem, relying on a reduced computational domain with simplified boundary conditions of constant temperature or constant heat flux imposed on the plane where the fins are attached (see, for example: [3]). The accuracy of uniform temperature boundary condition applied directly to the fin bases has been recently investigated in the context of tube-fin heat exchangers utilized in air-conditioning [4]. The conclusion reached has been that constant temperature boundary conditions are quite acceptable for design purposes, since they lead to errors in the estimation of heat flow rates that are always less than 2%. In the tube-fin heat exchangers investigated, however, the unfinned (internal) side was heated or cooled by convection and the ratio $_f / _b$ between the thicknesses of the fin and the base (the tube in this instance) was quite small, of the order of 0.1 at most. Thus, it was inferred that with relatively low heating and cooling loads and small $_f / _b$ ratios, the fins perturb the thermal field only in very limited zones close to their roots. A different conclusion, in fact, was reached in an analysis of coolant passages with arrays of pin fins [5]. In this application, a relatively large constant heat flux was imposed on the unfinned face of the plate and the ratio $D_h / _b$ between the hydraulic diameter of the pins and the plate thickness was

relatively large (of the order of 1). Thus, conduction allowed for a significant redistribution of heat flow lines in the whole plate, leading to a far from constant heat flux on the plane where the fins were attached. Even in this case, however, temperature variations on the plane where the fins were attached remained relatively small. As a consequence, if a reduced computational domain (excluding the plate) was chosen to limit the computational effort, the fixed temperature boundary condition was found to be the most appropriate.

The aim of the present work is to evaluate the accuracy reached with a reduced computational domain and a uniform temperature boundary condition on the fin bases in the context of heat sinks consisting of an array of relatively thick longitudinal fins attached to a solid plate. To this purpose we assume constant heat flux boundary conditions on the unfinned face of the plate and we solve the resulting, fully conjugate, heat transfer problem. In the simulations we consider various $_f / _b$ ratios and different Reynolds numbers in the laminar regime. Three-dimensional simulations are carried out using an in-house FEM code. Results and comparisons are presented in terms of Nusselt number, heat flux concentration factor, and Biot number referred to the base plate thickness.

2. STATEMENT OF THE PROBLEM

The study considered here refers to an incompressible, laminar flow of air treated as a constant property fluid. The governing equations are the Navier-Stokes and the energy equations (not reported here for brevity). In the numerical simulations, the Navier-Stokes equations are solved only in the fluid region, while the energy equation is solved in both the fluid and the solid regions. Obviously, in the solution of the energy equation in the whole domain, we refer to the pertinent thermophysical properties in each region, and we assume a zero velocity field in the solid region.

Appropriate conditions are imposed on external boundaries. At the inflow, uniform velocity and temperature are prescribed, to simulate the thermal and hydrodynamic development of the air flow. On the unfinned surface of the base plate a uniform heat flux is prescribed, while the opposite surface is considered adiabatic, as shown in Figure 1a.

In the numerical solution, convergence to steady state is obtained through a pseudo-stationary process, employing an in-house FEM code whose reliability had already been demonstrated through examples of application concerning compact heat exchangers of different kinds [3-6].

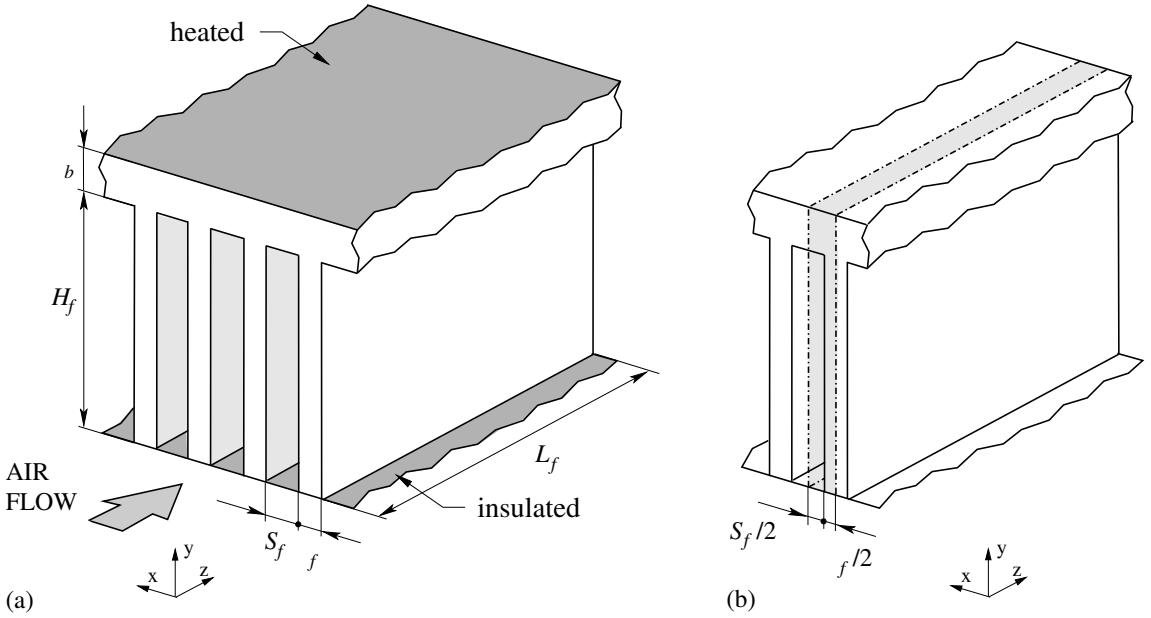

FIGURE 1. Schematization of a fin array (a) and the computational domain (b)

3. RESULTS AND DISCUSSION

The geometry analysed is represented in Figure 1a. It can be characterised by fin thickness $_f$, fin spacing S_f, fin length L_f, fin height H_f and base plate thickness $_b$. A single fin array geometry is considered, whose geometrical parameters, chosen with reference to a typical commercial heat sink, are: $S_f/\ _f = 1.5$, $H_f/\ _f = 8$ and $L_f/\ _f = 20$. The base plate thickness ranges from zero to $2\ _f$. Operating fluid is air, with a value of the Prandtl number Pr = 0.71, and the solid material has a thermal conductivity k_s = 100 W/(mK). A constant heat flux q''_b is imposed on the unfinned surface of the base plate. Different laminar flows have been considered with frontal velocities u_f varying in the range from 0.5 m/s to 2 m/s that lead to Reynolds numbers: $\mathrm{Re}_{Lf} = u\ L_f /$ (referred to the fin length L_f and to the mean fluid velocity u) ranging from 5,500 to 22,000.

Using existing symmetries, the computational domain can be reduced to the shaded region in Figure 1b, encompassing both the fluid and the solid regions. Final grids, made of hexahedral, non-uniform, structured elements, present a number on nodes ranging from a minimum of 110,352 (for $_b = 0$) to a maximum of 139,392 (for $_b = 2\ _f$).

As an example, Figure 2a shows the temperature field in the solid region of the domain (fin and base plate) in four different transverse sections for $_b/\ _f = 2$ and u_f = 1.0 m/s. The temperature field development from inlet to outlet, and its perturbations close to the fin root, can be clearly seen. In Figure 2b, temperatures on the horizontal planes $y = H_f$ (at the base fin) are shown for different base plate thicknesses; temperature variations are smaller for larger values of $_b$, due to the heat flux redistribution in the solid base.

As expected, the value of the average heat flux q''_f through the fin base is higher than the imposed constant value of the heat flux q''_b on the unfinned surface of the base plate. The concentration factor q''_f/q''_b is plotted in Figure 3a versus the ratio $_b/\ _f$. As remarked, simplified approaches neglect the base plate and impose boundary condition on the fin base plane. However, for a heat flux boundary condition, obviously we get $q''_f/q''_b = 1$, and thus we completely miss the concentration effect. On the contrary, as shown in Figure 3a , a physically reasonable result is given by the fixed temperature boundary condition.

The global thermal resistance can be considered as the sum of the equivalent convective resistance through the fluid and the solid (including the fins) and the conductive resistance through the base plate.

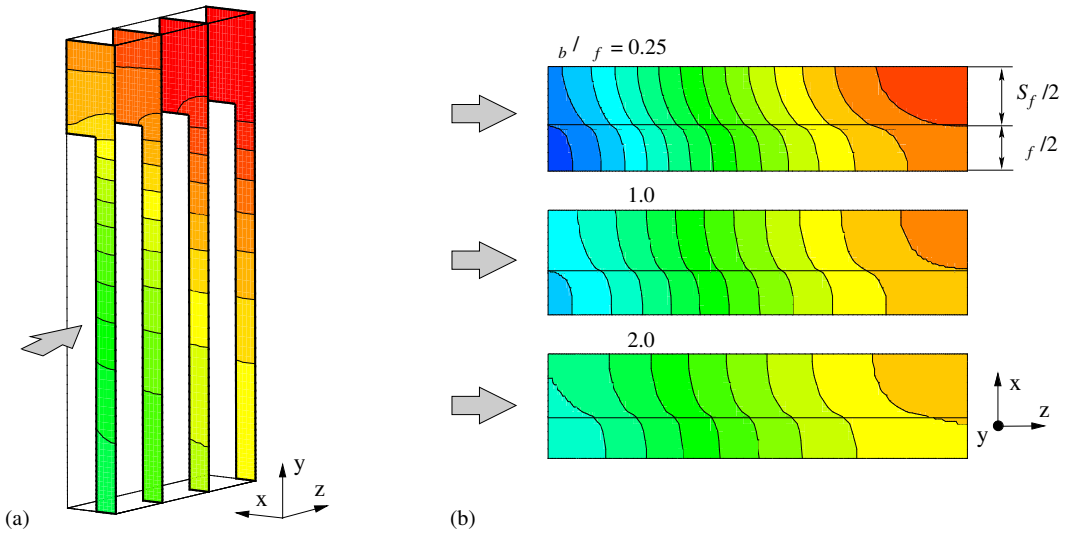

FIGURE 2. Temperature fields: (a) in the solid region for $_b/\ _f = 2$ and u_f = 1.0 m/s and (b) at $y = H_f$ for different values of $_b/\ _f$ and u_f = 1.0 m/s (figures not to scale in the z direction)

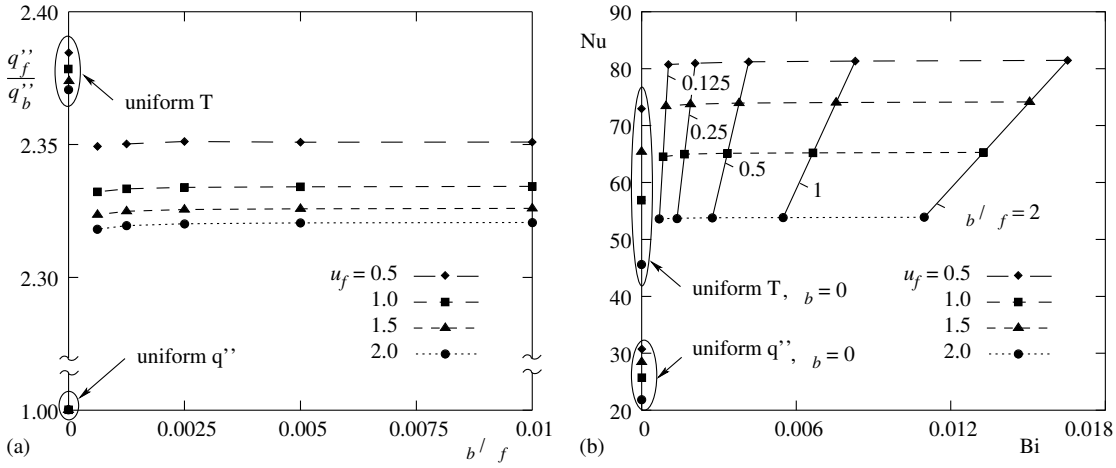

FIGURE 3. Concentration factor q''_f/q''_b versus $_b/_f$ (a) and Nusselt versus Biot numbers (b)

Therefore, we define the global thermal resistance U as the sum of two terms: $1/U = 1/h + {}_b/k_s$, where h is the equivalent convective coefficient of the fluid/fin system and ${}_b/k_s$ is the thermal resistance of the base plate. The total heat flux can be expressed as $q = UA\Delta t$, where the reference area A is the heated surface of the base plate and Δt is the log-mean temperature difference. Finally, the Nusselt number can be defined as $\mathrm{Nu} = (hD_h)/k_f$, where D_h is the hydraulic diameter of the fluid channel formed by adjacent fins. The Nusselt number takes into account the convective resistance of the fluid/fin system, and thus allows comparisons with the results of simplified solutions neglecting the base plate effect. The plot of the Nusselt number as a function of the base plate Biot number, $\mathrm{Bi} = (h\ {}_b)/k_s$, is reported in figure 3b. If we do not take into account the base plate to reduce the computational effort, the fixed temperature boundary condition yields again a quite reasonable approximation to the complete, fully coupled solution.

4. CONCLUSIONS

The conjugate heat transfer problem has been numerically solved in a typical finned heat sink used for electronic cooling. Results for different values of the base plate thickness have been presented in terms of Nusselt number and heat flux concentration factor. It was thus shown that a reduced computational domain with fixed temperature boundary conditions on the surface where the fins are attached yields results that are quite acceptable for design purposes.

REFERENCES

[1] F.P. Incropera, *Liquid cooling of electronic devices by single-phase convection*, Wiley, New York, 1999.

[2] B.W. Webb and S. Ramadhyani, Conjugate heat transfer in a channel with staggered ribs, *International Journal of Heat and Mass Transfer*, 28, 1679-1687, 1985.

[3] P. D'Agaro and G. Comini, Thermal performance evaluation of coolant passages with staggered arrays of pin fins, *Heat Mass Transfer*, 44, 815-825, 2008.

[4] G. Comini and S. Savino, Accuracy of one-dimensional design procedures for finned-tube heat exchangers, *Applied Thermal Engineering*, doi:10.1016/j.applthermaleng.2009.02.007, 2009.

[5] G. Comini, G. Croce and P. D'Agaro, Coupled conduction and convection in coolant passages with arrays of pin fins, CHT-08-233, ICHMT International Symposium on Advances in Computational Heat Transfer, May 11-16, 2008, Marrakech, Morocco.

[6] G. Comini, C. Nonino and S. Savino, Modeling of Coupled Conduction and Convection in Moist Air Cooling, *Numerical Heat Transfer, Part A*, 51, 23-37, 2007.

First International Conference on Computational Methods for Thermal Problems
ThermaComp2009, September 8-10, 2009, Naples, Italy
N.Massarotti and P.Nithiarasu (Eds.)

Numerical simulation of heat transfer between forced moist air and a flat plate with water condensation

Beatrice Pulvirenti
University of Bologna, Viale Risorgimento, 2, Bologna, Italy, beatrice.pulvirenti@unibo.it

Giampietro Fabbri
University of Bologna, Viale Risorgimento, 2, Bologna, Italy, giampietro.fabbri@unibo.it

ABSTRACT

The problem of heat transfer between forced moist air and a flat plate with water condensation is studied numerically by means of Fluent. The problem is modelled as a flow of a mixture of air and water vapour over a cooled vertical surface, with water condensation on the surface. The two-phase flow is modelled with a VOF model, with the gas flow flowing within a rectangular channel under a turbulent regime and exchanging heat with a cooled vertical surface. The water film or droplets creation on the surface is modelled by means of user defined functions (UDF) built *ad hoc*. The numerical solution is compared with experiments performed by Bozzoli *et al.* [1]. Local heat transfer coefficient is obtained in order to validate the UDF functions built to model source terms.

Key Words: *Computational heat transfer, water condensation, inverse heat transfer problem.*

1. INTRODUCTION

Film or droplets condensation occurs in various applications, such as heat exchangers in electronic cooling, automotive air conditioning, and refrigeration.
From the experimental point of view, the problem of condensation has been largely studied in the past few years. Cavallini et al. [2] dealt with condensation in a large range of tube section sizes and shape. Ad instance, they obtained the heat transfer coefficients for condensation of R134a inside multiport minichannels. Kim et al. [3] proposed a new technique to measure condensation heat transfer of R134a inside a smooth single tube. They found that the measured local heat transfer coefficients are close to the values predicted by the correlation of Shah for the lower mass fluxes. Koyama et al. [4] studied the condensation of refrigerant R134a in four kinds of multiport extruded aluminum channels. They measured the local heat transfer and pressure drop for smooth rectangular channels and for rectangular channels with straight microfins.
On theoretical side, a few studies have been conducted for condensation by means of numerical procedures. Zhang et al. [5] used the volume-of-fluid (VOF) method to simulate the capillary blocking in the convective condensation in horizontal tube channels. Comini et al. [6] dealt with the numerical simulation of moist air cooling in compact heat exchangers. They solved a coupled problem, with interface temperatures calculated at the same time as temperature distributions in adjacent fluid and solid regions. They solved energy equation in the whole domain, including the solid region, and the latent heat flux on the surfaces, where condensation occurs, is taken into account by means of an additional internal boundary condition.
The aim of this work is to study numerically the problem of heat transfer between forced moist air and a flat plate with water condensation. The problem is modelled as a flow of a mixture of air and water vapour over a cooled vertical surface, with water condensation on the surface. The water film or droplets creation on the surface is modelled by user defined functions (UDF) built *ad hoc*. The numerical solution is validated by a comparison with experiments performed by Bozzoli *et al.* [1]. Local heat transfer coefficient is obtained by numerical simulations and compared with experiments in order to validate the UDF functions chosen to model source terms.

2. MODELLING SETUP

The problem of heat transfer between forced moist air and a flat plate with water condensation is studied numerically by means of Fluent. The problem is modelled as a flow of a mixture of air and water vapour over a cooled vertical surface, with water condensation on the surface. The two-phase flow is modelled with a VOF model, with the gas flow flowing within a rectangular channel under a turbulent regime and exchanging heat with a cooled vertical surface. The water film or droplets creation on the surface is modelled by user defined functions (UDF) built *ad hoc*. For the phase change model it is assumed that:

- the condensation is homogeneous (i.e., no impurities are present to form nuclei);
- the droplet growth is based on average representative mean radii;
- the droplet is assumed to be spherical;
- the heat capacity of the fine droplet is negligible compared with the latent heat released in condensation.

The mass generation rate is modelled with two contributions for the droplets mass increase, the nucleation (the formation of critically sized droplets) and the growth/demise of these droplets. The expansion process is very rapid. Therefore, when the state path crosses the saturated-vapor line, the process will depart from equilibrium, and the supersaturation ratio will assume values greater than one. The condensation process involves two mechanisms, the transfer of mass from the vapor to the droplets and the transfer of heat from the droplets to the vapour in the form of latent heat. The formation of a liquid-phase in the form of droplets from a supersaturated phase is modelled by assuming the absence of impurities or foreign particles. The nucleation rate is modelled with source terms, added directly into momentum, energy, and scalar equations, by means of defined functions (UDF) for all the corresponding equations.
The numerical solution is validated by a comparison with experiments performed by Bozzoli *et al.* [1]. The experimental apparatus consists of a closed-loop wind tunnel, with a flow of air and water vapour up to the saturation point by the steam produced by a variable-power boiler. In order to regulate both the water vapour content and the temperature, the humid air stream is forced through a finned tube heat exchanger connected to a heat bath. It enters then into a settling chamber and then into a channel where the test section is arranged. On one vertical wall an aluminium plate is placed, with no geometrical discontinuities on the channels wall on which the aluminium plate is fitted. The test section is located downstream the channel inlet section, in order to assure that a fully developed boundary layer is achieved for the whole Reynolds number range under investigation. The temperature along three sides of the metallic fin is controlled by means of direct contact with a copper tube where a fluid coming from a circulator bath flows. The external surface of the metallic plate has been coated by a thin film of opaque paint with uniform and known emissivity. The surface temperature distribution has been acquired by means of an infrared thermographic system. When the infrared thermographic technique is adopted, like in the present investigation, some problems arise, due to the reduced detectors sensitivity at low temperatures shown by both cooled and uncooled sensors. The estimation procedure under question, based on the solution of the inverse heat conduction problem in the wall, has been here successfully adopted to estimate the local heat transfer coefficient for a humid air turbulent flow maintained at the saturation point, by considering three different Reynolds number values, ranging from 21000 to 35000. The heat transfer coefficient in wet condition is measured by means of an estimation technique of the local heat transfer coefficient, well established in single-phase conditions ([6]-[9]) and successfully applied to the two-phase convection problem which occurs when the water vapour carried by a humid air stream condenses on a cooled surface [9]. The interesting aspect of this estimation technique is related to the fact that it enables to recover the heat flux exchanged locally at the surface, while the majority of the experimental procedures available in literature regarding this argument enables to determine only spatially integrated heat transfer coefficient values.
The geometry considered for numerical simulations is a rectangular channel with the same dimensions of the test section in the wind tunnel described above, with a vertical cooled surface with the same dimensions. The same boundary conditions as those considered for experiments are imposed to the inlet flow and to the cooled surface. Local heat transfer coefficient is obtained by numerical simulations and compared with experiments in order to validate the UDF functions chosen to model source terms.

3. RESULTS AND DISCUSSION

First, numerical results without water condensation have been obtained, in order to compare the numerical single-phase heat transfer coefficient with experiments and with the literature. A good agreement has been found for air flow velocity u in the same range of the experiments, i.e. in the interval 8-13 m/s. The data obtained for average heat transfer coefficient, shown in Table 1, are in a good agreement both with experiments and with Dittus-Böelter correlation.

u (m/s)	h (W/m^2 K)	Dittus-Böelter
8	35	34.5
9	37	37.9
10	41	41.2
11	44	44.5
12	47	47.7
13	50	50.9

TABLE 1. Average heat transfer coefficient obtained without condensation

Then, water condensation model has been introduced. Figure 1 shows instantaneous temperature contours obtained for the case of air flow velocity u =13 m/s. Temperature profiles shown by the figure are on the cold plate, during droplets formation.

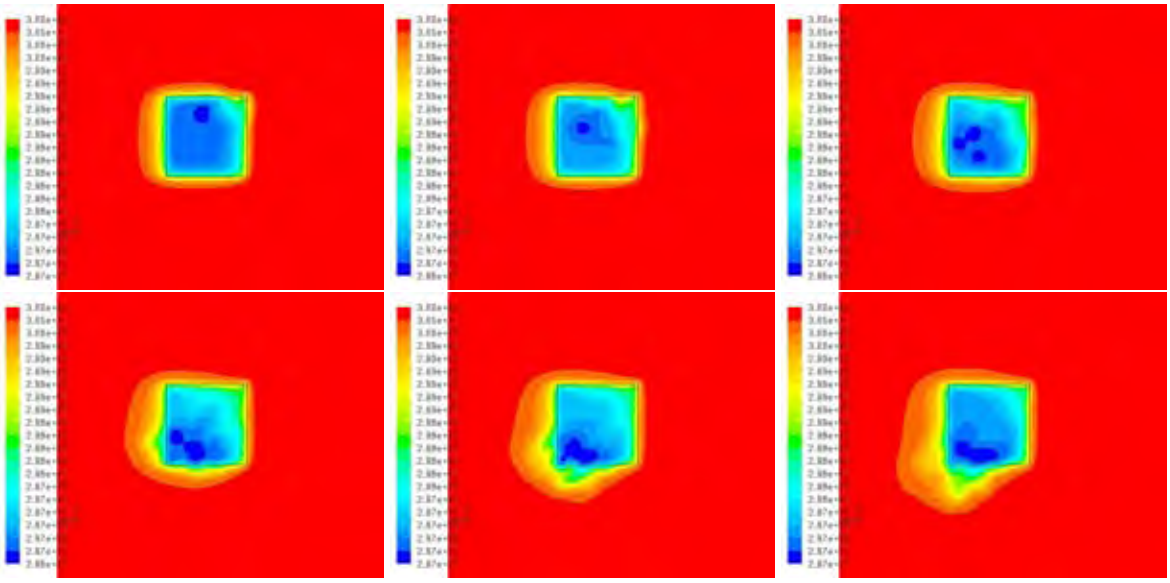

FIGURE 1. Temperature profiles (K) on the cold plate

The cold zones arise in correspondence of water droplets condensation. From temperature profiles, local heat transfer coefficients have been obtained. The results are plotted in Fig. 2, for the case of air flow velocity 13 m/s. In this figure, instantaneous plots of local h on the middle of the cold plate are shown. The condensation phenomenon improves heat transfer coefficient up to five times more than the case without condensation, as observed by Bozzoli *et al.* [1]. Also the averaged values obtained from the instantaneous plots shown by the figure have been found in a very good agreement with those measured by Bozzoli *et al.* [1].

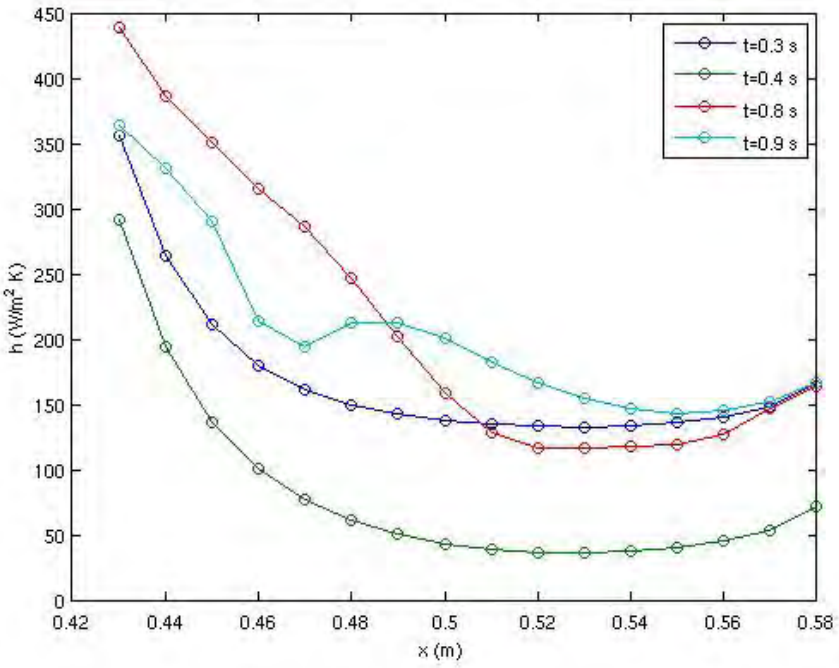

FIGURE 2. Local heat transfer coefficient

REFERENCES

[1] F. Bozzoli, S. Rainieri and G. Pagliarini: Estimation of the local heat transfer coefficient in forced convection of moist air in presence of water vapour surface condensation. *5th European Thermal-Sciences Conference*, The Netherlands, 2008.

[2] Cavallini A., Censi G. Del Col D., Doretti L., Longo G.A., Rosseto L.: Condensation heat transfer and pressure drop inside channels for AC/HP applicaiton. *12th Int. Heat Transfer Conference*, Grenoble, 2002.

[3] Kim M.H., Shin J.S., Huh C., Kim T.J., Seo K.W.: A study of condensation heat transfer in a single mini-tube. *First Int. Conference of Microchannels and Mini-channels*, Rochester, 2003.

[4] Koyama S., Kuwahara K., Nakashita K.: Condensation of refrigeratn in a multiport channel. *First Int. Conference of Microchannels and Mini-channels*, Rochester, 2003.

[5] Zhang Y, Faghri A., Shafii M.B.: Capillary blocking in forced convection two-phase flow. *Trans. ASME J. Heat Transfer*, vol. 123, pp. 501-511, 2001.

[6] Comini G., Nonino C. and Savino S.: Modeling of coupled conduction and convection in moist air cooling. *Numerical Heat Transfer*, vol. 51, pp. 23-37, 2007.

[7] Rainieri S. and Pagliarini G.: Data Filtering Applied to Infrared Thermographic Measurements Intended for the Estimation of Local Heat Transfer Coefficient. *Exp. Therm. Fluid Sci.* 26, pp.109114, 2002.

[8] Rainieri S., Bozzoli F. and Pagliarini G: Wiener Filtering Technique Applied to Thermographic Data Reduction Intended for the Estimation of Plate Fins Performance *Exp. Therm. Fluid Sci.* 28 Isuue 2-3, pp.179-183, 2004.

[9] Rainieri S. and Pagliarini: Thermographic Image Processing Intended for the Estimation of Local Heat Transfer Coefficient in Channel Flow Configuration *Proceedings of the 4th European Thermal Science Conference, Birmingham*, 2004.

[10] Rainieri S., Bozzoli F., Pagliarini G.: Experimental Inverse Estimation of the Local Heat Transfer Coefficient in External Forced Convection, *Proc. 6th World Conference on Experimental Heat Transfer, Fluid Mechanics, and Thermodynamics*, Matsushima, Japan, 17-21 April, 2005.

First International Conference on Computational Methods for Thermal Problems
ThermaComp2009, September 8-10, 2009, Napoli, Italy
N.Massarotti and P.Nithiarasu (Eds.)

FIRST NUMERICAL RESULTS ON FORCED-CONVECTION HEAT TRANSFER INSIDE A WAVY CHANNEL

Riccardo Mereu, Emanuela Colombo, Fabio Inzoli, Alfonso Niro
Dipartimento di Energia, Politecnico di Milano
Campus Bovisa, via Lambruschini, 4 – I-20156 Milano, Italy
alfonso.niro@polimi.it

ABSTRACT

This paper presents the first results of a numerical investigation on fluid dynamics and heat transfer characteristics of a forced air-flow inside a rectangular channel with the lower and upper walls wavy configured at Reynolds numbers ranging between 500 and 10000. The duct cross-section is 120 mm wide and 12 mm height whereas waviness have in streamwise direction a triangular profile of 68-mm pitch and 161° apex angle; the channel is operated with the wavy walls at fixed temperature and the side ones adiabatic. The numerical analysis is performed by means of a finite volume, commercial CFD code considering a three-dimensional fluid domain over a single module with periodic conditions; analysis over 6 modules and a 400-mm length, adiabatic inlet-duct are also performed. Results are compared with the data obtained by an experimental facility with the same geometry and operating conditions as the numerical model.

Key Words: *Heat Transfer, wavy channel, experimental approach, computational fluid dynamic, forced convection.*

1. INTRODUCTION

In designing compact heat exchangers, high values of heat transfer area per unit volume are looked for; however, increasing this parameter over a given value, thermal performances start worsening. Indeed, the higher the surface-to-volume ratio, the narrower the passages, and hence the air velocity has to be lowered to maintain acceptable pressure drops; in turn, narrow passages and low air velocities induce a laminar or weakly turbulent flow that is characterized by a quite poor convective coefficient which eventually defeats completely the area increase benefits. To overcome this limit, designer enhances heat transfer using specially configured extended-surfaces, such as offset or louvered or wavy fins, which are an efficient and cost-effective solution. These structured extended-surfaces modify the fluid dynamics by various mechanisms, such as periodic interruption of the boundary layer growth or periodic streamline deflection, and in addition they promote turbulence development as their characteristic size is close to the turbulent microscales (the lower the Reynolds number, the larger the size of dissipative structures).

As the shape of these structured extended-surfaces depends on the enhancement mechanisms employed, there is a large variety of geometries and consequently a large number of studies in the literature (Webb [1] reports near 40 papers). More precisely, several correlations deal with the offset and louvered fins (Joshi and Webb [2], Wieting [3], Davenport [4]), whereas the wavy-fin geometry is suffering from a some lack of data as well as of relevant correlations yet. For this reason, the authors are currently involved in an investigation on fluid dynamics and heat transfer characteristics of forced convection inside wavy channels. This paper reports on the numerical results on the convective coefficients and pressure drops of an air-flow inside a wavy channel, which reproduces geometry and operating conditions of an experimental facility; comparisons between numerical and experimental results are also presented.

2. NUMERICAL MODELLING

The wavy channel here investigated has a rectangular cross section whereas the corrugations, schematically showed in Figure 1, have in streamwise direction a triangular cross-section, with the apex on one wall coinciding with the throw on the other wall; it is noteworthy that corrugation dimensions, listed in the table also reported in the figure, are a scale modelling of a typical geometry used in compact heat exchangers with this kind of extended surfaces.

Geometry		
Duct width (W)	120	mm
Duct high (H)	12	mm
Aspect Ratio	10	
Wavy pitch (L)	68	mm
Hydraulic Diameter	21.5	mm
Corrugation angle ( )	161°	

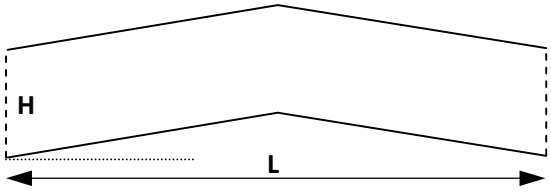

FIGURE 1. Geometrical characteristics of the wavy channel under analysis

The wavy channel experimentally investigated, which the present numerical analysis refers to, is 820 mm long, and hence there are 12 wavyness, and it is operated with the wavy walls at fixed temperature while the side ones being adiabatic. Upstream the wavy channel, there is an entry-section, which consists of a 400-mm long rectangular channel with the same transverse dimensions as the test section but with flat and adiabatic walls, in order to attain developed velocity conditions at the test channel entry. Room air flows through the test section by means of a blower operating in the suction mode since it is mounted as the last stage of the facility. Finally, air flow rates have been varied in order to investigate Reynolds numbers, based on the duct hydraulic diameter, between 500 and 10000.

From the modelling point of view, a three-dimensional fluid domain over a single module is used and considered as periodic, referred to as MODEL1, in order to reduce grid size and calculation time. Anyhow, to check the relevancy of the assumption of periodic conditions without taking into account neither the actual velocity-profile development of the air flow entering the test section during the experiments nor the consequent effects on thermal development, a second modelling approach is used which considers the entry section and 6 full periodicities without periodic conditions (MODEL2).

In both cases, the mesh strategy is based on a structured-like approach, as it can be seen from Figure 2, and the map scheme is used because almost orthogonal and uniform elements help in reducing numerical diffusion far as discretization is concerned. Special attention is also given, by means of a grading on the wall, to the boundary layer in order to properly capture the velocity and thermal profiles at wall. The total number of elements is almost 397,000 for the laminar cases and the MODEL1. For the turbulent cases, a further adaption up to 600,000 elements in the wall region was done in order to avoid wall functions. For the MODEL2 the mesh is obtained by repeating the mesh of the single corrugation.

The models are implemented and solved in a finite volume, commercial CFD code, i.e, FLUENT vers. 6.3.26. Due to the flow characteristics and the Reynolds number investigated, the Pressure Based solver is used and the SIMPLE algorithm is applied in velocity-pressure coupling. A second order scheme is used for the spatial discretization. A steady and unsteady laminar flow model is used for Reynolds number up to 1000 and a comparison between different two-equations RANS models is studied for the other Reynolds while keeping the same mesh size. A sensitivity analysis is computed on the grid, and the Grid Convergence Index is evaluated. The asymptotic convergence criterion for the mesh used is confirmed, and a numerical error band not greater than 10% for the turbulent cases and 1% for the laminar one was found.

Convergence is checked from both the numerical and physical point of view by using residual criterion, mass unbalance and by monitoring meaningful quantities stability.

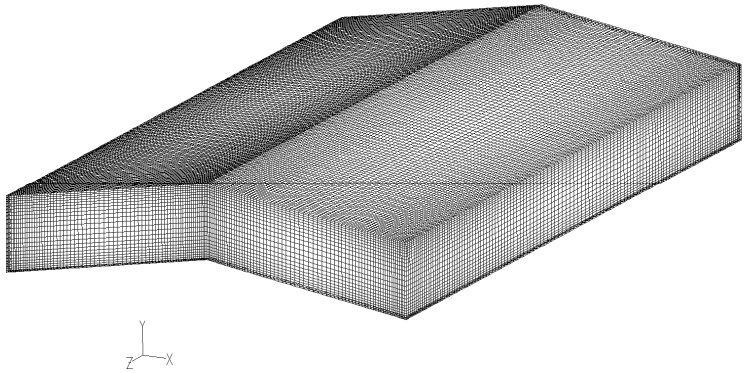

FIGURE 2. Model1: 3-D mesh

3. RESULT DISCUSSION AND CONCLUSIONS

Numerical results here reported are for Reynolds number ranging from 500 to 10000, and they are all grid independent; for Re>1000 a RNG k- turbulence model is used. Figure 3 (left) shows the per-module-average values of the Nusselt number, based on the hydraulic diameter as well, plotted versus the Reynolds number; for comparison, the figure also reports the corresponding values experimentally found. It is quite evident the laminar-turbulent transition starts at Re slightly greater than 1000. In laminar flow, numerical evaluations seem to be a 10% lower than the experimental one, but we have to take in mind they are obtained with the MODEL1 and therefore they are the thermally fully-developed values whereas the experimental Nu are values averaged over the entire test section which thus benefit of the entry region. Indeed, the Nu value found at Re=1000 with the MODEL2, which accounts for the first 6 modules, is quite coincident with the experimental datum. In transitional flow-regime, instead, numerical evaluations tend to slightly overpredict experimental values, but differences are within 20% while experimental uncertainties being around 10%. Anyway as Re increases, numerical and experimental values are again in good agreement. Heat transfer enhancement with a respect to a flat rectangular channel ranges between 20% and 60%. In Figure 3 (right) the apparent Darcy-Weisebach friction factor is plotted versus the Reynolds number.

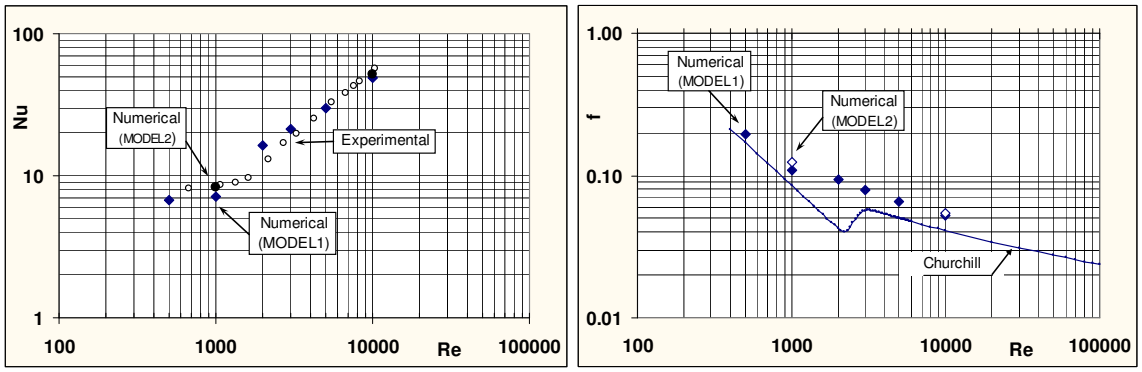

FIGURE 3. Per-module average Nusselt number (left) and Darcy-Weisebach friction factor (right) vs Reynolds number

Since at this time no experimental data are available yet, the figure reports as a light line the values calculated by means of the Churchill correlation adapted to a rectangular flat duct, with the same cross-section dimensions as the investigated channel, according to Shah and London. As it can be seen, there are no significant differences between the evaluations with the two models, and it is

confirmed that laminar-turbulent transition occurs for Re between 1000 and 2000. Penalization in pressure drops amounts to 30% on average.

Figures 4 and 5 report the velocity magnitude in the streamwise and spanwise directions, respectively, for Reynolds number of 1000 and 10000. Numerical results show the streamwise flow is deflected to the pressure-side wall and it separates on the peak corner while recirculation occurring inside the opposite corner, i.e., between the suction and pressure sides. The behaviour is more evident at low Reynolds numbers. Finally, it is noteworthy to highlight the wavy channel here investigated has some geometric characteristics, when compared to other wavy channels studied in the literature, that have to be taken into consideration. For instance, with respect to the channel considered by Hwang et al. [5] our channel has a wider cross section, a larger hydraulic diameter and, more important, a lower corrugation angle. This configuration, in some sense, is less critical than the Hwang's channel and it yields to a fluid dynamic behaviour more similar to the flat channel. This could explain why the Taylor-Görtler vortex pairs do not appear in neither the laminar and transitional cases. This consideration suggested to the authors a major parametric investigation with special attention to the corrugation angle which strongly effect fluid dynamic behaviour. The analysis is currently under processing.

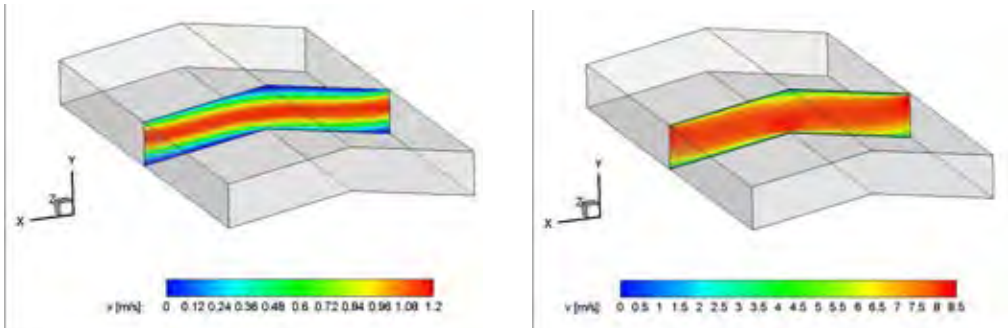

FIGURE 4. Velocity magnitude in the streamwise direction at Re 1000 (left) and 10000 (right)

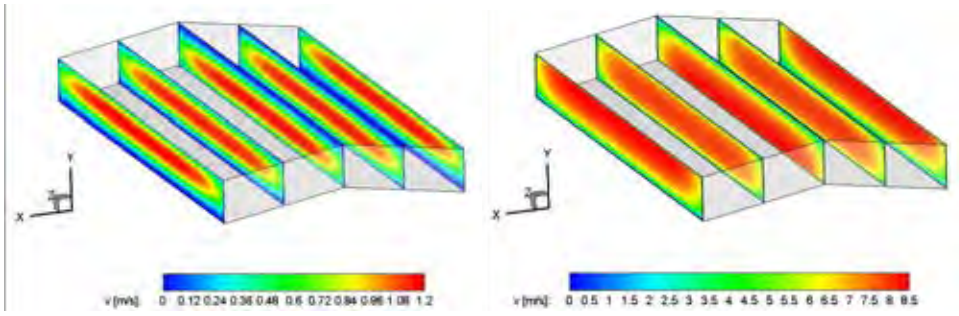

FIGURE 5. Velocity magnitude in the spanwise direction at Re 1000 (left) and 10000 (right)

AKNOWLEDGMENTS

This work is supported by MURST (the Italian Ministry for the University and the Scientific and Technicaal Research) via 2007 PRIN grants.

REFERENCES

[1] Webb, R.L., Principles of Enhanced Heat Transfer, John Wiley & Sons, cap. 9, pp. 228-284, 1994.

[2] Joshi, H.M., Webb, R.L., Prediction of heat transfer and friction in the offset strip fin array, Int. J. Heat and Mass Transfer, Vol. 30, No. 1, pp. 69-84, 1987.

[3] Wieting, A.R., Empirical correlations for heat transfer and flow friction characteristics of rectangular offset fin heat exchangers, J. Heat Transfer, Vol. 97, pp. 488-490, 1975.

[4] Davenport, C.J., Correlations for heat transfer and flow friction characteristics of louvered fin, Heat transfer-Seattle 1983, AIChE Symp. Ser., No. 225, Vol. 79, pp. 19-27, 1984.

[5] Hwang, S.D, Jang, I.H, Cho, H. H, Experimental study on flow and local heat/mass transfer characteristics inside corrugated duct, Int. J. Heat and fluid flow, 27 (2006) 21–32.

First International Conference on Computational Methods for Thermal Problems
ThermaComp2009, September 8-10, 2009, Napoli, Italy
N.Massarotti and P.Nithiarasu (Eds.)

NUMERICAL INVESTIGATION OF AIR FORCED CONVECTION IN CHANNELS WITH DIFFERENT SHAPED TRANSVERSE RIBS

Oronzio Manca
DIAM, Seconda Università degli Studi di Napoli, 81031 Aversa, Italy; oronzio.manca@unina2.it
Sergio Nardini
DIAM, Seconda Università degli Studi di Napoli, 81031 Aversa, Italy; sergio.nardini@unina2.it
Giuseppe Picardi
DIAM, Seconda Università degli Studi di Napoli, 81031 Aversa, Italy;
Daniele Ricci
DIAM, Seconda Università degli Studi di Napoli, 81031 Aversa, Italy; daniele.ricci@unina2.it

ABSTRACT

Heat transfer enhancement in fluids is very important in many industrial heating and cooling equipments. Convective heat transfer can be enhanced passively by adopting different solutions. A possibility for increasing the heat transfer with fluid is to employ extended surfaces. When a fluid flows in a channel, transversal ribs break the laminar sub-layer creating local wall turbulence but increasing pressure drops. In this paper a numerical investigation is carried out on air forced convection in a channel with constant flux applied on the external walls. Properties of fluid are considered temperature-dependent and flow regime is turbulent. Several shapes and arrangement of ribs are analyzed. The investigation is accomplished by means of the commercial code Fluent. The aim of this study is to find the shape and arrangement of ribs such to give high heat transfer coefficients and low pressure drops.

Key Words: *Heat Transfer, Forced Convection, Heat Transfer Enhancement.*

1. INTRODUCTION

Heat transfer enhancement technology has the aim to develop more efficient systems as demanded in many applications like heat exchangers for refrigeration, automotives, process industry, solar heater etc.. Bergles et al. [1] identified thirteen different techniques, segregated into two groupings: ‘passive’ and ‘active’ techniques. Passive techniques does not require external power supplies and employ special surface geometries, like coated surfaces, rough surfaces, swirl flow devices, fluid additives for enhancement [2]. The use of artificial roughness has been found to be as an efficient enhancement method. The ribs break the laminar sub-layer and create local wall turbulence due to flow separation and reattachment between consecutive ribs, which reduce thermal resistance and greatly augment the heat transfer. This behaviour overcomes the effect linked to the increased heat transfer area due to rib [3]. However, higher friction losses are expected and so turbulence must be created only in the region very close to the heat transferring surface and the core flow should not be unduly disturbed. Several experimental studies have been carried out but very few attempts of numerical investigation have been made due to complexity of flow pattern and computational limitations. Liou et al [4] have performed both numerical and experimental study the flow in a rectangular channel with periodic ribs mounted on one of the principal walls. Manca et al. [5] investigated the behavior of a rectangular channel with the heated walls provided with rectangular or square ribs at different dimensionless heights, pitches and Reynolds numbers.
The main target of the present analysis is to investigate the flow and the heat transfer characteristics of a two dimensional rib-roughned rectangular duct with the two principal walls subjected to uniform heat flux. The aim is to generate friction and heat transfer data, for different dimensionless pitches and Reynolds numbers in the range 20000-60000 for rectangular, triangular and trapezoidal shape.

2. NUMERICAL MODEL AND VALIDATION

A computational analysis of a two-dimensional rectangular duct model is carried out by means of the commercial code FLUENT. The length is 250 mm while the height is set equal to 10 mm and the hydraulic diameter, d_h, is 19.8 mm. The 3 mm thick wall is made up by aluminium and a constant heat flux equal to 10 kW/m^2 has been applied. On the duct wall ribs are introduced (fig. 1). Different fluid velocities are set at the inlet section and they vary in order to ensure Reynolds numbers in the range 20000 – 60000.

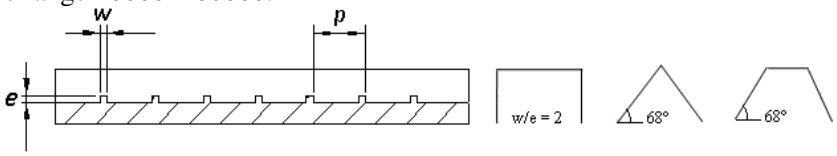

Figure 1 – Characteristic rib parameters.

Governing equations of continuity, momentum and energy are solved for a steady state turbulent flow and the *k- sst* turbulence model has been adopted. The working fluid is air and its properties are considered temperature-dependent. The considered roughness parameters are the height (*e*), the pitch (*p*), the width (*w*) and the shape of roughness elements. In this paper relative roughness pitches from 4 to 20 are considered and e/d_h is set equal to 0.05. A segregrated method is chosen to solve the governing equations and a second-order upwind scheme is chosen for energy and momentum equations. The SIMPLE coupling is chosen as scheme to couple pressure and velocity. The convergence criteria of 10^{-5} for the residuals of the velocity and energy components have been considered. It is assumed that the incoming flow is at a temperature equal to 300 K. Three different structured grid meshes are tested on ribs roughness, with p/e = 8, e/d_h=0.05 and w/e=0.5, to ensure that the calculated results are grid independent. They have 54600, 100100 and 185900 nodes, respectively. The second grid case has been adopted because it ensured a good compromise between the machine computational time and the accuracy requirements. The smooth model has been validated by comparing the obtained numerical data with the numbers calculated using the following correlations for Nu, f :

$$Nu_s = 0.024\,\mathrm{Re}_d^{0.8}\,\mathrm{Pr}^{0.4} \qquad (1)$$

$$f_s = 0.079\,\mathrm{Re}_d^{-0.25} \qquad (2)$$

Fig. 2 shows small percentage errors for the *sst k-* model both in terms of Nusselt number and friction factor.

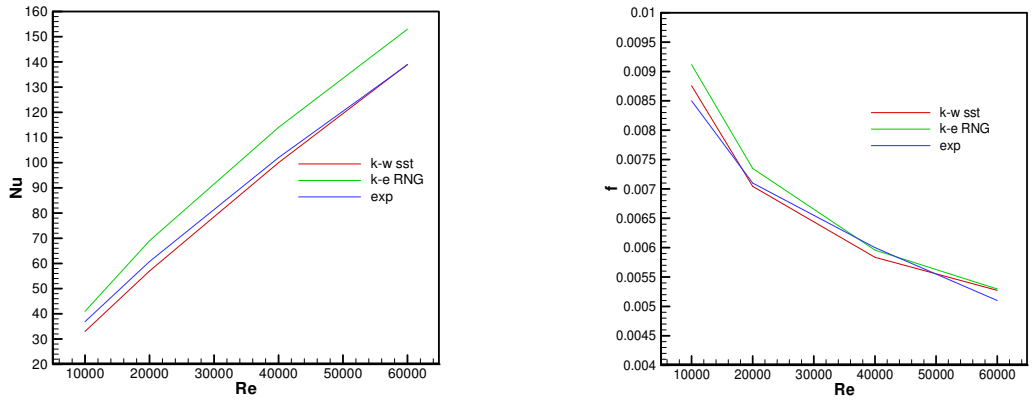

a) **b)**

Figure 2 – Validation of results: a) Nusselt number; b) friction factor.

3. RESULTS

Results show that Nusselt number increases as Re raises for all the considered configurations, as presented in figs. 3a and 4a. Nusselt numbers for triangular and trapezoidal ribs are, respectively, at least 1.58 times and 1.47 times higher than the smooth channel values. Triangular ribs ensures the

highest heat transfer coefficients; however, for both triangular and trapezoidal ribs the highest Nu are detected for p/e = 12 (fig. 3b). There are no significant differences among the solutions for different p/e ratios except for p/e = 4, where Nu is the lowest because the heat transfer is damaged by the very small distance between two adjacent cells. In fact, the rough behaviour associated to low pitches, called *d-rough* type, is observed. It is characterized by a single trapped eddy which hinders the heat transfer. For larger pitches the *k-type* behaviour is detected. The vortex length scale is comparable to the roughness height and the eddies characterized by a length scale of the order of roughness height are shed from roughness elements and penetrate into the bulk flow toward boundary layer. The friction factor increases as Re augments as shown in fig. 3c while for the trapezoidal ribs (fig. 4b) f tends to augment until Re = 40000 then it becomes constant attaining an asymptotic value which denotes the *fully rough* condition. It depends by the height of the roughness, in agreement with Moody chart. However, the value of the friction coefficient is almost six-times greater than one referred to the smooth case. Fig. 3d depicts the f profile depending on p/e ratio for the triangular ribbed channel. The highest value is detected for p/e = 10 for all the Reynolds numbers. This behaviour is observed for the trapezoidal ribs, too.
Figure 5 shows a comparison with rectangular ribs (w/e = 2) in terms of Nusselt number and f for p/e = 12 and p/e = 10, respectively. It is observed that this configuration expresses lower Nu and f. The Nu number is at least 4% lower and the asymptotic value of the fiction factor is about 0.118.

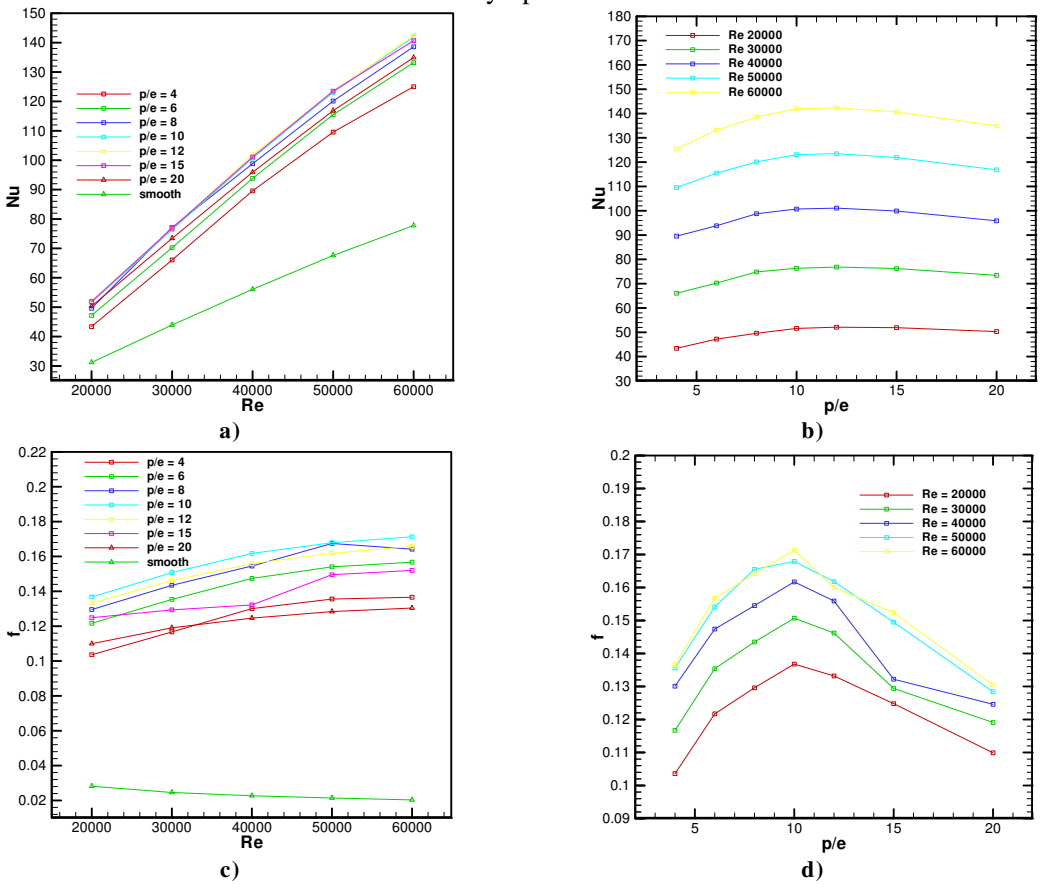

Figure 3 – Results for triangular ribs: a) Nusselt number depending on Reynolds number; b) Nusselt number depending on p/e ratios; c) friction factor depending on Reynolds number; d) friction factor depending on p/e ratios

4. CONCLUSIONS

In this work a 2-D rectangular duct with triangular, trapezoidal and rectangular ribs on the walls, heated by a constant heat flux equal to 10 kW/m^2 for e/d_h=0.05 and different pitches and Reynolds numbers was studied. The introduction of ribs augments both the heat transfer

coefficients, at most Nu = 1.84 Nu_s for triangular ribs, both friction coefficients, in comparison with a smooth duct. For both triangular and trapezoidal ribs, the highest Nusselt number was evaluated for p/e = 12, while regarding the friction coefficients, the maximum values were calculated for p/e = 10. Furthermore, it is shown that for trapezoidal ribs the friction coeffients are lower although the lowest values are detected for the rectangular ones. Nusselt numbers raise as Reynolds numbers increase. On the other hand losses augment although, for Re > 40000, f tends to an asymptotic value for the rectangular and trapezoidal shapes.

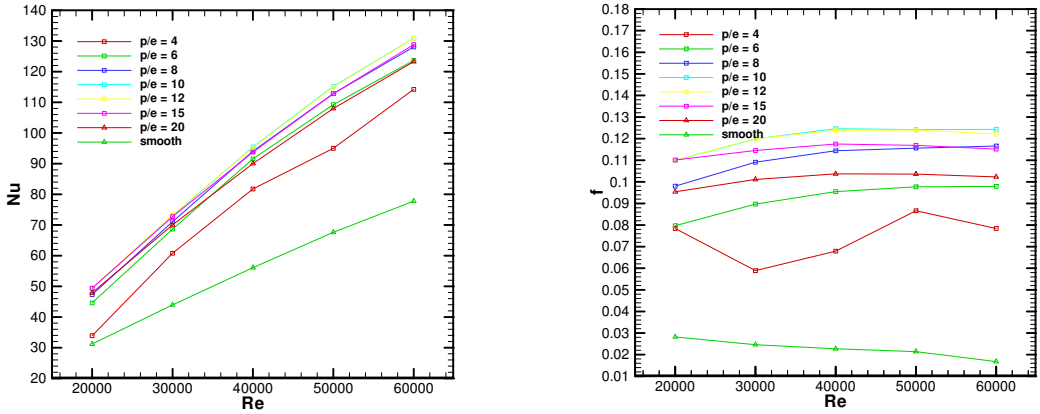

Figure 4 – Results for trapezoidal ribs depending on Reynolds number: a) Nusselt number; b) friction factor.

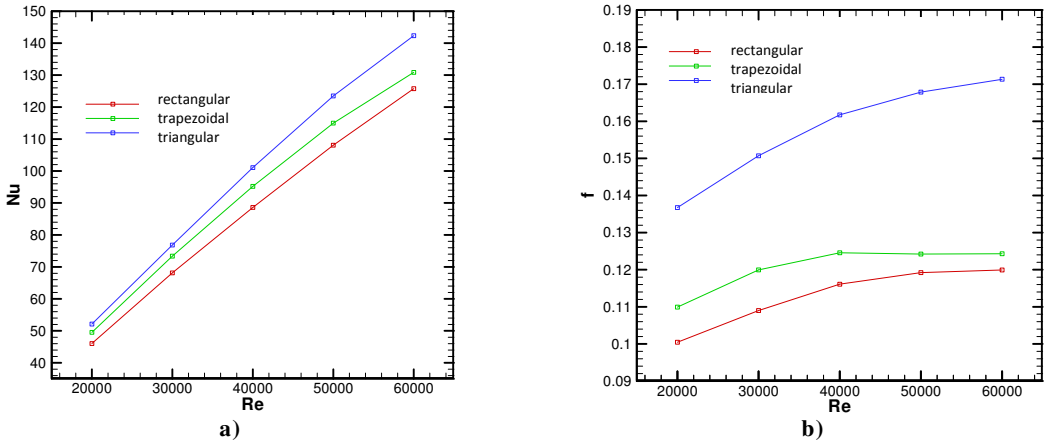

Figure 5 – Comparison with rectangular ribs: a) Nusselt number for p/e = 12; b) friction factor for p/e = 10.

REFERENCES

[1] A.E. Bergles, W.M. Rohsenow, J.P. Hartnett, E. Ganie, Techniques to augment heat transfer, *Handbook of Heat Transfer Application*, McGraw Hill, 1985.

[2] R.L. Webb, *Principles of enhanced heat transfer*, John Wiley&Sons, 303-319, 1994.

[3] C.K. Lee, S.A. Abdel Moneim, Computational Analysis of Heat Transfer in Turbulent Flow Past a Horizontal Surface with a 2-D Ribs, *International Communications in Heat and Mass Transfer*, 26, 161-176, 2001.

[4] T.M. Liou, J.J. Hwang, S.H. Chen, Simulation and measurement of enhanced turbulent heat transfer in a channel with periodic ribs on one principal wall, *International Journal of Heat and Mass Transfer*, 36, 507-517, 1993.

[5] O. Manca, G. Masullo, D. Ricci, Numerical investigation of air forced convection in channels with transverse ribs, *Proc. ASME IMECE Conference 2008*, Boston, 2008.

First International Conference on Computational Methods for Thermal Problems
ThermaComp2009, September 8-10, 2009, Napoli, Italy
N.Massarotti and P.Nithiarasu (Eds.)

FLUID FLOW AND HEAT TRANSFER IN WAVY CHANNELS WITH AND WITHOUT BAFFLES

Haitham M. S. Bahaidarah* Email: haithamb@kfupm.edu.sa
Islam A.A.Shabaneh Email: shabaneh@kfupm.edu.sa

*Dr. Haitham Bahaidarah, Assistant Professor, Department of Mechanical Engineering
King Fahd University of Petroleum and Minerals, P.O. Box 84 Dhahran, 31261 Saudi Arabia
966-3-860-1747 (Office), 966-3-860-2949 (Fax), 966-5-000-13450 (Mobile).

ABSTRACT

A two-dimensional steady developing fluid flow and heat transfer through periodic wavy passage (with and without baffles) will be numerically studied for a fluid with a Prandlt number of 0.7. The wavy walls will be studied for certain values of baffle length to module maximum height ratio. A representative runs will be made for different values of Reynolds number. The effect of each run on the velocity profile, streamline, and normalized temperature field will be compared to flow through a corresponding wavy walls channel without baffles. Domain disrectization will be carried out in body fitted coordinate system. The contravariant components of velocities will be used as the dependent variables. The governing equations will be solved using a finite volume technique. Fluent program is utilized to solve the problem. Grid independence study will be carried out and average Nusselt number and normalized pressure drop will be reported.

Key Words

wavy channel, heat transfer enhancement, vertical baffles

INTRODUCTION

Heat transfer enhancement is a matter of great importance in various engineering applications, especially those associated with compact heat exchangers. Flow interruptions provided by the corrugation patterns on the plate-surfaces in effect promote heat transfer enhancement in channels. The various applications considered in these types of studies include wavy-plate-fin cores [1-4], and dialysis devices and membrane oxygenators [5–10]. Numerous publications have been dedicated to the study of pioneering implementation of heat transfer enhancement strategies in compact heat exchangers [11-15]. One of the simplest geometry of the flow passage which is relatively easy to fabricate and can be used to enhance heat transfer, is the symmetrical corrugated or wavy walled channel. Of particular interest for a wide spectrum of usage in food, pharmaceutical, and chemical processing is the plate heat exchanger [16-18].

It has to be emphasized that the papers published in the literature are much related to each other in the aspect that they all consider symmetric wavy walls (triangular, sinusoidal, and arc-shaped wall). However, none of the above has probed a wavy channel with baffles the additional vertical baffles (X/L) as shown in Figure 1. The wavy channel with baffle will be studied for certain value of vertical baffles to module length ratio. Such an idea may have a considerable impact on the location of the recirculation size and strength which could affect the heat transfer augmentation.

The purpose of this study is to examine the effects of such change on the two-dimensional developing fluid flow and heat transfer characteristics.

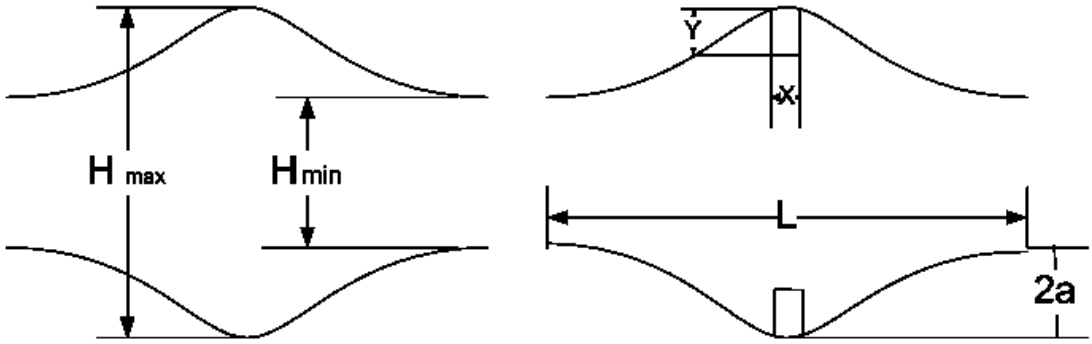

(a) (b)

Figure 1: Geometrical Flow Domains showing a wavy Channel with and without vertical baffles: (a) X/L = 0 and (b) X /L = 1/10.

DISCUSSION OF RESULTS

Representative results of (8) different parametric runs are presented in this work. The effect of each parameter on the velocity profile, streamline, normalized temperature field, normalized pressure drop, and module average Nusselt number will be discussed. Most of the cases attain periodically fully developed profiles downstream of the first module. Thus, discussion of the one of the interior module will be enough to show most of the details needed for examining the streamlines instead of showing the entire domain with dense repeated information. Figures 2 and 3 show the effect of Reynolds number on the non-dimensional stream function for one module for wavy channel with no vertical baffles and with vertical baffles, respectively.

When Reynolds number as low as 25 flow separation can hardly be detected. As Reynolds number increase, the separated flow covers a smaller portion of the domain until it completely covers the trough at higher Reynolds number. In fact, the entire area is occupied by recirculation for Re = 200 and 400, though the center of the recirculation is shifted slightly downstream closer to the next module at Re = 400. This significant difference is a result of a higher flow rate which pushes the recirculation further downstream.

Since the flow is attaining periodically fully developed behavior, it is clear that the values are nearly constant for a given Reynolds number. Therefore, it is reasonable to present the numerical data across one module as a function of the Reynolds number as shown in Figure 4 and 5. Minor variations were detected for the first and the last modules due to entrance and exit effects.

CONCLUSIONS

Fluid flow and heat transfer in periodic, corrugated wavy channels with and without vertical baffles have been numerically investigated for steady flow conditions using finite volume method for a fluid with Prandlt number 0.7, representative value for air. Flow attained periodically fully developed state and thermally periodically fully developed state downstream of the first module for all cases. Two different types of wavy geometry, wavy without vertical baffles and wavy with vertical baffles, were considered. The recirculation flow covers a smaller portion of the domain at lower Re values and it covers most of the domain at higher Reynolds numbers in case of no

vertical baffles. However, in case of vertical baffles, the recirculations take place at an upstream module due to the disturbance space available for the flow.

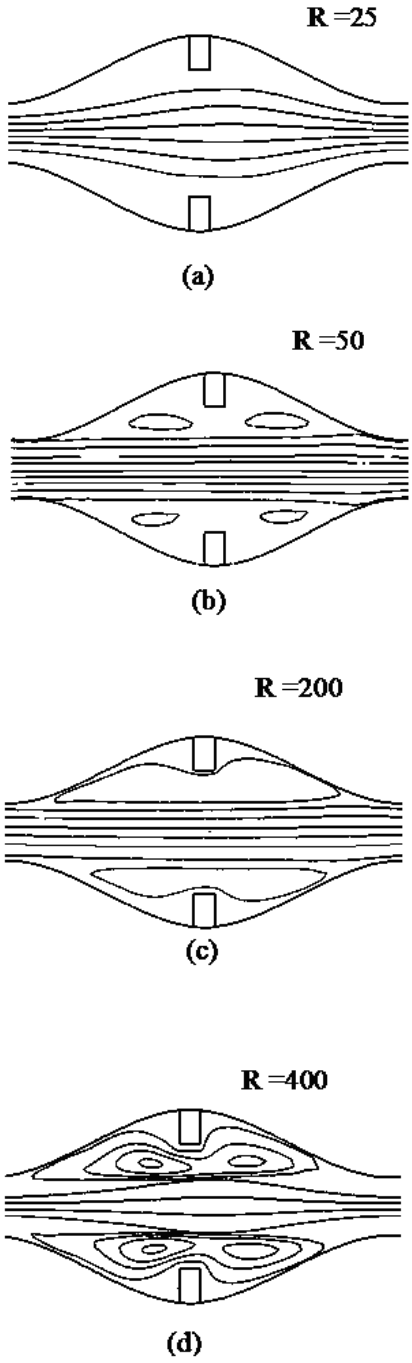

Figure 2: Effect of Reynolds number on the streamlines for one module of wavy channel configuration with vertical baffles.

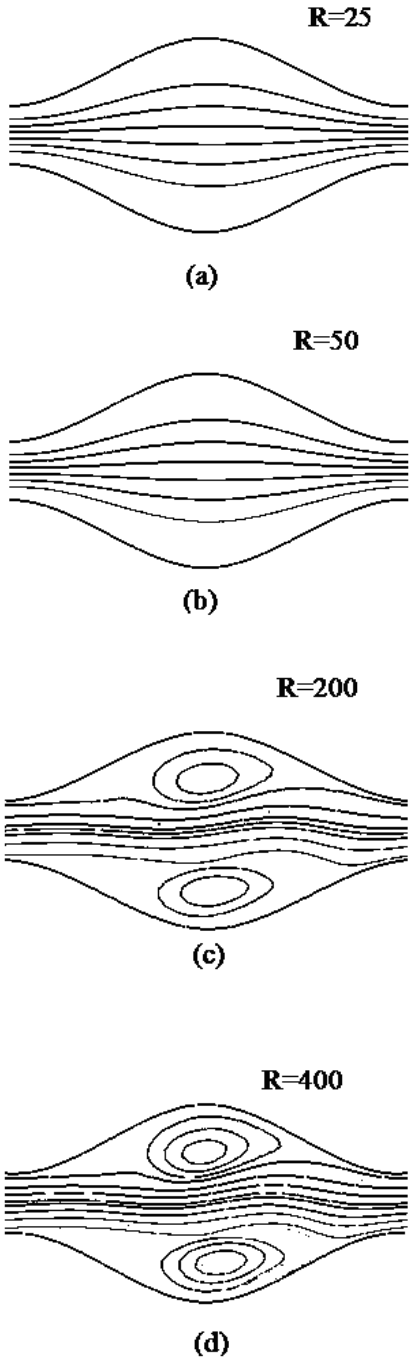

Figure 3: Effect of Reynolds number on the streamlines for one module of wavy channel configuration without vertical baffles.

Wavy channel without vertical baffles provide lower normalized pressure drop values when compared to wavy channel with vertical baffles. The module average Nusselt number monotonically increases as Reynolds number increases. However, it shows lower profile in the case of wavy channel without vertical baffles when compared to wavy channel with vertical baffles.

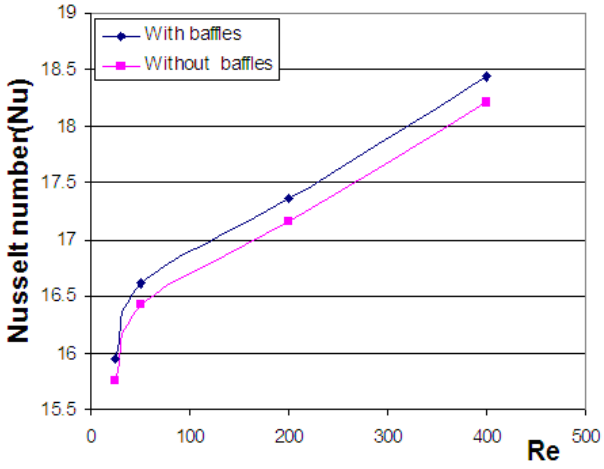

Figure 4: Effect of Reynolds number on Average Nusselt number (Nu) for the fifth module of both wavy channels with and without baffles.

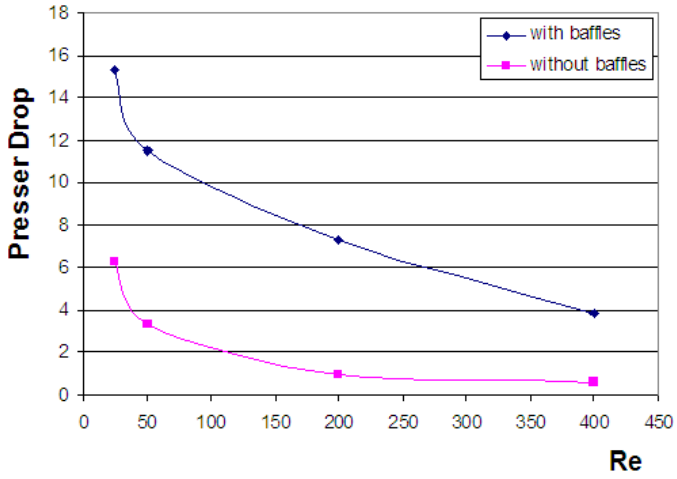

Figure 5: Effect of Reynolds number on Normalized Pressure Drop (PD) for the fifth module of both wavy channels with and without baffles

ACKNOWLEDGMENTS

Support for this research by King Fahd University of Petroleum and Minerals is gratefully appreciated.

REFERENCES

[1] J. E. O'Brien, and E. M. Sparrow, Corrugated-duct Heat Transfer, Pressure Drop, and Flow Visualization, J. Heat Transfer, vol. 104, pp.410-416, 1982.

[2] Y. Asako, and M. Faghri, Finite-volume Solution for Laminar Flow and Heat Transfer in a Corrugated Duct, J. Heat Transfer, vol. 109, pp.627-634, 1987.

[3] V. K. Garg, and P. K. Maji, Flow and Heat Transfer in a Sinusoidally Curved Channel, Int. J. Eng. Fluid Mech., vol. 1, No. 3, pp.293-319, 1988.

[4] L. C. Yang, Y. Asako, Y. Yamaguchi, and M. Faghri, Numerical Prediction of Transitional Characteristics of Flow and Heat Transfer in a Corrugated Duct, J. Heat Transfer, vol. 119, No. 1, pp.62-69, 1997.

[5] T. A. Rush, T. A. Newell, and A. M. Jacobi, An Experimental Study of Flow and Heat Transfer in Sinusoidal Wavy Passages, Int. J. Heat Mass Transfer, vol. 42, pp.154101553, 1999.

[6] B. J. Bellhouse, F. H. Bellhouse, C. M. Curl, T. I. MacMillan, A. J. Gunning, E. H. Spratt, S. B. MacMurung, and J. M. Nelems, A High Efficiency

Membrane Oxygenator and Pulsatile Pumping System, and its Application to Animal Trials, Trans. Am. Soc. Artificial Internal Organs, vol. 19, pp.72-78, 1973.

[7] T. Nishimura, Y. Ohori, Y. Kajimoto, and Y. Kawamura, Mass Transfer Characteristics in a Channel with Symmetric Wavy Wall for Steady Flow. J. Chem. Eng., Japan, vol. 18, pp-550-555, 1985.

[8] J. E. O'Brien, and E. M. Sparrow, Corrugated-duct Heat Transfer, Pressure Drop, and Flow Visualization, J. Heat Transfer, vol. 104, pp.410-416, 1982

[9] T. Nishimura, K. Yano, T. Yoshino, and Y. Kawamura, Occurrence and Structure of Taylor-Goertler Vortices Induced in Two-dimensional Wavy Channels for Steady Flow, J. Chem. Eng., Japan, vol. 23, No. 6, pp.697-703, 1990.

[10] T. Nishimura, S. Murakami, S. Arakawa, and Y. Kawamura, Flow Observation and Mass Transfer Characteristics in Symmetrical Wavy-walled Channels at Moderate Reynolds Numbers for Steady Flow. Int. J. Heat Mass Transfer, vol. 33, No. 5, pp-835-845, 1990.

[11] T. Nishimura, Y. Ohori, and Y. Kawamura, Y., Flow Characteristics in a Channel with Symmetric Wavy Wall for Steady Flow. J. Chem. Eng., Japan, vol. 17, pp-446-471, 1984.

[12] S. Kakac, R. K. Shah, and W. Aung, (Eds). Handbook of Single Phase Convective Heat Transfer, pp.17.1-17.62, Wiley, New York, 1980.

[13] R. L. Webb, Principles of Enhanced Heat Transfer, Wiley, New York, 1994.

[14] A. E. Bergles, Techniques to Enhance Heat Transfer, in W. M. Rohsenow, J. P. Hartnett, and Y.I. Cho (Eds.), Handbook of Heat Transfer, 2nd ed., McGraw-Hill, New York, 1998 (Chapter 11).

[15] R. M. Manglik, Heat Transfer Enhancement, in A. Bejan, and A. D. Kraus (Eds.), Heat Transfer Handbook, chap. 14, Wiley, New York, 2003.

[16] R. K. Shah, and W. W. Focke, Plate Heat Exchangers and their Design Theory, in R. K. Shah, E. C. Subbarao, and R. A. Mashelkar (Eds.), Heat Transfer Equipment Design, pp.227-254, Hemisphere, New York, 1988.

[17] R. M. Manglik, Plate Heat Exchangers for Process Industry Applications: Enhanced Thermal-hydraulic Characteristics of Chevron-plates, in R. M. Manglik, A. D. Kraus (Eds.), Process, Enhanced and Multiphase Heat Transfer, pp.267-276, Begell House, New York, 1996.

[18] L. Wang, B. Sunden, and R. M. Manglik, Plate Heat Exchangers: Design, Applications, and Performance, W.I.T. Press, Southampton, UK, 2007.

First International Conference on Computational Methods for Thermal Problems
ThermaComp2009, September 8-10, 2009, Naples, Italy
N.Massarotti and P.Nithiarasu (Eds.)

Thermal interaction effects in micro and nanofluid flows

Nikolaos Asproulis and Dimitris Drikakis
Fluid Mechanics & Computational Science Group
Department of Aerospace Sciences
Cranfield University, United Kingdom

ABSTRACT

In this study thermal phenomena in micro and nanofluid flows are investigated. A better insight on the thermal interactions involved inside micro and nanofluidic devices is essential for optimising their performance. The fidelity of the computational models employed for the thermal wall is examined. Molecular dynamics simulations are utilised to exploit the impact of the wall models on the heat transfer across the solid-liquid interface. The performed simulations revealed that the thermalisation procedure and the solid's bond stiffness have a direct impact on the thermal transfer to and from the solid boundary. Therefore, their selection has to be thoroughly examined.

Key Words: *Heat transfer, thermal walls, micro/nanofluid dynamics, molecular dynamics.*

1. INTRODUCTION

In recent years high-fidelity computational modelling of micro and nano fluid flows has emerged as a viable tool able to assist the design and optimise the performance of devices operating at these scales [1, 2]. Miniaturisation of the conventional macro scale devices offers numerous advantages including reduced operating volume, increased throughput and improved accuracy [3, 4]. As the operational dimensions shrink to smaller scales the surface-to-volume ratio increases and the inter-facial interactions dominate the phenomena observed inside the micro and nanofluidic devices. Computational techniques and specifically molecular dynamics (MD) simulations [5, 6, 7, 8] are employed to study from first principles these surface effects.

The majority of the numerical studies are mainly focused on the effects of the wall-fluid interactions to the existence of slip near the solid boundary. On the other hand, phenomena related to thermal transport across solid-liquid interfaces have not been equally exploited. Previous works[5] revealed that the main difficulty, associated with the thermal boundary conditions, is related to thermal wall models employed by the molecular simulations. Realistic modelling of the solid wall is a crucial issue for the accuracy of the numerical experiments and the primary objective of the current study.

Two are the main thermal wall models applied to MD simulations. In the first one [9, 8] the wall consists of a fixed lattice structure and interacts with the fluid through the intermolecular forces applied among the particles. Since the wall molecules are fixed in their lattice positions, a thermostat has to be applied in the fluid, to dissipate the excessive viscous heating of the system. This wall model cannot accommodate heat transfer from and to the solid boundary and therefore the thermal interactions cannot be realistically simulated. In the second wall model [6, 5] the solid particles are attached to their equilibrium lattice sites with a non linear spring potential. They are allowed to vibrate from their lattice position, imitating the thermal motion, and these thermal oscillations impact the momentum transfer across the interface. The walls operate as heat baths aiming to maintain the liquid's thermal equilibrium by circumventing the need for an additional thermostat.

In this paper, different thermal wall models are utilised to simulate heat transfer problems aiming to broaden our understanding of thermal transport across solid-liquid interfaces.

2. SIMULATION METHOD

The computational domain for the current molecular simulations consists of monoatomic fluid particles confined by two thermal walls separated by a distance H along the y direction. Periodic boundary conditions are applied in the x, y directions and the total size of the considered computational domain is 16.97σ, 34.64σ and 6.54 in the x, y and z direction, respectively.

The interatomic interactions of the wall and fluid particles are modelled by the shifted Lennard-Jones (LJ) potential and for a pair of atoms i and j with distance r_{ij} the potential is:

$$V_{ij}^{LJ} = 4\epsilon \left[\left(\frac{\sigma}{r_{ij}} \right)^{12} - \left(\frac{\sigma}{r_{ij}} \right)^{6} - \left(\frac{\sigma}{r_c} \right)^{12} + \left(\frac{\sigma}{r_c} \right)^{6} \right] \tag{1}$$

where ϵ is the characteristic energy level, σ is the molecular length scale and r_c is the cut-off distance. For the scope of this study liquid Argon particles are simulated particles with mass m, $\epsilon = 120K/k_B$ and $\sigma = 0.34nm$ with density $\rho_f = 0.8\ m\sigma^{-3}$, cut off distance $r_c = 2.2\ \sigma$. The parameters for the wall fluid interaction are $\epsilon_{wf} = 0.2\ \epsilon$ and $\sigma_{wf} = 0.72\ \sigma$.

Each wall consists of 528 atoms and the fluid of a total number of 2640 liquid Argon particles. The time step used in all the simulations is $\delta t = 5 \cdot 10^{-4}\tau$, where τ is the characteristic time $\tau = \left(m\sigma^2/\epsilon\right)^{0.5}$, and the simulations have been performed for $2,5 \cdot 10^6$ time steps to reach steady state and another $2,5 \cdot 10^6$ time steps for averaging.

For the scope of the current study two wall models are examined. In both models the walls are simulated as (111) fcc planes with density $\rho_w = 4.0\ m\sigma^{-3}$. The mass of the wall and fluid particles is equal and the wall's particles are attached to their equilibrium lattice sites with a non linear spring potential:

$$V_w = \frac{1}{2}\kappa r^2 \tag{2}$$

where κ is the spring stiffness. The value specified for the stiffness κ should not allow the mean square displacement of the wall atoms to be larger than the Lidemann criterion of melting [10, 6]. For the current simulations two values $\kappa = 100\epsilon\sigma^{-2}$ and $\kappa = 600\epsilon\sigma^{-2}$ have been assigned for the spring. The main difference between the two models is based on the wall's thermalisation process. In the $1^(st)$ model a velocity rescaling thermostat [11] is applied to the entire solid wall whereas in the $2^(nd)$ model the thermostat is applied to every layer of the wall separately.

3. RESULTS

In the first test case the temperature on both upper and lower walls of the channel is kept constant $T_w = 1.1\ \epsilon k_B^{-1}$. Two simulations for each wall model have been carried out for the two aforementioned values of the spring stiffness $\kappa = 100,\ 600\ \epsilon\sigma^{-2}$. Figure 1 shows the temperature profiles based on the corresponding numerical experiments. It can be identified the profiles obtained from simulations where the 1^{st} wall model has been encompassed, are not physically realistic and consistent. In the current test case the temperature of the fluid along the channel is expected to remain constant and equal to the walls' temperature. In the case where the 1^{st} wall model is applied, although the fluid's temperature remains constant, its value presents significant deviations compare to the one applied on the walls. Furthermore, major deviations are also observed for the different values of the spring stiffness. For the 2^{nd} wall model, as shown in Figure 1, the temperature profiles, from both values of the bond stiffness, remain constant and very close to the walls' temperature. The motion of the fluid's particles is primarily experienced by the solid molecules that belong to the first wall layer. As a consequence, the first solid layer has higher thermal velocity and higher temperature compared the averaged wall's values. Therefore, each of the layers has to be thermalised independently, to avoid any artifacts induced in the thermal transport.

In the second test case a temperature difference is applied between the walls and specifically the temperature for the lower and upper one is $T_{w,lower} = 1.1\ \epsilon k_B^{-1}$ and $T_{w,upper} = 1.3\ \epsilon k_B^{-1}$ respectively. Figure 2a shows the temperature distributions obtained when the 1^{st} wall model is engaged. The outcomes are not physically correct since the temperature remains constant, despite the temperature difference that

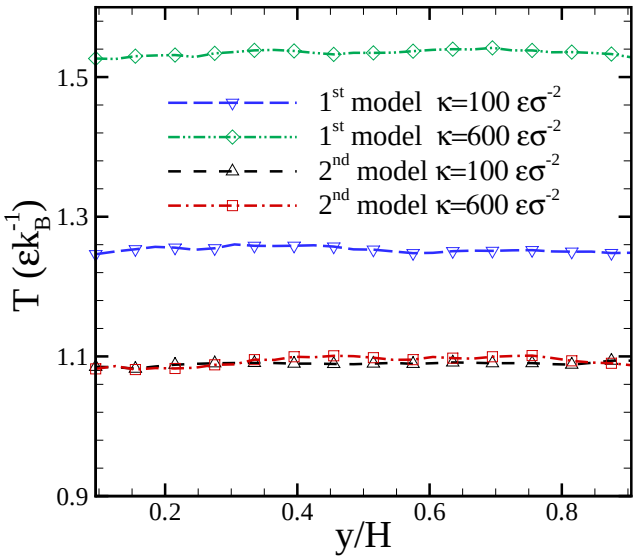

Figure 1: Temperature profiles for the examined wall models with various spring stiffness, when the same temperature is applied to both walls

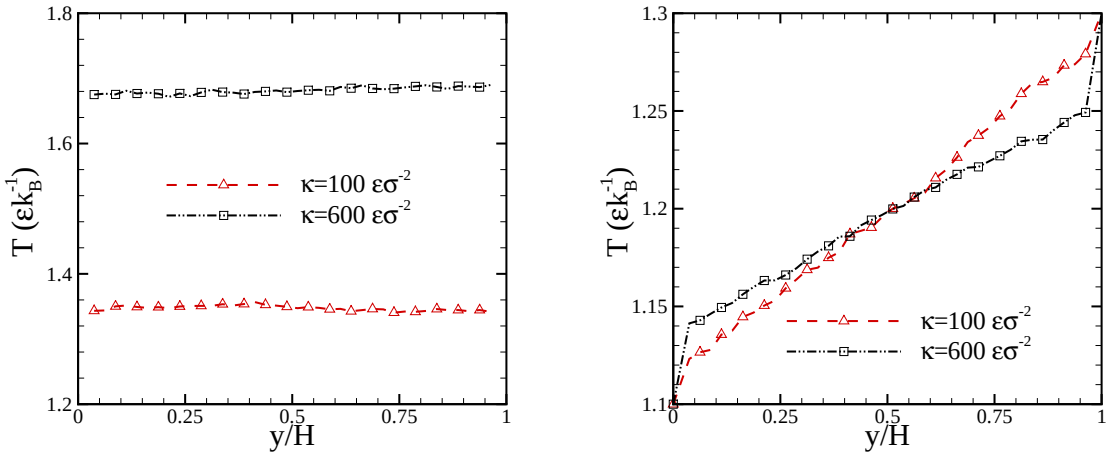

(a) Temperature profile when the 1^{st}wall model with various spring stiffness applied

(b) Temperature profile when the 2^{nd}wall model with various spring stiffness applied

Figure 2: Temperature profiles for the examined wall models with various spring stiffness, when a temperature difference is applied to the channel's walls

is applied between the walls, and in the case of spring stiffness $\kappa = 600\ \epsilon\sigma^{-2}$ is outside the applied temperature regime. Figure 2b shows the results obtained when the 2^{nd} wall model has been employed. The expected linear profile [5] is obtained. In addition a temperature jump is observed in the liquid solid interface. This jump can be quantified through the thermal (Kapitza) resistance and it varies with the spring stiffness, as shown in Figure 2b the temperature jump is higher for stiffness $\kappa = 600\ \epsilon\sigma^{-2}$.

4. CONCLUSIONS

An investigation of the different thermal wall models employed in molecular simulations has been presented. Two wall types have been examined for two fundamental heat transfer test cases. In both models the solid particles are attached to their equilibrium positions with a spring potential, and they are allowed to vibrate aiming to mimic the thermal oscillations. The main difference in the two approaches remains in the thermalisation process. The numerical experiments revealed that a thermostat has to be applied in every solid layer separately in order to represent realistically the thermal transport. Furthermore, the simulations showed a temperature jump in the solid liquid interface which is related also to the value of the bond stiffness of the wall.

REFERENCES

[1] G. Whitesides. The origins and the future of microfluidics. *Nature*, 442:368–373, 2006.

[2] L. O'Hare, D. A. Lockerby, J. M. Reese, and D. R. Emerson. Near-wall effects in rarefied gas micro-flows: some modern hydrodynamic approaches. *In. J. Heat Fl. Flow*, 28(1):37–43, 2007.

[3] R. Mukhopadhyay. When microfluidic devices go bad. *An. Chem.*, 77(21):429–432, 2005.

[4] M. Kalweit and D. Drikakis. Multiscale methods for micro/nano flows and materials. *J. Comput. Theo. Nano Sci.*, 5(9):1923–1938, 2008.

[5] B. H. Kim, A. Beskok, and T. Cagin. Thermal interactions in nanoscale fluid flow: Molecular dynamics simulations with solid-liquid interfaces. *Microfluidics and Nanofluidics*, 5(4):551–559, 2008.

[6] N. V. Priezjev. Effect of surface roughness on rate-dependent slip in simple fluids. *J. Chem. Phys.*, 127(14):144708, 2007.

[7] S. C. Yang. Effects of surface roughness and interface wettability on nanoscale flow in a nanochannel. *Microfluidics and Nanofluidics*, 2(6):501–511, 2006.

[8] J. Koplik, J. R. Banavar, and J. F. Willemsen. Molecular dynamics of fluid flow at solid surfaces. *Physics of Fluids*, 1(5):781–794, 1989.

[9] P. A. Thompson and S. M. Troian. A general boundary condition for liquid flow at solid surfaces. *Nature*, 389(6649):360–362, 1997.

[10] J. L. Barrat and J. P. Hansen. *Basic concepts for simple and complex liquids*. Oxford University Press, Oxford, 2003.

[11] M. P. Allen and D. J. Tildesley. *Computer simulation of liquids*. Oxford University Press, Oxford, 1987.

First International Conference on Computational Methods for Thermal Problems
ThermaComp2009, September 8-10, 2009, Naples, Italy
N.Massarotti and P.Nithiarasu (Eds.)

Numerical Investigation of an Electro-osmotic Cooling System

P.F.Eng
School of Engineering, Swansea University, P.Nithiarasu@swansea.ac.uk

P.Nithiarasu
School of Engineering, Swansea University, P.F.Eng@swansea.ac.uk

ABSTRACT

A conjugate heat transfer problem of an electroosmotic flow (EOF) based micro-cooling system has been numerically studied. The CBS-AC algorithm has been employed to temporally discretize the governing equations. The spatial discretization is carried out using the finite element method. Results clearly show that the increase in Biot number enhances the heat transfer. It is also obvious from the results that the temperature at a point above the micro-channel is reduced to between 3 to 6 ^oC when EOF is induced.

Key Words: *Electro-osmotic Flow, Thermal Management, Electronic cooling, Numerical modelling.*

1. INTRODUCTION

All electronic equipment produce heat during normal operating conditions. Microprocessor used in computing equipment, and power electronic devices are two examples where heat generation is a major issue. The hot spots developed on these equipment may shorten the life span of them. Air cooled heat sinks are the commonly employed form of heat dissipation mechanisms for microprocessors. Such systems in general are bulky and they can be difficult to employ at smaller scales. Attachment of heat sink to a microprocessor exhibits some thermal resistance between the microprocessor and heat sink. Therefore, integrated chip cooling methods are more attractive to remove heat and to reduce hot spots. Such a local cooling procedure is essential for high power applications.

Micro-channel liquid cooling is an alternative method for integrated local cooling system. Liquid systems extract more heat and operate with lower noise than a fan cooling system. It is obvious from the literature that a heat flux of 790 W/cm^2 can be removed using micro-channels [1]. In micro-cooling applications, pumping a liquid through micro-channels is an issue and it is a research problem. In the present work, we use electroosmotic flow (EOF) to drive the liquid. External EOF pump reported by Yao at el [2] has produced up to 1.3 atm of pressure and flow rates greater than 33 ml/min to support cooling heat load of 100 W. The reported works clearly show that the EOF has the potential to be used in electronic cooling. Such systems are free of mechanical moving parts and noise.

A numerical study of a EOF based heat spreader is presented here. The heat spreader proposed is located in the proximity of the microprocessor to reduce the hot spots more effectively. The design proposed reduces the complexity of the cooling system due to the absence of no piping or external connections. The schematic diagram of the heat spreader is shown in Figure 1. As seen the micro-channels are placed in between the microprocessor and the heat sink and sealed. The liquid inside is driven by EOF. The idea here is that use of liquid driven cooling system in between the heat sink and the microprocessor makes the heat flux more uniform and accelerates heat transfer. Thus, the heat sink size will be reduced.

In the present paper, the electric fields of EOF are solved separately from the Navier Stokes equations. The converged electric field is then represented by a source term to the momentum equations [3]. The characteristic based split (CBS) algorithm is employed to temporally discretise the governing equations

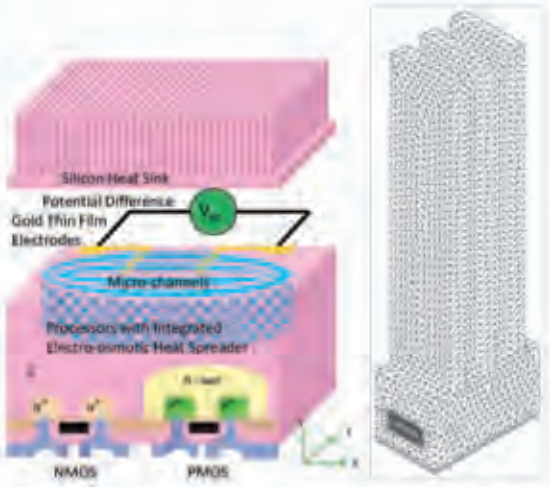

FIGURE 1. Proposed EOF Heat Spreader and Mesh

of electro-osmotic flow. This method is widely used in other incompressible flow applications [4,5]. This algorithm is used explicitly to solve EOF in micro-channels.

2. GOVERNING EQUATION

The non dimensional form of electric fields and the Navier Stokes equations take the following forms:

The Laplace and Poisson Boltzmann Equations:

$$\frac{\partial^2 \phi^*}{\partial x^{*2}} = 0 \qquad and \qquad \epsilon^* \frac{\partial^2 \psi^*}{\partial x^{*2}} = \kappa a^2 \sinh\left(\frac{\psi^*}{T^*+1}\right) \tag{1}$$

Continuity equation:

$$\frac{1}{\beta^{*2}} \frac{\partial P^*}{\partial t^*} + \rho^* \frac{\partial u_i^*}{\partial x_i^*} = 0 \tag{2}$$

Modified momentum equation:

$$\frac{\partial u_i^*}{\partial t^*} + u_j^* \frac{\partial u_i^*}{\partial x_i^*} = -\frac{\partial P^*}{\partial x_i^*} + Pr \frac{\partial \tau_{ij}^*}{\partial x_i^*} + J \sinh\left(\frac{\psi^*}{T^*+1}\right) \frac{\partial \phi^*}{\partial x_i^*} \tag{3}$$

where

$$\kappa = \sqrt{\frac{2n_0 z^2 e^2}{\epsilon_\infty \epsilon_0 k_B T_\infty}}; Pr = \frac{\mu}{\rho_\infty \alpha_\infty}; J = \frac{2n_0 k_B T_\infty L_\infty^2}{\alpha_\infty^2 \rho_\infty}; \tau_{ij}^* = \left(\frac{\partial u_i^*}{\partial x_j^*} + \frac{\partial u_j^*}{\partial x_i^*}\right) \tag{4}$$

Here, $\kappa a = W \times \kappa$ where W is the width of the channel and κ is Debye-Huckel Parameter. The Prandtl number, Pr and parameters, ka and J are defined using properties of electrolytes in room temperature and geometry that are known a priori for electrolyte and geometry used [6]. The non dimensional form of energy equation is written as:

$$\left(\frac{\partial T^*}{\partial t^*} + u_j^* \frac{\partial T^*}{\partial x_j^*}\right) = \alpha^* \frac{\partial^2 T^*}{\partial x_j^{*2}} \tag{5}$$

where $\alpha^* = \frac{\alpha}{\alpha_\infty}$. $\alpha_\infty = \alpha_{fluid}$, is used. In this paper, Joule heating is ignored because the external voltage used is small. For solid part of the heat spreader, the convective term is removed. Convective heat transfer between the fins and the ambient at a constant heat flux is assumed. Convective boundary conditions are given as:

$$\frac{\partial T}{\partial n} = BiT \qquad \text{where Biot number,} \qquad Bi = \frac{hL_\infty}{k_\infty} \tag{6}$$

where h is convective heat transfer coefficient, k is thermal conductivity and L is the characteristic length which refers to the width of the channel. Biot numbers used in the simulations are 0.1, 1 and 10.

TABLE 1. Conjugate heat transfer from a uniform heat source. Temperature distribution at point (0,0,0.5)

Biot number	Temperature without EOF	Temperature with EOF	Temperature Difference
0.1	48 ^oC (T^*=0.077)	44 ^oC (T^*=0.065)	4 ^oC
1.0	45 ^oC (T^*=0.067)	40 ^oC (T^*=0.052)	5 ^oC
10	41 ^oC (T^*=0.052)	35 ^oC (T^*=0.033)	6 ^oC

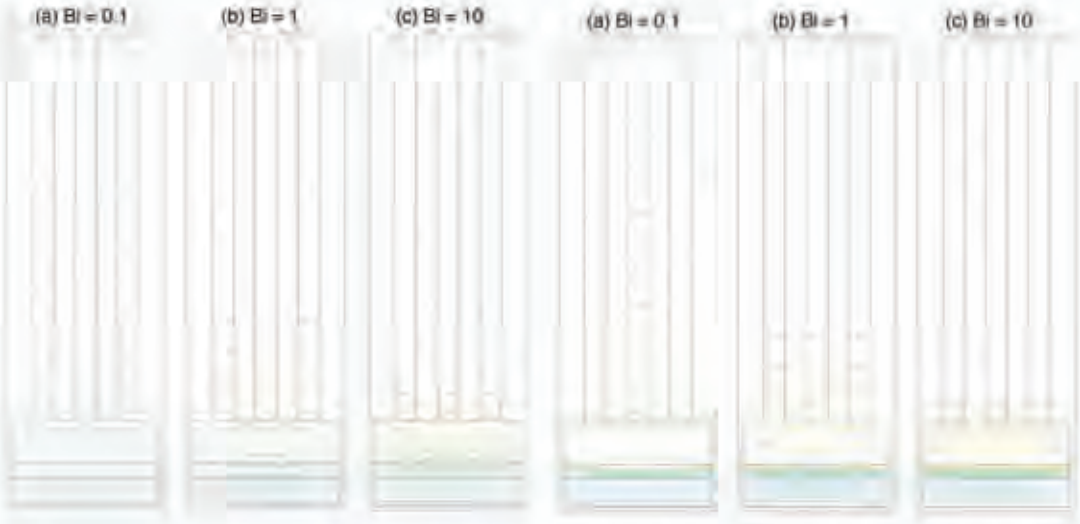

FIGURE 2. Conjugate heat transfer from a uniform heat source. (Left)without EOF (Right)with EOF at Biot numbers of (a) 0.1, (b) 1 and (c) 10

3. RESULTS

Two different cases are considered here. In the first case a uniform temperature that is higher than atmospheric temperature is prescribed at the bottom surface of the geometry (see Figure 1) (68^oC). In the second case, a non-uniform temperature distribution is assumed on the bottom surface.

3.1. **Uniform Heat Source.** Figure 2 shows the temperature distribution. The figures on the left shows the temperature distribution without EOF and the ones at the right are with EOF. The cuts of the heat spreader were taken through the geometry at (0,2,0). As seen the temperature difference is notably different when EOF is invoked, especially closer to the micro-channels. The temperature at the point (0,0,0.5) is shown in Table 1. At Biot number of 0.1, the temperature at the point (0,0,0.5) is about 48^oC and at $Bi = 1$ and 10, the temperature is reduced to 45 ^oC and 41 ^oC respectively. When EOF is invoked (right, Figure 2) the temperature is reduced from by 4^oC at $Bi = 0.1$. Similarly the temperature reduction is observed at $Bi = 1$ and $Bi = 10$. This clearly demonstrates that the EOF based heat spreader is effective.

3.2. **Nonuniform Heat Source.** In the second case studied, a non-uniform temperature is assumed along the bottom surface of the geometry. The maximum temperature of the surface is 68^oC. Figure 3 shows the temperature distributions without EOF on the left and with EOF on the right. As seen the difference between the two cases are clearly evident. Table 2 shows the temperature distribution at point (0,0,0.5). In all the three cases of Biot number considered, the temperature reduction due to EOF is about 3^oC. This may be due to the fact that the average temperature of the bottom surface here is much lower than the case studied in the previous section.

4. CONCLUSIONS

A conjugate heat transfer problem relevant to electronic cooling applications has been studied. It is clear from the studies that the Biot number has a great deal of influence on the heat transfer. In addition, the

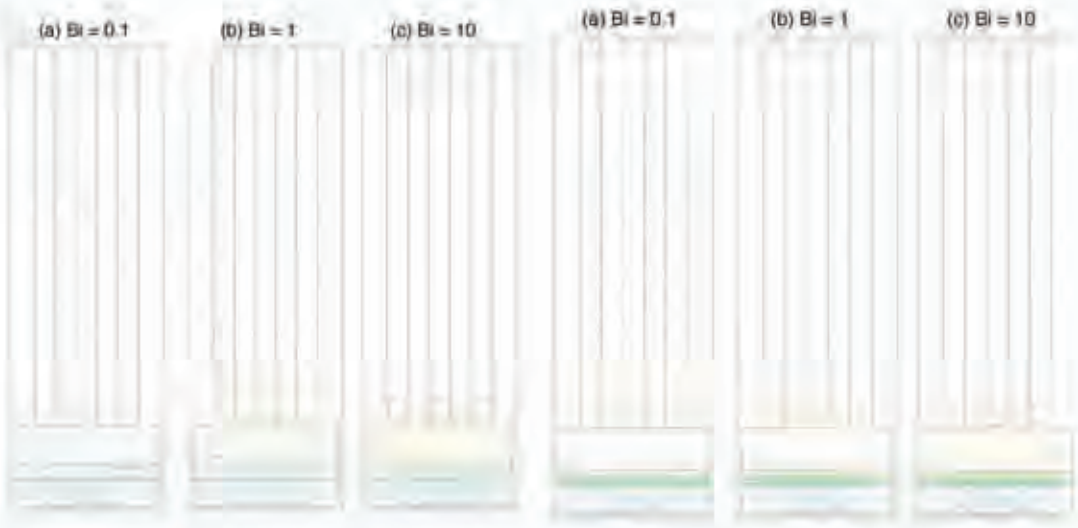

FIGURE 3. Conjugate heat transfer from a non-uniform heat source. (Left)without EOF (Right)with EOF at Biot numbers of (a) 0.1, (b) 1 and (c) 10

TABLE 2. Conjugate heat transfer from a uniform heat source. Temperature distribution at point (0,0,0.5)

Biot number	Temperature without EOF	Temperature with EOF	Temperature Difference
0.1	49 ^oC (T^*=0.080)	46 ^oC (T^*=0.069)	3 ^oC
1.0	46 ^oC (T^*=0.071)	43 ^oC (T^*=0.059)	3 ^oC
10	41 ^oC ^oC (T^*=0.055)	38 ^oC (T^*=0.044)	3 ^oC

study shows that the influence of electroosmotic flow (EOF) can not be underestimated. Use of EOF as a part of an electronic cooling system clearly demonstrates that EOF helps in reducing the size of heat sinks.

REFERENCES

[1] D.B. Tuckerman and R.F.W. Pease, High Performance Heat Sinking for VLSI, *IEEE Electron Device Letters*, 2, 126-129, 1981.

[2] S.L. Zeng, C.H. Chan, J.C. Mikkelsen and J.G. Santiago, Fabrication and characteristic of Electroosmotic Micropumps, *Journal of Sensors and Actuator B*, 79, 107-114, 2001.

[3] N.A. Patankar and H.H. Hu, Numerical Simulation of Electroosmotic Flow, *Analytic Chemistry*, 70, 1870-1881, 1998.

[4] O.C. Zienkiewicz, R.L. Taylor and P.Nithiarasu, *The Finite Element Method for Fluid Dynamics*, Elsevier, 2005.

[5] P. Nithiarasu, An Efficient Artificial Compressibility (AC) Scheme Based on the Characteristic Based Split (CBS) Method for Incompressible Flows, *International Journal for Numerical Methods in Engineering*, 56, 1815-1845, 2003.

[6] P. Nithiarasu and R.W. Lewis, A Short Note on Joule Heating in Electro-osmotic Flows: A Consistent Non-Dimensional Scaling, *International Journal of Numerical Methods for Heat and Fluid Flow*, 18, 919-931, 2008.

First International Conference on Computational Methods for Thermal Problems
ThermaComp2009, September 8-10, 2009, Napoli, Italy
N.Massarotti and P.Nithiarasu (Eds.)

COMPUTATIONAL STUDIES OF EFFECTS OF DIMENSION AND HEAT LOSS ON METHANE COMBUSTION IN A MICROCHANNEL

YanXia Li
Liang Feng
ZhongLiang Liu*
JingFu Wang
Key Laboratory of Enhanced Heat Transfer and Energy Conservation, Ministry of Education and
Key Laboratory of Heat Transfer and Energy Conversion, Beijing municipality,
College of Environmental and Energy Engineering, Beijing University of Technology, Beijing
100124, China

ABSTRACT

The effects of dimension and heat loss on methane combustion in a rectangle microchannel are numerically investigated. A two-dimensional model is solved to study the volumetric reaction of the premixed methane/air mixture in the microchannel by using Fluent 6.2. A one step irreversible reaction is used. It is found that under the adiabatic condition, large height and thick walls of the channel result in high wall temperature and more uniform temperature distribution. While the effect of 0.4mm-thick walls on the combustion characteristics has a little difference from that of the 0.8mm-thick walls. No oscillatory behavior is observed when the heat transfer coefficient is less than 50 W/(m^2·K). With the increase of heat transfer coefficient on the external walls of the channel, the wall temperature and downstream fluid temperature decrease. However, numerical simulation also shows that when the heat transfer coefficient is 100 W/(m^2·K), the steady flame is not obtained.

Key Words: *Micro-combustion, Methane, Dimensions, Heat loss.*

1. INTRODUCTION

Microscale power generation devices are increasingly applied in many fields recently, such as micro-spacecraft, micro-satellite, soldier portable power applications, and many other miniature space systems. Due to the large energy density of hydrocarbons (40-50MJ/kg)[1], people try to use combustion producing energy to meet the needs of these miniature devices. However, as one could understand, it is still a great technological challenge to burn fuels stably and efficiently in a confined and very small space. With the decrease of the combustor size to the micro-scale level, the time available in the channel for the combustion reaction is very short. Moreover, the surface-area-to-volume ratio for a micro-scale combustor is approximately two orders of magnitude larger than that of a typical combustor. The heat loss increases more rapidly than the heat production as the combustor size is reduced[2]. Therefore, homogeneous flames are often quenched when confined in the spaces with dimensions below 1-2mm[3]. Recent experiments have found flame could propagate stably in micro-combustor through preheating the feed or reducing heat loss to the surroundings[4-6]. While the mechanism of the flame stability and combustion characteristics of the micro-systems are poorly understood.

The numerical approach was widely used in studying micro-combustion process. Many scholars studied the catalytic combustion in microtubes. Kim[7] investigated the propagation of premixed

* Corresponding author. E-mail address: liuzhl@bjut.edu.cn (**ZhongLiang Liu).**

flame in small tubes without considering the thermal conduction within the walls. Norton[3, 8] firstly investigated the effect of walls on microcombustion. They studied the effects of many factors on combustion characteristics and analyzed the flames stability of premixed methane/air and propane/air mixtures in channels. Zhong[9,10] studied the extinction limits of CH_4/air premixed combustion in a microtube. They found the effect of heat transfer within the walls is significant and very important. The feeds are preheated by upstream heat transfer within the walls. This is necessary for flame ignition and stability. Whereas, the wall condutivity used in their model is small. In fact, the stainless steel is often used in engineering applications. Therefore, it is special importance to study the combustion characteristics in microchannels made of stainless steel. This paper intends to analyze the volumetric reaction of premixed methane/air mixture in rectangle channel in which the thermal conductivity of walls is 16.7 W/(m·K). Here we also take the heat conduction of the walls into consideration.

2. MODEL

The mixture of premixed methane/air are fed into a microchannel at a fixed velocity (v_0=0.5m/s). The stoichiometric ratio of methane/air mixture is 1. A two-dimension symmetry section is the computational domain. The schematic is shown in FIGURE 1. In this figure, H is the height of the channel, L is the length and L_w is the thickness of the walls. Three different sizes of the rectangle microchannel are simulated, the height and the length are 0.6mm×10mm, 1.0mm×10mm and 2.0mm×20mm, respetively.

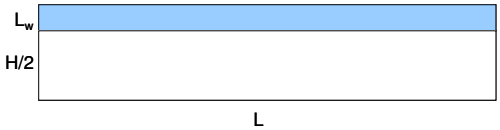

FIGURE 1. The computational domain.

A two-dimensional parabolic model is solved to study the effects of dimension and heat loss on combustion characteristics. Control equations are omitted here. Radiation is not included in the model and the effects of viscous dissipation and mass forces are also not considered. Fluent 6.2 is used to perform all the simulations. The finite difference method is used to discretize the two-dimension equations. The boundary and initial conditions are as follows. A fixed, uniform velocity profile is used at the inlet. Symmetry boundary condition is applied at the centerline of the channel. A fixed pressure condition is used at the exit. The Newton's cooling law is applied at the external walls. At the interface between the wall and fluid, no-slip boundary conditions and coupled conditions are applied. The heat flux at the solid-fluid interface is computed using Fourier's law. The continuity in temperature and heat flux links the fluid and solid phases. The thermal conductivity of the walls is set at 16.7 W/(m·K). The temperature of the inlet mixture is 300K.
Because of the low Reynolds numbers($<$1000), the Laminar Finite Rate model is used for all simulations.

3. RESULTS

The study is based on the parabolic model. The initial time step size is 0.0005s. After about forty thousands steps, the time step size is adjusted to be 0.05s. In all simulations of this paper, the results are all at steady state. The time for reaching the steady state is different for different cases.

3.1 The effects of the channel height on combustion characteristics

Three channels whose height are 0.6mm, 1.0mm and 2.0mm, respectively are studied. FIGURE 2 compares the influences of the channel height on axial temperature distribution and the reaction rate. As can be seen from this figure, increasing the channel height shifts the flame location downstream and increases the flame length. The maximum temperature also shifts to the down stream and decreases with the channel height. It is also disclosed that the smaller the height, the stronger the

reaction is. Furthermore the flame location is closer to the entrance as the height of the channel becomes shorter, and this in turn causes lower wall temperature and steeper temperature distribution.

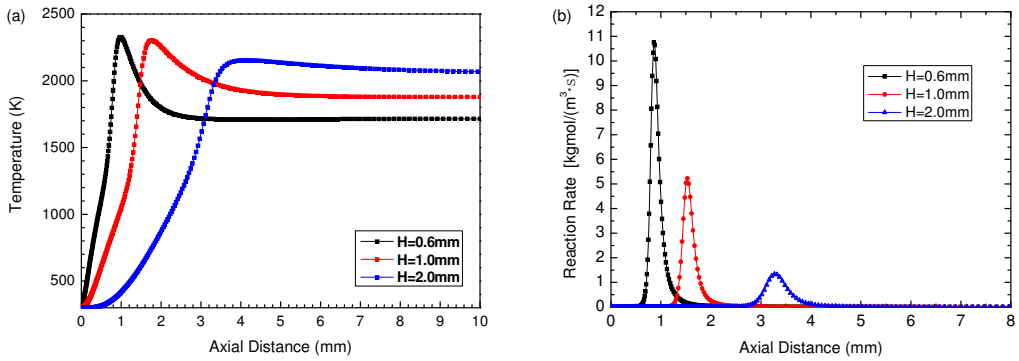

FIGURE 2. The profiles of (a) temperature; (b) reaction rate along the centerline.
(The wall thickness is 0.2mm, the heat transfer coefficient on the external wall is 0 W/(m^2·K))

3.2 The effects of wall thickness on combustion characteristics

FIGURE 3 shows the influences of the wall thickness on the combustion characteristics. The thermal conductivity of the wall material is 16.7 W/(m·K) and is relatively large. The wall temperature distribution along the axial direction is relatively uniform. The thicker the wall, the more uniform the temperature. This is because the thicker wall has larger equivalent area for axial thermal conduction. However this effect decreases as the thickness increases. As one can see, though the combustion characteristics of the 0.2mm-thick wall channel and that of the 0.4mm-thick wall channel shows significant difference, there is only a very slight difference between the 0.4mm-thick wall channel and the 0.8mm-thick wall.

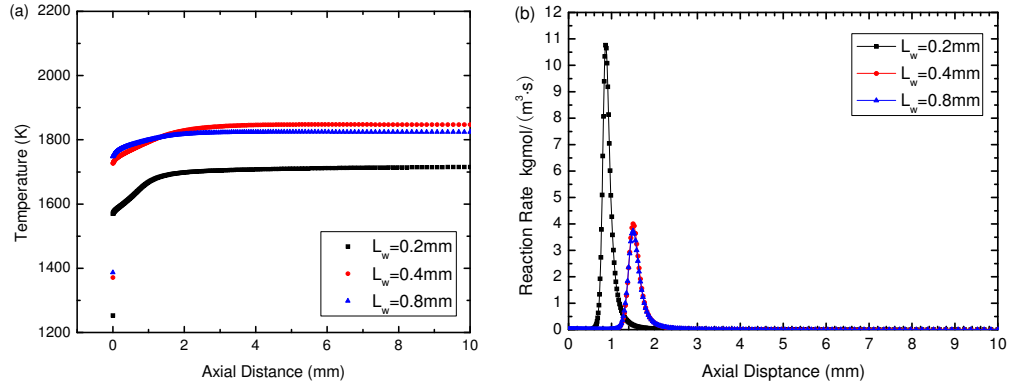

FIGURE 3. The profiles of (a) temperature ; (b) reaction rate along the central line.
(The channel's height is 0.6mm, the heat transfer coefficient on the external wall is 0 W/(m^2·K))

3.3 The effects of heat loss on combustion characteristics

In these simulations, the Newton's cooling law is applied at the exterior walls. The heat transfer coefficient is set at 0, 5, 10, 16, 50, 100 W/(m^2·K), separately. FIGURE 4 presents the axial profiles of temperature under different cooling conditions. As one may expect, the wall temperature and fluid temperature all decrease as the heat transfer coefficient increases. And furthermore, if the cooling is too strong, for example, when the heat transfer coefficient increases to 100 W/(m^2·K), the numerical simulations reveal that no stable flame could maintain.

4. CONCLUSIONS

The effects of dimension and heat loss on microcombustion of methane/air in a microchannel are investigated by solving a two-dimensional parabolic model. The thermal conductivity of wall

material is set at 16.7 W/(m·K) and the premixed, stoichiometric methane/air mixture are fed to the rectangle microchannel at 0.5m/s velocity. It is found that under the adiabatic condition, large height and thick walls of the channel result in high wall temperature and more uniform temperature distribution. While the effect of 0.4mm-thick walls on the combustion characteristics has a little difference from that of the 0.8mm-thick walls. No oscillatory behavior is observed when the heat transfer coefficient is less than 50 W/(m^2·K). With the increase of heat transfer coefficient on the external walls of the channel, the wall temperature and downstream fluid temperature decrease. However, numerical simulation also shows that when the heat transfer coefficient is 100 W/(m^2·K), the steady flame is not obtained.

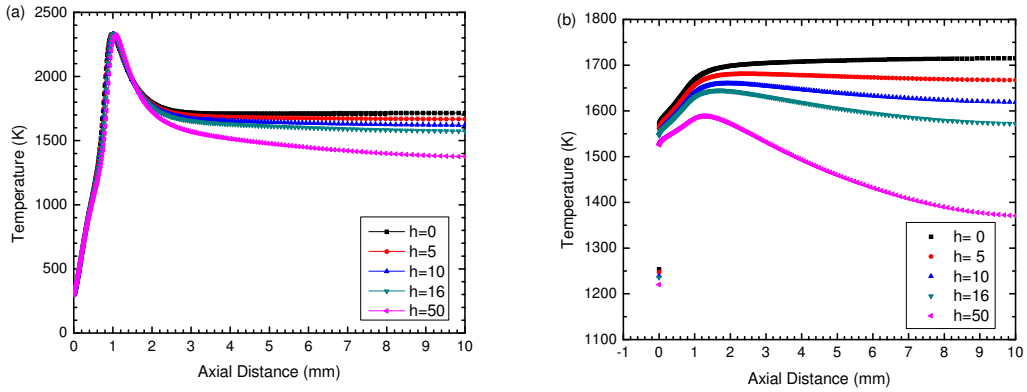

FIGURE 4. The profiles of (a) temperature along the centric axis; (b) temperature along the walls. (The wall thickness is 0.2mm, the channel's height is 0.6mm.)

REFERENCES

[1] C.C. Loy and F. Bo, The Development of a Micropower (Micro-thermophotovoltaic) device, Journal of Power Sources, 165, 455-480, 2007.

[2] J.W. Li and B.J. Zhong, Experimental investigaion on heat loss and combustion in methane/oxygen micro-tube combustor, Applied Thermal Engineering, 28, 707-716, 2008.

[3] D.G. Norton and D.G. Vlachos, Combustion Characteristics and Flame Stability at the Microscale: a CFD Study of Premixed Methane/Air Mixtures, Chemical Engineering Science, 58, 4871-4882, 2003.

[4] V.V. Zamashchikov, An investigation of gas combustion in a narrow tube, Combustion Science and Technology, 166, 1-14, 2001.

[5] K. Maruta, T. Kataoka, et al, Characteristics of combustion in a narrow channel with a temperature gradient, Proceedings of the Combustion Institute, 30, 2429-2436, 2005.

[6] W.M. Yang, S.K. Chou, C. Shu, Z.W. Li, H. Xue, Experimental study of micro-thermophotovoltaic system with different combustor configurations, Energy Conversion and Management, 48, 1238-1244, 2007.

[7] N.Il Kim and K. Maruta, A Numerical Study on Propagation of Premixed Flames in Small Tubes, Combustion and Flame, 146, 283-301, 2006.

[8] D.G. Norton and D.G. Vlachos, A CFD Study of Propane/Air Microflame Stability, Combustion and Flame, 138, 97-107, 2004.

[9] B. J. Zhong and J. Jiao, Extinction Limits of CH4/Air Premixed Combustion in a Microchannel, Journal of Tsinghua University(Science and Technology), 47, 2041-2044, 2007.

[10] J.A. Federici and D.G. Vlachos, A Computational Fluid Dynamics Study of Propane/Air Microflame Stability in a Heat Recirculation Reactor, Combustion and Flame, 153, 258-269, 2008.

First International Conference on Computational Methods for Thermal Problems
ThermaComp2009, September 8-10, 2009, Naples, Italy
N.Massarotti and P.Nithiarasu (Eds.)

Numerical Modelling of Heat Generated by Electroosmotic Flows in a T-Mixer

Perumal Nithiarasu
School of Engineering, Swansea University, Swansea SA2 8PP; P.Nithiarasu@swansea.ac.uk

ABSTRACT

In this paper, numerical modeling of Joule heating in electroosmotic flows in a T-mixer is described in some detail. The finite element method is used for the spatial discretization along with the characteristic based split (CBS) time discretization. A new non-dimensional scaling is also introduced. The non-dimensional scales and the numerical algorithm are demonstrated by solving the electroosmotic flow and heat generation in a T-mixer.

Key Words: *Micro channel flows, electroosmosis, heat generation, biomedical applications, numerical modeling.*

1. INTRODUCTION

Electro-osmotic flow (EOF) has been a basis for designing certain types of biomedical and micro-cooling devices for several years. EOF is used as pumping, valving, mixing, splitting and delivering mechanisms in "lab-on-chip" devices for biological and chemical analyses and medical diagnoses[1]. It is also used in cooling of electronic equipment[2]. In both these applications, Joule heating can be a factor in the design. In biological applications, increased use of low cost, but poor heat conducting materials[3], poses the problem of heat dissipation. In electronic cooling applications, Joule heating increases the temperature of the coolant and imposes an extra burden on the cooling system. Thus, Joule heating and it's the dissipation are of one of the major challenges currently faced by heat transfer engineers. Numerical modelling of Joule heating helps to estimate the approximate increase in the electrolyte temperature and thus leads to a better device design to dispose the heat generated.

A small number of modelling studies have been reported on Joule heating in EOF and different non-dimensional scalings have been adopted in these studies [4-8]. Though the scalings used in these works are correct, some of them may not always be convenient and they are not sufficiently general to use. Thus, we use a non-dimensional scaling scheme that is often adopted in the natural convection and conjugate heat transfer studies[9]. This scaling is general and it does not change with the boundary conditions or other variable parameters.

The objective of the present work is thus to introduce the new non-dimensional scales and also to solve the heat generation problem using the implicit-explicit approach[10]. Section 2 introduces the governing equations and the non-dimensional scales. The numerical algorithm is briefly presented in Section 3. Section 3 provides some results to demonstrate the non-dimensional scales and the numerical algorithm proposed.

2. GOVERNING EQUATIONS AND SOLUTION ALGORITHM

2.1. **Governing Equations.** Following scales are selected to non-dimensionalise the governing equations.

$$\phi^* = \frac{\phi}{\phi_\infty}; \psi^* = \frac{\psi}{\phi_\infty}; \beta^* = \frac{\beta L_\infty}{\alpha_\infty}; \mathbf{u}^* = \frac{\mathbf{u}L}{\alpha_\infty};$$
$$t^* = \frac{t\alpha_\infty}{L_\infty^2}; p^* = \frac{pL^2}{\rho\alpha_\infty^2}; T^* = \frac{T - T_\infty}{T_\infty} \quad (1)$$

where

$$\alpha_\infty = \frac{k_\infty}{(\rho c_p)_\infty} \tag{2}$$

and the subscript ∞ indicates a reference quantity. Assuming $\phi_\infty = k_b T_\infty / ze$ and substituting the above scales, we obtain the non-dimensional form of the equations as:

Laplace equation:

$$\nabla.(\lambda^* \nabla \phi^*) = \mathbf{0} \tag{3}$$

where $\lambda^* = \lambda/\lambda_\infty$. Poisson-Boltzmann equation:

$$\nabla.(\epsilon^* \nabla \psi^*) = ka^2 sinh(\frac{\psi^*}{T^*+1}) \tag{4}$$

where

$$\epsilon^* = \frac{\epsilon}{\epsilon_\infty}; ka = (\frac{2n_0 z^2 e^2 L_\infty^2}{\epsilon_\infty \epsilon_0 k_b T_\infty})^{\frac{1}{2}} \tag{5}$$

The non-dimensional form of the momentum equation is

$$\left(\frac{\partial \mathbf{u}^*}{\partial t} + \mathbf{u}^*.\nabla \mathbf{u}^*\right) = -\nabla p^* + Pr \nabla.\tau^* + J \sinh\left(\frac{\psi^*}{T^*+1}\right) \nabla \phi^* \tag{6}$$

where

$$\nu^* = \frac{\nu}{\nu_\infty}; J = \frac{2n_0 k_b T_\infty L_\infty^2}{\alpha_\infty^2 \rho}; Pr = \frac{c_p \mu_\infty}{k_\infty}; \tau^* = \nu^* \left(\nabla \mathbf{u}^* + \nabla \mathbf{u}^{*T}\right) \tag{7}$$

Finally, the non-dimensional form of the energy equation may be written as

$$\left(\frac{\partial T^*}{\partial t^*} + \mathbf{u}^*.\nabla T^*\right) = \nabla.(\alpha^* \nabla T^*) + Ju\ \lambda^* |\nabla \phi^*|^2 \tag{8}$$

where

$$\alpha^* = \frac{\alpha}{\alpha_\infty}; Ju = \frac{\lambda_\infty k_b^2 T_\infty}{k_\infty z^2 e^2}; \lambda^* = \frac{\lambda}{\lambda_\infty} \tag{9}$$

In the present work, the electrical conductivity, viscosity and thermal conductivity are assumed to be temperature dependent[9]. The important non-dimensional parameters identified above include the Prandtl number, Pr, and the parameters J, Ka and Ju. As seen, these parameters are defined using properties of the fluid and geometry that are known *a priori* for the electrolyte and the geometry used. Thus, determining these parameters independent of each other is straight forward. Table 1 lists various parameters, reference quantities and their values.

TABLE 1. EOF and Joule heating parameters.

Parameter	Value
α_∞	0.146 $\times$ 10^{-6} m^2/s
ϵ_∞	78.5
J	0.1 - 220 (micro-channel size between 1μm to 100 μm)
Ju	0 - 10^{-2} (depending on the reference electrical conductivity)
ka	10 - 80
k_∞	0.6138 W/mK
λ_∞	0.2 S/m
ν_∞	0.8666 $\times$ 10^{-6} m^2/s
ϕ_{in}; ϕ_{out}	134.4; 0.0 (equal to an electric field of 11.679 kV/m)
Pr	5.877
ζ	-3.7 (corresponding dimensional value is 95 mV)
T_∞	298 K

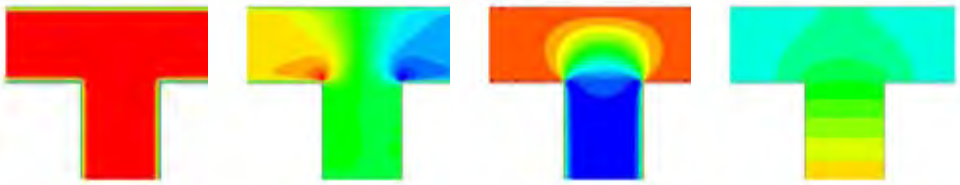

(a) EOF potential (b) Horizontal velocity (c) Vertical velocity (d) Temperature

FIGURE 1. EOF and Joule heating in a T-mixer. Contours of variables.

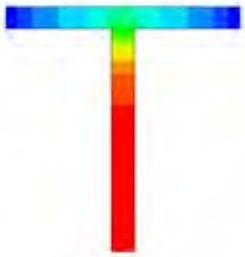

FIGURE 2. EOF and Joule heating in a T-mixer. Temperature contours

2.2. **Solution Procedure.** We solve the electric field equations using a GMRES solver[10]. To overcome standard difficulties, a fractional step algorithm involving three steps and the energy equation may be written as (asterisks are dropped from the non-dimensional equations for simplicity)

Step1: Intermediate momentum

$$\left(\frac{\Delta\tilde{\mathbf{u}}}{\Delta t}+\mathbf{u}^{n}.\nabla\mathbf{u}^{n}\right)=Pr\nabla.\tau^{n+\theta_1}+J\sinh\left(\frac{\psi}{T+1}\right)^{n+\theta}\nabla\phi^{n+\theta} \tag{10}$$

where $\Delta\tilde{\mathbf{u}}=\tilde{\mathbf{u}}-\mathbf{u}^{n}$ and $\tilde{\mathbf{u}}$ is an intermediate velocity field. Step2: Pressure calculation

$$(1-\theta_2)\left(\frac{1}{\beta^2}\right)^{n}\frac{\Delta p}{\Delta t}-\Delta t\nabla^2 p^{n+\theta_2}=-\nabla.\tilde{\mathbf{u}} \tag{11}$$

Step3: Momentum correction

$$\frac{\mathbf{u}^{n+1}-\tilde{\mathbf{u}}}{\Delta t}=-\Delta p^{n+\theta_2} \tag{12}$$

Energy equation:

$$\left(\frac{\Delta T}{\Delta t}+\mathbf{u^{n}}.\nabla T^{n}\right)=\nabla.\left(\alpha^{*}\nabla T^{n+\theta_1}\right)+Ju\left(\lambda|\nabla\phi|^{2}\right)^{n+\theta} \tag{13}$$

In the above equations θ_1 and θ_2 vary between 0 and 1 depending on whether equations are treated explicitly, implicitly or semi-implicitly. All the results given in the present work are generated by assuming $\theta=\theta_1=\theta_2=0$[9,11].

3. RESULTS

EOF and heat generation in a two-dimensional T-mixer is studied here. The total length and width of the mixer are ten times the width of the inlet or exit sections. The mixer is symmetric with respect to the vertical central axis. The electrolytes used at the two horizontal inlets are assumed to be identical for demonstration purposes. All the other properties used are given in Table1.

A total of more than one hundred thousand finite elements are used to generate the finite element mesh. The temperature boundary conditions used are zero non-dimensional temperature at the inlet and insulated boundary conditions on all the remaining surfaces including the exit. All the walls are prescribed with a constant zeta potential value and an external electric field is introduced between the inlets and exit.

Figure 1 shows the contours of EOF potential, velocity components and the temperature. As expected the distribution of variables is symmetric with respect to the vertical central axis due to the identical electrolytes assumed at both the horizontal exits. The high EOF potential gradient clearly introduces a very high velocity gradient all along the walls of the T-mixer. The full details of the temperature distribution are shown in Figure 2. In addition to the given parameter in Table1, a *Ju* value of 0.00001 is used in the calculation. The increase in temperature for the above parameters is approximately 0.8^oC.

4. CONCLUSIONS

A detailed modeling procedure for dealing with EOF based Joule heating was explained. The non-dimensional scales used are clearly an improvement over the existing scales. The formulation shows that the parameter Ju is the most important parameter in determining the heat generation.

REFERENCES

[1] F. Bianchi, R. Ferrigno, and H.H. Girault. Finite element simulation of an electroosmotic-driven flow division at a t-junction of microscale dimensions. *Analytical Chemistry*, 72:1987–93, 2000.

[2] L. Jiang, J. Mikkelsen, J-M. Koo, D. Huber, S. Yao, L. Zhang, P. Zhou, J.G. Maveety, R. Prasher, J.G. Santiago, T.W. Kenny, and K.E. Goodson. Closed-loop electroosmotic microchannel cooling system for vlsi cirsuits. *IEEE Transactions on Components and Packaging Technologies*, 25:347–355, 2002.

[3] D. Erickson, D. Sinton, and D. Li. Joule heating an heat transfer in poly(dimethylsiloxane) microfluidic systems. *Lab on a Chip*, 3:141–149, 2003.

[4] T.S. Zhao and Q. Liao. Thermal effects on electroosmotic pumping of liquids in microchannels. *Journal of Micromechanics and Microengineering*, 12(6):962–970, 2002.

[5] G.Y. Tang, C. Yang, C.J. Chai, and H.Q. Gong. Modeling of electroosmotic flow and capillary electrophoresis with the joule heating effect: The nernst-planck equation versus the boltzmann distribution. *Langmuir*, 19:10975–10984, 2003.

[6] K-D. Huang and R-J. Yang. Numerical modelling of the joule heating effect on electrokinetic flow focusing. *Electrophoresis*, 27:1957–1966, 2006.

[7] G.Y. Tang, D.G. Yan, C. Yang, H.Q. Gong, J.C. Chai, and Y.C. Lam. Joule heating and its effect on electrokinetic transport of solutes in rectangular microchannels. *Sensors and Actiators*, 139:221–232, 2007.

[8] P. Nithiarasu. A unified fractional step method for compressible and incompressible flows, heat transfer and incompressible solid mechanics. *International Journal of Numerical Methods for Heat and Fluid Flow*, 18:111–130, 2008.

[9] P. Nithiarasu and R.W. Lewis. A short note on Joule heating in electro-osmotic flows. a consistent non-dimensional scaling. *International Journal of Numerical Methods for Heat and Fluid Flow*, 18:919–931, 2008.

[10] S.P. Singh, P. Nithiarasu, P.F. Eng, R.W. Lewis, and A.K. Arnold. An implicit-explicit solution method for coupled electro-osmotic flows in three dimensions using unstructured meshes. *International Journal for Numerical Methods in Engineering*, 73:1137 – 1152, 2008.

[11] A.K. Arnold, P. Nithiarasu, and P.G. Tucker. Finite element modelling of electroosmotic flows using unstructured meshes. *International Journal of Numerical Methods for Heat and Fluid Flow*, 18:67–82, 2008.

First International Conference on Computational Methods for Thermal Problems
ThermaComp2009, September 8-10, 2009, Naples, Italy
N.Massarotti and P.Nithiarasu (Eds.)

A HYBRID APPROACH TO THE NUMERICAL ANALYSIS OF CROSS-FLOW MICRO HEAT EXCHANGERS

Carlo Nonino
Università degli Studi di Udine, Dipartimento di Energetica e Macchine,
Via delle Scienze 208, 33100 Udine, Italy
carlo.nonino@uniud.it

Stefano Savino
stefano.savino@uniud.it

Stefano Del Giudice
stefano.delgiudice@uniud.it

ABSTRACT

A hybrid technique, which has the advantage of accounting for all three-dimensional features of the flow field, but with a limited computational effort, is used for the solution of conjugate convection-conduction heat transfer problems in a cross-flow micro heat exchanger. The key feature of the procedure is represented by the separate computation of the velocity field in single microchannels. Then, such velocity fields are mapped onto a grid used to solve the thermal problem.

Key Words: *Finite elements, conjugate heat transfer, micro heat exchangers.*

1. INTRODUCTION

In most microscale thermal devices the area of the section of the solid material normal to the direction of the flow is comparable to the area of the channel cross-section. Therefore, it has long been recognized that the thermal performances of micro heat exchangers and heat sinks are strongly affected by the coupling of the heat conduction taking place in the solid walls and of the forced convection inside the flow passages [1].

Results of numerical simulations can give a useful support to experimental work, but, due to limited computational resources, the numerical solution of a complete micro heat exchanger has only seldom been carried out in the past [2, 3]. In general, the computational domain only corresponds to one or two microchannels and allows the analysis of the thermal behaviour of dissipators or of parallel-flow and counter-flow micro heat exchangers [4, 5].

In this paper, as an alternative to massive CFD, a hybrid technique [6], which has the advantage of accounting for all three-dimensional features of the flow field, but with a limited computational effort, is proposed for the solution of conjugate convection-conduction heat transfer problems in cross-flow micro heat exchangers.

2. STATEMENT OF THE PROBLEM AND MATHEMATICAL MODEL

The cross-flow micro heat exchanger considered here consists of a number of layers of 10 square microchannels each, as shown in Fig. 1(a). For the sake of simplicity, in this analysis the hot and cold fluids are assumed to have the same (constant) thermophysical properties. Moreover, the same mass flow rate is also assumed in all the microchannels, which all have the same height H (equal to their width). The thicknesses of the solid walls, both between two adjacent microchannels of the same layer

and between to adjacent layers, is equal to $H/2$. The length of the microchannels is $15H$. If only the part of the micro heat exchanger away from the external surfaces is considered, the computational domain, because of the existing symmetries, can be limited to two half-layers as illustrated in Fig. 1(b).

The adopted solution procedure implies a separate computation of the velocity field in single microchannels. Then, such velocity fields, which, in the present case are all equal, are mapped onto a grid used to solve the thermal problem [6]. Thus, a very efficient finite element procedure is first employed for the step-by-step solution of the parabolised momentum equations in a domain corresponding to the cross-section of each microchannel, which is discretized using a sufficiently fine grid [7]. Provided that the axial diffusion of momentum can be neglected, such an approach is very advantageous with respect to the one based on the steady-state solution of the elliptic form of the Navier-Stokes equations in a three-dimensional domain corresponding to the whole duct because of the high value of the ratio between the total length and the hydraulic diameter. Then, the three-dimensional hydrodynamically developing velocity field thus determined is mapped onto the parts of the three-dimensional mesh corresponding to the flow passages in the grid used to discretize the entire domain (solid and fluid parts) for the finite element solution of the steady-state energy equation. However, before solving the energy equation, the fulfilment of the discrete mass conservation constraint for the velocity field mapped onto the new grid is obtained by solving a Poisson equation for a velocity correction potential which allows the calculation of appropriate velocity corrections. This technique is standard in the context of fractional step methods, which are often used to solve the continuity and the Navier-Stokes equations.

As the velocity field is determined before the conjugate thermal problem is solved, the energy equation is the only equation that needs to be solved in a large and complex domain. This, of course, allows significant savings in computer time with respect to a situation where the Navier-Stokes equations also had to be solved in their elliptic form in the same domain. It must be pointed out that, even if here the same cross-sections, fluid thermophysical properties and mass flow rates have been assumed for all the microchannels, the procedure is much more general. In fact, if this is not the case, it is sufficient to determine and appropriately map a different velocity field for each combination of microchannel cross-section, fluid properties and mass flow rate.

3. RESULTS AND DISCUSSION

In this demonstrative analysis, two values of the Reynolds number ($\mathrm{Re} = 100$ and 200), chosen among those typical of microchannel applications, are considered together with a Prandtl number $\mathrm{Pr} = 5$ for both fluids and six values of the ratio k_s/k_f of the solid wall to fluid thermal conductivities, namely, $k_s/k_f = 2.5$, 8, 25, 80, 250 and 800. In particular, the first value has been selected to show the behaviour of the micro heat exchanger when walls are made of a low thermal conductivity material. The third and fifth ones, instead, have been chosen because they are representative of a condition where, if the fluid is water, the microchannel wall is made of stainless steel ($k_s/k_f = 25$) or of silicon ($k_s/k_f = 250$). The last value ($k_s/k_f = 800$), instead, corresponds to the combination silicon–refrigerant fluid.

The computational domain, whose overall size (width×height×length) is $15H \times 1.5H \times 15H$, is discreditezed using a non-uniform mesh of $240 \times 24 \times 240$ eight-node hexahedral (brick) elements, with a total of $1,452,025$ nodes. There are 16 subdivisions across each microchannel and 8 subdivisions across each solid wall separating two adjacent flow passages or layers. The two-dimensional domain where the parabolized Navier-Stokes equations are integrated corresponds to one half of the cross-section of one microchannel and is discretized using 60×30 bilinear elements, with sizes gradually increasing with increasing distance from the walls, with a total of 1891 nodes. The values of the dimensionless step $\Delta x/H$ adopted to march forward in the axial direction range from 1×10^{-4}, at the microchannel inlet, to 1×10^{-2}, at the outlet. Appropriate boundary conditions are applied to take into account that all external surfaces are considered adiabatic and that the hot and the cold fluids enter the microchannels at the temperatures t_h and t_c, respectively.

Sample results are shown in Figs. 2 to 4. The temperature distributions on five planes in the computational domain are reported in Fig. 2 for both Reynolds numbers and for $k_s/k_f = 2.5$ and 25 (expanded scale in the vertical direction). Those for higher values of k_s/k_f are not shown since, in this case, the solid wall is nearly isothermal.

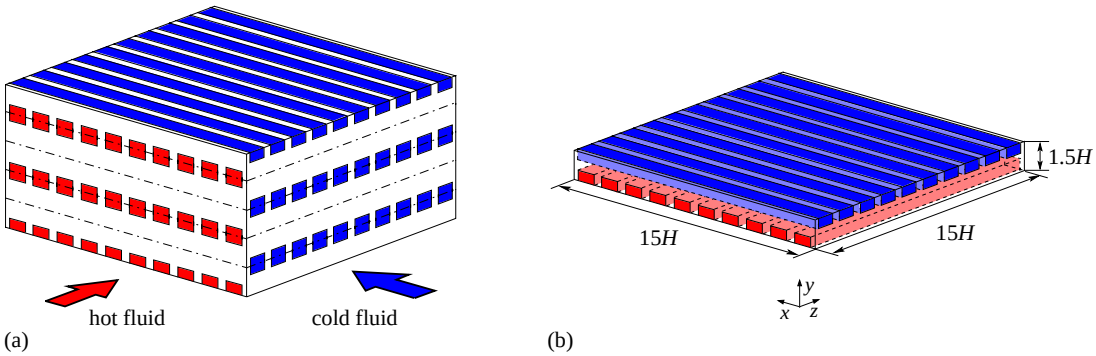

FIGURE 1. Cross-flow micro heat exchanger: (a) sketch of the geometry; (b) computational domain.

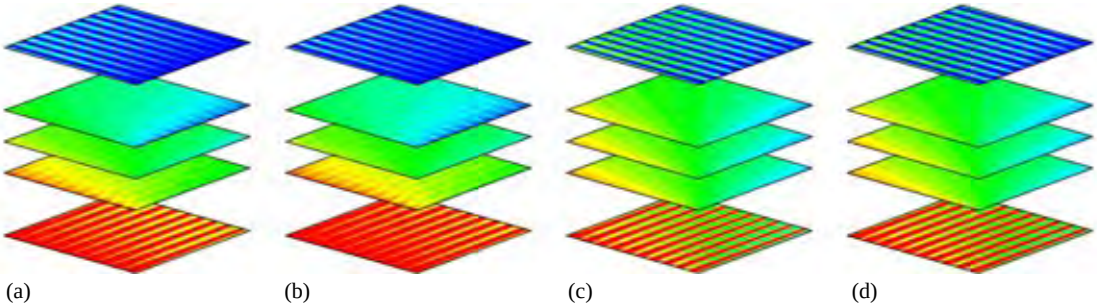

FIGURE 2. Temperature distributions on different planes in the computational domain (expanded scale in the vertical direction): (a) $\mathrm{Re} = 100$ and $k_s/k_f = 2.5$; (b) $\mathrm{Re} = 200$ and $k_s/k_f = 2.5$; (c) $\mathrm{Re} = 100$ and $k_s/k_f = 25$; (d) $\mathrm{Re} = 200$ and $k_s/k_f = 25$.

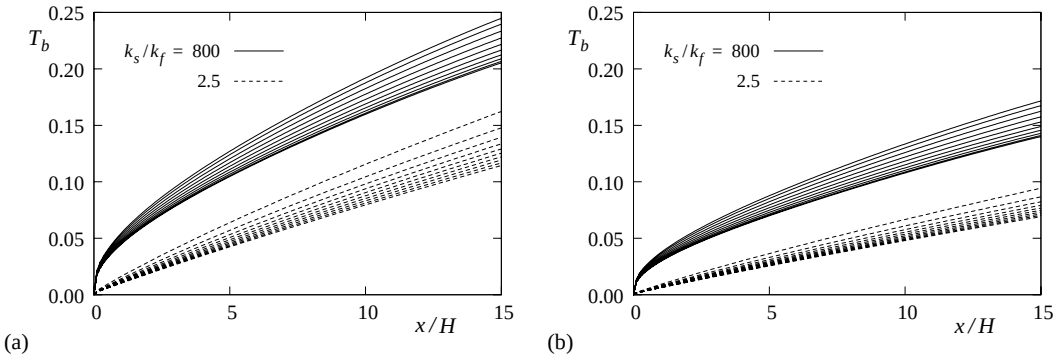

FIGURE 3. Axial distributions of the dimensionless bulk temperature T_b in different microchannels of the cold layer: (a) $\mathrm{Re} = 100$; (b) $\mathrm{Re} = 200$.

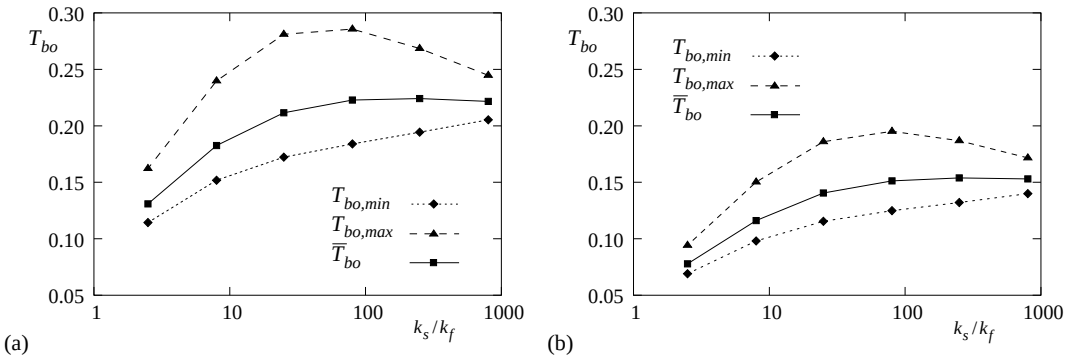

FIGURE 4. Minimum ($T_{bo,min}$), maximum ($T_{bo,max}$) and stream ($\overline{T}_{bo}$) dimensionless outlet bulk temperature of the cold fluid: (a) $\mathrm{Re} = 100$; (b) $\mathrm{Re} = 200$.

The axial distributions of the dimensionless bulk temperature

$$T_b = \frac{t_b - t_c}{t_h - t_c} \tag{1}$$

in all the microchannels of the cold layer are reported in Fig. 3 for $k_s/k_f = 2.5$ and 800 and the considered values of the Reynolds number. For a given axial position x/H, higher values of T_b refer to the microchannles closer to the inlet of the hot fluid. Obviously, higher values of T_b are also obtained for larger values of k_s/k_f and lower values of Re. It must be pointed out that, since the heat capacity rates are the same for all the microchannels of both the hot and cold streams, the dimensionless bulk temperatures of the hot fluid is the complement to one of that of the cold fluid at the same axial position.

Finally, the minimum and maximum values ($T_{bo,min}$ and $T_{bo,max}$) of the dimensionless bulk temperatures $(T_{bo})_i$ at the outlet of the microchannels of the cold layer are shown in Fig. 4 for different values of k_s/k_f, together with the dimensionless outlet bulk temperature of the whole cold stream

$$\overline{T}_{bo} = \frac{\overline{t}_{bo} - t_c}{t_h - t_c} = \frac{1}{10}\sum_{i=1}^{10}(T_{bo})_i \tag{2}$$

As expected, the temperature difference $T_{bo,max} - T_{bo,min}$ reaches its maximum for intermediate values of the ratio k_s/k_f, since it must tend to zero both for $k_s/k_f \to 0$ (zero flux, i.e., $(T_{bo})_i = 0$ for all the microchannels of the cold layer) and $k_s/k_f \to \infty$ (isothermal walls at $T = (t - t_c)/(t_h - t_c) = 0.5$). It must be pointed out that, in this case, the value of $\overline{T}_{bo}$ coincides with that of the effectiveness ε of the micro heat exchanger which can be expressed as

$$\varepsilon = \frac{\overline{t}_{bo} - t_c}{t_h - t_c} = \overline{T}_{bo} \tag{3}$$

As can be seen, also the effectiveness of the micro heat exchanger reaches a maximum for intermediate values of the ratio k_s/k_f.

4. CONCLUSIONS

As an alternative to massive CFD, a hybrid technique, which has the advantage of accounting for all three-dimensional features of the flow field, but with a limited computational effort, has been employed for the solution of conjugate convection-conduction heat transfer problems in cross-flow micro heat exchangers. Future plans include the application of this efficient method to more systematic analyses of micro heat exchangers of the same type.

REFERENCES

[1] G. Hetsroni, A. Mosyak, E. Pogrebnyak and L.P. Yarin, Heat transfer in micro-channels: Comparison of experiments with theory and numerical results, *Int. J. Heat Mass Transfer*, 48, pp. 5580-5601, 2005.

[2] I. Tiselj, G. Hetsroni, B. Mavko, A. Mosyak, E. Pogrebnyak and Z. Segal, Effect of axial conduction on the heat transfer in micro-channels, *Int. J. Heat Mass Transfer*, 47, pp. 2551-2565, 2004.

[3] M.K. Kang. J.H. Shin, H.-H. Lee and K. Chun, Analysis of laminar convective heat transfer in micro heat exchanger for stacked multi-chip module, *Microsyst. Technol.*, 11, pp. 1176-1186, 2005.

[4] H. Al-Bakhit and A. Fakheri, Numerical simulation of heat transfer in simultaneously developing flows in parallel rectangular ducts, *Applied Thermal Engng.*, 26, pp. 596-603, 2006.

[5] M.I. Hasan, A.A. Rageba, M. Yaghoubib and H. Homayoni, Influence of channel geometry on the performance of a counter flow microchannel heat exchanger, *Int. J. Thermal Sci.* (in press).

[6] C. Nonino, S. Savino and S. Del Giudice, Conjugate forced convection and heat conduction in micro heat exchangers: a hybrid approach, *Proc. 1st European Conference on Microfluidics*, Bologna, 2008 (on CD-ROM).

[7] C. Nonino, S. Del Giudice and S. Savino, Temperature dependent viscosity effects on laminar forced convection in the entrance region of straight ducts, *Int. J. Heat Mass Transfer*, 49, pp. 4469-4481, 2006.

First International Conference on Computational Methods for Thermal Problems
ThermaComp2009, September 8-10, 2009, Napoli, Italy
N.Massarotti and P.Nithiarasu (Eds.)

HEAT TRANSFER ENHANCEMENT IN A STRIAGHT CHANNEL VIA TRANSVERSLY OSCILLATING ADIABATIC CIRCULAR CYLINDER

Bayram Celik and Ali Beskok
Old Dominion University, Aerospace Engineering Department,
Norfolk, VA 23529-0247, USA.
Email: baycel@gmail.com and ABeskok@odu.edu

Mehrdad Raisee
School of Mechanical Engineering, University College of Engineering,
University of Tehran, Tehran, Iran.
Email: mraisee@ut.ac.ir

ABSTRACT

Vortex shedding from a transversely oscillating circular cylinder confined in a channel and its effect on the wall heat transfer of a channel under constant heat flux wall boundary condition are studied by utilizing an arbitrary Lagrangian Eulerian formulation based on h/p finite element algorithm. The numerical method exhibits spectral accuracy and allows large mesh deformation in the computational domain. The simulations are performed at Re=100 for a fixed maximum cylinder displacement of 0.4 times the cylinder diameter. For all these cases, blockage ratio is equal to 1/3. The simulation results show that the vortex shedding from the cylinder increases the heat transfer levels significantly. The transverse oscillation of the cylinder creates strong vortices close to the walls which results in an effective heat transfer mechanism from the channel walls. Numerical simulation results, conducted for a wide range of cylinder excitation frequencies, show that the highest heat transfer enhancement is arisen for the cylinder oscillation to natural vortex shedding frequency ratio of 0.75.

Key Words: *Heat Transfer, Transverse Oscillation, Vortex Dynamics, Vortex Shedding*

1. INTRODUCTION

The thermal performance of cooling systems can be substantially improved by various augmentation techniques. Heat transfer enhancement is often obtained by geometric modifications of the wall boundaries. For example, casting artificial roughness or putting obstacles on the solid boundary can substantially increase the wall heat transfer coefficient [1]. Such boundary modifications can generate vortices, which increase mixing, reduce the thickness of the thermal boundary layer, and thereby enhance heat transfer. Since the fluid velocities and characteristic length scales are relatively small in meso-scale heat transfer devices, flow Reynolds number is low or moderate. Therefore, these devices are operating at laminar condition usually. Moreover, the lengths of these devices are long enough that the flow is considered to be hydro-dynamically fully-developed. Utilizing a proper vortex generation mechanism can effectively enhance heat transfer in such devices [2-6]. When the cylinder is forced to oscillate in the cross-flow direction with a frequency that is in the vicinity of natural vortex shedding frequency, the vortex shedding synchronizes with the cylinder movement [7-9]. This synchronization condition is known as lock-in, and the cylinder excitation frequencies that yields this state is called primary lock-in regime. The main objective of the present study is to enhance the heat transfer in a straight channel by utilizing the vortex shedding mechanism from an adiabatic circular cylinder, which is subjected to forced transverse oscillation in cross flow direction at Re =100. The influences of the vortex dynamics on heat transfer from the channel walls, which are under constant heat flux, were studied systematically for wide range of cylinder excitation frequency values.

2. GOVERNING EQUATIONS AND NUMERICAL METHOD

The simulations presented here are based on the numerical solutions of two dimensional, unsteady, incompressible Navier-Stokes equations and energy equation in a moving domain. For a Newtonian fluid, non-dimensional Navier-Stokes equations are as follows:

$$\frac{\partial \mathbf{u}}{\partial t} + (\mathbf{u} - \mathbf{w}) \cdot \nabla \mathbf{u} = -\nabla p + \frac{1}{Re} \nabla^2 \mathbf{u} \tag{1}$$

The velocity field obtained from Eq. (1) satisfies the continuity equation written below.

$$\nabla \cdot \mathbf{u} = 0. \tag{2}$$

In a moving domain, non-dimensional form of the energy equation is as follows:

$$\frac{\partial T}{\partial t} + (u - w).\nabla T = \frac{1}{Pe} \nabla^2 T \tag{3}$$

where Pe can be written in terms of Re and Pr as below:

$$Pe = \frac{UD}{\alpha} = Re.Pr \tag{4}$$

In order to solve Eqs (1)-(3) in a moving domain, an arbitrary Lagrangian Eulerian (ALE) formulation based on h/p finite element algorithm is utilized in this study [10]. The algorithm uses third order time accurate operator splitting scheme [11-12].

3. PROBLEM DEFINITION

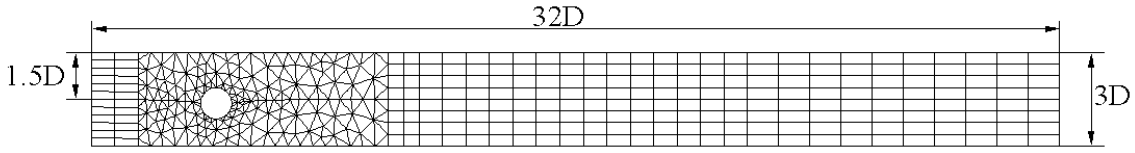

FIGURE 1. Details of the mesh that is utilized for the simulation of a flow past an oscillating circular cylinder confined in a straight channel, and the channel dimensions

The numerical mesh and the dimensions of the physical domain are depicted in Fig. 1. As can be seen from the figure, a circular cylinder that has a diameter of D, is surrounded by 314 triangular elements and the remaining portion of the computation domain is discretized into 232 quadrilateral elements. The centre of the cylinder is 4D and 1.5D away from the inlet and the channel walls, respectively. It is assumed that fully developed flow, which is parabolic in shape with a maximum velocity of 1.5 times the mean velocity, enters the channel with a constant temperature of T = 0.0. The cylinder is located at the centreline of the channel (y = 0.0) at t = 0.0, and it is subjected to a forced oscillation in cross-flow direction according to $y = y_{max} \sin(\quad t)$ where y_{max} is equal to 0.4D. On all of the solid boundaries, no-slip boundary conditions are applied. Zero heat flux (q˝ = 0.0) and constant heat flux, q˝ = 1.00, are applied on the cylinder surface and the channel walls, respectively. At the channel outlet, 31D away from the inlet, zero Neumann boundary conditions are applied for both velocity and temperature. For all of the simulations presented here, flow Reynolds number that is based on the cylinder diameter and average inlet velocity, is kept constant to be 100, while Pr number is 1. The simulation results showed that the solutions are grid independent for the polynomial discretization order of 7th and higher.

4. RESULTS

Computations were performed for fixed amplitude of 0.4·D and various frequencies. Fig.'s 2.(a) (c) and (e) respectively show the snapshots of vorticity contours for an oscillating cylinder confined in channel for F = 0.75, F = 1.00 and F = 1.25 at the instant when the cylinder passes the centreline during its upward motion. It is seen that the vortices are shed from the upper and lower sections of the cylinder and their size is larger than those found for non-oscillating cylinder. An interesting feature which can be observed from the vorticity contours is the fact that the vortices for F = 0.75 (Fig. 2(a)) are formed closer to the channel wall compare to those of F =1.0 and also F = 1.25.

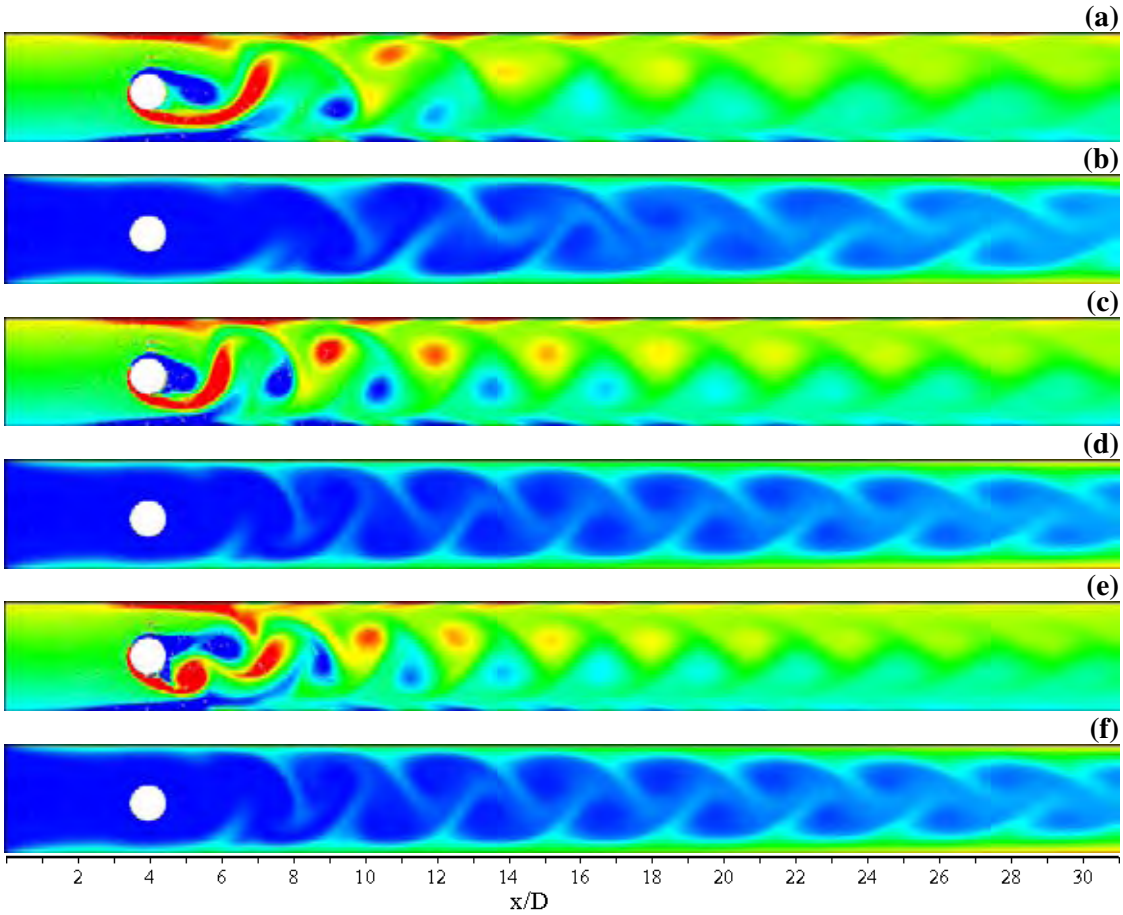

FIGURE 2: Vorticity and temperature contours for flows with F=0.75 (a), (b), 1.00 (c), (d) and 1.25 (d), (e) at Re=100, Pr=1.00

In order to show how vortex shedding from the oscillating cylinder influences the wall heat transfer, the corresponding temperature contour snapshot are presented in Figs 2.(b), (d) and (f). It is observed that the vortex street formed at the cylinder downstream substantially influences the thermal boundary layer development downstream of the cylinder. The shape of the thermal boundary layer is kind of corrugated shape. This is due to the recirculation motion of the vortices, which as they convect downstream; they transport the hot near-wall fluid to the main stream and vice versa. Qualitative comparisons of temperature contours shows that for F=0.75 (see Fig. 2(b)), the thickness of the thermal boundary layer is less than those for F = 1.0 and 1.25. This feature is consistent with the vorticity contours shown in Fig. 2 where the vortex cores for F = 0.75 are closer to the channel walls than those for higher frequencies.

The variations of time-averaged Nusselt number along the walls of the channels that have oscillating cylinder with F=0.75, 1.00, 1.25 and stationary cylinder are presented in Fig. 3 for comparison. It appears that oscillation of the cylinder does not significantly affect Nusselt number distribution upstream of the circular cylinder. On the hand, oscillation of the obstacle in cross-flow direction causes higher Nusselt number levels at cylinder downstream. This is because the vortices transport the low-temperature and high-speed core flow toward the heated regions of the channel. Also, the high-temperature wall flow is carried away from the heated regions of the channel to mix with the low-temperature core flow by transverse vortices. It is seen that the best heat transfer enhancement is obtained for frequency ratio of F = 0.75. This is because, as shown in Fig. 2 at this frequency ratio the vortices are closer to the heated walls.

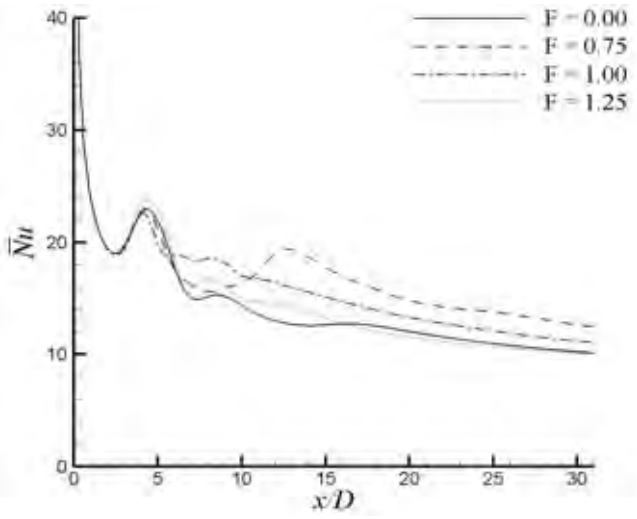

FIGURE 3. Time averaged Nusselt number variations along the channel walls for straight channel, stationary and oscillating cylinder confined in the channel at Re = 100, Pr = 1.0.

5. CONCLUSIONS

Vortex shedding from an oscillating cylinder confined in a channel can increase heat transfer from the wall. The level of heat transfer enhancement depends on the strength and the location of vortices respect to the wall. The maximum heat transfer coefficient and the lowest wall temperature is obtained for a circular cylinder with oscillating in the lock-in region at a frequency ratio of F=0.75.

REFERENCES

[1] R.L. Webb, E.R.G. Eckert, and R.J. Goldstein, Heat Transfer and Friction in Tubes with Repeated Rib Roughness, *International Journal of Heat and Mass Transfer*,14, 601-617, 1971.

[2] K. Sreenivasan, and A. Ramachandran, Effect of vibration on heat transfer from a horizontal cylinder to a normal air stream, *Int. J. Heat Mass Transfer*, 60-67, 1961.

[3] U.C. Saxena, A.D.K. Laird, Heat transfer from a cylinder oscillating in a cross flow, J. *Heat Transfer*, 100, 684-689, 1978.

[4] C. Gau, J.M. Wu, and C.Y. Liang, Heat transfer enhancement and vortex flow structure over a heated cylinder oscillating in the cross flow direction, *J. Heat Transfer* ,121, 789–795, 1999.

[5] T.S. Pottebaum, and M. Gharib, Using oscillations to enhance heat transfer for a circular cylinder, *International Journal of Heat and Mass Transfer*, 49, 3190–3210, 2006.

[6] S.J. Yang, Numerical study of heat transfer enhancement in a channel flow using an oscillating vortex generator, *Heat and Mass Transfer*, 39, 257–265, 2003.

[7] J. Carberry, J. Sheridan, and D. Rockwell, Forces and wake modes of an oscillating cylinder, *J Fluid Struct,* 15, 523-532, 2001.

[8] C.H.K. Williamson, and A. Roshko, Vortex formation in the wake of an oscillating cylinder, *J Fluid Struct*, 2, 355–381, 1988.

[9] B. Celik, U. Akdag, S. Gunes, and A. Beskok, Flow past an oscillating circular cylinder in a channel with an upstream splitter plate, *Physics of Fluids,* 20, 103603, 2008.

[10] A. Beskok, T.C. Warburton, An unstructured hp finite-element scheme for fluid flow and heat transfer in moving domains, *Journal of Computational Physics*, 174, 492-509, 2001.

[11] G.E. Karniadakis, and S.J. Sherwin, *Spectral/hp Element Methods for CFD*, Oxford University Press, Oxford UK, 2005.

[12] G.E. Karniadakis, M. Israeli, and S.A. Orszag, High-Order Splitting Methods for the Incompressible Navier Stokes Equations, *Journal of Computational Physics,* 97, 414-443, 1991.

First International Conference on Computational Methods for Thermal Problems
ThermaComp2009, September 8-10, 2009, Naples, Italy
N.Massarotti and P.Nithiarasu (Eds.)

Invariant Grids and Lattice Boltzmann Method for Combustion

Eliodoro Chiavazzo
Swiss Federal Institute of Technology (ETH), Institut f. Energietechnik ML L 17 Sonneggstrasse 3
8092 Zurich Switzerland, eliodoro.chiavazzo@gmail.com

Ilya V. Karlin
Swiss Federal Institute of Technology (ETH), Institut f. Energietechnik ML L 13 Sonneggstrasse 3
8092 Zurich Switzerland, karlin@lav.mavt.ethz.ch

Alexander N. Gorban
University of Leicester, Department of Mathematics University road LE1 7RH Leicester UK,
ag153@leicester.ac.uk

Konstantinos Boulouchos
Swiss Federal Institute of Technology (ETH), Institut f. Energietechnik ML J 39 Sonneggstrasse 3
8092 Zurich Switzerland, boulouchos@lav.mavt.ethz.ch

ABSTRACT

The lattice Boltzmann (LB) method is a relatively novel approach to numerical flow simulations, and recent studies have proved that it is highly competitive to traditional methods when simulating compressible and turbulent flows (in terms of accuracy and efficiency). Although this makes LB a good candidate for computing reactive flows, applications in this field are still limited by the stiffness of the governing equations and the large amount of fields to solve. In this sense, the present study intends to be a first step toward the efficient, yet accurate, solution to this problem. **Key Words:** *Combustion, lattice Boltzmann, invariant manifold.*

1. INTRODUCTION

Accurate modeling of reactive flows requires the solution of a large number of conservation equations as dictated by detailed reaction mechanism. In addition to the sometimes prohibitively large number of variables introduced, the numerical solution of the governing equations has to face the stiffness due to the fast time scales of the kinetic terms. These issues make computations of even simple flames time consuming, and have particularly negative impact on the lattice Boltzmann method, whose number of fields (distribution functions or populations) is significantly larger than the number of conventional fields (density, momenta, temperature, species mass fractions) by a factor ranging from tens to hundreds for 2D and 3D simulations. However, the dynamics of complex reactive systems is often characterized by short initial transients when the solution trajectories approach low-dimensional manifolds in the concentration space, known as the *slow invariant manifolds* (SIM). Thus, the construction of SIM enables to establish a simplified description of a complex system by extracting only the slow dynamics and neglecting the fast.

In our study, the reduced model is obtained using the *method of invariant grids* (MIG) [1, 2]. The detailed mechanism of Li et al [3] (9 species, 21 elementary reactions) for hydrogen combustion is considered, and we search for a reduced description with two degrees of freedom. To this end, let us construct the $2D$ quasi equilibrium manifold for a stoichiometric H_2-air mixture under fixed pressure $p = 1bar$ and enthalpy $\bar{h} = 2.8kJ/kg$, corresponding to the temperature $T_0 = 300K$ for the stoichiometric unburned mixture $H_2+0.5O_2+1.88N_2$. A QEM is obtained solving the following minimization

problem:

$$\begin{aligned} &min \quad G \\ &s.t. \quad \sum_i m_j^i Y_i = \xi^j, \quad j = 1, 2. \end{aligned} \tag{1}$$

Here, G represents the mixture-averaged entropy, and the vector set $\{\boldsymbol{m}_j = (m_j^1, ..., m_j^9)\}$ is used to re-parameterize the mass fractions Y_i in terms of new variables ξ^j, which are expected to follow a slow dynamics.

Many suggestions for defining slow lumped variables in chemical kinetics are known in the literature, and for our purposes here we use the *total number of moles* ξ^1 and *free oxygen* ξ^2, respectively (see, e.g., [4]). An approximated solution to (1), computed making use of the algorithm introduced in [5], is shown in Fig. 1, and it is called *quasi equilibrium grid* (QEG). The corresponding invariant grid is found by relaxation of the QEG Ω under the following film equation of dynamics [1]

$$\frac{d\Omega}{dt} = \vec{f} - \boldsymbol{P}\vec{f}, \tag{2}$$

where $\vec{f}$ and $\boldsymbol{P}$ denote the vector of motion in the phase space and a projector operator onto the manifold tangent space, respectively. Following [1], here we adopt the *thermodynamic projector* which enables to define the fast motions toward the slow manifolds. Finally, the refined grid, approximating the slow invariant manifold, is also shown in Fig. 1. More details can be found in the literature [6, 7, 8].

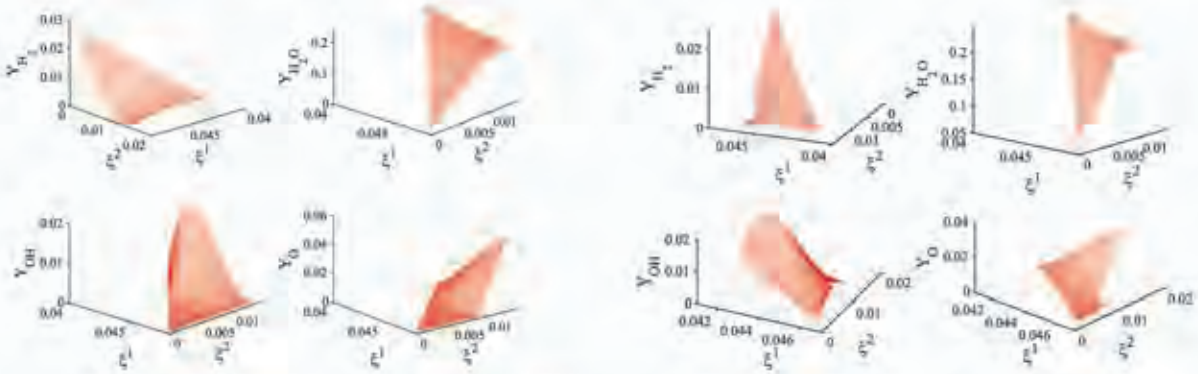

FIGURE 1. Quasi equilibrium grid (left) and refined grid (right): Four coordinates function of the parameters ξ^1, ξ^2.

2. DETAILED MODEL

Here, we consider the simplest lattice Boltzmann formulation suitable for simulations of combustion [9], whereas more elaborate LB models for mixtures [10] and compressible flows [11] shall be taken into account in the near future, too. According to [9], the flow field is treated as a single-component medium that can be described, in terms of pressure distribution functions p_α, by the following equation at an arbitrary lattice node $\boldsymbol{x}$ [13]:

$$p_\alpha(\boldsymbol{x} + \boldsymbol{e}_\alpha, t + \delta t) = p_\alpha(\boldsymbol{x}, t) - \frac{1}{\tau_F}\left[p_\alpha(\boldsymbol{x}, t) - p_\alpha^{eq}(p, \boldsymbol{u})\right], \tag{3}$$

where the equilibrium populations p_α^{eq} read:

$$p_\alpha^{eq} = w_\alpha p\left[1 + 3\left(\boldsymbol{e}_\alpha \boldsymbol{u}^T\right) + \frac{9}{2}\left(\boldsymbol{e}_\alpha \boldsymbol{u}^T\right)^2 - \frac{3}{2}\boldsymbol{u}^2\right]. \tag{4}$$

The pressure p and the fluid velocity $\boldsymbol{u}$ are given by:

$$p = \sum_\alpha p_\alpha, \quad \boldsymbol{u} = \frac{1}{p_0}\sum_\alpha \boldsymbol{e}_\alpha p_\alpha, \tag{5}$$

where the reference pressure $p_0 = \rho_0/3$, with ρ_0 denoting the reference density of the LB model. Let δt be the time step, the relaxation parameter τ_F is related to the kinematic viscosity ν by (see, e.g., [15])

$$\nu = \frac{2\tau_F - 1}{6}\delta t. \tag{6}$$

In general, the discrete velocities can be regarded as the nodes of a Gauss-Hermite quadrature applied to the Maxwell-Boltzmann distribution function, and each of them is characterized by a proper weight w_α (see also [13, 14]). According to [9], the flow field is not affected by the chemical reaction, transport coefficients are constant and Fick's law applies to the diffusion. Let $\bar{h}_0$ be a reference enthalpy, the evolution equations for enthalpy and concentration of species i are written as

$$\tilde{h}_\alpha\left(\boldsymbol{x}+\boldsymbol{e}_\alpha, t+\delta t\right) - \tilde{h}_\alpha\left(\boldsymbol{x}, t\right) = -\frac{1}{\tau_h}\left[\tilde{h}_\alpha\left(\boldsymbol{x}, t\right) - \tilde{h}_\alpha^{eq}\left(\tilde{h}, \boldsymbol{u}\right)\right] + w_\alpha Q_h, \tag{7}$$

$$Y_{i\alpha}\left(\boldsymbol{x}+\boldsymbol{e}_\alpha, t+\delta t\right) - Y_{i\alpha}\left(\boldsymbol{x}, t\right) = -\frac{1}{\tau_{Y_i}}\left[Y_{i\alpha}\left(\boldsymbol{x}, t\right) - Y_{i\alpha}^{eq}\left(Y_i, \boldsymbol{u}\right)\right] + w_\alpha Q_{Y_i}, \tag{8}$$

where

$$\tilde{h} = \bar{h}/\bar{h}_0 = \sum_\alpha \tilde{h}_\alpha, \quad Y_i = \sum_\alpha Y_{i\alpha}, \tag{9}$$

and the equilibrium populations $\tilde{h}_\alpha^{eq}$, $Y_{i\alpha}^{eq}$ are expressed as in (4) after replacing p with $\tilde{h}$ and Y_i, respectively. Assume t_0 is a factor for converting physical time into LB time units: $(t)_{LB} = (t)_{phys}\Big/t_0$, the source terms take the explicit form

$$Q_h = \frac{1}{h_0}\left(\sum_{i=1}^{9}\frac{\dot{\omega}_i W_i}{\bar{\rho}}h_i\right)t_0\delta t, \;\; Q_{Y_i} = \frac{\dot{\omega}_i W_i}{\bar{\rho}}t_0\delta t, \tag{10}$$

where $\bar{\rho}$ is the mixture-averaged density, while $\dot{\omega}_i$, W_i, h_i denote the rate of change, molecular weight and enthalpy of species i, respectively. The thermal diffusivity κ and diffusion coefficient D_i of species i are related to the relaxation parameters as follows

$$\kappa = \frac{2\tau_h - 1}{6}\delta t, \quad D_i = \frac{2\tau_{Y_i} - 1}{6}\delta t. \tag{11}$$

3. PREMIX COUNTERFLOW FLAMES

For simplicity, we use the assumption of equal diffusivity D for all species and Lewis number $Le = \kappa/D = 1$. In this case, the mixture enthalpy $\bar{h}$ and the element fractions remain constant throughout the domain, and the reduced dynamics takes place along a single invariant grid. Notice however that, the latter assumption is not restricting and a generalization is obtained by extending the invariant grid with enthalpy and element fractions as additional degrees of freedom. Moreover, in low-Mach combustion, the pressure p can be considered constant for most cases. Under the latter assumptions, the equations (8) can be written in terms of the slow manifold parameters ξ^1, ξ^2 as follows:

$$\xi_\alpha^j\left(\boldsymbol{x}+\boldsymbol{e}_\alpha, t+\delta t\right) - \xi_\alpha^j\left(\boldsymbol{x}, t\right) = -\frac{1}{\tau_\xi}\left[\xi_\alpha^j(\boldsymbol{x}, t) - \xi_\alpha^{jeq}\left(\xi^j, \boldsymbol{u}\right)\right] + w_\alpha Q_{\xi^j}, \tag{12}$$

where, the equilibrium populations for the reduced variables ξ^j read

$$\xi_\alpha^{jeq} = w_\alpha \xi^j\left[1 + 3\left(\boldsymbol{e}_\alpha \boldsymbol{u}^T\right) + \frac{9}{2}\left(\boldsymbol{e}_\alpha \boldsymbol{u}^T\right)^2 - \frac{3}{2}\boldsymbol{u}^2\right], \tag{13}$$

and the source terms take the form:

$$Q_{\xi^j} = \sum_{i=1}^{9} m_j^i Q_{Y_i}, \;\; \xi^j = \sum_{i=1}^{9} m_j^i Y_i. \tag{14}$$

Here, we consider the so-called counterflow laminar flame as a two dimensional benchmark of the suggested methodology. A well premixed stoichiometric H_2-air mixture is uniformly ejected from two parallel stationary flat nozzles, located at $y = \pm L_y$. When properly ignited, the fuel reacts generating two twin flames in this counterflow, while the burned gas exits the domain along the x-direction. Under

the assumption of symmetrical flow with respect to the stagnation lines $x = 0$ and $y = 0$, the computational domain can be restricted to the region where $x \geq 0$ and $y \geq 0$, and simulations can be carried out using the standard 2-dimensional lattice $D2Q9$. Species dynamics can be simulated by solving both the detailed model (7), (8) and the reduced one (12). In the latter case, the source terms Q_{ξ^j} are tabulated at each node of the invariant grid, and accessed through multi-variate linear interpolation. When simulating the reduced model, a remarkable saving, in terms of both memory (one-quarter of the density functions are stored at any lattice node) and number of time steps ($\delta t_{reduced} \cong 35\delta t_{detailed}$), can be achieved. In both models (detailed and reduced), the mixture, initially under room temperature $T_0 = 300K$, is ignited by placing a hot spot at the origin of the reference system. Very good agreement is demonstrated as reported in Fig. 2, where the time evolution of O radical concentration is shown.

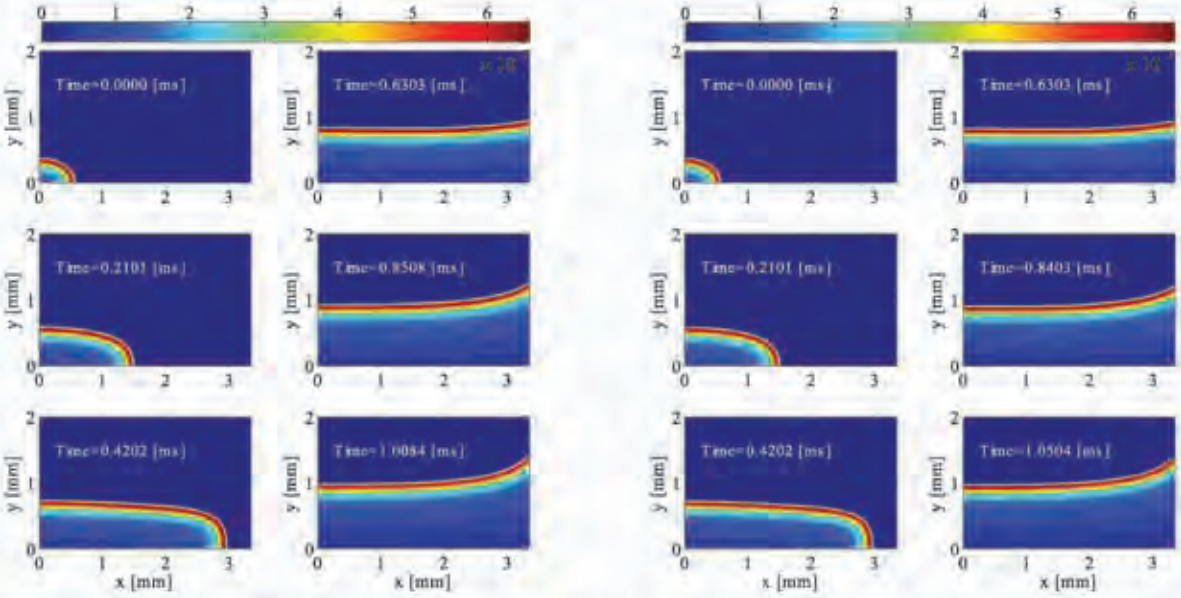

FIGURE 2. Detailed model (left) and reduced model (right) using the $D2Q9$ lattice: O mass fraction evolution

4. CONCLUSIONS

Here, we suggest a methodology for using accurate reduced chemical kinetics in combination with a lattice Boltzmann solver for simulating reactive flows. It has been shown that the method of invariant grids (MIG) is suitable for providing the reduced description of chemistry, and this approach enables to cope with stiffness when solving the LB species equations. This is particularly desirable in the case of explicit solvers, and it results in a remarkable speedup.

REFERENCES

[1] A. Gorban, I. V. Karlin, *Invariant Manifolds for Physical and Chemical Kinetics*. Springer, Berlin, 2005.
[2] A. N. Gorban, I. V. Karlin, A. Y. Zinovyev, *Physica A*, vol. 333, pp. 106–154, 2004.
[3] J. Li, Z. Zhao, A. Kazakov, F.L. Dryer, *Int. J. Chem. Kinet.*, vol. 36, pp. 566–575, 2004.
[4] Q. Tang, S. B. Pope, *Combust. Theory Model.*, vol. 8, pp. 255–279, 2004.
[5] E. Chiavazzo, I. V. Karlin, *Jour. Comput. Phys.*, vol. 227, pp. 5535–5560, 2008.
[6] E. Chiavazzo, A.N. Gorban, I.V. Karlin, *Comm. Comput. Phys.*, vol. 2, pp. 964–992, 2007.
[7] E. Chiavazzo, I.V. Karlin, C.E. Frouzakis, K. Boulouchos, *Proc. Combust. Instit.*, vol. 32, pp. 519-526, 2009.
[8] E. Chiavazzo, I. V. Karlin, A. N. Gorban, K. Boulouchos, *JSTAT*, (preprint), 2009.
[9] K. Yamamoto, X. He, G. D. Doolen *Jour. Stat. Phys.*, vol. 107, pp. 367–383, 2002.
[10] S. Arcidiacono, I. V. Karlin, J. Mantzaras, and C. E. Frouzakis, *Phys. Rev. E*, vol. 76, 046703, 2007.
[11] N. Prasianakis and I. V. Karlin, *Phys. Rev. E*, vol. 76, 016702, 2007.
[12] P. L. Bhatnagar, E. P. Gross, M. Krook, *Phys. Rev.*, vol. 94(3), pp. 511-525, 1954.
[13] S. Succi, *The Lattice Boltzmann Equation for Fluid Dynamics and Beyond*. Oxford University Press, Oxford, 2001.
[14] I. V. Karlin, A. Ferrante, H. C. Öttinger, *Europhys. Lett.*, vol. 47(2), pp. 182–188, 1999.
[15] S. Chen, G. Doolen, *Annu. Rev. Fluid Mech.*, vol. 30, pp. 329–364, 1998.

First International Conference on Computational Methods for Thermal Problems
ThermaComp2009, September 8-10, 2009, Napoli, Italy
N.Massarotti and P.Nithiarasu (Eds.)

FREE SURFACE LATTICE BOLZTMANN METHOD FOR HYDRAULIC PROBLEMS

Biscarini Chiara
Water Resources Research And Documentation Centre, University For Foreigners, Villa La Colombella 0634Perugia, Italy, biscarini.chiara@unistrapg.it

Di Francesco Silvia
H2CU, Honors Center of Italian Universities, University of Rome La Sapienza, Rome, Italy - Department of Civil and Environmental Engineering, University of Perugia, Via G. Duranti 93 06125 Perugia, Italy, silvia.difrancesco@unipg.it

Mencattini Matteo
Department of Mechanical Engineering, University of Rome Tor Vergata, Via del Politecnico 1 00133 Roma, Italy， matteo.mencattini@gmail.com

Pizzuto Luca
Department of Mechanical Engineering, University of Rome Tor Vergata, Via del Politecnico 1 00133 Roma, Italy, luca_pizzuto@hotmail.com

ABSTRACT

An algorithm for free surface simulations with the lattice Boltzmann method is presented. The method is chosen for its computational efficiency and ability to deal with complex geometries. Topic of the present research is the validation of the developed code with a typical case of environmental-hydraulic interest (i.e. dam break). A comparison with experimental result is performed.

Key Words: free surface, Lattice Boltzmann, BGK, hydraulic applications

1. INTRODUCTION

A potential candidate for detailed hydraulic simulations is the Lattice Boltzmann Method (LBM), which is emerging as an alternative to Navier-Stokes equations for the computational modelling of a wide variety of complex fluid flow problems. The macroscopic fluid dynamics is solved through a mesoscopic kinetic approach in which all details of molecular motion are removed except those that are strictly needed to recover hydrodynamic behaviour at the macroscopic scale (mass, momentum and energy conservation). Its major advantage is the simple form of the governing equations system, which is easy to implement and natural to parallelize. To simulate the typical hydraulic two phase problems, the LBM is combined here to the Volume Of Fluid (VOF) method, which is a surface-tracking technique applied to a fixed Eulerian mesh.

2. NUMERICAL MODEL

The Lattice Boltzmann Equation simulates transport phenomena by tracking the evolutions of density distribution functions (or populations), $f_i\left(\vec{x},\vec{e},t\right)$ that describe the probability to find a system of particles at site $\vec{x}$, at time t and with velocity $\vec{e}$.
The general form of the Lattice Boltzmann Equation (LBE) reads as follows:

$$f_i\left(\vec{x}+\vec{e}_i\Delta t,t+\Delta t\right)-f_i\left(\vec{x},t\right)+\Delta t\cdot F_i=\frac{\Delta t}{}\left[f_i\left(\vec{x},t\right)-f_i^{eq}\left(\vec{x},t\right)\right] \quad (1)$$

where F_i is an external force. The right hand side of eq. (1), called local collision operator, describes the particle density change due to collisions via a single–time relaxation towards local equilibrium f^{eq} (local Maxwellian expanded to second order in the fluid speed) on a typical timescale (called BGK approximation [2]). The velocity space is drastically reduced to only a few discrete points by assuming that at each site the particles can only move along a finite number of directions, described by a finite set of discrete particle velocity vectors. In this paper, the 9-bit bidimensional model (D2Q9) will be used [3].
The implemented algorithm consists of two steps: streaming and collision [4].

– Streaming: all the distribution functions are advected with their respective velocities to their neighbour lattice site.

$$f_i^{in}(x,t) = f_i^{out}(x - e_i \cdot \Delta t, t - \Delta t) \tag{2}$$

– Collision: after advection the particle distribution functions approach their equilibrium distributions due to a collision step

$$f_i^{out}(x,t) = f_i^{in}(x,t) - \frac{\Delta t}{}(f_i^{in}(x,t) - f_i^{eq}(x,t)) + \Delta t \cdot F_i \tag{3}$$

In eqs. (2) and (3) the incoming and outgoing distribution functions (i.e. before and after collision) are denoted with f^{in} and f^{out}, respectively.

The macroscopic density ρ and the velocity $\vec{u}$ are easily computed as:

$$= \sum_{i=1}^{9} f^{eq} \ , \quad \vec{u} = \sum_{i=1}^{9} \vec{e}_i f^{eq} \Big/$$

In the limit of weak departures from local equilibrium, i.e. small Knudsen numbers, and near the incompressible limit, i.e. small Mach numbers, it can be shown through a Chapman-Enskog analysis that the above formulation recovers the dynamic behaviour of a fluid with pressure $P = c_s^2$ and a kinematic viscosity $= c_s^2\left(- \Delta t/2\right)$, being c_s the lattice sound speed.

The simulation of free surfaces requires a distinction between liquid and no liquid regions. In order to track the motion, a layer of interface cells between liquid and no liquid regions is introduced [5, 6]. It is important to notice that direct state changes from liquid to gas and vice versa are not possible. Hence, liquid and gas cells are only allowed to transform into interface cells whereas interface cells can be transformed into both gas and liquid cells. The simulation and tracking of the free surface consists of three steps: the computation of the interface movement, the boundary conditions at the gas-liquid interface, and the re-initialization of the cell types.
The movement of the gas-liquid interface is tracked by the calculation of the mass that is contained in each cell. For this two additional values need to be stored for each cell, the mass m and the liquid fraction ε (the portion of the cell is filled with liquid fluid)

$$\begin{cases} (x) = 0, \forall x \in G \\ (x) = 1, \forall x \in L \\ 0 < \ (x) < 1, \forall x \in I \end{cases} \tag{5}$$

G: Empty cells, L: liquid cells, I: Interface cells

The mass m is related to ε as follows:

$$m = \ \cdot \tag{6}$$

For liquid cells the mass exchange in the i-th direction is given by:

$$\Delta m_i(x,t+\Delta t) = f_j(x+c_i,t) - f_i(x,t) \tag{7}$$

For interface cells, the mass can be exchanged in the common area :

$$\Delta m_i(x,t+\Delta t) = \left[f_j(x+c_i,t) - f_i(x,t) \right] * \frac{{}_i(x+c_i,t) + {}_i(x_i,t)}{2} \tag{8}$$

3. VALIDATION OF THE ALGORITHM BY EXPERIMENTAL RESULTS.

To check the ability of the algorithm to model extreme wave conditions, a breaking dam problem was simulated and compared to measurements from a wave tank. The test section of the tank is 4.6 m long, 0.5 m deep, and 0.3 m wide.
A removable wall is installed across the middle of the tank. Before the start of the experiment, the left-hand section is left empty and the right-hand section is filled with water up to a level of 0.46m. The wall is then abruptly removed, causing the water block to disintegrate and a fast running wave to be generated. The water shoots up, splashing against the top of the tank. The initial wave breaks, but a reflected wave begins to propagate in the opposite direction. In the experiment, the waves were followed for more than 10 seconds, which corresponds to about 3 full reflections. The simulation, compared with pictures deriving from the experimental results, shows a good agreement with the real behaviour (see figures 1 and 2).
The time evolution of water surface level has been evaluated for 4 vertical cross sections of the tank, located as reported in table 1.

In figure 3 the time evolution of water level at the study cross section is reported. Figure 4 shows the time evolution of water surface difference between section X4 and X3.

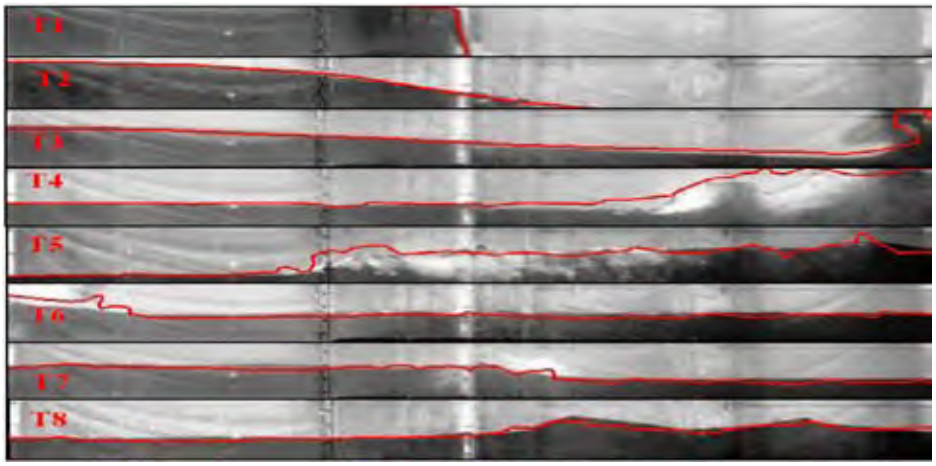

FIGURE 1: Real dam break (picture) and simulation's (red line) results

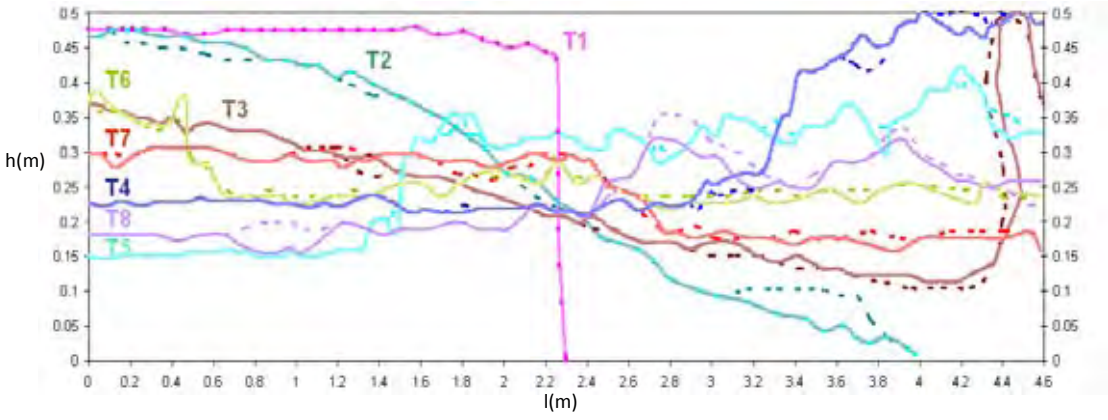

FIGURE 2: Comparison between computed and experimental results for time T1-T8. Continuous line: real water surface level, dashed line: simulated water surface level

Cross Section	X1	X2	X3	X4
Position (m)	0	2.3	3.8	4.6

TABLE 1: Location of reference Cross Sections X1, X2, X3, X4

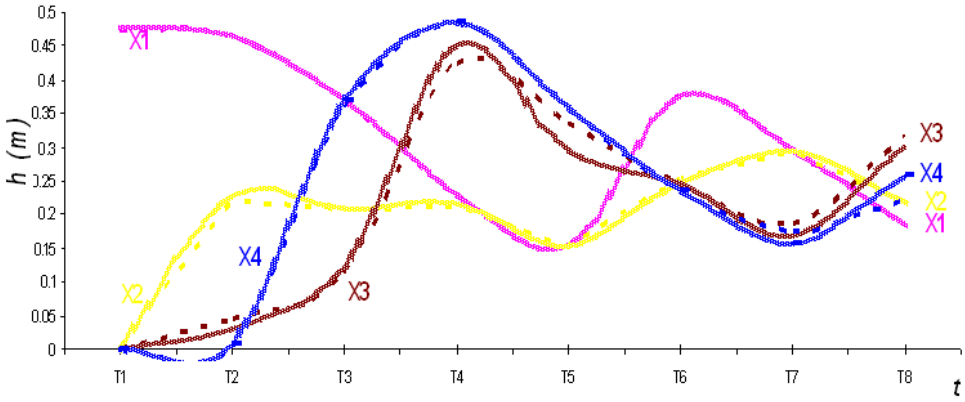

FIGURE 3: Water surface level at different time steps for sections X1, X2, X3 X4. Real behaviour: dashed line. Numerical results: continuous line

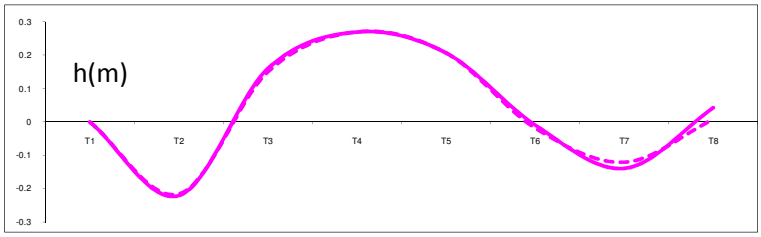

FIGURE: 4: Water level difference between X4 and X2. Real behaviour: dashed line. Numerical results: continuous line

REFERENCES

[1] Nils Thürey, Physically based Animation of Free Surface Flows with the Lattice Boltzmann Method, PhD thesis (2007)

[2] P. Bhatnagar, E. Gross, and M. Krook, Phys. Rev. E 50:511–525 (1954).

[3] D.D'Humiers, Y.H. Quian and P. Lallemand, Phys. Rev. Lett., 17, 479484, 1992

[4] Succi, S., 2001, The lattice Boltzmann equation for fluid dynamics and beyond, Clarendon, Oxford.

[5] Körner, Carolin et al., *FreeWIHR: Lattice Boltzmann Methods with Free Surfaces and their Application in Material Technology* In: Bode, Arndt; Durst, Franz (Hrsg.): *High Performance Computing in Science and Engineering, Garching 2004* (KONWIHR Results Workshop, Garching, 14.10.-15.10.2004) . Springer, 2005.

[6] C. Körner et al., Journal of Statistical Physics, Vol. 121, Nos. 1/2, October 2005

First International Conference on Computational Methods for Thermal Problems
ThermaComp2009, September 8-10, 2009, Naples, Italy
N.Massarotti and P.Nithiarasu (Eds.)

PHASE SEPARATION OF BINARY FLUIDS WITH DYNAMICAL TEMPERATURE

Giuseppe Gonnella
Dipartimento di Fisica, Università di Bari *and* INFN, Sezione di Bari, Via Amendola 173, 70126 Bari, Italy,
gonnella@ba.infn.it

Antonio Lamura
Istituto Applicazioni Calcolo, CNR, Via Amendola 122/D, 70126 Bari, Italy
a.lamura@ba.iac.cnr.it

Antonio Piscitelli
Dipartimento di Fisica, Università di Bari *and* INFN, Sezione di Bari, Via Amendola 173, 70126 Bari, Italy,
antonio.piscitelli@ba.infn.it

Adriano Tiribocchi
Dipartimento di Fisica, Università di Bari *and* INFN, Sezione di Bari, Via Amendola 173, 70126 Bari, Italy,
adriano.tiribocchi@ba.infn.it

ABSTRACT

Thermal phase separation process, which follows a sudden quench in the coexistence region, is considered for binary fluid mixtures. It is studied applying a new version of an hybrid lattice Boltzmann model, where non-ideal terms of the pressure tensor, which takes into account thermal and concentration gradient contribution, are included as a body force in the LBM equations, used to solve the Navier-Stokes equations. The equations for concentration and temperature are solved using a finite difference scheme. Domains are observed to order preferably with interfaces parallel to the cold walls and this behavior is more pronounced at higher viscosities. An intermediate regime with two characteristics scales for the domain size, one close to the walls and the other in the middle of the system, has been also observed.

Key Words: *Lattice Boltzmann Methods; Phase Separation*

1. INTRODUCTION

The process of phase separation for binary fluids aroused a lot of interest in the scientific community [1] and many important results have been obtained in numerical simulations for different physical system and by different methods [2]. The importance of these processes is due to the innumerable physical phenomena in which they appear and to the theoretical frameworks necessary to explain them. On the other hand, the most part of the studies was made for systems whose temperature is assumed constant. In recent years there was an increasing interest to the study of the processes with a non constant temperature, due to the great variety of phenomena in which a heat flow occurs, like boiling processes and droplet motion under thermal gradient [3] or phase separation [4,5]. Experimental studies of phase separation of polymer mixtures [6] suggest the possibility of controlling the morphology of the coarsening domains by exploiting thermal diffusion properties and proper heat sources.

In this paper we present some results about the phase separation of a binary fluid mixture with non homogeneous temperature and the system quenched by contact with cold walls. We use a theoretical

framework presented in [7], in which the set of thermo-hydrodynamic equations is written for fluids with entropy and internal energy functionals including gradient terms. A generalized Gibbs-Duhem relation, that takes into account the presence of interface, allows to obtain a pressure tensor with explicit contributions from thermal gradient. We focused our studies on the morphology of the domains and on their growth dynamics, showing how ordered lamellar patterns result perpendicular to the direction of thermal gradients while interfaces assume more circular shapes when the viscosity is decreased. In an intermediate temporal regime a phase separation with two characteristic length, one close to the cold walls and the other in the central part of the system, has been observed.

The set of thermo-hydrodynamics equations, used to study these processes, are solved using a hybrid lattice Boltzmann (LB) approach, in which the continuity and the Navier-Stokes equations are simulated by using a LB algorithm (with a forcing term for non-ideal contributions), while the equations for concentration and energy are implemented by using a finite-difference scheme [8]. This is a convenient tool for studying thermal phase separation from a mesoscopic point of view. The paper is organized as follows. In the next section a brief description of the hybrid LB algorithm is presented and in the successive section some numerical results are shown. Some conclusions follow in the last section.

2. THE MODEL

For a binary mixture the conservation equations of mass, momentum and energy, expressed in terms of the total density n and concentration difference φ, take the form

(1) $$\partial_t n + \partial_\alpha (n u_\alpha) = 0,$$

(2) $$\partial_t (n u_\beta) + \partial_\alpha (n u_\alpha u_\beta) = -\partial_\alpha (P_{\alpha\beta} - \sigma_{\alpha\beta}),$$

(3) $$\partial_t \varphi = -\partial_\alpha (\varphi u_\alpha) - 2\partial_\alpha J^d_\alpha,$$

(4) $$\partial_t \hat{e} = \partial_\alpha (\hat{e} u_\alpha) - (P_{\alpha\beta} - \sigma_{\alpha\beta})\partial_\alpha u_\beta - \partial_\alpha J^q_\alpha,$$

where u is the velocity field, $\hat{e}$ is the internal energy of the mixture, $P_{\alpha\beta}$ is the reversible stress tensor, $\sigma_{\alpha\beta} = \eta(\partial_\alpha u_\beta + \partial_\beta u_\alpha) + (\xi - 2\eta/d)\delta_{\alpha\beta}\partial_\gamma u_\gamma$ is the dissipative stress tensor. J^d and J^q are the diffusive and heat currents, respectively given by $J^d = -L_{11}\overrightarrow{\nabla}(\frac{\mu}{T}) + L_{12}\overrightarrow{\nabla}(\frac{1}{T})$ and $J^q = -L_{21}\overrightarrow{\nabla}(\frac{\mu}{T}) + L_{22}\overrightarrow{\nabla}(\frac{1}{T})$, where μ is the chemical potential and T is the temperature. The quantities L_{ij} are phenomenological coefficients given by $L_{11} = Tl_{11}$ and $L_{22} = Tl_{22}$, with l_{11} and l_{22} diffusion and heat conductivity constants, respectively. Moreover η is the shear viscosity, ξ is the bulk viscosity and the Greek indexes are related to the cartesian axes.

These equations describe the dynamics of the system with non homogeneous temperature. The thermodynamics of the mixture is fixed by the free energy

(5)
$$F = \int d\mathbf{r} \left(AT + \frac{n\lambda}{4}(1 - \frac{\varphi^2}{n^2}) - k_B T[n \ln n - \frac{n+\varphi}{2}\ln(\frac{n+\varphi}{2}) - \frac{n-\varphi}{2}\ln(\frac{n-\varphi}{2})] + \frac{1}{2}\kappa|\nabla\varphi|^2 \right),$$

where A is a constant, k_B is the Boltzmann constant and κ weights the interface contribution. From the above expression the chemical potential and the pressure tensor can be derived [11]. Moreover the constant λ is given by $\lambda = T_c/2$, where T_c is the critical temperature of the mixture.

To solve numerically the Eqs. (1)-(4), we use an hybrid approach in which a LB scheme solves Eqs. (1) and (2) and a finite difference scheme solves the Eqs. (3) and (4). The LB scheme is built starting from a two dimensional square lattice where each site $\mathbf{r}$ is connected to the first and second neighbors. Horizontal and vertical links have length Δx, diagonal links $\sqrt{2}\Delta x$ and Δt is the simulation time step. On each site nine velocity vectors $\mathbf{e}_i$ are defined, according to the D_2Q_9 scheme. A set of distribution function $\{f_i(\mathbf{r}, t)\}$, whose evolution equation is

(6) $$f_i(\mathbf{r} + \mathbf{e}_i\Delta t, t + \Delta t) - f_i(\mathbf{r}, t) = -\frac{\Delta t}{\tau}[f_i(\mathbf{r}, t) - f_i^{eq}(\mathbf{r}, t)] + \Delta t F_i,$$

is defined in each site. f_i^{eq} is the equilibrium distribution function, τ is a relaxation parameter related to the viscosity and F_i is a forcing term depending on the concentration through the chemical potential

and giving in the continuum by $\mathbf{F} = -\varphi\nabla\mu$. The mass and momentum are defined by

$$n = \sum_i f_i, \qquad n\mathbf{u} = \sum_i f_i \mathbf{e}_i + \frac{1}{2}\mathbf{F}\Delta t. \tag{7}$$

By using a Chapman-Enskog expansion and conservation laws for mass and momentum, the continuum equations can be recovered. The finite difference scheme consists of an explicit Euler algorithm that solves the Eqs. (3) and (4) implementing in two successive time steps the convective and the diffusive term, respectively. In the convective part the velocity comes from the solution of the LB equation and the gradient of the concentration is calculated by using a backward or a forward scheme if the velocity is positive or negative, respectively. Moreover for both the equations (3) and (4), the space and time steps are the same of the ones used in the LB scheme. This approach allows to have a better numerical stability.

3. RESULTS AND CONCLUSIONS

In this section we present some results obtained for a phase separation process in absence of hydrodynamic with symmetric composition. The system, initially in a disordered state above T_c, is quenched by contact with cold walls. The effects of the temperature evolution on the morphology of phase separation are shown on the left in Figure 1, for a system at very high viscosity. We used a lattice size $L_x \times L_y = 512 \times 512$ with $\Delta x = \Delta t = 1$ and $\Omega = 3/5$, where $\Omega = T/T_c$. In Figure 1 the cold walls are placed at the bottom and top sides at the same temperature. Moreover we set $\gamma = l_{22}/l_{11} = 1/10$ and $l_{12} = l_{21} = 0$. The bulk properties are controlled via the coefficients $a = k_B T/n - \lambda/2n$ and $b = k_B T/3n^3$, obtained by a φ^4 approximation of (5). At time $t = 250$ of the simulation, domains with well-defined interface are observed close to the walls while in the central region the system is still in the disordered phase. From time $t = 1000$ a stack of domains perpendicular to the temperature gradient can be observed in all the system, except close to the walls, where we imposed the neutral wetting condition, which means that $\vec{a} \cdot \vec{\nabla}\varphi|_{y=0,L_y} = 0$. The quantity $\vec{a}$ is the inward normal unit vector at the boundaries. The corresponding evolution of the temperature across the system is shown on the

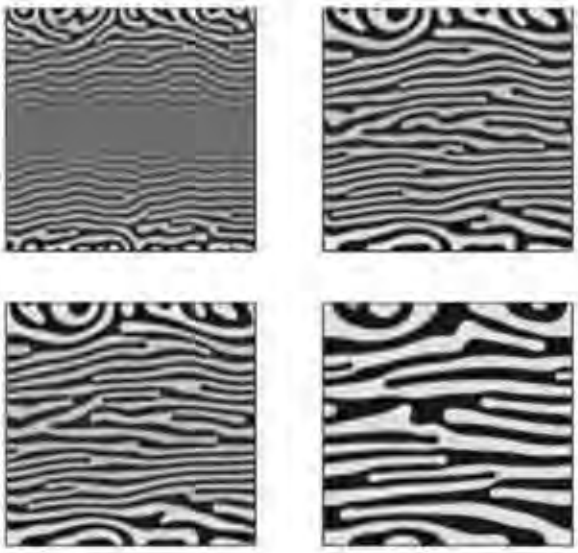

FIGURE 1. On the left a contour plot of φ at consecutive times (from the top left to the bottom right $t = 250, 1000, 1250, 5500$) during a phase separation in a system of size 512×512, with $\Omega = 3/5$. The mixture composition is symmetric

right in Figure 1. We also studied the phase separation with dynamical temperature at lower viscosity. In Figure 3 we show what happens at the value $\tau = 1$ in Eq. (6), on the same lattice and with $\Omega = 4/5$. During the phase separation one can observe two scales that characterize the growth of the domains in the bulk and close to the walls, where a more spherical shape can be observed. Further results have been obtained with asymmetric composition, in which the regular lamellar pattern obtained without hydrodynamics is substituted by circular domains that increase their size with different evolution and morphology depending on the value of viscosity.

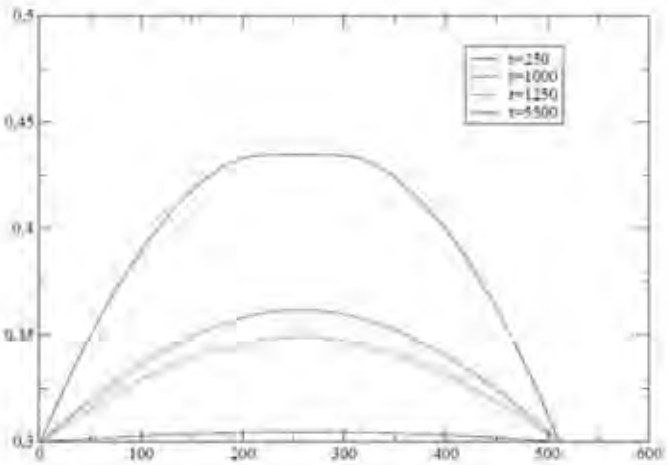

FIGURE 2. On the left the temperature profile across the system averaged along the x-direction, during a phase separation in a system of size 512×512, with $\Omega = 3/5$. The mixture composition is symmetric.

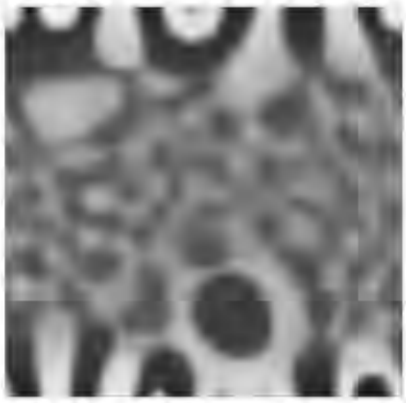

FIGURE 3. Contour plot of φ during a phase separation at $\tau = 1$ with $\Omega = 4/5$, in a system of size 512×512.

In conclusion we studied the phase separation process for a binary fluid where also the temperature is a dynamical quantity with a hybrid LB approach. We found that the morphology of the domains strongly depends on thermal diffusivity properties.

REFERENCES

[1] A.J.Bray, Theory of phase-ordering kinetics, *Adv. Phys.*, 43, 357, 1994

[2] Kinetics of Phase Transitions, Ed. S. Puri and V. Wadhawan, CRC Press 2009.

[3] A.Onuki, Dynamic van der Waals Theory of Two-Phase Fluids in Heat Flow, *Phys.Rev.Lett*, 94, 054501, 2005

[4] C.M.Pooley, O.Kuksenok, A.C.Balazs, Convection-driven pattern formation in phase-separating binary fluids, *Phys.Rev.E*, 71, 030501, 2005

[5] G. Gonnella, A. Lamura, and V. Sofonea, Lattice Boltzmann simulation of thermal nonideal fluids, *Phys.Rev.E*, 76, 036703 2007

[6] A.P.Krekhov and L.Kramer, Phase separation in the presence of spatially periodic forcing, *Phys. Rev. E*, 70, 061801, 2004

[7] G.Gonnella, A.Lamura, A.Piscitelli, Dynamics of binary mixtures in inhomogeneous temperatures, *J.Phys A: Math.Theor.*, 41, 105001, 2008

[8] A. Tiribocchi, N. Stella, G. Gonnella, A. Lamura, Hybrid lattice Boltzmann model for binary fluid mixtures, *arXiv:0902.3921v1 [cond-mat.soft]*, 2009

First International Conference on Computational Methods for Thermal Problems
ThermaComp2009, September 8-10, 2009, Naples, Italy
N. Massarotti and P. Nithiarasu (Eds.)

Lattice Boltzmann simulation of flow and heat transfer in porous media

Arkadiusz Grucelski, **Jacek Pozorski**

Institute of Fluid-Flow Machinery, Polish Academy of Sciences
ul. Fiszera 14, 80-952 Gdańsk, Poland, {agrucelski, jp}@imp.gda.pl

ABSTRACT

Two- and three- dimensional models of the lattice Boltzmann method (LBM) are applied for fluid flow through a simulated fragment of a porous medium with heat transfer. First, LBM results for drag and lift coefficients as well as the vortex shedding frequency in flow past a circular cylinder are obtained as a test case. Then, results for head loss (pressure vs. flow rate) are presented for a computer-created porous medium and shown to compare favourably with the Darcy and Forchheimer laws. Thermal problem is solved by adding internal energy density distribution function to the LBM for fluid flow. First results for heat transfer are presented, both for heated cylinder and a fragment of porous medium.

Key Words: *porous media flow, heat transfer, LBM, coking.*

1. INTRODUCTION

Coking plants are widely used in coal processing industry to obtain chemically cleaner coal (coke) and other products. From the fluid thermomechanics point of view, coking occurs in a bed of granular material (coal grains) that upon heating becomes a uniform porous medium. During coking process complicated phenomena occur at the level of a single grain (pore). They include fluid flows through deposit, thermal conduction, chemical reactions, plastic deformation of medium coupled with the temperature increase, and others. Seems that none of them can be effectively simulated by more traditional CFD methods, mostly because of complicated geometry of the domain.

Our longer-term objective is the physically sound simulation of the coking process. As an efficient numerical approach to simulation at the mesoscale or representative element of volume (REV) level, we have chosen the lattice Boltzmann method. The REV in present paper has been constructed in a simple manner: positions and radii of grains (pores) are randomized, but no distribution function of geometrical properties of natural medium has been used so far. As shown in the following, the LBM can be used with success for flow simulation, alike more traditional methods in fluids dynamics; additionally, we are also able to solve thermal problems.

2. GOVERNING EQUATIONS FOR LBM AND IMPLEMENTATION ISSUES

The LB method solves the Navier-Stokes equations for a viscous fluid in the incompressibility limit. This is done through the computation at the mesoscopic level and subsequent averaging [1, 2]. Using the Bhatnagar-Gross-Krook (BGK) approximation, the non-dimensional Boltzmann kinetic equation is written for the distribution function f_α in the discretized directions (identified by $\vec{e_\alpha}$ unit vectors):

$$f_\alpha(\vec{r}+\vec{e_\alpha}, t+\delta t) - f_\alpha(\vec{r}, t) = -\tau_\nu^{-1}(f_\alpha(\vec{r}, t) - f_\alpha^{eq}(\vec{r}, t)), \tag{1}$$

where the local equilibrium distribution function f_α^{eq} is approximated by ($\vec{u}$ is the mesoscale velocity):

$$f_\alpha^{eq} = \varepsilon_\alpha \rho \left(1 + 3\vec{e_\alpha}\cdot\vec{u} + \frac{9}{2}(\vec{e_\alpha}\cdot\vec{u})^2 - \frac{3}{2}(\vec{u})^2\right), \tag{2}$$

ε_α is weight coefficient. The viscous relaxation time is $\tau_\nu = 3\nu + 1/2$ (general form is given in [2]); the lattice streaming speed is equal one and the speed of sound $c_s = 1/\sqrt{3}$. Correctness of implementation

of LB method into the working software was proved by numerical experiments (laminar pipe flow with periodic inlet/outlet). Then, we have considered vortex shedding in a flow past a circular cylinder in function of Reynolds number. We have computed drag and lift coefficients, C_d and C_l, out of the force $\vec{F}$ exerted by the flow on the obstacle, using equations:

$$\vec{F} = \int_S \hat{\tau}\vec{n}ds \qquad \text{where} \qquad \vec{F} = F_d\vec{j_\perp} + F_l\vec{j_\parallel} \qquad \text{and} \qquad C_m = 2\frac{F_m}{\pi r u_o^2 \rho}, \tag{3}$$

where $m \in \{d, l\}$ correspond to drag and lift and $U_o\vec{j_\parallel}$ is velocity of undisturbed flow. Stress tensor $\hat{\tau}$ (for incompressible Newtonian fluid) was computed at nodes which form a surface of the obstacle. These nodes are also part of flow, so the Boltzmann kinetic equation is still used there. Spatial derivatives of velocity (needed to compute $\hat{\tau}$ in equation 3) are calculated with the finite difference scheme of second order. In considered flow cases we have used half-way bounce-back no-slip boundary conditions for obstacles. At the domain boundaries (parallel to the main flow direction) periodicity conditions were imposed. At the inlet, we gave a uniform velocity profile with unknown distribution functions calculated from non-equilibrium condition, $f_\alpha^{neq} = f_\beta^{neq}$ (where α, β meet $\vec{e_\alpha} = -\vec{e_\beta}$). At the outlet, unknown distribution functions were calculated from extrapolation condition [3]: $f_\alpha(\vec{x}, t) = 2f_\alpha(\vec{x} - \vec{e_\alpha}\delta t, t) - f_\alpha(\vec{x} - 2\vec{e_\alpha}\delta t, t)$.

As the second milestone, we have chosen to compute pressure drop curves in a simulated porous medium in function of flow rate corresponding to Darcy-Forchheimer equation. Last series of experiments provide the Nusselt number in function of Reynolds (Re) and Prandtl ($\mathsf{Pr} = \nu/\alpha$) numbers and change of Nusselt number in time. The results are presented in Sec. 3.

3. RESULTS FOR FLOW PAST OBSTACLES AND POROUS MEDIA FLOW

Main results for an unsteady flow over one obstacle include time records of drag and lift force (Fig. 1), and the vortex shedding frequency. The computed curve of lift coefficient was next used to determine the Strouhal number $\mathsf{St} = N_d/(tU_o)$ in function of the Reynolds number (Tab. 1); N_d is the number of lattice nodes per diameter of the obstacle, t number of time steps for a periodic solution.

mesh \ Re	75	100	200	250
190 x 380	0.176	0.189	0.214	0.221
240 x 480	0.175	0.188	0.212	0.219
300 x 600	0.175	0.188	0.213	0.220

TABLE 1. Computed Strouhal numbers for vortex shedding past a circular cylinder.

The second flow case considered was the flow over a number of obstacles (simulating REV, i.e., a simple fragment of a porous medium, Fig. 2a). Computed results include pressure loss as a function of the Reynolds number. The head loss δp was found, for medium with a constant porosity, by simple

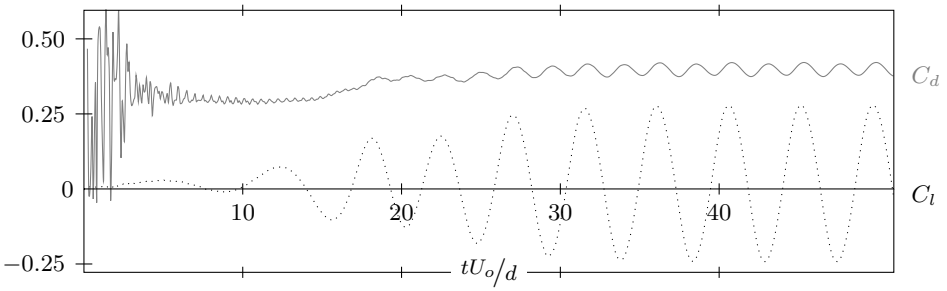

FIGURE 1. Drag and lift coefficients for an unsteady flow past a cylinder, LBM at Re = 350.

difference of mean pressure at the inlet and outlet for a given flow rate Q. We expect to retrieve Darcy's law for a viscosity-dominated flow (low Re), whereas for higher Re, the curve of pressure drop will be consistent with the Forchheimer equation [4]. For a viscosity-dominated flow, the permeability coefficient k was found from Darcy's equation ($\delta p = Q\nu/k$). From the second case, the pressure drop curve was used to determine coefficient β connected with flow inertia effects, from equation

a) 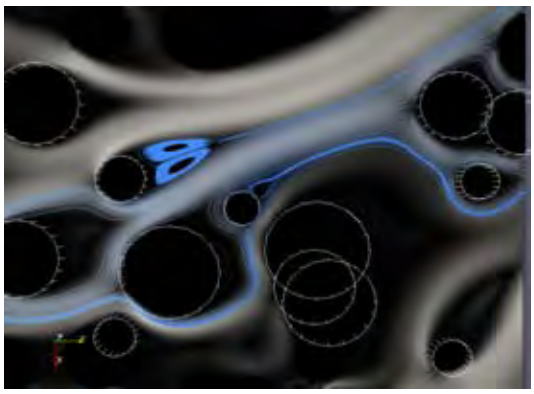 b) 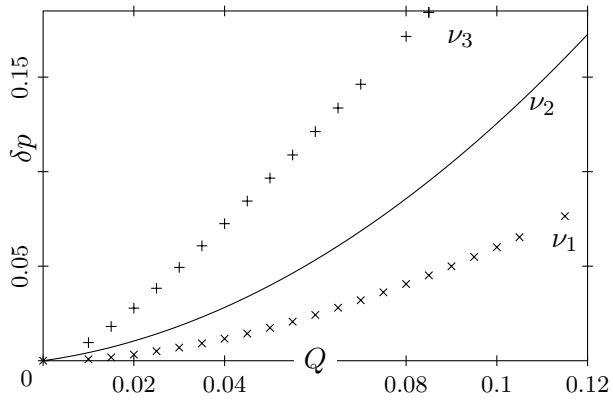

FIGURE 2. a) Example of flow path in a LBM-simulated porous medium. b) Head loss vs. the flow rate. Symbols: results for a few viscosity coefficients (or Reynolds numbers), where $\nu_1 < \nu_2 < \nu_3$. Solid line: best fit to the Forchheimer law for ν_2.

$\delta p = Q\nu/k + \beta\rho Q^2$. A slight discrepancy between simulation results and the best fit to the Darcy-Forchheimer law (Fig. 2b) is possibly a consequence of the assumption that β is constant (cf. [4]).

4. THERMAL LB METHOD, FIRST RESULTS

The issue of heat transfer in considered domain can also be solved by LB method [5, 6]; we implement the model for laminar flow of incompressible fluid, assuming that material properties of solid and fluid do not depend on temperature. An ultimate model for coking process has to be developed accounting for plastic deformation of grains, etc. In addition to Eq. (1), discrete thermal Boltzmann equation for heat transfer is written for the internal energy density distribution function (IEDDF) $g_\alpha(\vec{r}, t)$:

$$g_\alpha(\vec{r} + \vec{e}_\alpha, t + \delta t) - g_\alpha(\vec{r}, t) = -\tau_\theta^{-1}(g_\alpha(\vec{r}, t) - g_\alpha^{eq}(\vec{r}, t)), \tag{4}$$

where the local equilibrium distribution function and thermal relaxation time (for a phase f):

$$g_\alpha^{eq} = \omega_\alpha T\left(a_\alpha + b_\alpha\frac{\vec{e}_\alpha\cdot\vec{u}}{c^2} + d_\alpha\frac{(\vec{e}_\alpha\cdot\vec{u})^2}{c^4} - h_\alpha\frac{3}{2c^2}(\vec{u})^2\right), \qquad \tau_\theta = \frac{3}{2}\frac{\lambda^f}{\rho c_p^f\delta t} + \frac{1}{2} \tag{5}$$

where T is temperature. This function depends on direction (α) and on a specific model. We indicate, after Shu [6], that pressure is independent of the internal energy distribution. Full description of given equation can be found in [5], [6].

For one obstacle (as a classical problem) the Nusselt number $\mathsf{Nu} = \mathsf{Nu}(\mathsf{Re}, \mathsf{Pr})$, was calculated (cf. Fig. 3b). At the solid boundary we applied modified boundary condition, showed at [6]. Unmodified condition can be rewritten:

$$g_\alpha^{neq} - \vec{e_\alpha} f_\alpha^{neq} = -g_\beta^{neq} + \vec{e_\beta} f_\beta^{neq}. \tag{6}$$

Implemented and modified condition uses distribution functions, $f_\alpha = f_\alpha^{neq} + f_\alpha^{eq}$. As results show, this modification still gives results compatible with intuition; however we are rebuilding code to the original condition (6). We try to obtain a curve of Nusselt number in function of Re and Pr:

$$\mathsf{Nu} = -\int_S \frac{d}{T_w - T_{in}}\frac{\partial T}{\partial n}dS$$

where $\vec{n}$ is normal vector to the solid-fluid interface. In LBM computation we simulate isothermal fluid flow (with temperature T_{in}) past the obstacle. When vortex shedding becomes regular, in one time step temperature of the obstacle has been set to T_o and Nusselt number was calculated, cf. Fig. 3.

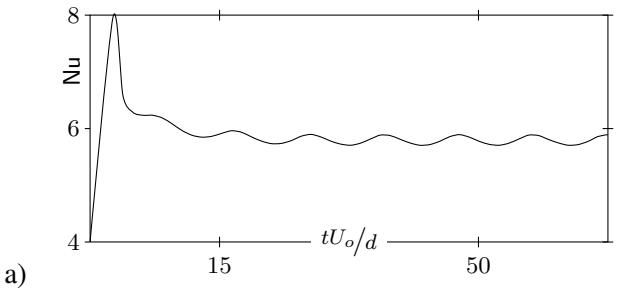

a)

Re \ Pr	air 0.7	water 7	refrig R12 4.5
150	15.24	5.26	5.05
200	17.36	5.63	5.26
250	19.73	6.19	5.55

b)

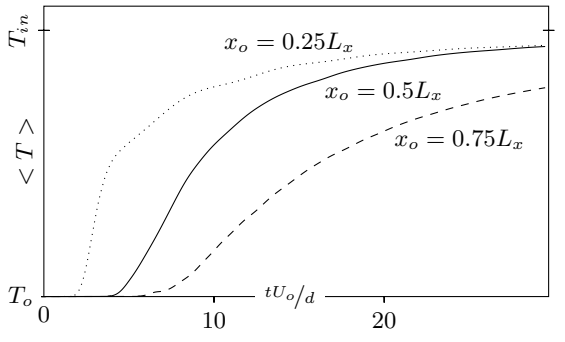

c)

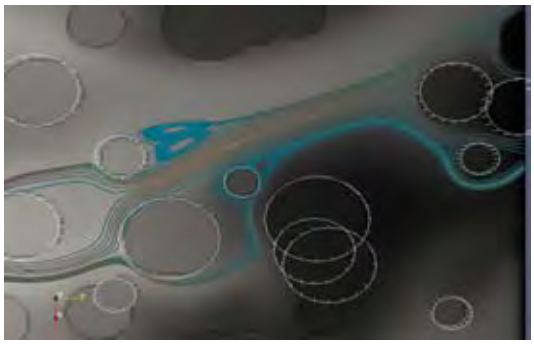

d)

FIGURE 3. a) Temporal record of the Nusselt number for flow past a heated cylinder; b) Nusselt number vs. Reynolds and Prandtl numbers; c) average temperature records at selected x_o stations in the porous medium; d) temperature field in REV.

5. CONCLUSIONS AND PERSPECTIVE

The lattice Boltzmann algorithm for fluid flow and heat transfer is implemented, and gives reasonable results. Pressure drop in function of flow rate (and Re) is consistent with the Darcy law (for low flow rates) and the Forchheimer law (for higher values). Changes of the Strouhal number in function of Reynolds number have also been shown; curves of lift force and drag force for a single obstacle are in accordance with physical intuitions. The same we can say about Nusselt number in function of time and dimensionless numbers. Thermal LB model is still under development. Full description of fluid flow and heat transfer on a representative volume element has to be reached for porous medium. It seems that for such complicated geometry as the coal bed (with property to change shape with increasing temperature), the LB method is a proper choice for simulating coking phenomenon with consideration of plasticity of grains. The problem has to be solved by usage of moving boundary model for LBM [7].

REFERENCES

[1] X. He, S. Chen and G.D. Doolen (1998). The lattice Boltzmann method in incompressible limit, *Annu. Rev. Fluid Mech.* **146**, 282–300

[2] C. Shuai, X.D. Niua, Y.T. Chewa and Q.D. Caib (2006). A fractional step lattice Boltzmann method for simulating high Reynolds number flows, *Math. Comput. Simul.* **72**, 201–205

[3] P.H. Kao, R.J. Yang (2008). An investigation into curved and moving boundary treatments in the lattice Boltzmann method, *J. Comput. Phys.* **227** 5671–5690

[4] L.S. Bennethum and T. Giorgi (1997). Generalized Forchheimer equation for two-phase flow based on hybrid mixture theory, *Transp. Porous. Med.* **26** 261–275

[5] J. Wang, M. Wang and Z. Li (2007). A lattice Boltzmann algorithm for fluid-solid conjugate heat transfer, *Int. J. Thermal Sci.* **46**, 228–234

[6] Y. Peng, C. Shu and Y.T. Chew (2003). A 3D incompressible thermal LBM and its application to simulate natural convection in a cubic cavity, *J. Comput. Phys.* **193**, 260–274

[7] F. Verhaeghe, Li-Shi Luo and B. Blanpain (1998). Lattice Boltzmann modeling of microchannel flow in slip flow regime, *J. Comput. Phys.* **146**, 282–300

[8] L.S. Luo (1998). Unified theory of LBM for non ideal gases, *Phys. Rev. Lett.* **81**, 1618–1621

First International Conference on Computational Methods for Thermal Problems
ThermaComp2009, September 8-10, 2009, Naples, Italy
N.Massarotti and P.Nithiarasu (Eds.)

Review on Lattice Boltzmann Methods for Heat Transfer

Frédéric Kuznik
Thermal Sciences Center of Lyon
CNRS, UMR 5008, INSA de Lyon, Université Lyon 1
Bât. Sadi Carnot, 9 rue de la Physique - 69621 Villeurbanne Cedex, France
frederic.kuznik@insa-lyon.Fr

Jean-Jacques Roux
Thermal Sciences Center of Lyon
CNRS, UMR 5008, INSA de Lyon, Université Lyon 1
Bât. Sadi Carnot, 9 rue de la Physique - 69621 Villeurbanne Cedex, France
jean-jacques.roux@insa-lyon.Fr

Gilles Rusaouen
Thermal Sciences Center of Lyon
CNRS, UMR 5008, INSA de Lyon, Université Lyon 1
Bât. Sadi Carnot, 9 rue de la Physique - 69621 Villeurbanne Cedex, France
gilles.rusaouen@insa-lyon.Fr

ABSTRACT

The development of Thermal Lattice Boltzmann Method (TLBM) for the prediction of heat transfer is a key to a wider use of LBM. The objective of this paper is to provide a comprehensive and coherent review on TLBM. In order to illustrate the different methods, the well known problem of the heated cavity with imposed temperatures is used. The paper and the presentation are proposed for the Minisymposium "Lattice Boltzmann methods for heat and mass transfer". **Key Words:** *Lattice Boltzmann Method, Heat Transfer, Review.*

1. PROPOSAL

In the last two decades, the Lattice Boltzmann method (LBM) has proved its capability to simulate a large variety of fluid flows ([1], [2], [3], [4], [5], [6], [7], ...). For the isothermal fluid flows, the LBM was found to be an accurate, stable and computationally "economic" method compared with classical computational fluid dynamics methods. The Lattice Boltzmann equation represents the minimal form of Boltzmann kinetic equation ([8]), and the result is a very elegant and simple equation for a discrete density distribution function $f_i(\overrightarrow{x}, t) = f(\overrightarrow{x}, \overrightarrow{c_i}, t)$. This density distribution function represents the probability to find a particle at lattice site $\overrightarrow{x}$, at time t and moving with speed c_i.

The thermal LBM model has been investigated first by [9]. The main limitation of using LBM in engineering applications is the lack of satisfactory model for the thermal fluid flows problems. Three methods for solving thermal LBM exist: the multispeed approach, the passive scalar approach and the double-population approach.

The multispeed approach, which is a straightforward extension of the isothermal LBM, uses a single distribution function, makes theoretically possible to express both heat flux and temperature in terms of higher order kinetic moments of particle distribution function ([10], [11]).

For the passive scalar approach, it consists in solving the velocity by the LBM and the macroscopic temperature equation independently. The macroscopic temperature equation is similar to a passive scalar evolution equation if the viscous heat dissipation and compression work done by pressure are

negligible. The coupling to LBM is made by adding a potential to the distribution function equation ([12], [13]).

The double-population approach introduces an internal energy density distribution function in order to simulate the temperature field, the velocity field stilling simulated using the density distribution function ([14]).

The validity of the models reviewed in this article is done through their application to natural convection in the square cavity. The number of papers available shows the great interest in this topic. The flow is laminar for Rayleigh numbers (Ra) less than 10^6, the transition occurs for $10^6 < Ra < 10^8$ and the flow becomes fully turbulent for $Ra \geq 1.82.10^8$. The numerical studies, used in this article, are, for the laminar flow, [15] and [16], and [17] and [18] for the transitional flow results.

2. RESULTS

The main objective of this study results is to compare different TLBM and validate the use of such models to predict the velocity and temperature fields in the case of natural convection in a square cavity for laminar and transitional flows. Moreover, a numerical stability analysis is presented depending on the TLBM and boundary conditions ([19]).

		$Ra = 10^3$	$Ra = 10^4$	$Ra = 10^5$	$Ra = 10^6$
u_{max}	[15]	3.649	16.178	34.730	64.630
	[16]	-	16.180	34.740	64.837
	double-population	3.636	16.167	34.962	64.133
y_{max}	[15]	0.813	0.823	0.855	0.850
	[16]	-	0.825	0.837	0.850
	double-population	0.809	0.821	0.854	0.860
v_{max}	[15]	3.697	19.617	68.590	219.360
	[16]	-	19.629	68.639	220.461
	double-population	3.686	19.597	68.578	220.537
x_{max}	[15]	0.178	0.119	0.066	0.038
	[16]	-	0.120	0.883	0.039
	double-population	0.174	0.120	0.067	0.038
Nu_0	[15]	1.117	2.238	4.509	8.817
	[16]	-	2.244	4.521	8.825
	double-population	1.117	2.246	4.518	8.792

TABLE 1. Example: Comparison of laminar flow with previous works for the square heated cavity with imposed temperatures.

		$Ra = 10^7$	$Ra = 10^8$
u_{max}	[17]	-	514.3
	[18]	148.580	321.876
	double-population	148.768	321.457
y_{max}	[17]	-	0.941
	[18]	0.879	0.928
	double-population	0.881	0.940
v_{max}	[17]	-	1812
	[18]	699.236	2222.39
	double-population	702.029	2243.36
x_{max}	[17]	-	0.0135
	[18]	0.021	0.120
	double-population	0.020	0.121
Nu_0	[17]	-	32.045
	[18]	16.523	30.225
	double-population	16.408	29.819

TABLE 2. Example: Comparison of transitional flow with previous works for the square heated cavity with imposed temperatures.

REFERENCES

[1] Higuera F.J., Succi S., Benzi R., Lattice Gas Dynamics with Enhanced Collisions, *Europhys. Lett*, 9, 345-349, 1989.

[2] Benzi R., Succi S., Vergassola M., The lattice Boltzmann equation: theory and applications, *Phys. Rep.*, 222, 145-197, 1992.

[3] Wolf-Gladrow D.A., *Lattice-Gas Cellular Automata and Lattice Boltzmann Models: An Introduction*, Springer, Berlin, 2000.

[4] Succi S., *The lattice Boltzmann - For Fluid Dynamics and Beyond*,Oxford University Press, 2001.

[5] Filippova O. and Hanel D., A novel BGK approach for low Mach number combustion, *J. Comput. Phys.*, 158, 139-160, 2000.

[6] Mei R., Shyy W., Yu D., Luo L.S., Lattice Boltzmann method for 3-D flows with curved boundary, *J. Comput. Phys.*, 161, 680-699, 2000.

[7] Lee T. and Lin C.L., A characteristic Galerkin method for Discrete boltzmann equation, *J. Comput. Phys.*, 171, 336-356, 2001.

[8] Higuera F.J. and Jimenez J., Boltzmann Approach to Lattice Gas Simulation, *Europhy. Lett.*, 9, 663-668, 1989.

[9] Massaioli F., Benzi R., Succi S., Exponential Tails in Two-Dimensionnal Rayleigh-Bénard Convection, *Europhy. Lett.*, 21, 305-310, 1993.

[10] Chen Y., Ohashi H., Akiyama M.A., Thermal lattice Bhatnagar-Gross-Krook model without nonlinear deviations in macrodynamic equations, *Phys. Rev. E*, 50, 2776-2783, 1994.

[11] Pavlo P., Vahala G., Vahala L., Soe M., Linear-stability analysis of thermo-lattice Boltzmann models, *J. Comput. Phys*, 139, 79-91, 1998.

[12] Crouse B., Krafczyk M., Kuhner S., Rank E., Van Treeck C., Indoor air flow analysis based on lattice Boltzmann methods, *Energy and Buildings*, 34, 941-949, 2002.

[13] D'Orazio A., Corcione M., Cielata G.P., Application to natural convection enclosed flows of a lattice Boltzmann BGK model coupled with a general purpose thermal boundary condition, *Int. J. Thermal Sciences*, 43, 575-586, 2004.

[14] He X., Chen S., Doolen G.D., A novel thermal model for the lattice Boltzmann method in incompressible limit, *J. Comput. Phys.*, 146, 282-300, 1998.

[15] de Vahl Davis G., Natural convection of air in a square cavity: a bench mark numerical solution, *Int. J. Numer. Meth. Fluids*, 3, 243-264, 1983.

[16] Hortmann M., Peric M., Scheuerer G., Finite volume multigrid prediction of laminar natural convection: bench-mark solutions, *Int. J. Numer. Meth. Fluids*, 11, 189-207, 1990.

[17] Markatos N.C., Pericleous K.A., Scheuerer G., Laminar and turbulent natural convection in an enclosed cavity, *Int. J. Heat Mass Transfer*, 27, 752-772, 1984.

[18] Le Quere P., Accurate solutions to the square thermally driven cavity at high Rayleigh number, *Computers and Fluids*, 20, 29-41, 1991.

[19] Lallemand P., Luo L.S. Theory of the lattice Boltzmann method: Acoustic and thermal properties in two and three dimensions, *Phys. Rev. E*, 68, 036706, 2003.

First International Conference on Computational Methods for Thermal Problems
ThermaComp2009, September 8-10, 2009, Naples, Italy
N.Massarotti and P.Nithiarasu (Eds.)

Enhanced thermal lattice Boltzmann method for heat and mass transfer applications

Nikolaos I. Prasianakis*
Paul Scherrer Institute, 5232 Villigen PSI Switzerland,
nikolaos.prasianakis@psi.ch

Ilya V. Karlin
ETH-Zurich, 8092 Zurich Switzerland & University of Southampton, SO17 1BJ UK,
karlin@lav.mavt.ethz.ch

ABSTRACT

A lattice Boltzmann model, suitable for simulation of fluid dynamics engineering applications that include heat and mass transfer, is presented. The basis is an energy conserving lattice Boltzmann model with an improved equilibrium population set. Correction terms are added to the discretized lattice BGK equation. They are tailored in such a way as to recover the full set of compressible Navier-Stokes and Fourier equations, for large temperature and density variation. Simulation results that are used for the validation of the model are also presented.

Key Words: *lattice Boltzmann, computational heat transfer, thermal flows*

1. INTRODUCTION

The lattice Boltzmann (LB) method has been used with a remarkable success as a powerful alternative tool for solving the hydrodynamic Navier–Stokes (NS) equations, with applications ranging from large Reynolds number flows to flows at the micron scale, porous media, and multiphase flows [1]. The success of the LB method is mainly in the low Mach number isothermal NS limit. The most commonly used LB models are the ones that reside on the so-called standard lattices, which are characterized by a relatively small number of discrete velocities. Populations f_i propagate only to their neighboring nodes during the streaming process. For $D = 2$ the most commonly used lattice is the D2Q9, and for $D = 3$ the D3Q15, D3Q19 and D3Q27 lattices are usually implemented. The discrete velocity populations, at equilibrium state f_i^{eq}, are polynomial expressions of density ρ and velocity u. For the simulation of flows where temperature and density variations play a significant role, the recently introduced LB thermal model on the D2Q9 lattice of Ref. [2, 3] can be used. The equilibrium populations are polynomial expressions of density ρ, velocity u and of the temperature T. Due to the minimal discrete velocity set, the hydrodynamic description is not accurate enough. In order to increase the accuracy and the stability of the algorithm, the lattice BGK equation is equipped with specifically designed counter terms. The full set of compressible NS and Fourier equations for large temperature and density variation are recovered. The Prandtl number can take arbitrary values, and external forcing fields as well as heat sources can be easily accommodated.

2. LATTICE BOLTZMANN MODEL FOR HEAT TRANSFER APPLICATIONS

The popular nine-velocity model is considered, the so-called D2Q9 lattice, for which the discrete velocities $c_{i\alpha}$, $i = 0, \ldots, 8$ (the $D2Q9$ lattice, see Fig. 1) are:

$$c_x = \{0, 1, 0, -1, 0, 1, -1, -1, 1\} ,$$
$$c_y = \{0, 0, 1, 0, -1, 1, 1, -1, -1\} .$$

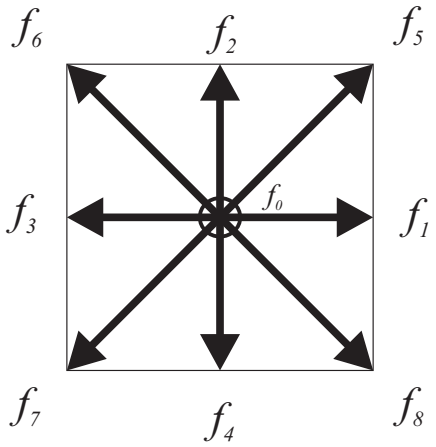

FIGURE 1. Two dimension - nine discrete velocities lattice (D2Q9 lattice)

The equilibrium populations are obtained after entropic minimization under specific constraints. The constraints require the conservation of mass, momentum and energy. Moreover, the equilibrium pressure tensor must have the same form as in the continuous kinetic theory [2]. The expressions of the equilibrium populations are:

$$f_i^{\mathrm{eq}} = \rho \prod_{\alpha=x,y} \frac{\left(1-2c_{i\alpha}^2\right)}{2^{c_{i\alpha}^2}} \left((c_{i\alpha}^2-1)+c_{i\alpha}u_\alpha+u_\alpha^2+T\right),$$

where ρ, u_α and T are the density, velocity and temperature fields, respectively which are defined as:

$$\begin{aligned}
\sum_{i=0}^{8} f_i^{eq} &= \sum_{i=0}^{8} f_i = \rho, \\
\sum_{i=0}^{8} c_{i\alpha} f_i^{eq} &= \sum_{i=0}^{8} c_{i\alpha} f_i = j_\alpha, \\
\sum_{i=0}^{8} c_i^2 f_i^{eq} &= \sum_{i=0}^{8} c_i^2 f_i = 2\rho T + \frac{j^2}{\rho},
\end{aligned}$$

The model presented so far, does not result to a fully correct description of thermo-hydrodynamic flows. In order to recover the NS and energy equations, the counter-terms Ψ_i and Φ_i must be added into the Boltzmann-BGK equation,

$$\partial_t f_i + c_{i\alpha}\partial_\alpha f_i = -\frac{1}{\tau}(f_i - f_i^{eq}) + \Psi_i + \Phi_i, \tag{1}$$

where τ is the relaxation rate toward the equilibrium state. Ψ_i and Φ_i are functions of ρ, u_α and T. Their purpose is to provide the precise macroscopic momentum (term Ψ_i) and energy (term Φ_i) equations. Their expressions are defined in [2]. After the introduction of these counter-terms into the kinetic equation (1), the latter recovers the compressible Navier-Stokes and Fourier equations in the hydrodynamic limit:

$$\begin{aligned}
\partial_t \rho &= -\partial_\gamma(\rho u_\gamma), \\
\partial_t u_\alpha &= -u_\gamma\partial_\gamma u_\alpha - \frac{1}{\rho}\partial_\alpha(\rho T) + \frac{1}{\rho}\partial_\gamma\left[\tau\rho T\left(\partial_\alpha u_\gamma + \partial_\gamma u_\alpha - \partial_\kappa u_\kappa \delta_{\alpha\gamma}\right)\right] + \rho g_\alpha, \\
\partial_t T &= -u_\alpha\partial_\alpha T - T\partial_\alpha u_\alpha + \frac{1}{\rho}\left[\partial_\alpha\left(\frac{2}{\mathrm{Pr}}\tau\rho T\partial_\alpha T\right) + \left(\partial_\gamma u_\alpha\right)\tau\rho T\left(\partial_\alpha u_\gamma + \partial_\gamma u_\alpha - \partial_\kappa u_\kappa\delta_{\alpha\gamma}\right)\right].
\end{aligned}$$

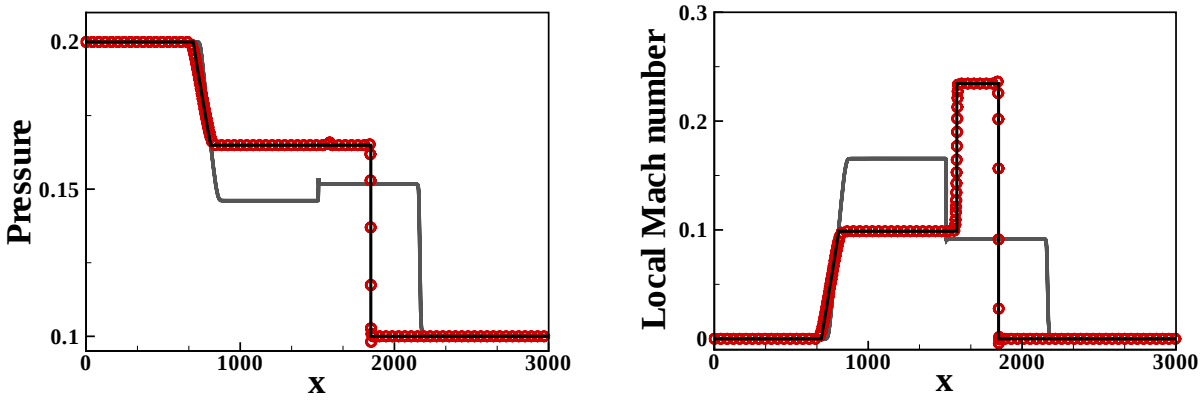

FIGURE 2. Shock tube simulation. Solid black line, represents the analytic solution of the flow. Symbols are the simulation results of the model with counter-terms implementation. Gray line represents the model without counter-term implementation.

The corresponding fluid obeys the ideal gas equation of state, $p = \rho T$, with the adiabatic exponent $\gamma = c_p/c_v = 2$. The viscosity coefficient μ and thermal conductivity κ are identified as:

$$\mu = \tau\rho T,\ \kappa = \frac{2}{\mathrm{Pr}}\tau\rho T.$$

The Prandtl number $\mathrm{Pr} = c_p\mu/\kappa$, and the speed of sound $c_s = \sqrt{2T}$ are tunable parameters. The model is suitable for simulations of flows that belong to the subsonic regime. In Ref. [5] flow simulations where the Mach number is as high as Ma=0.8 have been presented. The accuracy of the results shows that the low Mach number limitation, of the standard lattice Boltzmann method, has been removed. This model is a complete Galilean invariant model. The equilibrium populations remain positive if the temperature T is in the range $\delta T = \delta T_x \bigcap \delta T_y$, where $\delta T_{x,y} = \{T : |u_{x,y}| < T + u_{x,y}^2 < 1\}$. For low Mach numbers, $0 < T < 1$. In Ref. [3] a combustion relevant simulation with temperature variation of the order of ten has been presented.

3. RESULTS

The aforementioned thermal LB model can be used in a multitude of engineering applications [3, 4]. The compressibility of the model can be checked with the shock tube simulation. The tube is separated in two regions (left and right) which contain the same gas but at different density, temperature and pressure. When the barrier is removed, a shock wave and a rarefaction wave start propagating. For a given time step, the simulation results of the model are compared to the analytic solution of the flow. In Figure 2, the black line depicts the analytic solution while the symbols are the simulation results. The gray line represents the behavior of the model without correction term implementation. The initial conditions are:

$$\frac{T_l}{T_r} = 8, \frac{\rho_l}{\rho_r} = \frac{1}{4}, \frac{P_l}{P_r} = 2.$$

The local Mach number is defined as the ratio of the velocity u over the speed of sound c_s at a given point: $Ma(x,t) = u(x,t)/c_s$. Simulation results of the model with the counter-term implementation are in very good agreement with the analytic solution.

The present thermal model can be used for heat transfer simulations, e.g. for natural convection. For that, the fluid is considered to be enclosed between two parallel walls. The bottom wall has higher temperature than the top wall. Periodic boundary condition is applied on the side-walls and the gravity force is perpendicular to the top and bottom walls. The aspect ratio of the computational domain is 2:1. The heat transfer intensity can be described by the Nusselt number (Nu) and depends on the Rayleigh (Ra) and Prandtl (Pr) dimensionless numbers. Simulation results are shown in Fig.3.

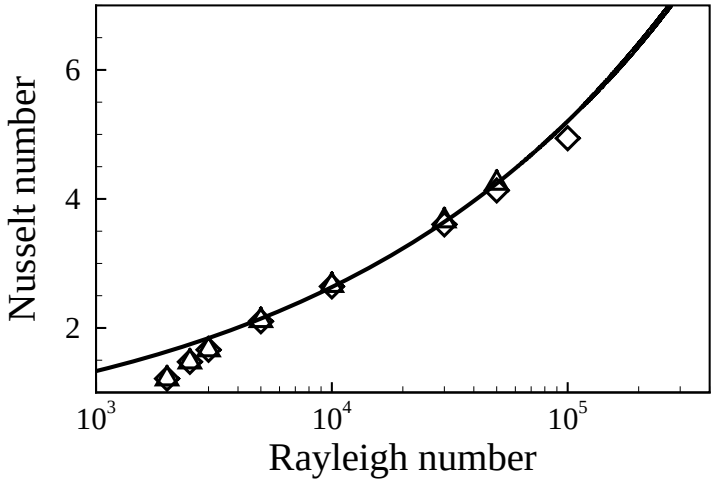

FIGURE 3. Rayleigh Benard natural convection. Dependency of the Nusselt number on the Rayleigh number. Triangles represent the reference data of Ref. [6]; the solid line is the theoretical power-law found in Ref. [6]; diamonds are the simulation results of the thermal lattice Boltzmann model

Finally, the present model has been shown to be able to serve as a basis model for combustion applications. A flow with distributed heat sources and heat sinks that mimics a combustion flow field was considered in Ref. [3].

4. CONCLUSIONS

A thermal lattice Boltzmann model has been presented. This model can be used for standard heat and mass transfer engineering applications. Simulation results of the shock tube, and the Rayleigh Benard natural convection have been presented in order to demonstrate the validity of the model.

REFERENCES

[1] S. Succi, *The Lattice Boltzmann Equation for Fluid Dynamics and Beyond*, (Oxford University Press, Oxford, 2001).
[2] N. I. Prasianakis, I.V. Karlin, Phys. Rev. E **76**, 016702 (2007).
[3] N. I. Prasianakis, I.V. Karlin, Phys. Rev. E **78**, 016704 (2008).
[4] N. I. Prasianakis, PhD thesis No. 17739, ETH Zurich (2008).
[5] N. I. Prasianakis, I.V. Karlin, I.Mantzaras, K. Boulouchos Phys. Rev. E **79**, 066702 (2009).
[6] R. M. Clever and F. H. Busse, J. Fluid Mech., **65**, 625 (1974).

First International Conference on Computational Methods for Thermal Problems
ThermaComp2009, September 8-10, 2009, Naples, Italy
N.Massarotti and P.Nithiarasu (Eds.)

Wall Boundary Conditions for Pseudo-Potential Multiphase Lattice Boltzmann Fluids

Giacomo Falcucci
University of Naples "Parthenope", Centro Direzionale - Isola C4, Naples, Italy
University of Rome "Tor Vergata", Viale Politecnico 1, Rome, Italy
falcucci@uniroma3.it

Daniele Chiappini
University of Rome "Tor Vergata", Viale Politecnico 1, Rome, Italy
chiappini@ing.uniroma2.it

ABSTRACT

In the behaviour of multiphase systems the contact angle problem is very challenging and it has a relevant influence in a lot of engineering and physics problems. The kinetic approach of LBM method allows characterizing this kind of phenomena in a detailed manner with short time simulation. For example the determination of liquid film shape due to a liquid drop impacting against a wall is one of the possible test cases which could be analyzed. The aim of this work is to present the results obtained by means of the Shan-Chen approach for non-ideal fluids in the Lattice Boltzmann model frame. First of all the theoretical background is presented, both for the standard multiphase approach due to Shan and Chen and for the recent enhancements of such a method; then the results of liquid drop impact on hydrophilic and hydrophobic surfaces are presented and compared to experimental measures in literature.

Key Words: *Lattice Boltzmann, multiphase, boundary conditions.*

I. INTRODUCTION

During last years many improvements have been done in the simulation of complex systems, as multiphase problems. One of the possibility, which is increasing its importance, is the use of a kinetic approach, the Lattice Boltzmann Method.
The Lattice-Boltzmann (LB) approach has proven to represent a powerful mesoscopic alternative to classical macroscopic methods for computational hydrodynamics [1, 2], especially in the field of non-ideal multiphase flows. The kinetic and *local* nature of LB methods, in fact, allows to account for the dynamics at the interface between the two fluids without the constraints of a continuum approach (Navier-Stokes) [3, 9, 20]. The pseudopotential method put forward a decade ago by Shan-Chen to endow Lattice Boltzmann (LB) models with potential energy interactions, is one of the most successfull outgrowth of basic LB theory [3, 4]. The Shan-Chen (SC) model is based on the idea of representing intermolecular interactions at the mesoscopic scale via a density-dependent nearest-neighbor pseudopotential $\psi(\rho)$. Despite its highly simplified character, the SC model provides the essential ingredients of non-ideal (dense) fluid behaviour, that is i) a non-ideal equation of state, ii) surface tension effects at phase interfaces. Because of its remarkable computational simplicity, the SC method is being used for a wide and growing body of complex flows applications, such as multiphase flows in chemical, manufacturing and geophysical problems. In spite of its undeniable success, the SC method has made the object of intense criticism. In particular, i) Lack of thermodynamic consistency, ii) Spurious currents at interfaces and iii) Surface tension tied-down to the equation of state. Problem i) refers to the fact that there is only one functional form, namely $\psi(\rho) \propto \rho$, securing compatibility between mechanical stability of the interface and equilibrium thermodynamics, i.e. Maxwell's area law in the Van der Walls loop of the non-ideal equation of state. However, recent studies [6] have clearly shown that use of suitable pseudopotentials such that $\psi(\rho) \rightarrow \rho$ in the limit of zero density, makes this problem largely irrelevant to any practical purposes. Problem ii) is general held responsible for setting a sharp limit on the density jumps across the dense/rarefied fluid interface to values around ten or less.

This is a rather severe limitation for many practical applications, in which two-three orders of magnitude density jumps are often encountered (typically $1:1000$ for air-water interfaces).
Recent studies indicate that the density ratio can be enhanced, the surface tension can be tuned independently of the equation of state and the onset of metastable multi-droplet configurations can be disclosed by introducing second-neighbor *repulsive* interactions [7, 8].
For what concerns the parasitic currents, it has been suggested that they can be significantly reduced in magnitude by reformulating the pressure gradient and the interface tension [9]−[13] or by incorporating the sharp interface dynamics into the LBE [14, 20], even though the total elimination of parasitic currents is not easy. In [11], it was first displayed that parasitic currents could be completely eliminated by replacing the pressure form of the surface tension force with the potential form. However, the numerical instability of this LBE method prevented it from being used for practical applications without the addition of a tiny correction term with a small amount of numerical viscosity.
Recently, it was shown [9, 16] that for van der Waals fluids, the use of the potential form of the surface tension and the isotropic finite difference eliminates parasitic currents to round-of and enables stable simulation of the liquid-vapor two-phase flows at a high density ratio. They reported, however, that the compressibility should be artificially increased in the case of a large density difference because of the finite equilibrium interface thickness that is usually a 3 to 4 grid distance.
In this work, the main aspects of the Shan-Chen theory and its recent enhancements are presented.
The wall boundary condition implementation is described for these two approaches and the results of liquid drop wall impingement are presented. The wall surface can be easily fixed to be either hydrophilic or hydrophobic and the obtained results in term of drop deformation are compared to experimental measures known from literature.

II. MAIN BODY

We consider the standard lattice Boltzmann (LB) equation with pseudopotentials

$$f_i(\vec{r}+\vec{c}_i,t+1)-f_i(\vec{r},t)=-\omega(f_i-f_i^{eq})+F_i \tag{1}$$

in which the term F_i is a body force term. Such a term can model non-ideal effects and can be written as [3, 4]:

$$F_i=G\psi(\vec{r},t)\sum_i w_i\ \psi(\vec{r}+\vec{c}_i,t)\ c_i \tag{2}$$

where $\psi(\vec{r},t)$ is the Shan-Chen *pseudoptential* for density interaction and w_i are the normalized weights.
As is well-known, the standard 1-belt, 8-speed lattice provides 4th-order isotropy and the weight values are $w_1=w_4=1/9; w_5=w_9=1/36$. In the standard Shan-Chen approach, the intermolecular density force is *attractive*, [3, 4]. Recently [7], the body force in eq. 1 was extended to the 2^{nd} Brillouin zone in the lattice (*belt*, for simplicity), providing interesting results in simulating spray-like fluids [8]. The scheme of the interaction is represented in Figure $1b$.
We consider generalized pseudoforces of the following form

$$\vec{F}(\vec{r})=\sum_{j=1}^{2}c_s^2G_j\psi_j^{n(j)}(\rho(\vec{r}))\sum_{i=1}^{b_j}p_{ij}\vec{c}_{ij}\psi_j^{n(j)}(\rho(\vec{r}+\vec{c}_{ij})) \tag{3}$$

In the above, the index j labels the Seitz-Wigner cell (*belt* for simplicity) defined by the condition $|\vec{r'}-\vec{r}|^2\leq 2j^2$, whereas $\vec{c_{ij}}$ denotes the set of discrete speeds belonging to the $j-th$ belt. The exponents $n(j)$ are chosen to be: $n(1)=1$ and $n(2)$ varying between 1 and $1/8$. Note that lattice units $\Delta x=\Delta t=1$ have been assumed here. In this work we shall confine our attention to the 24-neighbors, 2-belt lattice depicted in Figure $1a$. As stated before, the standard 1-belt, 8-speed lattice provides 4th-order isotropy, whereas the 2-belts, 24-speed lattice upgrades isotropy to 8th order, provided the weights are properly chosen. A suitable choice is reported in [7] To forestall any confusion, we wish emphasize that the 2-belt lattice is used *only* for the (pseudo)-force evaluation, whereas tha standard lattice Boltzmann dynamics still takes place in the original D2Q9 lattice. This is also the reason why we keep a separate notation for the weights w_i used for the lattice Boltzmann populations and the weights p_{ij} used for the force evaluation.

The implementation of boundary conditions is one of the greatest advatages in adopting the Lattice Boltzmann approach. In fact, the ability to easily incorporate complex solid boundaries is one of the most exciting aspects of these models for the great flexibility they allow.
The wall boundary condition can be fixed as $free-slip$ or $no-slip$.
The $no-slip$ or $bounceback$ condition is particularly simple and the only need is to designate a particular node

(a) (b)

FIG. 1: (a): two-belt lattice for force evaluation. Each node is labelled by the corresponding energy $|c_{ij}|^2$. Belt 1 contains eight speeds and two energy levels $(1, 2)$. Belt 2 contains sixteen speeds, distributed over three energy levels $(4, 5, 8)$. (b): sketch of the $2 - belt$ interaction.

(or layer of nodes) as a solid obstacle, without any other programming requirement. Moreover, the wall nodes inside an obstacle can be $deleted$ from the simulation, allowing a considerable spare in computational time.
The bouncback condition annihilates both normal and parallel components of the velocity vector in respect to the considered wall, as shown in Figure 2. The bounceback conditions on the appropriate populations of the nodes

$a)$ $b)$

FIG. 2: $a)$:Sketch of the $bounce - back$ boundary condition implementation; $b)$:Contact angle of a liquid droplet on a hydrophilic surface.

in the buffer have to be imposed: if $\vec{x}$ is the position of the last fluid node, i is the direction entering the wall and j the opposite direction, we can write

$$f_j(\vec{x} + \vec{c_i}, t) = f_i(\vec{x}, t) \tag{4}$$

To make an example, considering a $Nord$ wall in a 2D lattice scheme,

$$f_4(\vec{x} + \vec{c_2}, t) = f_2(\vec{x}, t) \tag{5}$$
$$f_8(\vec{x} + \vec{c_6}, t) = f_6(\vec{x}, t) \tag{6}$$
$$f_7(\vec{x} + \vec{c_5}, t) = f_5(\vec{x}, t) \tag{7}$$

In case of a $free - slip$ boundary condition, the above equations only apply to the population entering the wall. To define the hydrophilic or hydrophobic nature of a wall, the basic information needed regards the magnitude of the $contact\ angle$. The contact angle is the angle at which a liquid/vapor interface meets the solid surface. The contact angle is specific for any given system and is determined by the interactions across the three interfaces. The contact angle plays the role of a boundary condition. Contact angle is measured using a contact angle goniometer, see Figure $2b$). To set the magnitude of the contact angle, the $density$ of the wall must be specified [18].

III. RESULTS

Figure 3 highlights the different behaviour of a liquid droplet impacting on a hydrophilic and hydrophobic surface. It is interesting to measure the maximum deformation obtained in case of hydrophobic impact: it is possible to relate the magnitude of such deformation to the Reynolds and Weber number that characterize the undisturbed motion of the droplet. Clanet et al. [19] found and empirical law for the maximum droplet deformation, reported in Figure $3(c)$. Figure $3(c)$ reports the rsults we obtained applying the sytandard Shan-Chen and the 2-belt approach for the impinging droplet. The Figure highlights the perfect matching between the measured deformations and the experimental trend proposed by Clanet et al. [19]. It is woth noting that the above results have been obtained also with different values of the density ratio (in the limits of the Shan-Chen EOS-based approaches), thus hihghlighting the accuracy and stability of such a method.

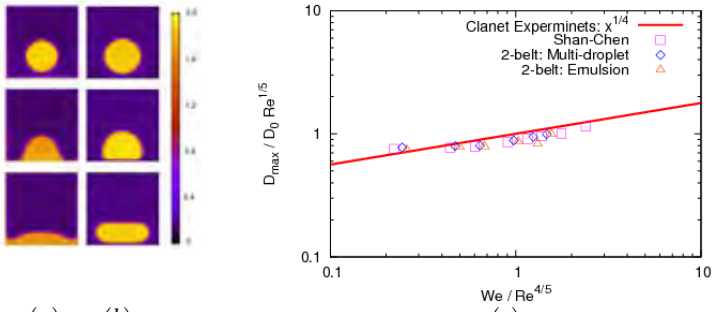

(a) (b) (c)

FIG. 3: Impact on hydrofilic (a) and hydrophobic (b) surfaces. In (c) it is shown the comparison between the maximum deformations obtained for the impinging droplet, as a function of Weber and Reynolds numbers between the results of the Shan-Chen and $2-belt$ approaches and experimental measures, [19].

IV. CONCLUSIONS

In this work, a review of the Shan-Chen model and its recent enhancements for non-ideal fluid simulation with Lattice Bolzmann models is presented.
The main aspects of wall boundary conditions in such a frame are presented, together with the results obtained in the field of liquid droplets wall impingement. The comparison with experimental data in literature shows a very good agreement, thus making the Lattice Boltzmann approach very promising in the field of wall impingement studies.

[1] Succi, S. "The lattice Boltzmann equation for fluid dynamics and beyond", Oxford Science Publications, 2001
[2] Benzi, R., Succi, S. and Vergassola, M. "The lattice Boltzmann equation: theory and applications" Phys. Rep. 222, 145-197, 1992
[3] Shan, X. and Chen, H. "Lattice Boltzmann model for simulating flows with multiple phases and components", Physical Review E, 47, 1993.
[4] Shan, X. and Chen, H. "Simulation of nonideal gases and liquid-gas phase transitions by the lattice Boltzmann equation", Physical Review E, 49, 1994.
[5] Benzi, R. "Private communication"
[6] Sbragaglia, M., Benzi, R., Biferale, L., Succi, S., Sugiyama, K. and Toschi, F. "'Generalized Lattice Boltzmann method with multi-range pseudo-potential", submitted.
[7] Falcucci G., Bella G., Chiatti , Chibbaro S., Sbragaglia M., and Succi S., Comm. in Comp. Phys., **2**, 1071 (2007).
[8] Falcucci G., Chibbaro S., Succi S., Shan X. and Chen H., Europhys. Lett., **82**, 24005, (2008).
[9] T. Lee, P.F. Fischer, Phys. Rev. E 74 (2006) 046709.
[10] A. Cristea, V. Sofonea, Int. J. Mod. Phys. C 14 (2003) 1251.
[11] A.J. Wagner, Int. J. Mod. Phys. B 17 (2002) 193.
[12] P. Yuan, L. Schaefer, Phys. Fluids 18 (2006) 042101.
[13] X. Shan, Phys. Rev. E 73 (2006) 047701.
[14] S.V. Lishchuk, C.M. Care, I. Halliday, Phys. Rev. E 67 (2003) 036701.
[20] P. Lallemand, L.-S. Luo, Y. Peng, J. Comput. Phys. 226 (2007) 1367.
[16] D. Chiappini, G. Bella, S. Succi, F. Toschi and S. Ubertini, submitted to Communication in Computational Phisics Under Review (2009)
[17] Shan, X. "Analysis of the spurious current near the interface in a class of multiphase lattice Boltzmann models", Physical Review E, 73, 2006
[18] R. Benzi, L. Biferale, M. Sbragaglia, S. Succi and F. Toschi, "Mesoscopic modeling of a two-phase flow in the presence of boundaries: the contact angle", Phys, Rev. E. **74**, 021509 (2006)
[19] C. Clanet, C. Beguin, D. Richard nad D. Quere, "Maximal deformation of an impacting drop", J. Fluid Mech. (2004), vol. 517, pp. 199208
[20] P. LAllemand, L.S. Luo, Y. Peng, *A Lattice Boltzmann Front-Tracking Method for Interface Dynamics with Surface Tension in Two Dimensions*, Journ. Comp. Physics 226 (2007) pp.1367-1384.

First International Conference on Computational Methods for Thermal Problems
ThermaComp2009, September 8-10, 2009, Napoli, Italy
N.Massarotti and P.Nithiarasu (Eds.)

THE LATTICE BOLTZMANN METHOD IN SOLVING RADIATIVE HEAT TRANSFER IN A PARTICIPATING MEDIUM

Antonio F. Di Rienzo
Department of Energetics, Politecnico di Torino, Turin - 10129, Italy, antonio.dirienzo@polito.it

Salvador Izquierdo
Department of Energetics, Politecnico di Torino, Turin - 10129, Italy, salvador.izquierdo@polito.it

Pietro Asinari
Department of Energetics, Politecnico di Torino, Turin - 10129, Italy, pietro.asinari@polito.it

Subhash C. Mishra[1]
Department of Energetics, Politecnico di Torino, Turin - 10129, Italy, scm_iitg@yahoo.com

Romano Borchiellini
Department of Energetics, Politecnico di Torino, Turin - 10129, Italy, romano.borchiellini@polito.it

ABSTRACT

A lattice Boltzmann method (LBM) is proposed in order to analyze radiation problems involving an absorbing, emitting and scattering participating medium. The LBM scheme has been tested by solving benchmark radiative transfer problems in 1-D and 2-D Cartesian geometry. Temperature and heat flux distributions have been obtained for a wide range of the values of the extinction coefficient. The LBM results have been compared against the results obtained from the finite volume method (FVM). A good comparison has been obtained.

Key Words: *Radiation, Lattice Boltzmann Method, Finite Volume Method.*

1. INTRODUCTION

The lattice Boltzmann method (LBM) is a new computational tool, that has been applied to a large class of fluid flow and heat transfer problems. Recently, the application of the LBM has also been extended to formulate and solve energy equation of heat transfer problems involving thermal radiation as well. In such problems, the volumetric thermal radiation was always computed using the conventional numerical radiative transfer methods such as discrete ordinates method (DOM), the discrete transfer method (DTM), the collapsed dimension method (CDM) and finite volume method (FVM). LBM has found to be superior over FVM for solving the energy equations of heat transfer problems involving thermal radiation. However, in none of the previous studies the computation of radiative information, which is the most time costing part, has been computed by using the LBM. Hence, the aim of the present work is to compute radiative informations in a participating medium through the lattice Boltzmann formulation.

2. MAIN BODY

A 2-D rectangular enclosure has been considered. The gray and homogeneous participating medium is absorbing, emitting and scattering. The south boundary of the enclosure is at temperature T_S and it is the source of radiation in the medium. The other three boundaries are cold. All four boundaries are diffuse and gray. The medium temperature is unknown and the thermal equilibrium in the system is only by radiation. Scattering is assumed to be isotropic and radiative equilibrium

[1] On leave from the Department of Mechanical Engineering, Indian Institute of Technology Guwahati, Guwahati – 781039, India

condition is considered. The extinction coefficient β is the reciprocal of the mean free path of radiation in the medium and $1/\beta$ causes a similar kind of dissipative effect to radiation as is done by the kinematic viscosity in the treatment of viscous flow and thermal diffusivity in the analysis of conduction heat transfer. We use $\vec{e}_i$ to indicate the generic component of the lattice and $e_i = |\vec{e}_i|$ for its magnitude. In the usual LBM formulation, radiation equation can be written as:

$$I_i\left(\vec{r}_n + \vec{e}_i \Delta t, t + \Delta t\right) = I_i\left(\vec{r}_n, t\right) + \frac{\Delta t}{i}\left[I_i^{(eq)}\left(\vec{r}_n, t\right) - I_i\left(\vec{r}_n, t\right)\right]$$

From the point of view of the solution procedure, the algorithm is split into two steps, viz., collision and streaming, which are, respectively:

$$I_i^*\left(\vec{r}_n, t\right) = I_i\left(\vec{r}_n, t\right) + \frac{\Delta t}{i}\left[I_i^{(eq)}\left(\vec{r}_n, t\right) - I_i\left(\vec{r}_n, t\right)\right]$$

$$I_i\left(\vec{r}_n + \vec{e}_i \Delta t, t + \Delta t\right) = I_i^*\left(\vec{r}_n, t\right)$$

3. RESULTS

The LBM formulation has to be validated. For this purpose, results of the FVM are considered benchmark. Both LBM and FVM are iterative methods and require a convergence criterion on one of the evolving parameters. In this work, this parameter was set on the incident radiation and when, between two successive iterations, the maximum change in incident radiation at any point was less than 1×10^{-6}, the solution was assumed to have converged. In Fig. 1 the distribution of the dimensionless heat flux along the south (hot) boundary have been compared between the LBM and the FVM. The comparisons have been made for three different values of the extinction coefficient. In both LBM and FVM runs were taken for 31x31 lattice/control volumes. The LBM results have been computed for D2Q16 lattice, which uses only 16 directions. It is observed from Figs. 1 that the LBM results are slightly offset from the FVM results. However, considering that fact that the LBM uses 8 times less number of directions than the FVM, the accuracy provided by the LBM is appreciable. The comparison of the LBM and the FVM results for the centerline ($x/X=0.5, y$) dimensionless emissive power has been shown in Fig. 2. It is seen from the Fig. 2 that for $\beta=1.0$, the emissive power distribution has a numerical oscillation. This oscillation is present in both the FVM and in the LBM. By increasing the number of control volumes, this unphysical numerical oscillation can be avoided. The emissive power computed using the LBM is found to match well with those of the FVM for other values of the extinction coefficient β. In Fig. 3 we compare the effect of lattices in the LBM and the number of directions in the FVM on dimensionless heat flux distributions along the south (hot) boundary. For the LBM, effects of D2Q8, D2Q16 and D2Q32 have been studied. While, for the FVM, effects have been studied for 2x4, 4x8 and 8x16 directions. Results improve by increasing the number of directions.

For the 1-D case, the X-dimension in the 2-D LBM code was stretched 10 times more than the Y-dimension. With this, practically the effects of the side walls (west and east) should have no influence on the heat flux at the center of the south wall and emissive power distributions long the centerline ($x/X = 0.5, y/Y$). Fig. 4 provides a comparison of the variation of the dimensionless heat flux on the hot (south) boundary with the extinction coefficient β. This comparison has been made for β value in the range [0.1: 10]. The LBM results show a good comparison with the FVM results. Dimensionless emissive power distributions in the medium have been compared in Fig. 5 for β = *1.0, 3.0, 5.0* and *10.0*. With an increase in the value of β, results of the two methods are found to compare well.

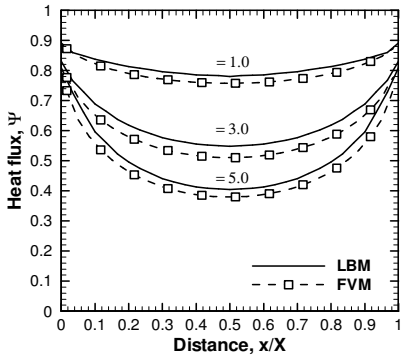

FIGURE 1. Dimensionless heat flux distribution along the south wall for $\beta = 1.0, 3.0, 5.0$

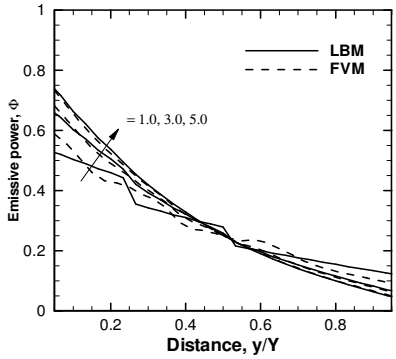

FIGURE 2. Dimensionless centerline emissive power distribution for $\beta = 1.0, 3.0, 5.0$

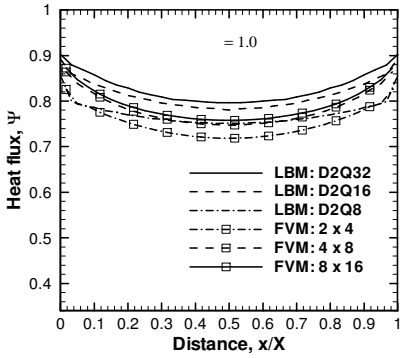

FIGURE 3. Dimensionless heat flux distribution along the south wall for D2Q8, D2Q16 and D2Q32 for $\beta = 1.0$

4. CONCLUSIONS

A 2-D formulation of the LBM was developed for the analysis of radiative transport problems. To compare the results of the LBM, the problems were also solved using the FVM. The FVM results were considered benchmark. Dimensionless heat flux distributions along the hot boundary and centerline emissive power distributions were compared for a wide range of values of the extinction coefficient. By stretching x-dimension of the 2-D enclosure, a 1-D planar medium situation was achieved and results for this case were compared with the 1-D FVM code. For all the situations, the LBM results were in close agreements with the FVM results. Considering the fact that the LBM used 8 times less number of directions, the accuracy obtained was satisfactory. The slight mismatch between the LBM and the FVM results can be offset by increasing the number of lattices.

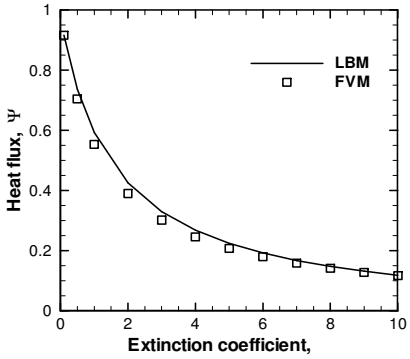

FIGURE 4. Comparison of variation of dimensionless heat flux distribution on the south boundary as function of the extinction coefficient

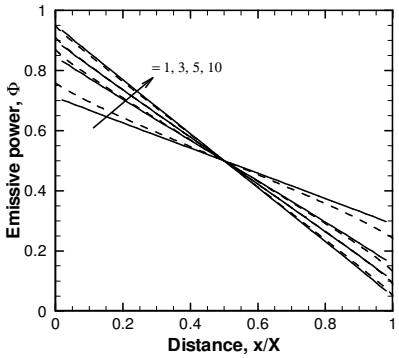

FIGURE 5. Distributions of dimensionless emissive power in the medium for $\beta = 1.0, 3.0, 5.0$

REFERENCES

[1] Modest, M.F., 2003. *Radiative Heat Transfer*, second ed., Academic Press, New York.

[2] Fiveland, W.A., 1984. "Discrete-Ordinates Solution of the Radiative Transport Equation for Rectangular Enclosures". *J. Heat Transfer,* 106, pp. 699–706.

[3] Mishra, S. C., Roy, H. K., Mishra, N. 2006, "Discrete Ordinate Method with a New and a Simple Quadrature Scheme". *J. Quant. Spectrosc. Radiat. Transfer*, 101, pp. 249-262.

[4] Anand, N., and Mishra, S.C., 2006, "The Discrete Transfer Method Applied to the Radiative Heat Transfer in a Variable Refractive Index Semitransparent Medium", *J. Quant. Spectrosc. Radiat. Transfer*, 102, pp. 432-440.

[5] Mishra, S.C., and Prasad, M., 2002, "Radiative Heat Transfer in Absorbing-Emitting-Scattering Gray Media Inside 1-D Gray Cartesian Enclosure using the Collapsed Dimension Method". *Int. J. Heat Mass Transfer*, 45, pp. 697-700.

[6] Chai J. C., and Patankar S.V., 2000. Finite volume method for radiation heat transfer, *Adv. Numerical Heat Transfer*, 2, pp. 110–135.

[7] Kim, M.Y., Baek, S.W., and Lee, C.Y., 2008., "Prediction of Radiative Heat Transfer Between Two Concentric Spherical Enclosures with the Finite Volume Method". *Int. J. Heat Mass Transfer*, 51, pp. 4820-4828.

[8] Mishra S.C. and Roy H.K., 2007. Solving Transient Conduction-Radiation Problems using the Lattice Boltzmann Method and the Finite Volume Method, *J. Computational Physics*, 223, pp. 89-107.

First International Conference on Computational Methods for Thermal Problems
ThermaComp2009, September 8-10, 2009, Napoli, Italy
N.Massarotti and P.Nithiarasu (Eds.)

NUMERICAL STUDY OF NATURAL CONVECTION IN A SQUARE CAVITY USING THE LATTICE BOLTZMANN METHOD

Elkin Flórez
Department of Mechanical Engineering, Rovira I Virgili Universtity, Av. Països Catalans, 26,
elkingregorio.florez@urv.cat

Clara Salueña

Department of Mechanical Engineering, Rovira I Virgili Universtity, Av. Països Catalans, 26,
clara.saluena@urv.cat

Jordi Pallares

Department of Mechanical Engineering, Rovira I Virgili Universtity, Av. Països Catalans, 26,
jordi.pallares@urv.cat

Ildefonso Cuesta

Department of Mechanical Engineering, Rovira I Virgili Universtity, Av. Països Catalans, 26,
ildefonso.cuesta@urv.cat

ABSTRACT

Numerical simulations of natural convection in a partially conducting square heated from one side wall, using the method of lattice Boltzman equation (LBE) with the Boussinesq approximation, and for highs Prandtl numbers are reported. Radiation heat transfer, compressibility effects, and variation of physical properties between the cold and the hot temperatures are neglected.

The velocity and temperature fields are computed using two different lattice schemes. The first one uses the same D2Q9 for both velocity and temperature [1] and the second one uses D2Q9 for velocity and D2Q5 for temperature. The two distributions functions follow their respective lattice Boltzmann transport equations with the single relaxation time Bhatnagar-Gross-Krook (LBGK) approximation.

The natural convection flow in a square cavity is studied in the range of $6 \leq \mathrm{Pr} \leq 50$ and for $10^3 \leq \mathrm{Ra} \leq 106$. The code used was validated with existing data for Ra-Be and cavity problems for Pr = 0,71. The numerical results are found in a good agreement with those reported in the literature and computed by Navier-Stokes solvers.

Key Words: *Heat Transfer, lattice Boltzmann method, Natural Convection.*

1. INTRODUCTION

From the end of the last millennium, a great amount of research of Computational Fluid Dynamics (CFD) using the lattice Boltzmann method (LBM) has been carried out. Latice Boltzmann method has become a relative novel alternative to traditional numerical methods such as finite differences, finite elements and finite volume methods for solving the Navier-Stoke and transport equations [1]. For the isothermal fluid flows, the LBM was found to be an accurate, stable and computationally economic method compared with classical computational fluid dynamics methods [2]. Nowadays, there are many engineering problems that can be studied by the LBM. Nevertheless, has been little attention to the study of natural convection flows, which hasn't been achieved much success due by

the requirements that big grids and by the numerical instabilities of the thermal LBM proposed in the literature [3].

In general, current LBM thermal models are classified into three categories: the multi-speed approach, the passive scalar approach and the doubled populations approach. The multi-speed approach is an extension of the LB isothermal model, in which only the density distribution function is used to calculate both, velocity and temperature. Two restrictions are in the multi-speed models, one its numerical instability and second the narrow range of temperature variations [4]. The passive scalar approach solves the velocity by the LBM, and the macroscopic temperature is calculated as a passive scalar. The disadvantages of this methodology are, first a drastic departure from a fully kinetic approach of the LBM, and second, the impossibility of incorporating the viscous heat dissipation and compression work done by pressure [5]. Finally, the double population approach has been implemented in this work, which is based on the work of He et al. [6]. This model introduces an internal energy density distribution function in order to calculate the temperature field, and the velocity field is obtained by the traditional density distribution function.

Different numerical schemes have been used to study natural convection in a square cavity have been performed using different Navier-Stokes solvers: Vahl Davis (1983) used the finite diffence method, M. Hortmann et al. (1990) applied a finite volume multigrid procedure and V. Heuveline (2003) with the finite element method. Previus work was carried out to simulated the 2D laminar flow for $10^3 \leq Ra \leq 10^6$ and Pr = 0,71. To solve this problem using LBM, Z. Guo (2002), Y. Peng et al. (2003), and A. D'orazio (2003) simulated the flow for $Ra \leq 10^6$, F. Kuznik et al. (2007) for $Ra \leq 10^8$, and H. N. Dixit and V. Babu (2006) for Ra until 10^{10}, for to name a few. All previous researchers have carried out simulations of these flows for Prandtl numbers less than 6, while in our work the natural convection flow in a cavity was studied for values of $6 \leq Pr \leq 50$ and also for a wide range of Rayleigh numbers.

2. NUMERICAL METHOD

The standard LBGK method to evaluate the macroscopic velocity based on square lattice with nine discret vector velocities for incompresible fluid flows is used, and for temperature field is evaluated using a simple LBGK method with a five vectors in the latticce. The two LBGK models are combined up into of the final one assuming the Boussinesq approximation for natural convection flows. The model makes use of two distribution functions, f and g, for the flow velocity field and the temperature field, respectively. The density and the temperature distribution function, f and g, are defined as the probability of particles at site x at time t moving with the discret particle velocity e_i during the time interval Δt in each lattice direction i. The two distribution obey their respective lattice Boltzmann transport equation,

$$f_i(x + e_i\Delta t, t + \Delta t) - f_i(x,t) = \frac{\Delta t}{\nu}\left[f_i^{eq}(x,t) - f_i(x,t)\right] + F_i \tag{1}$$

for the flow velocity field, and

$$g_i(x + e_i\Delta t, t + \Delta t) - g_i(x,t) = \frac{\Delta t}{T}\left[g_i^{eq}(x,t) - g_i(x,t)\right] \tag{2}$$

for the temperature field. Where de ν and T are the relaxation time for the flow and temperature lattice Boltzmann equation, respectively, and F_i is the momentum amount from the bouyant body force, calculated using the Boussinesq approximation by

$$F(x,t) = \rho(x,t) \cdot \quad_i \cdot g_0 \cdot \beta \cdot \left[T(x,t) - T_\infty\right] / c_s^2 \tag{3}$$

where $_i$ is the weighting factor, which can be determined to achieve isotropy of fourth-order tensor of velocities and Galilean invariance [7], is the thermal expantion coefficient, and the g_0 is the acceleration of the gravity in the the vertical direction, T_∞ is a refference temperature, and c_s=1/√3 is the speed of sound. The kinetic viscosity and the thermal diffusivity are given by their own relaxation time, $= c_s^2(\ _v - 0{,}5)$ and $= c_s^2(\ _T - 0{,}5)$. Furthemore, the local equilibrium distributions for f and g are:

$$f_i^{eq}(x,t) = \ _i\rho(x,t)\left[1+\frac{e_i\ \cdot V}{c_s^2}+\frac{V\ \cdot V}{2c_s^2}\left(\frac{e_i\ e_i}{c_s^2}-\Delta\ \ \right)\right] \tag{4}$$

$$g_i^{eq}(x,t) = \ _i\theta(x,t)\left[1+\frac{e_i\ \cdot V}{c_s^2}+\frac{V\ \cdot V}{2c_s^2}\left(\frac{e_i\ e_i}{c_s^2}-\Delta\ \ \right)\right], \tag{5}$$

respectively. In these expressions, the macroscopic variables, density , velocity V, and Temperture population are defined as: $= \sum f_i$, $V = \sum f_i e_i$ / , and $= \sum g_i$, where i and represent the cartesian coordinates. Using the Chapman-Enskog expansion, the continuity equation and the Navier-Stokes equation can be recovered with a second-order approximation from the equation (1) as is shown in [8]. Similarly, the transport equation for temperature can be obtained from equation (2), as can see in reference [9].

Typical bounce-back boundary conditions, for density distribution function, were used. Dirichlet condition was used to set wall temperatures, and Newman conditions for fixing wall heat fluxes.

The simulation of natural convection in a square cavity by LBM, requires an appropiate characteristic velocity ($V_c = \sqrt{\beta g_0 \Delta T H}$), the kinetic viscosity and thermal diffusivity, where H denotes the length scale, which is in our case the length of the cavity.

3. RESULTS

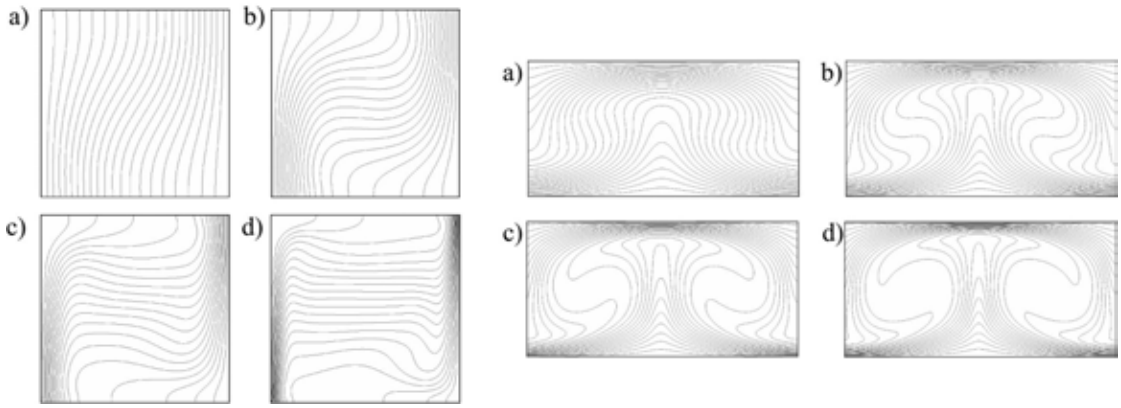

FIGURE 1. Isothermal lines for a cavity thermal flow and Ra-Be problem with Pr=0,71, a) Ra = 10^3, b) Ra = 10^4, c) Ra = 10^5, y d) Ra = 10^6

The numerical code developed in the present work, and suitable to study natural convection flows at high Pr numbers was validated by analyzing the natural convection flows at different Ra numbers, The results obtained in a two typical free convective problems, with fix Prandtl number (Pr = 0,71) in two different configurations; a differentially heated square cavity and the well reported Ra-Be

problem. The preliminaries results, including the temperature fields showed in Figure 1, agree well with those reported in [3, 10, 11] and [3,12], respectively.

The Figure 2 shows the horizontal velocity at the mid-width y/H = 0,5, for the differents Pr numbers. Grids from 51x51 to 301x301 was used and the relaxation times, both, smaller to 2.

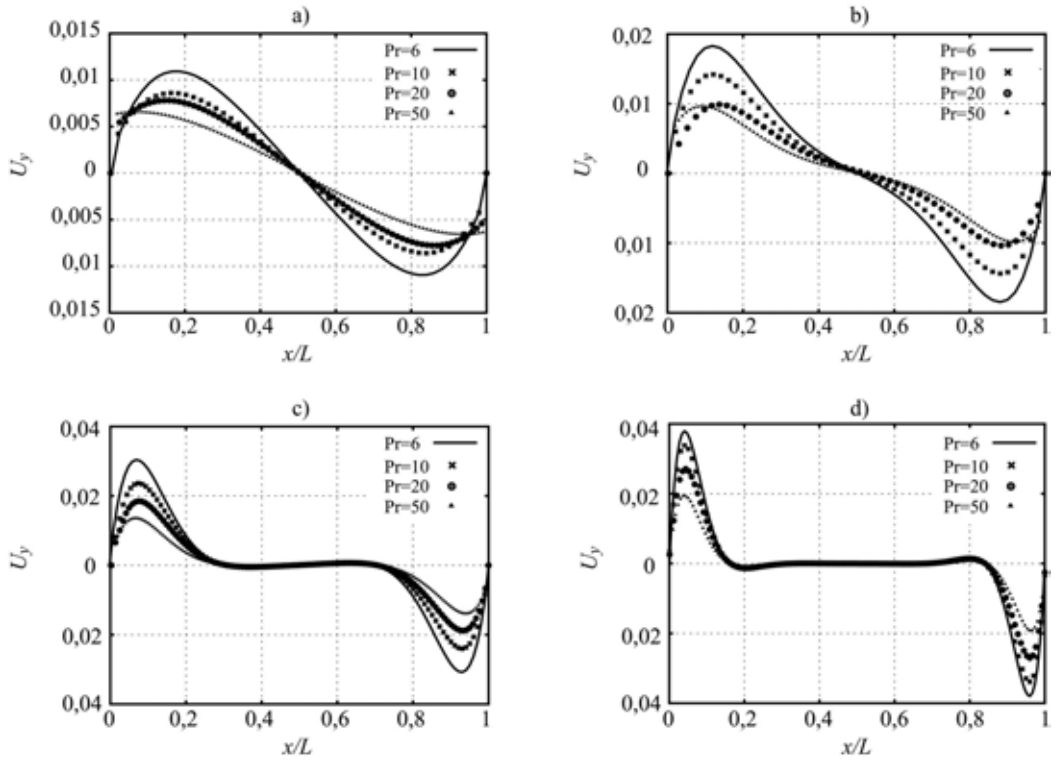

FIGURE 2. Vertical velocity at y/H = 0,5 for different Pr numbers and a) Ra = 10^3, b) Ra = 10^4, c) Ra = 10^5, y d) Ra = 10^6

3. CONCLUSIONS

A thermal lattice Boltzmann BGK model with doubled populations has been used to study the natural convection flow in a cavity for a wide range of Prandtl numbers.

The Rayleigh-Benard convection flow in a box was used to validate the developed code. Results of this flow show a good agreement of that reported in the literature.

This study shows that the LBM with uniform grid provides relatively reliable results over a range of 6≤Pr≤50. For higher Pr numbers, finer grids should be used to describe accurately the boundary layers.

REFERENCES

[1] X. He, S. Chen, G. D. Doolen, A novel thermal model for the lattice Boltzmann method in incompressible limit, *Journal of Computational Physics*, **146**, 282-300, 1998.

[2] S. Chen, G. Doolen, Lattice Boltzmann method for fluid flows, *Ann. Rev. Fluid Mech*. **30**, 329-64, 1998.

[3] F. Kuzmick, J. Vareilles, G. Rusaouen, G. Krauss, A double-population lattice Boltzmann method with non-uniform mesh for the simulation of natural convection in a square cavity, *Int. J. Heat and Fluid Flow*, **28**, 862-70, 2007.

[4] S. Succi, The lattice Boltzmann Equation for Fluid Dynamics and Beyond, Clarendon Press, Oxford, 2001.
[5] G. McNamara, A.L. Garcia, B.J. Alder, Stabilization of thermal lattice Boltzmann models, *J. Stat. Phys.*, **81**, 395-408, 1995.
[6] F. Kuznik, J. Vareilles, G. Rusaouen, G. Krauss, Application to natural convection enclosed flows of a lattice Boltzmann BGK model coupled with a general purpose thermal boundary conditions, *Int. J. of Thermal Sciences*, **43**, 575-86, 2004.
[7] Y. H. Quian, D. d'Humieres, P. Lalleman, Lattice BGK models for Navier-Stokes equation, *Europhys. Lett.* **17** (6), 479-484, 1992.
[8] Y. H. Quian, S. A. Orszag, Lattice BGK models for Navier-Stokes equation: non-linear deviation in compressible regimes, *Europhys. Lett.* **21**, 255-259, 1993.
[9] Z. Guo, B. Shi, and C. Zheng, A coupled BGK model for the Boussinesq equations, *Int. J. for Num. Meth. in Fluids*, **39**, 325-42, 2002
[10] Y. Peng, C. Shu, and Y. T. Chew, Simplified thermal lattice Boltzmann model for incompresible thermal flows, *Phys. Rev. E*, **68**, 026701, 1-8, 2003
[11] G. D. de Vahl, Natural convection of air in a square cavity a bench mark numerical solutions, *Int. J. For Meth. In Fluids*, **3**, 249-264, 1983
[12] X. Shan, Simulation of Rayleigh-Benard convection using a lattice Boltzmann method, *Phys Rev. E*, **55** (3), 2780-2788, 1996

First International Conference on Computational Methods for Thermal Problems
ThermaComp2009, September 8-10, 2009, Napoli, Italy
N.Massarotti and P.Nithiarasu (Eds.)

A STABILITY ANALYSIS FOR THE AC-CBS ALGORITHM FOR THE SOLUTION OF INTERFACE PROBLEMS IN PRESENCE OF LARGE SOURCE TERMS

Fausto Arpino
Department of Mechanics, Structures and Environment (DiMSAT), University of Cassino, Via G. Di Biasio 43, 03043 Cassino (FR), Italy. E-mail: f.arpino@unicas.it

Nicola Massarotti
Department for Technologies (DiT), University of Napoli "Parthenope", Isola C4, Centro Direzionale di Napoli, 80143 Napoli, Italy. E-mail: nicola.massarotti@uniparthenope.it

Alessandro Mauro
Department for Technologies (DiT), University of Napoli "Parthenope", Isola C4, Centro Direzionale di Napoli, 80143 Napoli, Italy. E-mail: alessandro.mauro@uniparthenope.it

Alberto Carotenuto
Department for Technologies (DiT), University of Napoli "Parthenope", Isola C4, Centro Direzionale di Napoli, 80143 Napoli, Italy. E-mail: alberto.carotenuto@uniparthenope.it

ABSTRACT

In this work, a stability analysis for the Artificial Compressibility (AC) Characteristic Based Split (CBS) algorithm in the presence of large source terms is carried out for the first time. The AC-CBS scheme was successfully used by the authors to solve both flows through porous media and porous medium-free fluid interface problems. The stability analysis has been performed on the basis of the order of magnitude analysis of the equations terms. The obtained results have been compared to the analytical, experimental and numerical results available in the literature for well-known benchmark problems, showing an excellent agreement. The CPU times have also been compared to the Semi Implicit (SI) version of the CBS algorithm, showing that the new stability condition drastically speeded up the AC-CBS scheme.

Key Words: *CBS, Stability analysis, Source terms, Interface, Matrix-inversion free.*

1. INTRODUCTION

Nowadays, more efficient, accurate and stable algorithms are needed to solve complex engineering problems. In fact, many commercial and proprietary codes can fail in finding the solution of complex thermo fluid dynamic problems mainly because of instability issues, especially in the presence of large source terms. The Artificial Compressibility version of the CBS algorithm [1-3] presents advantages with respect to the Semi-Implicit CBS version. In fact, the AC-CBS is a matrix free-inversion algorithm and, if properly stabilized, can drastically reduce the computational time. Even though the AC-CBS stability has been studied in the case of free fluid forced convection [3], such algorithm still presented poor performances in the presence of large source terms (natural convection problems, presence of porous domains, etc.), reducing significantly the capabilities of the algorithm in solving problems of practical interest. In the present paper the required stability conditions for the AC-CBS in the presence of very large source terms have been studied, by considering two different kind of source terms. The first one is related to the presence of a porous matrix, while the second one is due to buoyancy forces. In particular, the stability conditions have been derived on the basis of the order of magnitude analysis of the different terms constituting the governing equations, allowing to overtake the limitations shown by the AC-CBS in the simulation of problems involving natural convection or in the presence of free fluid-porous medium interfaces.

The stabilized AC-CBS algorithm performances have been tested by simulating well known test cases available in the literature, showing an excellent agreement with the available analytical and experimental results. The results obtained have also been compared to the Semi Implicit (SI) version of the CBS algorithm, showing a drastic reduction of the CPU time.

2. GOVERNING EQUATIONS

Incompressible viscous flow through a partially porous domain can be described by the generalized model, derived by averaging the Navier-Stokes equations over a representative elementary volume, using the well known volume averaging procedure [3, 4]. The governing equations are:

Mass conservation equation

$$\frac{1}{\ ^2}\frac{\partial p}{\partial t}+\frac{\partial u_i}{\partial x_i}=0 \tag{1}$$

Momentum conservation equation

$$\frac{}{\ ^f}\frac{\partial u_i}{\partial t}+\frac{\ ^f}{2}u_j\frac{\partial u_i}{\partial x_j}=-\frac{\partial p_d}{\partial x_i}+\frac{}{\ ^{eff}}\frac{\partial}{\partial x_j}\left(\frac{\partial u_i}{\partial x_j}\right)-\frac{}{\ ^f}u_i-\ _f\frac{F}{\sqrt{}}|\mathbf{u}|u_i+\ _\infty g_i\ _\infty\left(T-T_\infty\right) \tag{2}$$

Energy conservation equation

$$\left[\ \left(\ c_p\right)_f+\left(1-\ \right)\left(\ c_p\right)_s\right]\frac{\partial T}{\partial t}+\left(\ c_p\right)_f u_i\frac{\partial T}{\partial x_i}=\ _{eff}\frac{\partial^2 T}{\partial x_i^2} \tag{3}$$

The generalized model, based on a single domain approach, reduces to the Navier-Stokes equations in the free fluid domain ($\to 1$ and $\to\infty$) while, as the porosity $\to 0$ and $\to 0$, the equations reduce to the Darcy-Forchheimer model. In the presence of buoyancy forces, the well known Bousinnesq approximation has been adopted to derive the momentum conservation equations.

3. STABILITY CONDITION FOR THE SOURCE TERMS

The stability analysis of equations (1)-(3) has been performed on the basis of a order of magnitude approach of the different terms. In particular, once the conservation equations are discretized in time, they can be rewritten as follow:

$$\begin{aligned}
\frac{p^{n+1}}{p^n}&=1-\frac{^2\Delta t}{p^n}\left(\frac{\partial u_i}{\partial x_i}\right)^n\\
\frac{u_i^{n+1}}{u_i^n}&=1-\frac{\Delta t}{u_i^n}\left[-\frac{\partial p}{\partial x_i}+\frac{\ ^f}{2}u_j\frac{\partial u_i}{\partial x_j}-\frac{}{\ ^{eff}}\frac{\partial}{\partial x_j}\left(\frac{\partial u_i}{\partial x_j}\right)\right]^n\\
&\quad-\frac{\Delta t}{u_i^n}\left(\frac{}{\ ^f}u_i+\ _f\frac{F}{\sqrt{}}|\mathbf{u}|u_i\right)^n+\frac{\Delta t}{u_i^n}\left[\ _\infty g_i\ _\infty\left(T-T_\infty\right)\right]^n\\
\frac{T^{n+1}}{T^n}&=1-\frac{\Delta t}{\left[\ \left(\ c_p\right)_f+\left(1-\ \right)\left(\ c_p\right)_s\right]}\left[\left(\ c_p\right)_f u_i\frac{\partial T}{\partial x_i}-\ _{eff}\frac{\partial^2 T}{\partial x_i^2}\right]^n
\end{aligned} \tag{4}$$

The stability conditions have been derived by observing that the order of magnitude of each term in (4) has to be equal to 1. The application of the well known AC-CBS steps [2, 3], not presented here for brevity, leads to the following time-steps limitations, obtained neglecting the up-winding terms:

Stability conditions - Step 1

$$\Delta t_{i,conv}=\frac{h_i}{u_{i,conv}^n};\quad \Delta t_{diff}=\frac{h_i^2}{2\ _{eff}};\quad \Delta t_{i,por}=\frac{1}{P_i^n};\quad \Delta t_{i,b}=\frac{h_i}{\Delta t_{i,\min}^n g_i\ _\infty\left(T_i-T_\infty\right)^n} \tag{5}$$

where $P = \frac{f}{} + \ _f \frac{F}{\sqrt{}} |\mathbf{u}|$. The above time-steps limitations also allow the calculation of the artificial compressibility parameter as $\ _i = u^n_{i,conv} + \frac{h_i}{\Delta t_{i,\min}}$, and the other steps limitations are:

Stability conditions - Step2

$$\Delta t_{i,pr} = \frac{p^n_i h_i}{\ ^2_i u^n_{i,conv}} \tag{6}$$

Stability conditions - Step 3

$$\Delta t_{i,3} = \frac{h}{} \tag{7}$$

The algorithm stability is then achieved by employing, at each node, the minimum time-step value from equations (5)-(7).

4. RESULTS

The performances of the stabilized AC-CBS have been verified by simulating well known benchmark cases, for which numerical and experimental data are available in the literature. The first case studied is the forced convection in a partially porous channel, as available in [5]. The obtained velocity profiles are reported in Figure 2(a), while Figure 2(b) shows the convergence histories and the computational times for both the AC and SI versions of the CBS, showing that the SI-CBS is much more costly than the AC-CBS from the computational time point of view. The second case analysed is the natural convection in a partially porous square cavity. The problem definition and the reference results are available in [6]. Figure 2(a) shows the obtained temperature profiles, while Figure 2(b) reports the complete convergence history and the computational time. From the analysis of Figure 2 it is evident the excellent agreement of the AC-CBS with the experimental results available in [6]. Even though the study cases represent a real challenging test-case, the stabilized AC-CBS algorithm performed excellently, requiring less than 0.5 hours to achieve the convergence, while the SI-CBS required more than 24 hours.

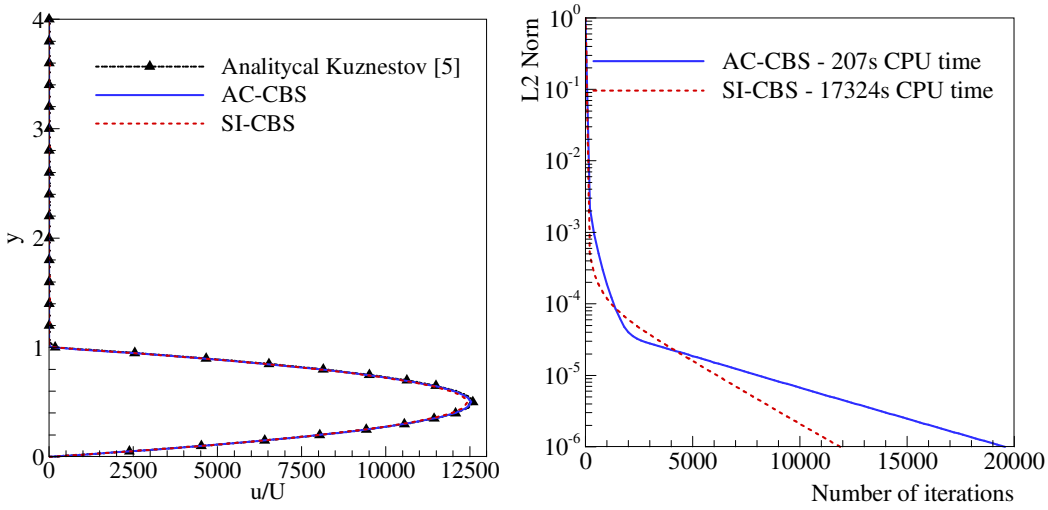

(a) (b)

Figure 1. Forced convention in a channel horizontally divided in free fluid and porous medium for Da=10^{-5}, Re=2 and a mesh of 4941 nodes: (a) velocity profiles; (b) convergence histories and computational times.

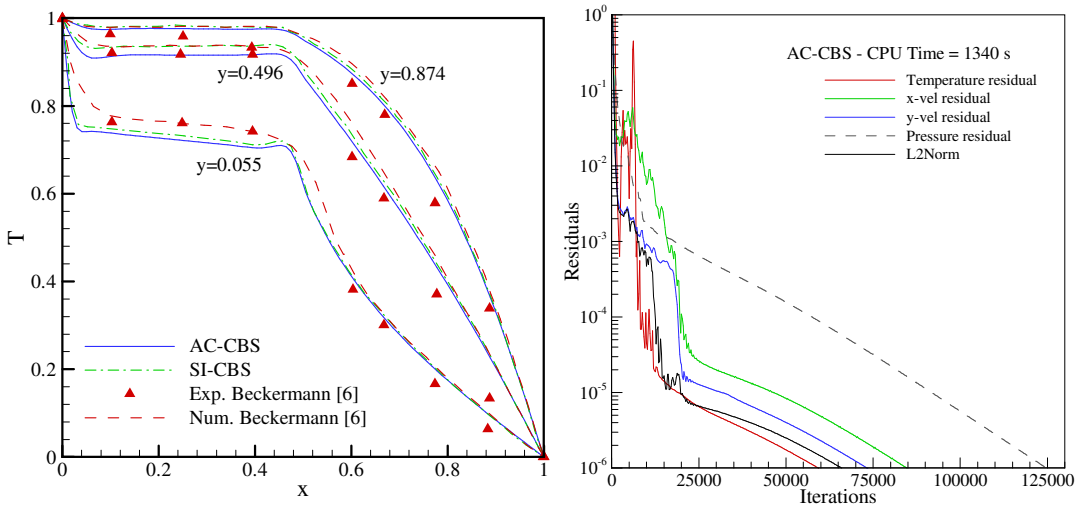

(a) (b)

Figure 2. Natural convection in a partial porous cavity: (a) temperature profiles; (b) convergence histories and computational times. $Ra = 3.028\times10^{7}$, $Da = 7.354\times10^{-7}$, $Pr = 6.97$ and $= 0.36$.

4. CONCLUSIONS

The stability analysis for the AC-CBS algorithm in the presence of large source terms developed by the authors has proved to be very efficient for all the problems considered. The stability conditions speeded up the process enormously. The computational times to achieve the steady state convergence by using the present scheme are firmly smaller than those obtained by using the original SI-CBS, while any destabilization has been observed even in presence of very large source terms.

REFERENCES

[1] N. Massarotti, et al., Explicit and semi-implicit CBS procedures for incompressible viscous flows, International Journal For Numerical Methods In Engineering, 66, 1618-1640, 2006.

[2] F. Arpino, N. Massarotti, A. Mauro and P. Nithiarasu, Artificial Compressibility Based CBS Scheme for the Solution of the Generalized Porous Medium Model. Numerical Heat Transfer, Part B; 55: 196-218, 2009.

[3] P. Nithiarasu, An efficient artificial compressibility (AC) scheme based on split (CBS) method for incompressible flows, International Journal for Numerical Methods in Engineering, 56, 1815-1845, 2003.

[4] N. Massarotti, P. Nithiarasu, and O.C. Zienkiewicz, Natural convection in porous medium-fluid interface problems, International Journal of Numerical Methods for Heat & Fluid Flow, 11 No. 5, 473-490, 2001.

[5] A.V. Kuznetsov, Influence of the stress jump condition at the porous-medium/clear-fluid interface on a flow at a porous wall, Int. Comm. Heat Mass Transfer, 24, No 3, 401-410, 1997.

[6] C. Beckermann, S. Ramadhyani, and R. Viskanta, Natural convection flow and heat transfer between a fluid and a porous layer inside a rectangular enclosure, ASME J. Heat Transfer, 109, 363-370, 1987.

First International Conference on Computational Methods for Thermal Problems
ThermaComp2009, September 8-10, 2009, Napoli, Italy
N.Massarotti and P.Nithiarasu (Eds.)

NATURAL CONVECTION IN CONVERGENT VERTICAL CHANNELS WITH POROUS MEDIA

Bernardo Buonomo
DIAM, Seconda Università degli Studi di Napoli, 81031 Aversa, Italy;
bernardo.buonomo@unina2.it
Oronzio Manca
DIAM, Seconda Università degli Studi di Napoli, 81031 Aversa, Italy; oronzio.manca@unina2.it
Sergio Nardini
DIAM, Seconda Università degli Studi di Napoli, 81031 Aversa, Italy; sergio.nardini@unina2.it
Salvatore Tamburrino
DIAM, Seconda Università degli Studi di Napoli, 81031 Aversa, Italy;
salvatore.tamburrino@unina2.it

ABSTRACT

In this paper natural convection in a vertical convergent channel with or without saturated porous medium is studied numerically at steady state. The investigation is carried out in laminar, two dimensional regime and employing the Brinkman-Forchheimer-extended Darcy model. The physical domain consists of two non-parallel plates which form a convergent channel. Both plates are heated at uniform heat flux. The solutions are achieved using the commercial code FLUENT. A finite-extension computational domain is employed to simulate the free-stream condition. A finite-extension computational domain is employed to simulate the free-stream condition. The results are obtained for different convergence angles, for 0° to 5°, and porosity coefficient (0.4, 0.6 and 0.9), a channel aspect ratio equal to 10, a Rayleigh number equal to 10^4 and a Darcy number equal to 0.01.

Key Words: *Natural Convection, Porous Medium, Vertical Convergent Channel.*

1. INTRODUCTION

Potential authors Convective heat transfer in fluid-saturated porous media has received considerable attention during the past several decades due to its applications in many engineering and geophysical systems [1,2]. These applications include packed bed reactors, porous insulation, beds of fossil fuels, nuclear waste disposal, usage of porous conical bearings in lubrication technology, fibrous insulation systems, grain storage, food processing, energy efficient drying processes, geophysics, and energy related engineering problems.

Multiple technological applications in different industrial equipments and electronic devices require the detailed knowledge of velocity and temperature fields under this particular situation. An interesting problem is that of heat transfer in a convergent channel with two uniformly heated flat plates [3,4]. Numerical investigations can give useful information on the effects of the heat flux, the convergence angle and the spacing. It seems that investigations for steady state conditions in natural convection, in vertical convergent channels with porous medium in the open-ended enclosure, have not received much attention. However, a deep knowledge of natural convection, in these geometries, should be carried out in order to have more information on the thermal and fluid dynamics behaviors of natural convection in vertical convergent channels with porous medium. As far as the present authors' knowledge is concerned, natural convection coupled in a vertical convergent channel open at both ends and filled with isotropic porous medium has not been dealt with. Then, in this paper, reference is made to natural convection in air in a convergent channel with porous media and the two principal flat plates at uniform heat flux. The numerical analysis is accomplished in laminar, two dimensional and steady state regime. The fluid between the two plates is air. The study is carried out employing the Brinkman-Forchheimer-extended Darcy model. The

numerical results are obtained using the commercial code FLUENT, which is based on the finite volume method. A finite-extension computational domain is employed to simulate the free-stream condition and allows to account for the diffusive effects which are peculiar to the elliptic model.

2. DESCRIPTION OF THE MODEL

The physical system and geometry under investigation are shown in Fig. 1a. It consists of two non-parallel plates that form a vertical convergent channel filled with a fluid-saturated porous medium and the fluid is air, Pr=0.71. The porous material is considered as homogeneous and isotropic. Both plates are heated at uniform heat flux. The imbalance between the temperature of the ambient air, T_0, and the temperature of the heated plates draws a mass of fluid into the vertical channel. It is assumed that the transient fluid flow and heat transfer in the channel are two-dimensional, laminar, incompressible. Viscous dissipation, heat generation and pressure work are all assumed to have negligible effect on the velocity and temperature fields and, thus, are neglected. All thermophysical properties of the fluid and the solid matrix of the porous medium are assumed constant except for the variation in density with temperature (Boussinesq approximation) giving rise to the buoyancy forces. The thermophysical properties of the fluid and the solid matrix of the porous medium are evaluated at the ambient temperature, T_0, which is equal to 300 K in all cases. In the porous medium region, the generalized flow model, known as the Brinkman-Forchheimer-extended Darcy model, is used in the governing equations. The permeability coefficient K and inertia coefficient C of porous medium are based on Ergun's experimental investigation [5] and it is expressed in [6].

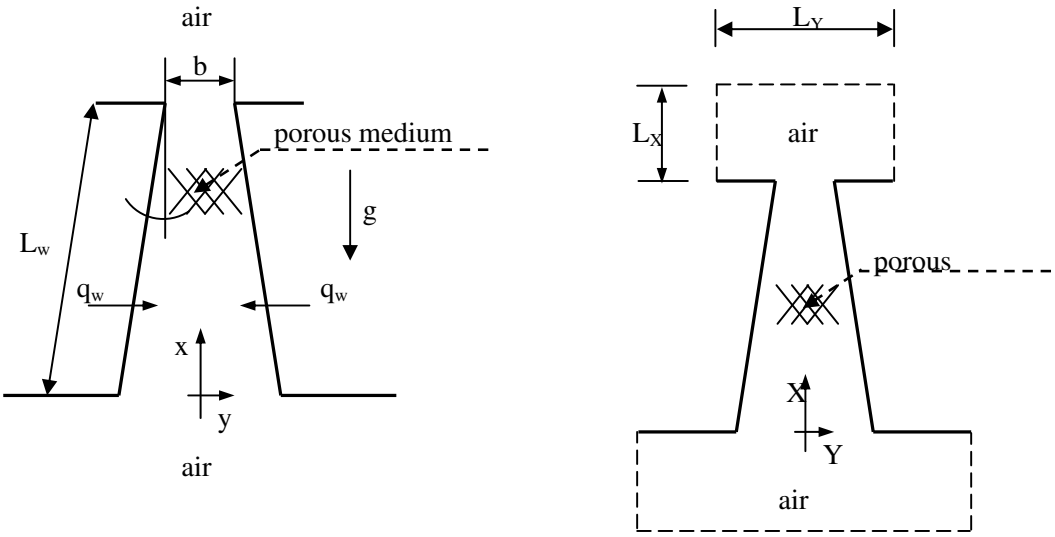

Figure 1. Geometric configuration: (a) physical domain; (b) computational domain.

3. NUMERICAL MODEL

Since the vertical convergent channel is in an infinite medium, from a numerical point of view the problem is solved with reference to a computational domain of finite extent, as shown in Fig. 1b. Following the approach given [7]. A finite-extension computational domain is employed to simulate the free-stream condition and allows to account for the diffusive effects which are peculiar to the elliptic model. The imposed boundary conditions are the following: in the inlet permeable surfaces of the lower reservoir the free stream conditions are considered and the air temperature is assumed equal to the ambient temperature. On the impermeable surfaces, in the lower and upper reservoir, the no slip condition are assumed and these surfaces are adiabatic. At the permeable surfaces of the upper reservoir the free stream conditions are considered whereas the thermal conditions are

adiabatic surfaces, if the fluid is outgoing, or the fluid is at ambient temperature, if the motion is incoming. On the solid wall in the channel no slip conditions and uniform heat flux are assumed. The commercial CFD code Fluent [8] is employed to solve the governing equations. The SIMPLE scheme is chosen to couple pressure and velocity. The model porous medium is active in the porous region. Computation starts with zero values of the velocity components and with pressure and temperature values equal to the ambient ones. The convergence criteria of 10^{-4} for the residual of continuity equation and velocity components and 10^{-8} for the residuals of energy are assumed. A grid dependence test is accomplished to realize the most convenient grid size by monitoring the average Nusselt number, for $Ra=10^4$, an aspect ratio equal to 10 and for a case without porous medium and with porous medium (Da=0.01 and =0.6).

4. RESULTS

The results are presented for aspect ratio equal to 5 and 10 and Rayleigh number, Ra, ranging from 10^2 to 10^6 and ranging from 0° to 5°. The porous material in the convergent channel has a value of Da=0.01 and the cases with porosity coefficient =0.4, 0.6 and 0.9 are considered and compared with the channel without porous medium (no porous case). The fluid is air and the solid matrix has a thermal conductivity 10 times the one of the air. Temperature and stream function fields for an aspect ratio equal to 10, $Ra=10^4$ and =0°, 2° and 5°, are reported in Figs. 2 and 3, respectively.

The fields are given for no porous and =0.9 cases. Temperature fields show that, for the case without porous medium inside the channel, in Figs. 2a-2c, in the central region of the channel the air temperature is equal to the ambient one and this zone increases increasing the convergence angle, according with [4]. This indicates that the flow in the channel is developing. In the upper region external to the channel, two thermal plumes are present and a slight oscillation appears in this zone. In presence of porous medium inside the channel, in Figs. 2d-2f, the flow seems developed and the isotherms have a parabolic size inside the channel. In the upper reservoir a single plume is detected and the oscillations are more evident. This unsteady condition in the upper reservoir does not have effect on flow inside the channel.

The stream function in the channel shows that the flow has a parallel motion for = 0°, in Fig. 3a. For ≥ 2°, in Fig. 3b and 3c, the flow presents the stream lines sparse in the inlet region and thick in the outlet region. In the upper reservoir the flow is slightly squeezed. In the cases with porous medium in the channel the trend is very similar to the previous but it has lower values of mass flow rate and the stream lines are more sparse. In the upper reservoir the plume is very thinner than the previous case.

REFERENCES

[1] K. Vafai, *Handbook of Porous Media*, vol. II, Marcel Dekker, New York, 2005.

[2] D.A. Nield, A. Bejan, *Convection in Porous Media*, third ed., Springer, New York, 2006.

[3] A. Bejan, A. K. da Silva, S. Lorente, Maximal heat transfer density in vertical morphing channels with natural convection, *Numerical Heat Transfer Part A*, 45, 135-152, 2004.

[4] N. Bianco, L. Langellotto, O. Manca, V. Naso, Numerical analysis of radiative effects on natural convection in vertical convergent and symmetrically heated channels, *Numerical Heat Transfer Part A*, 49, 369-391, 2006.

[5] S. Ergun, Fluid flow through packed columns, *Chemical Engineering Proceedings*, 48, 89-94, 1952.

[6] K. Vafai, Convective flow and heat transfer in variable porosity media, *Journal of Fluid Mechanics*, 147, 233-259, 1984.

[7] A. Andreozzi, O. Manca, Thermal and Fluid Dynamic Behaviour of Symmetrically Heated Vertical Channels with Auxiliary Plate, *International Journal for Heat and Fluid Flow*, 22, 424–432, 2001.

[8] Fluent Inc., *Fluent 6.3, User Manual*, Fluent, Inc., Lebanon, NH, 2006.

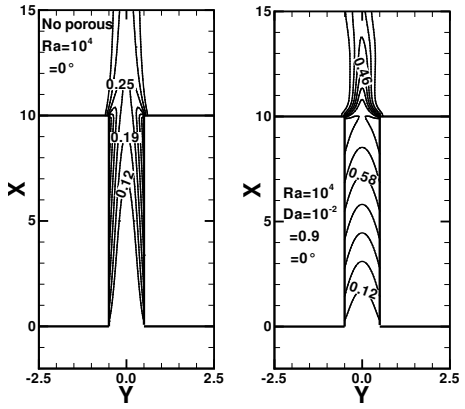

(a) (d)

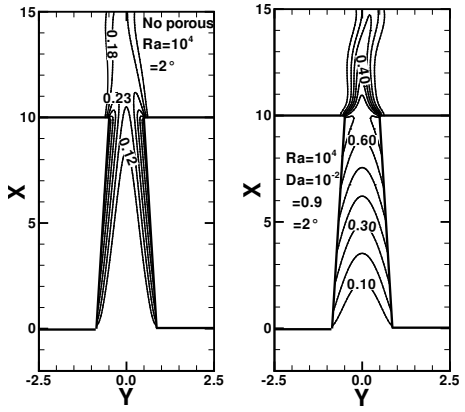

(b) (e)

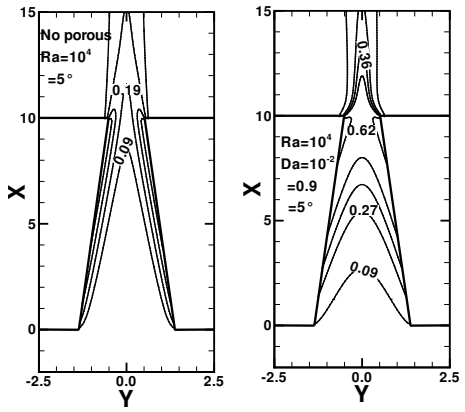

(c) (f)

Figure 2. Temperature fields for $Ra=10^4$, $Da = 10^{-2}$: (a)(d) =0°, (b)(e) =2°, (c)(f) =5°.

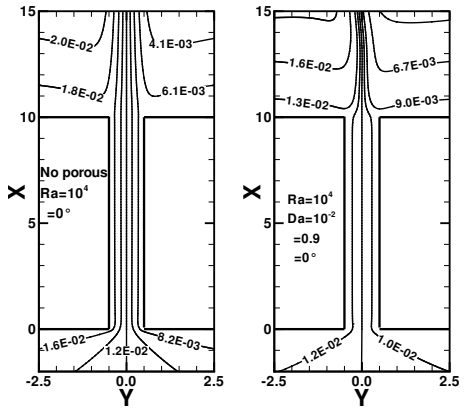

(a) (d)

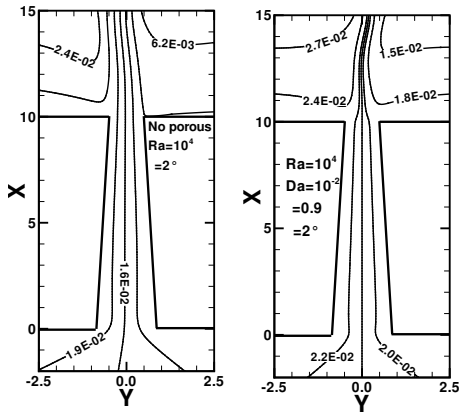

(b) (e)

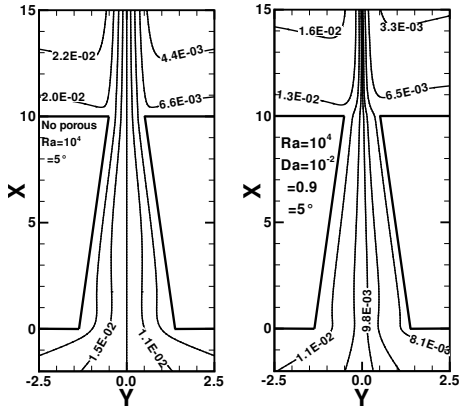

(c) (e)

Figure 3. Stream function fields for $Ra=10^4$, $Da=10^{-2}$: (a)(d) =0°, (b)(e) =2°, (c)(f) =5°.

First International Conference on Computational Methods for Thermal Problems
ThermaComp2009, September 8-10, 2009, Naples, Italy
N.Massarotti and P.Nithiarasu (Eds.)

Darcy Mixed Convection in a Fluid Saturated Square Porous Enclosure under Multiple Suction Effect

B. V. Rathish Kumar
Department of Mathematics and Statistics, Indian Institute of Technology, Kanpur -208016, India,
bvrk@iitk.ac.in

S. V. S. S. N. V. G. K. Murthy
Department of Mathematics and Statistics, Indian Institute of Technology, Kanpur-208016, India,
sgkmurthy@gmail.com,skmurthy@iitk.ac.in,

Vivek Sangwan
Department of Mathematics and Statistics, Indian Institute of Technology, Kanpur-208016, India,
sangwan.vivek@gmail.com

Mohit Nigam
Department of Mathematics and Statistics, Indian Institute of Technology, Kanpur-208016, India,
mohitsun@iitk.ac.in

Peeyush Chandra
Department of Mathematics and Statistics, Indian Institute of Technology, Kanpur-208016, India,
peeyush@iitk.ac.in

ABSTRACT

In this study volume averaged equations governing the steady mixed convection flow in a vertical square enclosure filled with a Darcian fluid saturated homogeneous porous medium is investigated numerically by Galerkin Finite Element Method. The forced flow conditions are imposed by providing multiple inlet windows at the bottom wall and multiple outlet windows with suction on the top wall. The free convection is induced by introducing a hot but isothermal temperature on the left vertical wall together with Boussinesq approximation on density. Detailed numerical simulations are carried out for a wide range of governing parameters such as Rayleigh Number (Ra), suction/injection velocity (a), suction/injection width (D/H), as fraction of the length of the square enclosure.

Key Words: *Mixed convection, Suction/Injection, Porous medium, Finite Element Method.*

1. INTRODUCTION

In many of the engineering applications such as solar central receivers exposed to wind currents, electronic devices cooled by fans, heat exchangers, vented enclosures filled with micro spheres, which require a detailed study on mixed convection process the spatial location of inlet / outlet windows become very vital [1-3]. In this study we continue our numerical investigation on Darcy mixed convection in a vertical porous enclosure with multiple fluid injections at the bottom wall and fluid multiple suctions at the top wall. Detailed numerical simulations are carried out by Galerkin finite element method for a wide range of parameters such as Rayleigh number (Ra), Suction / injection flow speed (a), and suction/injection width(D / H). Flow and temperature distribution is analyzed by tracing Streamlines, Isotherms, local / cumulative heat fluxes.

So far not much work has been reported on Darcy mixed convection in a vertical square porous enclosure. In particular mixed convection in vertical porous enclosure under simultaneous multiple Suction / Injection effects on opposite walls, which becomes very relevant in the context of electronic devices, environmental chamber for bacterial culture preservation etc., have not been considered so far.

2. MAIN BODY

We consider a two dimensional enclosure filled with a fluid saturated porous medium with the left vertical wall at the constant temperature 'T_w, right wall at ambient temperature and the other two horizontal walls are adiabatic, excluding the inlet/outlet portions at the top / bottom wall. The forced flow conditions are imposed by providing inlets at the bottom of the wall and outlets with suction at the top of the wall for out flow. It is assumed that 'D' is the width of the inlet and outlet, 'H' is the height of the Cavity. The inflow is considered to be at ambient temperature. The porous medium is assumed to be isotropic with permeability 'K' and Boussinesq approximation is valid in the momentum equation for the density term. Under the above mentioned assumptions, non-dimensional equations [1-3] governing the flow, heat and mass transport in a fluid saturated porous media can be written as follows.

$$\frac{\partial^2 \Psi}{\partial X^2} + \frac{\partial^2 \Psi}{\partial Y^2} = \frac{\partial \theta}{\partial X}$$

$$\frac{\partial \Psi}{\partial Y}\frac{\partial \theta}{\partial X} - \frac{\partial \Psi}{\partial X}\frac{\partial \theta}{\partial Y} = \frac{1}{Ra}\left(\frac{\partial^2 \theta}{\partial X^2} + \frac{\partial^2 \theta}{\partial Y^2}\right)$$

The appropriate boundary conditions in non-dimensional form are:

Left wall : $\Psi = 0, \theta = 1 \quad on \quad X = 0, \ 0 \leq Y \leq 1$

Right wall : $\Psi = 0, \theta = 0, \quad on \quad X = 1, \ 0 \leq Y \leq 1$

Permeable Bottom Wall :

$$\frac{\partial \Psi}{\partial Y} = 0, \quad \frac{\partial \theta}{\partial Y} = 0 \quad on \quad Y = 0, \quad 0 \leq X \leq X_1 \ and \ X_1 + (D/H) \leq X \leq X_2, X_2 + (D/H) \leq X \leq 1$$

Permeable Top Wall :

$$\frac{\partial \Psi}{\partial Y} = 0, \quad \frac{\partial \theta}{\partial Y} = 0 \quad on \quad Y = 1, \quad 0 \leq X \leq X_3 \ and \ X_3 + (D/H) \leq X \leq X_4, X_4 + (D/H) \leq X \leq 1$$

Inlet at Bottom wall : $\Psi = -aX_i, \ \theta = 0 \quad on \quad Y = 0, \quad X_i \leq X \leq X_i + (D/H) \quad for$ i=1,2

Outlet at Top wall : $\Psi = -aX_i, \ \frac{\partial \theta}{\partial Y} = 0 \quad on \quad Y = 1, \quad X_i \leq X \leq X_i + (D/H) \quad for$ i=3,4

3. RESULTS

The above non-dimensional governing equations with boundary conditions have been solved using Galerkin Finite Element method. To begin with code has been validated by comparing the results for Darcian case with reported in literature. To ensure grid independency of the results grid selection test has been carried out on four different mesh systems consisting of 20×20, 30×30, 40×40, 50×50 elements. It is observed that as one moves from 40×40 grid system to 50×50 grid system there is only a marginal variation (less than 1%) in 'Nu' values. Hence 40×40 grid system has been chosen for extensive numerical simulations for various values of the parameters. In Figure 1 Cumulative heat fluxes (CHFLXs) along the left vertical wall are plotted for Ra=100, (D/H)=0.1 and $0 \leq a \leq 0.5$. Global Nusselt number (Nu_g) decreases when 'a' increases. In all cases there is a steep raise in CHFLXs along the lower half of the left vertical wall. Further along the left vertical wall the increase in CHFLXs gradually fall with increasing suction/injection velocity thereby effectively leading Nu_g to decrease with increasing Suction/Injection (S/I) velocity. The flow and temperature fields are analyzed by tracing the streamlines and isotherms. Streamlines depict a complex flow pattern encompassing a dominant primary circulation with a clockwise rotation and semi-circular flows centered around S/I windows.

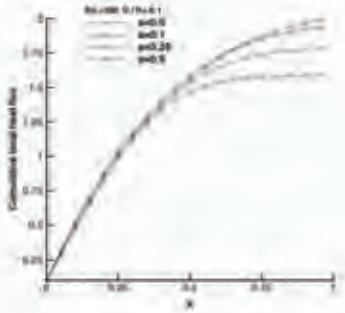

FIGURE 1. Cumulative heat fluxes for Ra=100, (D / H)=0.1 and $0 \leq a \leq 0.5$

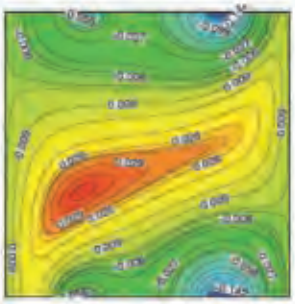

FIGURE 2. Streamlines for the case Ra=100, (D/H)=0.1 and a=0.5

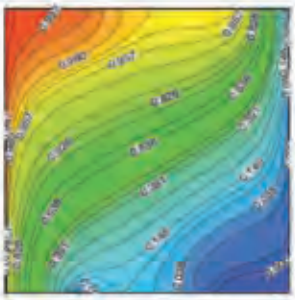

FIGURE 3. Isotherms for the case Ra=100, (D/H)=0.1 and a=0.5

Increasing S/I velocities lead to narrowing of a primary circulation zone with increasing horizontal stretch and to the merger of the two separated semi-circular patterns located adjacent to each other on the horizontal walls. Streamlines for the case Ra=100, (D/H)=0.1 and a=0.5 are shown in Figure 2. Isotherm pattern corresponding these set of parameters are shown in Figure 3. From this plot can notice the presence of thermal boundary layer(TBL) along the left vertical wall. Clearly the sharp TBL gets blunt as one moves from the bottom of the left vertical wall to the top. Detailed numerical simulations are also carried out w.r.t other parameters. Nusselt numbers increase with increasing 'Ra' and increasing S/I window slit size.

4. CONCLUSIONS

Both the flow and temperature fields are highly sensitive to magnitude of S/I velocity, S/I window slit size and 'Ra'. While heat fluxes along the isothermal left vertical wall decrease with increasing S/I velocities they are formed to increase with increasing '(D/H)' and 'Ra'. Multi cellular circulation pattern and TBLs are seen to manifest in flow and temperature fields respectively.

REFERENCES

[1] B. V. Rathish Kumar, S. V. S. S. N. V. G. Krishna Murthy, Vivek Sangwan, Mohit Nigam, Peeyush Chandra, Non-Darcy Mixed Convection in a Fluid Saturated Square Porous Enclosure Under Suction Effect Part-I, *(To appear in Journal of Porous Media-2009)*,

[2] B. V. Rathish Kumar, S. V. S. S. N. V. G. Krishna Murthy, Vivek Sangwan, Mohit Nigam, Peeyush Chandra, Non-Darcy Mixed Convection in a Fluid Saturated Square Porous Enclosure Under Suction Effect Part-II, *(To appear in Journal of Porous Media-2009)*,

[3] Shohel Mahmud and Ioan Pop, Mixed Convection in Square Vented Enclosure Filled with a Porous Medium, *International Journal of Heat and Mass Tranfer*, 49, 2190-06, 2006.

First International Conference on Computational Methods for Thermal Problems
ThermaComp2009, September 8-10, 2009, Napoli, Italy
N.Massarotti and P.Nithiarasu (Eds.)

A GEOTHERMAL DOWNHOLE HEAT EXCHANGER MODEL BASED ON AN EQUIVALENT POROUS MEDIUM APPROACH

Fausto Arpino
Dipartimento di Meccanica, Strutture, Ambiente e Territorio, Università di Cassino, Via G. Di Biasio 43, 03043 Cassino (Fr), Italy. E-mail: f.arpino@unicas.it

Alberto Carotenuto, Alessandro Mauro, Nicola Massarotti
Dipartimento per le Tecnologie, Università di Napoli "Parthenope", Isola C4, Centro Direzionale di Napoli, 80143 Napoli, Italy. E-mail: alberto.carotenuto@uniparthenope.it, alessandro.mauro@uniparthenope.it, massarotti@uniparthenope.it

ABSTRACT

The paper presents a numerical procedure for the simulation of heat and fluid flow in a low enthalpy geothermal energy system, using a generalised model for porous media flow and an equivalent porous medium approach for macroscopic description of the heat exchanger. The results obtained are validated against the experimental data available for a geothermal reservoir in the island of Ischia in Italy, which were available from previous work of one of the authors. The comparison shows that the proposed procedure can be successfully used for the simulation of this type of problems.

Key Words: *Geothermal energy, Porous media, interface problems.*

1. INTRODUCTION

The use of geothermal heat pumps may substantially increase the economical potential of geothermal energy, extending its use to countries that have not exploited this source so far, due to the lack of high enthalpy geothermal reservoirs. Still, in countries where the geothermal energy is already employed, the use of downhole heat exchangers for exploitation of low enthalpy geothermal reservoirs solves the problem of re-introducing the geothermal fluid into the reservoir, as requested by environmental and legislative restrictions. However, the heat withdrawn from the aquifer with this type of devices can be limited due to the interaction between the exchanger and the well. In fact, the circulation of the geothermal fluid in the porous matrix, which represents the aquifer, is necessary in order to withdraw heat from the aquifer.

Downhole heat exchangers have been studied extensively, both numerically and experimentally, in the last ten years, but still many aspects of the above mentioned interaction between aquifer and well as not completely clear [1], [2], [3]. In most of the modelling work available, the Darcy law is employed to describe porous medium flow, which complicates the mathematical coupling between the aquifer and the well. Therefore, some assumptions and simplifications have to be made, in order to obtain a numerical solution. At the same time, experimental data on the behaviour of the aquifer are very difficult and expensive to retrieve. In the end it is very difficult to validate the results obtained with simplified models.

It is therefore desirable to develop a simulation procedure that reduces the number of simplifications and assumptions that are needed, and uses boundary conditions and results that can be measured experimentally. In particular, such a complete simulation of the well, the aquifer and the heat exchanger as a whole system does not appear to be available. This type of analysis would

allow to understand some of the limitations in the use of downhole heat exchanger, and to more efficiently design the whole system.

In this work, a generalized model [4] is used to describe the macroscopic heat and fluid flow through porous medium. Such model allows the use of a single domain approach for the calculation of velocity and temperature in both the aquifer and the well. Furthermore, the same approach can be used to describe the flow through the downhole heat exchanger, if this is simulated as a porous medium with a uniform negative heat generation. This type of approach can better approximate the actual operating conditions of the entire system.

The finite volume method has been used to recover the numerical solution for the model developed. The results obtained show that the proposed procedure can be successfully used for the solution of the phenomena that occur in the well.

2. THE PROBLEM

An intensive experimental campaign was carried out by one of the authors of this work in order to test a new prototype of a geothermal convector, and to study its performance in an aquifer on the Island of Ischia in Southern Italy [1], [2]. The prototype was made of three main components: the condenser, the evaporator (geothermal convector) with a convection promoter, and an adiabatic connection between the two. A sketch of the actual plant and the computational domain with boundary conditions are given in Figure 1. The temperature of the well was monitored using five T-type thermocouples installed between the convection promoter and the tube casing of the well (Figure 1). Furthermore, during the experiments the heat transfer rate withdrawn from the aquifer was monitored together with the temperature in the well.

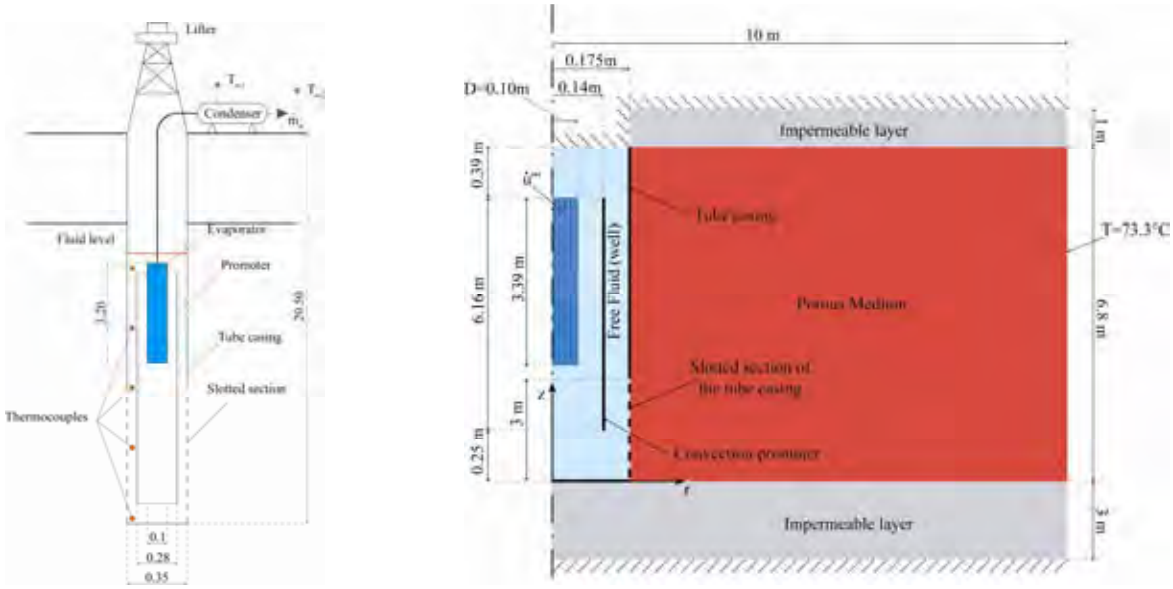

Figure 1: Geothermal plant on the Island of Ischia in Southern Italy (left), and computational domain used in the simulation (right).

The aquifer on Ischia was found at a depth of about 12 meters and had an unperturbed temperature of 73.3°C. The characteristics of the aquifer were determined on the basis of a number of tests that were performed on site and in laboratory [1].

The geometry considered is part of the geothermal well, whose dimensions are based on the actual well situated on the island of Ischia in Italy (Figure 1).

The heat exchanger, which is made of a system of 94 pipes with an external diameter of 16mm and a length of 2.8m [1], in the present work, is modelled as cylindrical porous medium from which a constant heat is withdrawn [4], [5], assuming a uniformly distributed negative heat source, $\dot{u}'''$ (W/m3). The equivalent porous cylinder has a radius of 10 centimetres and is about 3.4 meters tall, which corresponds to the actual encumbrance of the exchanger. The properties of the porous medium have been calculated on the basis of the relations available in literature [5] and on the basis of the heat exchanger's design [1].

The problem can be considered axis-symmetric with respect to the well axis, as the fluid-dynamic and thermal boundary conditions considered are symmetrical to the axis of the well, as described later in this section. The well has a diameter of 35 cm and the geothermal fluid depth is about 6.8 meters from the bottom of the well.

The extension of the aquifer domain was chosen on the basis of the results obtained in previous work [1], [2] , where it was shown that the disturbance due to the presence of the well does not penetrate into the well for more than 9 meters. Therefore, the domain considered has a radius of 10 meters, while the total height of the aquifer considered is of about 7 meters, and it is placed between two impermeable layers. The hight of these layers was chosen based on the same considerations made for the aquifer. After a mesh sensitivity analysis, the two-dimensional mesh used is constituted of 248764 nodes and 544310 elements. The mesh is refined near the heat exchanger and in the well region, where the highest gradients are expected.

3. RESULTS

The solution of the problem was obtained for different values of the total heat withdrawn from the well and considering the properties of the medium for which experimental results were available [1]. In particular, the permeability of the aquifer is considered to be 3×10^{-3} m/s and its effective conductivity is varied between the estimated minimum and maximum values, $1.5< {}_e<2.5$ W/(mK). Table 1 presents the main quantities used in the simulations. The properties of the geothermal fluid are considered to be constant, and are assumed to be those of water at the mean temperature of the well.

Table 1: Main parameter values used in the simulations.

Aquifer		*Geothermal fluid*		*Heat exchanger*	
	0.31	$_f$ [kg/m^3]	975.5 kg/m^3		0.36
$k_{e,a}$ [m/s]	3×10^{-3}	c_f [kJ/kg]	4190	$k_{e,HE}$ [m/s]	1.22
$_{e,a}$ [W/(m·K)]	1.5 and 2.5	$_f$ [kg/(m·s)]	3.91×10^{-4}	$\dot{Q}$ [kW]	10, 14 and 24
$T_{aquifer}$ [°C]	73.3	$_f$ [W/(m·K)]	0.668		

The results obtained are presented in terms of temperature profiles. Figure 2 presents a comparison of the calculated and measured temperatures along the annulus between the tube case and the convection promoter (see Figure 1), for transient and steady state. The plot shows a good comparison of the results obtained with those measured experimentally. However, it is noticed that the steady state solution was not fully reached during the experiments. In fact, the transient profile presented in Figure 2 is obtained 32 hours later the initial time, when the aquifer and the well were considered to be unperturbed (T=73.3°C as initial condition).

The results obtained at the steady state also show that the effect of the effective thermal conductivity of the well temperature does only affect the lower part of the well, where the temperature of the geothermal fluid is increased of less than 2 °C in the whole range of k_e considered.

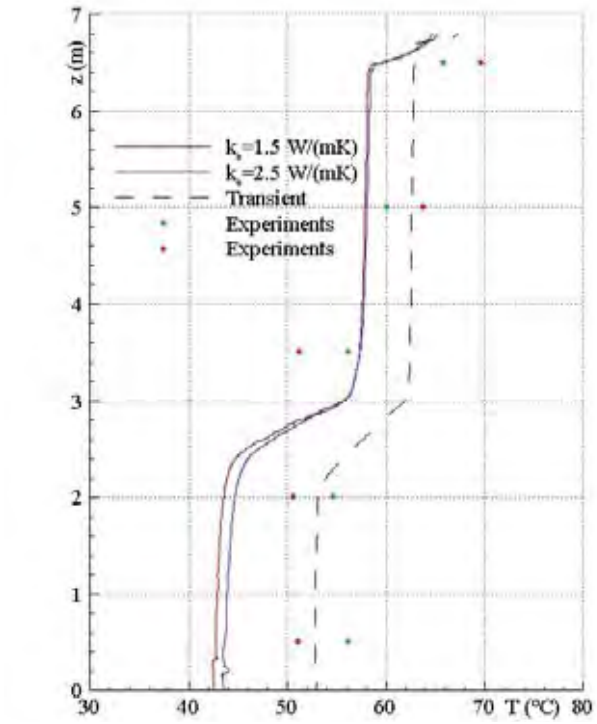

Figure 2: Comparison of calculated and measured temperatures in the well.

4. CONCLUSIONS

This paper presents a numerical procedure for the simulation of a downhole heat exchanger for the exploitation of low enthalpy geothermal reservoirs. Using a generalised model for the description of porous medium heat and fluid flows, the proposed procedure allows to calculate the velocity and temperature distribution in the well, the aquifer and the heat exchanger, without having to subdivide these domains and use non physical boundary conditions for each sub-domain. The results were validated against experimental data that had been obtained on a plant in southern Italy, and showed that the procedure can be successfully used in the prediction of the complex phenomena that occur in the interaction between the well and the aquifer. The procedure is used to verify some results that were previously obtained with more approximate models, and to gain a better understanding of the problem studied.

REFERENCES

[1] Carotenuto, A., Casarosa, C. and Martorano, L., 1999, The geothermal convector: experimental and numerical results, Applied Thermal Eng., 19, 349-374.

[2] Carotenuto, A., Casarosa, C. and Vanoli, L., 2001, Optimizing the position of the tube casing slotted section for geothermal wells with a downhole heat exchanger, Geothermics, 30, 133-157.

[3] Lund, J.W., 2003, The use of downhole heat exchangers, Geothermics, 32, 535-543.

[4] Massarotti, N., Nithiarasu, P. and Carotenuto, A., 2003, Microscopic and macroscopic approach for natural convection in enclosures filled with fluid saturated porous medium, Int. J. Num. Meth. Heat Fluid Flow, 13, 862-886.

[5] Nakayama, A. and Kuwahara, F., 2000, Numerical modeling using microscopic structures, Handbook of Porous Media, Vafai, K. (Ed.), Chapter 10, Marcel Dekker, New York.

PARALLEL SESSIONS

First International Conference on Computational Methods for Thermal Problems
ThermaComp2009, September 8-10, 2009, Napoli, Italy
N.Massarotti and P.Nithiarasu (Eds.)

APPLICATION OF IMPLICIT TVD SCHEME TO SIMULATION OF SEPARATED HYPERSONIC BOUNDARY LAYER STABILITY

Andrey V. Novikov
TsAGI, 140180, Zhukovsky, Russia; AndrewNovikov@yandex.ru

Ivan V. Egorov
TsAGI, 140180, Zhukovsky, Russia; ivan_egorov@tsagi.ru

Alexander V. Fedorov
Moscow Institute of Physics and Technology (MIPT), 140180, Zhukovsky, Russia; fedorov@falt.ru

ABSTRACT

An in-house code is applied to direct numerical simulation (DNS) of unsteady two-dimensional (2D) flow fields relevant to stability of the separated hypersonic boundary layer. An implicit second-order finite-volume TVD technique is used for solving the compressible Navier–Stokes equations. Numerical simulations of artificially excited disturbances propagating over a flat plate, compression corner and grooved plate are performed at the freestream Mach numbers 5–6. Calculations illustrate high robustness of the method, which allows for simulation of nonlinear dynamics of disturbance fields in flows with essential spatial irregularities. DNS predicts stabilization on high-frequency disturbances in separation bubbles.

1. INTRODUCTION

It is well known that laminar-turbulent transition leads to substantial increase of the aerodynamic drag and surface heating. The ability to predict the transition locus is of critical importance in design and optimization of aerospace planes. One of challenging problems here is instability of flows in separation bubbles formed over deflecting flaps or surfaces with metallic thermal protection panels bowed due to temperature gradients caused by aerodynamic heating [1] (for example, the windward surface of the X-33 flight test vehicle). The initial phase of transition is associated with amplification of unstable disturbances. For hypersonic flow and configurations considered herein these are the first and/or second boundary-layer modes. The wall cooling, which naturally occurs on hypersonic vehicle surfaces, strongly stabilizes the first mode while destabilizes the second mode. This indicates that it is important to simulate the second-mode instability. Since the most unstable second-mode waves are two-dimensional (2D), we perform 2D simulation and do not address 3D disturbances.

Numerical simulations of flow stability are often carried out using high-order shock-fitting schemes (for example weighted essentially non-oscillatory (WENO) scheme) or using the compressible nonlinear parabolised stability equations (NPSE) solvers with the mean flow predicted by DNS. Nevertheless low-order shock-capturing schemes are preferable for practical configurations. Their robustness is due to relatively high dissipation, which, however, may damp physically unstable disturbances. We attempt to develop a method, which could blend these opposite tendencies. The method is based on the total variation diminishing (TVD) finite volume second-order scheme adapted for non-uniform meshes associated with DNS on bodies of engineering interest.

In this paper we demonstrate that the developed method allows for simulation of unstable processes in the boundary layer despite its dissipative features. We discuss DNS results relevant to instability of 2D hypersonic flow with local separations. The Navier-Stokes equations are solved numerically for disturbances generated by a local forcing (periodic suction-blowing) for the freestream Mach number range 5-6 in the near-wall flow over a flat plate, compression corner and plate with wavy

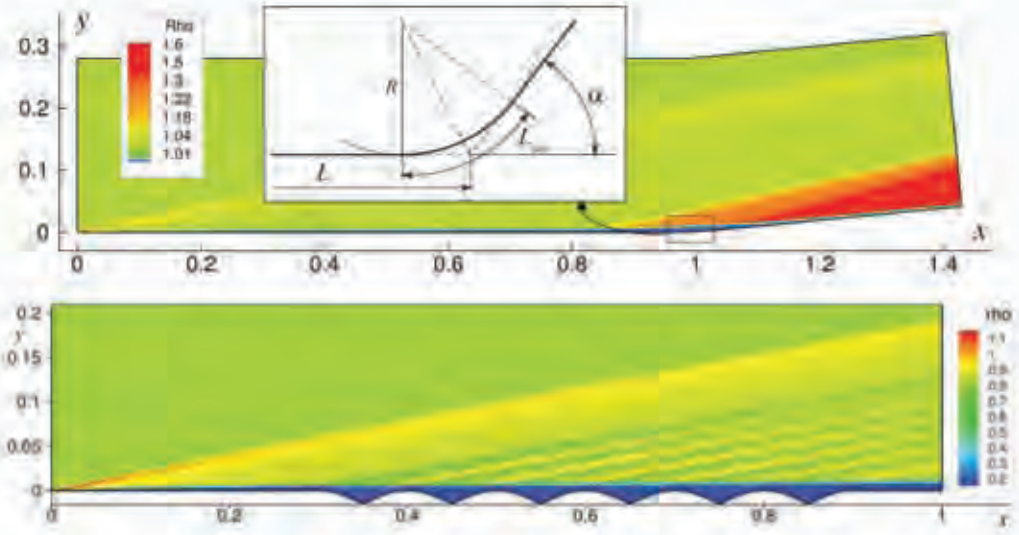

FIGURE 1. Density fields of steady flows and computation domain

surface. For a flat plate configuration, we compare numerical solutions with the linear stability theory (LST) to validate the method.

2. PROBLEM FORMULATION AND NUMERICAL METHOD

Herein we consider a standart dimensionless form of 2D Navier–Stokes equations, see for example [2]. The dependent variables are normalized in a standart way to the corresponding free-stream parameters. Computations of flow fields over a wavy plate were carried out at $M_\infty = 6$, $Re_\infty = 2\times10^6$ and over a compression corner at $M_\infty = 5.373$, $Re_\infty = 5.667\times10^6$. The viscosity-temperature dependence is approximated by the Sutherland's formula $\mu = T^{3/2}\left(T_\mu^* + 1\right)/\left(T_\mu^* + T\right)$, $T_\mu^* = 110\,\mathrm{K}$. The fluid is a perfect gas with the specific heat ratio $\gamma = 1.4$ and Prandtl number $Pr = 0.72$.

Numerical solutions are obtained using an implicit finite-volume method with the second-order approximation in space (13-points stencil) and time. A quasi-monotonic Godunov-type scheme (TVD scheme) is used with van Leer limiter. This gives a system of nonlinear algebraic equations, which is solved with the help of the modified Newton-Raphson iteration method. The Jacobi matrix is formed using the finite differences approach with a truncated stencil of 5 points. Usage of this stencil essentially reduces the computational time and memory despite some slowing of the convergence process. At every iteration step the corresponding linear system is solved using the iterative general minimum residual method *GMRes(k)* and *ILU*-decomposition as a preconditioner, where the iteration process is sufficiently stable (compared with the direct method). More details on the numerical method can be found in [2].

Computations are carried out for flows over compression corners of fixed angle $\alpha = 5.5°$ and different roundings (Figure 1 top) and over a grooved wavy wall with 6 cavities of the depth $H = 0.015$ (Figure 1 bottom), which approximately equals to the doubled boundary-layer thickness (2δ) at the station $x = 0.5$ located on the flat plate region.

The boundary conditions are: no-slip conditions on the lower boundary of computational domain ($u = v = 0$), the free-stream conditions on the left (inflow) and upper boundaries ($u = 1$, $v = 0$, $p = 1/\gamma M_\infty^2$, $T = 1$), and a linear extrapolation of dependent variables u, v, p, and T on the right

(outflow) boundary. The surface is adiabatic, $\partial T_w/\partial n = 0$, for the steady-state solution. In the unsteady problem, the wall temperature equals the adiabatic-wall temperature of steady solution, $T_w(x, t) = T_{aw}(x)$; i.e., the unsteady temperature disturbance is zero on the wall.

Computations are performed on a curved orthogonal grid with 2501 × 241 nodes. The grid is generated using numerical conformal mapping of a rectangle onto the computational domain [3]. This method gives a grid with high level of orthogonality. It is clustered near the surface, so that 55% of nodes are within the boundary layer and the separation region including the mixing layer.

The problem was solved in two steps. First, a steady laminar flow field was computed using a time-dependent method. Then, unsteady disturbances were imposed onto the steady solution – a local periodic suction-blowing was introduced on the wall via the boundary condition for the mass-flow perturbation $q_w(x,t) = \dfrac{\rho_w^* v_w^*}{\rho_\infty^* U_\infty^*} = \varepsilon \sin\left(2\pi \dfrac{x - x_1}{x_2 - x_1}\right) \sin(\omega t),\ x_1 \le x \le x_2$, where $x_1 = 0.0358$ and $x_2 = 0.0521$ are boundaries of the suction-blowing region. The majority of calculations were conducted at the dimensionless frequency $\omega = \omega^* L^* / U_\infty^* = 220$ for the wavy plate and $\omega = 450$ for the compression corner. To ensure linear evolution of disturbances before separation and, hence, to perform comparisons with LST, we chose a small forcing amplitude $\varepsilon = 10^{-3}$. The computation is continued until a time-periodic disturbance field sets in (this occurs at $t \sim 1.25$).

3. RESULTS

Flat plate. At first disturbance evolution is computed for a flat plate. At the actuator frequency $\omega \approx 220$ (for $\mathrm{Re}_\infty = 2\times10^6$) the second-mode instability waves are excited inside the computation domain and attains their maximum amplitudes near the outflow boundary. The second mode is typified by the structure shown on Figure 2: two-cells in the pressure field and rope-like formations in the temperature field. The x-location of growth curve agrees with that predicted by LST [4]. Comparison of the disturbance profiles at different x-stations (Figure 3) also shows good agreement. This allows us to conclude that the numerical method can be used for direct simulation of the boundary-layer instability.

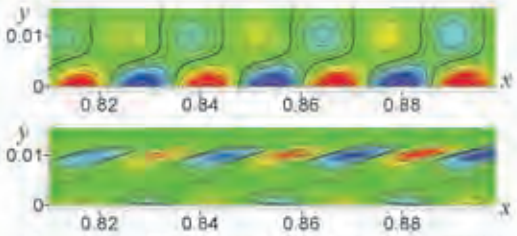

FIGURE 2. Pressure (top) and temperature (bottom) disturbances fields near the flat wall in the range of maximum growth rate

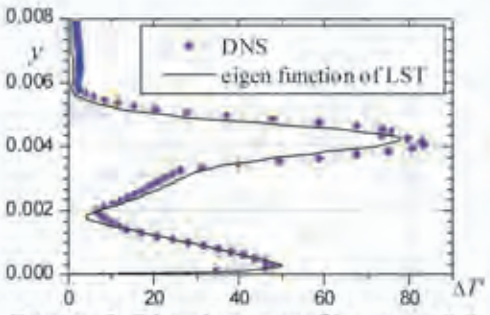

FIGURE 3. Disturbance profiles at $x = 0.8$

Compression corner. In the region $0.85 < x < 1.1$, disturbances on the wall damp sharply, while on the plate the second-mode disturbances have maximum amplitudes (Figure 4). Thus the separation bubble stabilizes oscillations of the frequency $\omega = 450$ induced by actuator. However, analysis of disturbance fields for different corner roundings shows that inside a long separation zone a waveguide is formed and acoustic waves of appreciable amplitudes are excited via a resonance mechanism that could be described using the WKB method.

These acoustic waves effectively generate the boundary layer disturbances which grow downstream the reattachment point.

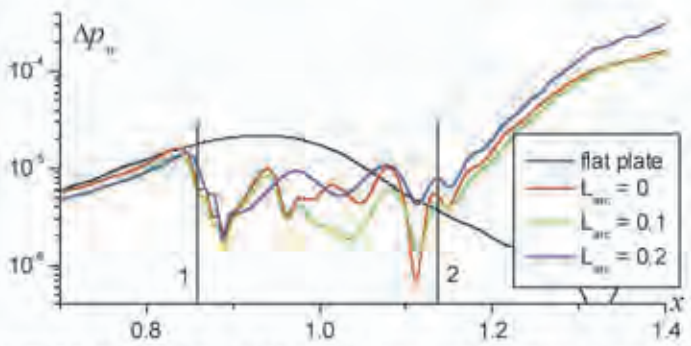

FIGURE 4. Envelope of the wall-pressure disturbances on the corner for $\omega = 450$. 1, 2 – separation and reattachment points

Wavy wall. On the wavy wall, the disturbance growth rate is lower then in the flat plate case. Thus the mixing layer, which bridges several cavities, stabilizes the boundary-layer waves of the considered frequency $\omega = 220$. Furthermore there is no strong growth of the disturbances downstream the wavy region like in the case of the aforementioned compression corner. It seems that this is because the separation bubbles within the cavities are short, that prevents from resonant excitation of acoustic disturbances. The boundary-layer reattachments on the bumps are smooth and relatively short that also prevents from the intensive second-mode growth in these regions.

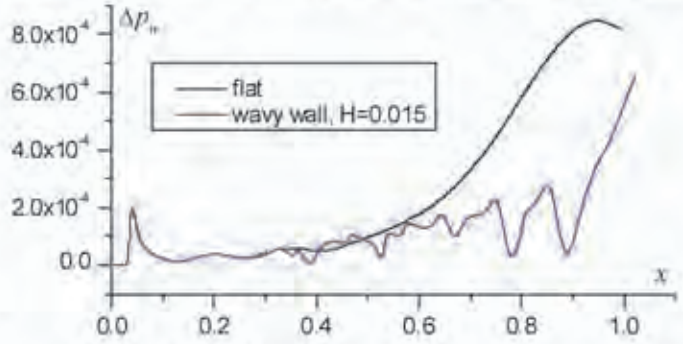

FIGURE 5. Envelope of the wall-pressure disturbances on wavy walls for $\omega = 220$

4. CONCLUSIONS

Numerical method based on the second-order TVD space discretization coupled with the second-order implicit temporal advance method were used for DNS of unstable disturbances in hypersonic separated boundary layer over a compression corner and wavy surface at free-stream Mach numbers 5–6. It was shown that the numerical method allows for simulation of unstable processes in near-wall flows. DNS disturbance fields helped us to apply a waveguide theory to disturbance dynamics inside relatively long separation bubbles. DNS predicts stabilization on high-frequency disturbances over the grooved plate. This prediction will be verified by the ongoing wind-tunnel experiments.

This work is supported by Russian Foundation for Basic Research (Project 09-08-00472).

REFERENCES

[1] Kontinos, D.A. & Palmer, G. Numerical Simulation of Metallic Thermal Protection System Panel Bowing, Journal of spacecraft and rockets, 36(6), 1999.

[2] Egorov, I.V., Fedorov, A.V., Soudakov, V.G. Direct numerical simulation of disturbances generated by periodic suction-blowing in a hypersonic boundary layer, *Theoret. Comput. Fluid Dynamics*, 20(1), 41-54, 2006

[3] Driscoll, T.A. & Vavasis, S.A. Numerical Conformal Mapping Using Cross-Ratios and Delaunay Triangulation, *SIAM J. Sci. Comput*, 19(6), 1783-1803, 1998.

[4] Fedorov, A.V. and Khokhlov, A.P. Prehistory of instability in a hypersonic boundary layer, *Theoret. Comput. Fluid Dynamics*, 14(6), 359-375, 2001.

First International Conference on Computational Methods for Thermal Problems
ThermaComp2009, September 8-10, 2009, Naples, Italy
N.Massarotti and P.Nithiarasu (Eds.)

A MULTILEVEL LAGRANGIAN CONSERVATIVE SCHEME

Valerio Grazioso
University of Naples 'Federico II' - DETEC, Dipartimento di Energetica Termofluidodinamica applicata e Condizionamenti ambientali, P.le Tecchio 80 - 80125 Naples, valerio.grazioso@unina.it

Nicola Massarotti
University of Naples 'Parthenope' - Dipartimento per le Tecnologie, Centro Direzionale - Is. C4 - 80143 Naples, massarotti@uniparthenope.it

Carlo Meola
University of Naples 'Federico II' - DETEC, Dipartimento di Energetica Termofluidodinamica applicata e Condizionamenti ambientali, P.le Tecchio 80 - 80125 Naples, cmeola@unina.it

Carlo Scalo
Queens University - Department of Mechanical and Materials Engineering, 130 Stuart Street, Kingston, Ontario, scalo@appsci.queensu.ca

ABSTRACT

In this paper we present the Multilevel Lagrangian Conservative Scheme (MLCS) for the convective fluxes numerical evaluation. It is based on a lagrangian approximate solution with a control of spurious oscillations by means of suitable reconstruction technique and a subsequent gaussian high order time integration for the evaluation of the numerical fluxes. A scalar, vectorial and multidimensional analysis is presented.

Key Words: *Accurate and wiggling reduced fluxes, non linear convection, Burgers, Euler and Navier-Stokes equations* .

1. INTRODUCTION

Convection schemes are of great importance in the design of computational fluid dynamics codes. Due to the difficulties of the analysis for the multidimensional system, it is a common practice to test advection schemes and their properties in 1D. In last four decades -after Godunov's theorem- the attempts to conjugate high order with further properties, like the stability and/or entropic ones, have been directed to less ambitious goals (e.g. monotonic, TVD, TVB, Muscl, ENO, WENO, etc.), but more robust for the multidimensional extension. The early Von Neumann idea of using conservative schemes and adding a proper amount of artificial viscosity still holds even if such numerical diffusion effects are introduced in a not explicit and not stationary way. Flux and slope limiters as well as solution adapted reconstruction are the main ingredients of most popular codes. Here we combine a lagrangian prediction (based on a solution adapted reconstruction) for the set up of low and high order Richtmyer-Lax-Wendroff fluxes obtaining a new scheme, successfully checked for both 1D scalar case and 3D Navier-Stokes equations.

2. PRINCIPLES OF LAGRANGIAN CONSERVATIVE APPROACH

Let us refer to the 1D scalar case of the conservation equation and its usual single step discretized form:

$$\frac{\partial u}{\partial t} + \frac{\partial f(u)}{\partial x} = 0 \tag{1}$$

$$\bar{u}_i^{n+1} = \bar{u}_i^n - \lambda[\tilde{f}_{i+1/2} - \tilde{f}_{i-1/2}] \tag{2}$$

where $f(u)$ is any smooth function of u, $\bar{u}$ is a space average of u, $\tilde{f}$ is a time average of $f(u)$ (numerical flux), $\tau \in [0, \Delta t^n]$ and λ is the ratio of the time and space interval measures. The Multilevel Lagrangian Conservative Scheme (MLCS) furnishes an estimate of the numerical fluxes based on a combination of low order and high order numerical fluxes, as usual in the practice of limiters. See for instance [1], [2]. Its innovative contribution relies upon the high order part F_h:

$$\tilde{F}_h\left(x_{i-1/2}, t^n\right) \approx \frac{1}{\Delta t} \int_{t^n}^{t^{n+1}} f\left[u_L\left(x_{i-1/2}, \tau\right)\right] d\tau \tag{3}$$

where $u_L\left(x_{i-1/2}, \tau\right)$ is a suitably accurate and robust prevision of the exact solution that we call *Lagrangian Approximate Solution* (LAS) and the time integral is evaluated by means of Gauss numerical integration so that u_L is required only on the gaussian (time level) nodes.
In order to clarify the last point let us firstly consider the scalar case and the Burgers' equation for which $f(u) = \frac{u^2}{2}$, $f_u = u$, $f_{uu} = 1$. In this case the exact solution $u\left(x_{i-1/2}, t^n + \tau\right)$ - briefly $u_e(\tau)$- is available in an implicit form, i.e.:

$$u_e(\tau) = u\left(x_{i-1/2} - \tau\, u_e(\tau), t^n\right) \triangleq u^n\left(x_{i-1/2} - \tau\, u_e(\tau)\right). \tag{4}$$

Unluckily the explicit form for $u_e(\tau)$, even for the Burgers' case, may require the solution of a nonlinear equation as a consequence of the (general) nonlinear dependence of $u(x, t^n)$ upon x, and such a solution can result to be multi-valued. However, it is possible to derive a family of explicit approximations, i.e. the above mentioned LAS, by substituting the $u_e(\tau)$ in the right hand side of (4) with some truncated Taylor time-expansion $u_T(\tau)$:

$$u_L(\tau) = u^n\left(x_{i-1/2} - \tau\, u_T(\tau)\right) \tag{5}$$

where

$$u_T(\tau) = (u^n)_{x_{i-1/2}} - \tau\left(u^n \frac{\partial u^n}{\partial x}\right)_{x_{i-1/2}} + \frac{\tau^2}{2!}\left(2u^n\left(\frac{\partial u^n}{\partial x}\right)^2 + (u^n)^2 \frac{\partial^2 u^n}{\partial x^2}\right)_{x_{i-1/2}} + \dots \tag{6}$$

Obviously the coefficient expression of $\tau^3, \tau^4, \dots, \tau^k$ becomes increasingly complex and could be determined with a symbolic computational approach. However it is important to note here that $u^n(x)$, because of the space discretization, is not exactly and/or continuously known and the order of the u_T truncation is constrained by the reconstruction order of u^n.
For the non scalar case of conservation laws, as the fluidynamic models, the extension of (3) to vectorial quantities $\mathbf{u}$ and related fluxes $\mathbf{f}(\mathbf{u})$ is not directly written because, in general, does not exist an easy vectorial extension of the exact solution, even in the implicit form (4). In fact the gasdynamic conservation model that includes the energy balance instead of the the entropy conservation does not admit Riemann Invariants that could allow a (very complex, implicit) expression of the exact solution. Therefore for compressible flows the finding of a suitable expression of an approximated and/or *exact* solution $\mathbf{u}$ that has to be substituted in the right hand side of the possible vectorial extension of equation (3) has been object of the last fifty years of research in the CFD community. The first attempt that produced the Lax-Wendroff families of schemes (Richtmyer, Lapidus, etc.) were based on the tenso-vectorial form of the Taylor expansion (6). At the same time and later on *local exact solution* (mainly Riemann Problem solutions and/or k-wave solutions) were introduced either after suitable cell reconstruction of $\mathbf{u}^n$ (Godunov, Osher, Van Leer, etc.) either by adopting a frozen (constant) evaluation of the jacobian matrix $\mathcal{A} = \frac{\partial \mathbf{f}}{\partial \mathbf{u}}$ (Roe, Beam-Warming, etc.). The extension of (3) and its related research to the 3D case is extremely complex and some problems as ensuring the physical relevance of the numerical solutions is still an open question as it is the existence, the uniqueness or multiplicity of such solutions [3].
Here we consider only slightly compressible flows so that it is numerically convenient to consider, instead of a thermodynamic pressure, a p scalar field having the role of a Lagrangian multiplier that constrains the density flow divergence to have a prescribed value (i.e. $\frac{\partial \rho}{\partial t}$). Therefore we will here consider only vector balances for the vector $\mathbf{u} = \left[\rho v, \rho v^2\right]$ in 1D or its 2-3D extensions $\mathbf{u} = \left[\rho \mathbf{v}, \rho |\mathbf{v}|^2\right]$ (i.e. momentum and kinetic energy) end the related purely convective fluxes (i.e. pressure free). Moreover such flux reduction corresponds to the so called *advection upstream splitting of momentum* (AUSM) widely adopted in multidimensional compressible flow simulation [4]. As a consequence we have that the matrix $\mathcal{A}$ in 1D case has already a diagonal (scalar) structure (i.e. $u_2/u_1\, \mathbf{I}$) as well as in 3D case

the correspondent flux Jacobians $\mathcal{A}_1, \mathcal{A}_2, \mathcal{A}_3$ still result to be simply $v_1\,\mathbf{I}, v_2\,\mathbf{I}, v_3\,\mathbf{I}$. Such a choice for the matrices $\mathcal{A}_i$ explains our definition of LAS for the $\mathbf{u}_L$. Moreover the kinetic energy (i.e. velocity quadratic norm $|\mathbf{v}|^2$) may not require a real computation if one adopts suitable conservative schemes for the balances of ρ and $\rho\mathbf{v}$, as earlier demonstrated by Arakawa and others [5]. As conclusive result of the presented remarks and assumptions the extension of equation (3) to the to the 3D case for the general pressure free momentum numerical fluxes $\mathbf{f} = \rho\mathbf{v}\mathbf{v}$ has the following LAS form:

$$\int_{t^n}^{t^{n+1}} \left(\int_{S_k} \mathbf{f}_k \left[\mathbf{u}_L \left(\mathbf{P}\left(S_k\right), \tau \right) \right] dS_k \right) d\tau \approx \sum_i w_i \mu\left(S_k\right) \bar{\mathbf{f}}_k \left[\mathbf{v}\left(\mathbf{P}\left(S_k\right) - \mathbf{s}_i, t^n\right), \rho\left(\mathbf{P}\left(S_k\right) - \mathbf{s}_i, t^n\right) \right] \quad (7)$$

where $\mathbf{s}_i = \tau_i \mathbf{v}\left(\mathbf{P}\left(S_k\right), t^n\right)$ is an estimate of the Lagrangian displacement in the time fraction τ_i, w_i are the gaussian time integration coefficients, S_k is the boundary surface of the control volume normal to the k^{th} direction, $\mu\left(S_k\right)$ is the S_k measure and the overbar on $\mathbf{f}$ indicates the S_k average. It can be clarifying for the understanding of equation (7) to read in it a variant of the early Richtmyer's version of two step Lax-Wendroff scheme with the meaningful differences of either the multipoint Gaussian time integration, either the substitution of Lax-Friedrich prevision at $\Delta t/2$ with the Lagrangian prevision on the Gaussian time points. Last but not least, further improvements and advantages for the presented schemes comes from the use in the multidimensional case of recent fast interpolative procedures. Observe in fact that functions $\mathbf{v}\left(\cdot, t^n\right), \rho\left(\cdot, t^n\right)$ have to be continuously reconstructed i.e. the required values for (7) need an interpolation of the available grid values. Such a reconstruction when practiced by means of high order polynomials and/or splines may produce strong wiggles and uncontrolled TV. In the present proposal the high order reconstructions are obtained by subgrid piecewise constant reconstruction that mimic the continuos high order ones. In such a way one get a fine control of the artificial viscosity and the associated stability effect. For sake of clearness in the following we will describe in full details the implementation of Multilevel Lagrangian Conservative Scheme and the classical Burgers test case while some results of its application to multidimensional Navier-Stokes equations can be found in [6].

3. IMPLEMENTATION AND RESULTS FOR BURGERS TEST CASE

The numerical solution of Burgers equation is a popular and simple test case on which most of the different class of schemes for non linear PDE have been applied. Here the initial condition adopted is a rectangular window function, and the discretization structure of time evolution given in (2) is:

$$\bar{u}_i^{n+1} = \bar{u}_i^n - \frac{\Delta t}{\Delta x}\left[\widetilde{\left(\frac{u^2}{2}\right)}_{i+1/2} - \widetilde{\left(\frac{u^2}{2}\right)}_{i-1/2} \right]. \quad (8)$$

Adopting the Richtmyer Two-Step Lax-Wendroff method the time averaged fluxes, for instance on $x_{i-1/2}$, are obtained by evaluating $\widetilde{\left(\frac{u^2}{2}\right)}_{i-1/2}$ as $\frac{1}{2}\left(u_{LF}\right)^2_{i-1/2}$ where u_{LF} is the Lax-Friedrich prevision of $u_{i-1/2}$ at time $t^n + \frac{\Delta t}{2}$ - i.e. $\left(u_{LF}\right)^{n+\frac{1}{2}}_{i-1/2} = \frac{1}{2}\left(u^n_{i-1} + u^n_i\right) - \frac{\lambda}{2}\left[f(u^n_i) - f(u^n_{i-1})\right]$. In order to reduce the strong TV increase of the Richtmyer scheme, and to get an improved time and space accuracy, the present scheme introduces the following modifications:

- the single prevision at time $t^n + \frac{\Delta t}{2}$ is substituted with at least two intermediate time points previsions. For the two-points Gaussian integration $\alpha_1 \Delta t$ and $\alpha_2 \Delta t$, time fractions are: $\alpha_1 = \frac{3-\sqrt{3}}{6}$ and $\alpha_2 = \frac{3+\sqrt{3}}{6}$
- the u previsions themselves are not the Lax-Friedrich's ones but are based, after a subgrid discretization of a space continuous high order reconstruction of $u\left(\cdot, t^n\right)$, on a Lagrangian estimation of the space coordinates points from which such values are assumed to come from unchanged.

In practice the first step consists of interpolating with a given order the nodal values of the velocity u from the first grid (*grid 1*) to a second grid (*grid 2*) which is derived from *grid 1* by refining the mesh

with additional $nsbgr-1$ cells or $nsbgr$ cell centers in between two cell centers of *mesh 1*. Therefore the values of u_- and u_+ at the α_1 and α_2 points used for computing the time averaged Burgers' numerical fluxes as $\frac{u_1^2+u_2^2}{4}$ are calculated as follows:

$$u_{\mp} = u^n \left(x_{i-1/2} - \frac{3 \mp \sqrt{3}}{6} \, \Delta t \, u^*_{i-1/2} \right) \quad \text{with} \quad u^*_{i-1/2} = \frac{1}{2} \left(u_{i-1} + u_i \right).$$

Observe that the $u_{\mp}$, after that the high order interpolation has been done from *grid 1* to *grid 2*, are easily obtained with a *nearest value* interpolation, in order to provide a controlled amount of artificial viscosity while substantially preserving the main part of high-order spatial variation.

Here the Multilevel Lagrangian Conservative Schemes (MLCS) scheme is compared with the Richtmyer two-step Lax-Wendroff method and then is controlled with a superbee limiter

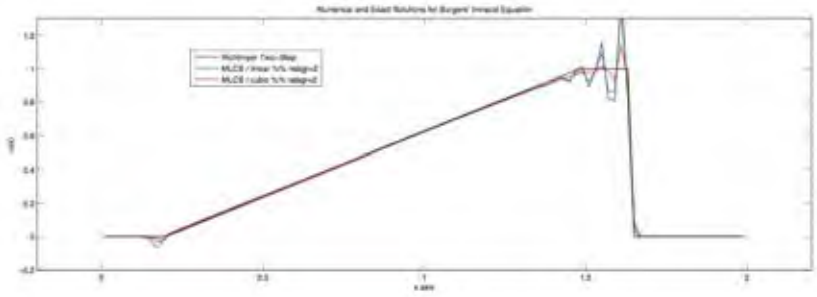

FIG 1. Multilevel Lagrangian Conservative scheme with 2 sub-grid points vs. Lax-Richtmyer

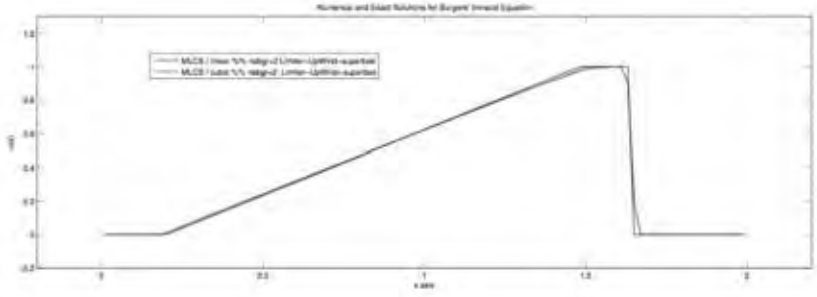

FIG 2. MLCS with 2 sub-grid points and SuperBee limiter.

REFERENCES

[1] F. Grasso and C. Meola , *Euler and Navier-Stokes equation for compressible flows: finite volume methods - chapter 4 of: Handbook of Computational Fluid Mechanics*, edited by R. Peyret, Academic Press, 2000.

[2] R.J. Leveque, *Finite Volume Methods for Hyperbolic Problems*, Cambridge University Press, 2002.

[3] A. Majda, *Compressible fluid flow and systems of conservation laws in several space variables*, Springer-Verlag, 1984.

[4] M.S. Liou, C. Steffen, *A New Flux Splitting Scheme*, J Comput Phys, J Comput Phys, 107, 23-39, 1993.

[5] Y. Morinishi, T.S. Lund, O.V. Vasilyev, P. Moin *Fully conservative higher order finite difference schemes for incompressible flow*, J Comput Phys, 143, 90-124, 1998.

[6] G. de Felice, V.Grazioso, C. Meola and C. Scalo, *High level languages implementation and analysis of 3D N.S. solvers - ThermaComp2009*, Submitted abstract.

First International Conference on Computational Methods for Thermal Problems
ThermaComp2009, September 8-10, 2009, Napoli, Italy
N.Massarotti and P.Nithiarasu (Eds.)

NUMERICAL STUDY OF INSTABILITY OF HIGH-SPEED BOUNDARY LAYERS USING WENO AND TVD SCHEMES

V.G. Soudakov
TsAGI, 140180, Zhukovsky, Russia, vit_soudakov@mail.ru

I.V. Egorov
TsAGI, 140180, Zhukovsky, Russia, ivan_egorov@falt.ru

ABSTRACT

A numerical algorithm and code are developed and applied to direct numerical simulation (DNS) of unsteady two-dimensional flow fields relevant to receptivity and stability of the high-speed boundary layer. An implicit second-order finite-volume technique is used for solving the Navier–Stokes equations. Numerical simulation of unsteady disturbances in the boundary layer on a flat plate is performed at free-stream Mach number equal to 6. It is shown that numerical method using TVD and WENO scheme allows for simulation of unstable processes.

Key Words: *DNS, Receptivity, Stability, Boundary Layer, WENO, TVD.*

1. INTRODUCTION

Prediction of laminar-turbulent transition is important for aerothermal design and drag calculations of high-speed vehicles. In “quiet” free streams, transition on aerodynamically smooth surfaces includes receptivity, linear phase and nonlinear breakdown to turbulence. This explains high interest in DNS of different phases of hypersonic transition during the last two decades.

Zhong et al. [1] conducted a series of numerical simulations related to receptivity and stability of hypersonic flow over a flat plate. These studies were carried out using a high-order shock-fitting scheme. DNS of transition of supersonic boundary layer at Mach 3 was performed in [2] using high-order finite difference scheme. However, these schemes are not applicable to a small region near the leading edge, which may play an important role in receptivity to free-stream disturbances. Balakumar *et al.* [3] numerically investigated stability of hypersonic boundary layer over a compression corner using high-order weighted essentially non-oscillatory (WENO) shock-capturing scheme. Egorov *et al.* [4, 5] carried out a series of numerical investigations of receptivity and stability of hypersonic boundary layer over flat plate at Mach 6 using second order TVD (Total Variation Diminishing) scheme.

Shock-capturing schemes are preferable for practical configurations. However, their robustness is due to relatively high dissipation, which may damp physically unstable disturbances. In this paper we compare methods based on TVD and WENO spatial discretization applied to the problem of receptivity and stability of hypersonic boundary layer.

2. PROBLEM FORMULATION

Viscous two-dimensional unsteady compressible flows are governed by the Navier-Stokes equations. The fluid is a perfect gas with the specific heat ratio $\gamma = 1.4$ and Prandtl number $\mathrm{Pr} = 0.72$. The viscosity-temperature dependence is approximated by the power law $\mu^* / \mu_\infty^* = \left(T^* / T_\infty^* \right)^{0.7}$. Calculations are carried out for supersonic flow over a flat plate with sharp leading edge at the free-stream Mach number $M_\infty = 6$ and the Reynolds number

$\mathrm{Re}_\infty = \rho_\infty^* U_\infty^* L^* / \mu_\infty^* = 2\times10^6$. Hereafter ρ_∞^* is free-stream density, U_∞^* is free-stream velocity, L^* is plate length, asterisks denote dimensional variables. Flow variables are made nondimensional using steady-state free-stream parameters and plate length L^*.

The computational domain is a rectangle with its bottom side corresponding to the plate surface. The no-slip boundary conditions are imposed on the plate surface. The wall temperature corresponds to the adiabatic condition for the steady-state solution. Details on the problem formulation and governing equations are given in [4]. The problem is solved in two steps. Firstly, the steady-state solution is calculated to provide the mean flow field. This flow field is presented in [4]. Then, unsteady disturbances are induced on boundaries of computational domain at the initial time moment and the unsteady problem is integrated.

For modelling of receptivity to small disturbances, a plain monochromatic wave is imposed on the free stream given by $\left(u', v', p', T'\right)_\infty^T = \left(|u'|, |v'|, |p'|, |T'|\right)_\infty^T \exp\left[i\left(k_x x + k_y y - \omega t\right)\right]$, where $|u'|, |v'|, |p'|, |T'|$ are non-dimensional perturbation amplitudes. For slow acoustic wave with zero angle of incidence we have:

$$|p'| = \varepsilon, \quad |T'| = (\gamma - 1) M_\infty^2 |p'|, \quad |u'| = M_\infty |p'|, \quad |v'| = 0, \; k_\infty = \omega M_\infty / (M_\infty - 1).$$

Here ε is amplitude of incident wave; $k_x = k_\infty$, $k_y = 0$ are wavenumber components; $\omega = \omega^* L^* / U_\infty^*$ is circular frequency. Here we consider waves of small amplitude $\varepsilon = 5\times10^{-5}$ at which the receptivity process is linear. The disturbance frequency is $\omega = 260$ at which the maximum disturbance amplitude in the boundary layer is observed at the station $x \approx 0.9$ and associated with the second mode wave. The temperature disturbance is zero on the plate surface, $T'|_{y=0} = 0$.

3. NUMERICAL METHOD

The problem is solved numerically using a conservative finite-volume method [4]. For calculations of steady-state solution providing the mean flow field, the implicit scheme is more preferable. Calculations of unsteady disturbances, in which the time step is very small to provide sufficient accuracy in simulating unstable waves, require less computational time than does the steady-state problem because the steady solution should be obtained with very low numerical residual in the case of small disturbances. Therefore, the implicit numerical scheme is used for both steady and unsteady problems.

A second-order Godunov-type scheme with the Roe approximate Riemann solver are used for the inviscid part of the intercell flux. A piece-wise linear reconstruction with a TVD limiter is used to represent the components of the conserved vector at the boundary of a cell:

$$\mathbf{Q}_L = \mathbf{Q}_j + \frac{1}{2} m\left(\mathbf{Q}_j - \mathbf{Q}_{j-1}, \mathbf{Q}_{j+1} - \mathbf{Q}_j\right), \; \mathbf{Q}_R = \mathbf{Q}_{j+1} - \frac{1}{2} m\left(\mathbf{Q}_{j+1} - \mathbf{Q}_j, \mathbf{Q}_{j+2} - \mathbf{Q}_{j+1}\right)$$

where *m(a, b)* is the van Leer limiter function. Second-order central-difference approximations are used for the viscous part of the intercell flux.

The use of a second-order implicit time descritization results in a system of nonlinear equations, which is solved using the modified Newton–Raphson method. The Jacobian matrix of the system is evaluated using a truncated stencil with three points in each direction. During the iteration process, a solution of the linear algebraic system is obtained with the help of the iteration general minimum residual method GMRES(k) and ILU-decomposition as a preconditioner. More details on the numerical method can be found in [4].

The TVD scheme allows for modelling of the disturbance dynamics in the leading-edge vicinity. Nevertheless, this computational scheme damps physical waves, especially near the peaks and valleys. Another type of numerical schemes which do not have this disadvantage is WENO schemes

[6]. In our work, third-order WENO scheme is used where the interpolation of the dependent variables on the boundary of an elementary cell is:

$$Q_R = \omega_{0R} Q_{0R} + \omega_{1R} Q_{1R}\,,\ \omega_{0R} = \alpha_{0R} \big/ \left(\alpha_{0R} + \alpha_{1R}\right),\ \ \omega_{1R} = \alpha_{1R} \big/ \left(\alpha_{0R} + \alpha_{1R}\right)$$

$$\alpha_{0R} = \frac{d_0}{\left(\varepsilon + \beta_{0R}\right)^2};\qquad \alpha_{1R} = \frac{d_1}{\left(\varepsilon + \beta_{1R}\right)^2},\ d_0 = \frac{2}{3};\ \ d_1 = \frac{1}{3},\ \varepsilon = 10^{-6}$$

$$\beta_{0R} = \left(Q_j - Q_{j+1}\right)^2;\qquad \beta_{1R} = \left(Q_{j+1} - Q_{j+2}\right)^2,\ Q_{0R} = \frac{1}{2}\left(Q_{j+1} + Q_j\right);\qquad Q_{1R} = -\frac{1}{2} Q_{j+2} + \frac{3}{2} Q_{j+1}$$

The value of Q_L is derived from symmetry.

In our calculations the computational grid has 2001×301 nodes. In the boundary-layer region, the grid nodes are clustered in the direction normal to the body surface.

4. RESULTS

The pressure disturbance field, defined as the difference between an instantaneous flow field and the mean flow field, induced by the acoustic wave is shown in figure 1. The shock wave weakly disturbs the acoustic field pattern. Major distortions are observed in the near-wall region and associated with the interaction of acoustic disturbances with the boundary layer. Pressure disturbances in free stream are presented in figure 2 for $0.8 \le x \le 0.9$. The figure shows the comparison of TVD and WENO3 results with the theory near the upper boundary of computational domain, where grid stretching is used. Wall pressure disturbances are shown in figure 3 ($0 \le x \le 1$ – left figure, $0.8 \le x \le 0.9$ – right figure). One can see that the difference in amplitude between TVD and WENO3 scheme is small in the boundary layer and large enough in free stream. Moreover, TVD scheme shows larger phase error.

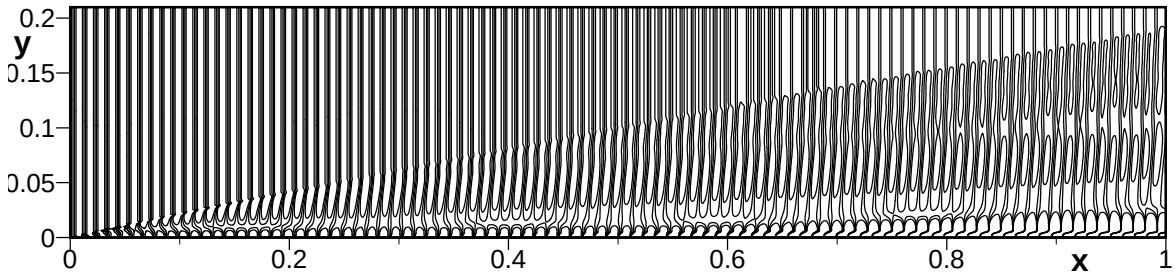

FIGURE 1. Pressure disturbance field induced by acoustic wave

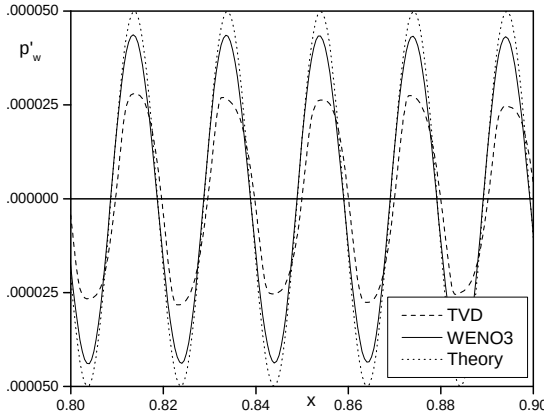

FIGURE 2. Free-stream pressure disturbance obtained with TVD and WENO3

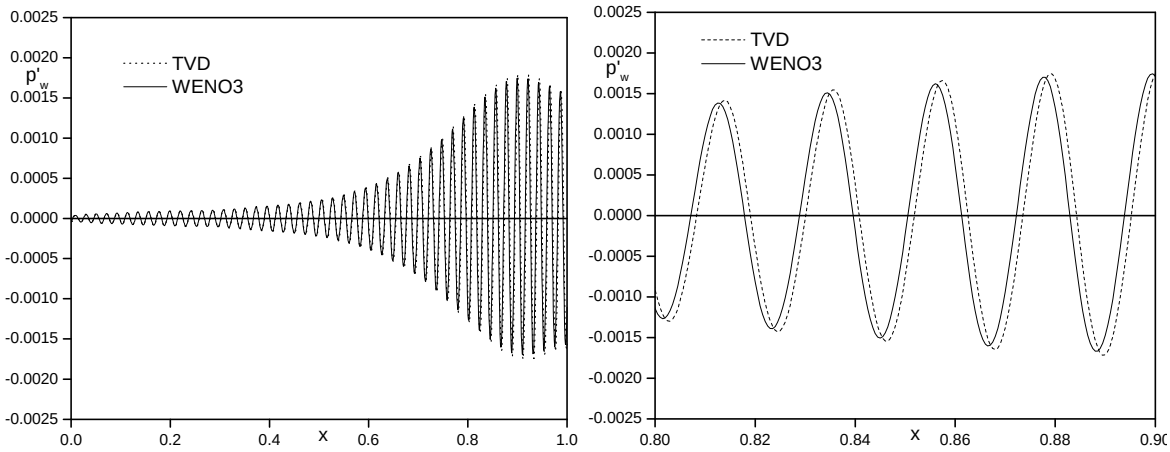

FIGURE 3. Wall pressure disturbance obtained with TVD and WENO3

4. CONCLUSIONS

Numerical methods based on second-order TVD and third-order WENO space discretization coupled with second-order implicit temporal advance method are used for DNS of unstable disturbances in hypersonic boundary layer over a flat plate at free-stream Mach number 6. The difference in amplitude between TVD and WENO scheme is relatively small in the boundary layer, but becomes important in the free stream (where grid stretching is used). Moreover, TVD scheme gives a larger phase error. It is shown that both numerical methods allow for simulation of unstable processes in the boundary layer.

Authors thank Dr V. Titarev (Cranfield University, UK) for numerous discussions on WENO methods.

The work is supported by Russian Foundation for Basic Research under Grant 09-08-00472 and AVCP RNPVSh 2.1.1/200.

REFERENCES

[1] Y. Ma, and X. Zhong, Receptivity of a supersonic boundary layer over a flat plate. Part 2. Receptivity to free-stream sound, *Journal of Fluid Mechanics*, 488, 79-121, 2003.

[2] F. Husmeier, C.S.J. Meyer, and H.F. Fasel, Investigation of Transition of Supersonic Boundary layers at Mach 3 Using DNS, *AIAA Paper 2005-95*, 2005.

[3] P. Balakumar, H. Zhao, and H. Atkins, Stability of hypersonic boundary-layer over a compression corner, *AIAA Paper 2002-2848*, 2002.

[4] I.V. Egorov, A.V. Fedorov, and V.G. Soudakov, Direct numerical simulation of disturbances generated by periodic suction-blowing in a hypersonic boundary layer, *Theoretical and Computational Fluid Dynamics*, 20(1), 41-54, 2006.

[5] I.V. Egorov, A.V. Fedorov, and V.G. Soudakov, Receptivity of a hypersonic boundary layer over a flat plate with a porous coating, *Journal of Fluid Mechanics*, 601, 165-187, 2008.

[6] G.S. Jiang, and C.W. Shu, Efficient Implementation of Weighted ENO Schemes, *J. Comput. Phys.*, 126, 202-228, 1996.

First International Conference on Computational Methods for Thermal Problems
ThermaComp2009, September 8-10, 2009, Naples, Italy
N.Massarotti and P.Nithiarasu (Eds.)

SPECTRAL FINITE DIFFERENCE ANALYSIS IN A DOUBLY-CONNECTED REGION

Yoshihiro Mochimaru
Tokyo Institute of Technology, Tokyo 152−8550, Japan,
ymochima@o.cc.titech.ac.jp

ABSTRACT

Natural convection heat transfer in a doubly-connected region formed in terms of Mathieu functions is effectively analyzed, using a spectral finite difference scheme for a variety of parameters, to get streamlines, isotherms, a mean Nusselt number, and total force acting on the body placed inside.

Key Words: *Spectral Analysis, Doubly-Connectedness*

1. INTRODUCTION

Analysis of natural convection heat transfer is one element of heat and fluid flow problems, e.g. heat transfer to liquid metals from cylinders [1]. Recently-developed spectral finite difference schemes [2] are very effective to analytical or numerical treatment especially of fluid flow problems or of heat and fluid flow problems in two-dimensional or in axisymmetrical solutions. Mathematical introduction of multiply-connectedness is required as shown in [3] (doubly-connected), and [4] (triply-connected). Special attention is necessary to a problem for forming a conformal mapping system [5]. The spectral finite difference scheme has the following property: mathematically exact spatial spectral decomposition, high spatial resolution, high speed computation, and accepting non-uniform grid spacing.

2. ANALYSIS

Steady-state two-dimensional natural convection from a heated object to fluid enclosed in a finite region (doubly-connected region) is analyzed, using a spectral finite difference scheme [2], later supplemented with a mathematical condition for multiply-connectedness [3, 4]. Under a boundary-fitted conformal mapping coordinate system (α, β) and a Boussinesq approximation neglecting dissipation terms, the dimensionless governing equations (ψ : stream function, ζ : vorticity, T : temperature) are:

$$J\frac{\partial \zeta}{\partial t} + \frac{\partial(\zeta,\psi)}{\partial(\alpha,\beta)} = \frac{1}{\sqrt{Gr}}\left(\frac{\partial^2}{\partial\alpha^2} + \frac{\partial^2}{\partial\beta^2}\right)\zeta + \frac{\partial(T,y)}{\partial(\alpha,\beta)}\ , \tag{1}$$

$$J\zeta + \left(\frac{\partial^2}{\partial\alpha^2} + \frac{\partial^2}{\partial\beta^2}\right)\psi = 0\ , \tag{2}$$

$$J\frac{\partial T}{\partial t} + \frac{\partial(T,\psi)}{\partial(\alpha,\beta)} = \frac{1}{Pr\sqrt{Gr}}\left(\frac{\partial^2}{\partial\alpha^2} + \frac{\partial^2}{\partial\beta^2}\right)T\ \ ,\ \ J \equiv \frac{\partial(x,y)}{\partial(\alpha,\beta)}\ , \tag{3}$$

where Gr and Pr stand for a Grashof number and a Prandtl number respectively. The following mapping

$$\mathrm{e}^{\alpha+i\,\beta} = \frac{1+i\,\eta(z)}{1-i\,\eta(z)}$$

is a general mapping such that $\alpha = 0, |\beta| \le \pi$ stands for an outer wall where $\eta(z)$ takes a single real value and along which the value varies from $-\infty$ to $+\infty$ monotonously. Another wall inside is assumed to be given by $\alpha = \alpha_0(< 0)$ if $\Im(\eta) \ge 0$. One-to-one correspondence in the conformal mapping gives

$\eta'(z) \neq 0$ inside the domain and vice versa[6]. Special focus is placed on a new configuration different from [2, 3, 4] given by the following with a parameter q:

$$\eta \equiv \frac{1}{\mathrm{se}_1(z,q)} + \mathrm{se}_1(z,q) - i\,\mathrm{ce}_1(z,q) \ , \ \Im(z) \leq 0 \ , \tag{4}$$

where $z \equiv x + iy$: physical dimensionless Cartesian coordinate, y : vertically upward, and $\mathrm{se}_1, \mathrm{ce}_1$ stand for the sine-elliptic and cosine-elliptic Mathieu functions of order 1 respectively; $\alpha_0 \leq \alpha \leq 0$. Characteristic values a_1 for ce_1 and b_1 for se_1 of the Mathieu functions are specified through the infinite continued fractions

$$1 - a_1 + q = \frac{q^2/(1^2 \cdot 3^2)}{1 - a_1/3^2} - \frac{q^2/(3^2 \cdot 5^2)}{1 - a_1/5^2} - \frac{q^2/(5^2 \cdot 7^2)}{1 - a_1/7^2} - \cdots \ , \tag{5}$$

$$1 - b_1 - q = \frac{q^2/(1^2 \cdot 3^2)}{1 - b_1/3^2} - \frac{q^2/(3^2 \cdot 5^2)}{1 - b_1/5^2} - \frac{q^2/(5^2 \cdot 7^2)}{1 - b_1/7^2} - \cdots \tag{6}$$

with $\lim_{q \to 0} a_1 = 1, \lim_{q \to 0} b_1 = 1$ [7]. Here as ususal, the following restriction is imposed: q is real and positive. For the one-to-one correspondence of the conformal mapping ($\eta' \neq 0$ in the domain),

$$0 < q \leq q_0 \approx 0.539 \ , \tag{7}$$

where

$$\frac{1}{\mathrm{se}_1(i\,H_0, q_0)} + \mathrm{se}_1(i\,H_0, q_0) + i\,\mathrm{ce}_1(i\,H_0, q_0) = 0 \ , \tag{8}$$

$$\mathrm{se}_1'(-i\,H_0, q_0) \left\{ 1 - \frac{1}{\mathrm{se}_1^2(i\,H_0, q_0)} \right\} - i\,\mathrm{ce}_1'(-i\,H_0, q_0) = 0 \ , \tag{9}$$

$$H_0 > 0$$

and $'$ denotes a derivative with respect to the first argument. Multiply-connectedness leads at $\alpha = \alpha_0$, as in [3, 4], to

$$\oint_{\alpha = \alpha_0} \frac{\partial p}{\partial \beta}\, d\beta = 0 \ , \tag{10}$$

which becomes

$$\frac{1}{\sqrt{Gr}} \oint \frac{\partial \zeta}{\partial \alpha} d\beta + \oint T \frac{\partial y}{\partial \beta} d\beta = 0 \tag{11}$$

(under a no-slip flow condition at a stationary wall), where p stands for pressure. Dynamical boundary conditions are specified through no slip flow conditions, i.e., without loss of generality as

$$\psi(\alpha_0, \beta) = \text{const} \ , \ \psi(0, \beta) = 0 \ , \ \frac{\partial}{\partial \alpha}\psi(\alpha_0, \beta) = 0 \ , \ \frac{\partial}{\partial \alpha}\psi(0, \beta) = 0 \ , \ |\beta| \leq \pi \ . \tag{12}$$

As a thermal boundary condition, the following Dirichlet type (the inner and outer walls are kept at a higher and lower constant temperature respectively) is considered:

$$T(\alpha_0, \beta) = 1 \ , \ T(0, \beta) = 0 \ , \ |\beta| \leq \pi \ . \tag{13}$$

In this case the thermal and fluid flow field is symmetric with respect to the y-axis. Thus, spectral decomposition is, not necessarily restricted to, but based on the Fourier series as

$$\begin{bmatrix} \zeta \\ \psi \end{bmatrix} = \sum_{n=1}^{\infty} \begin{bmatrix} \zeta_{sn}(\alpha, t) \\ \psi_{sn}(\alpha, t) \end{bmatrix} \sin n\beta \ , \tag{14}$$

$$T = \sum_{n=0}^{\infty} T_{cn}(\alpha, t) \cos n\beta \ . \tag{15}$$

Total force $\boldsymbol{F}$ acting on the inner surface $\alpha = \alpha_0$ is given by

$$\boldsymbol{F} = \frac{i}{\sqrt{Gr}} \oint z' \zeta d\beta - \frac{i}{\sqrt{Gr}} \oint z \frac{\partial \zeta}{\partial \alpha} d\beta \ , \tag{16}$$

(17) $$z' \equiv \frac{dz}{d(\alpha + i\beta)} \ .$$

Mean Nusselt number along the inner wall, Nu_m, is given by

(18) $$Nu_m = - \oint \frac{\partial T}{\partial \alpha} d\beta \Big/ \oint \sqrt{J} d\beta \ .$$

In Eqs.(16) and (18), integration is assumed to be carried out at $\alpha = \alpha_0$.

3. RESULTS

As an example, Figs. 1 and 2 show steady-state streamlines and isotherms respectively at $Gr = 10^4, Pr = 0.7, \mathrm{e}^{\alpha_0} = 0.1, q = 0.5$. In Fig.1 difference of streamlines $\delta\psi = 0.0025$, and in Fig. 2 temperature difference between isotherms $\delta T = 0.1$, $Nu_m = 10.2$, $\boldsymbol{F} = 0.0115\, i$, height of the outer circumference = 0.843, where the top point of the circumference is at $z = 0$. Figure 3 shows steady-state streamlines at $Gr = 10^4, Pr = 0.7, \mathrm{e}^{\alpha_0} = 0.1, q = 0.37$, where $Nu_m = 11.8, \boldsymbol{F} = 0.0085\, i$, height of the outer circumference = 0.711 .

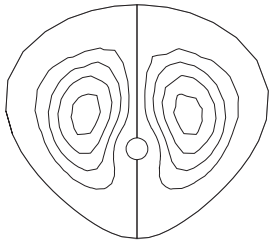

Fig.1 Steady-state streamlines at $Gr = 10^4, Pr = 0.7, \mathrm{e}^{\alpha_0} = 0.1, q = 0.5, \delta\psi = 0.0025$.

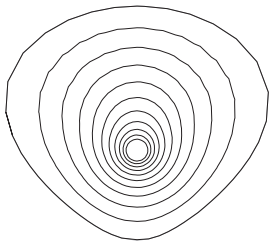

Fig.2 Steady-state isotherms at $Gr = 10^4$, $Pr = 0.7$, $\mathrm{e}^{\alpha_0} = 0.1, q = 0.5, \delta T = 0.1$.

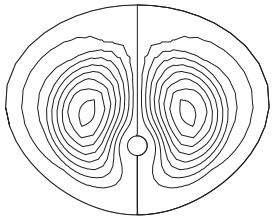

Fig.3 Steady-state streamlines at $Gr = 10^4$, $Pr = 0.7$, $\mathrm{e}^{\alpha_0} = 0.1, q = 0.37, \delta\psi = 0.001$.

4. CONCLUSIONS

Thermal and fluid flow of natural convection heat transfer in a doubly-connected region is successfully analyzed, using a spectral finite difference scheme. Information on lift force, total flow rate, and a mean Nusselt number is obtained for a variety of parameters.

5. REFERENCES

[1] S.C. Hyman, C.F. Bonilla, and S.W. Ehrlich, Natural convection transfer processes: I. Heat transfer to liquid metals and nonmetals at horizontal cylinders, *Chem. Eng. Prog. Sym. Ser.*, 49(1953), 21−31.

[2] Y. Mochimaru, Effectiveness of a spectral finite difference scheme, *Computational Fluid Dynamics Review* , 1(1998), 379−394.

[3] Y. Mochimaru and M-W. Bae, Natural convection heat transfer in a doubly-connected region, using a spectral finite difference scheme, *International J. Pure and Applied Mathematics*, 32(2006), 51−60.

[4] Y. Mochimaru and M-W. Bae, Spectral finite difference analysis in a triply-connected region, *International J. Computational and Numerical Analysis and Applications*, 4(2003), 91−104.

[5] Y. Mochimaru, Existence / Non-existence of Conformal Mapping in Some Family of Functions, *International J. Pure and Applied Mathematics*, 49 (2008), 497−503.

[6] P. Henrici, *Applied and Computational Complex Analysis*, 1(1974), Wiley−Interscience.

[7] N.W. McLachlan, *Theory and Application of Mathieu Functions*, (1964), Dover.

First International Conference on Computational Methods for Thermal Problems
ThermaComp2009, September 8-10, 2009, Naples, Italy
N.Massarotti and P.Nithiarasu (Eds.)

An upwind method for incompressible flows with heat transfer

J C Mandal
Professor, Aerospace Engg. Dept, IIT Bombay Mumbai India, mandal@aero.iitb.ac.in

Anesh S Iyer
Master's Student, Aerospace Engg. Dept, IIT Bombay Mumbai India, aneshiyer@aero.iitb.ac.in

Key Words: *Pseudo-compressibility method, upwind method, heat transfer, incompressible flow*

1. INTRODUCTION

The motivation for the present work is to formulate an efficient method of numerical solution for incompressible viscous flows with heat transfer. Two common approaches used in solving incompressible flow problems are the so called pressure based method introduced by Patankar and density based (pseudo- compressibility) method proposed by Chorin. The pseudo-compressibility formulation is considered here because of its superior performance in terms of convergence and robustness. Furthermore, all advanced techniques for compressible flows can be extended to incompressible flow computations in pseudo-compressibility formulation.

Mainly two approaches are used for numerically discretizing the Navier-Stokes equations with pseudo-compressibility formulation; namely, central differencing scheme by Jameson, and flux difference splitting scheme by Roe. While Jameson scheme requires addition of artificial dissipation (which needs tuning depending on the problem) for stability, the derivation of flux difference splitting scheme of Roe is not proper due to violation of the homogeneity property of flux vector in pseudo-compressibility formulation. Although the results reported in the literature do not show the effect of above deficiency of Roe's scheme, a need is felt to develop an alternate upwind method. Thus, the authors proposed a novel Harten Lax and van Leer with contact (HLL-C) type method for pseudo-compressibility formulation which is cost effective and free from above drawbacks[1]. The new method has been found to produce excellent results for a wide range of incompressible flows without heat transfer[1]. In the present work, above HLLC-type method is modified to include energy equations with the Navier Stokes equations in order to solve heat transfer problems.

2. GOVERNING EQUATIONS AND NUMERICAL FORMULATION

The pseudo-compressibility formulation for 2D incompressible flow with heat transfer is given by

$$\frac{\partial \mathbf{U}}{\partial t} + \frac{\partial \mathbf{E}}{\partial x} + \frac{\partial \mathbf{G}}{\partial y} = \mathbf{S} \tag{1}$$

where $\mathbf{U} = (p, u, v, T)^T$, $\mathbf{S} = (0, 0, g_t\beta_t(T - T_{ref}), 0)^T$, $\mathbf{E} = \mathbf{E}^c - \mathbf{E}^v$ and $\mathbf{G} = \mathbf{G}^c - \mathbf{G}^v$. The expressions for the convective fluxes $\mathbf{E}^c$ and $\mathbf{G}^c$, and viscous fluxes $\mathbf{E}^v$ and $\mathbf{G}^v$ are

$$\mathbf{E}^c = \begin{Bmatrix} \beta u \\ u^2 + p \\ uv \\ uT \end{Bmatrix}, \quad \mathbf{G}^c = \begin{Bmatrix} \beta v \\ uv \\ v^2 + p \\ vT \end{Bmatrix}, \quad \mathbf{E}^v = \begin{Bmatrix} 0 \\ \nu(2\frac{\partial u}{\partial x}) \\ \nu(\frac{\partial v}{\partial x} + \frac{\partial u}{\partial y}) \\ \alpha\frac{\partial T}{\partial x} \end{Bmatrix}, \quad \mathbf{G}^v = \begin{Bmatrix} 0 \\ \nu(\frac{\partial v}{\partial x} + \frac{\partial u}{\partial y}) \\ \nu(2\frac{\partial v}{\partial y}) \\ \alpha\frac{\partial T}{\partial y} \end{Bmatrix}$$

Here, u and v are the Cartesian components of velocity, p is the modified pressure (normalized with density), T the temperature, ν the kinematic viscosity, α the thermal diffusivity, β_t the coefficient of thermal expansion, g_t acceleration due to gravity and T_{ref} the reference temperature. The term β represents artificial compressibility.

Integrating them over an arbitrary finite volume and changing the volume integral over the flux vectors to the surface integral, we have

$$\int\int_{\Omega} \frac{\partial \mathbf{U}}{\partial t} dxdy + \oint_A [\mathbf{E}n_x + \mathbf{G}n_y]dA = \int\int_{\Omega} \mathbf{S}dxdy \tag{2}$$

where n_x and n_y are the direction cosines for the face of area A which is enclosing the cell volume Ω.

Discretizing Eq.(2), the normal components of the inviscid flux $\mathbf{F}_{ij} = (\mathbf{E}^c n_x + \mathbf{G}^c n_y)$ at the face between two cells are evaluated based on the proposed new upwind method for pseudo-compressibility formulation. This method is an extension of the upwind method developed by the present authors for incompressible flow without heat transfer[1]. The interface inviscid flux is given by

$$\mathbf{F}_{i,j} = \begin{cases} \mathbf{F}_L & 0 \le S_L \\ \mathbf{F}_L^* = \mathbf{F}_L + S_L(\mathbf{U}_L^* - \mathbf{U}_L) & S_L \le 0 \le S^* \\ \mathbf{F}_R^* = \mathbf{F}_R + S_R(\mathbf{U}_R^* - \mathbf{U}_R) & S^* \le 0 \le S_R \\ \mathbf{F}_R & 0 \ge S_R \end{cases} \tag{3}$$

where S_L, S_R and S^* are the wave speed estimates. $\mathbf{F}_L$ and $\mathbf{F}_R$, are the inviscid fluxes on the left and right of the interface between cells i and j. The primitive variable vectors, $\mathbf{U}_L$ and $\mathbf{U}_R$, are evaluated at left and right states using a piecewise linear reconstruction presented by Barth and Jespersen.

Realizing that the flux Jacobian for the above system has eigenvalues u_n, u_n, $u_n - a$ and $u_n + a$, the fastest left and right running waves are estimated as $S_L = min[(u_n - a)_L, (u_n - a)_R]$; $S_R = max[(u_n + a)_L, (u_n + a)_R]$; and the middle wave as $S^* = u_n^*$ with the artificial speed of sound $a = \sqrt{u_n^2 + \beta}$. Note that the subscripts L and R denote left and right states at the interface respectively.

The unknown vectors defining the star quantities $\mathbf{U}_L^* = [p^*\, u_n^*\, v_n^*\, T^*]_L^T$ and $\mathbf{U}_R^* = [p^*\, u_n^*\, v_n^*\, T^*]_R^T$ in Eq.(3) are evaluated in the following manner. As shown in Fig. 1(a), there exists jumps in all primitive variables across the fastest left and right running waves (S_L,S_R). Based on generalized Riemann Invariant analysis similar to that in reference[1], it is noted that there is a jump in the face tangential velocity and temperature across the intermediate wave with wave speed S^*, while the pressure and normal component of velocity remains invariant across the middle wave. Therefore, the intermediate (star) quantities for pressure and normal velocity can be obtained from the two wave system while tangential velocity components and the temperature in the intermediate (star) region, i.e. v_{nL}^*, v_{nR}^*, T_L^* and T_R^*, are determined by solving the Rankine Hugnoit conditions across the waves S_L and S_R.

The primitive variables in the intermediate region as evaluated above are used to evaluate the convective flux as in Eq.(3).This convective flux is added with viscous flux to give the total flux across the edge.The viscous flux is evaluated in a conventional central differencing manner.

3. RESULTS AND DISCUSSIONS

The present method is validated with two square cavity test problems; one involving natural convection flow[2], and the other involving mixed convection flow[3]. The geometry for both the cases is identical with change in the boundary conditions for each case. The 41×41 grided domain is shown in Fig. 1(b). The flows considered here are laminar. The density variation because of buoyancy effects are taken into account by Boussinesq hypothesis. Air with Prandtl number 0.71 is chosen as the fluid medium. Gravitational body force is assumed to act in the negative y direction.

3.1. **Natural convection flow.** The vertical walls (x=0,x=1) are differentially heated and the horizontal walls (y=0,y=1) are insulated while the lid of the cavity is held at rest. Heat transfer through the walls cause density changes and leads to buoyancy driven flows.The reference fluid temperature is taken as $T_0 = 293K$ while $T_h = 303K$ and $T_c = 283K$ are the temperatures of hot and cold wall respectively.

The temperature and velocity contour plots for $Ra = 10^6$ are also shown in Fig. 2. The computed velocity components at the domain center-lines are shown in Fig. 3(a) as non-dimensional form (using $\frac{\alpha}{D}$ as a scale factor, where α is the thermal diffusivity and D is the cavity width) for Rayleigh numbers $Ra = 10^5, 10^6$. The important quantities for the problem considered, e.g. the Nusselt number and the maximum velocities are summarized in Table 1. The table shows the computed Nusselt numbers at the

hot wall for $Ra = 10^4, 10^5, 10^6$. A comparison with the available literature [2] is also shown in the table.

3.2. **Mixed convection flow.** The results presented are that of computations carried out for various Grashof numbers of $Gr = 10^2, 10^4, 10^6$ and Reynolds Number of $Re = 100, 400, 1000$. It has been observed that for $\frac{Gr}{Re^2} << 1$, the mechanical effect of sliding lid is more prominent than that of the buoyancy effects and vice versa for $\frac{Gr}{Re^2} >> 1$. The velocity profiles at the cavity mid planes are shown in Fig. 3(b) for $Gr = 10^2, 10^6$ and $Re = 1000$ values. The streamline plot and temperature contours are also shown in Fig. 4 for $Re = 1000$ and $Gr = 10^6$. The Nusselt Number at the top wall, which indicates the measure of heat transfer, is computed and compared with the values given in the literature[3] as shown in Table 2 for all the above cases.

4. CONCLUSION

A new upwind method is proposed for solving incompressible flows with heat transfer which has superior features as compared to the existing methods for pseudo-compressibility formulation. Extensive validation exercise conducted with test cases of natural and mixed convective flows, demonstrate that the computed solutions from the present method have very good agreement with benchmark solutions reported in the literature.

REFERENCES

[1] J.C. Mandal and A.S. Iyer, An upwind method for incompressible flow computations using pseudo-compressibility approach, *AIAA Paper No. AIAA-2009-3541, 19th Computational Fluid Dynamics Conference, 22- 25 June 2009, San Antonio, USA*.

[2] G.de Vahl Davis and I.P. Jones, Natural convection in a square cavity-a comparison exercise, *International Journal for Numerical Methods in Fluids* , 3, 227-248, 1983.

[3] R.Iwatsu, J.M.Hyun, K.Kuwahara, Mixed convection in a driven cavity with a stable vertical temperature gradient, *International Journal of Heat and Mass Transfer*, 36, 1601-1608, 1993.

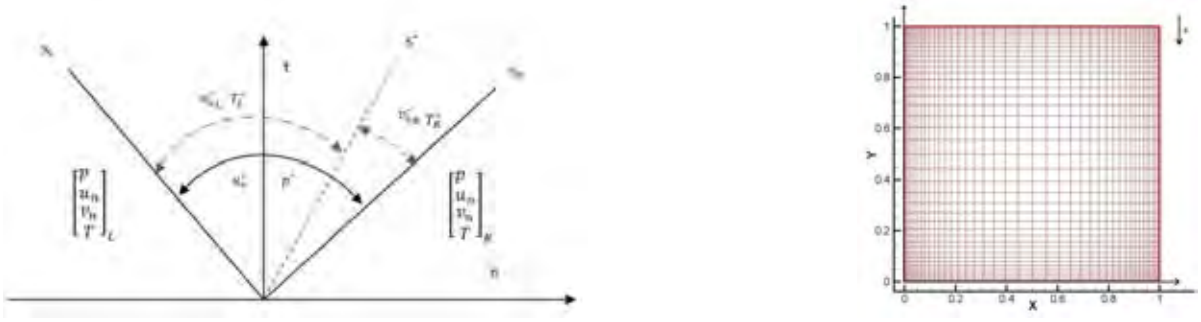

(a) Three wave system

(b) 41 X 41 grid

FIGURE 1. Three wave system and grid used for the problem

TABLE 1. Comparison at different Ra Numbers

Parameter	$Ra = 10^4$	$Ra = 10^5$	$Ra = 10^6$
Nu_{max}	3.52(3.528)	7.80(7.717)	17.79(17.925)
y_{Numax}	0.1407(0.1425)	0.0826(0.081)	0.0382 (0.0378)
Nu_{min}	0.512(0.586)	0.646(0.729)	0.898 (0.989)
Nu	2.32(2.243)	4.61(4.519)	8.51 (8.779)
u_{max}	16.16(16.178)	34.25(34.73)	63.82 (64.63)
y_{umax}	0.823(0.823)	0.855(0.855)	0.852 (0.850)
v_{max}	19.42(19.617)	68.24(68.59)	217.66 (217.36)
y_{vmax}	0.115(0.119)	0.064(0.066)	0.034 (0.0379)

* Values in the brackets() are taken from ref[2] and [3].

TABLE 2. Nu Number at Top wall

Re	$Gr = 100$	$Gr = 10^4$	$Gr = 10^6$
100	1.97(1.94)	1.31(1.34)	-(1.02)
400	3.78(3.84)	3.61(3.62)	1.18 (1.22)
1000	6.41(6.33)	6.32(6.29)	1.81 (1.77)

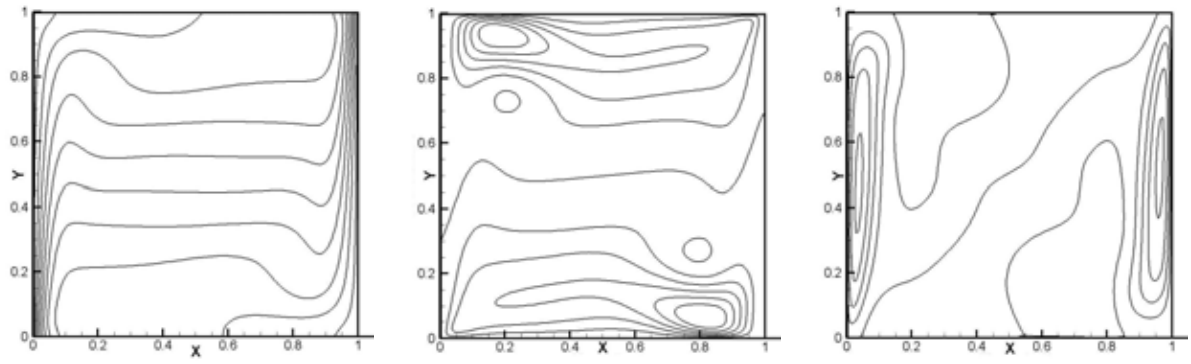

(a) Temperature contour (b) u velocity contour (c) v velocity contour

FIGURE 2. Natural convection with Rayleigh Number 10^6

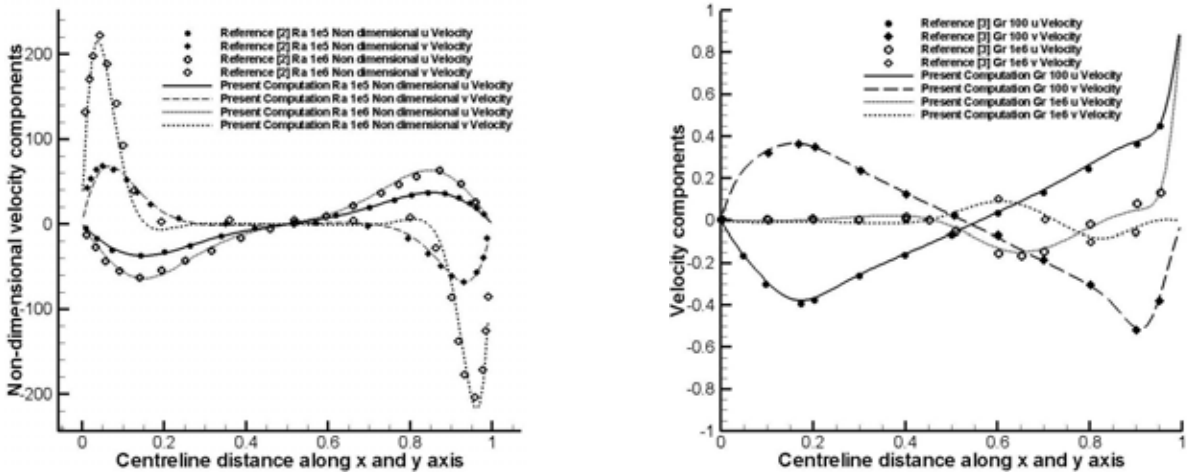

(a) Natural convection $Ra = 10^5, 10^6$ (b) Mixed convection $Gr = 100, 10^6$

FIGURE 3. Velocity components along centerline

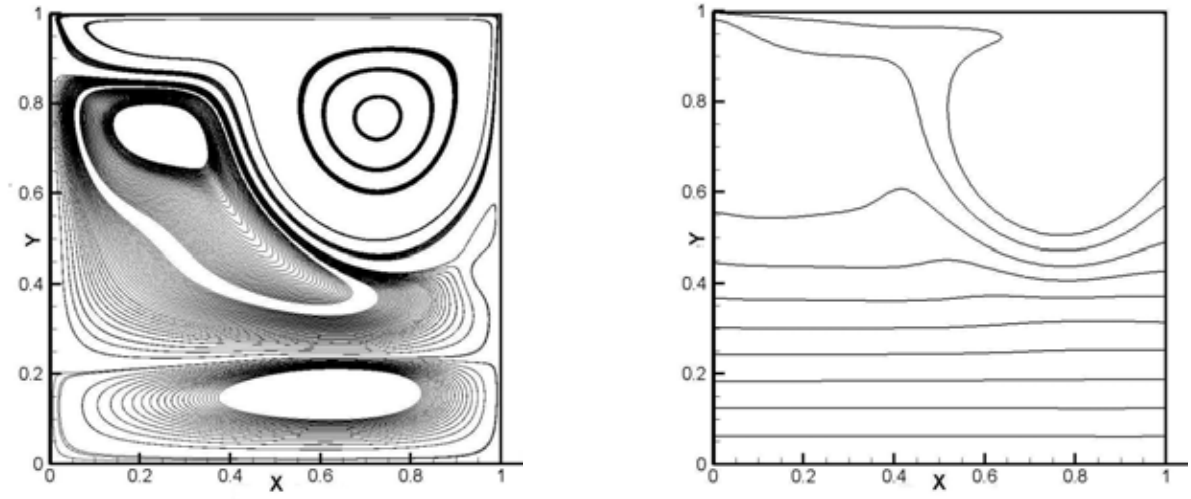

(a) Streamline plot (b) Temperature contours

FIGURE 4. Mixed convection with Reynolds Number 1000 Grashof Number 10^6

First International Conference on Computational Methods for Thermal Problems
ThermaComp2009, September 8-10, 2009, Naples, Italy
N.Massarotti and P.Nithiarasu (Eds.)

Numerical Computations of Energy Balances in Thermal Convection Problems

***TAGAMI, Daisuke**
Faculty of Mathematics, Kyushu University
6-10-1, Hakozaki, Higashi-ku, Fukuoka 812-8581, JAPAN
E-mail: tagami@math.kyushu-u.ac.jp
URL: http://www2.math.kyushu-u.ac.jp/~tagami/

ABSTRACT

Numerical computations of energy balances are introduced in thermal convection phenomena, and its error estimates are established. As for a practical example to apply the justified scheme, some results are shown in case of an electrical melting furnace.

Key Words:*Energy Balance, Thermal Convection Problem, Error Estimate, Finite Element Method.*

1. INTRODUCTION

The design for glass furnaces with lower fuel consumption and with less CO_2 emission requires us to find precisely convection phenomena in the melting process. For a grasp of phenomena, the use of numerical computations is growing in acceptance, and there encounter many researches on the computations; see, for example, Choudhary [1], Ungan and Payli [8], and Ungan and Viskanta [9]. Because the physical properties of raw glass materials dependent on the temperature, a choice to approximate physical coefficients is treated with care in justifying numerical schemes. Recently, we have mathematically justified a class of finite element methods for thermal convection problems with temperature-dependent coefficients; see Tabata [3] and Tabata and Tagami [5]. As for a practical example to apply the justified scheme, we focus our attention to numerical computations of energy blances in a glass melting process.

Owing to the Boussinesq, the Rosseland, and the infinite Prandtl number approximations, the velocity u, the pressure p, and the temperature θ of the raw material in the furnace with the electric boosting are governed by the thermal convection equations with the Joule heat, which is regarded as the external heat source; see Tagami and Tabata [7].

The equations are discretized by the backward Euler method in time and by the conforming finite elements in space; for details, see [7]. Tagami and Itoh [6] have established the optimal error estimates of such scheme, although the physical coefficients are assumed to be constants. On the other hand, the physical coefficients are regarded as functions of the temperature in practical glass process. In practical finite element codes, some approximation may be introduced to variable coefficients, that is, they are replaced by interpolants. Therefore, some conditions are required to maintain the same error estimates as in the constant coefficient case. In [3] and [5] we have established the estimates in the variable coefficient case, where the equations correspond to the case without the Joule heat.

Moreover, the energy given into raw materials through the throat is descretized by a consistent flux method, which is well-known as an accurate and simple method for computing boundary quantities; see, for example, Gresho et al. [2] and Tabata and Tagami [4]. This process reduces error estimates of the energy balances to those of the velocity, the pressure, and the temperature. From this descretization, we have also established the estimates on energy balances.

Using the numerical scheme mentioned above, we compute thermal convection phenomena in a model furnace with the Joule heat. As the first step of the design for furnaces, an attempt is made to investigate qualitative differences among some electrode configurations on the temperature distribution and convection pattern in the furnace, and on the energy given into raw materials through the throat.

2. FORMULATION

Here, a nonstationary thermal convection problem with temperature-dependent coefficients is considered as follows: Find the velocity u, the pressure p, and the temperature θ

$$
\begin{cases}
\partial_t u + (u\cdot\nabla)\,u - \nabla\cdot\left[\nu(\theta)D(u)\right] + \nabla p - \beta(\theta)\,\theta = f & \text{in } \Omega\times(0,T), \quad \text{(1a)}\\
\nabla\cdot u = 0 & \text{in } \Omega\times(0,T), \quad \text{(1b)}\\
\partial_t\theta + (u\cdot\nabla)\,\theta - \nabla\cdot\left(\kappa(\theta)\nabla\theta\right) = g & \text{in } \Omega\times(0,T), \quad \text{(1c)}
\end{cases}
$$

where T (>0) denotes a time; Ω a bounded domain in $\mathbb{R}^d$ ($d=2,3$) with Lipschitz-continuous boundary Γ that consists of three parts, Γ_B, Γ_T, and Γ_W; $(f,\ g)$: $\Omega\times(0,T)\to\mathbb{R}^d\times\mathbb{R}$ a set of external force and heat source; $(\nu,\ \kappa,\ \beta)$: $\Omega\times(0,T)\times\mathbb{R}\to\mathbb{R}^+\times\mathbb{R}^+\times\mathbb{R}^d$ a set of generalized viscosity, thermal conductivity, and thermal expansion coefficients; $D(u)$ the strain-rate tensor defined by $D(u)\equiv(\nabla u+\nabla u^T)/2$. The boundaries Γ_B, Γ_T, and Γ_W correspond an inflow, an outflow, and a fixed boundaries, respectively; for example, see Figure1. A mathematical model of thermal convection problems is obtained by adding appropriate boundary and initial conditions to (1).

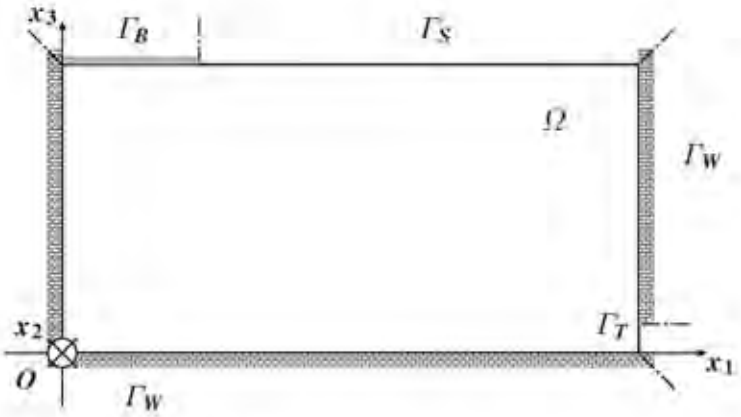

FIGURE 1. A domain Ω.

The problem (1) is discretized by the backward Euler method in time and by the kth order conforming finite elements in space. Then, the optimal error estimates have been established, that is, errors of the finite element solution converge with $O(\tau+h^k)$ under the appropriate conditions (see [5] and [6]), where τ denotes a time increment and h a space descretization parameter.

3. ENERGY BALANCES

As an example of representative quantities appearing in energy blances, the outflow energy "OE" is defined by an integral on the boundary Γ_T as follows:

$$
\mathrm{OE}\equiv\int_{\Gamma_T}\theta\,u\cdot n\,ds.
$$

"OE" corresponds an energy obtained by the raw material through the boundary Γ_T. We note that the approximate "OE" can be computed by a consistent flux method, which is well-known as an accurate and simple method for computing boundary quantities; see, for example, Gresho et al. [2] and Tabata

and Tagami [4]. Then, when the corresponding approximate solutions and functions are denoting by subscripts "$_h$", an approximate "OE" is defined by

$$\mathrm{OE}_h^n \equiv -\int_\Omega D_\tau \theta_h^n \, \phi_{Oh} \, dx + \int_\Omega u_h^{n-1} \cdot \nabla \phi_{Oh} \, \theta_h^n \, dx - \int_\Omega \nabla \theta_h^n \, \nabla \phi_{Oh} \, dx + \int_\Omega g^n \, \phi_{Oh} \, dx,$$

where $\phi_O = 0$ on $\Gamma_B \cup \Gamma_S$, $\phi_O = 1$ on Γ_T, and $D_\tau \theta^n \equiv (\theta^n - \theta^{n-1})/\tau$. Owing to the error estimates of the finite element solution, errors of the approximate "OE" converge with $\mathcal{O}(\tau + h^k)$.

4. NUMERICAL RESULTS

A glass furnace is considered as for the practical model problem in Figure 2.In this model, the source term g in (1) is given by the Joule heat, $\sigma(\theta)|\nabla\phi|^2/2$. Here ϕ is the electric scalar potential defined by

$$\begin{cases} -\nabla \cdot \big(\sigma(\theta)\nabla\phi\big) = 0 & \text{in } \Omega \times (0,T), \quad \text{(2a)} \\ \phi = \phi_D & \text{on } \Gamma_E \times (0,T), \quad \text{(2b)} \\ \dfrac{\partial \phi}{\partial n} = 0 & \text{otherwise}, \quad \text{(2c)} \end{cases}$$

where Γ_E denotes a union of the electrode boundaries, $\Gamma_{E_1} \cup \Gamma_{E_2} \cup \Gamma_{E_3}$, and $\sigma : \Omega \times (0,T) \times \mathbb{R} \to \mathbb{R}^+$ is electrical conductivity depending on x, t, and θ. The physical coefficients ν, κ, σ, and β are taken as

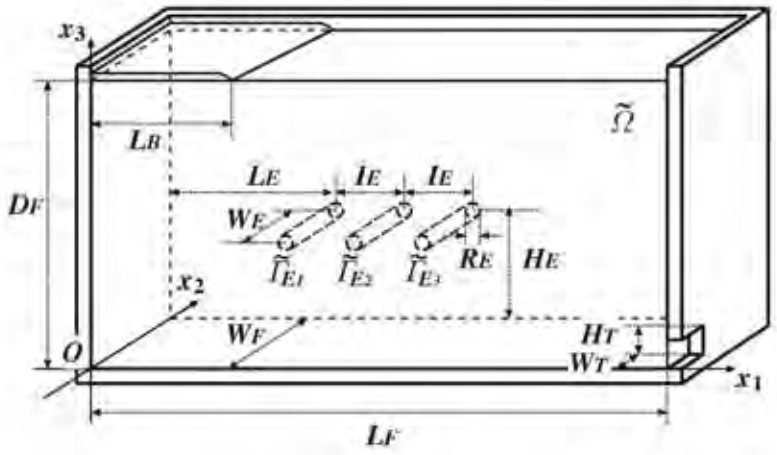

FIGURE 2. A model furnace.

$$\nu \equiv 0.01 \, \exp\Big(\frac{50}{10+\theta}\Big), \qquad \kappa \equiv 0.01 \, \theta^2 + 0.2 \, \theta + 1,$$

$$\sigma \equiv 55 \, \exp\Big(\frac{-50}{15+\theta}\Big), \qquad \beta \equiv (0, \, 20000).$$

These coefficients are obtained by normalizing with 1500 [K] and by rounding those of a raw glass material given in [9]. Three cases of the electric potential values on the electrodes are considered as in Table 1. In Case A, the values are obtained by normalizing and rounding the root-mean-square values

TABLE 1. The electric potential ϕ imposed on Γ_E.

Case	Γ_{E_1}	Γ_{E_2}	Γ_{E_3}
A	6	-3	-3
B	-3	6	-3
C	-3	-3	6

of the complex potentials given in [9]. In Cases B and C, the locations of the positive potential are different from those in Case A.

Table 2 shows energy balances computed by the method introducing above. "Given", "Out", "Int", and "Loss" mean the external heat in the furnace, outflowing energy from the furnace, internal energy used in the temperature elevation, and lost energy in convective motions. More precisely, these values are defined as follows:

$$\text{Given} \equiv \frac{1}{2}\int_0^T\int_\Omega \sigma(\theta)|\nabla\phi|^2\,dxdt, \qquad \text{Out} \equiv \int_0^T\int_{\Gamma_T} (\theta\, u\cdot n - \theta_0\, u_0\cdot n)\,dsdt,$$

$$\text{Int} \equiv \int_\Omega (\theta(T)-\theta_0(T))\,dx, \qquad \text{Loss} \equiv \int_0^T\int_{\Gamma_B\sqcup\Gamma_S}\left(\kappa(\theta_0)\frac{d\theta_0}{dn} - \kappa(\theta)\frac{d\theta}{dn}\right)dsdt.$$

"Ratio" is defined by Out/Given. From point of view on energy efficients, Case B is better than the other cases.

TABLE 2. Comparison of heat balances.

Case	Given	Out	Ratio[%]	Int	Loss
A	16.5	0.47	2.8	2.11	14.9
B	7.7	0.46	6.0	1.28	6.5
C	16.6	0.51	3.1	1.96	15.2

5. CONCLUSIONS

Numerical computations of energy balances have been introduced in thermal convection phenomena, and its error estimates have been established. As for a practical example to apply the justified scheme, some results have been shown in case of an electrical melting furnace. From point of view on energy efficients, the best allocation has been found by the numerical computations mentioned above.

REFERENCES

[1] CHOUDHARY, M., "Three-dimensional mathematical model for flow and heat transfer in electric glass furnaces", *Heat Transfer Eng.*, **6** (1985), 55–65.

[2] GRESHO, P.M., ET AL., "The Consistent Galerkin FEM for Computing Derived Boundary Quantities in Thermal and/or Fluids Problems", *Int. J. Numer. Methods Fluids*, **7** (1987), 371–394.

[3] TABATA, M., "Finite element approximation to infinite Plandtl number Boussinesq equations with temperature-dependent coefficients—thermal convection problems in a spherical shell", *Future Gener. Comput. Syst.*, **22** (2006), 521–531.

[4] TABATA, M. AND TAGAMI, D., "Error Estimates for Finite Element Approximations of Drag and Lift in Nonstationary Navier–Stokes Flows", *Japan J. Indust. Appl. Math.*, **17** (2000), 371–389.

[5] TABATA, M. AND TAGAMI, D., "Error estimates of finite element methods for nonstationary thermal convection problems with temperature-dependent coefficients", *Numer. Math.*, **100** (2005), 351–372.

[6] TAGAMI, D. AND ITOH, H., "A finite element analysis of thermal convection problems with the Joule heat", *Japan J. Indust. Appl. Math.*, **20** (2003), 193–210.

[7] TAGAMI, D. AND TABATA, M., "Numerical computations of a melting glass convection in the furnace", *Proceedings of The Seventh China-Japan Seminar on Numerical Mathematics*, Edited by Shi, Z.-C. and Okamoto, H., Science Press, 149–160, 2006.

[8] UNGAN, A. AND PAYLI, R. U., "Numerical Study of Coupling between Flow and Electrical Fields in an Electrical Glass Melter", *Int. J. Appl. Electromagn. Mater.*, **5** (1994), 241–250.

[9] UNGAN, A. AND VISKANTA, R., "Three-dimensional numerical simulation of circulation and heat transfer in an electrically boosted glass melting tank", *IEEE Trans. Ind. Appl.*, **IA-22** (1986), 922–933.

First International Conference on Computational Methods for Thermal Problems
ThermaComp2009, September 8-10, 2009, Naples, Italy
N.Massarotti and P.Nithiarasu (Eds.)

HIGH LEVEL LANGUAGES IMPLEMENTATION AND ANALYSIS OF 3D N.S. SOLVERS

Giuseppe de Felice
University of Naples 'Federico II' - DETEC, Dipartimento di Energetica Termofluidodinamica applicata e Condizionamenti ambientali, P.le Tecchio 80 - 80125 Naples, giudefel@unina.it

Valerio Grazioso
University of Naples 'Federico II' - DETEC, Dipartimento di Energetica Termofluidodinamica applicata e Condizionamenti ambientali, P.le Tecchio 80 - 80125 Naples, valerio.grazioso@unina.it

Carlo Meola
University of Naples 'Federico II' - DETEC, Dipartimento di Energetica Termofluidodinamica applicata e Condizionamenti ambientali, P.le Tecchio 80 - 80125 Naples, cmeola@unina.it

Carlo Scalo
Queens University - Department of Mechanical and Materials Engineering, 130 Stuart Street, Kingston, Ontario, scalo@appsci.queensu.ca

ABSTRACT

In this work we present PRIN-3D (*PR*oto-code for *I*nternal flows modeled by *N*avier-Stokes equations in *3-D*imensions), a new high level algebraical language (Matlab®) code and its *solving kernel* based on a *quasi-segregation* technique of the pressure equation.

Key Words: *Computational fluid dynamics, high level algebraical languages, segregation, preconditioner.*

1. INTRODUCTION

In order to design a computational fluid dynamics code that enables the user to perform several tests ranging from algebraic analysis of the equations' structure to modular implementation of virtually any kind of Fluid Dynamic model, it is convenient to adopt high level algebraical languages (like Python, Scilab, Octave, etc.) and in particular Matlab®. This choice is made considering the opportunities that this kind of programming languages offer in terms of easy user interfacing, fast libraries and packages integration (i.e. NAG, LAPACK, UMFPACK, etc.) and increasing usage of natively multi-threaded functions. In comparison with low level programming languages (like C or Fortran) they result to be easier to use and more portable across platforms because of their strong abstraction from the details of the computer, also taking into account their "natural" and "native" handling of fundamental linear algebra objects like matrices, and the extensive amount of libraries and functions available for a lot of simple and complex operations like matrix manipulation or 3D graphics and visualization. Moreover high level algebraical languages have also an easy parallelization capability by means of specifically designed toolboxes (MPI based) and packages (like Star-P®). Following such considerations and with the purpose in mind of designing a flexible code (sometimes referred to as *proto-code*) with turbulent and reactive capabilities and oriented to the study of new mathematical and numerical models and to the development or optimization of new numerical algorithms, we decided to write from scratch a new numerical code called PRIN-3D (*PR*oto-code for *I*nternal flows modeled by *N*avier-Stokes equations in *3-D*imensions) tailored to the general structure of the mathematical models that we want to solve (in particular the incompressible and the slightly compressible Navier-Stokes model) but also flexible enough to easy implement new models by exploiting the fast built in functions of such high level algebraical languages. The focus is also on the introduction of advanced numerical solvers with pressure

segregation by means of preconditioning techniques, and to the study of different linear (iterative as well as direct) solvers.

2. MAIN BODY

The structure of PRIN-3D linear solver for the system of equations yielded by the discretization of the incompressible Navier-Stokes partial differential equations is the *solving kernel* for every incompressible or even slightly compressible model being resolved. An implicit time discretization for the diffusive part, weighing with θ the unknowns at time $n+1$ and $(1-\theta)$ the known values at time n, is adopted (the most common choice for the value of θ is 1/2 and this leads to the Cranck-Nicolson scheme with a truncation error $e = O(\Delta t^2) + O(\Delta x^2)$). All non linear terms are left on the right hand side of the discrete equations, that is to say the evaluation of such terms is only done on the basis of values at time t^n. The pressure gradient has been collocated directly at the time $t^{(n+1)}$ and this is to stress the fact that the vector field $\frac{\partial P^{n+1}}{\partial x_j}$ has to correct the divergence of the finally computed field at time $t^{(n+1)}$ and that in incompressible flows pressure has barely no physical meaning and so does any attempt to assign a time collocation to it. The solving process is carried out with a *quasi-segregation* technique of the pressure equation. Introducing a spatial discretization, the system of discretized equations can be restated in terms of algebraic operators:

$$\begin{pmatrix} \mathcal{F} & \mathcal{G} \\ \mathcal{D} & 0 \end{pmatrix} \begin{pmatrix} v \\ p \end{pmatrix}^{n+1} = \begin{pmatrix} q \\ g \end{pmatrix}^{n} \tag{1}$$

where $\mathcal{F}$ is a block-diagonal elliptic operator $\left(\begin{smallmatrix} F & 0 & 0 \\ 0 & F & 0 \\ 0 & 0 & F \end{smallmatrix}\right)$. With simple algebraic manipulation (considering Richardson iterations with the left preconditioner $\mathcal{P} = \left(\begin{smallmatrix} \mathcal{F} & 0 \\ \mathcal{D} & -I \end{smallmatrix}\right)$) system (1) can be rewritten as

$$\begin{pmatrix} I & \mathcal{F}^{-1}\mathcal{G} \\ 0 & \mathcal{D}\mathcal{F}^{-1}\mathcal{G} \end{pmatrix} \begin{pmatrix} v \\ p \end{pmatrix}^{n+1} = \begin{pmatrix} \mathcal{F}^{-1}q \\ \mathcal{D}\mathcal{F}^{-1}q - g \end{pmatrix}^{n}$$

obtaining the typical structure of a segregated system where velocity and pressure variable computations have been uncoupled, and the latter has to satisfy the classic pressure *segregated* Poisson's equation $\mathcal{D}\mathcal{F}^{-1}\mathcal{G}p^{n+1} = \mathcal{D}\mathcal{F}^{-1}q - g$. If the matrices $\mathcal{F}^{-1}$ and $\mathcal{F}^{-1}\mathcal{G}$ were directly computed, both would turn out to be completely full and their storage would be dramatically demanding on memory resources. Of course also matrix $\mathcal{D}\mathcal{F}^{-1}\mathcal{G}$ is completely full and has to be inverted. Considering the following polynomial expansions of the inverse of F (and so of the whole block diagonal matrix $\mathcal{F}$): $F^{-1} = (I - \nu\theta\Delta t\ \nabla^2)^{-1} = I + \sum_{p=1}^{\infty}(\nu\theta\Delta t\ \nabla^2)^p$, it can be truncated at the N-th order so that to obtain the following approximate inverse operator

$$\tilde{F}_N^{-1} = I + (\nu\theta\Delta t\ \nabla^2) + (\nu\theta\Delta t\ \nabla^2)^2 + \cdots + (\nu\theta\Delta t\ \nabla^2)^N$$

with an obvious reduced sparsity if N increases. Repeating the segregation process with the approximate inverse $\tilde{\mathcal{F}}_N^{-1}$ instead of $\mathcal{F}^{-1}$, and bearing in mind that $\tilde{F}_N^{-1}F = I - B_N = I - (\nu\theta\Delta t\ \nabla^2)^{N+1}$ this yields

$$\begin{pmatrix} I - \mathcal{B}_N & \tilde{\mathcal{F}}_N^{-1}\mathcal{G} \\ -\mathcal{D}\mathcal{B}_N & \mathcal{D}\tilde{\mathcal{F}}_N^{-1}\mathcal{G} \end{pmatrix} \begin{pmatrix} v \\ p \end{pmatrix}^{n+1} = \begin{pmatrix} \tilde{\mathcal{F}}_N^{-1}q \\ \mathcal{D}\tilde{\mathcal{F}}_N^{-1}q - g \end{pmatrix}^{n}.$$

The pressure variables in this system are quasi-segregated since $\mathcal{B}_N$ is different from zero but of the $(N+1)^{th}$ order. Every term with $\mathcal{B}_N$ can be somehow neglected or used to start the iterative method:

$$\begin{pmatrix} I & \tilde{\mathcal{F}}_N^{-1}\mathcal{G} \\ 0 & \mathcal{D}\tilde{\mathcal{F}}_N^{-1}\mathcal{G} \end{pmatrix} \begin{pmatrix} v \\ p \end{pmatrix}^{n+1,i+1} = \begin{pmatrix} \mathcal{B}_N & 0 \\ \mathcal{D}\mathcal{B}_N & 0 \end{pmatrix} \begin{pmatrix} v \\ p \end{pmatrix}^{n+1,i} + \begin{pmatrix} \tilde{\mathcal{F}}_N^{-1}\,q \\ \mathcal{D}\tilde{\mathcal{F}}_N^{-1}q - g \end{pmatrix}^{n}.$$

For every i-iteration step, the following pressure segregated equation has to be solved:

$$\mathcal{D}\tilde{\mathcal{F}}_N^{-1}\mathcal{G}p^{n+1,i+1} = \mathcal{D}\mathcal{B}_N v^{n+1,i} + \mathcal{D}\tilde{\mathcal{F}}_N^{-1}q - g.$$

It is possible to split the approximate inverse operator $\tilde{F}_N^{-1}$ into two parts

$$\tilde{F}_N^{-1} = I + \sum_{p=1}^{N_{lhs}}(\nu\theta\Delta t\ \nabla^2)^p + \sum_{p=N_{lhs}+1}^{N}(\nu\theta\Delta t\ \nabla^2)^p = (I + F_1) + F_2$$

and with such splitting, pressure segregated equation is ready to be solved with the following "nested" iterative scheme indicated with the counter k:

$$\mathcal{D}(I+\mathcal{F}_1)\mathcal{G}p^{n+1,i+1,k+1} = -\mathcal{D}\mathcal{F}_2\mathcal{G}p^{n+1,i+1,k} + \mathcal{D}\mathcal{B}_N v^{n+1,i} + \mathcal{D}\tilde{\mathcal{F}}_N^{-1}q - g.$$

A third nested iterative cycle can be introduced to solve pressure equation finding alternative types of pressure variable ordering to the standard lexicographic, so that the elliptic operator $\mathcal{D}(I+\mathcal{F}_1)\mathcal{G}$ assumes a block-structured pattern. This also allows a parallel resolution for such equation. As a matter of fact the user can choose between a sequential block Gauss-Siedel solver and a parallel block Jacobi solver. This last choice is possible only if the Star-P software has been installed together with Matlab. Star-P is a client-server parallel-computing platform that has been designed to work with high level languages. Several convection schemes have been implemented in PRIN-3D, ranging from simple lagrangian to high order conservative ones with flux limiters, and a new Multilevel Lagrangian Conservative scheme (MLC) has been introduced [2].

3. RESULTS

Three-dimensional geometry handling is one of the toughest steps in a CFD code design. An effort has been made to guarantee the maximum of flexibility with respect to the user's demands in within a not too limited class of 3D domains. The actual version of the code is intended to handle a specific class of three-dimensional domains, *right prisms*. The user defines a basic 2D polygon and the height of the prism which extends along the third dimension. The computational grid is a 3D block-structured grid obtained by a staircase approximation of the user defined boundary geometry and the mesh is evenly spaced ($\Delta x = \Delta y = \Delta z$). The *partially-staggered* grid system appears to be a fair trade off between *colocated* and *staggered* grid systems. Boundary Conditions (BC) available for the velocity's components *u,v,w* are *Dirichlet* (for all faces) and *Extrapolation* (for Outflow faces only) (*Pressure Inlet* and *Neumann* BC are supported in the code but not yet tested). It is also possible to assign *lid driven* faces or even *swirled*. The same kind of BC apply for transported scalars and other model-related quantities (Turbulent Energy K, Energy Dissipation rate ε, Mixture Fraction Z, etc...). One of PRIN-3D numerical applications is the numerical combustion with the flamelet model. Here we present a simulation of a methane-air laminar diffusion flame compared with experimental data obtainable in [3]. The experimental setup consists of a coannular burner made up of a 1.1-cm-diameter fuel tube and a concentric 10.2-cm-diameter air annulus which is used to establish the laminar diffusion flames. The air and fuel flow rates are respectively set to 1300 cm^3/s and 9.8 cm^3/s. The very first simulations of such flame have been carried out with a 2D cartesian geometry. The flames evolve in the y-z plane while spanwise periodic boundary conditions (along the x-direction) are imposed. The simulation numerical data are shown in Table 1. In this 2D simulation the flame surface's position (i.e. the maximum Temperature

$Lx = .01$	$Ly = .15$	$Lz = .8$	`'Periodic'='x-x'`	pres.arrang. 2
$Re_{OX} = 112.44$	$Re_{OXcell} = 1.284$	$numiter_i = 1$	$numiter_k = 1$	$numiter_l = 1$
$ncp = 200715$	$ncpx = 5$	$ncpy = 87$	$ncpz = 463$	$nvel = 438976$

TABLE 1. 2D flame simulation: general data

value contour) is not stationary probably due to the extrapolating outflow boundary conditions. Furthermore as it can be seen in [3] at 7.5 cm the flame should be approximately 1 cm wide. This mismatch can be explained by the 2D nonrealistic approximation. A truly 3D combustion simulation have been

`'rdt'=0.1`	`'rlxFL'=0.1`	$nvel = 392040$	$ncp = 200715$	$ncpx = 67$
$ncpy = 67$	$ncpz = 91$	$Lx = .11$	$Ly = .11$	$Lz = .15$

TABLE 2. 3D flame simulation: general data

also carried out. Axisymmetric boundary conditions (as far as the staircase approximation's limited

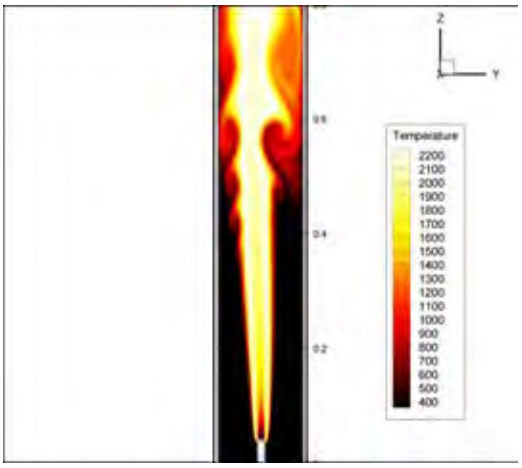

FIG 1. 2D flame temperature profile.

reconstruction capability is concerned) are reproduced. In Table 2 all PRIN-3D numerical parameters of the 3D flame simulation are shown. In this case the flame is steady and the maximum temperature

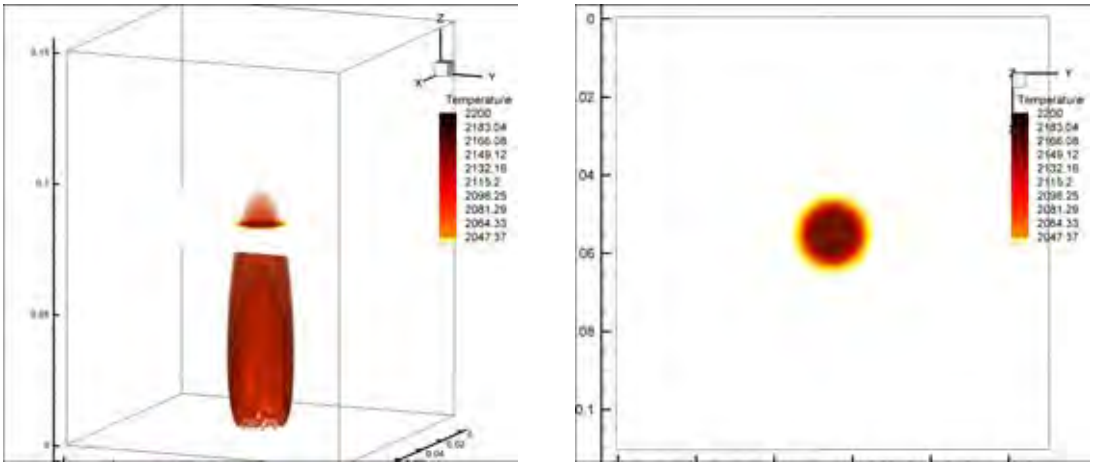

FIG 2. 3D flame temperature isosurfaces with slicing plain at $Z = 0.75$ meters.

profile (flame surface intersection with plane $Z = 0.75$) has approximately a 1 centimeter diameter.

4. CONCLUSIONS

PRIN-3D is an high level algebraical proto-code oriented to the study of new mathematical and numerical models and to the development or optimization of new numerical algorithms. Its numerical solving kernel is based on the quasi-segregation of pressure elliptic equation and subsequent resolution by means of nested iterative processes with parallel capabilities. First non trivial numerical tests show good agreement with experimental data.

REFERENCES

[1] S. Badia and R. Codina, Algebraic Pressure Segregation Methods for the Incompressible Naveri-Stokes Equations, *Arch Comput Methods Eng*, 15, 343-369, 2008.

[2] V.Grazioso, N. Massarotti, C. Meola and C. Scalo, *A Multilevel Lagrangian Conservative scheme - ThermaComp2009*, Submitted abstract.

[3] R. Puri, R. J. Santoro and K. C. Smyth, The Oxidation of Soot and Carbon Monoxide in Hydrocarbon Diffusion Flames, *Combustion and Flames*, 97, 125-144, 1994.

[4] H. Elman, D. Silvester, and A. Wathen, *Finite Elements and Fast Iterative Solvers*, Oxford University Press, 2005.

First International Conference on Computational Methods for Thermal Problems
ThermaComp2009, September 8-10, 2009, Napoli, Italy
N.Massarotti and P.Nithiarasu (Eds.)

POD-BASED REDUCED ORDER DYNAMICAL MODEL OF A CIRCULATING FLUIDIZED BED COMBUSTOR

Katarzyna Bizon
Istituto Ricerche Combustione CNR, Via Diocleziano 328, 80124 Naples, Italy,
katarzyna.bizon@irc.cnr.it

Gaetano Continillo
Department of Engineering, Università del Sannio, Piazza Roma 21, 82100 Benevento, Italy,
gaetano.continillo@unisannio.it

ABSTRACT

Spectral reduction of the 1-D distributed dynamic model of a non isothermal circulating fluidized bed combustor (CFBC) is developed and presented. The continuum model is first approximated by a finite-difference method and integrated in time by means of Adams method to provide a "reference" solution. Then, Proper Orthogonal Decomposition (POD) with Galerkin projection is introduced to derive a reduce order model (ROM). The POD modes are then tested in the low-order approximation of the system evolution. ROM model proves to be effective, being able to reproduce steady-state with a low number of basis functions and significant speed up of the calculation.

Key Words: *Fluidized Bed Combustion Modelling, Model Reduction, Proper Orthogonal Decomposition, Spectral Methods.*

1. INTRODUCTION

The fluidized bed combustion (FBC) technology has many advantages over traditional methods of solid fuel combustion, such as higher process efficiency, fuel flexibility and lower pollution. However, there are still many uncertainties in predicting FBC behaviour, which depends on many operational parameters i.e. excess air, solid properties, geometry of the reactor and many others. Prediction of FBC behaviour and parametric studies can be conducted by means of mathematical models of different levels of complexity [1] – starting from the 1-D plug flow systems to 3D models based on Navier-Stokes equations. However, most of these models, despite of addressing many specific phenomena, are limited to steady state operation. Hence there is still need for mathematical modelling and simulation of the dynamic behaviour of the FB boilers, for example in order to predict the response of the system to sudden changes of process conditions during operation.

It is well recognized that even when the model details are kept to a minimum, in order to emphasize the dynamical aspects, in many cases the complexity of the first principle models of chemically reactive systems require quite significant time of computation. This is caused by a high number of ODEs resulting from the discretization of the original PDEs system. Hence, it is desirable to express the original model as a set of ordinary differential equations of the lowest possible order. Spectral methods, such as for example Galerkin method [2], provide an interesting framework in that, by proper choice of the functional basis, one can reduce the number of ODEs necessary to accurately describe the dynamics of the original PDEs model. One of the possible choices is use of the empirically derived orthogonal basis functions that can be determined by conducting Proper Orthogonal Decomposition (POD) of the spatiotemporal profiles of the system obtained from the full model simulation.

Aim of this work is to report on the development of a 1-D dynamical model of circulating fluidized bed combustor (CFBC), which integrate simplified hydrodynamics, fuel combustion and heat transfer. The model consist of eight mass and heat balance equations. A combination of the Galerkin spectral method with empirical orthogonal basis functions obtained by means of POD is then applied to build a light yet faithful reduced order model (ROM).

2. CFBC MODEL

The circulating fluidized bed system is idealized as a 1-D distributed, unsteady tubular reactor with solids recycle [4]. The quasi-steady approximation is made for interphase momentum exchange. Combustion is modelled as a single one-step heterogeneous reaction ($C+O_2 \rightarrow CO_2$). Moreover, both volatile matter and ash content of the fuel have been neglected and the balance equation for the solids have been limited to fixed carbon lumped into two phases of different particle diameter, namely *coarse* and *fine* char.

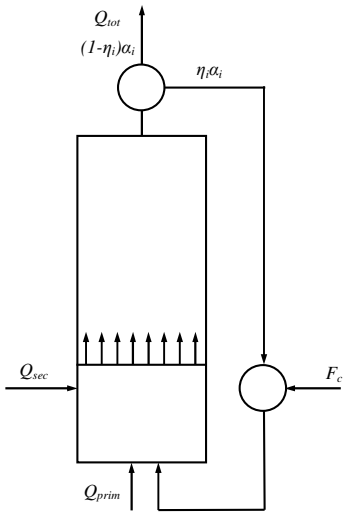

FIGURE 1. Idealized scheme of CFBC

Riser height	H_{ex} [m]	10
Riser diameter	D [m]	1
Temperature	T [K]	1123
Pressure	P [kPa]	101.325
Inert particle diameter	d_b [μm]	300
Inert material density	ρ_b [kg/m^3]	2600
Coarse diameter	d_c [mm]	3
Fine diameter	d_f [μm]	100
Char density	ρ_c [kg/m^3]	1500
Cyclone efficiency for coarse	η_c [-]	1
Cyclone efficiency for fine	η_f [-]	0.9
Slip multiplier for coarse	γ_c [-]	0.5
Slip multiplier for fine	γ_f [-]	1

TABLE 1. Main parameter values

Mass balances, in dimensionless form, for the coarse phase, which is depleted both by combustion and attrition, and for the fine phase, enriched by attrition and depleted by combustion, are given respectively, in dimensionless form, by:

$$\frac{\partial}{\partial} + \frac{\partial(v_c)}{\partial} = - \quad - \quad$$

$$\frac{\partial}{\partial} + \frac{\partial(v_f)}{\partial} = \quad - \quad$$

The mass balances for gas phase, for O_2 and CO_2 , are:

$$\frac{\partial(\quad)}{\partial} + \frac{\partial(v_g \quad)}{\partial} = -k_1(\quad + \quad)$$

$$\frac{\partial(\quad)}{\partial} + \frac{\partial(v_g \quad)}{\partial} = k_1(\quad + \quad)$$

Energy balances for solid phases and gas phase are:

$$\frac{\partial(\quad)}{\partial} + \frac{\partial(v_c \quad)}{\partial} = \quad - \Phi_{c-g} h_c (\quad - \quad) - \quad$$

$$\frac{\partial(\quad)}{\partial}+\frac{\partial(\quad)}{\partial}=\quad-\Phi_{f-g}h_f\quad\left(\quad-\quad\right)+\quad$$

$$\frac{\partial((1-\quad)\quad)}{\partial}+\frac{\partial(\quad(1-\quad)\quad)}{\partial}=-\Phi_{b-g}h_b(1-\quad)\left(\quad-\quad\right)-\Phi_{b-w}h_w\left(\quad-\quad\right)$$

$$\frac{\partial(\quad c_{pg}\quad)}{\partial}+\frac{\partial(\quad c_{pg}\quad)}{\partial}=k_3\Phi_{c-g}h_c\quad\left(\quad-\quad\right)+k_3\Phi_{f-g}h_f\quad\left(\quad-\quad\right)+k_3\Phi_{b-g}h_b(1-\quad)\left(\quad-\quad\right)$$

3. MODEL REDUCTION

The objective of the POD approach is to determine an empirical set of orthogonal functions basing on the spatiotemporal simulation data $u_t(x)$ [3]. Sampled data can be represented, in matrix form:

$$U=\begin{bmatrix} u_1(x_1) & u_2(x_1) & \cdots & u_M(x_1) \\ u_1(x_2) & u_2(x_2) & \cdots & u_M(x_2) \\ \vdots & \vdots & \ddots & \vdots \\ u_1(x_N) & u_2(x_N) & \cdots & u_M(x_N) \end{bmatrix}$$

where N is the number of position in the spatial domain and M is the number of samples taken in time. The POD basis $\Phi=\{\ _1,\ _2,\ldots,\ _N\}$ is then determined by solving the eigenvalue $C\Phi=\ \Phi$, where C is the time-averaged autocorrelation matrix. Using the POD modes, the solution can be then expressed as:

$$\tilde{u}_t(x)=\sum_{k=1}^{K}a_k(t)\ _k(x)$$

where $K<N$ is the number of modes used for truncation and $a_k(t)$ are modal coefficients to be determined by means of Galerkin projection of the system of PDEs onto POD modes.

4. RESULTS

A finite difference method with staggered grid, employing 501 spatial nodes was used for approximation of the PDEs. Then Adams implicit method was used to solve resulting ODEs, in order to build the reference solution and collect the snapshots. Typical sets of equally spaced snapshots from transient and steady state collected during simulation of the full order model for solid density are shown in Figure 2.

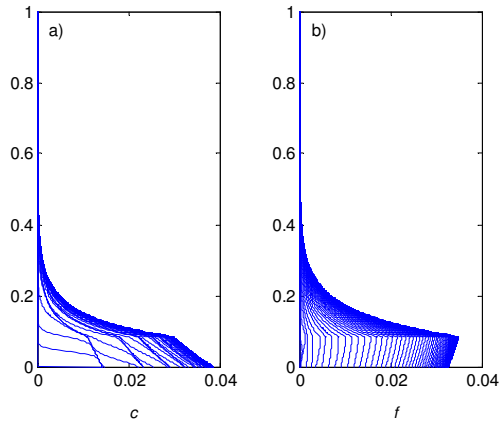

FIGURE 2. Set of snapshots collected for coarse (a) and fine char (b).

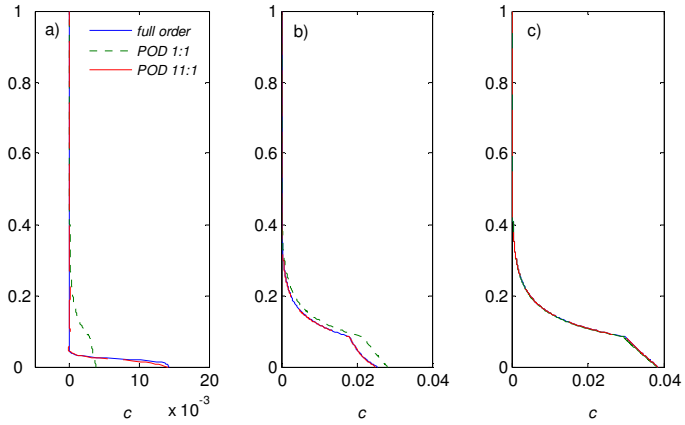

FIGURE 3. Comparison of vertical concentration profile of coarse in early transient and steady state; τ=40 (a), τ=560 (b) and τ=10000 (c).

Following the POD procedure, collected data sets are combined into matrices of snapshots for each state variable separately and manipulated to produce four sets of orthogonal basis. The reduced order model was determined by performing Galerkin projection of the governing equations onto the modes. The resulting ODEs were integrated in time using Adams implicit method as for the full model. Preliminary results referring to isothermal operation are reported here. Axial profiles of coarse char concentration in the early transient and steady state are shown in Figure 3. The cusp in the profiles corresponds to the separation from the dense bed and the freeboard. Two cases are reported: Results from the model obtained by the projection of the PDEs onto one POD mode for each state variable (POD 1:1) and model obtained by the projection of the balances for solids and gas onto 11 and 1 modes (POD 11:1), respectively. POD 1:1 model is unable to capture the solution at the early transient, due to the characteristic shape of the leading POD mode, whereas the higher order model captures quite accurately both transient and steady state behaviour.

5. CONCLUSIONS

A distributed dynamical model of CFBC has been developed for isothermal operation and a POD/Galerkin method has been illustrated and applied to produce reduced order models. We have shown that, at least in the case of non-oscillatory regime, the system can be successfully projected onto just four POD modes, while retaining all qualitative features of the spatial distribution and, to engineering purposes, even quantitatively at steady–state. To provide accurate results in the transient, 24 modes are found to be sufficient.

REFERENCES

[1] P. Basu, Combustion of coal in circulating fluidized-bed boilers: a review, *Chemical Engineering Science,* 54,5547-5557, 1999.

[2] J.S. Hesthaven, S. Gottlieb, D. Gottlieb, *Spectral methods for time dependent problems*, Cambridge University Press, 2007.

[3] P. Holmes, J.L. Lumley, G. Berkooz, *Turbulence, coherent structures, dynamical systems and symmetry*, Cambridge University Press, 1996.

[4] D. Barletta, A. Marzocchella, P. Salatino, S.G. Kang, P.T. Stromberg, Modeling fuel and sorbent attrition during circulating fluidized bed combustion of coal, *17th International Fluidized Bed Combustion Conference, 2003.*

First International Conference on Computational Methods for Thermal Problems
ThermaComp2009, September 8-10, 2009, Napoli, Italy
N.Massarotti and P.Nithiarasu (Eds.)

LOCAL COLLOCATION APPORACH FOR SOLVING TURBULENT THERMO-FLUID PROBLEMS

Robert Vertnik
Technical Development, Štore-Steel, Železarska 3, SI-3220, Štore, Slovenia, robert.vertnik@p-ng.si

Božidar Šarler
Laboratory for Multiphase Processes, University of Nova Gorica, Vipavska 13, SI-5000, Nova Gorica, Slovenia, bozidar.sarler@p-ng.si

ABSTRACT

The application of the mesh-free Local Radial Basis Function Collocation Method (LRBFCM) [1-4] in solution of incompressible turbulent combined forced and natural convection is explored in this paper. The turbulent flow equations are described by the low - Re number $k-$ model with Launder and Sharma [5] closure coefficients. The involved temperature, velocity, pressure, turbulent kinetic energy and dissipation fields are represented on overlapping 5-noded sub-domains through collocation by using multiquadrics Radial Basis Functions (RBF). The involved first and second derivatives of the fields are calculated from the respective derivatives of the RBF's. The involved equations are solved through the explicit time stepping. The pressure-velocity coupling is based on Chorin's fractional step method [6]. The adaptive upwinding technique, proposed by Gu and Liu [7] is used because of the convection dominated situation. The solution procedure is represented in 2D for upward channel flow with differentially heated walls. The results have been assessed by achieving reasonable agreement with the direct numerical simulation of Kasagi and Nishimura [8] for Reynolds number 4494, based on the channel width, and Grashof number 9.6×10^5. The advantages of the represented mesh-free approach are its simplicity, accuracy, similar coding in 2D and 3D, and straightforward applicability in non-uniform node arrangements.

Key Words: *Turbulent Combined Convection, Two-Equation Turbulence Model, Radial Basis Function, Collocation, Meshless Method*

1. INTRODUCTION AND GOVERNING EQUATIONS

The principal goal of the present paper represents the development of the LRBFCM for turbulent thermo-fluid problems. This novel meshless technique [1] has been previously successfully applied to diffusion problems [2], convection-diffusion problems [3], and laminar thermo-fluid problems [4]. Consider a connected fixed domain Ω with boundary Γ filled with a fluid that exhibits incompressible turbulent flow. The flow is described (in a two-dimensional Cartesian coordinate system with base vectors $\mathbf{i}_\varsigma;\varsigma=x,y$ and coordinates $p_\varsigma;\varsigma=x,y$, i.e. position of point $\mathbf{p}$ is determined as $\mathbf{p}=\mathbf{i}_\varsigma p_\varsigma;\ \varsigma=x,y$) by the following time-averaged Reynolds equations for mass, energy, and momentum conservation

$$\frac{\partial v_x}{\partial p_x}+\frac{\partial v_y}{\partial p_y}=0, \qquad c_p\frac{\partial T}{\partial t}+\nabla\cdot\left(c_pT\mathbf{v}\right)=\nabla\cdot\left[\left(+ _t\right)\nabla T\right], \tag{1,2}$$

$$\frac{\partial v_x}{\partial t}+v_x\frac{\partial v_x}{\partial p_x}+v_y\frac{\partial v_x}{\partial p_y}=-\frac{1}{}\frac{\partial p}{\partial p_x}+\frac{\partial}{\partial p_x}\left[\left(+ _t\right)2\frac{\partial v_x}{\partial p_x}\right]+\frac{\partial}{\partial p_y}\left(+ _t\right)\left(\frac{\partial v_x}{\partial p_y}+\frac{\partial v_y}{\partial p_x}\right), \tag{3}$$

$$\frac{\partial v_y}{\partial t}+v_x\frac{\partial v_y}{\partial p_x}+v_y\frac{\partial v_y}{\partial p_y}=-\frac{1}{}\frac{\partial p}{\partial p_y}+\frac{\partial}{\partial p_y}\left[\left(\quad+\quad_t\right)2\frac{\partial v_y}{\partial p_y}\right]+\frac{\partial}{\partial p_x}\left[\left(\quad+\quad_t\right)\left(\frac{\partial v_y}{\partial p_x}+\frac{\partial v_x}{\partial p_y}\right)\right],$$

(4)

with v_x, v_y and T standing for the time averaged velocity components and time averaged temperature, respectively, and p, t, , , $_t$, c_p, and $_t$ are standing for pressure, time, density, molecular kinematic viscosity, turbulent kinematic viscosity, specific heat, molecular thermal conductivity and turbulent thermal conductivity, respectively. Molecular kinematic viscosity is defined as = / where is molecular dynamic viscosity. Turbulent kinematic viscosity is defined as $_t = c\ f\ k^2/$ with c and f standing for closure coefficients of the turbulence model, and k and are the turbulent kinetic energy and dissipation, calculated by the following transport equations

$$\frac{\partial k}{\partial t}+v_x\frac{\partial k}{\partial p_x}+v_y\frac{\partial k}{\partial p_y}=\frac{\partial}{\partial p_x}\left(\quad+\frac{_t}{_k}\right)\frac{\partial k}{\partial p_x}+\frac{\partial}{\partial p_y}\left(\quad+\frac{_t}{_k}\right)\frac{\partial k}{\partial p_y}+P_k-\quad+D\,, \tag{5}$$

$$\frac{\partial}{\partial t}+v_x\frac{\partial}{\partial p_x}+v_y\frac{\partial}{\partial p_y}=\frac{\partial}{\partial p_x}\left(\quad+\frac{_t}{}\right)\frac{\partial}{\partial p_x}+\frac{\partial}{\partial p_y}\left(\quad+\frac{_t}{}\right)\frac{\partial}{\partial p_y}+\left(c_1\ f_1-c_2\ f_2\ \right)\frac{}{k}+E\,, \tag{6}$$

where P_k, D, and E are the shear production of turbulent kinetic energy, source term in k equation and source term in equation, respectively. They are given by $P_k = {}_t\left(2\left(\partial v_x/\partial p_x\right)^2+2\left(\partial v_y/\partial p_y\right)^2+\left(\partial v_x/\partial p_y+\partial v_y/\partial p_x\right)^2\right)$ $D=-2\ \left[\left(\partial\sqrt{k}/\partial p_x\right)^2+\left(\partial\sqrt{k}/\partial p_y\right)^2\right]$, $E=2\ {}_t\left[\left(\partial^2 v_x/\partial p_y^2\right)^2+\left(\partial^2 v_y/\partial p_x^2\right)^2\right]$. The closure coefficients c , f , c_1 , f_1, c_2 , f_2, $_k$ and of the low-Reynolds turbulent model [Launder and Sharma (1974)] are defined as $c\ =0.09$, $f\ =\exp\left[-2.5\left(1+\mathrm{Re}_t/50\right)\right]$, $c_1\ =1.44$, $f_1=1.0$, $c_2\ =1.92$, $f_2=1-0.3\exp\left(-\mathrm{Re}_t^2\right)$, $_k=1.0$, $\quad=1.3$, $_t=0.9$. The turbulent Reynolds number is $\mathrm{Re}_t=k^2/$. The turbulent thermal conductivity is $_t=\ _t\ c_p/\ _t$, where $_t$ is the turbulent Prandtl number. In order to determine the turbulent flow, the system of Eqs.1-6 has to be solved, together with the problem-specific initial and boundary conditions.

2. NUMERICAL METHOD

A suitable model equation of Eqs.1-6, for explaining the numerical method used in this paper, is the general transport equation $\partial/\partial t\left(\ \Phi\right)+\nabla\cdot\left(\ \mathbf{v}\Phi\right)=\nabla\cdot\left(\underline{\mathbf{D}}\nabla\Phi\right)+S$, with $\ ,\Phi,t,\mathbf{v},\underline{\mathbf{D}}$, and S standing for density, transport variable, time, velocity, diffusion matrix, and source, respectively. The solution of the governing equation for the transport variable at the final time $t_0+\Delta t$ is sought, where t_0 represents the initial time and Δt the positive time increment. The representation of function and its derivatives over a set l of (in general) non-equally spaced $_lN$ nodes $_l\mathbf{p}_n;\ n=1,2,...,{}_lN$ is made in the following way $\Phi\left(\mathbf{p}\right)\approx\sum_{k=1}^{_lK}{}_l\ {}_k\left(\mathbf{p}\right){}_l\ {}_k$, $\frac{\partial^i}{\partial p_\varsigma^i}\Phi\left(\mathbf{p}\right)\approx\sum_{k=1}^{_lK}\frac{\partial}{\partial p_\varsigma}{}_l\ {}_k\left(\mathbf{p}\right){}_l\ {}_k;i=1,2,\ \varsigma=x,y$, where ${}_l\ {}_k$ stands for the shape functions, ${}_l\ {}_k$ for

the coefficients of the shape functions, and $_lK$ represents the number of the shape functions. The left lower index l represents the overlapping sub-domain $_l\Omega$ on which the coefficients $_{l\ k}$ are determined. Each of the sub-domains $_l\Omega$ includes $_lN$ grid-points of which $_lN_\Omega$ are in the domain and $_lN_\Gamma$ are on the boundary. The coefficients are calculated from the sub-domain nodes by collocation. The radial basis functions, such as multi-quadrics $_k(\mathbf{p})=\left[(\mathbf{p}-\mathbf{p}_k)\cdot(\mathbf{p}-\mathbf{p}_k)+c^2\right]^{1/2}$ can be used for the shape function, where c represents the shape parameter. The general transport equation can be transformed into the following expression $\Phi=(\ _0/\ )\Phi_0-(\Delta t/\ )\nabla\cdot(\ _0\mathbf{v}_0\Phi_0)+(\Delta t/\ )\nabla\cdot(\underline{\mathbf{D}}_0\nabla\Phi_0)+(\Delta t/\ )S_0$, by taking into account the explicit discretization, from which the unknown function value Φ_n in grid-point $\mathbf{p}_n$ can be explicitly evaluated. The involved derivatives are calculated through the described RBF collocation. The details of the novel numerical method are described in [1-4]. Fractional step method [6] is used for solving the pressure-velocity coupling, and the adaptive upwinding is used in the collocation of the velocity derivatives [7].

3. NUMERICAL EXAMPLE

The geometry of the problem is a vertical channel of width Δ and height h, $h/\Delta=120$. The flow with constant uniform velocity and temperature is entering into the channel at the bottom and leaving the channel at the top. Vertical walls are kept at different (left wall hot, right wall cold), but constant temperatures. At the outlet, the flow is assumed to be fully developed. The forced flow and the buoyancy force drive the flow upward near the hot wall (adding flow at the left wall), and downward near the cold wall (opposing flow at the right wall). The Reynolds number based on the channel width is set to 4494, and the Grashof number based on the temperature difference between the vertical walls and the channel width is 9.6×10^5. The non-uniform node arrangement with 13847 nodes (81x171 nodes – 4 corner nodes) and $\Delta t=0.001\mathrm{s}$ is used. Node arrangement is adapted near the walls to achieve the position of the first point to be in the range $y^+\le5$. y^+ is the non-dimensional distance from the wall $y^+=xu\ /\ $, u is the friction velocity and x is the distance from the vertical wall. Friction velocity is $u\ =\sqrt{\ _w/\ }$ and the wall shear stress is $_w=\ \partial v_y/\partial x$. The results are compared with the results obtained by the DNS [8]. Fig. 1 represents the mean dimensionless velocity profile $u^+=v_y/u$ of the fully developed flow in wall coordinates, and dimensionless temperature profile $T^+=(T_w-T)/T$, with T_w and T standing for wall temperature and friction temperature $T\ =q_w/\ c_pu_t$ (q_w is the heat flux at the wall), respectively.

3. CONCLUSIONS

This paper probably for the first time represents the solution of the incompressible turbulent thermo fluid problem by a meshless method. The low-Re k- model with the closure coefficients proposed by Launder and Sharma (1974) is used. The novel numerical solution is based on the local collocation with the radial basis functions for spatial disretization and first order (backward Euler) explicit method for time discretization. Due to its locality and explicit time stepping, the method is very appropriate for parallelization. The partial differential equations are solved in their strong formulation and no integrations are needed. The transition from two-dimensional to three-dimensional cases is quite straightforward. The results were compared with the DNS for problem of

combined forced and natural convection with a very good agreement. In the future, the method will be extended to cope with the turbulent flow with solidification, as encountered in the continous casting of steel. With this, the new LRBFCM will most probably achieve a reasonable maturity and technological relevance.

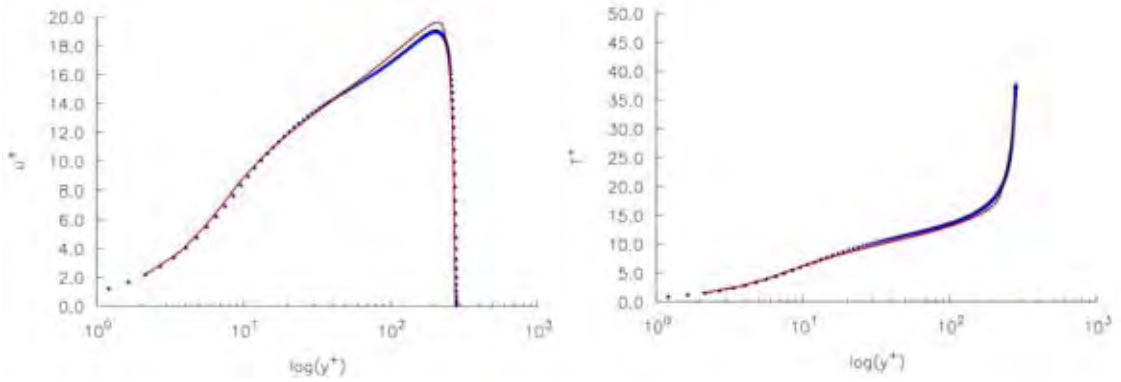

Figure 1: Mean dimensionless velocity profile (left) and dimensionless temperature (right) of the opposing flow in wall coordinates. Blue stars-DNS solution [8], solid red line-present LRBFCM.

Acknowledgement: The authors would like to express their gratitude to Slovenian Technology Agency (RV) and Slovenian Research Agency (BŠ) for funding of the represented research.

REFERENCES

[1] B. Šarler, From Global to Local Radial Basis Function Collocation Method for Transport Phenomena, in: V.M.A. Leitao, C.J.S. Alves, C. Armando-Duarte, *Advances in Meshfree Techniques, (Computational Methods in Applied Sciences, Vol.5)*, Springer Verlag, Dordrecht , 257-282, 2007.

[2] B. Šarler, and R.Vertnik, Meshfree local radial basis function collocation method for diffusion problems, *Computers and Mathematics with Application*, 51, 1269-1282, 2006.

[3] R.Vertnik, and B.Šarler, Meshless local radial basis function collocation method for convective diffusive solid-liquid phase change problems, *International Journal of Numerical Methods in Heat and Fluid Flow*, 16, 617-640, 2006.

[4] G. Kosec, and B.Šarler, Solution of heat transfer and fluid flow problems by the simplified explicit local radial basis function collocation method, *International Journal of Numerical Methods for Heat & Fluid Flow*, Vol. 18, pp. 868-882, 2008.

[5] B.E. Launder**,** and B.I. Sharma, Application of the energy-dissipation model of turbulence to the calculation of flow near a spinning disc. *Letters in Heat and Mass Transfer*, 1, 131–138, 1974.

[6] A.J. Chorin, A numerical method for solving incompressible viscous flow problems, *Journal of Computational Physics*, 2, 12-26, 1967.

[7] Y.T. Gu, G.R. Liu, G.R. Meshless technique for convection dominated problems. *Computational Mechanics*, 38, 171-182, 2005.

[8] N. Kasagi, and M. Nishimura, Direct numerical simulation of combined forced and natural turbulent convection in a vertical plane channel, *International Journal for Heat and Fluid Flow*, 18, 88-99, 1997.

First International Conference on Computational Methods for Thermal Problems
ThermaComp2009, September 8-10, 2009, Naples, Italy
N.Massarotti and P.Nithiarasu (Eds.)

Immersed volume method for radiative heat transfer: Theory and validation

T. Kloczko
École des Mines de Paris, Centre de Mise en Forme des Matériaux (CEMEF), UMR CNRS 7635,
Sophia-Antipolis, France.
Thibaud.Kloczko@mines-paristech.fr
E. Hachem
Elie.Hachem@mines-paristech.fr
T. Coupez
Thierry.Coupez@mines-paristech.fr

ABSTRACT

The moment-based models coupled to our immersed volume method (IVM) are considered in order to simulate radiative fields and their interactions with the matter in the context of the heat treatment of industrial parts. This first presentation aims at introducing the basics of the IVM and validating the radiation hydrodynamic coupling on academic cases.

Key Words: *Radiative heat transfer, P-1 approximation, M-1 model, stabilized Finite Elements, immersed volume method, anisotropic mesh adaptation, level set function.*

1. INTRODUCTION

Radiative transfers are involved in many industrial applications but the resolution of the full radiative transfer equation is often too expensive. In recent years, new alternatives were proposed to derive cheaper models which overcome the deficiencies of the simplest methods such as the so called P-1 approximation [1]. The M-1 model presented in [2] enables in particular to preserve the shadow cone in transparent region. On the other hand, the numerical simulation of heat transfers in industrial applications often require the knowledge of exchange coefficients to ensure, as a boundary condition, the heat transfer at the fluid/solid interface. For instance, the convective and radiative heat exchanges at the contact interface Γ_i between a fluid and a solid is usually computed as follows:

$$F_C = \int_{\Gamma_i} h_c \left(T - T_{\text{ext}}\right) \mathrm{d}\Gamma \quad \text{and} \quad F_R = \int_{\Gamma_i} \sigma_r \varepsilon \left(T^4 - T_{\text{ext}}^4\right) \mathrm{d}\Gamma \tag{1}$$

where h_c is the convective heat transfer coefficient, T_{ext} is the averaged temperature of the surroundings, and ε is the emissivity of the solid. However, the assessment of coefficients h_c and ϵ can become a prohibitive task since it needs experimental data and often requires solving many inverse problems. It can be therefore a limiting issue for practical applications especially when one needs to change the geometry of the treated parts, the physical parameters, the number and the position of the parts, the surrounding fluid (air, water, etc.).

An alternative to circumvent this drawback is to consider single grid for both the fluid and the solid for which only one set of equations need to be solved. This technique, known as immersed volume method (IVM), makes the use of a signed distance function that allows turning thermodynamic properties of each component into homogeneous parameters. In this way, there is no need of empirical data so as to determine the exchange coefficients.

The present work aims at coupling the moment-based models and the IVM to compute coupled radiative hydrodynamic flows.

2. MATHEMATICAL MODELS

2.1. **Hydrodynamics equations.** Let $\Omega \subset \mathbb{R}^d$, $d = 2, 3$, be the spatial computational domain with boundary $\partial\Omega$. The computation of the heat transfer and the fluid flow requires to solve simultaneously the Navier-Stokes and energy equations:

$$(2) \qquad \begin{cases} \boldsymbol{\nabla} \cdot \mathbf{u} = 0 & \text{in } \Omega \\ \rho\left(\partial_t \mathbf{u} + \mathbf{u} \cdot \boldsymbol{\nabla}\mathbf{u}\right) - \boldsymbol{\nabla} \cdot \left(2\mu\, \dot{\boldsymbol{\gamma}}(\mathbf{u}) - p\, \mathbf{I_d}\right) = \rho_0 \beta (T - T_0)\, \mathbf{g} & \text{in } \Omega \end{cases}$$

where $\mathbf{u}$ is the velocity vector, ρ the density, p the pressure, T the temperature, μ the dynamic viscosity, $\dot{\boldsymbol{\gamma}}(\mathbf{u}) = (\boldsymbol{\nabla}\mathbf{u} + {}^t\boldsymbol{\nabla}\mathbf{u})/2$ the deformation-rate tensor, ρ_0 and T_0 reference density and temperature, β the thermal expansion coefficient and $\mathbf{g}$ the gravity vector. The heat transfers are governed by the energy equation:

$$(3) \qquad \rho C_p(\partial_t T + \mathbf{u} \cdot \boldsymbol{\nabla} T) - \boldsymbol{\nabla} \cdot (\lambda \boldsymbol{\nabla} T) = f - \boldsymbol{\nabla} \cdot \mathbf{F}_{\mathrm{R}} \quad \text{in } \Omega$$

where T is still the temperature, C_p the constant pressure heat capacity, λ the specific conductivity, f a source term and $\mathbf{F}_{\mathrm{R}}$ the radiative heat flux.

2.2. **Moment-based models for radiative transfer.** In order to close the system (2)-(3), the divergence of the radiative heat flux is needed. To achieve this, the grey medium approximation is assumed and two approaches are considered:

i) The well-known P-1 approximation [1] gives rise to the radiative energy E_{R} equation as follows:

$$(4) \qquad \boldsymbol{\nabla} \cdot \left(-\frac{c}{3\kappa}\, \boldsymbol{\nabla} E_{\mathrm{R}}\right) + \kappa c E_{\mathrm{R}} = 4\kappa\sigma_r T^4 \ \text{ in } \ \Omega$$

with c the speed of light, κ the mean absorption coefficient and σ_r the Stefan-Boltzmann constant. The divergence of the radiative heat flux is then computed through:

$$(5) \qquad \boldsymbol{\nabla} \cdot \mathbf{F}_{\mathrm{R}} = 4\kappa\sigma_r T^4 - \kappa c E_{\mathrm{R}}$$

ii) The M-1 model [2] involves two equations coupling the radiative energy and the radiative flux:

$$(6) \qquad \boldsymbol{\nabla} \cdot \mathbf{F}_{\mathrm{R}} + \kappa c E_{\mathrm{R}} = 4\kappa\sigma T^4 \ \text{ in } \ \Omega \quad \text{and} \quad \boldsymbol{\nabla} \cdot (c E_{\mathrm{R}} \mathbb{D}) + \kappa \mathbf{F}_{\mathrm{R}} = 0 \ \text{ in } \ \Omega$$

where $\mathbb{D}$ is the Eddington tensor defined by:

$$(7) \qquad \mathbb{D} = \frac{1-\chi}{2}\, \mathbb{I} + \frac{3\chi - 1}{2}\, \frac{\mathbf{f} \otimes \mathbf{f}}{||\mathbf{f}||^2} \quad \text{with} \quad \mathbf{f} = \frac{\mathbf{F}_{\mathrm{R}}}{c E_{\mathrm{R}}} \quad \text{and} \quad \chi = \frac{3 + 4\,||\mathbf{f}||^2}{5 + 2\sqrt{4 - 3\,||\mathbf{f}||^2}}\,,$$

$\mathbb{I}$ is the identity tensor, $\mathbf{f}$ the normalized flux and χ the Eddington factor.

A stabilized Finite-Element method [3] is used to solve the coupled systems (2)-(3)-(4) and (2)-(3)-(6). The presentation will bring further details on this part.

3. IMMERSED VOLUME METHOD

The immersed volume method is based on three key ingredients, namely a signed distance or level set function, an anisotropic mesh adaptation procedure and the use of appropriate mixing laws. The contact interface between fluid and solid is represented using the zero level of a smooth signed distance function. Let Ω_f, Ω_s and Γ_i be respectively the fluid domain, the solid domain and the interface such that $\Omega_f \cup \Omega_s = \Omega$ and $\Omega_f \cap \Omega_s = \Gamma_i$. For each node of the computational domain Ω, the level set function α which is the signed distance from the interface reads:

$$(8) \qquad \alpha(\mathbf{x}) > 0 \text{ if } \mathbf{x} \in \Omega_f, \quad \alpha(\mathbf{x}) = 0 \text{ if } \mathbf{x} \in \Gamma_i, \quad \alpha(\mathbf{x}) < 0 \text{ if } \mathbf{x} \in \Omega_s.$$

The sharp variations of physical and thermodynamic properties across the interface are taken into account using a smooth Heaviside function given by:

$$(9) \qquad H(\alpha) = 1 \text{ if } \alpha > \varepsilon\,, \quad H(\alpha) = 0.5\left(1 + \alpha/\varepsilon + 1/\pi \sin\left(\frac{\pi\alpha}{\varepsilon}\right)\right) \text{ if } |\alpha| \le \varepsilon\,, \quad H(\alpha) = 0 \text{ if } \alpha < -\varepsilon$$

where ε is a small parameter such that $\varepsilon = O(h)$, with h the averaged mesh size in the vicinity of the interface. Then, the global material properties introduced in the previous section, such as density,

initial temperature, dynamic viscosity, constant pressure heat capacity, mean absorption coefficient, are defined as follows:

$$\varphi = \varphi_f H(\alpha) + \varphi_s(1 - H(\alpha)) \quad \text{with} \quad \varphi = \rho,\ \mu,\ \kappa,\ \rho C_p,\ \rho C_p T. \tag{10}$$

As far as the thermal conductivity is concerned, one has to resort to the following law to ensure the conservation of the heat flux:

$$\lambda = (H(\alpha)/\lambda_f + (1 - H(\alpha))/\lambda_s)^{-1} \tag{11}$$

Accurate calculation of the temperature distribution along the fluid-solid interface is critical for a correct modelling of industrial experiments. If the interface is not aligned with the element edges, it may intersect the element arbitrarily such that the accuracy of the finite element approach can be compromised. In order to circumvent this issue, the level set process is coupled with an anisotropic mesh adaptation as described in [4]. The mesh becomes locally refined which enables to sharply define the interface and to save a great number of elements compared to classical isotropic refinements. This anisotropic adaptation resorts to a so-called metric which is a symmetric positive defined tensor representing a local base that modify the distance computation, such that:

$$||\mathbf{x}||_{\mathrm{M}} = \sqrt{{}^t\mathbf{x} \cdot \mathbf{M} \cdot \mathbf{x}}\,, \quad < \mathbf{x}, \mathbf{y} >_{\mathrm{M}} = {}^t\mathbf{x} \cdot \mathbf{M} \cdot \mathbf{y}\,. \tag{12}$$

The metric $\mathbf{M}$ can be regarded as a tensor whose eigenvalues are related to the mesh sizes, and whose eigenvectors define the directions for which these sizes are applied. For instance, using the identity tensor, one recovers the usual distances and directions of the Euclidean space. In our case the direction of mesh refinement is given by the unit normal to the interface which corresponds to the gradient of the level set function: $\mathbf{x} = \nabla\alpha/||\nabla\alpha||$. A default mesh size, or background mesh size, h_d is imposed far from the interface and it is reduced as the interface comes closer. A likely choice for the mesh size evolution is the following:

$$h = h_d \ \text{ if } |\alpha(\mathbf{x})| > e/2\,, \quad h = \frac{2h_d(m-1)}{m\,e}|\alpha(\mathbf{x})| + \frac{h_d}{m} \ \text{ if } |\alpha(\mathbf{x})| \leq e/2 \tag{13}$$

Eventually, at the interface, the mesh size is reduced by a factor m with respect to the default value h_d. Then this size increases until equalling h_d for a distance that corresponds to the half of a given thickness e. The unit normal to the interface $\mathbf{x}$ and the mesh size h defined above, lead to the following metric:

$$\mathbf{M} = C\,(\mathbf{x} \otimes \mathbf{x}) + \frac{1}{h_d}\,\mathbf{I_d} \quad \text{with} \quad C = \begin{cases} 0 & \text{if } |\alpha(\mathbf{x})| \geq e/2 \\ \dfrac{1}{h^2} - \dfrac{1}{h_d^2} & \text{if } |\alpha(\mathbf{x})| < e/2 \end{cases} \tag{14}$$

where $\mathbf{I_d}$ is the identity tensor. This metric corresponds to an isotropic metric far from the interface (with a mesh size equal to h_d for all directions) and to an anisotropic metric near the interface (with a mesh size equal to h in the direction $\mathbf{x}$ and equal to h_d in the others). In practice, the mesh is generated in several steps using, through the CIMLIB library, the MTC mesher and remesher [4]. The figure 1 shows the result of a refinement process applied to a 2D square body immersed in a cavity.

FIGURE 1. Mesh adaptation process from an isotropic distribution to an adapted anisotropic mesh in the vicinity of the interface.

The mesh is gradually refined orthogonally to the interface. In this way, additional nodes are added in this region only, while the rest of domain keeps the same background size.

4. NUMERICAL VALIDATION

4.1. **Conduction and radiation heat transfer.** A circular solid, initially at a temperature of $T = 1000°C$, is cooled in presence of air at atmospheric conditions. The transient is computed using two different methods. The first one consists in treating the solid as a single entity (*cf.* figures 2(a)). The radiative exchange with the surrounding air is computed by the means of the exchange coefficients previously presented. The second method is our immersed volume technique. The body is immersed

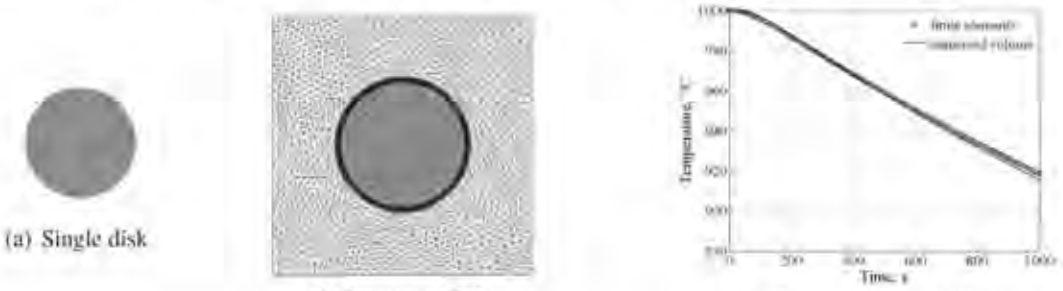

(a) Single disk (b) Immersed disk (c) Temperature evolution

FIGURE 2. Comparison of computational domains and temperature evolution for each method.

inside a square cavity filled by the air. The remeshing process coupled to the level set function enables to capture accurately the air-solid interface as shown in figures 2(b). The radiative exchange is naturally taken into account inside the equation without need of any coefficient. The comparison of the temperature evolution in figure 2(c) shows a good agreement between both methods validating the proposed IVM.

4.2. **Free streaming radiative beam.** During the talk, we will also consider the case of a free streaming beam adjacent to some section of dense, opaque material (*cf.* fig. 3) in order to compare both P-1 and M-1 approaches when shade phenomenon is at stake.

FIGURE 3. Free streaming beam adjacent to an opaque material.

5. CONCLUSIONS

A newly method coupling moment-based model for radiation and immersed volume technique has been proposed. The IVM enables to avoid the tricky definition of heat exchange coefficients while moment models allows to take radiative effects into account with a very good accuracy.

REFERENCES

[1] M. F. Modest, *Radiative Heat Transfer*, Mc Graw Hill, New York, 1993.

[2] B. Dubroca and J.-L. Feugeas, *Hiérarchie de modèles aux moments pour le transfert radiatif*, C. R. Acad. Sci., Série I. pp 915-920, tome 334, Paris.

[3] E. Hachem, E. Massoni and T. Coupez, *Immersed volume technique for solving natural convection, conduction and radiation of a hat-shaped disk inside an enclosure*, 15th Int. Conf. on Finite Elements in Flow Problems, Tokyo, 2009.

[4] C. Gruau and T. Coupez, *3D Tetrahedral, Unstructured and Anisotropic Mesh Generation with Adaptation to Natural and Multidomain Metric*, Comput. Methods Appl. Mech. Engrg., v194, pp 4951-4976, 2005.

First International Conference on Computational Methods for Thermal Problems
ThermaComp2009, September 8-10, 2009, Napoli, Italy
N.Massarotti and P.Nithiarasu (Eds.)

UNIFIED INTEGRAL TRANSFORMS IN CONVECTION-DIFFUSION: THE UNIT CODE WITH SYMBOLIC COMPUTATION

Renato M. Cotta and Carolina P. Naveira-Cotta
Mechanical Eng. Dept., POLI & COPPE, Universidade Federal do Rio de Janeiro, Brasil

Leandro A. Sphaier
Mechanical Eng. Dept., Universidade Federal Fluminense, Niteroi, RJ, Brasil

João N. N. Quaresma
Chemical Eng. Dept., Universidade Federal do Pará, Belém, PA, Brasil

ABSTRACT

The present work summarizes the development of a mixed symbolic-numerical computational code that provides unified solutions for partial differential equations via integral transforms. The reported research was performed by making use of the symbolic computation platform *Mathematica 7.0* and the hybrid numerical-analytical methodology Generalized Integral Transform Technique – GITT, in accurately handling coupled partial differential equations, readily applicable to heat and fluid flow formulations. The aim is to illustrate detailed modeling and robust simulation of various problems in steady and transient convection-diffusion, and providing a brief tutorial of this open source code of symbolic computations in heat and fluid flow.

Key Words: *Integral Transforms, Symbolic Computation, Heat Transfer, Convection, Diffusion.*

1. INTRODUCTION

This contribution is part of a wider project titled "UNIT Project: Hybrid Methods in Engineering and Multiphysics" headed by the Federal University of Rio de Janeiro (COPPE/UFRJ), which is in synthesis a coordinated effort towards consolidating and constructing computational simulation tools based on hybrid numerical-analytical methodologies for multiphysics engineering problems.

The second half of the 20th century, due to the increasing availability of computational performance based on both the hardware enhancement and numerical methods development, witnessed the continuous advancement of the role of computational simulation in physical sciences analysis and engineering design. Discrete numerical methods for differential equations were responsible for most of the simulation of processes and prototypes, which are nowadays accomplished technologies, and are the most frequently employed in commercial software for multipurpose use. While commercial simulation packages based on purely numerical methods are still far from perfect in terms of cost-effectiveness, reliability, flexibility, and accuracy, their presence in routine tasks of academia, industry and consulting companies is an undeniable fact, which, in turn, brings an increasing demand for improvements. Recently, for instance, software manufacturers are being pressed to move into multiphysics systems, by integrating different computational platforms even originated from different companies, which are being progressively merged.

The analytical-type approaches were not, however, fully abandoned during this period of the computer boom. Rather they were advanced, unified and further formalized by a few research groups [1]. These researchers were in part motivated since they could be useful to the technological revolution on numerical methods then under progress, by offering benchmark results for validation and calibration of numerical schemes. Most important, however, these researchers made contributions by producing the theoretical background for bridging new developments on hybrid analytical-numerical approaches. In this context, a number of hybrid methodologies have appeared

in the open literature, that, to within different degrees of success, attempt to match the classical analytical ideas with the present knowledge basis on numerical analysis, in the search for more accurate, robust and economical options to the now well-established discrete solution methods.

For instance, this period has witnessed the development of a hybrid method for solving diffusion and convection-diffusion problems, called the Generalized Integral Transform Technique (GITT) [2-6], which was progressively advanced to overcome barriers posed by different classes of problems that were before supposed to be handled solely by discrete-type methods. Those include, among others in the heat and fluid flow field, nonlinear physical properties, moving boundaries, irregular geometries, boundary layer equations and the Navier-Stokes equations. This technique naturally evolved from the classical analytical approach, bringing up a more flexible and applicable methodology than the classical one. The relative merits of such an approach over purely numerical procedures include the automatic global accuracy control feature and the mild increase on computational cost for multidimensional nonlinear situations. The GITT adds to the available simulation tools, either as a companion in co-validation tasks, or as an alternative approach for analytically oriented users. In addition, hybrid methods become even more powerful and applicable when making use of symbolic manipulation systems, which were widely disseminated along the last two decades as well. The present hybrid approach has been progressively implemented within mixed symbolic-numerical environments, allowing for a marked reduction on formula derivation and analysis effort while providing integrated algorithms for numerical computations and graphical representation. From this experience, the goal became to conduct an effort to integrate the knowledge on a multipurpose computational code, here named UNIT (UNified Integral Transforms), which would initially be intended to bridge the gap between simple problems that allow for a straightforward analytical solution, and those more complex and involved situations that unavoidably require expensive commercial software systems. Rather than a market oriented user friendly software, the open source UNIT code is thus an implementation and development platform for researchers and engineers interested on hybrid integral transform solutions of convection-diffusion problems.

2. PROBLEM FORMULATION

As an illustration of the class of problems handled by the formal integral transform procedure, a transient convection-diffusion problem of *n* coupled potentials (for instance velocity, temperature or concentrations) is considered. These parameters are defined in the region *V* with boundary surface *S* and including non-linear effects in the convective and source terms as follows:

$$w_k(\boldsymbol{x})\frac{\partial T_k(\boldsymbol{x},t)}{\partial t} = \nabla K_k(\boldsymbol{x})\nabla T_k(\boldsymbol{x},t) - d_k(\boldsymbol{x})T_k(\boldsymbol{x},t) + P_k(\boldsymbol{x},\mathrm{t},\mathrm{T}_\ell),$$

$$\boldsymbol{x}\in \mathrm{V},\quad \mathrm{t}>0,\quad \mathrm{k},\ell = 1,2,...,\mathrm{n} \tag{1.a}$$

with initial and boundary conditions given, respectively, by

$$T_k(\boldsymbol{x},0) = f_k(\boldsymbol{x}),\qquad \boldsymbol{x}\in \mathrm{V} \tag{1.b}$$

$$\left[\quad _k(\boldsymbol{x}) + \quad _k(\boldsymbol{x})K_k(\boldsymbol{x})\frac{\partial}{\partial \boldsymbol{n}}\right]T_k(\boldsymbol{x},t) = \ _k(\boldsymbol{x},t,\mathrm{T}_\ell),\qquad \boldsymbol{x}\in S,\qquad \mathrm{t}>0 \tag{1.c}$$

where $\boldsymbol{n}$ denotes the outward-drawn normal to the surface S.

Equations (1) are sufficiently general once all nonlinear and convection terms are grouped within the equations and boundary source terms. For linear source terms, i.e., $P \equiv P(\boldsymbol{x},t)$, and $\equiv$ $(\boldsymbol{x},t)$, this example becomes a class I linear diffusion problem according to the classification in [1]. Exact analytical solutions were in this situation obtained through the classical integral transform technique. Otherwise, this problem is not *a priori* transformable, and the ideas in the generalized integral transform technique [2-10] can be utilized to develop hybrid numerical-analytical solutions

to this class of problem. Following the solution path previously established for convection-diffusion and purely diffusive non-linear problems, the formal solution of the posed nonlinear problem requires the proposition of eigenfunction expansions for the associated potentials. The linear situation above commented that allows for an exact solution via the classical integral transform approach, naturally leads to the eigenvalue problems to be preferred in the analysis of the nonlinear situation as well. They appear in the direct application of separation of variables to the linear homogeneous purely diffusive version of the above problem. Thus, the recommended set of auxiliary problems is given by

$$\nabla K_k(\boldsymbol{x})\nabla \quad _{ki}(\boldsymbol{x}) + [\ ^{2}_{ki} w_k(\boldsymbol{x}) - d_k(\boldsymbol{x})]\ _{ki}(\boldsymbol{x}) = 0, \qquad \boldsymbol{x} \in V \tag{2.a}$$

$$\left[\ _{k}(\boldsymbol{x}) + \ _{k}(\boldsymbol{x}) K_k(\boldsymbol{x}) \frac{\partial}{\partial \boldsymbol{n}} \right] \ _{ki}(\boldsymbol{x}) = 0, \qquad \boldsymbol{x} \in \mathrm{S} \tag{2.b}$$

where the eigenvalues, $_{ki}$, and related eigenfunctions, $_{ki}(\boldsymbol{x})$, are assumed to be known from exact analytical expressions or application of computational methods for Sturm-Liouville type problems [1,2]. The problem indicated by Eqs.(2.a,b) allows, through the associated orthogonality property of the eigenfunctions, definition of the integral transform pairs [2]. Then, the integral transformation of the partial differential system (1) results in a coupled system of ordinary differential equations for the transformed potentials. Once the transformed potentials have been computed from numerical solution of the ODE system, the inversion formula is recalled to reconstruct the original potentials $T_k(\boldsymbol{x},t)$, in explicit form.

3. RESULTS AND DISCUSSION

The constructed UNIT code encompasses all of the symbolic derivations that are required in the GITT formal solution, besides the numerical computations that are required in the solution of the eigenvalue problem and the transformed ODE system. The user essentially needs to specify the problem formulation, according to eqs.(1), and then choose how to present results according to the specific needs. The coefficients in the transformed system can be obtained by analytical integration, if feasible, or by the automatic adaptive numerical integration available in the *Mathematica* system. An alternative semi-analytical integration procedure is also implemented, which is particularly convenient in nonlinear formulations that might require costly numerical integration. For instance, the integral transformation of the equation source term for homogeneous filtered boundary conditions would then be evaluated as:

$$\overline{g}_{ki}(t,T_l) = \int_v \tilde{}_{ki}(\boldsymbol{x}) P_k(\boldsymbol{x},t,\mathrm{T}_\ell) dv = \sum_{m=1}^{M} \int_{v_m} \tilde{}_{ki}(\boldsymbol{x}) \hat{P}_{k,m}(\boldsymbol{x},t,\mathrm{T}_\ell) dv \tag{3}$$

where $\hat{P}_{k,m}(\boldsymbol{x},t,\mathrm{T}_\ell)$ are simpler representations of the source term, defined in sub-regions $\mathrm{V_m}$, for which analytical integration of the eigenfunctions is still obtainable. Several previously solved problems by GITT have been revisited to test and evaluate the general procedure that has been constructed, and we have here chosen the nonlinear Burgers equation example [7] to illustrate the UNIT code behaviour. The mathematical formulation of the problem here considered is:

$$\frac{\partial\ T(x,t)}{\partial\ \mathrm{t}} + u(T)\frac{\partial T(x,t)}{\partial\ \mathrm{x}} = \quad \frac{\partial^2 T(x,t)}{\partial \mathrm{x}^2}\ , \qquad 0<x<1, \qquad t>0 \tag{4.a}$$

$$T(x,0)=1\ , \qquad 0 \le x \le 1 \tag{4.b}$$

$$T(0,t)=1\ ; \qquad T(1,t)=0\ , \qquad \mathrm{t}>0 \tag{4.c,d}$$

and for the present application the non-linear function $u(T)$ is taken as:

$$u(T) = u_o + bT \tag{4.e}$$

Table 1 illustrates the behavior of the UNIT code solution, for N=30 terms in the eigenfunction expansion, and different number of sub-regions in the semi-analytical integration (M=60, 120, 180 and 240) with a linear representation of the source term, so as to demonstrate the adequacy of this enhancement in the algorithm introduced in the present implementation. The results are compared for typical values of the governing parameters $t = 0.1\,(u_o = 1.0;\ \ b = 0.5\ and\ 5.0;\quad = 1.0)$ where the increase in the parameter b is offered to enhance the nonlinear effect in the formulation. The last two columns correspond to results already reported in ref.[7], corresponding to the GITT solution also with N=30 but with analytical integration, and the discrete solution by the Method of Lines then obtained from the NDSolve routine of the *Mathematica* system under default precision control. One may conclude that only for the case with M=60 sub-regions in the analytical integration, the numerical results from the UNIT code start changing in the last significant digit provided, with respect to the fully converged solution of ref.[7], offering a reliable and automatic integral transform solution of the proposed problem, with more accuracy than the NDSolve solution.

M / *x*	60	120	180	240	GITT [7]	Numerical*
$t = 0.1(u_o = 1.0;\ \ b = 0.5;\quad = 1.0)$						
0.1	0.98463	0.98462	0.98462	0.98462	0.98462	0.98461
0.3	0.93245	0.93243	0.93243	0.93243	0.93243	0.93238
0.5	0.81774	0.81773	0.81772	0.81772	0.81772	0.81764
0.7	0.59405	0.59404	0.59404	0.59403	0.59403	0.59395
0.9	0.23099	0.23099	0.23099	0.23099	0.23099	0.23095
$t = 0.1(u_o = 1.0;\ \ b = 5.0;\quad = 1.0)$						
0.1	0.99851	0.99851	0.99851	0.99851	0.99851	0.99851
0.3	0.98900	0.98898	0.98897	0.98897	0.98897	0.98896
0.5	0.94776	0.94772	0.94771	0.94771	0.94771	0.94769
0.7	0.79328	0.79328	0.79328	0.79328	0.79328	0.79324
0.9	0.35416	0.35424	0.35425	0.35426	0.35426	0.35423

TABLE 1. Convergence of UNIT code solution (GITT with N=30 terms in eigenfunction expansion) varying the number of sub-regions in semi-analytical integration (M).
*Function NDSolve, *Mathematica* (default precision).

REFERENCES

[1] M.D. Mikhailov and Ozisik, M.N., *Unified Analysis and Solutions of Heat and Mass Diffusion*, John Wiley, New York, 1984; also, Dover Publications, 1994.

[2] R.M. Cotta, Hybrid Numerical-Analytical Approach to Nonlinear Diffusion Problems, *Num. Heat Transfer, Part B*, 127, 217-226, 1990.

[3] R.M. Cotta, *Integral Transforms in Computational Heat and Fluid Flow*, CRC Press, FL, 1993.

[4] R.M. Cotta, Benchmark Results in Computational Heat and Fluid Flow: - The Integral Transform Method, *Int J. Heat & Mass Transfer* (Invited Paper), 37, Suppl. 1, 381-394, 1994.

[5] R.M. Cotta and M.D. Mikhailov, *Heat Conduction: Lumped Analysis, Integral Transforms, Symbolic Computation*, Wiley-Interscience, Chichester, UK, 1997.

[6] R.M. Cotta and M.D. Mikhailov, Hybrid Methods and Symbolic Computations, in: *Handbook of Numerical Heat Transfer*, 2nd edition, Chapter 16, Eds. W.J. Minkowycz, E.M. Sparrow, and J.Y. Murthy, John Wiley, New York, 2006.

[7] R. Serfaty and R.M. Cotta, Hybrid Analysis of Transient Nonlinear Convection-Diffusion Problems, *Int. J. Num. Meth. Heat & Fluid Flow*, 2, 55-62, 1992.

First International Conference on Computational Methods for Thermal Problems
ThermaComp2009, September 8-10, 2009, Napoli, Italy
N.Massarotti and P.Nithiarasu (Eds.)

TRANSPORT OF HIGH VISCOSITY OIL IN LONG PIPELINES

Terje Sira[1], Dag Lindholm[1], Bin Hu[1], Gunnar Flaten[2], Steinar Øyulvstad[3], Olav Sendstad[1], Peter Borg[1] and Knud Lunde[2]

[1] Institute for Energy Technology, P.O. Box 40, NO-2027 Kjeller, Norway.
[2] StatoilHydro ASA, NO-0246 Oslo, Norway.
[3]Aker Solutions, P.O. Box 94, NO-1324 Lysaker, Norway.

terje.sira@ife.no, dag.lindholm@ife.no, bin.hu@ife.no, gunnarfl@statoilhydro.no, steinar.oyulvstad @akersolutions.com, olav.sendstad@ife.no, peter.borg@ife.no and knudl@statoilhydro.no

ABSTRACT

Detailed computation of the free convection heat loss in heavy oil transport lines typically involves extreme grid aspect ratios, since the pipe length to diameter ratio may be of the order of 100000. In order to remedy this situation, we use a scaling technique for the equations. Using this technique we are able to do realistic simulations on very long pipelines. Some of these results are shown.

Key Words: *Heat Transfer, Natural Convection, High Viscosity, Laminar Flow.*

1. INTRODUCTION

Heavy oil often has such a high viscosity that the oil flow through a transport pipeline can be laminar. Moreover, the oil viscosity often varies strongly with temperature. Typically the oil is fairly hot at the pipe inlet and is then cooled gradually towards the ambient temperature along the pipe. How fast the oil is cooled will then determine the pressure drop. Correct modelling of the heat loss to the surroundings is therefore very important.

When the main flow is laminar, heat is transported from the oil to the pipe wall through free convection flow in the pipe cross section. The free convection velocities are typically of the order of fractions of a mm/s, while the typical transport velocities in the axial direction are of the order of 1 m/s. Moreover, in the cross section the velocities and temperature will vary over length scales of some mm to some cm, while variations in the axial direction will typically be over a length scale of some km.

Computation of the steady state temperature and velocity fields along the pipeline is a parabolic problem; the velocities and temperatures in a cross section can be computed based on the velocities and temperatures in the upstream cross section. However, due to practical considerations and the slow variation in the axial direction, we would typically like a grid-spacing of the order of 100 m in the axial direction. The huge grid aspect ratio in this situation gives rise to numerical problems. In order to remedy this situation, we use a scaling of the equations, where we effectively do the computations on a much shorter pipeline. This scaling is valid under very reasonable assumptions.

Using this scaling we are able to do robust, realistic and fast simulations for real pipelines. Studies have been done for two pipelines in the North Sea. The first study was for a 220 km pipeline, which now is in operation. The simulations done for this pipeline were instrumental for the choice of the transport concept. The second study was for a field development project with a potential 50 km transport line.

This work describes the applied methodology and the assumptions made for the scaled set of

equations. A verification of the method is followed by simulation results for highly viscous oil transported in a 220 km long pipeline.

2. METHODOLOGY

In the three-dimensional CFD simulations the problem is solved using a set of scaled equations that are valid for laminar flow. Both the length of the pipe and the flow rate in the pipe are reduced with a factor c. From the computed solution the solved variables are scaled back to a solution for the real pipe. The equations are expressed in a Cartesian coordinate system: x_1 is the coordinate in the pipe axial direction, x_2 and x_3 are coordinates in the pipe cross section, with x_3 being the vertical direction.

The scaling assumptions are:

- The transient terms and the convective momentum transfer term are ignored.
- We ignore the axial velocity gradients in the viscous term in the Navier-Stokes equation and the axial heat conduction.
- The pressure in the pipe can be written as an average pressure over the pipe cross section plus a deviation pressure, i.e. $p(x_1, x_2, x_3) = \overline{p}(x_1) + p_d(x_1, x_2, x_3)$. We ignore the deviation pressure when evaluating the pressure gradient in the axial pipe direction.

Based on these assumptions we get the following set of un-scaled equations:

$$\frac{\partial \overline{p}}{\partial x_1} - \left(\frac{\partial}{\partial x_2}\mu\frac{\partial}{\partial x_2} + \frac{\partial}{\partial x_3}\mu\frac{\partial}{\partial x_3}\right)\cdot u_1 = 0 \qquad \frac{\partial p}{\partial x_2} - \left(\frac{\partial}{\partial x_2}\mu\frac{\partial}{\partial x_2} + \frac{\partial}{\partial x_3}\mu\frac{\partial}{\partial x_3}\right)\cdot u_2 = 0$$

$$\frac{\partial p}{\partial x_3} - \left(\frac{\partial}{\partial x_2}\mu\frac{\partial}{\partial x_2} + \frac{\partial}{\partial x_3}\mu\frac{\partial}{\partial x_3}\right)\cdot u_3 - \rho\cdot g = 0 \qquad \frac{\partial u_1}{\partial x_1} + \frac{\partial u_2}{\partial x_2} + \frac{\partial u_3}{\partial x_3} = 0$$

$$\rho\cdot c_p\cdot\left(u_1\frac{\partial T}{\partial x_1} + u_2\frac{\partial T}{\partial x_2} + u_3\frac{\partial T}{\partial x_3}\right) = \left(\frac{\partial}{\partial x_2}\lambda\frac{\partial}{\partial x_2} + \frac{\partial}{\partial x_3}\lambda\frac{\partial}{\partial x_3}\right)T + S$$

In the above equations g is the gravity, c_p is the specific heat capacity, S is a source term for frictional heat dissipation, T is the temperature, u_i is the velocity component in the direction x_i, is the density, is the thermal conductivity and is the dynamic viscosity. Assuming that p, u_i and T are a solution to the equations shown above, we define a new solution that includes a scaling parameter c. This solution is based on the following scaling:

$$\tilde{p}(x_1, x_2, x_3) = c^{-2}\cdot\overline{p}(cx_1) + p_d(cx_1, x_2, x_3) \qquad \tilde{\overline{p}}(x_1) = c^{-2}\cdot\overline{p}(cx_1)$$

$$\tilde{u}_1(x_1, x_2, x_3) = c^{-1}u_1(cx_1, x_2, x_3) \qquad \tilde{u}_2(x_1, x_2, x_3) = u_2(cx_1, x_2, x_3)$$

$$\tilde{u}_3(x_1, x_2, x_3) = u_3(cx_1, x_2, x_3) \quad \tilde{T}(x_1, x_2, x_3) = T(cx_1, x_2, x_3) \quad \tilde{S}(x_1, x_2, x_3) = S(cx_1, x_2, x_3)$$

This scaled solution is then inserted into the set of un-scaled equations, and we see that if (p, u_i, T) is a solution, then ($\tilde{p}, \tilde{u}_i, \tilde{T}$) is also a solution. The final set of scaled equations becomes:

$$\frac{\partial \overline{p}(cx_1)}{\partial cx_1} - \left(\frac{\partial}{\partial x_2} \quad \frac{\partial}{\partial x_2} + \frac{\partial}{\partial x_3} \quad \frac{\partial}{\partial x_3}\right)\cdot u_1(cx_1, x_2, x_3) = 0$$

$$\frac{\partial p_d(cx_1, x_2, x_3)}{\partial x_2} - \left(\frac{\partial}{\partial x_2} \quad \frac{\partial}{\partial x_2} + \frac{\partial}{\partial x_3} \quad \frac{\partial}{\partial x_3}\right)\cdot u_2(cx_1, x_2, x_3) = 0$$

$$\frac{\partial p_d(cx_1, x_2, x_3)}{\partial x_2} - \left(\frac{\partial}{\partial x_2} \quad \frac{\partial}{\partial x_2} + \frac{\partial}{\partial x_3} \quad \frac{\partial}{\partial x_3}\right)\cdot u_3(cx_1, x_2, x_3) - \quad \cdot g = 0$$

$$\frac{\partial u_1(cx_1,x_2,x_3)}{\partial cx_1}+\frac{\partial u_2(cx_1,x_2,x_3)}{\partial x_2}+\frac{\partial u_3(cx_1,x_2,x_3)}{\partial x_3}=0$$

$$\rho\cdot c_p\cdot\left[u_1(cx_1,x_2,x_3)\frac{\partial T(cx_1,x_2,x_3)}{\partial cx_1}+u_2(cx_1,x_2,x_3)\frac{\partial T(cx_1,x_2,x_3)}{\partial x_2}+\right.$$

$$\left.u_3(cx_1,x_2,x_3)\frac{\partial T(cx_1,x_2,x_3)}{\partial x_3}\right]=\left(\frac{\partial}{\partial x_2}\ \frac{\partial}{\partial x_2}+\frac{\partial}{\partial x_3}\ \frac{\partial}{\partial x_3}\right)T(cx_1,x_2,x_3)+S(cx_1,x_2,x_3)$$

A parabolic solver is applied to calculate the steady-state condition. Buoyancy is modelled by means of the well-known Boussinesq approximation. The scaling approach is adapted to the commercial available CFD software Phoenics [1].

3. RESULTS AND DISCUSSION

Two different simulations, with a scale factor of 10 and 100 respectively, were used to verify the method of scaling. In Figure 1 the resulting pressure and temperature profiles are shown for a 90 km long pipeline. The agreement is in overall very good, although a slight discrepancy is seen in the pressure in the first part of the pipe. This is believed to be caused by entrance effects which do not scale according to the scale factors used.

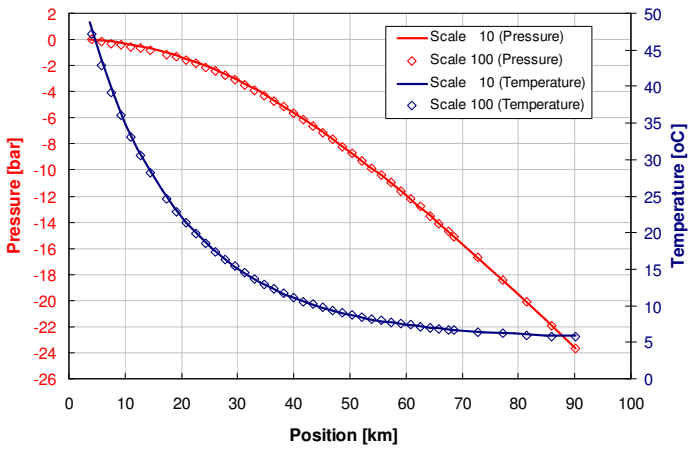

FIGURE 1. Pressure and temperature profiles based on different scale factors.

The approach developed in this paper has been applied to two viscous oil pipelines in the North Sea. Figure 2 shows the typical temperature and velocity fields obtained in the single-phase laminar flow simulations. Of most importance is the stratification behaviour of the fluid; a cold layer is formed at the bottom with hot liquid flowing above. Stronger convection effects are seen in the hot layer. This stratification behaviour clearly demonstrates that a 1D model with an average heat loss coefficient to the surroundings would be inappropriate, although such models are commonly used today for oil pipeline design.

Accurate prediction of temperature variation and pressure drop along a long viscous oil pipeline is crucial for correct design. During transport of highly viscous fluid, flows are initially turbulent due to low viscosity at high export temperature and gradually become laminar as the temperature drops along the line. In this study, the turbulent flow region has been simulated by the commercial software OLGA [2], which uses a 1D heat transfer model accepted widely in the literature. The additional mixing in turbulent flow significantly reduces the cross-sectional temperature variation. The laminar flow region is simulated using the scaling approach described above. Figure 3 illustrates the temperature and pressure profiles obtained in a 220 km long pipeline for given export

temperature (90 ºC) and pressure (120 bara). It also shows the extent of the turbulent/transition flow zone and the laminar flow zone. The decreases in pressure and temperature from inlet to outlet are in better agreement with the field data (not shown) than a general 1D model.

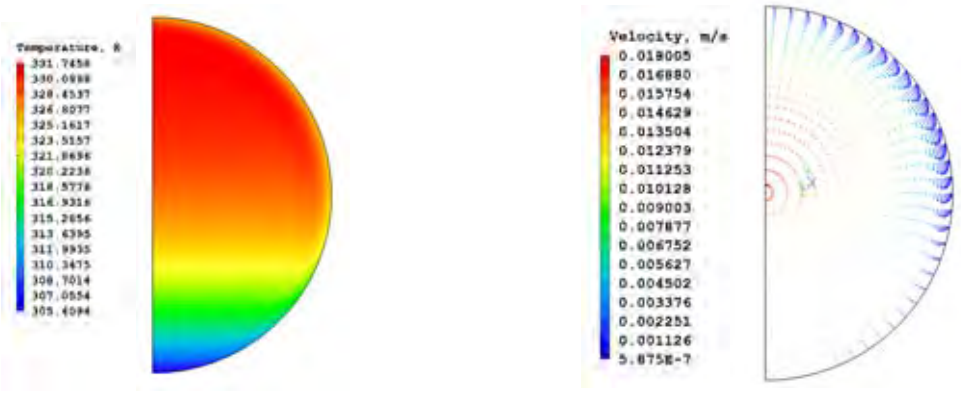

(a) (b)

FIGURE 2. Typical temperature distributions (a) and velocity vector fields (b).

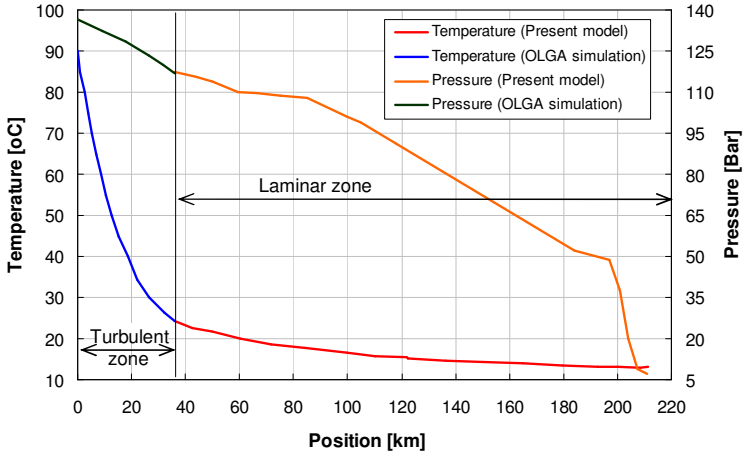

FIGURE 3. Typical temperature and pressure profiles along a long viscous oil pipeline.

4. CONCLUSIONS

Highly viscous oils are difficult both to produce and to transport. The pressure drop in the pipeline should be as low as possible to limit the pump power and to enable long transport distances. Such oils typically have a viscosity that depends strongly on the temperature. This, combined with the natural convection that takes place as the oil is slowly cooled down, makes such flow conditions challenging to simulate. In this work a special scaling technique has been presented that enables the heat and fluid flow in the full-scale pipeline to be represented by a significantly shorter pipeline with unchanged pipe diameter. This technique both promotes convergence of the problem and significantly reduces the consumed computer time. The scaling method has been verified and used for simulation on two pipelines in the North Sea with good results.

REFERENCES

[1] Concentration, Heat and Momentum Limited (CHAM), London, UK. Website: www.cham.co.uk
[2] Bendiksen K.H., Malnes D., Moe R. and Nuland S. - The Dynamic Two-Fluid Model OLGA: Theory and Application. SPE Production Engineering, 1991, pp 171-180.

First International Conference on Computational Methods for Thermal Problems
ThermaComp2009, September 8-10, 2009, Naples, Italy
N.Massarotti and P.Nithiarasu (Eds.)

Improving of Parameter Estimates Obtained from the Thermal Response Tests

T.V. Bandos
Instituto Universitario de Matemática Pura y Aplicada, Universidad Politécnica de Valencia,
Camino de Vera s/n, 46022 Valencia, Spain, tbandos@uv.es

Á. Montero
Departamento de Física Aplicada, Universidad Politécnica de Valencia,
Camino de Vera s/n, 46022 Valencia, Spain, almonter@upvnet.upv.es

J.F. Urchueguía
Instituto Universitario de Matemática Pura y Aplicada, Universidad Politécnica de Valencia,
Camino de Vera s/n, 46022 Valencia, Spain, jfurchueguia@fis.upv.es

P.J. Fernández de Córdoba
Instituto Universitario de Matemática Pura y Aplicada, Universidad Politécnica de Valencia,
Camino de Vera s/n, 46022 Valencia, Spain, pfernandez@mat.upv.es

ABSTRACT

This paper compares the solution to the three dimensional finite line source model for ground coupled borehole heat exchangers with thermal response test data, taking into account the heat transfer to the ambient air. Also infinite line source model is applied. To estimate effective thermal conductivity of the ground surrounding borehole fitting of model temperature time dependence to the experimental data is carried out on the base of regression analysis.

Key Words: *Geothermal borehole heat exchangers, convection-diffusion equation, regression analysis*

1. INTRODUCTION

Thermal response test (TRT) is designed to measure *in-situ* ground thermal conductivity for sizing ground source heat pump systems. These in situ tests are based on studying of the thermal response of the borehole heat exchanger (BHE) to a constant heat injection or extraction. The outputs of the TRT are the inlet and outlet temperatures of the heat carrier fluid as a function of time. From these experimental data, and with an appropriate model describing the heat transfer problem between the fluid and the ground, the thermal conductivity of the surroundings is inferred.

Evaluating TRT data based on the Kelvin's infinite line-source (ILS) model assumes that i) there is no heat transfer between the heat carrier fluid and the ambient air, and ii) there are no significant effects of boundary conditions for the vertical temperature profile in the ground surrounding the borehole heat exchanger. It is difficult to thermally insulate external parts of the test rig completely; there is often heat transfer between the ambient and the fluid: depending on air temperature the heat carrier fluid can gain or loss heat to the ambient. This may influence the estimate of the ground thermal conductivity. In this paper, results of measurements are compared to the finite-length corrections for the average ground temperature from the finite line-source (FLS) model (Bandos et al, 2009).

Strong influence of the diurnal temperature on the measured fluid temperature was pointed repeatedly and this study addresses this effect on the estimation of the thermal conductivity of the ground. In order to obtain more reliable results from the TRT measurements comparison based on the ILS model and the FLS model is carried out for intermediate times of the experiment. The main objective is to

apply finite size corrections for the average borehole temperature from the finite line source model to the experimental data after removing the unwanted atmospheric effect on the parameter estimates.

In addition, the influence of length of data interval on the thermal conductivity estimation is presented.

In this extended abstract, it is described a new method of field data preprocessing to estimate the ground thermal conductivity by making use of the regression technique.

2. Line-Source Theory

Within the infinite line-source (ILS) approach commonly applied for the estimates of thermal response test data, the ground is assumed to be a homogeneous infinite medium characterized by its thermal conductivity λ. In the surroundings of the borehole the results of the infinite line-source model for sufficiently large time values give

$$T(r,t) = T_0 - \frac{q_z}{4\pi\lambda} Ei(-\frac{r^2}{4\alpha t}) \approx \frac{q_z}{4\pi\lambda}\left\{ln\frac{4\alpha t}{r^2} - \gamma + O\left(\frac{r^2}{4\alpha t}\right)\right\} + T_0, for \frac{4\alpha t}{r^2} >> 1 \qquad (1)$$

The function $Ei(u)$ denotes the exponential integral, q_z is heat flow per length unit, γ is Euler's constant, α is ground thermal diffusivity and T_0 is identified with the undisturbed ground temperature. It is usually assumed that the heat is released at a constant rate from the borehole heat exchanger (BHE), in the 'radial' direction orthogonal to it, and is transferred by the mechanism of thermal conductivity.

In the frame of the finite line-source (FLS) model in the semi-infinite region, the approximation of the ground temperature, averaged along the BHE, for the times corresponding to the TRT was proposed by Bandos et al. (2009). The average ground temperature response for $t_z >> t >> \frac{r^2}{4\alpha}$ is given by

$$< T(r,z,t) - T_0 >= \frac{q_z}{4\pi\lambda}\left\{ln\frac{4\alpha t}{r^2} - \gamma - \frac{3}{\sqrt{\pi}}\sqrt{\frac{4t}{t_z}} + \frac{3r}{H} - \frac{3}{\sqrt{\pi}}\frac{r^2}{H^2}\sqrt{\frac{t_z}{4t}}\right\}, \qquad (2)$$

where $t_z = H^2/\alpha$ is the characteristic axial scale of time, and H is the depth of the borehole.

3. Analysis of TRT data: climatic effect on parameter estimates.

In the data acquisition system the apparatus used to monitor the thermal response is connected to the BHE by insulated 1-m long tubes. The field test was performed on the borehole with radius r_b of 0.15m, and $H = 25$m. Figure 1a illustrates correlation between changes of measured fluid temperature and

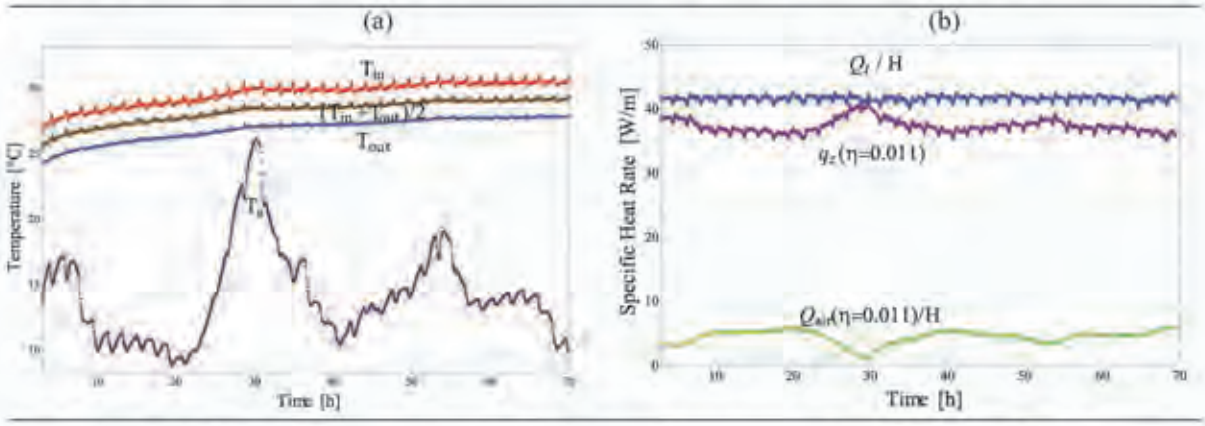

FIGURE 1. *(a) Influence of varying ambient air temperature (purple line) on the average fluid (brown line) temperature in the injection mode. (b) Measured total heat rate Q_t (blue line), variable heat rate $q_z H$ transferred to ground (purple line), Q_{air} calculated with the fitting parameter $\eta = 0.011$ (green line) vs time.*

temperature of the air. To provide the constant heat rate (of 1000 W as shown in Fig.1b), the difference between temperature of the circulating fluid on the input and output of the ground loop were hold constant as well as the volume flow rate of fluid, G. The test parameters were monitored every 3 minutes by a data logger. Figs.1 present the plots of 1418 readings after data averaging over 30 points. In the numerical calculations the ground thermal diffusivity α in Eqs.(1, 2) was set equal to $1.21\ 10^{-6} m^2/s$. Although pipes connecting the test rig with the borehole are insulated, undesirable correlation between the air temperature and the mean temperature of fluid is usually observed (as also shown in Figure 1a). Heat exchange between the air and the pipe work connecting the test rig with the borehole changes the

heat transferred to the borehole because of the heat dissipated outside the BHE. Then, total heat rate Q_t can be written as $Q_t = Q_{air} + q_z H$, where Q_{air} is the heat rate transferred to the ambient air, and $q_z H$ is the actual heat rate transferred to the ground. Besides diurnal variations of the air temperature, the interior temperatures of the test rig affect the efficiency of the system operation.

The fluid temperature changes with coordinate along the plastic pipes outside the borehole due to the undesirable heat exchange with the ambient air. At the quasi steady-state case, the heat transport by the fluid along the pipes, accompanied by the transverse heat flux to the air, is governed by the convection equations (Hellström, 1991). To account for climatic influence the dimensionless parameter η is used hereafter; it appears in the solution of the convection equations for T_{in} (T_{out}), the fluid input (output) temperature at the point of the external pipe on the ground surface level, and can be calculated using physical parameters of the fluid, flow rate of the heat carrier, the thermal resistance for the heat flow from fluid to the air, the length of the pipe between the point of measurement of the fluid temperature at the test rig and the corresponding point, at which the flow upwards/downwards the subsurface. This parameter influences both the heat rate and mean fluid temperature $\overline{T_f}$ as:

$$q_z(\eta, t)H = C_f G(2T_a(t)\sinh\eta - e^{\eta}T^*_{out} + e^{-\eta}T^*_{in}), \tag{3}$$
$$\overline{T_f}(\eta, t) = (T_{out}(t) + T_{in}(t))/2 = T_a(t)(1 - \cosh\eta) + (e^{\eta}T^*_{out} + e^{-\eta}T^*_{in})/2,$$

where T^*_{in} (T^*_{out}) corresponds to the fluid temperature at the point of measurement related to the input (output) of the borehole. Fig.1b shows that $q_z(\eta, t)H$ and $Q_{air}(t)$ change with time, but Q_t remains the same by keeping the temperature difference $T^*_{in} - T^*_{out}$ constant during the TRT.

To estimate the effective thermal conductivity, time-dependence of the ground temperature approximation is compared with time-dependence of the measured fluid temperature. The parameter λ of the ILS model depends on the η through the late time slope k of the linear approximation in the semi-logarithmic scale for the experimental $\overline{T}_f(ln(t))$ curve and mean $q_z(\eta; t)$ as $\lambda =< q_z(\eta; t) >_t /(4\pi k(\eta))$, where $\langle \dots \rangle_t$ denotes time averaging. A lower heat injection rate gives a lower estimate value for the ground thermal conductivity.

On the pre-processing stage of the test analysis, the model parameter η is to be evaluated. The energy rate balance and model set the relationship between η and p-th part of the total heat rate transmitted to the air, $\langle Q_{air} \rangle_t = p\langle Q_t \rangle_t$, as $\eta = p\langle T^*_{in}(t) - T^*_{out}(t) \rangle_t / \langle T^*_{out}(t) + T^*_{in}(t) - 2T_a(t) \rangle_t$ if the heat loss to the ambient is a small part of the total injected heat rate ($p << 1$), i.e. for small η values. One can use the above equation to select η. There is some arbitrariness involved in exact quantity of the total measured heat rate is transferred to the ambient air. The idea behind the proposed method of preprocessing TRT data is to use the freedom in choosing η to suppress the influence of the air temperature oscillations. The effect of the air temperature variation is mitigated for $T_{out}(t)$ if the fitting parameter η is set equal to 0.011 given $p = 0.1$, so that the fluid temperature of outward flow from the borehole $T_{out}(t)$ appears to be a sufficiently smooth function of time, see Fig.1a.

On the next stage, when fitting $T_b = T(r = r_b, t)$ to the experimental data for the mean heat carrier temperature, the thermal resistance R_b between the borehole wall and the fluid must be taken into account,

$$R_b C_f G(T_{in} - T_{out}) = R_b(Q_t - Q_{air}(t))/H = \overline{T_f}(\eta, t) - T_b(t), \tag{4}$$

where C_f is the volumetric heat capacity of fluid. Notice that the borehole temperature T_b is influenced by the measured fluid temperatures T^*_{in}, T^*_{out} and $T_a(t)$ through the $Q_{air}(t)$ that is $Q_{air}(t) \approx 2\eta C_f G((T^*_{in} + T^*_{out})/2 - T_a(t))$ for small η values. The thermal resistance parameter R_b is also obtained from the TRT. Below the proposed formulas for substraction of climatic influence on the TRT are applied to the parameter estimation analysis and the results of these application are presented.

4. RESULTS

The assessment of the late-time TRT data allows to estimate λ and to obtain extrapolated value for T_0 (Hellström, 1991). The statistical theory is used to analyze test data, when estimating the regression parameters (Hastie et al, 2001). The data obtained from the 71-h TRT were evaluated and compared by making use of the ILS and FLS models along with the introduced method of account for the heat transfer to the ambient characterized by η. To find suitable model parameters, Eqs.(1,2), are matched to the heat carrier fluid temperature data by using regression; the average heat rate, $< q_z(\eta, t) >_t$, is applied when heat rate variations of $q_z(\eta, t)$ are caused by $T_a(t)$ fluctuations as described before.

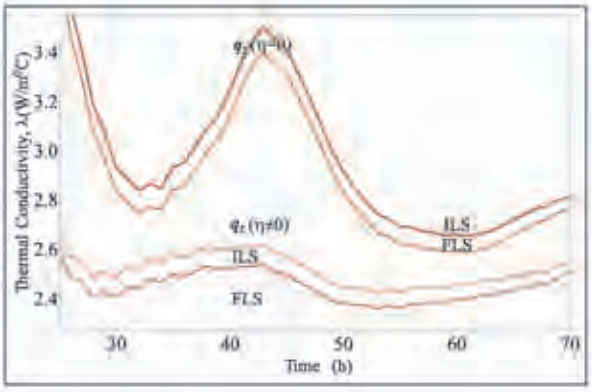

FIGURE 2. *Comparison between dependence of thermal conductivity from the ILS (red line) and FLS (orange line) model on the time estimation interval for the same test data. Estimates of thermal conductivity based on the ILS and FLS models when the end of the evaluation interval is fixed, while starting time increases: (i) without heat loss to the ambient ($\eta = 0$)- solid lines (ii) with heat loss to the ambient ($\eta = 0.011$)- dot-dashed lines.*

Figure 2 compares the λ values estimated from both the ILS and FLS models on different length of data interval of the same test, for $\eta = 0$ and $\eta = 0.011$. Transient early-time data influenced by borehole itself, i.e. by its geometry, thermal properties of the tubes, grout and fluid are omitted. Fig.2 reveals the cyclicity in the temperature response for $\eta = 0$ because of influence of the outside perturbation: small changes in the fluid temperature curve are significantly amplified for λ that is inverse to its time derivative. Fig.2 also shows that these fluctuations are almost disappear for $\eta \neq 0$, $R_b \approx 0.09 m^\circ C/W$ when using three parameter regression. Therefore, the developed method successfully removes cyclic distortions caused by the diurnal temperature cycle.When energy loss to the air is absent, the values of λ calculated from both ILS and FLS models are higher than ones evaluated with the proposed method of decoupling climatic influence from the TRT data; this is the effect of the heat transfer to the ambient. For $\eta \neq 0$ as well as for $\eta = 0$, the comparison between the results of finite line-source and infinite line-source models based on the TRT data shows that the effective thermal conductivity value of ground is overestimated by the ILS model (Bandos et al, 2009).

5. CONCLUSIONS

In this paper the effect of the finite size corrections on the evaluation of the ground thermal conductivity has been studied on a data set and the method of subtraction of the influence of outside perturbations has been developed. Parameter estimation from the test data has shown that the ground thermal conductivity is lower, when accounting dissipation on the external pipes of the test rig for the heat injection regime. Removal of climatic effect from the test data successfully damps oscillations of ground conductivity with increasing length of the time series. This holds true for both calculations made in the frame of infinite and finite line-source models. In agreement with the preliminary study in (see Bandos et al, 2009), the leading order depth corrections for the mean borehole temperature result in decreasing ground thermal conductivity estimate from test data, with or without accounting for climatic effect, and improve accuracy of the evaluation.

REFERENCES

[1] T. Hastie, R. Tibishirani and J. Friedman, *The Elements of Statistical Learning*, Springer-Verlag New York, NY, USA, 2001, pp. 536.

[1] G. Hellström, *Thermal Analysis of Duct Storage System*, Dep. of Mathematical Physics, University of Lund, Sweden, 1991, pp. 536.

[2] T.V. Bandos, Á. Montero, E. Fernández, J.L.G. Santander, J.M. Isidro, J. Pérez, P.J. Fernández de Córdoba and J.F. Urchueguía, *Finite line-source model for borehole heat exchangers: effect of vertical temperature variations*, Geothermics, 38, 2009, pp. 263-270.

First International Conference on Computational Methods for Thermal Problems
ThermaComp2009, September 8-10, 2009, Napoli, Italy
N.Massarotti and P.Nithiarasu (Eds.)

Sensitivity Analysis of Horizontal Air-Ground Heat Exchangers

Paolo Maria Congedo, Leda Bonfantini, Simone Occhilupo

University of Salento, Department of Engineering for Innovation, via per Arnesano, I-73100 Lecce, Italy, e-mail: paolo.congedo@unisalento.it

ABSTRACT

This work will assess the performance of an horizontal air-ground heat exchangers (HAGHEs), varying the depth of burial and the air mass flow rate. The comparison will be done through simulations in the CFD code Fluent 6.3. Two depths of burial and four mass flow rates have been investigated, depth of 2.5 and 3.5 meters and mass flow rates of 150-250-350-450 m^3/h, respectively. The analysis shows that there is no substantial difference changing depth, although a burial at a depth of 3.5 meters involves cost certainly more of a burial at a depth of 2.5 meters.

Key Words: *Air-Ground, heat exchanger, heat pumps, geothermal.*

1. INTRODUCTION

The energy consumptions reduction and the following decrease of CO_2 emissions are the first priority for the environment preservation and industrial development. Despite of international and national regulations about this issue, such as Kyoto Protocol, the social cost of greenhouse gas emissions and the deployment of fossil energy sources have led to a critical point. This work explores the potential of horizontal air-ground heat exchangers to reduce the energy consumption of ventilation and air conditioning systems. It has been already demonstrated that the substitution of traditional air coupled heat pumps with Ground Source Heat Pump (GSHPs) results in a good reduction of CO_2 emissions (Genchi et al., 2002) and a good return of the investment in the case of large size applications such as commercial buildings (Starace et al., 2005). The consumption and emissions reduction compared to traditional heat pump is due to the increase of COP in GSHP system, both in summer and in winter (Lazzarin, 2001). Also the HAGHEs can show good performance in terms of high efficiency of the total system and low environmental impact, operating on the ventilation air, in particular with passivhaus building (Congedo et al., 2008). The main cost for the installation of HAGHEs is comparable to GSHPs cost, due to drilling cost (Bloomquist, 2001). Ground temperature variations are damped and phase delayed, compared to the air temperature ones, because of the ground thermal inertia and heat capacity (higher than air) and these aspects, together with the higher heat transfer coefficient of the ground, are responsible of the higher efficiencies. The seasonal delay, that depends on the depth and the ground composition, can be as long as some weeks. This phenomenon is exploited at the beginning of the hot season, when the ground temperature is still lower than air, with lower energy consumption needed for conditioning. This study shows the thermal behavior of HAGHEs placed in south of Italy. Measurements show that the ground temperature below a certain depth, remains relatively constant throughout the year (see figure 1). At sufficient depth, the ground temperature is always higher than outside air temperature in winter, lower in summer. It can be used to preheating in winter and pre-cooling in summer the ventilation air by operating a HAGHE. It basically consist of pipes which are buried in the ground at the depth of about 2.5 meters, coupled with an air system which forces the

outside air through the pipes and eventually mixes it with the indoor air of the building. For a large number of applications it is necessary to know the influence of each parameters on the thermal performance of HAGHE as well as the pipes layout and the ground properties.

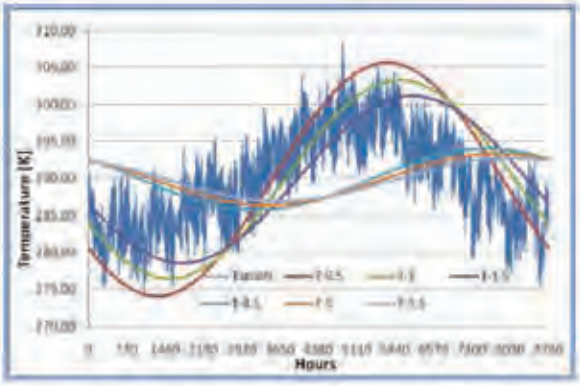

Figure 1 - Temperature distribution at all depths, Λ=2 [W/(Mk)]

2. MAIN BODY

The CFD study of the system was performed with the help of the CFD code Fluent 6.3 and the pre-processor Gambit 2.0. The numerical study was carried in unsteady conditions with an optimized 3D year analysis for the pipe heat flux transferred to air in the horizontal heat exchanger. Air mass flow rate was set at four different levels 150, 250, 350, 450 m^3/h respectively. Entering air temperatures were supposed variable equal to the external temperature varying hour by hour. The activation period of the heating and cooling system in winter was from 15th November to 31st March and each day from 8.00am to 7.00pm (typical of offices, farms, etc.). The activation period in summer was from 1st June to 31st August and each day from 8.00am to 7.00pm.

Figure 2. Geometry of geothermal heat exchanger model (only half-pipe)

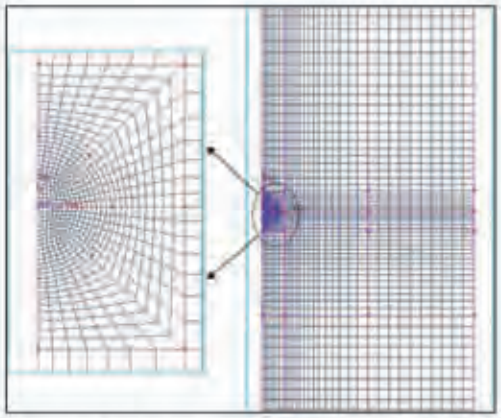

Figure 3. Mesh of calculus domain and a detail (Number of cells is about 171800)

The 3D analysis used a parallelepiped domain of 5.0 m x 2.0 m x 4.0 m [length x width x depth] with 200 mm diameter polyethylene (PE) semi-cylinder pipe with a length (as the domain) of 5.0 m. Two depths of burial of the geothermal probe have been tested 2,5 m and 3,5 m, respectively. The geometry represents only half of the ground-pipe heat exchanger, because of the geometrical and fluid-dynamic symmetry (see figure 2). The structured grid is composed of hexahedral cells,

stretched towards the curved lateral surface of the semi-cylinder into the ground parallelepiped. In table 1, the main parameters of the ground properties are shown, supposed homogeneous at all depths. The investigation concerned 3 different soil thermal conductivity: λ = 1,2,3 W/m K. Weather data relating to a climatic station, located in Brindisi (Latitude 40°65' North and Longitude 17°95' East, Elevation 10 m), were generated using Meteonorm Version 5. The ground temperature distribution as a function of time and depth is a complex function because of the interactions of the soil with sun radiation, wind and air temperature during all the year. This function (Kusuda et al., 1965) models the vertical temperature distribution of the ground given the mean ground surface temperature for the year, the amplitude of the ground surface temperature for the year, the time difference between the beginning of the calendar year and the occurrence of the minimum surface temperature, and the thermal diffusivity of the soil.

	Pipe (PE)	Ground	Air
ρ [kg/m^3]	946	2723.23	Ideal gas
λ [W/(m K)]	0.35	1; 2; 3	0.0242
c_p [J/(kg K)]	1920	837.338	1006.43
μ[kg/s]			1.7894E-5

Table 1. Materials properties

3. RESULTS

It is reported, for brevity, a comparison between the two tested depths of burial, with a conductivity of the soil amounted to 2 W/(mK). The results reported are for the weeks where you have the most extreme weather conditions. The week from 11 to 17 February has, in fact, the peak minimum temperature of the year, for the station of Brindisi; back, the week 19-25 in July with the peak maximum.

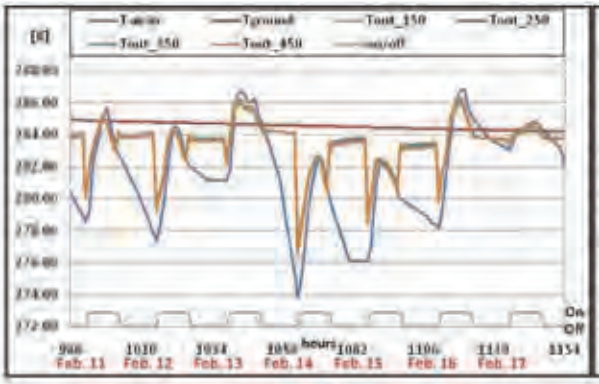

Figure 4. Comparison between outlet air temperatures varying the air mass flow, 11-17 February, depth of burial: 2,5 m

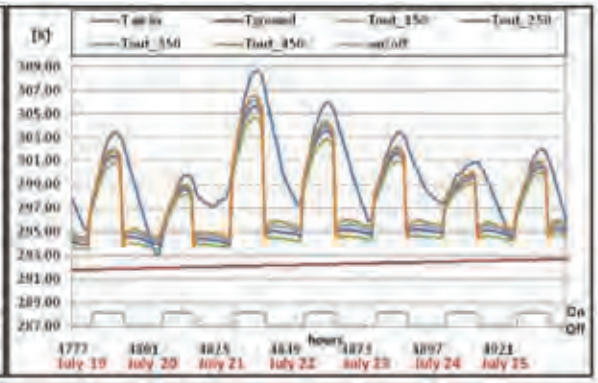

Figure 5. Comparison between outlet air temperatures varying the air mass flow, 19 – 25 July, depth of burial: 2,5 m

The comparison between the performance of the exchanger with two different depths of burial does not show substantial differences. The heat flux is negative when the air transfers heat to the soil; this behavior is, clearly, negative in winter. Therefore the plant, with a burial depth of 3.5 meters, is more efficient in heating the air in winter. But, when comparing the peaks in temperature of figure 4 and 7, we see that the difference in the winter, is under half a degree. The comparison between figure 5 and figure 8, shows a difference of temperature of about one degree. According to this

analysis, we must carefully evaluate the relationship between the costs related to the excavation for the installation of the exchanger, and the actual performance benefits of the transaction.

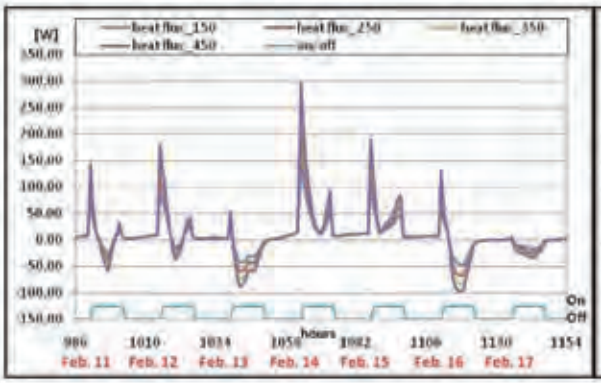

Figure 5. Thermal power transferred from ground to air for different air mass flow rates, 11-17 February, depth of burial: 2,5 m

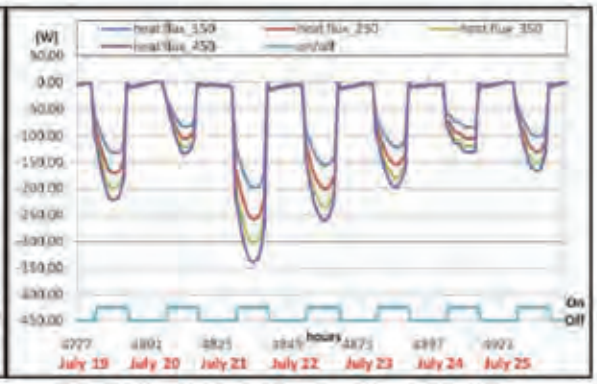

Figure 6. Thermal power transferred from ground to air for different air mass flow rates, 19-25 July, depth of burial: 2,5 m

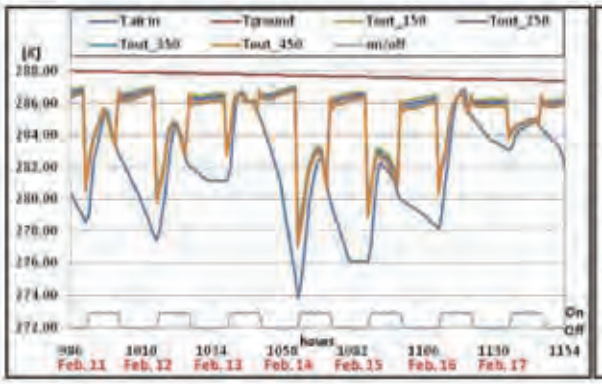

Figure 7. Comparison between outlet air temperatures varying the air mass flow, 11-17 February, depth of burial: 3,5 m

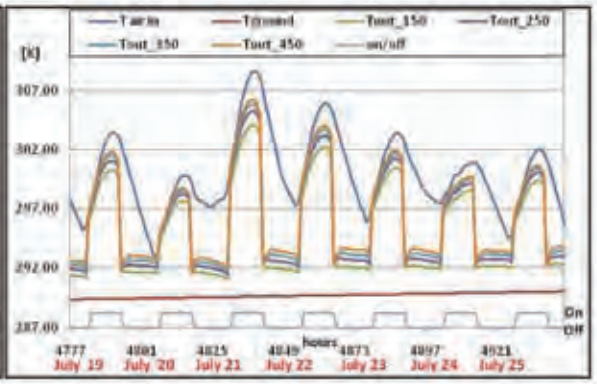

Figure 8. Comparison between outlet air temperatures varying the air mass flow, 19 – 25 July, depth of burial: 3,5 m

REFERENCES

[1] Genchi Y., Kikegawa Y., Inaba A., 2002, CO2 payback–time assessment of a regional-scale heating and cooling system using a ground source heat–pump in a high energy–consumption area in Tokyo, Applied Energy 71:147–160.

[2] Starace G., Congedo P.M., Colangelo G., 2005, Horizontal heat exchangers for GSHPs efficiency and cost investigation for three different applications, ECOS 2005 conference - Trondheim, Norway, June 20-23.

[3] Lazzarin R., 2001, Ground as a Possible Heat Pump Source, Geothermische Energie, 32-33.

[4] P.M. Congedo, L. Bonfantini, "Horizontal Air-Ground Heat Exchangers for Conditioning Systems", TCN CAE 2008 International Conference on Simulation Based Engineering and Sciences, 16-17th October 2008, Venice, Italy.

[5] Bloomquist R. G., 2001, The Economics of Geothermal Heat Pump Systems for Commercial and Institutional Buildings, Proceedings Conference on Geothermal Energy in Underground Mines, Ustron, Poland.

[6] Kusuda, T., & Achenbach, P. R. (1965). Earth temperature and thermal diffusivity at selected stations in the United States.

First International Conference on Computational Methods for Thermal Problems
ThermaComp2009, September 8-10, 2009, Napoli, Italy
N.Massarotti and P.Nithiarasu (Eds.)

Prefered Coiling Entry Temperature In Hot Metal Rolling

Nando Troyani
Centro de Métodos Numéricos en Ingeniería, Universidad de Oriente, Apdo. 4327, Puerto La Cruz, Venezuela, e-mail: ntroyani@cantv.net
Orlando M. Ayala
Centro de Métodos Numéricos en Ingeniería, Universidad de Oriente, Apdo. 4327, Puerto La Cruz, Venezuela, e-mail: ayalah@cantv.net

ABSTRACT

Temperature evolution in hot metal mills determines the uniformity of metallurgical and mechanical properties of the finished product. A numerical strategy to determine an estimate for the preferred distribution of temperature at the exit of the roughing stands of bars to be coiled in hot metal milling operations, based on a three-dimensional mathematical model for the evolution of temperature is presented, as well as the corresponding numerical solution strategy. The governing partial differential equation of transient heat diffusion is solved by integrating a two dimensional geometrically adaptive finite element solution, for a shape changing domain, with a finite difference one-dimensional solution in the width wise direction of the bar, using a novel numerical separation of variables strategy. Time is discretized according to a Crank-Nicolson scheme. Numerical results indicating preferred entry temperature are shown.

Key Words: *Metal Coiling, Coilbox, Finite elements, Finite differences*

1. INTRODUCTION

To minimize energy losses to the environment and for metallurgical uniformity manufacturing processes for flat hot strips, often shape the hot bars into coils, Fig. 1, The Coilbox®, [1-2], is just an example of a specific device utilized in strip coiling. The mathematical model for the problem consists of the three-dimensional (3-D) parabolic partial differential equation (PDE) of heat diffusion together with the necessary additional conditions.

The utilized three dimensional (3-D) model is resolved using an approach that integrates a one dimensional (1-D) finite difference (FD) solution in the width wise direction and a two dimensional (2-D) finite element (FE) solution in the lengthwise direction. Figure 1. For this integrated solution a novel numerical version of the separation of variables principle (NSVP) was used.

Due to symmetry only the lengthwise half of the metal strip is retained throughout the calculations. Geometrically adaptive FE's (8 node isoparametric quadrilaterals) are used in the coiling plane. Time is discretized according to a Crank-Nicolson implicit approach for both the FD and the FE solutions with the same time step for both individual solutions, that is, they march together in time.

Given the complexities of the physics of the problem only a reasonable approximation to a near optimal entry distribution of temperature can be achieved, that is, a distribution of temperature that is as flat as possible (as a function of x, y and z) as the metal strip enters the finishing stands.

The stated preferred distribution of temperature at the exit of the roughing stands, is determined in terms of the optimal initial temperature difference (OITD), between bar head and bar tail.

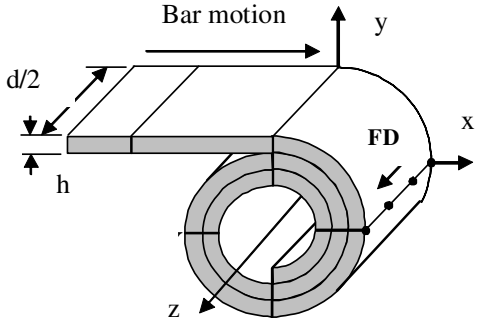

Figure 1. Partially coiled half bar showing significant geometric parameters.

2. MATHEMATICAL MODEL

The equation describing the temperature evolution in the bar is the well known parabolic partial differential equation of heat diffusion, given by:

$$k\left[\nabla^2 T\right] = c \quad \frac{\partial T}{\partial t} \qquad \forall (x, y, z) \quad \in \quad \Omega_{xyz}(t) \tag{1}$$

to be solved in the following (shape time dependent) domain

$$\Omega_{xyz}(t) = \left\{ (x, y, z) \middle| 0 \le x \le L, 0 \le y \le h, -d/2 \le z \le d/2, 0 \le t \le t^f \right\} \tag{2}$$

The initial shape of the bar is represented as a flat sheet of hot metal.

The boundary conditions (BC), prior to contact due to coiling, are the combined convective and radiative boundary conditions given by

$$-k \frac{\partial T}{\partial} = h_{cr} (T - T_\infty) \quad \forall \quad (x, y, z) \in \partial \Omega_{xyz}(t) \tag{3}$$

Symbols represent: T temperature, t time, c heat capacity, k thermal conductivity, density t^f, prescribed final time, h bar thickness, d bar width, L bar length, $T\infty$ far away temperature, h_c convective coefficient of heat transfer, h_r equivalent radiative coefficient of heat transfer respectively. Where $h_{cr} = h_c + h_r$, and $\partial\Omega_{xyz}(t)$ represents the boundary of the domain. The indicated derivative represents the outward normal derivative.

Applicability of the NSVP requires that all the different components of the 3-D model must be separable. The initial distribution of temperature satisfies it as well as long as it can be expressed as a 3-D function of x, y and z separable into three functions with the following general form,

$$T(x,y,z,0) = T^*(x)T^*(y)T^*(z) \;\forall\; (x,y,z) \in \Omega_{xyz}(0) \tag{4}$$

Thermal exchange between layers of the metal strip as they become in contact during coiling and loose contact during uncoiling is handled by defining an equivalent heat transfer film coefficient consistent with either radiation heat exchange between adjacent layers with a view factor value of 1, or consistent with experimentally determined values of the thermal contact conductance used in the following form

$$-k\frac{\partial T}{\partial} = h_{tccf}(T - T_\infty) \;\forall\; x,y,z \in \partial\,\Omega_{xyz}(t) \tag{5}$$

In this expression, T is the heat emitting surface temperature, and T_∞ is the heat receiving surface temperature in contact. Usage of this scheme entirely avoids the problems associated with the topology changes associated with coiling.

The problem posed in equations (1) through (5) is solved by a numerical strategy that at each time step integrates via the NSVP a 2-D FE solution (T_{FE}^{xy}) in the x-y plane (the coiling plane) with a 1-D FD solution (T_{FD}^{z}) in the z direction, width wise direction, of the bar, Fig. 2, resulting in a fully integrated 3-D solution. The NSVP is used here as follows:

$$T(x,y,z,t) = [T_{FE}{}^{xy}(x,y,t)]\left[\frac{T_{FD}{}^{z}(z,t) - T_\infty}{T^{z}(z,0) - T_\infty}\right] \tag{6}$$

3. NUMERICAL RESULTS

The numerical results presented below correspond to a 0.015 m thick, 1.0 m wide and 50.0 m long steel bar, in a 30.0 ºC environment, with the following average thermal properties for the bar steel. Thermal Conductivity 27.2 [W/m ºC]; Density 7520.0 [kg/m]; Heat Capacity 670.0 [J/kgºC].

For the particular cases under analysis, the thermal contact conductance consistent film coefficient h_{tccf} is calculated for each pair of elements engaged in thermal contact, assuming typical radiation exchange between adjacent layers, Troyani [2], with the following expression

$$h_{tccf} = F\frac{(T^4 - T^4{}_\infty)}{(T - T_\infty)} \tag{7}$$

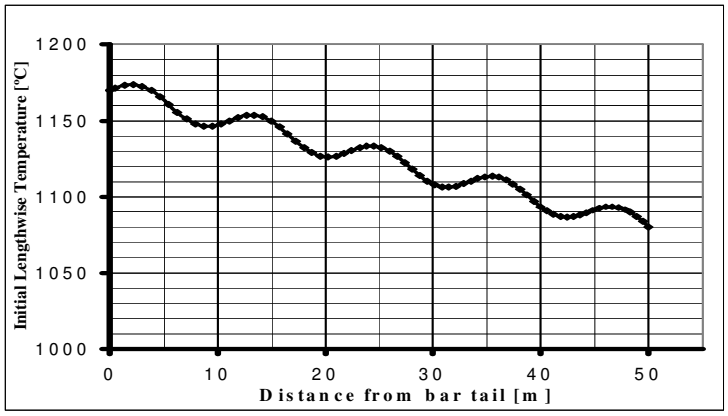

Figure 2. Typical Initial distribution of temperature for a 50 m long bar.

Fig. 3, below, shows the distribution of temperature (after coiling and uncoiling) as the bar enters the finishing milling stands. Fig. 3 shows no difference between the temperature longitudinal entry distribution at z = 0.0 m and at z = 0.5 m due to the fact that lateral heat loss has been entirely shielded.

The results for a set of computer simulations as a function of lateral radiation effectiveness for preferred both initial bar head temperature and bar tail temperatures are shown in Fig 4.

Comparisons with available experimental results were performed for both uncoiled and coiled parts of the bar. Hollander (1967) reports, from experimental measurements, that a 0.027 m thick carbon steel bar exposed to the environment loses temperature at an average rate of 2.256 ºC/s in the range of 1120.0 ºC-980.0 ºC to be compared with an average rate of 2.289 ºC/s for the same range using the present approach. For the coiled portion of a 0.0254 m thick bar Stelco (the Coilbox® manufacturer), also from experimental measurements, reports an average loss of temperature of 0.0556 ºC/s to be compared with 0.0544 ºC/s using the present approach.

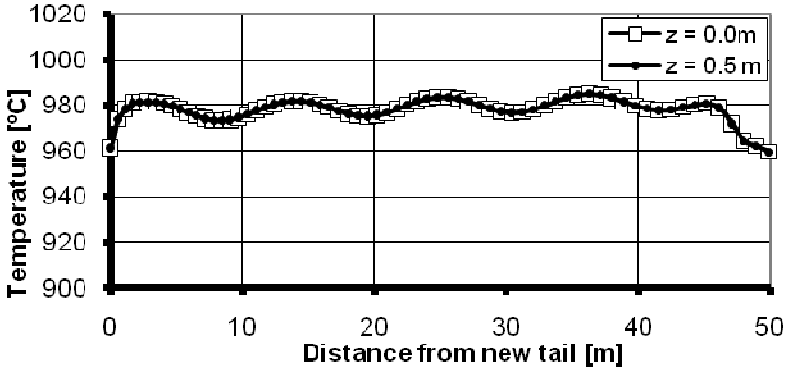

Figure 3. Finishing stands entry longitudinal distribution of temperature for z = 0.0 m and z = 0.5 m and full lateral radiation shielding.

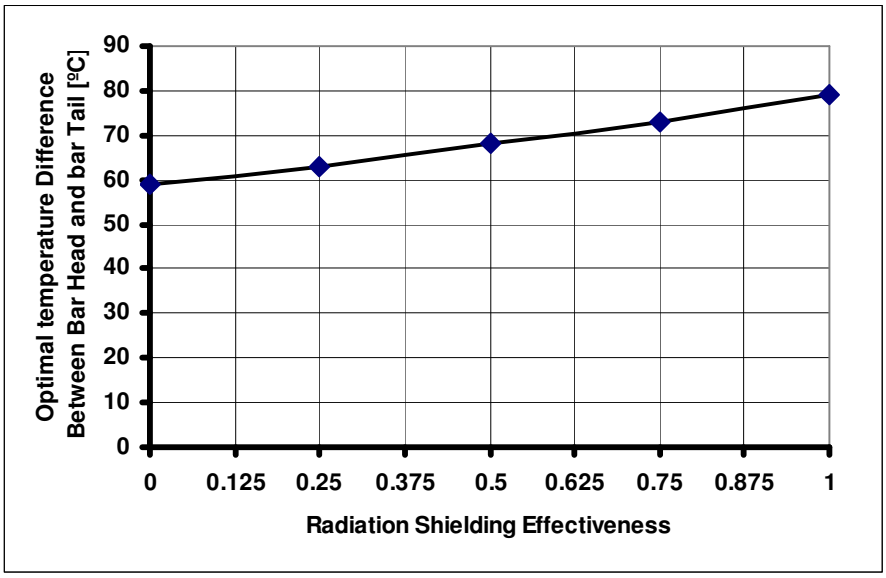

Figure 4. Optimal initial temperature difference as a function of lateral reradiating effectiveness.

4. CONCLUSIONS

A mathematical model of temperature evolution in hot metal mills is presented together with a novel integrated FE-FD solution of the corresponding partial differential equation. The described scheme is applied to a particular set of data to illustrate its applicability.

REFERENCES

[1] Smith W., 1981,The Coilbox: A New Approach to Hot Strip Rolling, AISE Year Book, pp. 432-436.

[2] Troyani N., 1996, Nonlinear Geometrically Adaptive Finite Element Model of the Coilbox, Numerical Heat Transfer, Part A, pp. 849-858.

[3] Hollander F., 1967, A Model to Calculate the Complete Temperature Distribution in Steel During Hot Rolling , AISE Year Book , pp 46-78.

First International Conference on Computational Methods for Thermal Problems
ThermaComp2009, September 8-10, 2009, Napoli, Italy
N.Massarotti and P.Nithiarasu (Eds.)

NUMERICAL ANALYSIS OF LAMINAR NATURAL CONVECTION IN ISOSCELES TRIANGULAR ENCLOSURES

E. Fuad Kent

Istanbul Technical University, Faculty of Mechanical Engineering, Inonu Cad. No: 87, 34437, Gumussuyu, Istanbul, Turkey, kente@itu.edu.tr

Key Words: *Natural convection, isosceles triangular enclosures, Nusselt number.*

1. INTRODUCTION

In the last years, a further increase of studies of natural convection in triangular enclosures has been observed in the literature because of its applicability in various fields such as heat transfer in air-filled attic spaces of houses and buildings with sloped roofs and horizontal suspended ceilings, triangular built-in-storage type solar collectors, solar stills and electronic equipment cooling. Representative works that have dealt with this topic are those of [1-6]. In solar engineering applications, triangular built-in-storage type solar water heaters, which result in higher solar gain and enhances the natural convection, leading to better heat transfer between the absorbing surface and the water stored in the heater are another practical application of triangular geometry heated from top inclined surface. Natural convection has been and still likely remains a promising option in the cooling of electronic equipment because of noiseless, simplicity and economy are the important factors in engineering design. The electronic components are usually mounted on boards, which form rectangular or triangular cavities.

In this work, numerical analysis of laminar natural convection in an enclosure of isosceles triangular cross section has been performed for different boundary conditions.The numerical solutions are obtained for a wide range of aspect ratios in order to investigate the effect of the base angles on the flow structure and heat transfer. The objective of our study is to assess the heat transfer rate across the bottom wall of the enclosure with the base angle.

2. FORMULATION OF THE PROBLEM

The geometric configuration of the physical system is shown in Figure 1.

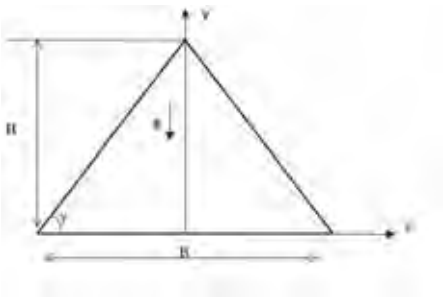

FIGURE 1: The schematic diagram of the physical system.

The enclosure is filled with a viscous, incompressible Newtonian fluid. Two notable cases involving prescribed wall temperatures are examined: Case 1, the base is cooled and the two top hypotenuses are symmetrically heated; and Case 2, the base is heated and the two top hypotenuses are symmetrically cooled. The flow field and heat transfer are conceived two-dimensional. The Boussinesq approximation is assumed valid and constant fluid properties are considered except the density variations.

Under the above approximations, the non-dimensional governing equations for steady natural convection flow using conservation of mass, momentum and energy can be written as

$$\frac{\partial U}{\partial X}+\frac{\partial V}{\partial Y}=0 \tag{1}$$

$$U\frac{\partial U}{\partial X}+V\frac{\partial U}{\partial Y}=-\frac{\partial P}{\partial X}+\Pr\left(\frac{\partial^2 U}{\partial X^2}+\frac{\partial^2 U}{\partial Y^2}\right) \tag{2}$$

$$U\frac{\partial V}{\partial X}+V\frac{\partial V}{\partial Y}=-\frac{\partial P}{\partial Y}+\Pr\left(\frac{\partial^2 V}{\partial X^2}+\frac{\partial^2 V}{\partial Y^2}\right)+\mathrm{Ra}\,\Pr \tag{3}$$

$$U\frac{\partial}{\partial X}+V\frac{\partial}{\partial Y}=\frac{\partial^2}{\partial X^2}+\frac{\partial^2}{\partial Y^2} \tag{4}$$

Where the non-dimensional variables are defined as follows:

$$X=\frac{x}{H},\quad Y=\frac{y}{H},\quad U=\frac{uH}{\quad},\quad V=\frac{vH}{\quad},\quad =\frac{T-T_C}{T_H-T_C},\ P=\frac{pH^2}{\ 2},\quad \Pr=—,\quad \mathrm{Ra}=\frac{g\ \ (T_H-T_C)H^3}{} \tag{5}$$

The transformed boundary conditions are:

- U=V=0 on all the walls.

The thermal boundary conditions are:

- On the base =0, and on the inclined walls =1 for the heating from the top (Case 1);
- On the base =1, and on the inclined walls =0 for the heating from the bottom (Case 2).

Subsequently, the dimensionless form of the mean heat transfer coefficient $\bar{h}$ and the mean Nusselt number are obtained from the relations

$$\overline{Nu}_H=\frac{\bar{h}H}{k}=\frac{H\bar{q}_w}{k(T_H-T_C)} \tag{6}$$

where the height of the enclosure H is taken as the characteristic length in the definition of Nusselt number and k is the thermal conductivity of the fluid.

3. RESULTS

In this study, numerical computations are carried out for five different base angles , which are 15°, 30°, 45°, 60° and 75°. Rayleigh numbers are varied from 10^3 to 10^5 and Prandtl number is taken as 0.71 that corresponds to air.

Governing equations which are discretized with finite volume method are solved by Fluent 6.0.12 commercial software by using SIMPLE method to solve the pressure-velocity couple, while second order upwind difference scheme is employed to discretize the convective terms. Iterations are continued until the global convergence is guaranteed by controlling the residuals of the descriptive mass, momentum and energy conservation equations by setting its variations to less than 10^{-10}. Trial calculations are made using various grid sizes in order to obtain grid independent solutions. The computational domain is created and meshed using the grid generation software Gambit 2.2.30.

Equilateral triangular elements are employed to form the computational grid. Nonuniform grid structures are utilized in the computational domain where high velocity gradients are expected.

To check the validity of the numerical results, the dimensionless temperature variation along the mid-plane of the isosceles triangular enclosure having a base angle of 45° is compared with the experimental data of Flack [1] for the cavity heated from the top. Figure 2(a) shows the variation in the computed dimensionless temperature along the mid-plane of the isosceles triangular cavity symmetrically heated from the top for the Grashof number $Gr = 2.84 \times 10^6$ used by Flack.

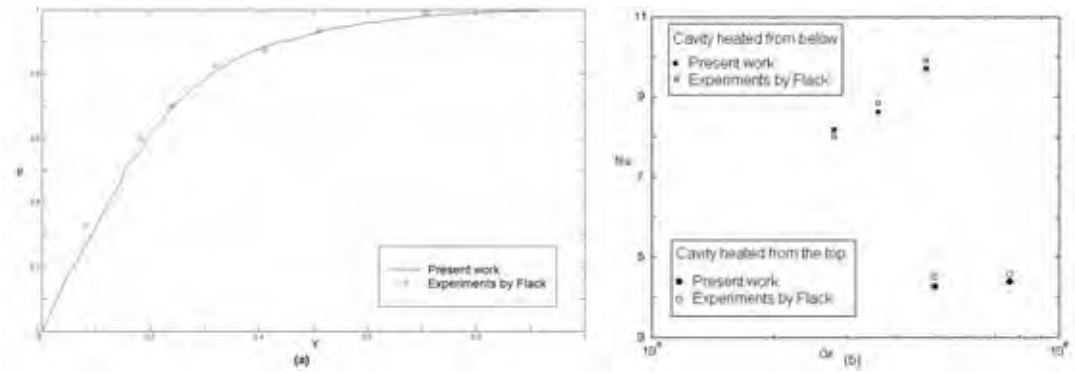

FIGURE 2: Comparison between the numerical results and experimental data of Flack [1]: (a) Dimensionless temperature variation along the mid-plane of the enclosure for the cavity heated from above with $Gr = 2.84 \times 10^6$. (b) Comparison between the numerical and experimental mean Nusselt numbers for the cavity heated from the top and for the cavity heated from below.

When compared with the experimental observations of Flack [1], it is seen that the numerical predictions overlap perfectly with the experimental measurements. The non-dimensional temperature profile is also in good agreement with the experimental data for the cavity heated from the bottom. Figure 2 (b) shows a comparison between the numerical and experimental mean Nusselt numbers for the two cases. A good agreement is found with the experimental data of Flack. The concordance found between the abovementioned numerical predictions and the corresponding experimental data validates the numerical codes of the present study.

Figure 3 represents the streamlines and isotherms in the enclosure heated from the bottom (case 2) for the base angle of =45° and $Ra = 10^5$. It should be noted that Holtzman et al. [2] reported the critical Grashof number for the pitchfork bifurcation to be $Gr_c = 16200$. This corresponds to a value of $Ra_c = 1.15 \times 10^4$. Thus, the flow in Figure 3 for $Ra = 10^5$ are not symmetric, while the boundary conditions are symmetric. Figure 4 shows the streamlines and isotherms in the enclosure heated from the top (case 1) for the base angle of =30° and $Ra = 10^5$.

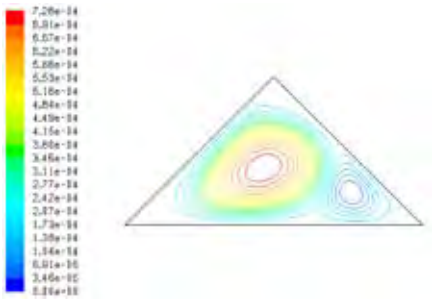

FIGURE 3: Streamline and isotherms for =45° and $Ra = 10^5$ (case 2).

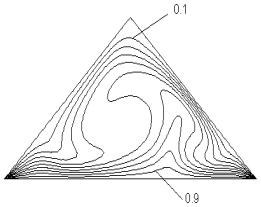

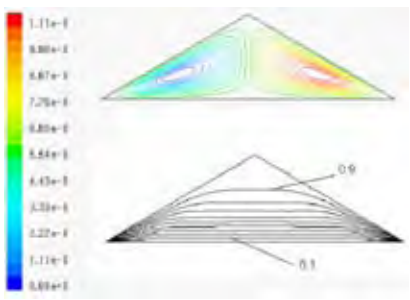

FIGURE 4: Streamline and isotherms =30° and $Ra = 10^5$ (case 1).

4. CONCLUSIONS

The aim of the current work is to examine the flow field and temperature distribution with detailed analysis on heat transfer evaluation for natural convection in isosceles triangular enclosures.

For the cold base and hot inclined walls (case 1), regardless of the value of Ra, all cases investigated are always stable and the stratified isotherms resembling pure conduction are found in the enclosure. The mean Nusselt numbers increase very slightly with Rayleigh numbers for all the base angles investigated. On the other hand, it is observed that the base angle has a considerable influence on both of the flow structure and heat transfer. As the base angle decreases, the isothermal region greatly diminishes in size and the recirculation cells fill entirely the enclosure. The distance between cold and hot walls becomes relatively small. This causes higher heat transfer rates at low base angles. It is found that, an enclosure of 75° base angles transfers 3.4 times less heat than that of an enclosure of 15° base angles.

For the hot base and cold inclined walls (case 2), the base angle has a profound influence on the average convective Nusselt numbers. For $Ra=10^3$, we observe that for all base angles, temperature distribution is the same as in the pure conduction case and two counter rotating symmetric cells are seen in the enclosure. For the Rayleigh numbers above the critical Rayleigh numbers Ra_c (Ra_c is depended on the base angle), asymmetric solutions exhibiting pitchfork bifurcations are obtained. For a given Rayleigh number, the higher the base angle, the less the heat transfer across the base wall. Multi-cellular asymmetrical streamline patterns and thermal plumes, which enhance the heat transfer, are obtained in the enclosures for low base angles and high Rayleigh numbers. In wintertime conditions, at $Ra=10^5$, it is seen that a roof of 75° base angles transfers 1.47 times less heat than that of a roof of 15° base angles.

Some general considerations can be drawn concerning the assessment of building energy needs: Heat transfer from the attics can be controlled changing the base angle of the roof according to architectural design of the building. In the calculation of heat transfer from the roof, attention must be paid on the base angle. The roofs having a low base angle are not suitable for wintertime conditions because of high heat transfer rates from the isosceles triangular attic space of the building to the environment.

REFERENCES

[1] Flack, R. D., The experimental measurement of natural convection heat transfer in triangular enclosures heated or cooled from below, *Journal of Heat Transfer*, 102, 770–772, 1980.

[2] Holtzman, G. A., Hill, R. W. and Ball, K. S., Laminar natural convection in isosceles triangular enclosures heated from below and symmetrically cooled from above, *Journal of Heat Transfer,* 122, 712-717, 2000.

[3] Akinsete, V. A., and Coleman, T. A., Heat transfer by steady laminar free convection in triangular enclosures, *International Journal of Heat and Mass Transfer*, 25, 991-998, 1982.

[4] Poulikakos, D., and Bejan, A., The fluid mechanics of an attic space, *Journal of Fluid Mechanics*, 131, 251–269, 1983.

[5] Asan H. And Namli L., Laminar natural convection in a pitched roof of triangular cross-section: summer day boundary conditions, *Energy and Buildings*, 33, 69-73, 2000.

[6] Asan H. and Namli, L., Laminar natural convection in a pitched roof of triangular cross-Section: winter day boundary conditions, *Energy and Buildings*, 33, 753-757, 2001.

First International Conference on Computational Methods for Thermal Problems
ThermaComp2009, September 8-10, 2009, Napoli, Italy
N.Massarotti and P.Nithiarasu (Eds.)

EVALUATION OF THERMAL RADIATION MODELLING IN TUNNEL FIRES

Paolo Ciambelli, Maria Grazia Meo, Paola Russo, Salvatore Vaccaro

Department of Chemical and Food Engineering, University of Salerno,
via Ponte don Melillo 84084 Fisciano (SA) Italy,
pciambelli@unisa.it, mgmeo@unisa.it, parusso@unisa.it, svaccaro@unisa.it

ABSTRACT

Modelling based on Computational Fluid Dynamics (CFD) is by now effectively used in fire research and hazard analysis. Depending on the scenario, radiative heat transfer can play a very important role in enclosure combustion events such as complex tunnel fires. In this work, the importance of radiation and the effect of different approaches or models to account for it were assessed. This was made firstly by performing small-scale tunnel fire simulations by the *CFX* code and comparing the results with experimental data, then simulating realistic full-scale scenarios. The results highlight the capability of CFD modelling to reproduce with good approximation tunnel fires. Radiation proved to be noteworthy mainly at full-scale. Among the various approaches accounting for radiation, modelling radiation and the effect of participating media gives the most accurate results. However, the simplest and far less computationally expensive fractional heat loss approach can provide remarkable overall predictions. Finally, the futures of the use of CFD in quantitative fire hazard analysis is highlighted.

Key Words: *CFD, Radiation Modelling, Tunnel Fires.*

1. INTRODUCTION

Quantitative fire hazard analysis (FHA) is becoming the fundamental tool of modern fire safety engineering practice. The goal of a FHA is to determine the expected outcome of a specific set of conditions called a fire scenario. This outcome determination can be made by expert judgment, by probabilistic methods using data from past incidents, or by deterministic means such as fire models. These include empirical correlations, computer programs, full-scale and reduced-scale models, and other physical models. Although empirical correlations and simplified computer models allow a rapid assessment of a fire scenario quickly yielding a value of the variables of interest, they are heavily limited by experimental conditions and simplifying assumptions. The trend today is to use models whenever possible supplemented, if necessary, by expert judgment [1]. In this context, the use of CFD techniques may represent an effective way to account for case and site specific details because they allow the estimation of the flow patterns of the fire-induced air velocity, temperature, pollutants and smoke concentration in large and complex enclosures, like tunnels.

Enclosure fires are, in general, very complex in nature. Their complexity arises from the fact that the physical and chemical processes (i.e. turbulence, combustion, radiation) controlling fire and smoke development interact with each other and with the surroundings. Radiation can play a very important role in the overall heat transfer, typically when temperatures are above 600 K [2]. According to many authors [2,3], radiative heat transfer can account for 30-40% of the heat output of a large fire. The main radiation sources are CO_2 and H_2O, emitting energy in discrete bands, and soot, which emits at all wavelengths [3,4]. While heat convection and conduction are easily handled and modelled by the energy equation, radiative heat transfer is not actually a flow phenomenon, and so cannot be modelled as such. In the energy equation the effect of radiation is accounted for by use of a source term, which must be supplied by a separate radiation model. In problems where thermal radiation is significant, as for fires in enclosures, the proper choice of the radiation model will affect not only the quality of the

solution, but also the computational time. A complete radiation model is very expensive. In practice, there are a range of simplifying assumptions that may be appropriate for a given problem. Among the different modelling approaches available, the most common used in large fires [2] are the following: i) Fractional heat loss due to radiative heat transfer: this method simply ignores the percentage of the heat release rate from a fire that turns into radiation by reducing the amount of HRR to be used in the energy balance equation [2,3]; ii) Discrete Transfer model: it aims to solve the radiative transfer equation for discrete representative radiative rays, and its accuracy is dependent on the ray directions chosen as well as the number of rays [5]; iii) Monte Carlo model: it simulates the underlying processes which govern the system of interest, i.e., the physical interactions between photons and the environment, and the computational cost is high when the model is applied to fires and smoke movement in large complex spaces [2,5].

In this work the *CFX* code by *ANSYS* was used [5] to evaluate the effect of different thermal radiation models on the conditions established in a tunnel when a gasoline pool fire occurs. The Discrete Transfer and the Monte Carlo models were used in the simulations. The absorption-emission characteristics of the combustion products were either modelled by a constant absorption coefficient (Grey model) or by a Multigrey model, to account for the dependence on the local gas composition. Finally, in the perspective of CFD use for fire hazard analysis, simulation results in terms of incident radiation were also compared with results from empirical correlations available in the literature [3].

2. SIMULATIONS

Preliminary simulations were run using the *CFX* code for a small-scale steady-state tunnel fire reported by Xue *et al*. [6]. In order to ascertain the importance of radiation modelling, the radiation was either not solved or modelled by Discrete Transfer or Monte Carlo model, in the grey assumption. The quality of the results of the simulations was evaluated by comparison with experimental data [6].

Then, realistic tunnel fires were simulated under the following hypotheses: a three-lane tunnel, compliant with current national guidelines, 100 m long and with an arched cross section of 12x7 m^2, with tunnel portals at atmospheric pressure and ambient temperature, 298 K; a 2x2 m^2 gasoline pool at the tunnel centre. According to literature data, the mass loss rate of a burning pool of gasoline is about 0.05 kg/m^2s [3] and an "ultra ultra fast" growth rate can be assumed [3]. Hence, the HRR curve was imposed to rise rapidly (in 90 s) up to 8 MW, remaining constant for about 10 min and, then, decaying exponentially within 30 min. The k-ε model was used for turbulence, the Eddy-Dissipation model was set for combustion and the Magnussen soot formation model was solved in conjunction with the combustion reaction. The radiative heat transfer was either modelled by the Discrete Transfer model or the Monte Carlo model, in grey or multigrey assumptions, or not modelled at all. The fractional radiative heat loss approach was also assessed by assuming a 30% reduction in HRR.

3. RESULTS

From the comparison with experimental data, the results pertaining to small-scale tunnel fire simulations showed that, due to the peculiar characteristics of the scenario (HRR of 3.15 kW), radiative phenomena were of moderate extent and, therefore, small differences were found between the predicted results when using different approaches. As an example, results reported in Fig.1a show that modelling the heat transfer by radiation contribute to lowering the predicted temperature values in the upper hot layer, and also that predicted temperature profiles are similar regardless of the radiation model used. Actually, calculated temperature profiles along the tunnel height did not rise as gradually as experimental data does, thus resulting in a different trend at intermediate levels and yielding a relatively poor prediction for the cold layer and the smoke layer interface heights. On the whole, the Discrete Transfer model for radiation modelling allowed the best compromise between computing time and accuracy: it ensured a computational rate of 12.8 iterations/min and a good heat balance closure (90%) after 3200 iterations. Instead, with the Monte Carlo model the calculation rate was only 3.6 iterations/min and the program needed 8000 iterations for balances closure. The main features of the experimental fire-induced airflow (upstream backflow (Fig.1b), stratification (Fig.1b and c) and

recirculating flow downstream (Fig.1c)) were reproduced with fair agreement, as shown in Fig.1d.

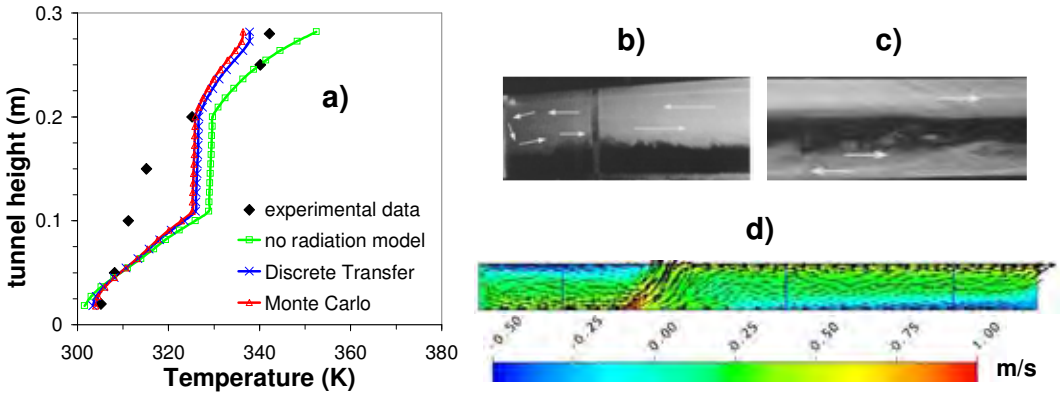

FIGURE 1. Small-scale tunnel fire. a) Temperature profiles along the height at the tunnel centreline, 3.6m downstream the fire. b) Experimental flow pattern upstream the fire. c) Experimental flow pattern downstream the fire. d) Predicted gas velocity distribution at the tunnel middleplane

Similarly, also with regard to fire simulations performed in the full-scale tunnel, predicted temperature profiles were comparable each other regardless of the radiation model used. However, the Monte Carlo model needed much more computational resource compared to the Discrete Transfer model. In addition, the Multigrey model gave more reasonable gas absorption-emission characteristics with respect to the assumption of constant grey characteristics over the whole domain. For the sake of clarity, only the results relevant to Discrete Transfer with multigrey model are reported in Fig. 2 and are compared with those pertaining to the simulations carried out without any radiation model and with 30% reduction in the fire HRR. Fig. 2 reports the predicted temperature profiles along the tunnel height, on the tunnel centreline and at 90 s after the fire starting. Specifically, those above the pool fire are displayed in Fig.2a and those at a distance of 25 m downstream the fire in Fig.2b.

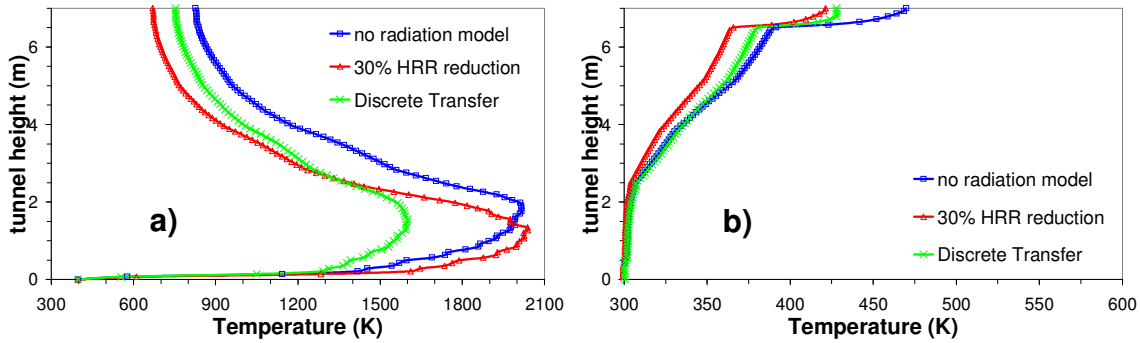

FIGURE 2. Full-scale tunnel fire. Temperature profiles along the height and at the tunnel centreline, t = 90 s. a) above the pool; b) at 25 m from the fire

Above the pool (Fig.2a) temperature values from all the simulations are consistent with the range of adiabatic flame temperature of gasoline-air mixtures (1632-2251 K). At a distance of 25 m from the fire (Fig.2b), the smoke and hot gases stratification is more stable being the predicted temperatures higher the upper the layer. Generally speaking, simulations with the fractional radiative heat loss approach result in a significant drop in gas temperature in comparison with that obtained without any radiation model. When radiation is modelled by Discrete Transfer, the gas temperatures above and near the fire (up to 10 m) are significantly lower than those calculated by imposing a reduced HRR (Fig 2a). Instead, far from the fire predicted temperatures by radiation modelling are higher because of radiative heating of gases, especially at elevated heights where gas stratification occurs (Fig.2b). Such

comparison underlines the noticeable influence of the radiation at full-scale. In order to give evidence of the benefit of CFD use in the fire hazard analysis, in Fig.3 results of CFD simulations in terms of radiant heat flux to a target at different heights and distances from the pool fire were compared with those obtained from empirical correlations (solid flame radiation model [3]). It appears that, except at small distances from the fire (< 3 m), the incident radiation values computed by simulations overestimate those yielded by the empirical correlations and, hence, they are more conservative with a view to FHAs. Moreover, correlations are based on assumptions (e.g. pool size, flame height and shape, time-averaged size of the visible envelope, average emissive power, wind, enclosure size) which limit their applicability, and have inherent limitations in their predictive capabilities. On the contrary, CFD models are validated and applicable to a wider range of conditions and scenarios.

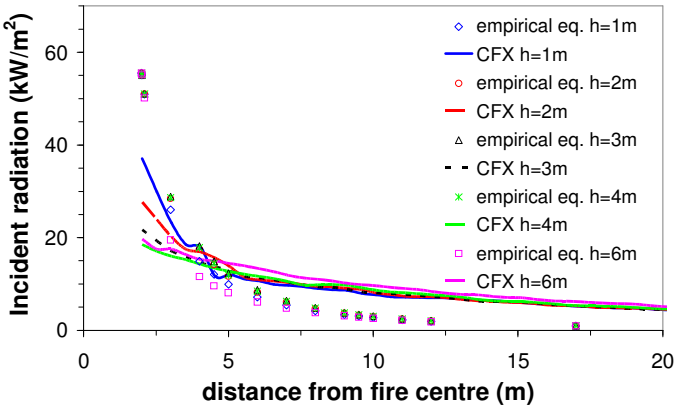

FIGURE 3. Full-scale tunnel fire. Incident radiation flux calculated by CFD simulations and by empirical correlations at different distances and heights (h) from the pool fire, t = 90 s

4. CONCLUSIONS

The results obtained in this study highlight the potential of CFD modelling to reproduce small-scale and full-scale tunnel fires, in order to assess the relative influence of heat transfer by convection and by radiation, which in some cases may play a very important role in confined combustion. Radiation proves to be a significant phenomenon above all in the case of real severe fires, so it should be properly taken into account to achieve reliable predictions by numerical simulations. However, failure to model radiation is expected to lead to conservative results. The simplest fractional radiative heat loss approach proves to give noteworthy predictions in the upper layer and beyond the fire. Modelling radiation and the effect of participating media like combustion gases allows the correct evaluation of consequences of heat transfer throughout the domain. Among those tested here, the Discrete Transfer and Multigrey model allows the best compromise between computing time and accuracy.

REFERENCES

[1] *Fire Protection Handbook*, 20th Edition (A.E. Cote *et al.* Eds.), National Fire Protection Association, Quincy (USA), 2008.

[2] N. Gobeau, H.S. Ledin, and C.J. Lea, Guidance for HSE Inspectors: Smoke movement in complex enclosed spaces, Assessment of Computational Fluid Dynamics, *HSL Report 29*, 2002.

[3] *The SFPE Handbook of Fire Protection Engineering*. 2nd Edition (P.J. DiNenno *et al.* Eds.), National Fire Protection Association, Quincy (USA), 1995.

[4] *Perry's Chemical Engineers' Handbook.* 7th Edition (R. H. Perry *et al.* Eds.), McGraw-Hill, New York (USA), 1997.

[5] ANSYS, *CFX help*, Release 11.0, 2007.

[6] H. Xue, J.C. Ho, and Y.M. Cheng, Comparison of different combustion models in enclosure fire simulation. *Fire Safety Journal*, 36, 37-54, 2001.

First International Conference on Computational Methods for Thermal Problems
ThermaComp2009, September 8-10, 2009, Napoli, Italy
N.Massarotti and P.Nithiarasu (Eds.)

RADIATIVE EFFECTS ON MIXED CONVECTION IN A UNIFORMLY HEATED VERTICAL CONVERGENT CHANNEL WITH A MOVING PLATE

Assunta Andreozzi
DETEC – Università di Napoli Federico II, P.le Tecchio, 80 – 80125, Napoli, Italy
assunta.andreozzi@unina.it

Nicola Bianco
DETEC – Università di Napoli Federico II, P.le Tecchio, 80 – 80125, Napoli, Italy
nicola.bianco@unina.it

Vincenzo Naso
DETEC – Università di Napoli Federico II, P.le Tecchio, 80 – 80125, Napoli, Italy
vincenzo.naso@unina.it

ABSTRACT

Mixed convection is of a paramount interest in many applications, such as thermal control in electronics and cooling of nuclear reactors. One of the most critical research areas in applied thermo-fluid-dynamics is just that concerned with technological processes.

Mixed convection in air induced by the interaction between a buoyancy flow and a moving plate induced flow in a vertical convergent channel is numerically investigated, in order to analyze the effects of the radiative heat transfer.The principal walls of the channel are heated at uniform heat flux. In the mid-plane of the channel an unheated plate moves at a constant velocity in the buoyancy force direction. The problem is solved numerically and results are obtained by means of a finite volume method. Heat conduction in the heated walls and radiative heat transfer are considered.

Key Words: *Mixed convection, Moving surfaces, Convergent channels, Radiative effects.*

1. INTRODUCTION

Mixed convection due to moving surfaces is very important in a wide variety of materials processing systems, such as soldering, welding, extrusion of plastics and other polymeric materials, hot rolling, cooling and/or drying of paper and textiles, Chemical Vapor Deposition (CVD), composite materials manufacturing, as reviewed in [1-3]. Mixed convection with continuously moving vertical surfaces in a quiescent fluid was mostly investigated with reference to a single moving plate, as recently reported in [4].

The effects of radiation and conduction in the plate in the numerical and analytical analysis of heat transfer from a moving plate to the environment are very important. Karwe and Jaluria [5] investigated numerically the heat transfer from a continuously moving isothermal plate to a still environment and compared predictions obtained by solving boundary layer equations with those obtained by solving complete elliptic equations. The effects of variable viscosity and variable thermal conductivity on heat transfer from moving surfaces in a micropolar fluid through a porous medium with radiation were studied in [6].

Mixed convection as a result of buoyancy and motion of one of the channel walls has received little research attention and few guidelines for choosing the best performing channel configuration are available. A study on this topic is presented in [7], where the conjugate mixed convection and conduction heat transfer induced by a continuous moving plate in a parallel channel flow was

numerically investigated. A numerical investigation on mixed convection in air due to the interaction between a buoyancy flow and a moving plate induced flow in a convergent vertical channel was carried out in [8].

In the present study the numerical investigation presented in [8] has been extended to the analysis of the radiative effects. The principal walls of the channel are heated at uniform heat flux. In the mid-plane of the channel an unheated plate moves at a constant velocity in the buoyancy force direction. The problem is solved numerically and results are obtained by means of a finite volume method. Heat conduction in the heated plate together with radiative heat transfer is considered. The effects of the channel spacing, the converging angle, the heat flux and the moving plate velocity are investigated. The temperatures of the channel walls and of the moving plate and correlations among dimensionless parameters are presented. The comparison with the case where radiative heat transfer is neglected is carried out.

2. MATHEMATICAL DESCRIPTION AND NUMERICAL PROCEDURE

The investigated system is sketched in fig.1a. It consists of a convergent vertical channel with a moving plate placed in its mid-plane. The moving plate, also termed "belt" in this work, is unheated and moves at a constant velocity in the buoyancy force direction. Both channel walls are conductive and heated at uniform heat flux, q_w. The length of the heated walls is L and the channel minimum spacing is b. The working fluid is air. Mixed convective flow in the convergent vertical channel is assumed to be incompressible and the system is assumed to be wide enough along the third coordinate to allow a 2D approximation. All thermophysical properties of the fluid are assumed to be constant, except for the dependence of density on the temperature (Boussinesq approximation). The governing equations for the fluid region in steady state regime are the time-averaged mass, Navier-Stokes and energy equations. A two-dimensional conduction model in the heated walls is employed.

An enlarged computational domain has been chosen. It is made up of the convergent channel and of two reservoirs of height L_x and width L_y, downstream and upstream of it, that simulate the free-stream conditions of the flow far away from the region thermally disturbed by the heated channel walls (fig. 1b). The $L_x = 0.400$ m and $L_y = 0.800$ m reservoirs dimensions ensure that solution to the problem is independent of the reservoirs size. The moving plate extends from the lower to the upper reservoir and its height is $L_b = L \cos + 2L_x$. Due to thermofluidynamic and geometrical symmetries, in solving the problem reference was made to half the domain, as shown in fig.1b. The

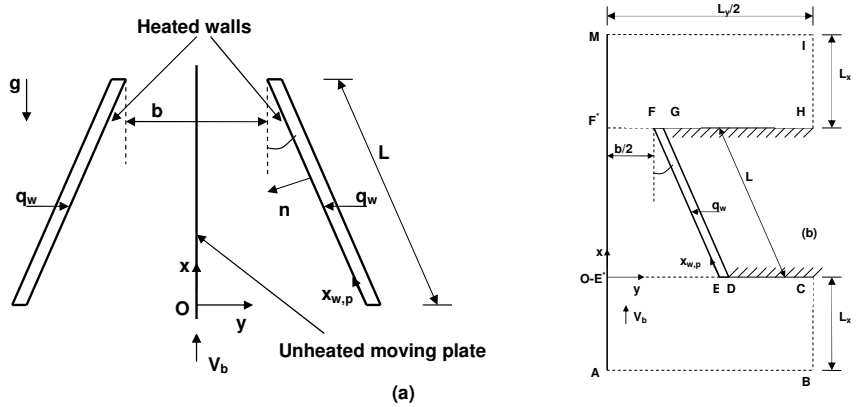

FIGURE 1. Sketch of the system: (a) physical domain; (b) computational domain

commercial Fluent CFD code was employed to solve the governing equations. The SIMPLE scheme was chosen to couple pressure and velocity. The discrete ordinates model (DO) was chosen to simulate radiative heat transfer. Walls are assumed to be grey.

3. RESULTS

In this study numerical results are presented for air (Pr = 0.71), for a heated plate length L = 406 mm, for minimum channel spacings b = 10 and 20 mm, for wall heat fluxes q_w = 30 and 120 W/m^2, for convergence angles = 0°, 2°, 10° and for a belt velocity V_b = 0.5 and 1 m/s. In this abstract results for b = 20 mm, q_w = 120 W/m^2 and V_b = 1 m/s are presented and a comparison with the case where radiative heat transfer is neglected is carried out. For the cases where radiative heat transfer is taken into account, the emissivity of the heated walls and of the belt is assumed to be $_p$ = 0.90 and $_b$ = 0.20, respectively, and the surroundings are assumed to be a black body at T_0=300 K.

Heated plate temperature profiles for = 0°, 2°, 10°, b = 20 mm, q_w = 120 W/m^2 and V_b = 1.0 m/s are reported in fig. 2a, for the cases where radiative heat transfer is taken into account, and in fig. 2b for the cases where radiative heat transfer is neglected. The comparison between the two cases shows that temperature profiles for = 0° are nearly the same, except in the upper part of the walls, where temperatures are larger when radiative heat transfer is not accounted for, because of the larger values of both walls temperature and view factor toward the surroundings in this part of the channel. Differences between temperature profiles in the two compared cases increase as the converging angle increases, due to the increasing view factor toward the lower reservoir.

The comparison with the case with negligible radiative heat transfer, in terms of belt surface temperature profiles, is reported in fig.3 for the same values of process parameters as those in the previous figure. For the parallel walled channel (= 0°), belt temperatures in the heated channel (0 ≤ x ≤ 406 mm) are slightly larger in the case with thermal radiation than in the other case ($_p$ = $_b$ = 0.0), where the radiative heat transfer from the heated plate to the moving belt does not contribute to the heating of the moving plate. Outside of the heated channel, belt temperatures for the case with thermal radiation are smaller than those for the other case, because of the larger cooling rate, caused by the radiative heat losses toward the surrounding. One can notice that in the case without thermal radiation the moving belt temperature begins to increase at an x value nearly equal to 0.12 m, where the thermal boundary layer thickness becomes equal to the channel spacing and the hot fluid heats the moving plate. When radiative heat transfer is taken into account, moving belt temperatures begin to increase at the heated channel inlet section, because of the radiative heat transfer and the view factor between the heated plate and the belt. Increasing the converging angle the abscissa at which the moving belt temperature begins to increase, decreases when radiative heat transfer is taken into account (fig. 3a) whereas it increases when radiation is neglected (fig. 3b).

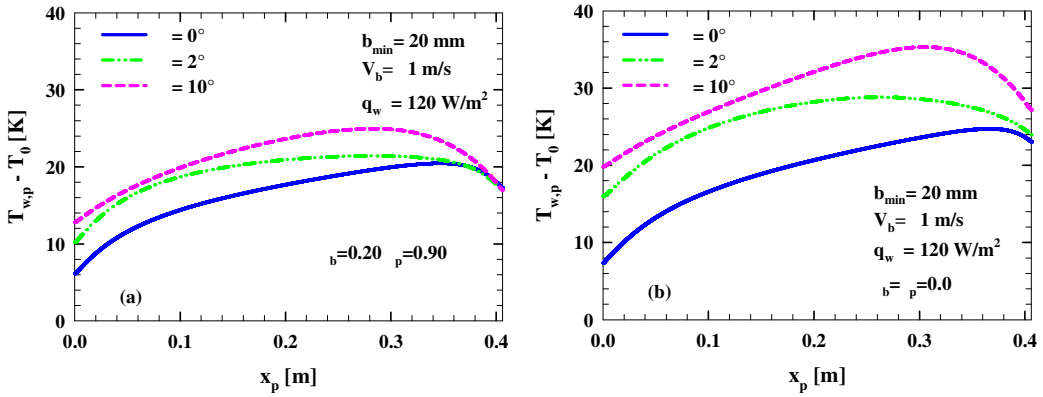

FIGURE 2. Heated temperature profiles, for b=20 mm, q_w = 120 W/m^2 and V_b = 1 m/s: a) $_p$=0.90, $_b$ = 0.20; b) $_p$= $_b$ = 0.0.

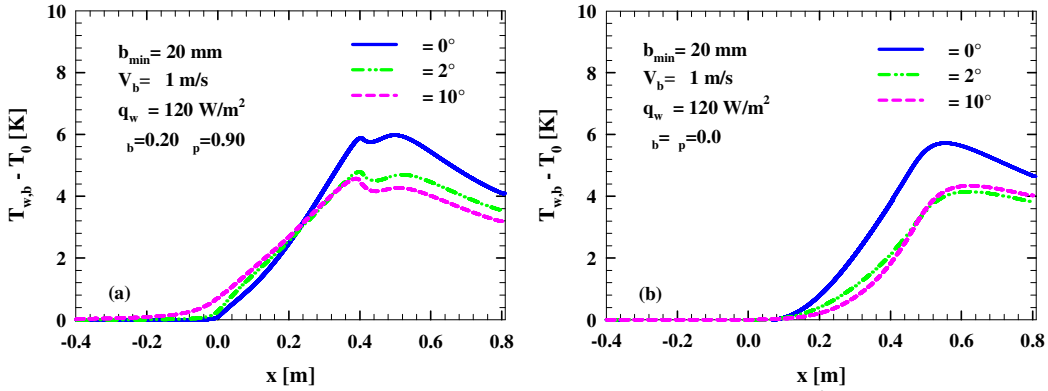

FIGURE 3. Belt temperature profiles, for b=20 mm, $q_w = 120$ W/m^2 and $V_b = 1$ m/s: a) $_p=0.90$, $_b = 0.20$; b) $_p = _b = 0.0$.

4. CONCLUSIONS

Mixed convection in air induced by the interaction between a buoyancy flow and a moving plate induced flow in a vertical convergent channel is investigated numerically, in order to analyze the effects of the radiative heat transfer. The comparison with the case where radiative heat transfer is neglected is carried out. Results show that the larger the converging angle the larger the radiative effects, due to the large view factor toward the surroundings. Particularly, the abscissa at which the moving belt temperature begins to increase, decreases at increasing converging angles when radiative heat transfer is taken into account, whereas the opposite occurs when radiative heat transfer is neglected.

REFERENCES

[1] R. Viskanta and T. L. Bergman, *Heat transfer in materials processing*, in: Rohsenow W. M., Hartnett J. P., Cho Y. I. (Eds.), Handbook of Heat Transfer, McGraw-Hill, New York, 1998.

[2] Y. Jaluria, 2001, Fluid flow phenomena in material processing, *Journal of Fluid Engineering*, 123, 173-210, 2001.

[3] Y. Jaluria, 2003, Thermal processing of materials: from basic research to engineering, *Journal of Heat Transfer*, 125, 957-979, 2003.

[4] S. A. Al-Sanea, Convection Regimes and Heat Transfer Characteristic along a Continuous Moving Heated Vertical Plate, *International Journal of Heat and Fluid Flow*, 24, 888-991, 2003.

[5] M. V. Karwe and Y. Jaluria, Numerical Simulation of Thermal Transport Associated with a Continuously Moving Flat Sheet in Materials Processing, *ASME Journal of Heat Transfer*, 113, 612-619, 1991.

[6] E. M. E. Elbarbary and N. S. Elgazery, Chebyshev, Finite Difference Method for the Effects of Variable Viscosity and Variable Thermal Conductivity on Heat Transfer from Moving Surfaces with Radiation, *International Journal of Thermal Sciences*, 43, 889-899, 2004.

[7] Y. Jaluria and B. H. Kang, Heat Transfer from Continuously Moving Material in Channel Flow for Thermal Processing, *Journal of Thermophysics and Heat Transfer*, 8, 546-554, 1994.

[8] A. Andreozzi, N. Bianco, G. Lacasa and V. Naso, Mixed Convection Heat Transfer in a Convergent Vertical Channel with a Moving Plate, *Proc. 8th Biennial ASME Conference on Engineering Systems Design and Analysis (ESDA)*, paper n. ESDA2006-95502, Torino, July 4-7, 2006.

First International Conference on Computational Methods for Thermal Problems
ThermaComp2009, September 8-10, 2009, Naples, Italy
N.Massarotti and P.Nithiarasu (Eds.)

Immersed volume method for solving 3D natural convection, conduction and radiation of a hat-shaped disk inside an enclosure

E. Hachem
École des Mines de Paris, Centre de Mise en Forme des Matériaux (CEMEF), UMR CNRS 7635, Sophia-Antipolis, France.
Elie.Hachem@mines-paristech.fr

T. Kloczko
Thibaud.Kloczko@mines-paristech.fr

T. Coupez
Thierry.Coupez@mines-paristech.fr

ABSTRACT

An immersed volume method for time-dependent, three-dimensional, conjugate heat transfer and fluid flow is presented in this paper. The incompressible Navier-Stokes equations and the heat transfer equations are discretized using a stabilized finite element method. The interface of the immersed disk is defined and rendered by the zero isovalues of the level set function. This signed distance function allows turning different thermal properties of each component into homogeneous parameters and it is coupled to a direct anisotropic mesh adaptation process providing a better capturing of the interface without affecting the initial background mesh. Thus, a single set of equations is solved for both fluid and solid with different thermal properties which can reduce the computational costs. On the other hand, using stabilized finite element method for the Navier-Stokes and the convection-diffusion equations allows the control of spurious oscillations and thermal shocks yielding very accurate results. The proposed method demonstrates the capability of the model to simulate an unsteady three-dimensional heat transfer flow of natural convection, conduction and radiation in a cubic enclosure with the presence of a conduction body (inconel 718). Results are assessed by comparing the predictions with the experimental data.

Key Words: *Stabilized FEM, natural convection, heat conduction, radiative transfer, immersion volume method*

1. INTRODUCTION

The development of efficient methods to understand and simulate conjugate heat transfer for multi-components system is one of the most challenges in engineering and industrial applications, especially the heat treatment of high-alloy steel by a continuously cooling. Usually, the heat treatment sequence involves heating to a high temperature followed by a controlled cooling so as to enhance the particular microstructures and the combinations of properties such as hardness, toughness and resistance. Fully hardened steel can be only obtained at a sufficiently high rate of cooling conditions. Usually, in the industry we carry out many experimental tests to attain this critical rate of cooling. Hence, resorting to numerical experiments is expected to save both time and economical resources. A first step to design an industrial numerical tool for simulating a quenching process is the modelling of air cooling of a heated body inside an enclosure. The main interest in this present is to present a direct method to study and analyse all the phenomena taking place in such a complex configuration, from a fluid dynamics and heat transfer point of view. We especially insist on the representation of the physical domains (air and solid), and how to deal with these domains both in terms of accuracy and computational costs. In recent years, there has been increasing interest in studying numerically a variety of engineering applications

that involve coupling between different physical phenomena such as conduction, convection and radiation. Most of the time, such analyses may be accomplished by dividing the global domain into several local subdomains over each of which a local model (equation to be solved) can be analyzed independently. The global solution can then be constructed by suitably piecing together local solutions from individually modelled subdomains. However, during the assembly, it is often too cumbersome, or even infeasible, to coordinate the meshes over separate subdomains. Alternate approaches that have also been applied for multi-phase flows problems are available in the literature. The idea was to introduce enrichment functions for material interfaces and voids by means of the level set representations of surfaces. Nevertheless, when using all these techniques, one still need to know the value of the heat transfer coefficients between the two domains which ensures, as a boundary condition, the heat transfer at the air/solid interface. In practice, industrials perform many experimental tests to obtain these heat transfer coefficients. But, when dealing with a large diversity of shapes, dimensions and physical properties of these metals to quench, such operations can become rapidly very costly and time consuming.

An alternative method to overcome this drawback is to consider a single grid for both air and solid for which only one set of equations need to be solved. This technique, known as immersed volume method (IMV), makes the use of a signed distance function (level-set function method) that allows turning thermal properties of each component into homogeneous parameters. Consequently , there is no need of empirical data so as to determine the exchange coefficients which are replaced naturally by solving the convective fluid in the whole domain and in particularly at the interface. At the same time, solving the radiative transport equation (RTE) in both domains generates a volume source term rendered by the sharp discontinuity of the temperature and the materials properties. Moreover, we make the use of our advanced research in the anisotropic mesh adaptation to adapt the interface between two different materials. The proposed mesh generation algorithm allows the creation of meshes with extremely anisotropic elements stretched along the interface, which is an important requirement for conjugate heat transfer and multi-component devices with surface conductive layers [1-2].
From a numerical point of view, the sudden cooling of hot solid immersed inside a gas fluid is at the origin of so-called thermal shocks which cause spurious oscillations in the solution. In order to circumvent this issue, a stabilized Finite-Element method is introduced for both Navier-Stokes and the convection-diffusion equations [3-4]. As far as the radiative terms are concerned, the radiative transfer equation is solved separately using the so-called P-1 method [5].

2. GOVERNING EQUATIONS

The governing equations are considered to be three-dimensional, unsteady and incompressible. Thermophysical and mechanical properties are assumed to depend on both the temperature and the relative position (air/solid) in the computational domain. The computation of the heat transfer and the fluid flow requires to solve simultaneously the Navier-Stokes and energy equations. Moreover, in order to take into account the radiation effects, the radiative transfer equation has to be solved. Hence, the resulting governing equations are the following:

$$\text{(1)} \qquad \begin{cases} \boldsymbol{\nabla} \cdot \mathbf{u} = 0 & \text{in } \Omega \\ \rho \left(\partial_t \mathbf{u} + \mathbf{u} \cdot \boldsymbol{\nabla} \mathbf{u} \right) - \boldsymbol{\nabla} \cdot \left(2\mu \, \dot{\boldsymbol{\gamma}}(\mathbf{u}) - p \, \mathbf{I_d} \right) = \rho_0 \beta (T - T_0) \, \mathbf{g} & \text{in } \Omega \end{cases}$$

where $\mathbf{u}$ is the velocity vector, ρ the density, p the pressure, T the temperature, μ the dynamic viscosity, $\dot{\boldsymbol{\gamma}}(\mathbf{u}) = (\boldsymbol{\nabla}\mathbf{u} + {}^t\boldsymbol{\nabla}\mathbf{u})/2$ the deformation-rate tensor, ρ_0 and T_0 reference density and temperature, β the thermal expansion coefficient and $\mathbf{g}$ the gravity vector. The heat transfers are governed by the energy equation:

$$\text{(2)} \qquad \begin{cases} \rho C_p (\partial_t T + \mathbf{u} \cdot \boldsymbol{\nabla} T) - \boldsymbol{\nabla} \cdot (\lambda \boldsymbol{\nabla} T) = f - \boldsymbol{\nabla} \cdot \mathbf{q_r} & \text{in } \Omega \\ T(\mathbf{x}, t) \; = \; T_{\text{wall}} & \text{in } \partial\Omega \\ T(\mathbf{x}, 0) \; = \; T_0(\mathbf{x}) & \text{in } \partial\Omega \end{cases}$$

where C_p the heat capacity, λ the specific conductivity, f a source term and $\mathbf{q_r}$ the radiative heat flux.

The contribution of the radiations to the heat transfers is assessed using the radiative transfer equation (RTE) coupled with the so-called P-1 radiation method. This latter enables to simplify the RTE equation

so that the incident radiation is found solving the following system:

$$\begin{cases} \boldsymbol{\nabla} \cdot \left(\dfrac{1}{3\kappa} \boldsymbol{\nabla} G \right) - \kappa G = 4\kappa\sigma T^4 \quad \text{in } \Omega \\ \dfrac{\partial G_w}{\partial n} = \dfrac{3\kappa\epsilon_w}{2(2-\epsilon_w)} \left(4\sigma T_w^4 - G_w\right) \text{ in } \partial\Omega \end{cases} \tag{3}$$

where G is the incident radiation, κ is the mean absorption coefficient which is calculated using the Bouger law, σ the Stefan-Boltzmann constant and ϵ_w the emissivity of the wall surfaces. Under gray gas assumption (see [4]), the divergence of the radiative flux from equation (2) is then computed as follows:

$$-\boldsymbol{\nabla} \cdot \mathbf{q_r} = \kappa \left(G - 4\kappa\sigma T^4\right) \tag{4}$$

Equations (1-3) are discretized using a space-time stabilized finite element methods to control the convection dominated flow as well as the sharp gradients of temperature (see [3-4] for further details).

3. IMMERSED VOLUME METHOD

The material distribution between each physical domains and the refined interface are described by means of the so-called level set method. For each node of the computational domain Ω, the level set function α reads:

$$\alpha(\mathbf{x}) = \begin{cases} > 0 & \text{if } \mathbf{x} \in \Omega_{fluid}, \\ 0 & \text{if } \mathbf{x} \in \Gamma_{interface}, \\ < 0 & \text{if } \mathbf{x} \in \Omega_{solid}. \end{cases} \tag{5}$$

The physical and thermodynamic properties in the domain are then calculated as a function of α; for instance, the mixed density is calculated using a linear interpolation between the values of the density in the fluid and the solid:

$$\rho = \rho_f H(\alpha) + \rho_s (1 - H(\alpha)) \tag{6}$$

where H is a smoothed Heaviside function given by:

$$H(\alpha) = \begin{cases} 1 & \text{if } \alpha > \varepsilon \\ \dfrac{1}{2}\left(1 + \dfrac{\alpha}{\varepsilon} + \dfrac{1}{\pi}\sin\left(\dfrac{\pi\alpha}{\varepsilon}\right)\right) & \text{if } |\alpha| \leq \varepsilon \\ 0 & \text{if } \alpha < -\varepsilon \end{cases} \tag{7}$$

ε is a small parameter such that $\varepsilon = O(h)$, where h is the averaged mesh size in the vicinity of the interface. The proposed mesh generation algorithm allows the creation of meshes with extremely anisotropic elements stretched along the interface, which is an important requirement for conjugate heat transfer and multi-component devices with surface conductive layers. The grid is only modified in the vicinity of the interface which keeps the computational work devoted to the grid generation low. This anisotropic adaptation is performed by constructing a metric map that allows the mesh size to be imposed in the direction of the distance function gradient : $\mathbf{x} = \boldsymbol{\nabla}\alpha / ||\boldsymbol{\nabla}\alpha||$. The constructed metric will take the following form:

$$\mathbf{M} = C\,(\mathbf{x} \otimes \mathbf{x}) + \frac{1}{h_d}\,\mathbf{I_d} \tag{8}$$

where $\mathbf{I_d}$ is the identity tensor and C is the signed tensor. Finally we obtain an isotropic mesh far from the interface (with a mesh size equal to h_d for all directions) and an anisotropic mesh near the interface (with a mesh size equal to h in the $\mathbf{x}$-direction and equal to h_d elsewhere).Further details about the algorithm used in here are available in [1].

4. NUMERICAL VALIDATION

A 3D Inconel-718 hat shape disk is initially taken at a temperature of 1160 ^oC and placed inside an enclosure filled by air at atmospheric conditions. The complete setup of this experiment is given in figure 1. We start by deriving an anisotropic adapted mesh that describes very accurately the interface between air and solid. Once the mesh is well adapted along the interface, the physical properties are

FIGURE 1. Problem setup and anistropic mesh adaptation

mixed and the coupled flow and heat transfer problem is solved iteratively. The heat transfer between

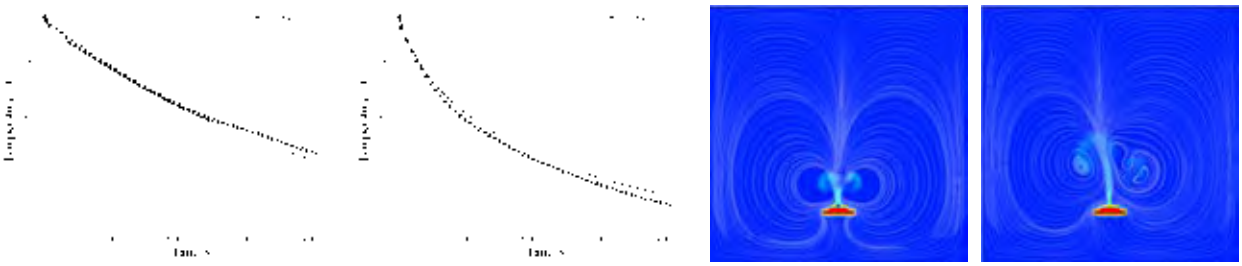

(a) (b) (c) (d)

FIGURE 2. Temperature evolution and streamlines.

the solid and the air at the interface has been treated "naturally", *ie* without the use of any heat transfer coefficient. Figure 2 shows the evolution of the temperature at the center (a) and close to the surface (b) of the disk as well as the convective effects from the Boussinesq model (c-d). The numerical solutions are in good agreements with the experimental data.

5. CONCLUSIONS

An immersed volume method for natural convection, conduction and radiation in a cubic enclosure with the presence of a conduction body (inconel 718) has been presented. The proposed method showed very promising results and can be used for any different geometry. It only requires to define the composite material properties without previous knowledge of the heat transfer coefficient between the solid and the surrounding fluid.

REFERENCES

[1] C. Gruau and T. Coupez, 3D Tetrahedral, Unstructured and Anisotropic Mesh Generation with Adaptation to Natural and Multidomain Metric, *Comput. Methods Appl. Mech. Engrg.*, 194, 4951-4976, 2005.

[2] T. Coupez, H. Digonnet and R. Ducloux, Parallel meshing and remeshing, *Appl. Math. Modelling*, 25, 2000.

[3] T.J.R. Hughes, Multiscale phenomena: Green's functions, the Dirichlet to Neuman formulation, subgrid scale models, bubbles and the origin of stabilized methods, *Comput. Methods Appl. Mech. Engrg.*, 127, 387-401, 1995.

[4] E. Hachem, H. Digonnet, E. Massoni and T. Coupez, Enriched finite element spaces for transient conduction heat transfer, *Int. J. for Num. Methods in Engng.*, submitted Nov 2008.

[5] M.F. Modest, *Radiative Heat Transfer*, McGraw Hill, New York, 1993.

First International Conference on Computational Methods for Thermal Problems
ThermaComp2009, September 8-10, 2009, Naples, Italy
N.Massarotti and P.Nithiarasu (Eds.)

An adaptive mesh refinement strategy for the solution of 3D inverse heat conduction problems using point-wise temperature observations

Yi Heng, **Maka Karalashvili**, **Adel Mhamdi**, **Wolfgang Marquardt**

AVT-Process Systems Engineering, RWTH Aachen University, D-52064 Aachen, Germany,
{yi.heng, maka.karalashvili, adel.mhamdi, wolfgang.marquardt}@avt.rwth-aachen.de

ABSTRACT

We present an algorithm for the fast solution of inverse heat conduction problems arising in pool boiling. The state equation is governed by the three-dimensional (3D) transient heat equation. The inverse problem is solved by an iterative regularization strategy. To reduce the computational effort, the numerical solution strategy considers local mesh refinement controlled by an a- posteriori error estimation procedure. The algorithm is applied to a real pool boiling experiment. The estimation results and the computational efficiency are analyzed.

Key words: *Local heat flux estimation, iterative regularization, adaptive mesh refinement.*

1. INTRODUCTION

Despite the huge research effort in the past decades, the mechanistic understanding of boiling phenomena is still not yet well understood. The reconstruction of the unmeasurable local boiling heat fluxes serves as a basis for the analysis of boiling heat transfer mechanisms. In recent years, one particular pool boiling experiment has been taken by our collaboration partner at TU Berlin and transient temperature observations at a few micro-thermocouples (MTC) mounted below the solid-liquid contact surface have been measured. These provide indirect information about the surface temperature and surface heat flux. Details of the experimental setup can be found in [1].

The reconstruction of the unknown surface heat flux from measured temperatures inside a heater body is an ill-posed inverse heat conduction problem (IHCP) [2]. Appropriate regularization methods, e.g. Tikhonov regularization, have been developed for its solution [2-4,7].

In our previous work [5,6], we proposed an iterative regularization strategy based on the conjugate gradient method for the solution of considered 3D IHCP problems arising in pool boiling. In this work, we consider the development of an a-posteriori error estimator for local mesh refinement to reduce the required computational time. Its application is important for the reconstruction of local boiling heat fluxes along the entire boiling curve, which is the basis for the systematic development of suitable heat transfer models describing the transient boiling process with local resolution.

2. THE INVERSE HEAT CONDUCTION PROBLEM

We consider the simple model governed by the transient heat equation defined on a 3D domain Ω with boundary $\partial\Omega = \Gamma_H \cup \Gamma_B \cup \Gamma_A$ (cf. Fig. 1)

$$\rho c_p \frac{\partial T}{\partial t} = \nabla \cdot (\lambda \nabla T), \qquad \text{in } \Omega \times (0, t_f), \tag{1}$$

$$T(\cdot, 0) = 0, \qquad \text{on } \Omega, \tag{2}$$

$$\lambda \frac{\partial T}{\partial n} = 0, \qquad \text{on } (\Gamma_H \cup \Gamma_A) \times (0, t_f), \tag{3}$$

$$\lambda \frac{\partial T}{\partial n} = q, \qquad \text{on } \Gamma_B \times (0, t_f), \tag{4}$$

where $(0, t_f)$ is the time interval. ρ, c_p and λ denote density, heat capacity and heat conductivity, respectively. They could be functions of the spatial and temporal coordinates.The considered inverse problem corresponds to the reconstruction of the unknown heat flux q from temperature observations measured by the MTC (cf. Fig. 1). Equations $(1)-(4)$ establish a linear relation between the heat flux q at the boiling surface and the temperature distribution T. Although, the initial and boundary conditions are often not zero in reality such that the mapping relation between q and T is affine-linear, it can be simplified to the formulation $(1)-(4)$ [5]. Since the temperature observations are available only at m

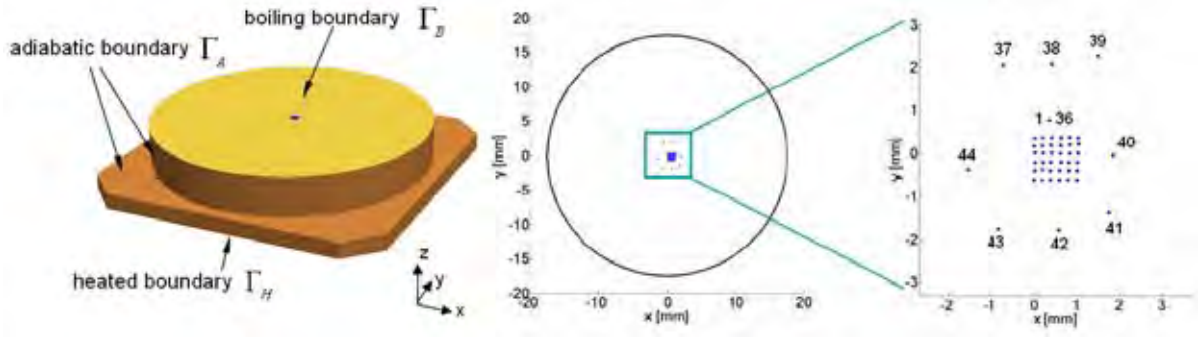

FIGURE 1. Left: The considered heater geometry. Right: the x-y position of 44 measurement sensors, which are located 3.6 μm below the boiling surface Γ_B.

finite locations $x \in M \subset \Omega$ and the time resolution is assumed to be sufficiently high, we choose the data space $\mathcal{Y} = L^2(0, t_f; \mathbb{R}^{N_m}) = \{T_m^i(t) \in L^2(0, t_f) : i = 1, \ldots, N_m\}$. To achieve the uniqueness, we seek the solution q in the function space $\mathcal{X} = L^2(0, t_f; H^1(\Gamma_B))$ [7]. By introducing the notation $T_m := T|_M$, the equations $(1)-(4)$ define implicitly the operator K

$$K : \mathcal{X} \to \mathcal{Y}, \qquad q \to T_m, \tag{5}$$

which corresponds to the forward problem. The inverse problem corresponds to the solution of the operator equation $Kq = T_m$ for q. Details of the mathematical analysis can be found in [6].

3. SOLUTION ALGORITHM ON A FIXED MESH

The solution of the considered inverse heat conduction problem is obtained by the minimization of the following least-squares functional,

$$J(q^\delta) := \|Kq^\delta - T_m^\delta\|^2, \tag{6}$$

where δ denotes the noise level of the unperturbed temperature observations T_m. This is equivalent to solving the normal equation (NE)

$$K'Kq^\delta = K'T_m^\delta\,, \tag{7}$$

with K' the adjoint operator with respect to the space $\mathcal{X}$. The conjugate gradient applied to the normal equation (CGNE) algorithm is employed here for its solution. Details of the implementation issues of the CGNE-algorithm can be found in [6].

4. ADAPTIVE MESH REFINEMENT STRATEGY

To enhance the performance of our solution procedure, we propose an adaptive mesh refinement procedure using a sequence of gradually refined meshes $\mathcal{T}_h^k, k = 1 \ldots L$. Due to lack of better information, the computation starts on a coarse mesh with zero initial value for q. On each subsequent finer mesh level, the heat flux computed on previous mesh refinement level is used as initial value for the solution of the inverse problem on the current mesh refinement level. The maximal number of levels corresponds to the mesh at which the discretization error of the forward problem meets the order of the data error δ. The proposed adaptive mesh refinement scheme is summerized in algorithm 1.

Algorithm 1 (Adaptive mesh refinement)**.**

1. Choose an initial mesh $\mathcal{T}_h^1$ and set $k = 1$, $\hat{q}_0^1 = 0$
2. Construct the finite element space
3. Solve the inverse problem on $\mathcal{T}_h^k$ to obtain the solution $\hat{q}^k$
4. Evaluate the *a posteriori* error estimator
5. If error $\leq$ TOL , stop
6. Refine $\mathcal{T}_h^k \longrightarrow \mathcal{T}_h^{k+1}$ using information from (4) and set initial value $\hat{q}_0^{k+1} = \tilde{q}^k$, with $\tilde{q}^k$ being the interpolation of the solution $\hat{q}^k$ on the finer mesh.
7. Increment k and go to 2

To perform the steps 4 and 6, we consider the a-posteriori error estimate with respect to the cost functional J of the following form:

$$J(q^\delta) - J(\hat{q}^k) \approx \eta_h^k. \tag{8}$$

Since the time resolution of the available measurements is very high, in this work we consider only the space discretization error denoted by η_h^k, which can be evaluated from the computed discrete solution. The explicit form of the used error estimator is defined by

$$\eta_h^k|_i := \|T(\hat{q}^k)|_i - Y_i\|^2 = \int_0^{t_f} (T(\hat{q}^k)|_i - Y_i)^2 \, dt, \tag{9}$$

where i denotes the index of the measurement position. Y_i and $T(\hat{q}^k)|_i$ correspond to the measured and computed temperatures at spatial position i, respectively.

The heuristics behind step 6 is to refine only regions close to measurement positions using the information of error estimator (9). Explicitly speaking, if the error level at a certain measurement position i is lower than the chosen tolerance TOL, no mesh refinement for i is carried out, otherwise the region close to i has to be refined. This refinement procedure continues until the errors at all measurement positions, and also their average value, are lower than TOL. Compared to the use of a pre-defined fine mesh discretization, the proposed adaptive approach enables the automatical selection of a discretization model with much smaller size. This leads to significant reduction of total computational effort.

5. ESTIMATION RESULTS WITH REAL EXPERIMENTAL DATA

In this section, we consider the pool boiling experiement presented in [1]. The chosen values for material properties are given in [6]. The observation time interval is 30 ms with a time step of 0.04 ms. For the space discretization, we choose a finely discretized mesh $\mathcal{T}_h^{\text{fine}}$ (cf. first row in the Table 1) for the illustration of the single-level optimization strategy. The adaptive mesh refinement algorithm starts with a coarse mesh $\mathcal{T}_h^1$; subsequent meshes $\mathcal{T}_h^2$ and $\mathcal{T}_h^3$ (cf. Fig 2(b)-(d)) are automatically generated base on the error estimator during an iterative process. The pre-defined tolerance TOL is chosen on the base of investigated temperature noise level $\delta = 0.025$ K. As we can see from Table 1, nearly 94% reduction of the computational efforts could be achieved with solutions of comparable quality (cf. Fig. 3).

6. CONCLUSIONS

An iterative regularization method combined with an adaptive mesh refinement strategy has been proposed for the solution of a 3D transient inverse heat conduction problem using pointwise temperature observations. Compared to our previous work, the computational effort has been significantly reduced and comparable estimation results are obtained. Future work will be devoted to the development of different types of error estimators and their comparison with respect to the obtained computational efficiency and estimation quality.

ACKNOWLEDGEMENT

The authors acknowledge the financial support by DFG through a joint research project on fundamentals of boiling heat transfer and SFB 540. We would like thank Hein Auracher and co-workers for giving access to experimental data [1].

TABLE 1. Numerical results with real experimental data using single-level and adaptive mesh refinement strategy; M: number of elements, N: number of time steps, it: number of optimization iterations.

	M	N	η_h	it	$time$
$\mathcal{T}_h^{\text{fine}}$	164,484	750	5.881×10^{-4}	54	8919.9 s
$\mathcal{T}_h^1$	3,156	750	6.229×10^{-3}	50	75.4 s
$\mathcal{T}_h^2$	11,418	750	1.545×10^{-3}	50	273.9 s
$\mathcal{T}_h^3$	17,430	750	6.047×10^{-4}	26	224.9 s

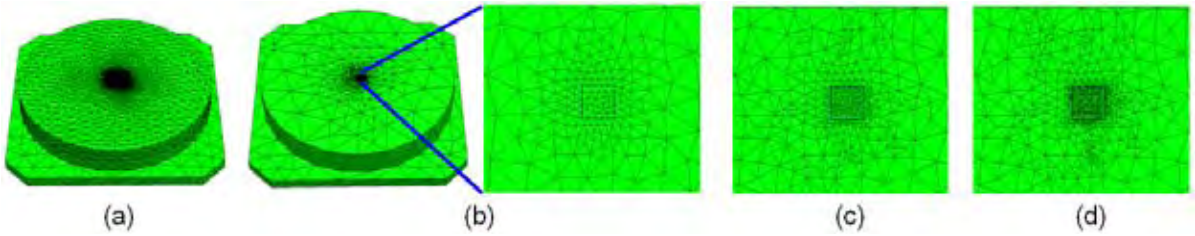

FIGURE 2. (a) Mesh $\mathcal{T}_h^{\text{fine}}$, (b) Mesh $\mathcal{T}_h^1$ and zoomed center view, (c) Zoomed center view of mesh $\mathcal{T}_h^2$, (d) Zoomed center view of mesh $\mathcal{T}_h^3$

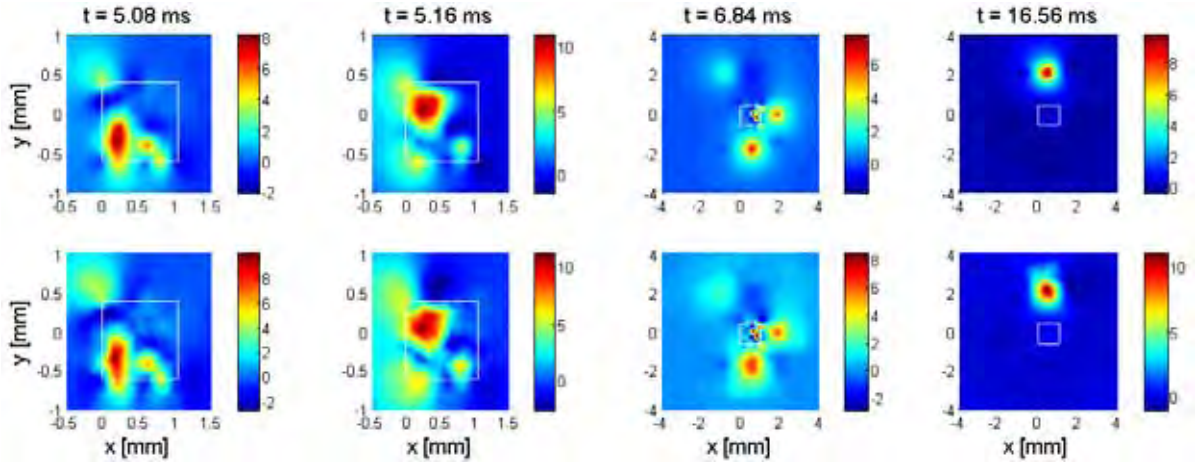

FIGURE 3. A comparison of selected estimated surface boiling heat fluxes (MW/m^2) obtained using single-level optimization (upper row) and adaptive mesh refinement strategy (lower row).

REFERENCES

[1] M. Buchholz, H. Auracher, T. Lüttich and W. Marquardt, *J. Heat Fluid Flow*, 25, 243-261, 2004.

[2] O.M. Alifanov, *Inverse Heat Transfer Problems*, Springer, Berlin, 1994.

[3] A.N. Tikhonov and V.Y. Arsenin, *Solutions of Ill-posed Problems*, V.H. Winston and Sons, New York, Washington, 1977.

[4] B. Kaltenbacher, A. Neubauer and O. Scherzer, *Iterative Regularization Methods for Nonlinear Ill-Posed Problems*, Walter de Gruyter, 2008.

[5] Y. Heng, A. Mhamdi, S. Groß, A. Reusken, M. Buchholz, H. Auracher and W. Marquardt, *Int. J. Heat Mass Transfer*, 51, 5072-5087, 2008.

[6] H. Egger, Y. Heng, W. Marquardt and A. Mhamdi, *Submitted to Inverse Problems*.

[7] H. W. Engl, M. Hanke, and A. Neubauer, *Regularization of Inverse Problems*, Kluwer Academic Publishers, Dordrecht, 1996.

First International Conference on Computational Methods for Thermal Problems
ThermaComp2009, September 8-10, 2009, Napoli, Italy
N.Massarotti and P.Nithiarasu (Eds.)

INVERSE DETERMINATION OF THERMAL CONDUCTANCE FOR BUILDING WALLS

Gaspare Giovinco
Dipartimento di Meccanica, Strutture, Ambiente e Territorio (DiMSAT) – University of Cassino,
Via G. Di Biasio 43 – 03043 Cassino (FR) - Italy, giovinco@unicas.it

ABSTRACT

Heat flow meter (HFM) is widely used for on site measurements of thermal conductance and transmittance of building envelopes. This method, in particular, requires a post-processing of the acquired data about measured temperature and heat flows, by means of suitable algorithms such as the "black-box" and the progressive mean ones. The progressive mean algorithm is enough reliable but, on the other hand, it requires extremely long measurement times, especially for high inertia walls. On the contrary, the "black-box" method requires short measurement times since it is based on time series analysis and, sometimes, it can lead to very high errors.

The aim of the present paper is to compare the above mentioned methods to a new one based on the solution of an inverse problem in order to obtain useful results for short time measurements and for measurement conditions involving high temperature variations both for the inner and outer environment which are typical for summer, spring and winter conditions with heated rooms in intermittent mode.

Key Words: *Heat Transfer, Inverse Problems, Thermal Conductance.*

1. HFM MEASUREMENT PRINCIPLE

As known, wall thermal conductance is defined as the ratio between the heat flow normal to the wall and the temperature difference between inner and outer wall surface.

Therefore, in order to evaluate such parameters, it is necessary to measure heat flow and inner and outer wall temperatures. The outer temperature variability in accordance with the daily conditions (and sometimes also the inner temperature ones in accordance with the heating or the HVAC plant operating conditions) coupled to heat flow variations due to the building envelope thermal inertia (and often to the inner and outer convective and radiative conductances) makes the instantaneous conductance measurement almost useless and misleading.

The thermal balance applied to the wall in unsteady conditions gives:

$$\dot{q}_{in} \cdot A = \dot{q}_{out} \cdot A + \frac{\partial}{\partial \vartheta} \int_{V.C} \cdot c \cdot T \cdot dV + \dot{Q}_{disp} \tag{1}$$

where $\dot{Q}_{disp}$ is the dispersed heat transfer rate, $\dot{q}$ is the heat flux, T is the absolute temperature of the wall, is the density, c is the specific heat, A is the normal surface of the wall and ϑ is the time.

As shown, in the presence of 1D thermal field, $\dot{Q}_{disp} = 0$, the difference between the inner and outer heat flow is due only to the heat accumulation term.

Therefore, for 1D and steady thermal conditions it is possible to measure the heat flow only on one wall surface, and the thermal conductance C is given by:

$$C = \frac{\dot{q}}{T_{w,i} - T_{w,e}} \tag{2}$$

where $T_{w,i}$ and $T_{w,e}$ are the internal and external wall temperatures.

2. POST PROCESSING

Dynamic test conditions require temperature and heat flow data acquisition for time intervals long enough. In the Italian standards [1-3] and scientific literature [4-6] several post-processing algorithms are proposed.

In the present paper, an alternative method is proposed, based on the solution of an inverse heat transfer problem in 1D unsteady thermal conditions, once the inner and outer wall surface temperatures and the heat flow are known as time varies.

3. INVERSE PROBLEM DEFINITION

A building wall is usually formed by a finite number of layers, each one having its thermophysical properties which can be considered constant along its thickness also for temperature variations. For an existing wall, if endoscopic investigations are not performed, generally it is not possible to know either the number of layers or the material of each layer.

Under the hypothesis of 1D thermal field, the following equation can be written:

$$(x)\cdot c(x)\cdot\frac{\partial T(x,\vartheta)}{\partial\vartheta}=\frac{\partial}{\partial x}\left(k(x)\cdot\frac{\partial T(x,\vartheta)}{\partial x}\right)\ \text{for}\ x\in[0,L]\ \text{and}\ \vartheta\geq 0 \tag{3}$$

where L is the wall thickness, with the following boundary conditions:

$$T(x=L,\vartheta)=T_{w,e}(\vartheta);\quad -k(x=0)\cdot\frac{\partial T(x=0,\vartheta)}{\partial\vartheta}=\dot{q}(\vartheta)\quad\text{for}\ \vartheta\geq 0 \tag{4}$$

by using the acquired $T_{w,e}(\vartheta)$ as term for minimization in eq. (6).

Therefore, the following functions must be determined (initial temperature conditions and thermophysical properties):

$$T(x,\vartheta=0);\quad k(x);\quad \Omega(x)\qquad\qquad\text{for}\ x\in[0,L] \tag{5}$$

where $\Omega(x)=(x)\cdot c(x)$.

In order to solve the inverse problem, eqs. (3)-(4) where solved by the finite differences method (fully implicit scheme) [7] with a number of calculation points determined through a mesh sensitivity analysis. The punctual values of the functions in eqs. (5) where obtained through the solution of the following minimisation problem in Scilab through the conjugate gradient method [8]:

$$min\left(\int_{\vartheta=0}^{\vartheta=\vartheta_{max}}\left(T(x=0,\vartheta)-T_{w,e}(\vartheta)\right)^2\cdot d\vartheta+\underbrace{\int_{\vartheta=0}^{\vartheta=\vartheta_{max}}\int_{x=0}^{x=L}\frac{k(x)}{T(x)}\cdot\left(\frac{\partial T(x)}{\partial x}\right)^2 dx d\vartheta}_{regolarization\ term}\right) \tag{6}$$

where the regularization term represents the entropic production, considered as in equilibrium conditions [10-11] and ϑ_{max} is the time corresponding to the end of the data acquisition.

4. NUMERICAL RESULTS

The proposed methodology was compared to the two most diffused post-processing algorithms: the progressive mean method [9] and the “black box” [5] one.

For this purpose the direct problem described by eqs. (3)-(5) was solved through the finite element software Femlab 3.1 ®, by applying the temperature boundary conditions reported in Fig. 1 to a wall of high thermal inertia whose characteristics are reported in Table 1, with internal and external thermal conductances equal to 7.69 W/(m^{2}K) and 25 W/(m^{2}K) respectively [1].

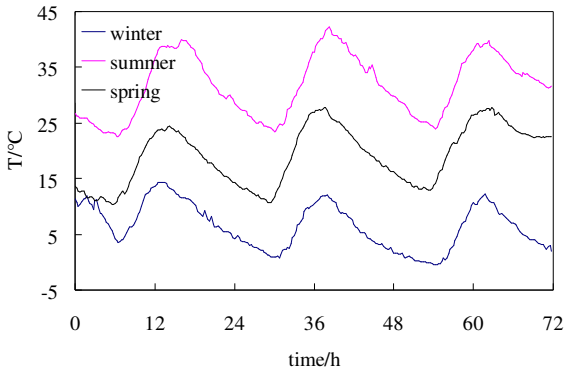

External temperatures

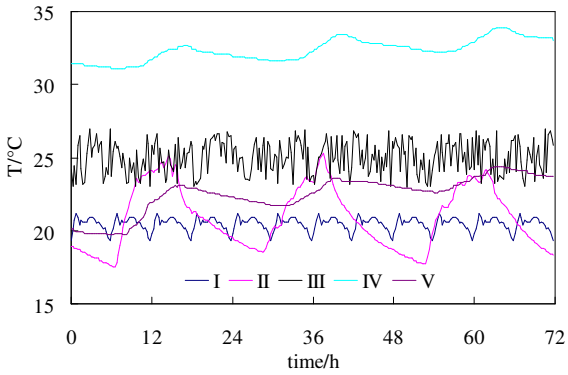

Internal temperatures

FIGURE 1. Applied temperature boundary conditions: (I) winter conditions with continuous heating, (II) winter conditions with 8 hours heating, (III) summer conditions with continuous climatisation, (IV) summer conditions with continuous climatisation and (V) summer conditions without climatisation .

These thermal conditions were recorded by the weather station of the University of Cassino during the year 2007 and refers to the period 23-25 August, 15-17 December and 10-12 April, during which the highest, the lowest temperatures and thermal inversion can be observed, respectively. Moreover, it was considered that as initial thermal condition the wall was subjected to uniform temperature equal to 20°C:

In particular, the aim was to test the consistency of the proposed methodology during the periods in which heat flow inversion is observed (i.e. spring and autumn).

Layer	Material	thickness/mm	k/(W m^{-1} K^{-1})
1	Plaster	15	0.9
2	Hollow tile	120	0.19
3	Polystyrene	100	0.033
5	Hollow tile	120	0.19
6	Plaster	16	0.9

Table 1. Tested wall

As regards the proposed methodology, it must be pointed out that as guess values for the minimization problems the following values were assumed:

$$T\left(x,\vartheta=0\right)=T_{p,i}\left(\vartheta=0\right)-\frac{T_{p,e}\left(\vartheta=0\right)-T_{p,i}\left(\vartheta=0\right)}{L}\cdot x;\quad k\left(x\right)=1;\quad \Omega\left(x\right)=10^{6}\text{ for }x\in\left[0,L\right] \tag{7}$$

and:

$$C=1\Big/\left(\sum_{i=1}^{n-1}\frac{x_{i+1}-x_i}{k_i}\right) \tag{8}$$

where n represents the number of nodes in which the domain was dicretised.

The number of unknowns is then equal to: i) n-2 for the initial temperature (the initial values for x=0 and x=L are known), ii) n_s for $k\left(x\right)$ and iii) n_s for $\Omega\left(x\right)$, where n_s is the number of equal thickness slab in which the wall is divided, for a total number of $n+2n_s-2$.

From a sensitivity analysis, the optimal number of points and slabs is equal to 32 and 4 respectively, granting a variation on C lower than 0.1% both for n and n_s unitary increment.

The obtained results are reported in Table 2.

Post-processing algorithm	Winter conditions with continuous heating	Winter conditions with 8 hours heating	Summer conditions with continuous climatisation	Summer conditions with continuous climatisation	Summer conditions without climatisation
Expected value	0.271	0.271	0.271	0.271	0.271
Progressive mean	0.314 (16%)	0.287 (5.9%)	0.332 (23%)	0.410 (51%)	0.235 (-13%)
Black box	0.293 (8.1%)	0.140 (-48%)	0.192 (-29%)	0.220 (-19%)	0.193 (-29%)
Proposed algorithm	0.278 (2.6%)	0.283 (4.4%)	0.276 (1.8%)	0.281 (3.7%)	0.282 (4.1%)

TABLE 2. Numerical results and comparison with the other post-processing algorithms (in brackets the percentage differences respect to the expected value)

As shown in Table 2, the proposed method obtains a percentage difference that is always lower than 5%, optimal results if compared to the other post-processing algorithms which are not so encouraging especially if applied to summer and spring measurements.

5. CONCLUSIONS

In the present paper, a post-processing algorithm based on the solution of an inverse 1D heat transfer problem was applied to HFM measurements for the determination of a wall thermal conductance. In particular, the proposed methodology was compared to the most used post-processing algorithms as the "black-box" and the progressive mean ones. The obtained results are very encouraging especially if applied to summer and spring measurements.

Future developments will involve the application of the proposed methodology to 2D and 3D problems to characterize complex building components.

These paper was developed within the "Numerical and experimental characterization of building innovative components for energy saving" project financed by MIUR (2007S8yKTR_004/2007).

REFERENCES

[1] UNI EN ISO 6946: 2008 Componenti ed elementi per edilizia - Resistenza termica e trasmittanza termica - Metodo di calcolo.

[2] EN 15603:2008 Energy performance of buildings – Overall energy use and definition of energy ratings

[3] ISO 9869:1994 Thermal insulation – Building elements – In-situ measurement of thermal resistance and thermal transmittance

[4] M. Cucumo *et al.*, A Method for the Experimental Evaluation In-Situ of the wall Conductance, *Energy and Buildings*, 38, 238-244, 2006.

[5] A. Panzeri, Acquisizione dati involucro: Metodi impiegabili ai fini della certificazione energetica degli edifici, *neo-Eubios*, 14, 13-18, 2005.

[6] L. Laurenti *et al.*, Determination of the thermal resistance of walls through a dynamic analysis of in-situ data, *Int. J. of Thermal Sciences*, 43, 297–306, 2004

[7] A. Quarteroni, R. Sacco, and F. Saleri, *Numerical Mathematics*, 2nd ed, Springer, 2004.

[8] Gene H. Golub and Charles F. Van Loan, *Matrix computations*, 3rd ed., Chapter 10, John Hopkins University Press, 1996.

[9] prEN 12494:1996 European Standard Building Components and Elements, In-Situ Measurement of the Surface-to-Surface Thermal Resistance

[10] Yu. A. Lyashenko, O. A. Shmatko, Entropy production as a regularization factor in solving an inverse diffusion problem, *Russian Physics Journal*, 49(6), 658-663, 2006.

[11] H. Yapici *et al.*, *"Numerical study on transient local entropy generation in pulsating turbulent flow through an externally heated pipe"*, SADHANA-Academy Proc. in Engineering Sciences, 30(5), 625-648, 2005

First International Conference on Computational Methods for Thermal Problems
ThermaComp2009, September 8-10, 2009, Napoli, Italy
N.Massarotti and P.Nithiarasu (Eds.)

MODELLING AND SIMULATION OF THE NATURAL VENTILATION OF A TRANSFORMER SUBSTATION

Maximiliano Beiza
Ph. D. student, mbeiza@tecnun.es

Jon Gastelurrutia
Ph. D. student, jgastelurrutia@tecnun.es

Alejandro Rivas
Associate Professor, arivas@tecnun.es

Juan Carlos Ramos
Associate Professor, TECNUN (University of Navarra), Paseo de Manuel de Lardizábal 13, 20018 San Sebastián, Spain, jcramos@tecnun.es

ABSTRACT

The ventilation by natural convection and radiation of an underground prefabricated transformer substation has been modelled using *CFD* techniques. The results of the model are the distributions of temperature and velocity in the air and the surface temperatures of the transformer and the walls of the substation. The obtained values are compared with the experimental measurements realized under different ventilation and load conditions in order to validate the model.

Key Words: *Computational Fluid Dynamics, Natural Convection, Thermal Model.*

1. INTRODUCTION

Underground prefabricated transformer substations are used for electrical power distribution in public networks and private installation load-centres. These buildings are usually made of prefabricated concrete, having a personnel access and some ventilation grilles. Inside of the enclosure, one of two distribution transformers with their Low Voltage boards, Medium Voltage cubicles, and interconnecting and auxiliary devices are found. In the transformer and the LV boards there are heat generation due to power losses. This heat is removed by the natural convection of the air circulating through the ventilation grilles and by the radiation exchanges with the walls of the substation.

The International Standards [1-2] indicates that the criterion of good performance of a transformer substation is given by the maximum temperature achieved by the top oil. This temperature must be limited to extend the operation life of the transformer. As the experimental tests must be done with the real substation, the obtaining of an over limited temperature would invalidate the built substation, requiring a new design and new casts. In order to avoid this slow and expensive task, it would be very useful to have a mathematical model of the ventilation of the substation and to perform a simulation of this model to determine the temperatures.

One possible approach to the thermal modelling of transformer substations is the equivalent thermal circuit model developed by Radakovic and Maksimovic in [3]. This type of so simplified models permits to obtain the top oil transformer temperature but not to analyse and optimise the whole ventilation of the substation.

To get a better understanding of the ventilation of the transformer substations, it is necessary to develop a more complete model that takes into account the air circulation. Ramos *et al.* in [4]

presented a mathematical thermal model of the ventilation of a half-buried transformer substation using *CFD* techniques. The model presented in this paper is an improvement of that model.

2. MODELLING OF THE TRANSFORMER SUBSTATION

2.1. Description of the system

The substation that has been modelled contains two transformers with an input voltage of 36 kV and a power of 1000 kVA. The height of the transformers is approximately 1 m and the height of the enclosure is approximately 3 m.

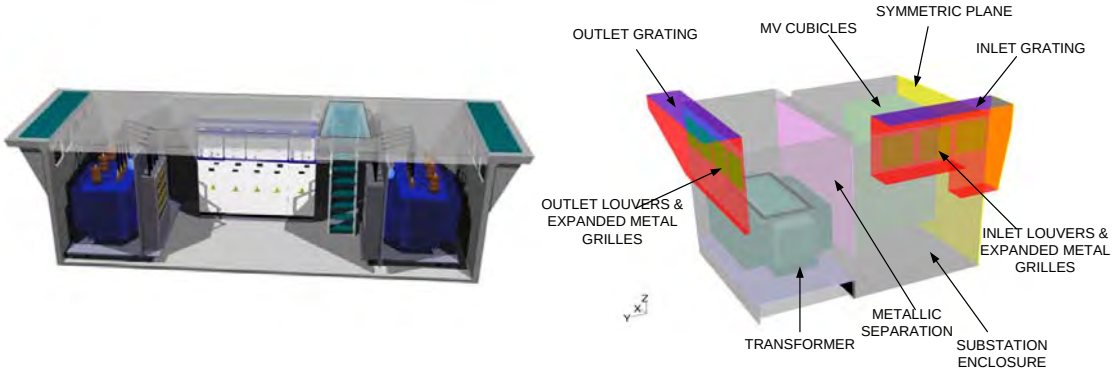

FIGURE 1. Images of the real (left) and the modelled (right) transformer substation

As it can be seen in Figure 1 (left), the configuration of the substation is almost symmetric: each transformer, with a set of outlet ventilation grilles, is located at the lateral extremes of the enclosure and there are inlet ventilation grilles in the middle of the longitudinal wall (not shown on the image). This set of inlet grilles is presented on the right part of Figure 1, which shows the flow domain of the model of the substation with its limits and its main components.

2.2. Description of the mathematical model

2.2.1 Governing Equations

The equations that represent the air flow and the heat transfer inside the substation are the steady Reynolds Average Navier-Stokes (*RANS*) equations, used to include turbulence effects in the mean flow variables, and the energy equation [5]

The RNG k-ε turbulence model [6] has been used with a 2 layer near wall approach [7].

The Ideal Gas equation is used to model the variation of the air density with the temperature. The rest of the air properties, like molecular viscosity, thermal conductivity and specific heat, are also temperature dependent.

The radiation heat exchange is considered by means of the Discrete Ordinates (DO) model [8]. Each octant of the angular space has been discretized into 9 solid angles that determine 72 directions where the radiation intensity is computed. It has been assumed that the air does not participate in the radiation and that the different surfaces in the domain are gray and diffuse.

2.2.2 Flow domain

The computational domain covers the air inside a half of the substation, due to the symmetry, as shown in Figure 1. The external limits of the domain are the walls of the enclosure, the symmetry plane and the inlet and outlet gratings. The internal limits are the surfaces of the transformer, the LV boards and the MV cubicles.

The model has about $21 \cdot 10^6$ elements. The resolution of the mesh is higher (approx. $7 \cdot 10^6$ elements) in the zone close to the transformer because it is the main heat source and a fine grid is needed to

model accurately the heat transfer and the air movement. The type of elements is hexahedral in the entire domain.

2.2.3 Boundary Conditions

In the inlet and the outlet boundaries, the atmospheric pressure and the ambient temperature were imposed. The inlet and outlet gratings, louvers and expanded metal grilles are modelled imposing a curve pressure loss - normal velocity for the air passing through them. These head loss curves have been obtained from mathematical models and book data [9].

The walls of the substation are modelled as solid walls with one-dimensional heat conduction and mixed (convection and radiation) external boundary conditions. The LV boards are considered as a box with a uniform heat flux imposed on the surface. The MV cubicles are considered adiabatic.

Initially, the experimental temperatures are imposed on the surfaces of the transformer. From this simulation, values of uniform heat fluxes on the different surfaces of the transformer (lid, fins, base) are obtained to be imposed in the next cases, simulating the different ventilation conditions of the experiments.

2.2.4 Discretization and resolution

The Finite Volume Method is used to discretized the governing differential equations. The steady state has been considered in the simulations and a segregated implicit solver has been used. Equations are linerized and then sequentially solved using Gauss Seidel algorithm accelerated by an Algebraic Multigrid method. Pressure-Velocity coupling is achieved through the use of SIMPLE algorithm. Diffusive and convective terms of the equations are discretized using second order upwind schemes. The Body Force Weighted scheme is chosen in the discretization of pressure to deal with this buoyancy driven flow. The entire numerical procedure is implemented in the unstructured *CFD* code Fluent V.6.3.26 [10].

2.2.5 Convergence criteria

Three principal convergence criteria have been considered to know when a simulation has reached a valid solution. The first one is the balance between the total energy dissipated from the surfaces of the transformer and the energy lost through the external limits of the domain. The second one is to reach perdurable stationary values for selected surface temperatures and for the mass flow rate through the ventilation grilles. And the last one is to obtain values of scaled residual below certain magnitudes (10^{-3} for mass, momentum and turbulence equations and 10^{-6} for energy equation).

3. RESULTS AND DISCUSSION

3.1. Experimental Tests

Three experimental tests, changing the conditions of ventilation and the transformer load, have been made. In Test 01 the substation is with full open ventilation (without any grille) and with transformer full load. Test 02 represents the service state: normal ventilation and full load power. In Test 03 the normal ventilation is maintained, but the transformer works at half power.

In the realization of the experiments 87 thermocouples for temperature measurements in specific positions, 5 hot-wire anemometers to measure the velocity of the air and a thermographic camera for the capture of the radiant image of the substation were used.

3.2. Comparison of the results of the model with the experiments

Table 1 shows some of the temperature results for the different tests and their comparison with the results of the simulations of the model.

Firstly, it can be observed that, for the three experimental tests, the model predicts acceptably the air temperatures in two specific positions above the transformer and at the outlet grating (maximum difference of -3.5 ºC). The same can be concluded for the walls of the substation (maximum

difference of -5.3 ºC). This is a demonstration that the model predicts well the global energy transport and the heat transfer in the external boundaries.

Relating the temperatures of the surface of the transformer and of the air between the fins, the results of the model are not totally acceptable. An adequate correlation between the results of the model and the tests is found in the temperatures of the lid for Test 02 and in the extreme fin for Test 02 and 03. The rest of results are excessively away from the experimental data.

Description	Test 01			Test 02			Test 03		
	T_{exp} [ºC]	T_{mod} [ºC]	Dif. [ºC]	T_{exp} [ºC]	T_{mod} [ºC]	Dif. [ºC]	T_{exp} [ºC]	T_{mod} [ºC]	Dif. [ºC]
Air above the transformer	48.0	48.3	0.4	53.9	54.3	0.4	39.0	37.3	-1.7
Air in the outlet grating	40.0	37.9	-2.1	41.7	38.2	-3.5	30.4	31.7	1.2
Interior surface of lateral wall	27.7	28.8	1.2	30.3	30.9	0.6	24.3	22.8	-1.5
Exterior surface of lateral wall	34.5	33.6	-0.8	39.1	36.7	-2.4	28.5	25.8	-2.7
Interior surface of rear wall	33.4	30.7	-2.6	37.8	32.5	-5.3	27.5	23.7	-3.8
Exterior surface of rear wall	26.0	26.8	0.8	27.6	28.0	0.4	22.2	28.0	5.8
Central Position of the lid	81.2	86.4	5.2	88.6	87.4	-1.2	59.7	52.4	-7.3
Average Surface Lid	79.9	85.7	5.8	87.3	86.2	-1.1	58.9	55.5	-3.4
Central Fin - High Position	80.5	93.8	13.3	88.7	98.4	9.7	58.6	63.4	4.8
Central Fin - Medium Position	71.7	80.3	8.6	80.4	83.6	3.1	52.0	52.9	0.9
Central Fin - Down Position	57.0	56.8	-0.1	65.7	55.7	-10.0	41.7	37.8	-4.0
Central Fin - Average	74.2	70.1	-4.1	76.5	79.0	2.5	49.7	51.1	1.3
Extreme Fin - High Position	78.1	86.5	8.4	85.4	89.3	3.8	57.5	57.3	-0.2
Extreme Fin - Medium Position	70.8	78.8	8.0	78.1	81.2	3.1	51.4	53.1	1.7
Extreme Fin - Down Position	61.9	67.8	5.9	70.0	67.4	-2.6	44.4	43.2	-1.2
Extreme Fin - Average	73.6	67.5	-6.0	75.9	74.0	-1.9	49.3	49.1	-0.2
Air between central fins - High	48.9	39.4	-9.5	57.4	46.7	-10.7	39.6	34.0	-5.6
Air between central fins - Down	34.5	25.8	-8.6	41.1	27.3	-13.8	29.9	23.1	-6.9

TABLE 1. Comparison between experimental and simulation temperatures

A possible reason to explain these differences is that the heat fluxes imposed as boundary conditions on the surfaces of the transformer are incorrect. These uniform heat fluxes have been calculated proportionally to the ones obtained from a simulation of the model imposing on the transformer the experimental temperatures of Test 01.

Therefore, the results obtained in the central fin for the three tests indicate that in this zone is necessary to impose a non-uniform heat flux that varies with the vertical coordinate. Moreover, in the extreme fins, the acceptable results obtained for Test 02 and 03 show that when the substation is working with the normal ventilation the use of a uniform heat flux boundary condition is not so bad. Lastly, the results in the lid for Test 03 indicate that a uniform heat flux obtained from a transformer working at 100% of power, divided by 2, is not applicable to a transformer working at 50% of load.

The inappropriate uniform heat fluxes imposed in the central fins are also affecting to the results obtained for the air between them. However, qualitatively, the model can be used to analyse the air temperature distribution and the air movement, as shown in Figure 2.

4. CONCLUSIONS

A mathematical model, representing the thermal performance of an underground prefabricated transformer substation, has been developed using CFD techniques. The results of the model have been compared with the experimental ones obtained under three different ventilation and load

conditions. The developed air model has shown a good capacity to represent the thermal behavior of the entire substation. The temperatures obtained by the model in the surface of transformer are not totally acceptable. As future work, the heat fluxes imposed as boundary conditions on the transformer are going to be modified (non-uniform and including vertical variation) in order to improve the results of the model and to validate it.

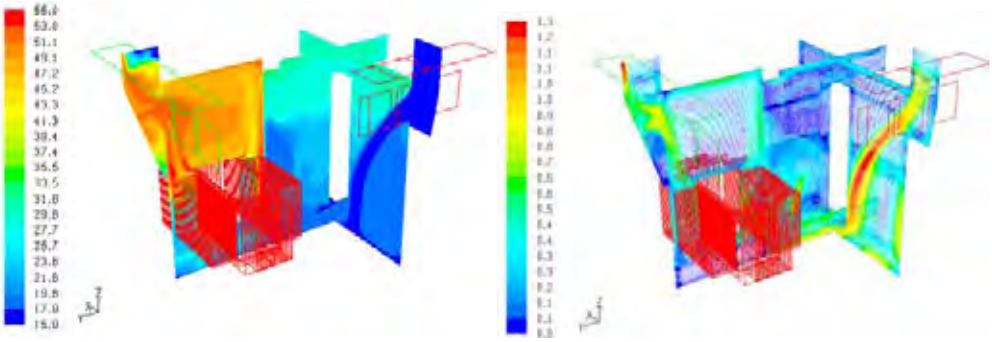

FIGURE 2. Air temperatures in ºC (left) and velocities in m/s (right) in two perpendicular sections of the modelled transformer substation

ACKNOWLEDGMENTS

This work is been carried included in the research project called CRISÁLIDA with the support of Grupo Ormazabal. CRISÁLIDA is funded by Ministerio de Industria, Turismo y Comercio through the program CENIT (Consorcios Estratégicos Nacionales en Investigación Técnica). The financial support of Cátedra Fundación Antonio Aranzábal–Universidad de Navarra is gratefully acknowledged.

REFERENCES

[1] IEC 60076-2:1997, *Power Transformers Part 2: Temperature Rise*, 2nd edition, IEC Standard, 1997.

[2] IEC 1330:1995, *High voltage/low voltage prefabricated substations*, IEC Standard, 1995.

[3] Z. Radakovic, S. Maksimovic., Non-Stationary Thermal Model of Indoor Transformer Stations, *Electrical Engineering*, 84, 109-117, 2002.

[4] J. C. Ramos, A. Rivas, J. M. Morcillo, Numerical Thermal Modelling of the Natural Ventilation of a Half-Buried Tranformer Substation using CFD Techniques, *Progress in Computational Heat and Mass Transfer*, Lavoisier, Paris, France, vol. 2, 929-934, 2005.

[5] F. M. White, *Viscous Fluid Flow*, 2nd Edition, McGraw-Hill, New York, 1991.

[6] D. Choudhury, Introduction to the Renormalization Group Method and Turbulence Modelling, *Fluent Inc. Technical Memorandum*, TM-107, 1993.

[7] T. Jongen, *Simulation and Modelling of Turbulent Incompressible Flows*, Ph. D. Thesis, EPF Lausanne, Lausanne, Switzerland, 1992.

[8] G. D. Raithby and E. H. Chui, A Finite Volume Method for Predicting a Radiant Heat Transfer in Enclosures with Participating Media, *Journal of Heat Transfer*, 112, 415-423, 1990.

[9] I. E. Idelchik, *Handbook of Hydraulic Resistance*, 3rd Edition, Jaico Publishing House, Mumbai, India, 2003.

[10] ANSYS-Fluent, *Fluent User's Guide*, Cavendish Court, Lebanon, NH, USA, 2006.

First International Conference on Computational Methods for Thermal Problems
ThermaComp2009, September 8-10, 2009, Napoli, Italy
N.Massarotti and P.Nithiarasu (Eds.)

On the Heat Transfer Modelling for the Prediction of the Human Thermoregulatory Response to the Thermal Environment

Gino Lopardo
Università degli Studi di Salerno – DIMEC – Dipartimento di Ingegneria Meccanica – Via Ponte Don Melillo, 1 – 84084 – Fisciano (Italy) – email: glopardo@unisa.it

Boris Igor Palella and Giuseppe Riccio
Università degli Studi di Napoli Federico II – DETEC – Dipartimento di Energetica Termofluidodinamica Applicata e Condizionamenti Ambientali – Piazzale V. Tecchio 80, 80125 Naples (Italy) – corresponding author email: palella@unina.it

ABSTRACT

The main goal of this work is just a short review of the role of heat transfer phenomena on the modelling of the human response to the surrounding environment. Aiming to show the most interesting facets and emphasize future research needs, fundamental equations and methods usually adopted by research of the thermal environment field will be showed. As application of heat transfer modelling, the main results of a thermoregulation model will be also presented.

Key Words: *Heat Transfer, Human Thermoregulation Models, Thermal Environment*

1. INTRODUCTION

In the last fifteen years, an increasing need for predicting thermal behaviour of the human body under typical indoor environment situations (or even in outdoor) resulted in a very strong acceleration of the research on heat transfer mechanisms involving the human body and the surrounding environment [1-3]. Due to an improved know-how, assisted by more and more powerful computers and user-friendly calculation codes, in most cases specialists are able to predict the human mean response to the microclimate with a certain reliability [1,3,4]. This is a very important goal towards both a more sustainable approach of the building envelope energetic efficiency and a more reliable precautionary occupational hygiene.

2. HEAT TRANSFER MODELLING IN THE THERMAL ENVIROMENT FIELD

Due to the human body peculiarities, heat transfer equations have to be slightly modified.

2.1 Heat transfer by convection

The heat loss by convection from the outer surface of the clothed body, C, is expressed by the equation:

$$C = A_b f_{cl} h_c (t_{cl} - t_a) \quad (1)$$

where h_c can be evaluated through special correlations as a function of the temperature difference or relative velocity between the subject and the air flow [5-8]. According to equation (1) the evaluation of the convective thermal flow needs for a preliminary evaluation of the clothing surface temperature, t_{cl}, which is usually attained by means of an iterative procedure based on the heat balance of the human body [6,7]. Body surface area takes into account the presence of clothing covering a part of it. Thus, a special clothing area factor, reported on tables in ISO 9920 standard for several clothing ensembles as a function of the static clothing resistance, has to be preliminary evaluated [5]. We highlight that convective heat transfer takes place in the respiration also. Its modelling is based on equations as a function of the metabolic rate and others microclimatic parameters [6-8]:

$$C_{res} = m_{a,res} c_p (t_{ex} - t_a) \begin{cases} C_{res} = 0,014M(34 - t_a) \\ C_{res} = 0,015M(28,56 + 0,885t_a + 0,641p_{v,a}) \end{cases} \quad (2)$$

2.2 Heat transfer by radiation

Generally for the radiative heat flow, R, the following relation is used:

$$R = f_{cl} A_b f_{eff} \varepsilon\sigma[(t_{cl}+273)^4 - (t_r+273)^4] \quad (3)$$

where the radiating surface takes into account both the presence of clothing and the mutual heat transfer between some body parts by means of a special coefficient $f_{eff}=A_r/A_{cl}$. Equation (3) is reliable when outer surface of the subject behaves as a gray body and the subject surrounding environment can be considered as a radiantly black enclosure (very realistic situation in case of large rooms but not in cars, where the classic evaluating methods of radiative heat transfer have to be used). The first hypothesis is verified if the subject receives radiations of high wavelength, situation that generally occurs in indoor environment. In the far infrared both skin and clothing are gray and their emissivity is assumed at 0,97 [6,7]. The main difficulty to estimate R from the Equation (3) is the evaluation of the mean radiant temperature, t_r, which can be calculated or measured [9] from: (a) the view factors, (b) the globe temperature, (c) the plane radiant temperatures. As alternative to equation (3), which treats the radiation in a global way ignoring that occupants of indoor environments are frequently exposed to inhomogeneous radiation (i.e. near cold windows, hot radiators, in the presence of solar radiation transmitted through glazed facades) several studies report a direct evaluation of the radiative flow by means of a 3-D modelling of the human body often characterised by more than ten thousand meshes [1,3]. An alternative for taking into account the overall thermal flow exchanged by convection and radiation is collapsing both in one term, H, defined dry heat loss, according to following equations:

$$H = C + R = f_{cl} A_b h (t_{cl} - t_o) = \frac{A_b (t_{sk} - t_o)}{R_{cl} + R_a} \quad (4)$$

based on the linearization of the equation (3) by means of the introduction of the operative temperature, t_o, defined as uniform temperature of an imaginary black enclosure in which an occupant would exchange the same amount of heat by radiation plus convection as in the actual non-uniform environment. Such temperature can be considered the average between the air temperature and the mean radiant temperature only if the relative air velocity is small (< 0,2 m/s) or if the difference between mean radiant and air temperature is small (< 4 °C), [9].

2.3 Heat transfer by evaporation from the skin surface

The heat loss by evaporation from the skin surface, E_{sk}, is evaluated by means of the following equations:

$$\begin{cases} E_{sk} = w(p_{vs,sk} - p_{v,a}) / R_{e,T} \\ R_{e,T} = R_{e,cl} + R_{e,a} \end{cases} \quad (5)$$

$R_{e,a}$ can be calculated from h_c by means of the well known Lewis relation for the air-water system, whereas $R_{e,cl}$ depends on the vapour permeability of clothing, which can be evaluated starting from the dimensionless permeability index, i_m, and the static clothing insulation, R_{cl}, reported in several standards [5,7].

Evaporative heat flow related to the respiration is modelled similarly to that previously reported for the convective heat transfer [6-8]:

$$E_{res} = \lambda m_{a,res} (x_{ex} - x_a) \begin{cases} E_{res} = 0,023M(44 - p_{v,a}) \\ E_{res} = 0,0173M(p_{ex} - p_{v,a}) \\ E_{res} = 0,00127M(59,34 + 0,53t_a + 11,63p_{v,a}) \end{cases} \quad (6)$$

2.4 Clothing modelling

The clothing plays a crucial role on the thermal response of the human body since it is the layer trough the heat transfer between the human body and the surrounding environment takes place. Its static thermal resistance is usually evaluated by means of thermal manikins. Havenith's group [2,5] highlightened how the presence of openings in clothing (i.e. collars, cuffs) results in an additional air flow inside clothing (pumping effect), increasing with increasing of body movement, resulting in a reduction of the insulation value. A similar effect occurs in the presence of high air velocities through the reduction of clothing layers thickness. In order to take into account these complex phenomena, special correlations as a function of the relative air velocity and the walking speed of the subject have been introduced by [2,5-8].

2.5 CFD Approach

Equation (1) treats the convective thermal flow in a global way since the whole of proposed correlations for h_c take into account neither the real body shape of the human body nor the fluid dynamics of surrounding environment induced also by the presence of HVAC systems. More in-depth analyses are starting to be obtained by means of CFD simulations [1,3] allowing a detailed analysis of involved thermal flows. Anyway, such tool requires an in-depth treatment of boundary conditions especially as far as the body surrounding is concerned since clothing and/or skin temperatures are strictly related to the thermal physiological response of the human body. In order to obtain reliable temperature values on the body surface the research is working at two different levels:

- development of computational thermal manikins (CTM) to be used in a coupled simulation environment to simulate the human thermoregulatory response in buildings [10,11];
- coupling CFD analysis with more promising thermoregulation models [1,3].

3. THERMOREGULATION MODELS

Several thermoregulation models have been developed aiming to predict the thermal behaviour of the human body in the widest range of indoor (and outdoor) situations [1-3]. Among them, in this paper we will briefly outline the main features of THERMODE 193 recently developed by our group [4]. With respect to the native Stolwijk's model proposed in Seventies, several changes have been introduced. In detail, the model is based on a thorough division of the human body made by 48 body segments each divided in four concentric layers (skin, fat, muscle and core) reaching 192+1 (blood) nodes. Aiming to simulate non homogeneous environments, microclimatic input data are made by a set triplets (t_a, t_r, $p_{v,a}$) for each node. The evaluation of the plane radiant temperature of each compartment has been carried out starting from the surface temperatures of a standard room without windows [4,9]. Moreover, the body is clothed and the effect of its movements on the static clothing insulation has been taken into account. The control system has been revised in order to improve its performances especially under slightly cold situations and with respect to the need for an enhanced thermal response prediction of hands and feet which are affected by great errors due to the irregular shape and the complex heat transfer modelling between blood into the veins and in arteries. THERMODE 193 is able to predict the local skin temperatures and the core temperature of the human body with a satisfactory degree of accuracy with only slightly differences between experimental and model temperatures [4].

4. CONCLUSIONS

In this paper heat transfer mechanisms between humans and the environment were briefly reviewed trying to highlight the crucial role of different approaches in the treatment of each mechanisms involved in the heat balance equation of the human body. This will be a real challenge for heat transfer specialists because: 1) the attainment of high energetic performances of a building has to be obtained in the presence of an acceptable comfort level of the occupants [12]; 2) the protection of

workers under hot or cold extreme situations cannot ignore the thermoregulatory response of the human body.

REFERENCES

[1] S. Tanabe, K. Kobayashi, J. Nakano, Y. Ozeki, M. Konishi, Evaluation of thermal comfort using combined multi-node thermoregulation (65MN) and radiation models and computational fluid dynamics (CFD), *Energy and Buildings* 34, 637-646, 2002.

[2] K.C. Parsons, G. Havenith, I. Holmér, H. Nilsson and J. Malchaire, The Effects of Wind and Human Movement on the Heat and Vapour Transfer Properties of Clothing, *Annals of Occupational Hygiene*, 43(5), 347-352, 1999.

[3] K. Kubaha, D. Fiala, J. Toftum, A. H. Taki, Human Projected area factors for detailed direct and diffuse solar radiation analysis, *Int. Journal of Biometereology*, 49, 113-129, 2004.

[4] F.R. d'Ambrosio Alfano, B.I. Palella, G. Riccio, THERMODE 193: an enhanced Stolwijk thermoregulation model of the human body, *Proceedings of 7th International Thermal Manikin and Modelling Meeting, September 2008 3-5th, University of Coimbra, Portugal. M.C. Gameiro da Silva Editor*, 8 pages on CD ROM, 2008.

[5] ISO. Ergonomics of the thermal environment - Estimation of thermal insulation and water vapour resistance of a clothing ensemble. ISO Standard 9920. Geneva: ISO, 2007.

[6] ISO. Ergonomics of the thermal environment - Analytical determination and interpretation of thermal comfort using calculation of the PMV and PPD indices and local thermal comfort criteria – ISO Standard 7730. Geneva: ISO, 2005.

[7] ISO. Ergonomics of the thermal environment – Analytical determination and interpretation of heat stress using calculation of the predicted heat strain – ISO Standard 7933. Geneva: , 2004.

[8] Ergonomics of the thermal environment - Determination and interpretation of cold stress when using required clothing insulation (IREQ) and local cooling effects – ISO Standard 11079. Geneva: ISO, 2007.

[9] ISO. Thermal environments - Instruments and methods for measuring physical quantities. ISO Standard 7726. Geneva: ISO, 2002.

[10] S. Murakami, Analysis and design of micro-climate around the human body with respiration by CFD, *Indoor Air* 14(7), 144-156, 2004.

[11] Y. Tong Yang, P.C, Cropper, M.J. Cook, R. Yousaf and D. Fiala, A New Simulation System to predict Human-Environment Thermal Interactions in Naturally Ventilated Buildings, *Proceedings of Building Simulations Conference, Beijing, September 03-06th, 2007*, 751-756, 2007.

[12] European Union Council Directive of 16 December 2002 on the energy performance of buildings (2002/91/EC), 2002.

Symbol	Meaning	Units	Symbol	Meaning	Units
A_b	Body surface area	m^2	$R_{e,a}$	Boundary air layer vapour resistance	m^2kPa/W
A_{cl}	Surface area of the clothed body	m^2	R_{cl}	Effective clothing resistance	m^2K/W
A_r	Effective radiating body area	m^2	$R_{e,cl}$	Clothing vapour resistance	m^2kPa/W
C_{res}	Respiratory convective heat flow	W/m^2	$R_{e,T}$	Overall vapour resistance of clothing and boundary layer	m^2kPa/W
c_p	Specific heat of dry air at constant pressure	J/kgK	t_a	Air temperature	°C
E_{sk}	Evaporative heat flow at the skin	W/m^2	t_{cl}	Clothing surface temperature	°C
E_{res}	Respiratory evaporative heat flow	W/m^2	t_{ex}	Expired air temperature	°C
f_{cl}	Clothing area factor	-	t_o	Operative temperature	°C
f_{eff}	Effective area coefficient	-	t_r	Mean radiant temperature	°C
h	Overall heat transfer coefficient	W/m^2K	t_{sk}	Mean skin temperature	°C
h_c	Convective heat transfer coefficient	W/m^2K	w	Skin wettedness	-
M	Metabolic rate	W/m^2	x_a	Humidity ratio of air	kg/kg
$m_{a,res}$	Respiratory dry air mass flow	kg/s	x_{ex}	Humidity ratio of expired air	kg/kg
$p_{v,a}$	Vapour pressure in the air	kPa	ε	Mean clothed body emissivity	-
$p_{vs,sk}$	Saturated vapour pressure at the skin temperature	kPa	λ	Evaporation latent heat of water	J/kg
R_a	Boundary air layer thermal resistance	m^2K/W	σ	Stefan-Boltzmann constant	W/m^2K^4

TABLE 1. Main symbols used in the text.

First International Conference on Computational Methods for Thermal Problems
ThermaComp2009, September 8-10, 2009, Napoli, Italy
N.Massarotti and P.Nithiarasu (Eds.)

MODELLING BUOYANT POINT AND LINE HEAT SOURCES USING A COMMERCIAL SOFTWARE PACKAGE – AN INITIAL INVESTIGATION

Pierre S. Farrugia
Department of Physics, University of Malta, Msida MSD 2080 Malta,
Email:pierresandre.farrugia@um.edu.mt

Alfred Micallef
Department of Physics, University of Malta, Msida MSD 2080 Malta,
Email:alfred.micallef@um.edu.mt

ABSTRACT

The study of buoyant point or line heat sources forms the basis of the analysis of buoyant heat sources of any shape or dimension. The reason for this is that analysing the behaviour of the buoyant plume at a sufficient distance from a heat source of a generic shape, one will find that its shape and behaviour are much similar to those of a point or line heat source that has as origin some point in space called the virtual origin. One way of carrying out the analysis is through the use of Computational Fluid Dynamic (CFD) simulations. However, currently one finds that it is more time effective to use general commercial software for the analysis rather than building the CFD code from scratch. This approach raises the issue, addressed in the present work, of determining effective ways of simulating heat sources with readily available software. The problems encountered when modelling a point and line heat source in an open environment and under displacement ventilation are presented and explained. Possible methodologies that can be employed to overcome the problems are put forward, together with their effect on the original flow.

Key Words: *Point Heat Sources, Heat Transfer, Natural Ventilation, Displacement Ventilation, Commercial CFD software, Fluent*

1. INTRODUCTION

Point and line heat sources are the simplest type of heat sources that one encounters. However, at a certain distance from a heat source of a general shape, usually just a few multiples of the characteristic length of the heat source, the evolving plume has the same characteristics as that of a line or point heat source [1]. This makes it practical to study the behaviour of the simple sources and try to extrapolate to that of the more complex ones. For this reason, point and line heat sources have been widely investigated both analytically and numerically under different conditions including homogenous and stratified environments [2,3], natural ventilation [4,5], and closed chambers [6].

Nowadays, when it comes to numerical modelling, it is no longer time effective to build the source code; a commercial CFD package is usually employed. However, this comes at a cost. When using a CFD package one is faced with the limitations of the package being used. This raises the question of what is the best way of simulating point and line heat sources.

The published numerical studies indicate that when the source is almost completely subject to wall boundary conditions – such as in natural ventilation – the available software is capable of simulating effectively the evolution of the plume [5]. However, no study concerning this type of modelling using a commercial CFD package could be found in which the source has a point or line configuration in an open environment. The work that approaches most closely this set up was that for a sphere in an open environment, where the CFD package CFX was used [7].

While such a situation might seem to be rather simplistic, obtaining results using the CFD package Fluent was not as easy as expected. It took some time to realise that the boundary conditions available in Fluent – which did not include the far field boundary used in [7] since in Fluent this boundary condition is not available with the Boussinesq approximation that is customary to use for such flows – were interfering with the expected physical pattern. In order to stabilise the process, displacement ventilation was introduced and then the inlet velocity was decreased gradually in an attempt to reduce it to zero and thus obtain the result sought. However, it was found that decreasing the inlet velocity below a certain value would, once again, cause instability.

Thus this work discusses the problems encountered with setting up a point or line heat source in a homogeneous environment and gives reasonable explanations that account for the instabilities observed when the Fluent was used. It will be shown that these instabilities arise both as a consequence of what is being modelled as well as, and from, the limits of the software package used.

2. MAIN BODY

The first limitation that one encounters in simulating a point or a line heat source is the confinement of the domain to a finite region of space. This means that the boundaries used can affect the system.

Similar problems and difficulties were encountered when simulating a point and a line heat source. Hence, only the setup used for the line heat source will be discussed in detail. To further simplify matters only a two dimensional setup was considered, and this is shown in Figure 1(a) with the source at the origin of the coordinate system used. The heat source was modelled as a wall with a constant heat flux. The size of the heat source was set equal to the grid spacing to mimic as much as possible a very small source. The walls at the sides were set to 10 m from the source. Considering that the plume is contained within half a metre, this meant that the boundaries were set at a factor of 20 times the largest characteristic length of the plume. A symmetry boundary condition was also introduced vertically above the source to limit the computational time.

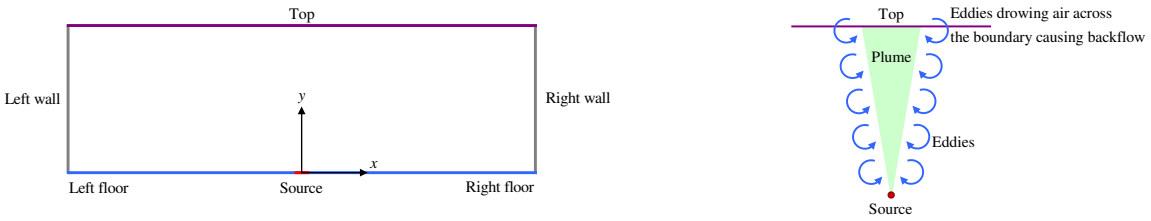

(a) (b)

FIGURE 1. (a) Line source model under investigation; (b) Schematic illustration of how the eddies at the edge of the plume cause backflow at the pressure outlet boundary.

Initially the floor was set as an adiabatic wall with the top being either a pressure outlet or simply an outlet. When this setup was solved using Fluent the result was far from what one would expect to see physically. It was observed that the pressure outlet or the outlet boundary conditions were causing small numerical fluctuations that grew with the iterations. These fluctuations coupled with the fact that buoyancy flows involve very small speeds and temperature differences, caused instabilities that resulted in the observed unexpected flow.

This potential effect of the boundary on the flow was verified when a setup consisting of a room of unit dimensions, with adiabatic walls and floor, and pressure outlet or outlet as the top was investigated. When this setup was solved using Fluent, the result was the formation of an air flow pattern. This contrasted with what was expected, i.e. no noticeable air motion. It was also noted that

the air flow pattern was less noticeable when using the pressure outlet than when using the outlet boundary condition. Thus the pressure outlet was chosen for further experimentation.

The next step taken, in order to overcome the problem caused by the numerical instabilities, was to introduce displacement ventilation by changing the floor to a velocity inlet. The idea was that the inlet velocity would superimpose on the numerical instabilities that were of a much smaller magnitude, preventing them from affecting the system. It was initially envisaged that it would have been possible to reduce the velocity to zero to reach the desired output. However, it turned out that this was not possible.

At a certain point when decreasing the velocity, backflow from the pressure outlet sets off and as a consequence the residuals stabilise to a rather high value. The most probable responsible mechanism was identified as being the eddies or vortices at the edge of the plume, which cause a downward flow at the boundary as illustrated schematically in Figure 1(b).

It was decided to use an extrapolation technique to determine the distribution of the temperature of the plume at zero velocity for comparison with the relevant empirical equation [8]:

$$\Delta T = \Delta T_{\text{Max}} e^{-41\frac{x^2}{y^2}} \text{ where } \Delta T_{\text{Max}} = 0.26 \frac{T_0}{gy} \left(\frac{gQ}{c_p \ _0 T_0} \right)^{\frac{2}{3}}, \quad (1)$$

with T_0 being the reference temperature, taken to be 293 K (20°C), g is the acceleration due to gravity, c_p is the specific heat capacity at constant pressure which was considered to be $1047 \text{ J kg}^{-1} \text{ K}^{-1}$, $_0$ is the free stream density that had a value of 0.616 kg m^3 and Q is the heat emitted per unit length which was assigned a value of 200 J, in order to establish the validity of the results.

The employed turbulence model was the RNG k- turbulent model since according to the literature it gives more reliable results than the standard one. To simplify computation the Boussinesq approximation was employed. As regards the discrimination, PRESTO! was used for the pressure – this being the recommended scheme in the case of buoyant driven flows – while QUICK was used for all the other quantities. The pressure-velocity coupling was obtained using the SIMPLEC algorithm.

3. RESULTS

The important parameters to be derived were the maximum temperature and the width, taken to be the position where the temperature falls to 1/e of it maximum value. While the maximum extent of the width of the plume was found to be grid independent, the maximum temperature varied substantially with grid resolution. A suitable grid resolution around the source was found to be 400 grid lines per metre. Interesting enough this was found to exceed substantially the resolution used in most of the work done on heat sources. Furthermore, for most of the quantities under investigation it did not make any difference whether half the domain was used and a symmetry boundary condition was introduced, or if the whole domain was incorporated. Differences were noted only close to the source to a height of around 0.1 m.

An attempt to linearise eq. 1 by taking the log to base e on both sides and use a least square fit in order to determine the maximum temperature and the width, did not produce very good results. Thus the maximum temperatures were obtained directly from Fluent and then used to calculate the width at different heights. Using the values for each height at different inlet velocities it was possible to use a linear fit to extrapolate the values that would be obtained with zero inlet velocity.

In the case of the variation of the width at zero velocity with height, this showed a good linear trend and the gradient was 0.0513 as compared to the expected 0.1562. The intercept of this graph gave the position of the virtual origin and after correcting accordingly, it was possible to analyse the

trend of the maximum temperature with the reciprocal of the distance from the virtual source. In this case, even though the correlation coefficient for linear regression was high (0.985), variation appeared to be more a shallow curve than a straight line. However, the gradient obtained was $1.432\ \mathrm{K\ m^{-1}}$ which compares rather well with the expected $3.696\ \mathrm{K\ m^{-1}}$.

This analysis showed that the width of the plume depends strongly on the inlet velocity. In fact the inlet velocity acted like an air curtain preventing the entrainment of adjacent air.

4. CONCLUSIONS

In this paper, possible approaches for modelling a line or point heat source in an open environment using the commercial software Fluent were presented. It was shown that due to numerical instabilities of the boundary conditions it is not possible to carry out a direct simulation. However, it is possible to extrapolate the properties of the plume in natural conditions by adding displacement ventilation and obtain the variation of a quantity with inlet velocity.

The results indicate that while the total width of the plume is not dependent on the grid, the maximum height is. It can be concluded that convergence can be assessed by ensuring that the maximum temperature at different locations vertically above the source does not change.

It is evident that some of the properties of the plume depend on the inlet velocity. This might have applications in determining the most appropriate positions for air inlets in displacement ventilation systems and also in determining the most appropriate speed to use at such inlets.

REFERENCES

[1] A. Bouzinaoui, R. Devienne, J.R. Fontaine, An experimental study of the thermal plume developed above a finite cylindrical heat source to validate the point source model, *Experimental Thermal and Fluid Science*, 31(7), 649-659, 2007.

[2] B.R. Morton, G. Taylor, and J.S. Turner, Turbulent Gravitational Convection from Maintained and Instantaneous Sources, *Proceedings of the Royal Society of London. Series A, Mathematical and Physical Sciences,* 234, 1-23, 1956.

[3] V.N. Kurdyumov and A. Liñán, Free convection from a point source of heat, and heat transfer from spheres at small Grashof numbers, *International Journal of Heat and Mass Transfer*, 42(20): 3849-3860, 1999.

[4] P.F. Linden, G.F. Lane-Serff, and D.A. Smeed, Emptying filling boxes: the fluid mechanics of natural ventilation, *Journal of Fluid Mechanics*, 212, 309-335, 1990.

[5] I.E. Abdalla, M.J. Cook, J.R. Simon, and Z. Yang, Large-eddy simulation of buoyancy-driven natural ventilation in an enclosure with a point heat source, *International Journal of Computational Fluid Dynamics*, 21(5): 231-245, 2007.

[6] R.J.M. Bastiaans, C.C.M. Rindt, F.T.M. Nieuwstadt, and A.A. van Steenhoven, Direct and large-eddy simulation of the transition of two- and three-dimensional plane plumes in a confined enclosure, *International Journal of Heat and Mass Transfer*, 43(13): 2375-2393, 2000.

[7] S.K.S. Boetcher, and E.M. Sparrow, Numerical Simulation of Axisymmetric, Turbulent Buoyant Plumes - Application to Displacement Ventilation, *Numerical Heat Transfer, Part A: Applications*, 51(11), 1023-1040, 2007.

[8] H. Rouse, W.D. Baines, and H.W. Humphrey, Gravitational convection from a bundary source, *Tellus*, 4, 201-210, 1952.

First International Conference on Computational Methods for Thermal Problems
ThermaComp2009, September 8-10, 2009, Napoli, Italy
N.Massarotti and P.Nithiarasu (Eds.)

Copper Foam for Capillary Structures in Heat Pipes

Wessel W. Wits
Faculty of Engineering Technology, University of Twente
7500 AE Enschede, The Netherlands, w.w.wits@utwente.nl

ABSTRACT

In heat pipe design, capillary structures with good capillary performance are of great importance. Important parameters for a capillary structure of metal foam are investigated. Low pore radii are sought after, as this increases the capillary pressure and thus heat pipe performance. However, low pore radii negatively influence the permeability of the working fluid through the capillary structure. To optimize the trade-off between pore size and permeability, the permeability of copper foam was determined experimentally. The investigated copper foam shows improved capillary performance compared to the currently used microgroove structures.

Key Words: *Porous Media, Capillary Flow, Metal Foam, Heat Pipes.*

1. INTRODUCTION

Thermal management plays an increasingly dominant role in the design process of electronic products. Component sizes decrease while performance demands increase, resulting in more power dissipation on smaller surfaces. Two-phase cooling solutions, such as heat pipes, vapor chambers, etc., offer a better thermal performance than conventional air cooling. Therefore, two-phase cooling is increasingly used in the design of electronic products. In a previous publication of this study [1] a new heat pipe design was presented. A heat pipe was fully integrated into a Printed Circuit Board (PCB), using standard PCB production and Surface Mount Device (SMD) assembly techniques, as shown in Figure 1(a).

(a) technology demonstrator (b) basic heat pipe structure

FIGURE 1. Heat pipe integrated into a printed circuit board.

Inside a heat pipe, a capillary structure is required to return the condensed vapor to the evaporator region. The capillary structure of this integrated heat pipe design consisted of many axially oriented microgrooves, as shown in Figure 1(b). Measurements done on the prototype proved the integrated concept to be promising. However, the measurements also showed that the microgrooves were not able to transport liquid straight up against gravity. Hence, another capillary structure that could fulfill this task was researched, leading to the subject of this publication: copper foam.

A metal foam is an interconnected network of cells available in many types of metal: copper, aluminum, iron based, etc. They are already used in many other applications, such as flow diffusers, sound absorption and lightweight optics [2]. As the material used to be rather expensive, it was mostly used in advanced technologies as aerospace and military. However, nowadays one can buy a metal foam sheet as a semi-manufactured good at a reasonable price. For this reason and due to the fact that it has promising capillary potential, this research aims to use a metal foam as the capillary structure inside the integrated heat pipe design.

From literature, the smaller the pore size of the capillary structure, the larger the capillary pressure. However, as frictional effects also increase for smaller pore sizes, a trade-off must be made. Both effects are correlated proportionally to each other [3]. The frictional effects of a capillary structure are characterized by its permeability. Due to the random nature of a foam, determining the permeability of this non-uniform structure is best done experimentally [4]. Therefore, this study seeks an (reliable) empirical value that can be used in heat pipe performance simulations, rather than determining a computational value computed by, for instance, finite element modeling.

To prevent unwanted electro-chemical reactions inside the heat pipe, only one type of metal should be used. In this case, as the cavity and sealing is already made of copper, the metal foam must also be made of copper. To predict possible heat pipe performance, a strip of copper foam was cut from a commercially procured copper foam sheet and characterized experimentally.

2. EXPERIMENTAL SET-UP

A common approach to characterize a capillary structure is to do a capillary rise test. Here, gravitational forces are balanced with the height a liquid is pulled up inside the capillary structure. This balance leads to a permeability that is characteristic for the foam in question. However, in this case, this method had two drawbacks: (1) one must wait for the liquid to reach a stationary level, which may take a long time, and (2) a stationary level must be reached. Although the latter seems peculiar, as the procured sheets were only 100mm long this was quite relevant.

Hence, another approach had to be used to characterize the copper foam. By measuring the flow of a fluid through the capillary structure at a certain pressure gradient, the permeability can also be determined. This approach is also known as a flow discharge test.

In the experimental set-up a vacuum system was used to induce the flow through the copper foam. The fluid used was water, as this is also the working fluid for the heat pipe application. Water was taken from a reservoir. By measuring the (decreasing) mass of the water inside the reservoir, the mass flow through the copper foam can be determined, assuming water acts as an incompressible fluid.

The copper foam that was tested had an average pore size of 220μm and a thickness of 0.93mm. These values were taken from the supplier's datasheet and website [5]. Also, according to the supplier, the foam had a porosity of approximately 70% and a permeability between $1.30 \cdot 10^{-11}$ and $1.37 \cdot 10^{-9} m^2$; a rather wide range. The strip of copper foam used in the test set-up was cut down to 20mm wide, approximately the width of the intended heat pipe application, and 100mm long. The test set-up, with its retained copper foam, is shown in Figure 2.

FIGURE 2. Copper foam inside the experimental set-up.

Water from the reservoir enters the copper foam through the tube on the left hand side; whereas the vacuum system was connected to the tube on the right hand side. To smoothen the flow through the foam, the water runs through a pre-mesh before it enters the foam. The pores of this pre-mesh are significantly larger than that of the foam; hence, this will not influence the measurement results. To force the water through the foam, all other paths had to be sealed off airtight. This was done by sandwiching the foam and both inlet and outlet tubes between a glass plate and a synthetic foil with tacky tape.

3. MEASUREMENT RESULTS

The recorded mass flow and pressure drop of three measurements are shown in Figure 3. An initial start-up effect is visible, due to some residual air in the system that must be pumped out first. This causes the cavity between the foil and the glass plate around the foam to be depressurized.

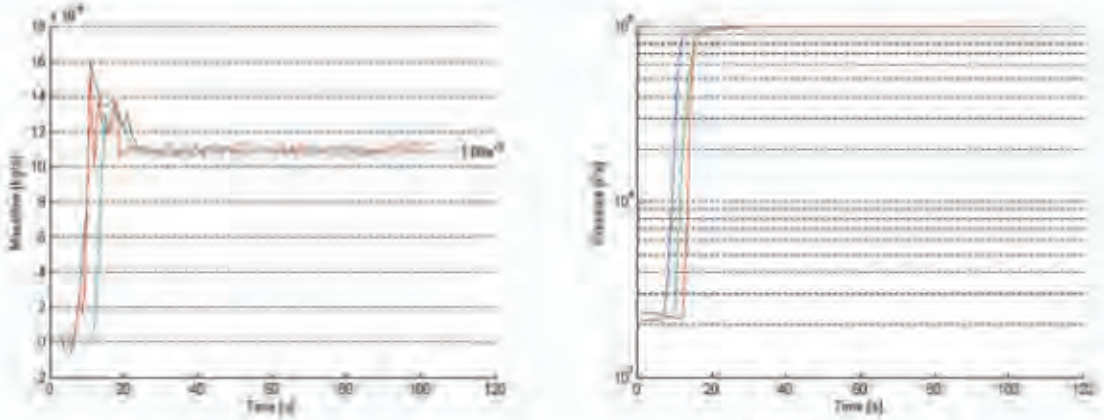

(a) mass flow (b) pressure drop

FIGURE 3. Results of 3 flow discharge measurements.

As shown in the figure, after approximately 24s the maximum pressure of 1 atmosphere is reached and the mass flow is settling to a steady state. The recorded average steady state mass flow was $1.09 \cdot 10^{-3}$kg/s with a standard deviation of $1.81 \cdot 10^{-5}$kg/s.

According to Darcy's law the pressure drop (dp/dx) and fluid velocity (v) are proportionally related to each other, as:

$$\frac{dp}{dx} = -\frac{\mu}{K} v \tag{1}$$

Here, the pressure drop is considered one dimensional along the length of the capillary structure. During the measurements a uniform flow front perpendicular to the flow direction was observed, hence confirming this assumption. In Equation (1), μ and K denote the fluid's viscosity and the foam's permeability, respectively. Due to the fluid's low velocity, the influence of turbulence and inertia (i.e. the Hazen-Dupuit-Darcy model) is disregarded in this case [6].

As the foam has a uniform cross section across its length, Equation (1) can be rewritten as:

$$\Delta p = -\frac{\mu L}{\rho A K} \dot{q} \tag{2}$$

Here, A and L denote the cross sectional area and length of the foam, respectively, and $\dot{q}$ represents the mass flow of the fluid. Hence, from Figures 3(a) and 3(b) and by correcting for geometric features and fluid properties, the foam's permeability can be computed. This is shown in Figure 4.

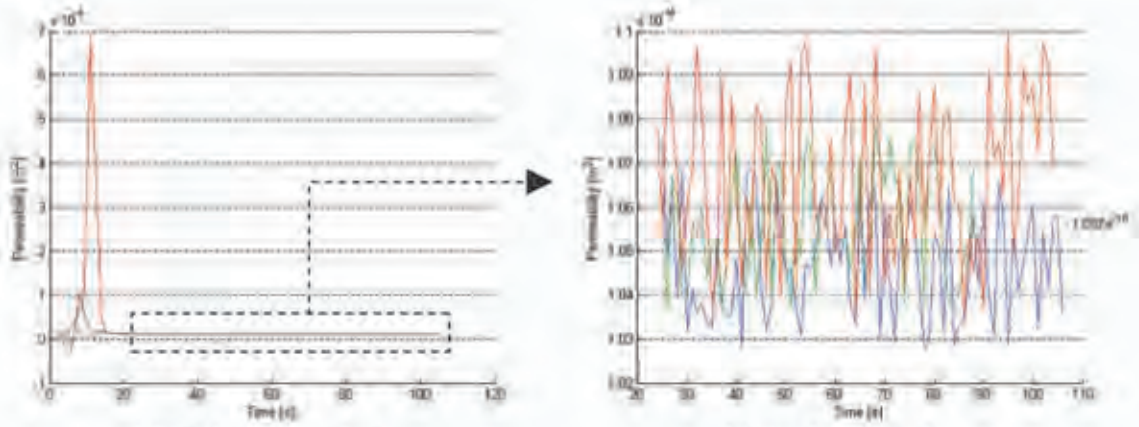

(a) total measurement (b) steady state values

FIGURE 4. Permeability of the copper foam sample.

The figure shows that the permeability of the copper foam reaches a steady state after some initial dynamics caused by the start-up effects discussed earlier. At steady state, an average permeability of $106 \cdot 10^{-12} m^2$ with a standard deviation of $1.74 \cdot 10^{-12} m^2$ was recorded over the three measurements. This value lays approximately halfway the specified range by the supplier. The computed Reynolds number during the experiments was approximately 40, indicating laminar flow. Hence, Darcy's law, as discussed earlier only applicable to viscous flow, could be used.

4. CONCLUSIONS

Using a flow discharge test, the capillary structure of a copper foam was characterized in terms of permeability and pore size. These are important parameters for the selection of capillary structures in heat pipe design. Table 1 lists these parameters for the currently used microgrooves and the investigated copper foam.

TABLE 1. Comparison of capillary structures.

Capillary structure	Pore size [μm]	Permeability [m^2]
Microgrooves	100	$190 \cdot 10^{-12}$
Foam	220	$106 \cdot 10^{-12}$

The foam has a pore size which is more than double the value of the microgrooves. The foam's permeability is however less than double the microgroove value. Hence, as both effects are proportionally related to each other, switching from microgrooves to a copper foam would increase the capillary effect. Consequently, this would improve heat pipe performance.

REFERENCES

[1] W.W. Wits, R. Legtenberg, J.H. Mannak and B. van Zalk, "Thermal management through in-board heat pipes manufactured using printed circuit board multilayer technology", in *Proc. of the 31st International Conference on Electronic Manufacturing and Technology*, pages 55-61, Petaling Jaya, Malaysia, 2006.

[2] L.P. Lefebvre, J. Banhart and D. Dunand, *Porous metals and metallic foams*, Proc. of the fifth International Conference on Porous Metals and Metallic Foams, Montreal, Canada, 2007.

[3] T.P. Cotter, *Theory of heat pipes*, Technical Report No. LA-3246-MS, Los Alamos Scientific Laboratory, 1965.

[4] A. Faghri, *Heat pipe science and technology*, Taylor & Francis, Washington, DC, USA, 1995.

[5] Metafoam Technologies Inc, http://www.metafoam.com/copper_foam_properties.html.

[6] M. Kaviany, Principles of heat transfer in porous media, 2nd edition, Springer, 1995.

First International Conference on Computational Methods for Thermal Problems
ThermaComp2009, September 8-10, 2009, Napoli, Italy
N.Massarotti and P.Nithiarasu (Eds.)

HIGH RAYLEIGH NUMBER NATURAL CONVECTION IN RECTANGULAR CAVITIES WITH DIFFERENT ASPECT RATIOS SOLVED BY USING A STABILIZED FINITE ELEMENT ALGORITHM

Fausto Arpino
Department of Mechanics, Structures and Environment (DiMSAT), University of Cassino, Via G. Di Biasio 43, 03043 Cassino (FR), Italy. E-mail: f.arpino@unicas.it

Nicola Massarotti, Alessandro Mauro
Department for Technologies (DiT), University of Napoli "Parthenope", Isola C4, Centro Direzionale di Napoli, 80143 Napoli, Italy. E-mail: nicola.massarotti@uniparthenope.it, alessandro.mauro@uniparthenope.it

ABSTRACT

In this work, high Rayleigh number natural convection has been solved for the first time by using a stabilized Artificial Compressibility (AC) Characteristic Based Split (CBS) algorithm. The authors have carried out a stability analysis, based on the order of magnitude analysis of all the terms present in the conservation equations, in order to solve problems in presence of very large source terms. A new benchmark problem for high Rayleigh number natural convection in rectangular cavities with different aspect ratios has been detected by the authors. This new benchmark case is the only one for which experimental data are available. The stabilized AC-CBS scheme is successfully used to solve the present benchmark problem. The efficiency and the accuracy of the AC-CBS algorithm are verified through comparison with the experimental data for the new benchmark problem and with the numerical solutions available in the literature for well known problems. The interest in the AC-CBS scheme has increased since it offers the possibility of an easy and efficient parallelization procedure.

Key Words: *CBS, Stability, Laminar free convection, Large source terms, Matrix-inversion free.*

1. INTRODUCTION

High Rayleigh number natural convection is a complex physical problem to simulate numerically, because of the large source terms involved in the governing equations. Natural convection is very important in many engineering applications such as energy transfer in rooms and buildings, nuclear reactors, electronic packaging, and solar collectors. Very few works deal with numerical simulation of natural convection with a Rayleigh number higher than 10^7 [1-4]. Furthermore, steady state laminar natural convection with Rayleigh number higher than 10^8 has not be yet well investigated, while turbulent natural convection with Rayleigh number higher than 10^8 has been simulated only by [4, 5].

The present work has two aims: i) introduce new benchmark quality solutions for natural convection with Rayleigh numbers higher than 10^8, in cavities with different aspect ratios, for which experimental data are available; ii) show the efficiency and the accuracy of the stability analysis for the Artificial Compressibility (AC) Characteristic Based Split (CBS) algorithm in presence of large source terms, carried out by the authors for the first time.

Even though the robustness of such a method was proved to be excellent in the past for free fluid forced convection [6] and flows through saturated porous media [7], such algorithm still presented some difficulties in solving problems where large source terms appeared (i.e. high Rayleigh number natural convection problems), therefore reducing significantly the capabilities of the algorithm in solving problems of practical interest. Moreover, the interest in the AC-CBS scheme for

incompressible fluid dynamic studies has increased since it offers the possibility of an easy and efficient parallelization procedure and easy implementation. For these reasons, the authors have made an effort in developing a detailed study of the AC-CBS algorithm stability, succeeding in the development of a stable, efficient and accurate numerical scheme, applicable to complex problems that appear in real applications.

The efficiency and the accuracy of the present stabilized AC-CBS algorithm are verified through comparison with the experimental solution [8] for the new benchmark problem and with the numerical solutions [1-3] available in the literature for well known problems. The authors consider different natural convection problems with high Rayleigh number: i) the classical square cavity with the vertical walls maintained at different temperatures, with Rayleigh number equal to 10^8; ii) a new natural convection benchmark problem where the top wall is heated as well as the left vertical one. For this last problem, different aspect ratios are considered for the cavity and the Rayleigh number is maintained at about $1.3 \cdot 10^8$.

2. GOVERNING EQUATIONS

The non-dimensional form of the equations for natural convection problems, in vector notation, can be written as:

$$\frac{\partial \mathbf{W}}{\partial t} + \frac{\partial \mathbf{F}_j}{\partial x_j} - \frac{\partial \mathbf{G}_j}{\partial x_j} = \mathbf{S} \tag{1}$$

with

$$\mathbf{W} = \begin{pmatrix} u_1 \\ u_2 \\ T \end{pmatrix}, \quad \mathbf{F}_j = \begin{pmatrix} u_j \\ u_1 u_j + p\Delta_{1j} \\ u_2 u_j + p\Delta_{2j} \\ T u_j \end{pmatrix}, \quad \mathbf{G}_j = \begin{pmatrix} 0 \\ {}_{1j} \\ {}_{2j} \\ \dfrac{\partial T}{\partial x_j} \end{pmatrix}$$

$$\mathbf{S} = \begin{pmatrix} 0 \\ 0 \\ Ra \Pr T \\ 0 \end{pmatrix}$$

The non-dimensional form of the deviatoric stress is defined by:

$${}_{ij} = \Pr\left(\frac{\partial u_i}{\partial x_j} + \frac{\partial u_j}{x_i} - \frac{2}{3} \frac{\partial u_k}{\partial x_k} \Delta_{ij} \right) \tag{2}$$

3. STABILITY ANALISYS FOR THE AC-CBS ALGORITHM

The stability analysis of the conservation equations is performed on the basis of the order of magnitude of all the terms [6, 7]. The stability conditions are derived by observing that the order of magnitude of each term [6, 7] must be smaller than 1. This approach is applied to the steps of the AC-CBS scheme [6, 7]. The time-step restrictions obtained by adopting the present analysis are shown in the followings:

Stability conditions - Step 1

$$\Delta t_{conv} = \frac{h}{u^n_{,conv}}; \quad \Delta t_{diff} = \frac{h^2}{\Pr}; \quad \Delta t_b = \frac{h}{Ra \Pr T^n} \frac{1}{\Delta t^{n-1}} \tag{3}$$

Stability conditions - Step2

$$= u^n_{conv} + \frac{h}{\min\left(\Delta t_{conv}, \Delta t_{diff}, \Delta t_b\right)}; \quad \Delta t_2 = \frac{p^n_{art} h}{{}^2 u^n_{conv}} \tag{4}$$

Stability conditions - Step 3

$$\Delta t_3 = \frac{h}{} \tag{5}$$

Stability conditions - Step 4

$$\Delta t_{convT} \leq \frac{h}{u^n_{conv}}; \quad \Delta t_{diffT} \leq \frac{h^2}{} \tag{6}$$

4. RESULTS

The AC-CBS scheme is successfully applied to the well known benchmark problem of natural convection, with Rayleigh number equal to 10^8, in a square cavity with the vertical walls maintained at different temperatures (Figure 1(a)), for which numerical solutions are available in the literature [1-3]. Figure 2(a) shows the nondimensional vertical velocity at midheight of the square cavity. The present results compare excellently with the numerical solutions available in the literature [1, 3].

The results are validated against the experimental data of the new benchmark problem (Figure 1(a)) identified by the authors for natural convection, with a Rayleigh number equal to $1.3 \cdot 10^8$, in rectangular cavities with three different aspect ratios [8]. Figure 2(b) shows the nondimensional temperature profiles at different heights of a cavity with aspect ratio L/H=0.5. The left wall nondimensional temperature is one, the top wall nondimensional temperature is 1.42, the right and bottom walls are at zero nondimensional temperature. There is an excellent agreement between the present results and the experimental data [8].

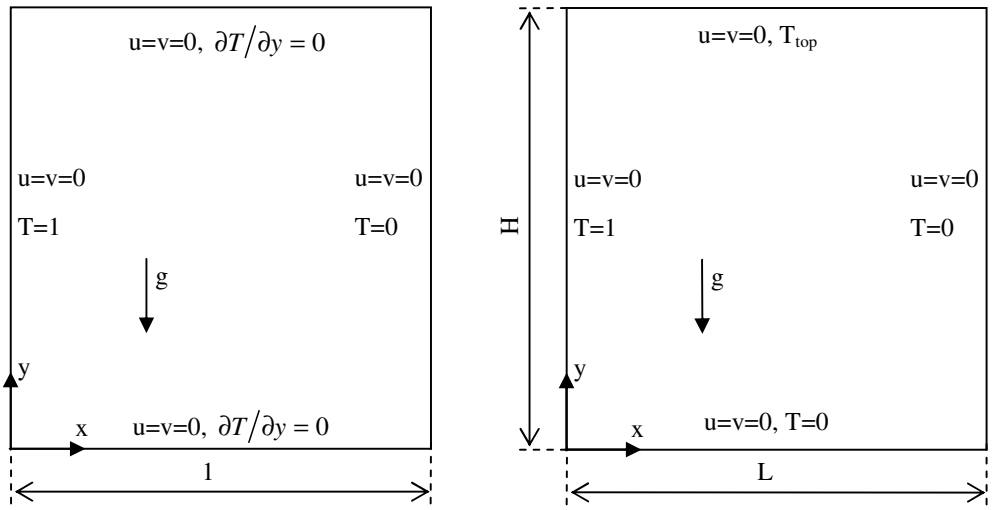

(a) (b)

Figure 1. Computational domain and boundary conditions employed: (a) square cavity; (b) new natural convection benchmark problem.

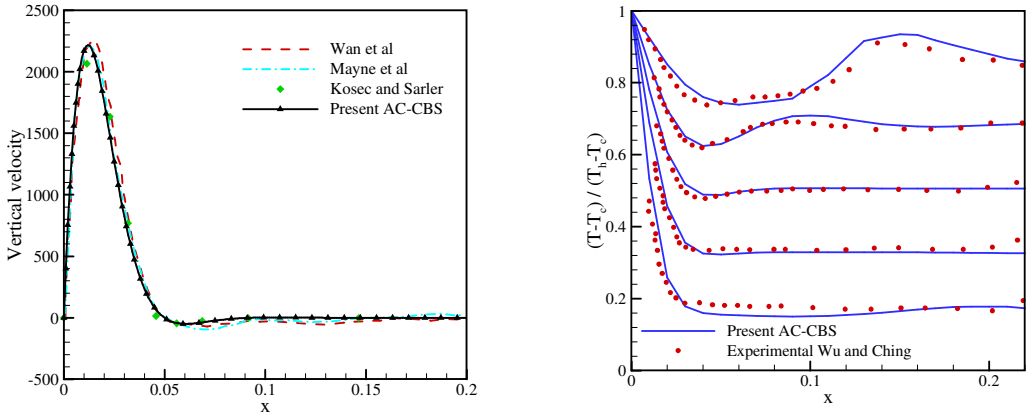

(a) (b)

Figure 2. High Rayleigh number natural convection: (a) square cavity; (b) new benchmark problem.

4. CONCLUSIONS

A new stabilized, efficient and accurate AC-CBS scheme has been presented for the solution of high Rayleigh number natural convection in cavities with different aspect ratios. A new benchmark quality solution has been introduced by the authors for natural convection, to test the efficiency of the stabilization analysis developed by the authors. The well known benchmark problem of natural convection in square cavity has also been solved. The results obtained for all the problems considered are in excellent agreement with the numerical and experimental data available in the literature.

REFERENCES

[1] D.A. Mayne, A.S. Usmani, M. Crapper, h-adaptive finite element solution of high Rayleigh number thermally driven cavity problem, International Journal of Numerical Methods for Heat and Fluid Flow, Vol. 10, pp. 598-615, 2000.

[2] D.C. Wan, B.S.V. Patnaik, G.W. Wei, A new benchmark quality solution for the buoyancy-driven cavity by discrete singular convolution, Numerical Heat Transfer, Part B, 40: 199-228, 2001.

[3] G. Kosec, B. Sarler, Solution of thermo-fluid problems by collocation with local pressure correction, International Journal of Numerical Methods for Heat and Fluid Flow, Vol. 18, pp. 868-882, 2008.

[4] H.N. Dixit, V. Babu, Simulation of high Rayleigh number natural convection in a square cavity using the lattice Boltzmann method, International Journal of Heat and Mass Transfer, 49, 727-739, 2006.

[5] N.C. Markatos, K.A. Pericleous, Laminar and turbulent natural convection in an enclosed cavity, Int. J. Heat Mass Transfer 27, 755–772, 1984.

[6] P. Nithiarasu, An efficient artificial compressibility (AC) scheme based on split (CBS) method for incompressible flows, International Journal for Numerical Methods in Engineering, 56, 1815-1845, 2003.

[7] F. Arpino, N. Massarotti, A. Mauro and P. Nithiarasu, Artificial Compressibility Based CBS Scheme for the Solution of the Generalized Porous Medium Model. Numerical Heat Transfer, Part B; 55: 196-218, 2009.

[8] W. Wu, C.Y. Ching, The effect of the top wall temperature on the laminar natural convection in rectangular cavities with different aspect ratios, Journal of Heat Transfer, vol.131, 5, 2009.

First International Conference on Computational Methods for Thermal Problems
ThermaComp2009, September 8-10, 2009, Napoli, Italy
N.Massarotti and P.Nithiarasu (Eds.)

COMPARISON OF HEAT TRANSFER ENHANCEMENT OF AN INTERNAL BLADE TIP WITH METAL OR INSULATING PINS

Gongnan Xie **Bengt Sundén***

Division of Heat Transfer, Lund University, SE-22100, P.O. Box 118, Lund, Sweden.
*Email: bengt.sunden@energy.lth.se (*B.Sundén*)

ABSTRACT

Cooling methods are needed for the turbine blade tips to ensure a long durability and safe operation. A common way to cool the tip is to use serpentine passages with 180-deg turn under the blade tip-cap taking advantage of the three-dimensional turning effect and impingement like flow. Improving internal convective cooling is therefore required to increase the blade tip life. In the present study, the augmented heat transfer of an internal blade tip with pin-fin arrays has been investigated numerically using a conjugated heat transfer approach. The computational models consist of a two-pass channel with 180-deg turn and an array of pin-fins mounted on the tip-cap, and a smooth-tip two-pass channel. The computational domain includes the fluid region and the solid pins as well as the tip regions. Turbulent convective heat transfer between the fluid and pins, and heat conduction within pins and tip are simultaneously computed. The main objective of the present study is to observe the effect of the pin material on heat transfer enhancement of pin-finned tips. It is found that due to the combination of turning impingement and pin-fin crossflow, the heat transfer coefficient of the pin-finned tip is a factor of 2.4 higher than that of a smooth tip at the cost of an increased pressure drop by about 10%. Disregarding the factor of the increased active heat transfer area, the tip with metal Aluminium pins provides around 15% and 7% higher heat transfer enhancement than the tips with insulting Wood pins and Renshape pins, respectively.

Key Words: *Heat Transfer Enhancement, Tip-wall, Pins, Thermal conductivity.*

1. INTRODUCTION

Numerical simulations are effective means to investigate the details of fluid flow and heat transfer characteristics resulting from augmented surfaces. During recent years, application of *Computational Fluid Dynamics* (CFD) techniques to predict the flow field and heat transfer coefficient distribution in turbomachineries has attracted many researchers[1-6]. For examples, Hwang et al. [1] predicted turbulent heat transfer in a rotating two-pass channel using a modified two-equation k-ε turbulence model. Chen et al. [2] calculated the 3D flow and heat transfer in a rotating two-pass square channel with smooth walls or $45^o/60^o$ angled ribs by a second-moment closure model and a two-layer k-ε isotropic eddy viscosity model. Iacovides and Raisee [3] computed fluid flow and heat transfer in 2D rib-roughened passages using modified low-Re differential second-moment (DSM) closure turbulence models, Nonino and Comini [4] computed 3D laminar forced convective heat transfer in ribbed square channels with velocity-preesure coupling SIMPLER algorithm based on the finite element method. Jia et al. [5] and Sunden et al. [6] numerically studied turbulent heat transfer and/or impingement cooling in rib-roughened ducts using the in-house code CACL-MP. From the above-mentioned references, it is indicated that heat transfer and cooling in gas turbine channels might be predicted effectively by CFD simulations with various computational approaches.

For turbine blades in particular operation, the hot leakage flow results in high thermal loads on the blade tip. It is therefore very essential to cool the turbine blade tip and the region near the tip. A

very common way to cool the blade tip is to adopt internal cooling by designing serpentine (two-pass, three-pass or multi-pass) channels with a 180-deg turn/bend inside the blade (as shown in Fig. 1). Taking the advantage of impinging and turning effects, the tip can be cooled to some certain extent. Consequently, augmenting internal convective cooling is required to increase the blade tip life. Fortunately, it is well documented that many augmented devices, i.e., fins, ribs, pins, dimples, can be used to improve the heat transfer significantly. Many previous investigations have proven that pin-fins can improve the cooling in low aspect ratio channels for gas turbines, typically at the trailing edges. The application of pin-fins has received much attention for enhancing heat transfer in cooling channels, e.g., turbine blades, heat sinks, compact heat exchangers. Most recently, Bunker [7] presented a method to provide substantially increased convective heat flux on an internal cooled blade tip-cap, where arrays of discrete shaped pins were fabricated and placed. It was found that the effective heat transfer coefficient could be increased up to a factor of 2.5 while the tip turn pressure drop was negligible compared to that of a smooth surface.

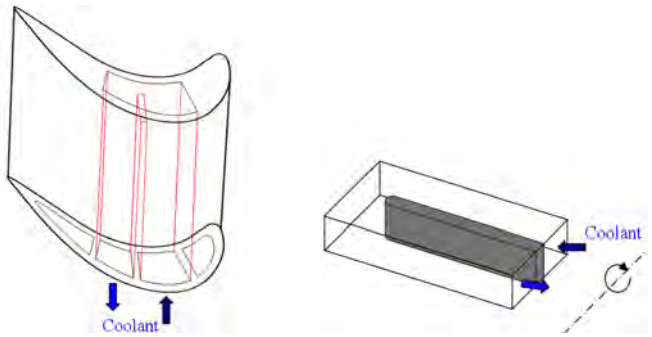

FIGURE 1. A typical serpentine passage inside a turbine blade

Even though similar heat transfer results in two-pass channels with pin-fins can be found in the experimental work by Bunker [7], limited details of the heat transfer and flow field on the pin-fins and tip-walls are available. Furthermore, most previous studies were concerned about the heat transfer on the leading or/and trailing walls of two-pass channels, and thus very limited information is available for tip walls. For these reasons, it is desirable to present more details on the heat transfer enhancement over tip walls, and to facilitate better understanding of three dimensional flow and heat transfer for pin-finned tips. Besides, few comprehensive studies focused the pin materials on augmented surfaces heat transfer, thus the main objective of the present study is to investigate the effect of pin material on heat transfer enhancement over pin-finned tips in a rectangular two-pass channel at high Reynolds number. Detailed flow field and heat transfer are presented, and the overall performances of pin-finned-tip two-pass channels are compared and evaluated.

2. DESCRIPTION OF PHYSICAL MODELS

A schematic diagram of the geometrical models considered in this study is provided in Fig. 2. The detailed geometrial parameters can be found in [8-10]. Figure 2(a) shows the smooth-tip two-pass channel. It is used for performance comparison with the pin-finned-tip two-pass channel as shown in Fig. 2(b). The numerical models of the rectangular two-pass channels are similar to those in the experiments by Bunker [7], but the pin-fin configurations and arrangements in the present study and the experiments are different. In Fig. 2(b), pin-fin arrays are mounted on the tip, and the pin-fins are in staggered arrangement. In all simulations, the pin-fins are assumed to be perfectly circular without base-fillet or tip-radius. Three kinds of pin materials are considered in this study: aluminum, wood and Renshape. The material properties are listed in Table 1.

Material	Aluminum	Wood	Renshape
Density, kg/m^3	2719	700	1800
Specific Heat, J/(kg.K)	871	2310	1180
Thermal conductivity, W/(m.K)	202.4	0.173	1

TABLE 1. Material properties for computations

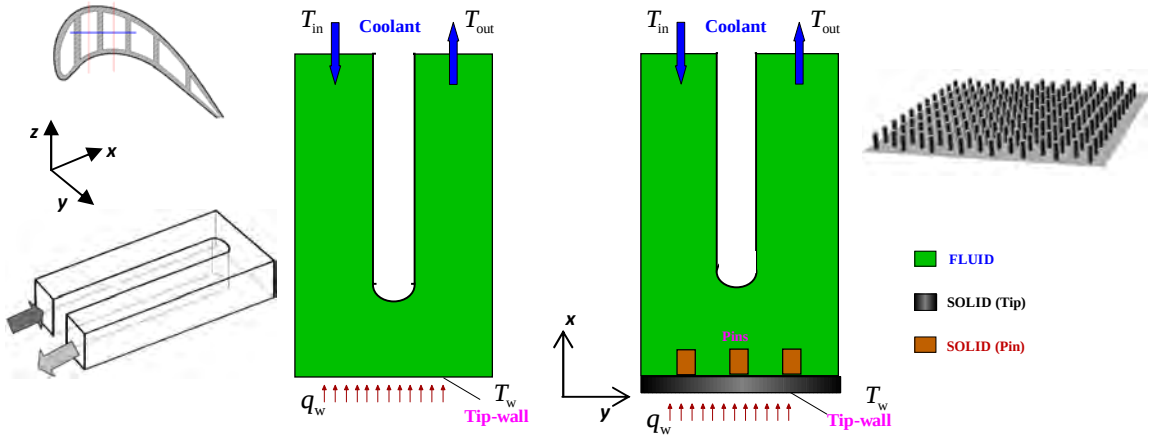

(a) smooth-tip channel (b) pin-finned-tip channel

FIGURE 2. Schematics of computational models: smooth-tip channel and pin-finned-tip channels

3. COMPUTATIONAL METHOD

Overview: In the present study, the finite volume modelling was conducted by applying the simulation software FLUENT version 6.3.26. This code uses the finite volume method to solve the governing equations of fluid flow and heat transfer with appropriate boundary conditions. The pressure and velocity fields are linked by the Semi-Implicit Method for Pressure Linked Equations Consistent (SIMPLEC) algorithm. Another commercial software GAMBIT version 2.4.6 providing geometry generation, geometry import and mesh generation capabilities was used to set up the computational models. *Due to the space for extended abstract, the details of conjugated heat transfer approach and others (grid study, turbulence model, governing equations and boundary conditions) are not presented. Similar details can be found in[8-10]. >>Awaiting more...*

4. RESULTS AND DISCUSSION

This section is awaiting for results, it needs 1~2 months to obtain all computational results, since a typical CPU time for one computation at a Re will take two days. >>Awaiting more...

Typical local Nusselt number is shown in Fig.3. It can be seen that larger regions of large local heat transfer are produced by pin-finned-tip channels. Disregarding increased active heat transfer, the heat transfer of different pins is compared in Fig.4. It can be found that the tip with metal Aluminium pins provides around 15% and 7% higher heat transfer enhancement than the tips with

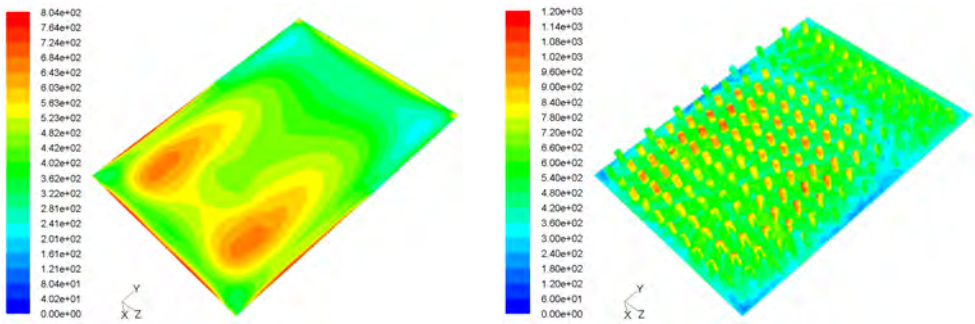

FIGURE 3. Local Nusselt number distributions of smooth-tip and pin-finned-tip channels

insulting Wood pins and Renshape pins, respectively. >>*Awaiting more...*

Other interesting results can be referred to [8-10].

5. CONCLUSIONS

The three-dimensional turbulent flow and convective heat transfer over the tips in rectangular two-pass channels have been numerically investigated. The main findings from this study are summarized as follows: (1) Due to combination of turn, impingement and pin-fin crossflow, the pin-fins are very effective heat transfer enhancement devices for gas turbine blade tips. The pin-fins force the vortices towards the tip wall and thereby improve the turbulent mixing of the approaching cold fluid and hot fluid near the tip. (2) Compared to the smooth tip channel, the heat transfer enhancement of the pin-finned tip channel is up to 2.4. >>*Awaiting more...*

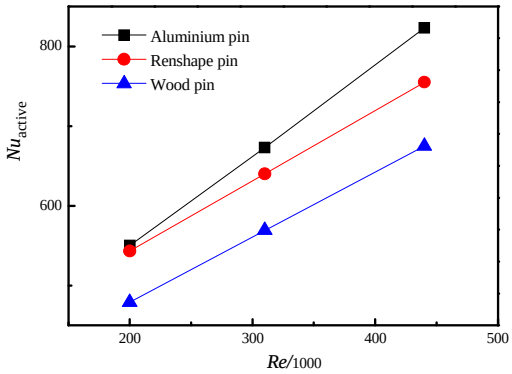

FIGURE 4. Active heat transfer of different fins

Other interesting conclusions can be found in [8-10].

REFERENCES

[1] J.J. Hwang, T.Y. Lia, and S.H. Chen, Prediction of turbulent fluid flow and heat transfer in a rotating periodical two-pass square duct, *International Journal of Numerical Methods for Heat and Fluid Flow*, 8, 519-538, 1998.

[2] H.C. Chen, Y.J. Jang, and J.C. Han, Computation of heat transfer in rotating two-pass square channels by a second-moment closure model, *International Journal of Heat Mass Transfer*, 43, 603-1616, 2000.

[3] H. Iacovides, and M. Raisee, Computation of flow and heat transfer in two-dimensional rib-roughened passages using low-Reynolds-number turbulence models, *International Journal of Numerical Methods for Heat and Fluid Flow*, 11, 138-155, 2001.

[4] C. Nonino, and G. Comini, Convective heat transfer in ribbed square channel, *International Journal of Numerical Methods for Heat and Fluid Flow*, 12, 610-628, 2002.

[5] R. Jia, M. Rokni, and B. Sundén, Impingement cooling in a rib-roughened channel with cross-flow, *International Journal of Numerical Methods for Heat and Fluid Flow*, 11, 642-662, 2001.

[6] B. Sundén, R. Jia, and A. Abdon, Computation of combined turbulent convective and impingement heat transfer, *International Journal of Numerical Methods for Heat and Fluid Flow*, 14, 116-133, 2004.

[7] R.S. Bunker, The augmentation of internal blade tip-cap cooling by arrays of shaped pins, Proceedings of GT2007, ASME Turbo 2007. *Paper no. GT2007-27009*. Also in *ASME J. Turbomachinery*, 130, 041007.

[8] G.N. Xie, B. Sundén, L. Wang, and E. Utriainen, Enhanced heat transfer on the tip-wall in a rectangular two-pass channel by pin-fin arrays, *Numerial Heat Transfer-Part A*, 55, 739-761, 2009.

[9] G.N. Xie, B. Sundén, L. Wang, and E. Utriainen, Augmented heat transfer of an internal blade tip-wall with a pin-fin array. *Proceedings of GT2009, ASME Turbo Expo 2009*, June 8-12, 2008, Orlando, USA. *Paper.no GT2009-59410.*

[10] G.N. Xie, and B. Sundén, Effect of pin base-fillet on heat transfer enhancement of an internal blade pin-finned tip-wall, *Proceedings of 2009 ASME Heat Transfer Conference, HT2009,* July 19-23, 2009, San Francisco, USA. *Paper.no HT2009-88116.*

First International Conference on Computational Methods for Thermal Problems
ThermaComp2009, September 8-10, 2009, Napoli, Italy
N.Massarotti and P.Nithiarasu (Eds.)

QUENCHING PROCESS SIMULATION FOR IC ENGINE CYLINDER HEADS

David GREIF
AVL AST d.o.o., Maribor. Slovenia, david.greif@avl.com

Maik SUFFA
AVL List GmbH, Graz, Austria, maik.suffa@avl.com

Vedanth SRINIVASEN
AVL Powertrain Inc., Plymouth, Michigan, USA, vedanth.srinivasen@avl.com

DeMing WANG
AVL Powertrain Inc., Plymouth, Michigan, USA, deming.wang@avl.com

Zlatko KOVACIC
AVL AST d.o.o., Maribor. Slovenia, zlatko.kovacic@avl.com

ABSTRACT

The paper describes the results obtained by simulating a cylinder head of a 4 cylinder gasoline engine. Separate computational domains constructed for the quenched solid part and the liquid domain are numerically coupled at the interface. The program handles multiphase flow dynamics in the liquid domain in conjunction with the temperature evolution in the solid region in coupled fashion. Comparison between measured and computed temperatures at different monitoring positions shows very good agreement for the two investigated cylinder head orientations O1 (upside down, cam shaft (top) side submerged first) and O2 (intake down, intake port flange side submerged first). Strong non-uniformity in temperature distribution within the structure was found, which is of great importance in evaluating residual stresses and fatigue patterns within the quenched object. Effects on the structure resulting from the quenching process are presented through sample Finite Element Method results.

Key Words: *Heat Transfer, CFD, Nucleate boiling, Film boiling, Quenching.*

1. INTRODUCTION

In order to meet the increasingly stringent regulations on tail pipe emissions also secondary measures, such as weight reduction, are taken. Aluminum was found to be a promising alternative to the heavy cast iron that was originally used for cylinder head manufacturing [1].

The use of aluminum cylinder heads requires heat treatment to achieve the required mechanical properties Part of that treatment is the so-called quenching: the reduction of the temperature of the hot aluminum alloy from about 700 to 800K to below 300K. Common methods to achieve this temperature drop include the use of air as well the use of liquids, such as water or polymers.

In-depth literature overview related to quenching is available from Srinivasan et al. [2, 3].

Using air as quenchant was initially found to result in lower residual stresses and higher fatigue values while the process itself is long-lasting and expensive. Therefore, especially if the manufacturing of large numbers of cylinder heads is planned, it is desirable to perform quenching with the help of liquids.

The paper provides details about a novel modeling procedure to simulate the quenching process by means of liquids using the commercial Computational Fluid Dynamics code AVL FIRE ®.

2. CYLINDER HEAD QUENCHING

Submerging the heated cylinder head into a sub-cooled liquid bath is triggering boiling mass transfer. As a result two-phase flow with boiling phase change is handled using the Eulerian two-fluid method [12]. Mass transfer effects are considered based on either film or nucleate boiling regime.

The framework of the AVL FIRE ® Multiphase module, described in detail in [4], has been extended by a boiling model, capable of handling both nucleate and film boiling. Since the mass transfer predominantly controls heat transfer, it is reasonable to apply the analogy and assume that the phase change rate (vapor formation) is proportional to the heat transfer rate [5]. The phase change rate (written for the continuous phase – liquid in the present study) due to the boiling process is computed as

$$\Gamma_c = C_m C_b \cdot \tilde{h}_b \cdot A_{\text{int}} \Delta T / \widetilde{H}_{fg}$$

with A_{int} the interfacial area, C_b boiling correction coefficient, C_m the closure coefficient, h_b the boiling heat transfer coefficient, H_{fg} the latent heat of vaporization, $\Delta T = T_w - T_{sat}$ being the wall superheat. The closure coefficient C_m is used to correct the interfacial area density to obtain the effective mass exchange [4]. The boiling heat transfer coefficient h_b assumes the value of film boiling coefficient [6] when the metal surface temperature is higher than the Leidenfrost temperature. If not, h_b is provided with a modified transition boiling heat transfer coefficient computed based on the fluid parameters [2]. Strong variations in Critical Heat Flux variations [11, 12, 13] in conjunction with alterations to the Minimum Heat Flux calculations [11, 14, 15] are used to construct corresponding mass transfer limits. Details of the implemented mass transfer model can be obtained from Srinivasan et al. [2].

3. RESULTS

In the simulations presented in this study water was used as quenchant. Its temperature was maintained close to liquid saturation temperature. Variable temperature dependent specific heat and thermal conductivity properties in the solid region was employed. A Leidenfrost approximation close to 600K was applied.

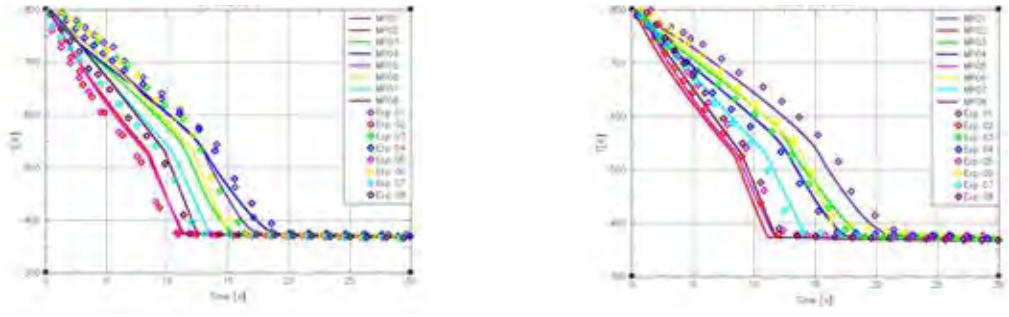

Figure 1: Comparison of metal temperature histories generated by quenching simulation of the O1(left) and O2 (right) orientation.

Figure 1 shows the predicted metal temperature history in comparison with the experimental observations at 8 different monitoring locations for both dip-in directions. At all locations the

computed metal temperature slopes, both in the film and transition boiling regime, are in good agreement with the measured data. Slowest and fastest cooling spots are separated by over 5s for O1 and almost 10s for O2 resulting in local temperature gradients.

As shown in figures 2 and 3 for both cases at time t=5s, intense cooling throughout entire metal surface is evident. With developing time, t=10s, highly non-uniform temperature can be observed: there are spots where temperature has dropped substantially; however, the bottom-most corner where the material has the highest thickness is still at rather high temperature. Even though temperature has fallen further at t=15 and 20s, regions of higher temperatures are still prevalent. This information provided by the numerical model is useful in order to understand and further analyze potential zones prone to higher residual stresses and thus minimize and/or eliminate resulting material dynamics such as cracks, fatigue etc. Figures 3 and 4 furthermore confirm that cooling is faster in orientation O1 as opposed to O2.

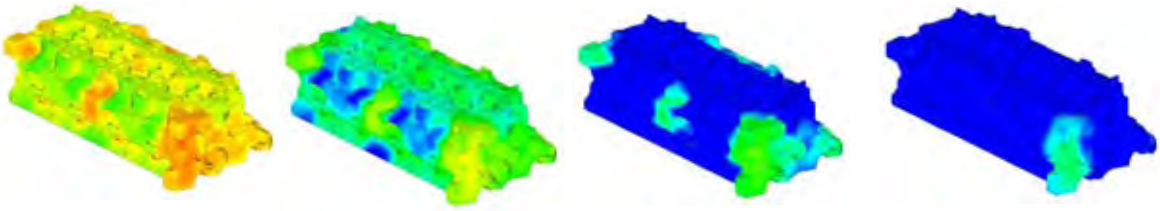

Figure 2: Temperature distribution at different time instants 5s, 10s, 15s, 20s (from left to right). Simulation results from O1 orientation

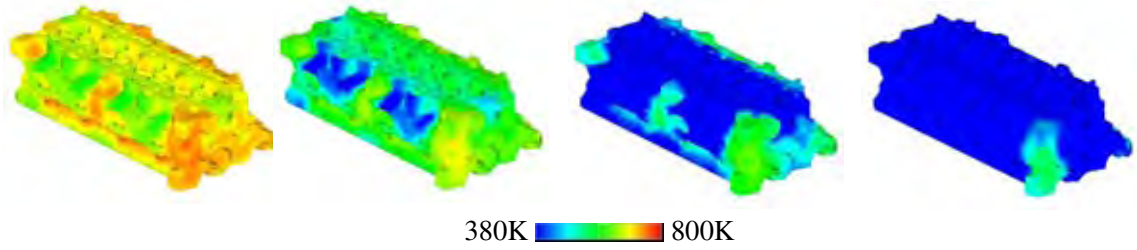

Figure 3: Temperature distribution at different time instants 5s, 10s, 15s, 20s (from left to right). Simulation results from O2 orientation

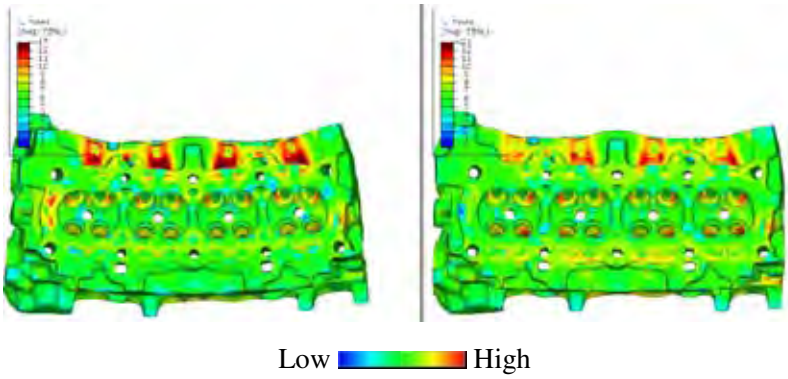

Figure 4: Stress distribution in the structure for orientation O1 (left) and O2 (right) 3 seconds after start of submerging. Deformations are overscaled by a factor of 100.

The results obtained in during the CFD simulation are applied as transient boundary conditions in a consequent prediction of stresses and deformations using commercial Finite Element Analysis (FEA) software. The two dipping orientations discussed above result in clearly different transient solid temperature fields and consequently in stresses and deformations that are locally visibly higher for orientation O1 compared to O2 (see figure 4).

4. CONCLUSIONS

Numerical simulations of a real-time cylinder head quenching process using the commercial code AVL FIRE ® have been performed successfully. Two different cylinder head orientations have been simulated. The computed cooling rates are in very good agreement with the experimental data wherever available. Quenching rates associated with the film boiling regime are tracked particularly well. Orientation O1 features faster overall cooling, which was not expected. This fact only proves the necessity to perform simulations of this type to predict temperature distributions within the solid. Computed temperature distribution emphasized non-uniform behavior driven by varying material thickness. The information is of great importance in consequent stress and strain analyses.

REFERENCES

[1] Allison, J., Li, M., Wolverton, C., Su, X., Virtual Aluminum Castings: An Industrial Application of ICME, JOM, November 2006.

[2] Srinivasan, V., Moon, K., Greif, D., Wang, D.M., Kim, M., Numerical Simulation of Immersion Quench Cooling Process: Part I, Proceedings in the International Mechanical Engineering Congress and Exposition, IMECE2008, Paper no: IMECE2008-69280, Boston, Massachusetts, USA, 2008.

[3] Srinivasan, V., Moon, K., Greif, D., Wang, D.M., Kim, M., Numerical Simulation of Immersion Quench Cooling Process: Part II, Proceedings in the International Mechanical Engineering Congress and Exposition, IMECE2008, Paper no: IMECE2008-69281, Boston, Massachusetts, USA, 2008.

[4] AVL FIRE ® Manual, 2008.

[5] Ho, K., Pehlke, R. D., Metal-Mold Interfacial Heat Transfer, Metallurgical Trans. B., Vol. 16B, pp. 585-594, 1985.

[6] Bromely, L. A., Heat transfer in stable film boiling. Chem. Eng. Prog. 58: 67-72, 1950.

[7] Dhir, V. K., Boiling Heat Transfer, Annu. Rev. Fluid Mech., Vol. 30, pp.365-401, 1998.

[8] Gogonin, I. I., Kutateladze, S. S., Critical Heat Flux as a Function of Heater Size for a Liquid Boiling in a Large Enclosure, J. Engg. Phy. Thermophysics, Vol. 33, No. 5, pp. 1286-1289, 1977.

[9] Kandlikar, S. G., Critical Heat Flux in Subcooled Flow Boiling – An Assessment of Current Understanding and Future Directions for Research, Multiphase Science Tech., Vol. 13, No. 3, pp.207-232, 2001.

[10] Hsu, Y. Y., A Review on Film Boiling, NASA Technical Mem., NASA TM X-52837, 1970.

[11] Dougall, R. S., Film Boiling on the Inside of Vertical Tubes With Upward Flow of the Fluid at Low Qualities, Ph.D Thesis, Massachusetts Institute of Technology, 1963.

[12] Wang, D.M., Alajbegovic, A., Su, X.M. and Jan, J., Numerical simulation of water quenching process of an engine cylinder head, Proceedings of ASME FEDSM 2003, 4th ASME JSME Joint Fluids Engineering Conference, Honolulu, Hawaii, USA, July 6 -10, 2003.

First International Conference on Computational Methods for Thermal Problems
ThermaComp2009, September 8-10, 2009, Napoli, Italy
N.Massarotti and P.Nithiarasu (Eds.)

CFD–ASSISTED DESIGN OF A HOUSEHOLD PELLET BOILER

Francesco Saverio Marra and **Daniela Menghini** [1]
IRC-CNR, Via Diocleziano 328, 80124 Naples, Italy, marra@irc.cnr.it

Gaetano Continillo
Università del Sannio, Piazza Roma 21, 82100 Benevento, Italy, continillo@unisannio.it

ABSTRACT

Two 3D detailed CFD models of a wood fuelled stove were employed sequentially to maximize the global heat efficiency and reduce the risk of boiling of water. First, the volume and shape of the gas-phase domain was optimized assuming Dirichlet boundary conditions at the walls separating the hot smokes and water. Then the computed heat fluxes on these surfaces were assumed as Neumann boundary conditions for the computation of the liquid-phase flow and thermal field.

Key Words: Heat Transfer, CFD, Wood stoves, Optimization.

1. INTRODUCTION

Wood combustion represents a large amount of energy production in household appliances. Manufacturers of wood stoves face optimization problems with respect to various aspects, as overall size and beauty of flame, manufacturing and operation costs, subject to pollution regulation constraints. The use of biomass energy obviously reduces CO_2 emissions, provide wildlife habitat, and help maintaining forest health through better management [1]. Among biomass, wood and its wastes are the most common fuels (64%) and their direct combustion is the most important and mature technology nowadays available for their utilization. Nevertheless wide margins for improvement with respect to efficiency, emissions, and cost are still available [2]. To pursue such improvements, Computational Fluid Dynamic (CFD) can be a very useful tool. Various approaches are suggested in literature aimed at increasing efficiency and reducing pollutant emissions. Ravi et al. [3] focus on the improvement of thermal efficiency through the optimization of geometric parameters and present an approach in which detailed CFD simulations of the flow, heat transfer, and chemical processes are conducted for a simple sawdust stove. Bryden et al. [4] use CFD analysis coupled to a graph–based evolutionary algorithm to improve heat transfer in a cookstove by changing position and size of some baffles that influence the swirl of the gas flow. Scharler et al. [5] simulate, with simplified chemistry, two different combustion chambers and grate systems to determine the effect of recirculation of gas flow and air staging. Optimization of such systems by CFD simulations is quite complex due to the large number of variables involved. For instance, the geometry of the stove is one of the main design options and the creation of a computational mesh is a complex and time consuming task that cannot be automated for substantial geometry changes. Even if optimization algorithms can be used to reduce computing efforts [6], the development of simplified computational procedures can greatly help to extend investigation to a wider set of configurations and achieve a better optimization of the appliances.

The analysis made for the prototypal design was based on the separation of the gas-phase problem from the water-phase problem, by decoupling the problems through the boundary conditions. The gas-phase boundary condition was chosen to be a Dirichlet Boundary Conditions (B.C.) since the water temperature can be safely assumed around 350 K. As a consequence, heat fluxes computed from the gas-phase problem must be used as Neumann B.C. for the water-phase problem. The

[1] currently at General Motors Powertrain Europe srl, 10100 Turin, Italy

analysis was conducted separately: Gas-phase analysis, aimed at the maximization of the heat recovery from the fumes, involving design and simulation of alternative gas path configurations; Liquid-phase analysis, aimed at avoiding local overheating and making as uniform as possible the temperature field in the liquid. This also involves conceiving and simulating alternative liquid path configurations, within the volume and shape of the metal interface, resulting from the gas-phase optimization. The procedure just described was adopted to determine the thermal optimization of a conceptual wood stove, reported in Figure 1a, designed to burn 3.6 kg/h wood pellets.

2. GAS PHASE AND LIQUID PHASE COMPUTATION AND OPTIMIZATION

Having determined a computational splitting of the problem between gas-phase and liquid-phase, we firstly describe the computational procedure adopted for the gas phase and how boundary data to be transferred to the solid-phase are collected. The results have been obtained with the CFD-ACE+ commercial software package by ESI-Group [7]. It is a control-volume-based CFD code that solves balance equations for mass, species, momentum and energy. Here the RANS formulation of the equation is adopted to take into account turbulence. Radiative heat transfer is included, being an important contribution to the total heat transfer problem. Combustion is modelled as a heat source located in the volume of the pellet burner. With 40% excess air, we estimate an inlet stream temperature of 2330 K. For all wet boundaries, Dirichlet boundary conditions for the temperature fixed to 345 K were assigned, whereas external boundaries exchange with the external ambient air by convection with a heat transfer coefficient of 6 W/(m^2 K) and ambient temperature of 300 K. Keeping a constant value for the water temperature during the gas-phase computations will not influence significantly the results: temperature is expected to take values within few tens of degrees, always below the boiling point.. The effective satisfaction of this preliminary assumption has to be verified at the end of the whole optimization procedure, to validate the obtained results.

FIGURE 1. Wood stove layout and computational mesh adopted for the gas-phase simulations

Numerical solutions are obtained by firstly defining the computational mesh directly from the CAD plan of the appliance, shown in Figure 1a, adopting an octree mesh with clustering of points near the walls and close to regions where maximum gradient of the state variable are expected, as shown in Figure 1b. Second order schemes both in space and time are used. Turbulence was modeled using the RNG k-ε Model [8], while the Discrete Ordinate Method was adopted for radiative heat transfer resolution [9]. The non-linear set of algebraic equations is solved by the SIMPLEC method suggested by Van Doormaal and Raithby [10]. Following indications coming from previous works [11], different geometry optimizations have been considered: introduction of a separating set to split the main chamber into an almost purely radiative heat exchanger and almost purely conductive and convective heat exchanger; change in the number and length of channels for the head of the combustion chamber; increasing to 6 the number of pipes in the descending path of fumes. These modifications finally led to a total heat flux recovery of 78%, as compared to 71.5% for the original

design with only two large pipes for the descending path and inclusion of a separator in the combustion chamber. The final design is shown in Figure 2, yielding a net power of 13500 W.

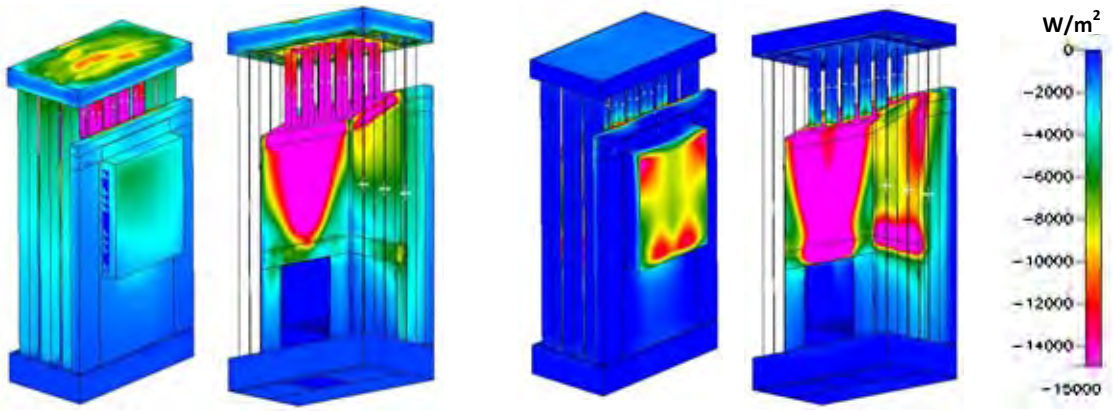

FIGURE 2. From left to right, front and rear view of the sum of conductive and convective heat flux and of radiative heat flux (W/m^2) for the final optimized configuration of the stoves.

The remaining task, i.e. optimization of the liquid phase circuit of the stove, corresponds to ensuring that local water temperature not exceeds the boiling point, while maintaining a reasonable pressure drop. Model equations are now the balance equation for mass, momentum and energy for an incompressible flow. Inlet temperature is assigned to 333 K, a typical value for household heating plants. A mass flow rate of 0.13 kg/s corresponds to a temperature increase of 25 K. The exchange of boundary data between the two simulations is done by averaging heat fluxes computed in the gas–phase simulation over each of the parts of the gas–liquid boundary (Figure 3). Water CFD was conducted with a different code, namely FLUENT [12], simply because more familiar to the person in charge of conducting this separate simulation. The governing equations were solved as laminar, being the local Reynolds number well below 1000 everywhere. Various configurations were tested: the final introduces several baffles to force the water into a circuit resembling a counter-current heat exchanger. Further elements were added in the side chambers to limit the formation of recirculation zones were values of the temperature exceeded the safety value of 90 °C (Figure 4). Water temperature never exceeds 360 K, with highest values at rear top of the combustion chamber.

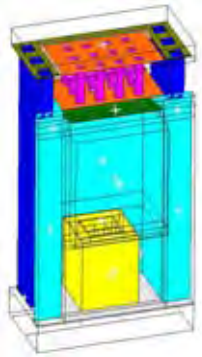

walls	Surface [m^2]	Heat power [W]	Heat flux [W/m^2]
Front	*0.0757*	*1001.6*	*13231.3*
Burner, rear	*0.1673*	*3623.7*	*21660.3*
Burner, right	*0.1003*	*1981.3*	*19754.1*
Burner, left	*0.1003*	*1861.3*	*18557.4*
Top	*0.0241*	*148.5*	*6164.3*
Floor	*0.0241*	*46.6*	*1932.3*
Central pipes	*0.1046*	*1291.2*	*12344.1*
Side pipes	*0.6378*	*1689.1*	*2648.3*
Top pipe array	*0.0431*	*408.2*	*9472.1*
Bottom pipe array	*0.0431*	*1284.2*	*29796.6*

FIGURE 3. Average heat fluxes for each interface element between the gas-phase and the liquid-phase, with the corresponding values of heat flux and surface area reported in the Table.

3. CONCLUSION

The proposed strategy of boundary-decoupled and combined CFD simulations of gas-phase and liquid-phase thermal flow allowed geometric optimization of a wood pellet stove by increasing from 71.5% to 78% total heat flux recovery without causing boiling in the liquid water phase.

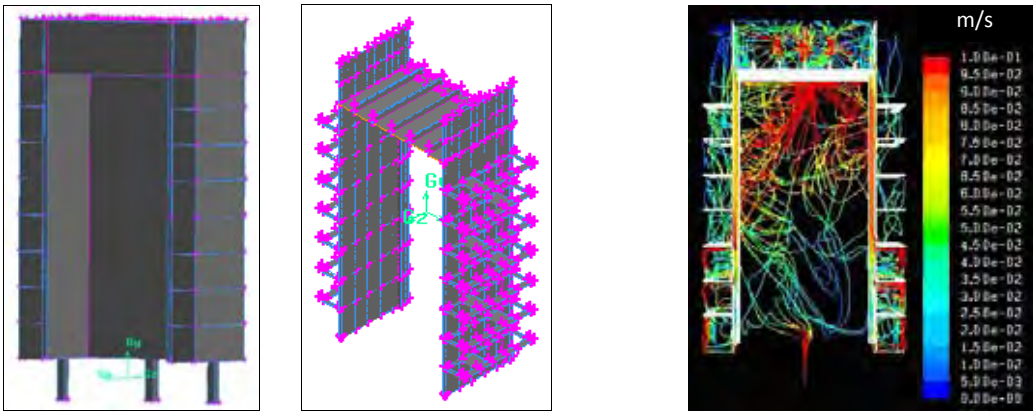

FIGURE 4. From left to right, external view of the domain of the water circuit, inner baffles in the water domain and resulting streamlines with indication of the local velocity magnitude in m/s.

REFERENCES

[1] A. Demirbas, Potential applications of renewable energy sources, biomass combustion problems in boiler power systems and combustion related environmental issues, *Progress in Energy and Combustion Science*, 31, 171-192, 2005.

[2] T. Nussbaumer, 12th European Conference and Technology Exhibition on Biomass for Energy, Industry and Climate Protection, Amsterdam, Holland, June 2002.

[3] M.R. Ravi, S. Kohli and A.Ray, Use of CFD Simulation as a Design Tool for Biomass Stoves, *Energy for Sustainable Development*, 6, 20-27, 2002.

[4] K. M. Bryden, D.A. Ashlock, D.S. McCorkle and G.L. Urban, Optimization of heat transfer utilizing graph based evolutionary algorithms, *International Journal of Heat and Fluid Flow*, 24, 267-277, 2003.

[5] R. Scharler, I. Obernberger, G. Längle and J. Heinzle, CFD Analysis of Air Staging and Flue Gas Recirculation in Biomass Grate Furnaces, 1st World Conference on Biomass for Energy and Industry, Sevilla, Spain, June, p. 1935 (2000).

[6] R.W. Johnson, M.D. Landon and E.C. Perry, Design Optimization, in *Computational Fluid Dynamics in Industrial Combustion*, Edited by Baukal C. E., Gershtein V. Y., Li X., CRC Press, Boca Raton, 2001.

[7] CFD-ACE+, ESI-Group CFD, AL (USA), website: www.esi-cfd.com, 2008

[8] V. Yakhot, S.A. Orszag, S. Thangam, C.G. Speziale and T.B. Gatski, Development of turbulence models for shear flows by a double expansion technique, *Physics of Fluids*, A4, 1510, 1992.

[9] W.A. Fiveland, Threedimensional radiative heat transfer solution by the discrete ordinates method, *Journal Thermophysics and Heat Transfer*, 2, 309-316, 1988.

[10] J.P. Van Doormaal and G.D. Raithby, Enhancements of the Simple Method for Predicting Incompressible Fluid Flows, *Numerical Heat Transfer*, 7, 147-163, 1984.

[11] D. Menghini, F. S. Marra, C. Allouis, F. Beretta, Effect of air excess on the optimization of heating appliances for biomass combustion, *Experimental Thermal Fluid Science Journal*, 32, 1371–1380, 2008.

[12] Fluent 6.1 user's guide, Fluent Inc., Centerra Research Park, 10 Cavendish Court, Lebanon, NH 03766, USA, 2003.

First International Conference on Computational Methods for Thermal Problems
ThermaComp2009, September 8-10, 2009, Naples, Italy
N.Massarotti and P.Nithiarasu (Eds.)

COMPUTATIONAL ANALYSIS OF A HEAT TRANSFER EXPERIMENT INCLUDING THERMALLY INDUCED DEFORMATIONS

Matthias Haupt
Institute for Aircraft Design and Lightweight Structures, Technical University Braunschweig, Hermann-Blenk-Str. 35, D-38108 Braunschweig, m.haupt@tu-bs.de

Reinhold Niesner
Volkswagen AG, D-38436 Wolfsburg, formerly: Institute for Aircraft Design and Lightweight Structures, Technical University Braunschweig, reinhold.niesner@volkswagen.de

Peter Horst
Institute for Aircraft Design and Lightweight Structures, Hermann-Blenk-Str. 35, D-38108 Braunschweig, p.horst@tu-bs.de

Burkard Esser
German Aerospace Center, Institute of Aerodynamics and Flow Technology, Wind Tunnels, Linder Höhe, D-51147 Köln, Burkard.Esser@dlr.de

Ali Gülhan
German Aerospace Center, Institute of Aerodynamics and Flow Technology, Wind Tunnels, Linder Höhe, D-51147 Köln, Ali.Guelhan@dlr.de

ABSTRACT

The simple configuration is described and used for computational and experimental investigations including thermal and mechanical fluid structure interactions for hypersonic flow conditions. The numerical modelling includes all relevant heat transfer mechanisms and takes into account the changes due to the heated and deformed structure.

Key Words: *Fluid-structure-interaction, heat transfer, radiation, deformation, coupled problem.*

1. INTRODUCTION

Spacecraft engineering requires the careful consideration of the high temperature loading conditions. The tragedies of the space shuttle accidents underline the importance of an accurate design taking into account all relevant phenomena and physical interactions. Computational analyses provide the tools to predict the spacecraft behaviour under complex loading scenarios. An important aspect is the validation of the nowadays multidisciplinary analysis tools, which become more and more complex. Computational heat transfer under hypersonic conditions including thermally induced deformations and their interactions with the flow field is a rarely documented domain and validation examples are mostly treating only one interaction. Here a validation configuration was developed including both, the thermal and the mechanical interactions.

2. CONFIGURATION

The design of the considered configuration was done under the requirements of well defined thermal and mechanical boundary conditions and reproducibility, to perform a variety of experiments. The test configuration is shown in Figure 1. The test specimen is a thin metallic plate (200mm$\times$200mm$\times$1mm) made of Incoloy 800HT which is mounted into a thick support frame as well made of Incoloy 800HT.

The frame acts as mechanical as well as thermal 'boundary' condition due to its stiffness and its capacity respectively. All this is insulated by Kapyroc against the windtunnel mount. It has a water cooled leading edge inducing an oblique shock for hypersonic fluid flow.

The experiment was designed to provide a validation database of thermal and mechanical fluid structure interactions at high Mach numbers and high temperature levels repectively. It includes the following heat transfer mechanisms:

- convection between the hypersonic and here laminar fluid flow and the structure,
- radiation between the structural surface and the environment, i.e. the wind tunnel walls,
- conduction in the structure, especially the thinwalled panel,
- active and capacitive cooling due to the boundary conditions and the support frame.

The experimental test procedure works as follows. The initial state of the structure is the undeformed one at room temperature. After start up the model is traversed into the established fluid flow with the conditions $Ma_\infty = 7.62$, $T_\infty = 463.7$ K, $p_\infty = 52$ Pa, $\rho_\infty = 3.1310^{-4}$ kg/m^3 and $U_\infty = 3690$ m/s. Due to the aerodynamic heating the temperature in the plate increases, reaches after a few seconds the critical thermal buckling temperature and the panel bends into the flow field. This alters the shape, the flow field and the resulting heat flux. After 120 s the complete model is traversed out of the fluid flow.

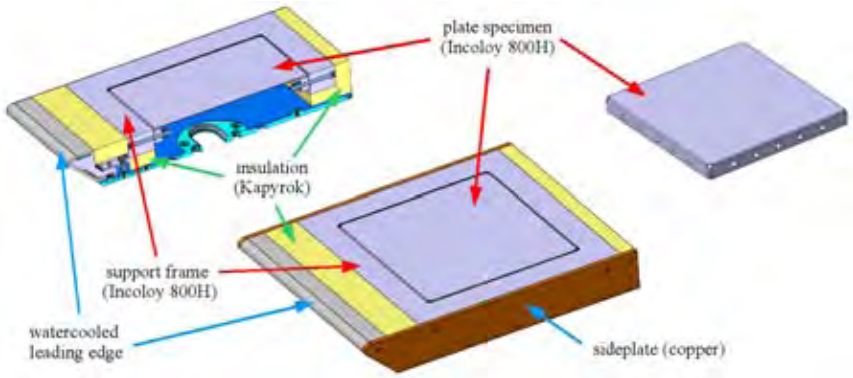

FIGURE 1. CAD model of the validation configuration

3. COMPUTATIONAL ANALYSIS

The computational analysis of the experiments was done with a partitioned approach using individual codes for the different domains, here the fluid and structural domains.

The CFD code DLR-Tau [1] solves in this analysis the classical RANS equations with a finite volume discretization including the AUSMDV upwind scheme, solved by a 3-stage Runge-Kutta integration and a multigrid-acceleration. Ideal gas with adopted gas constant $R = 346$ J/kgK and isentropic exponent $\kappa = 1.462$ and laminar flow is assumed because of the low Reynolds number $Re = 18800$ with respect to the model length of 0.4 m. Due to the symmetry only one half of the model needs to be simulated. To reduce the computational effort in parameter studies a simplified CFD 2.5D model was also used. On both longitudinal edges of the structure symmetry planes are assumed in the CFD grid neglecting the flow around the edges. Both grids are shown in Figure 2.

The FEM code ANSYS® was used to analyse the transient thermal state of the structure. The structural model includes the radiation between the surface and the surrounding environment. The FEM code Ansys provides as well the mechanical analysis including the geometric nonlinearities to predict large deformations of thin panels. One uncertainty in the material properties is the emissivity of the oxidized Incoloy surface, because it was not measured. The temperature dependent material properties especially required for Incoloy were taken from literature and used in the simulations.

The heat transfer between fluid and structure was modeled with a numerical coupling scheme, which iterates an equilibrium of temperature and heat flux on the wetted coupling surface in each time step of the coupled analysis. The same is valid for the deformations and the fluid forces. Due to the slow

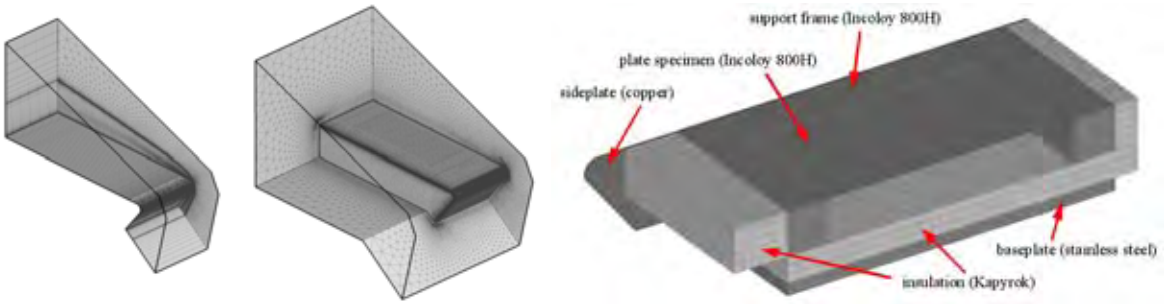

FIGURE 2. Left: 2.5D and 3D CFD grids, Right: FEM model of the structure

thermal deformation velocity the mechanical problem is treated quasi-stationary, i.e. in each thermal time step the stationary nonlinear deformation state is calculated for the actual temperature distribution. The deformations are incorporated into the CFD grid by a grid deformation algorithm.

The iteration procedure and the architecture of the implemented software is shown schematically in Figure 3. Details about the numerical scheme solving the partitioned equations and exchanging the state variables on the coupling surface for nonconforming discretizations on the fluid and the structural side are given in more detail in [2].

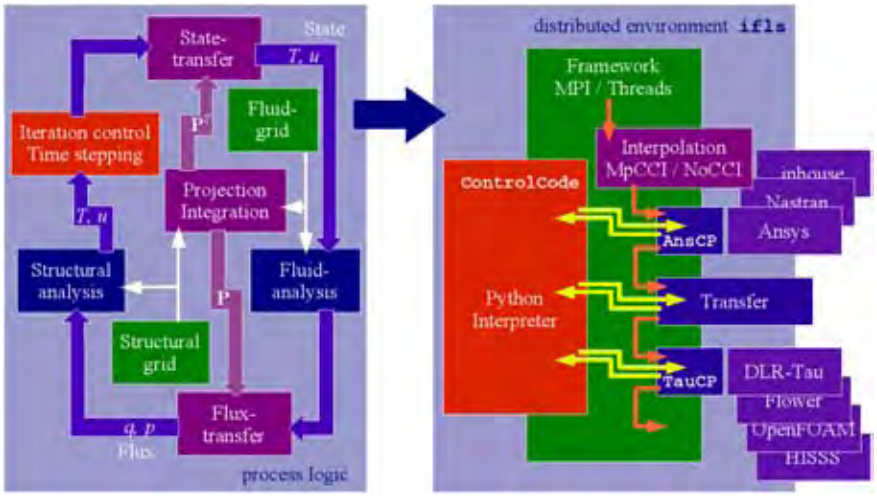

FIGURE 3. Process logic of the coupling algorithms and the corresponding software architecture

4. RESULTS

Figure 4 shows the time history of the plate's midpoint for temperature and deflection of the 1 mm thick plate. The experimental results are compared with the computational ones, taking the values 0.5 and 0.8 for the surface emissivity ϵ. In the first period 40 - 60 s the plate is heated up from room temperature to over 1000 K. At time 80 s a nearly steady thermal state is reached. After 120 s the test configuration is traversed out of the wind tunnel test section and cools down. The cooling process is simulated without any aerodynamic heat flow. Parallel to the temperature increase the plate bends up and reaches a wavy deformation pattern (see Figure 5) with a maximum amplitude of about 14 mm.

The calculation with $\epsilon = 0.8$, which is normally used for oxidized technical radiators, underestimates the temperature level for times over 30 s. Temperatures over 800 K are reached and the radiation becomes more important. As a consequence the bending amplitudes of the simulation are too small compared with the experiments due to the lower temperature level. For $\epsilon = 0.5$ the agreement becomes better for higher temperatures. In the beginning the simulations with both emissivities are in good agreement with experimental data. This indicates a good prediction of the aerodynamic heat flux by the CFD code and the low impact of the radiative heat transfer.

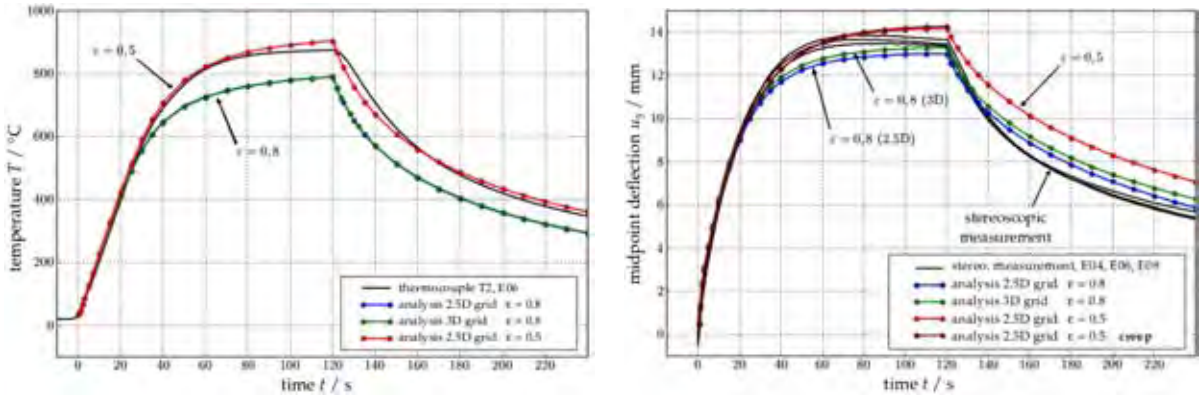

FIGURE 4. Left: temperature history, Right: deformations history of plate's midpoint

The differences between the 3D and the 2.5D aerodynamic models are relative small. For this reason the numerically more efficient 2.5D models are be used, e.g. for parameter studies with different flow conditions and plate thicknesses.

For times over 80 s the structural deformation decreases slightly in the experiments. This effect may be caused by the heating of the support frame - this should be covered by the FEM model - or by a more complex material behaviour. Up to now only a temperature dependend material law was used and further phenomena, e.g. creep or viscoplasticity, were neglegted. As a first attempt simple creep was included by Norton's law. The influence of this creep model is in this example insignificant. Nevertheless the material law should be improved for the high temperature range.

Figure 5 shows on the right hand side the comparison between the numerical analysis (top) and the stereoscopic measurement (bottom). The agreement in the complicated bending pattern is impressive.

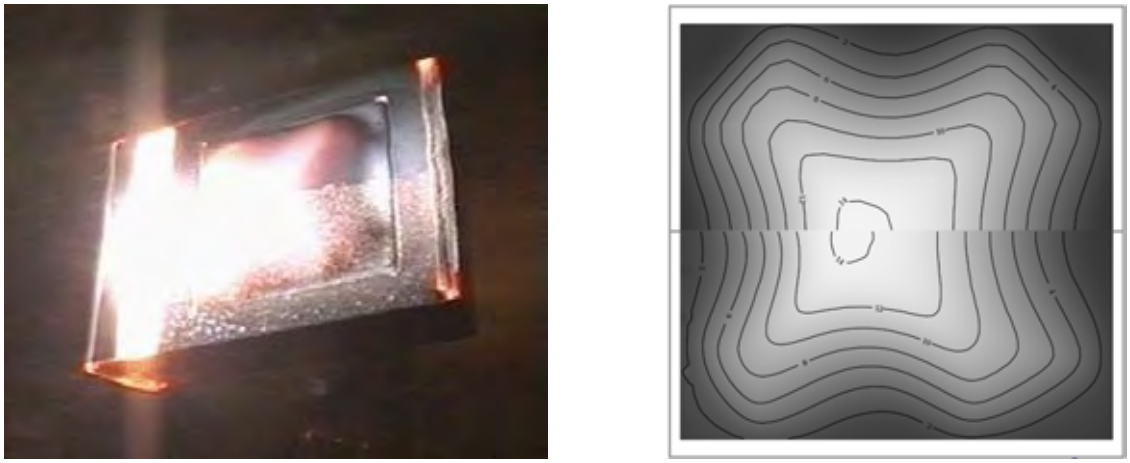

FIGURE 5. Left: Video capture of the experimental configuration, Right: comparison between numerical (top) and experimental results (bottom)

REFERENCES

[1] D. Schwamborn, T. Gerhold, and R. Heinrich, The DLR-TAU-Code: Recent applications in research and industry, *Proc. of ECCOMAS CFD*, 2006.

[2] M.C. Haupt, R. Niesner, R. Unger, and P. Horst, Computational aero-structural coupling for hypersonic applications, *AIAA Paper 2006-3252*, 2006.

First International Conference on Computational Methods for Thermal Problems
ThermaComp2009, September 8-10, 2009, Napoli, Italy
N.Massarotti and P.Nithiarasu (Eds.)

ELASTOPLASTIC-DAMAGE CONSTITUTIVE MODELING IN COUPLED CHEMO-THERMO-HYGRO-MECHANICAL PROCESS FOR CONCRETE AT HIGH TEMPERATURE

Xikui Li
Department of Engineering Mechanics, Dalian University of Technology, Dalian, China 116024
xikuili@dlut.edu.cn

Rongtao Li
College of Civil and Architectural Engineering, Dalian University, Dalian, China 116622
lirongtao@dl.cn

ABSTRACT

A coupled elastoplastic-damage model taking into account chemo-induced elastoplastic-damage effects for the modeling of coupled chemo-thermo-hygro-mechanical behavior of concretes at high temperature is proposed. A three-step operator split algorithm and consistent tangent modulus matrices for coupled chemo-thermo-hygro-mechanical analysis are derived. Numerical results demonstrate the validity of the presented algorithm and illustrate the capability of the proposed constitutive model in reproducing coupled chemo-thermo-hygro-mechanical behavior in concretes.

Key Words: *Elastoplastic-damage modeling, Coupled chemo-thermo-hygro-mechanical process, Concrete, reactive deforming porous medium, high temperature.*

1. INTRODUCTION

The fundamental study of the failure phenomena characterized by the thermal spalling of concrete is required to acquire a deep understanding of its physical origin observed on concrete exposed to rapid heating. To numerically study the complex multi-chemo-physical process which occurs in concretes subjected to fire, a hierarchical mathematical model for analyses of coupled chemo-thermo-hygro-mechanical behavior of concretes at high temperature was developed [2] based on the previous work of Gawin et al. [1]. Concretes are modeled as unsaturated deforming reactive porous media filled with pore fluids in immiscible-miscible levels. In the primary level, the two pore fluids, i.e. the gas mixture and the liquid mixture flow through the pore channels in an immiscible pattern. In the secondary level, dry air and vapor within the gas mixture phase, and the dissolved matrix components and pore water within the liquid mixture phase are homogeneously miscible between each other. The thermo-induced dehydration and desalination processes are integrated into the model. The chemical effects of both dehydration and desalination on the material damage and the degradation of the material strength are taken into account. The mathematical model consists of a set of coupled, partial differential equations governing the mass balance of the dry air, the mass balance of the water species, the mass balance of the matrix components dissolved in the liquid phases, the energy balance and momentum balance of the whole medium mixture. The present paper aims to develop a relevant constitutive model, in the frame of the mathematical model mentioned above, which can quantitatively describe the interrelated multi-chemo-physical process and progressive failure phenomena in concrete members subjected to fire.

To account for the complexity of coupled chemo-thermo-hydro-mechanical behavior in concrete subjected to fire and the fact that occurrence and evolution of the micro-crack or micro-void growth are accompanied with plastic flow process observed in concretes, a coupled elastoplastic-damage constitutive model with consideration of chemo-induced elastoplastic-damage effects is proposed in

the present work to model the realistic failure phenomena, i.e. loss of both the strength and stiffness, characterized by thermal spalling. The model is developed on the basis of the damage model by Mazars and the Willam-Warnke elastoplastic yield criterion for concrete at room temperature. The chemical softening and chemical damage, in addition to plastic strain hardening/softening, suction hardening and mechanical damage, are taken into account in the model. Based on the work of Ju [3] and Li et al. [4], a three-step operator split algorithm for the proposed coupled chemo-elastoplastic-damage model is derived. Consistent tangent modulus matrices with consideration of the fully coupled effects are formulated.

Numerical results demonstrate not only the capability of proposed model in reproducing coupled chemo-thermo-hygro-mechanical behavior and failure phenomena in concretes subjected to fire and thermal radiation, but also the validity and capability of the derived algorithm in numerical modeling and computation for isotropic, chemo-elastoplastic-damage porous continuum.

2. COUPLED CHEMO-ELASTOPLASTIC-DAMAGE MODELING AND COMPUTATIONAL ALGORITHM

The desalination of concretes with increasing temperature causes the reduction of the mechanical stiffness of the concrete material. The effect can be described with the chemical damage parameter d_s, the evolution of which depends on the mass concentration of the dissolved matrix component c_p. To quantitatively describe the damage effect due to the dehydration, the chemical damage parameter d_h is introduced as a function of the hydration degree . The chemical damage parameter d_c due to both the dehydration and desalination effects given by

$$d_c = 1-(1-d_s)(1-d_h) \tag{1}$$

It is remarked that with consideration of degradation of the elastic modulus of concrete skeleton due to the dehydration and desalination caused by increasing high temperature, the growing thermal damage due to chemical deterioration of concrete is taken into account in the proposed model.

In combination of chemical damage parameter with mechanical damage parameter d_m defined in the Mazars model, the total damage parameter d, which synthesizes both chemically and mechanically induced damage effects can be defined as below

$$d = 1-(1-d_m)(1-d_c) = 1-(1-d_m)(1-d_s)(1-d_h) \tag{2}$$

with $d \in [0,1]$ and $\dot{d} \geq 0$. Then the net stress tensor $\boldsymbol{\sigma}''$ linked to the effective stress tensor $\overline{\boldsymbol{\sigma}}''$ taking into account the damage effect can be written as

$$\boldsymbol{\sigma}'' = (1-d)\overline{\boldsymbol{\sigma}}'' \tag{3}$$

In the proposed model, the generalized Willam-Warnke yield criterion depending on the three stress invariants is employed to describe the coupled chemo-elastoplastic behavior occurring in concrete, with consideration of mechanically induced strain softening/hardening, suction hardening and chemo- plastic softening due to the dehydration and desalination.

It is noted that the cohesion $c(\bar{}_p, p_c, \ , c_p)$ in the generalized Willam-Warnke yield criterion depends on the equivalent plastic strain $\bar{}_p$, the capillary pressure p_c and $, c_p$ of the dissolved matrix component. With the piecewise linear hardening/ softening assumption, the cohesion parameter $c(\bar{}_p, p_c, \ , c_p)$ of concrete can be expressed in the form

$$c(\bar{}_p, p_c, \ , c_p) = c_0 + h_p \bar{}_p + h_s p_c + h\ (1- \ ) + h_c c_p \tag{4}$$

where c_0 is the initial cohesion pressure, $h_p, h_s, h\ , h_c$ are material hardening /softening parameters.

Thus the cohesion will decrease due to both the dehydration and the desalination developed with increasing temperature, the growing thermal de-cohesion due to chemical deterioration of concrete can be taken into account in the proposed model.

The total strain rate vector $\dot{\boldsymbol{\varepsilon}}$ is additively decomposed as

$$\dot{\boldsymbol{\varepsilon}} = \dot{\boldsymbol{\varepsilon}}^{m,e} + \dot{\boldsymbol{\varepsilon}}^{T,e} + \dot{\boldsymbol{\varepsilon}}^{s,e} + \dot{\boldsymbol{\varepsilon}}^{,e} + \dot{\boldsymbol{\varepsilon}}^{c,e} + \dot{\boldsymbol{\varepsilon}}^{m,p} \tag{5}$$

where $\dot{\boldsymbol{\varepsilon}}^{m,e}, \dot{\boldsymbol{\varepsilon}}^{m,p}, \dot{\boldsymbol{\varepsilon}}^{T,e}, \dot{\boldsymbol{\varepsilon}}^{s,e}, \dot{\boldsymbol{\varepsilon}}^{,e}, \dot{\boldsymbol{\varepsilon}}^{c,e}$ are denoted respectively as elastic and plastic portions of the strain rate $\dot{\boldsymbol{\varepsilon}}$ due to mechanical effect, strain rates due to thermal expansion, capillary pressure, the hydration and the desalination effects.

The net stress vector $\boldsymbol{\sigma}''$ linked to $\overline{\boldsymbol{\sigma}}''$ and further $\boldsymbol{\varepsilon}^{m,e}$ can be expressed as

$$\boldsymbol{\sigma}'' = (1-d)\overline{\boldsymbol{\sigma}}'' = (1-d)\mathbf{D}\boldsymbol{\varepsilon}^{m,e} \tag{6}$$

where $\mathbf{D}$ is elastic modulus matrix. The backward-Euler return algorithm for the model results in

$$\dot{\overline{\boldsymbol{\sigma}}}'' = \overline{\mathbf{D}}^{m}_{edpc}\dot{\boldsymbol{\varepsilon}} + \overline{\mathbf{D}}^{T}_{edpc}\dot{T} + \overline{\mathbf{D}}^{s}_{edpc}\dot{p}_c + \overline{\mathbf{D}}^{c}_{edpc}\dot{c}_p \tag{7}$$

With Eq. (6) the rate net stress vector may then be written as

$$\begin{aligned}\dot{\boldsymbol{\sigma}}'' &= (1-d)\dot{\overline{\boldsymbol{\sigma}}}'' - \dot{d}\overline{\boldsymbol{\sigma}}'' \\ &= \mathbf{D}^{m}_{edpc}\dot{\boldsymbol{\varepsilon}} + \mathbf{D}^{T}_{edpc}\dot{T} + \mathbf{D}^{s}_{edpc}\dot{p}_c + \mathbf{D}^{c}_{edpc}\dot{c}_p\end{aligned} \tag{8}$$

The consistent chemo-thermo-elastoplastic tangent modulus matrices are given in the closed forms. Based on the work of Ju [3] and Li et al. [4] a three-step operator split algorithm for the integration of the rate constitutive equations of the chemo-elastoplastic-damage model is developed. The algorithm is composed of elastic predictor, plastic return mapping corrector and damage corrector.

3. NUMERICAL EXAMPLE AND RESULTS

The example presented by Gawin et al. [1] is performed to illustrate the capability of the proposed constitutive model in reproducing coupled chemo-thermo-hygro-mechanical behavior as well as in modeling deteriorations in both strength and stiffness in concretes subjected to fire and thermal radiation. The example deals with a square concrete column of cross section $40\text{cm}\times 40\text{cm}$ exposed to fire. The time step size taken from its initial value $\Delta t = 1\,\text{s}$ varies up to $\Delta t_{\max} = 20\,\text{s}$ in the heating period. By symmetry, only one quarter with sizes $20\text{cm}\times 20\text{cm}$ is taken and discretized with a 15×15 eight-node serendipity element mesh. The column is heated at the surface of the column according to the curve $T = 298 + 0.5\cdot t\,[\text{K}]$ up to $T_{\max} = 798\,\text{K}$ at $t_{\max} = 1000\,\text{s}$. Fig. 1 shows the results obtained for the distributions of temperature, vapor pressure, equivalent plastic strain and total damage parameter due to both dehydration and desalination effects at $t = 16$ min. It is observed that moisture content decreases rapidly with increasing temperature in the zone close to the heated surface, where rapid evaporation develops and causes an increase of vapour pressure up to 0.7 MPa at $t = 16$ min. It is noted that chemical damage parameter due to coupled dehydration and desalination takes a significant portion up to 16% of total damage parameter at the corner at time $t = 16$ min and therefore the effect of chemical damage considerably deteriorates the material failure of the zone close to the heated surface as shown in Fig. 1d. High values of both the vapor pressure and total damage parameter at the corner zone close to the heated surface constitute a potential source to trigger the explosive spalling.

4. CONCLUSIONS

The main features of the proposed constitutive model can be summarized as follows:
(1) The developed coupled model is capable of simulating occurrence and evolution of the micro-

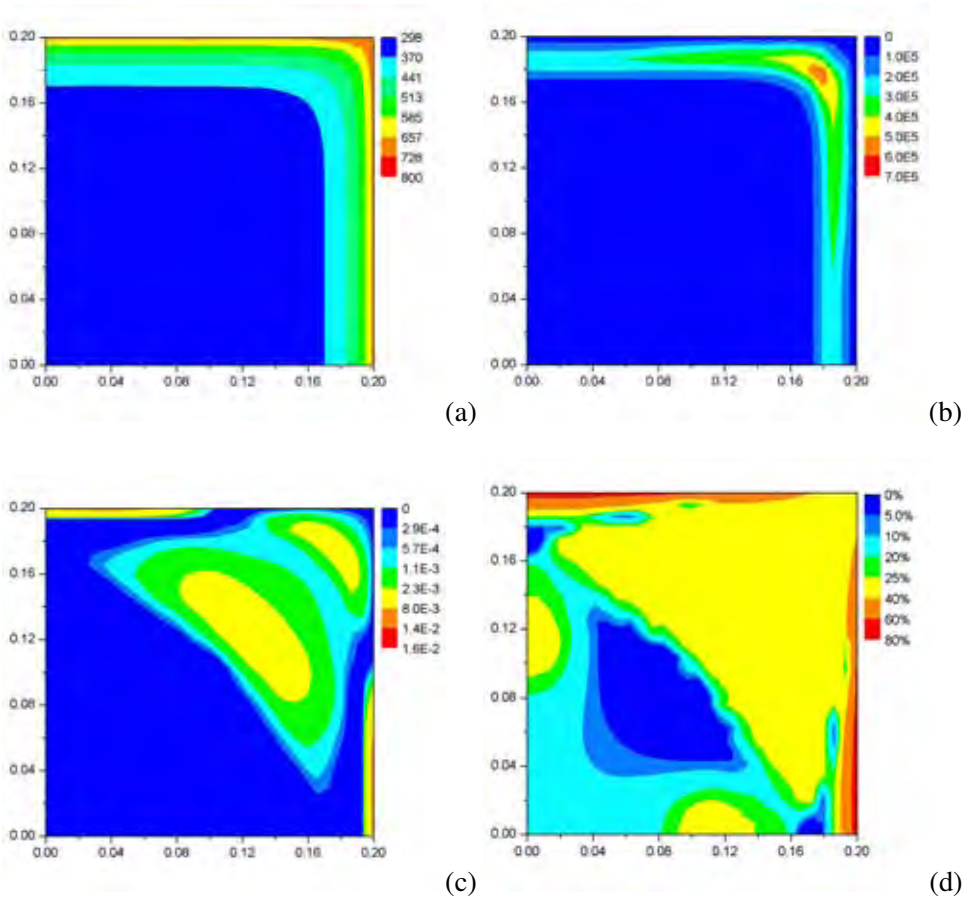

Figure 1. The distributions of variables in concrete column at $t = 16$ min
(a) Temperature, (b) Vapor pressure, (c) Equivalent plastic strain, (d) Total damage

crack or micro-void growth measured by damage parameters as well as accompanied plastic yielding observed in concretes in terms of effective plastic strain.

(2) The thermally-induced chemical effects of both desalination and dehydration processes on the material failure such as the deterioration of the Young's modulus and the loss of the material strength are taken into account.

(3) A three-step operator split algorithm for the integration of rate constitutive equations and consistent tangent modulus matrices for coupled nonlinear chemo-thermo-hygro-mechanical constitutive modeling are formulated to ensure the second order convergence rate of the global iterative solution procedure.

REFERENCES

[1] D. Gawin, F. Pesavento, and B.A. Schrefler, Modelling of hygro-thermal behaviour of concrete at high temperature with thermo-chemical and mechanical material degradation, *Computer Methods Appl. Mech. Engng*., 192, 1731–1771, 2003.

[2] X.K. Li, R.T. Li and B.A. Schrefler, A coupled chemo-thermo-hygro-mechanical model of concrete at high temperature and failure analysis, *Int. J. Numer. and Anal. Methods in Geomechanics*, 30, 635–681, 2006.

[3] J.W. Ju, On energy-based coupled elastoplastic damage theories: constitutive modeling and computational aspects, *International Journal of Solids and Structures*, 25, 803–833, 1989.

[4] X.K. Li, P.D. Duxbury and P. Lyons, Coupled creep-elastoplastic-damage analysis for isotropic and anisotropic nonlinear materials, *Int. J. of Solids and Structures*, 31:1181–1206, 1994.

First International Conference on Computational Methods for Thermal Problems
ThermaComp2009, September 8-10, 2009, Naples, Italy
N.Massarotti and P.Nithiarasu (Eds.)

FETCH - A COMPUTATIONAL FRAMEWORK FOR COMPLEX MULTI-PHYSICS MODELLING

Jefferson L.M.A. Gomes, Christopher C. Pain, Matthew D. Eaton and Tony Goddard
Imperial College London, Department of Earth Science and Engineering, Applied Modelling and Computation Group (AMCG), SW7 2AZ
j.gomes, c.pain, m.eaton, a.goddard@imperial.ac.uk

ABSTRACT

The FETCH (Finite Element Transient Criticality) model was created at Imperial College in the 1990s through support from the United Kingdom's regulator, the Health and Safety Executive. It was intended to model complex systems not fully amenable to experiment, through the detailed treatment of physical, spatial and temporal processes. The purpose of this paper is to summarise the coupled multi-fluids and neutron radiation transport models embedded in the FETCH code and show a very computationally demanding criticality problem involving granular materials.

Key Words: *Computational Multi-Fluid Dynamics (CMFD), Neutron Radiation Transport, Coupled Models, Criticality Studies, MoX Powder, Phase Change, Granular Flows.*

1. INTRODUCTION

The modelling approach developed by the authors applies detailed spatial and temporal modelling so that the criticality dynamics evolve naturally. This is in contrast to point kinetics models [1] which, although often having adequate accuracy, require correlation with existing data when the material evolves within the transient, such as in fissile liquid transients [2] and nuclear fluidised beds [3]. Others have used space-dependent kinetics to model transients in fissile liquids as reported by [4].

The FETCH model is used here to improve the understanding of a postulated criticality scenario involving the mixing of MOX powders with two different enrichments and zinc stearate (ZnSt) lubricant material (the ZnSt is used as a lubricant to help homogenising the MOX powders and its moderator properties introduce a ramp reactivity into the system) during fuel processing.

2. THE FETCH MODEL

The FETCH spatially and temporally coupled modelling framework uses three dimensional finite elements to describe the many interacting quantities of interest together with a numerically robust adaptive time stepping procedure [3, 5]. FETCH comprises a neutron kinetics module (EVENT) [6] and a computational multi-fluid dynamics (CMFD) with structural response module (FLUIDITY) [7, 3].

The neutron kinetics and the CMFD modules are linked by an interface module that interpolates the nuclear data cross-section based upon temperature, density and void fraction. Additionally, the FLUIDITY module provides the delayed neutron precursor concentration to the EVENT module. Conversely, the EVENT module provides heat sources, fission distributions and delayed neutron sources to the FLUIDITY module. A schematic of the information flow between the EVENT, FLUIDITY and the interface module is shown in Fig. 1. At each time step the interface module organises the feedback from FLUIDITY of spatial temperature, density and delayed neutron precursor distributions into the EVENT neutronics module. It also updates the spatial distribution of multi-group neutron cross-sections for EVENT from a pre-calculated nuclear cross-section library which was generated using the WIMS9

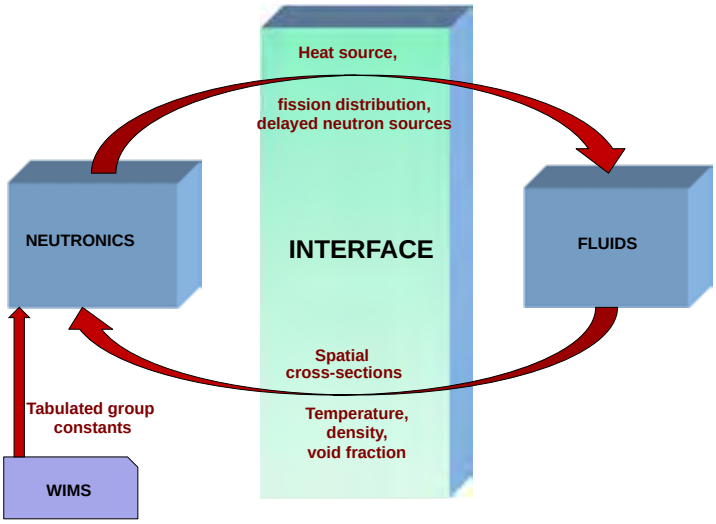

FIGURE 1. Schematic representation of the flow of information in the FETCH model.

code. For a given element of the FE mesh, a new set of nuclear cross-section are obtained by interpolating in temperature and mixing ratio (or number density) of all materials. This feature allows various fissile and non-fissile material concentrations to be tracked through the solution domain and the appropriate spatially varying nuclear cross-sections to be calculated from these concentrations. The neutronics module subsequently generates for the fluids module the spatial distribution of fission-power and delayed neutron generation rates.

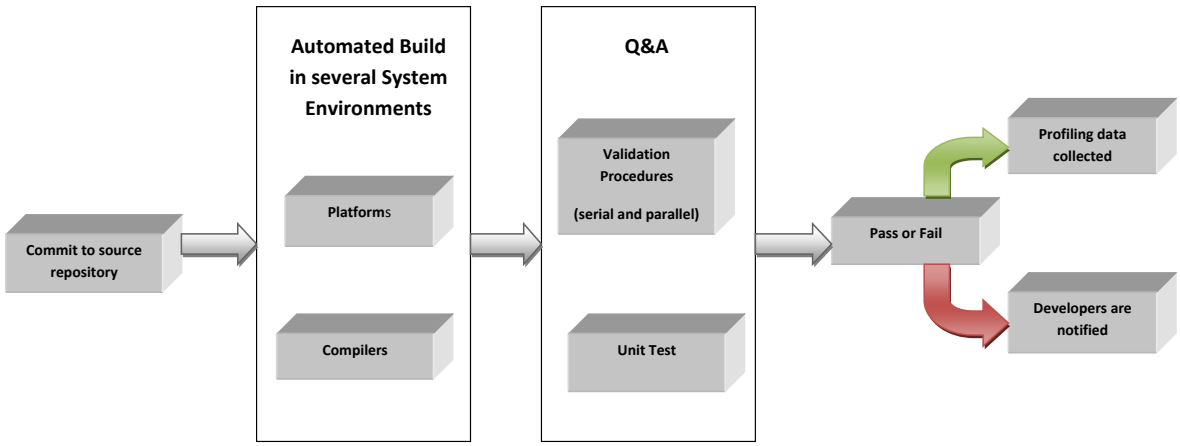

FIGURE 2. Automated and continuous QA system for CFD and RT codes embedded in the FETCH model.

2.1. **FLUIDITY: The Multiphase Thermo-Fluids Module.** The compressible thermo-fluids-structural response module, FLUIDITY, is able to solve both single and multiphase flow problems with options for a porous medium, fluidised granular material and bubbly solutions. The model also solves structural mechanics equations and therefore can resolve, in a fully coupled manner, the cracking of surrounding materials, granulation, phase changes and the ensuing movement of cracked material. The multiphase fluid flow is modelled throught the two-fluid granular temperature approach [7] in which all phases are modelled as a fully interpenetrating continua and corresponding mass, momentum, thermal energy and fluctuation energy balance equations are solved with interaction terms representing the coupling between the phases. Each phase is described by separated conservation equations with interaction terms representing the coupling between the phases. Closure laws are used to fulfill the remaining requirements for the balance as described by [8] (see [7] for a full description of the closure laws used by the CFMD model).

The momentum equations are discretized with an implicit non-linear Petrov-Galerkin method [8] and the other conservation equations are solved using an implicit high resolution method [5]. The high-resolution method is globally second order accurate in space and time. Locally the high-resolution scheme switches smoothly between first-order accurate schemes in space (upwind discretisation) and time (backward-Euler) and higher-order accurate schemes. The higher-order accurate fluxes for the spatial discretisation of the high resolution method are obtained from a FE interpolation of the solution variables (which are second-order accurate). The time-discretisation is based upon the θ time-stepping method where the value of θ is spatially varying. The value of θ varies locally based upon mathematically rigorous TVD (Total Variation Diminishing) numerical stability criteria. The TVD criteria ensure that the scheme optimizes numerical accuracy while imposing the constraint of minimizing any spurious numerical artifacts such as oscillations in the solution. Additionally, hexahedral elements are employed which have a bi-linear variation of velocity and a piecewise variation of pressure, density and all other advected quantities. This element has a single pressure associated with each element and a velocity node (collocation point) at the corners of the element with C^0 variation of velocity between elements. Within each time step the equations are iterated upon using a projection-based pressure determination method until all equations balance simultaneously [8]. As a result the non-linear continuity equations are strictly satisfied, ensuring mass conservation.

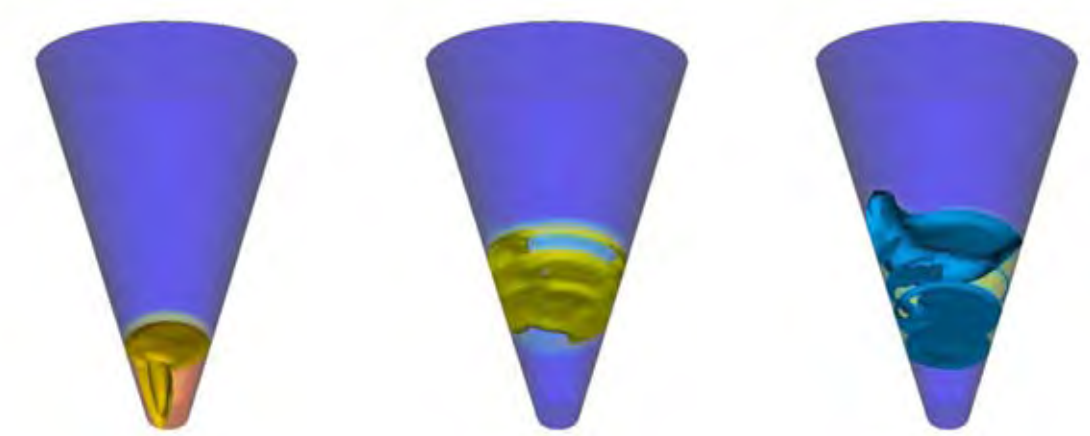

(a) (b) (c)

FIGURE 3. 3D numerical simulations: isosurfaces of normalised concentration of (a) MOX (33%), (b) MOX (18%) and (c) ZnSt at 0.0738 s of the simulation with the screw mixer.

2.2. **EVENT: The Neutron Kinetics Module.** EVEn parity Neutron Transport – EVENT is a stand-alone neutron transport code capable of performing time-dependent and time-independent eigenvalue and fixed source calculations with delayed neutrons but excludes the effects of burn-up on nuclide concentrations. Rather than solving the first-order form of the linear Boltzmann transport equation for neutrons EVENT solves a second-order form (see [6] for further details). This second-order form of the transport equation is based upon separating the neutron angular flux into its even and odd parity components that leads to a second-order rather than first order equation. The formulation embodied in the EVENT module can also be interpreted as a Galerkin weighting of the original even-parity within a weak formulation. It is an extremely robust numerical formulation and leads to symmetric positive definite global finite element matrices which are ideal for solution via iterative procedures such as pre-conditioned conjugate gradient schemes. In the EVENT module, the neutron transport equation is solved using FE in space, spherical harmonics (PN) in angle, multi-group in energy and implicit two level time discretisation methods.

3. THE CONTINUOUS AND AUTOMATED QUALITY ASSURANCE PROCEDURE

Due to the complexity associated with the coupled CMFD and RT codes, the AMCG has developed an automated system for source code control and quality assurance. A source code control system (SCCS) aims to take copies of files at specified locations, as so as it is possible to keep track of the history of code changing and to store earlier versions of files. In the AMCG, developers are able to: (a)

retrieve a copy of the source code, (b) make changes locally and (c) commit them back to the source repository. The SCCS merges changes in the case where another developer commits a change between a retrieving and a commit. When a developer commits to the source code repository, the code is changed and the prior verification and validation procedures are no longer valid. Thus, the SCCS notifies the software development continuous integration tool (SDCIT) that the source code has changed. The SDCIT compiles the source code across a number of system platforms and compilers and engages into a number of verification and validation procedures. If the modifications introduced by the developers fail in any of the V&V test-cases, a warning message is sent to all developers. A summary of the code control flow is shown in Fig. 2.

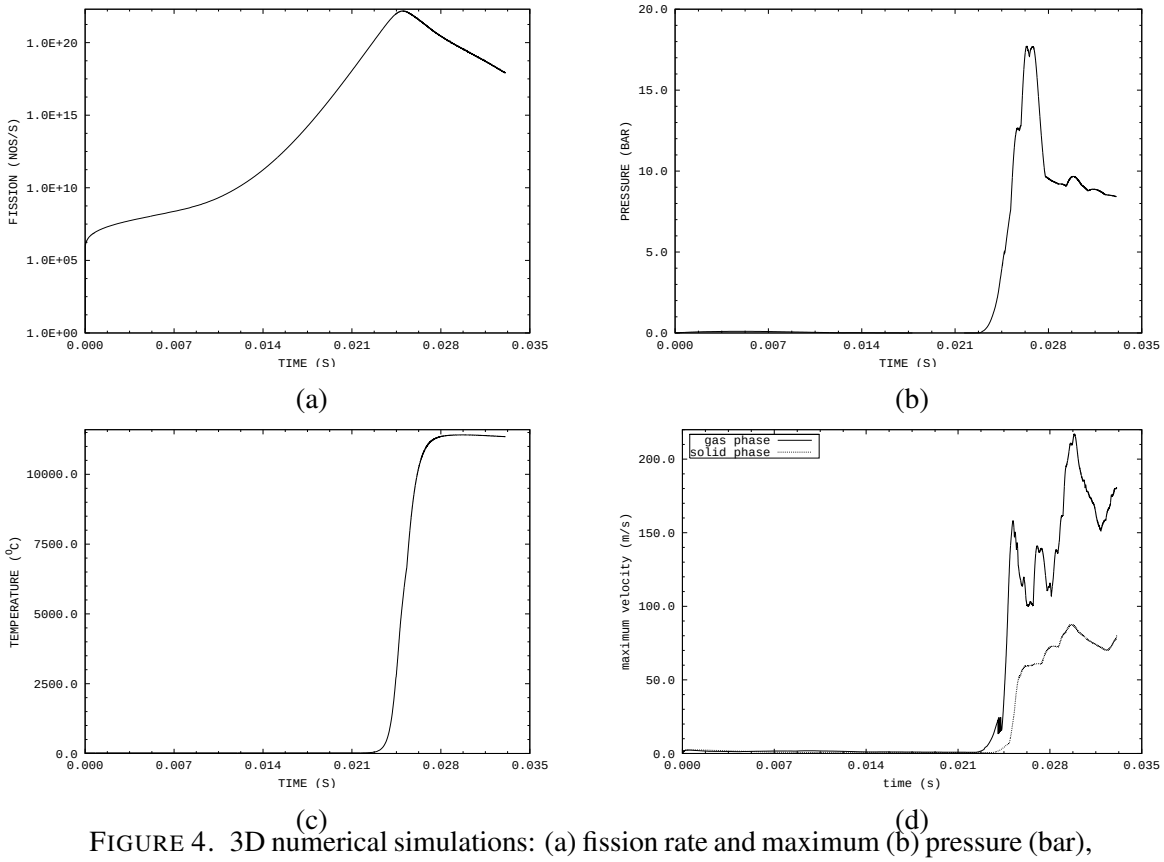

(a) (b) (c) (d)

FIGURE 4. 3D numerical simulations: (a) fission rate and maximum (b) pressure (bar), (c) particle temperature (^{o}C), (d) velocities (m/s).

4. NUMERICAL SIMULATIONS - MODELLING CRITICALITY IN A MIXED POWDER SYSTEM

This problem was addressed to understand the physics of criticality in mixed powder system, where the fissile quantities were raised significantly above those to be used in practise. The geometry of the powder mixing system can be described as a conical frustum shape, the diameter of the bottom and top being 24.14cm and 120.67cm, respectively. The total height of the vessel is 211.43cm. The walls are made of stainless steel, surrounded by polyethylene having a thickness of 10cm. MOX (UO_2 and PuO_2) powders with 18% and 33% enrichment Pu-239 and zinc stearate (lubricant) are allocated within the vessel in alternate stratified layers. A mixing impeller device (a set of 4 orthogonal paddles) is placed into the central region of the system.

For the description of temperature-dependent processes, transitions of components between the phases, coupled with an exchange of thermal energy, have to be taken into account in addition to the flow of the individual phases. Therefore, the formulation of a mathematical/numerical model requires an idealization of the physical processes in such a way that the natural systems are simplified but, at the same time, the characteristic properties of the processes in a system is maintained. In this work, MOX

ZnSt and air are mixed in thermodynamical equilibrium and the PVT behavior of these components are taken into account in the multicomponent and multiphase flow model used here. The multicomponent balance in the granular phase and its relationship with the equations of state and thermal properties used for each of the particles are fully described in [10].

The simulation was impulsively initialised, with the gas and powders at rest and the mixer instantaneously accelerated to its maximum velocity (0.5 rps). Isosurfaces representing the normalised MOX and ZnSt concentrations at 0.07 seconds into the transients are shown in Fig. 3. Temperature and pressure fluctuations during the simulation reached 10000^oC and 18 bar (Fig. 4), respectively, leading to a partial melting and vaporisation of the powder systems (see [9, 10]) indicating an extreme sensitivity of the ramp reactivity introduced by the mixing of the powder layers.

5. CONCLUSIONS

In this work, the coupled CMFD and neutron radiation models embedded in the FETCH code is introduced to model criticality problems in 3D mixing powder systems. A multicomponent submodel is introduced to deal with the different powders and a novel screw-mixer parameterization was developed to enable the consequences of forced-mixing of the powders to be studied. Additionally, the continuous and automated V&V system developed for the code suites is summarised.

Although the stratified ZnSt and MOX layered system is only initialized with a small reactivity insertion, it has a very rapid positive criticality feedback due to the initial small mixing between the powder layers. The system is under-moderated and quickly transitions to near optimal moderation with very large reactivity insertions. After the powders are fully mixed the reactivity decreases again. This behaviour accounts for the large increases in temperature of the system. Such temperatures are large enough to melt and vaporise the MOX and ZnSt powders.

6. ACKNOWLEDGEMENTS

Dr. Jefferson Gomes has been supported in part by the UK EPSRC under the 'Keep the Nuclear Option Open' (KNOO) programme. The authors wish to acknowledge the support of JAEA (Dr Yuishi Yamane) in the conduct of the research into mixing of layered fissile powders.

REFERENCES

[1] D.L Hetrick D.L. *Dynamics of Nuclear reactors*, American Nuclear Society, Illinois.

[2] C.C. Pain, C.R.E de Oliveira, A.J.H. Goddard and A.P. Umpleby, Transient Criticality in Fissile Solutions - Compressibility Effects, *Nuclear Science and Engineering*, 138, 78-95, 2001.

[3] C.C. Pain, J.L.M.A. Gomes, M.D. Eaton, C.R.E. de Oliveira, A.J.H. Goddard and A.P. Umpleby, A Model of Heat Transfer Dynamics of Coupled Multiphase-Flow and Neutron-Radiation: Application to a Nuclear Fluidized Bed Reactor, *International Journal of Numerical Methods for Heat and Fluid Flow*, 15, 765-807, 2005.

[4] R.H. Kimpland and D.E. Korneich, A Two-Dimensional Multi-Region Computer Model for Predicting Nuclear Excursions in Aqueous Homogeneous Assemblies, *Nuclear Science and Engineering*, 122, 204-211, 1996.

[5] J.L.M.A. Gomes, C.C. Pain, M.D. Piggott, C. Wilson, G.J. Gorman, Numerical Transport Methods for Multi-Phase Fluid Flow and Radiation Modelling, *International Journal of Numerical Methods in Fluids* (2009). Submitted.

[6] C.R.E de Oliveira, An arbitrary geometry finite element method for multi-group neutron transport equation, *Progress in Nuclear Energy*, 18, 227-238, 1996.

[7] J.L.M.A. Gomes, C.C. Pain, C.R.E. Oliveira, A.J.H. Goddard and F.B.S. Oliveira, Numerical Investigation of Heat Transfer Mechanisms in Gas-Solid Fluidized Beds using the TFGTM, *Heat Transfer Engineering*, 28, 576-597, 2007.

[8] C.C. Pain, S. Mansoorzadeh, C.R.E de Oliveira and A.J.H. Goddard, Numerical modelling of gas-solid fluidized beds using the two-fluid approach, *International Journal of Numerical Methods in Fluids*, 36, 91-124, 2001.

[9] J.L.M.A., C.C. Pain, M.D. Eaton, A.J.H. Goddard, M.D. Piggott, K. Ziver, C.R.E. Oliveira and Y. Yamane, Investigation of Nuclear Criticality within a Powder using Coupled Neutronics and Thermofluids, *Annals of Nuclear Energy*, 35, 2073-2098, 2008.

[10] J.L.M.A. Gomes, C.C. Pain, M.D. Eaton, , A.J.H. Goddard, M.D. Piggott, K. Ziver and Y. Yamane, Coupled Neutronics-Fluids Modelling of Criticality within a MOX Powder System – Part II: Transient Analysis, *Nuclear Science and Engineering* (2009) Awaiting Publication.

[11] C.K.K. Lun, S.B. Savage, D.J. Jefferey and N. Chepurniy, Kinetic theories for granular flow: inelastic particles in couette flow and slightly inelastic particles in a general flowfield, *Journal of Fluid Mechanics*, 140, 223-256, 1984.

First International Conference on Computational Methods for Thermal Problems
ThermaComp2009, September 8-10, 2009, Napoli, Italy
N.Massarotti and P.Nithiarasu (Eds.)

A COUPLED APPROACH FOR AEROTHERMAL MECHANICAL MODELLING FOR TURBOMACHINERY

Dario Amirante
University of Surrey, GU2 7XH, Guildford, UK, d.amirante@surrey.ac.uk

Nicholas J. Hills
University of Surrey, GU2 7XH, Guildford, UK, n.hills@surrey.ac.uk

Christopher Barnes
Rolls-Royce plc, DE24 8BJ, Derby, UK, christopher.barnes@rolls-royce.com

ABSTRACT

A coupling methodology has been developed for coupled fluid/solid modelling accounting for the geometry deflections predicted by the structural analysis. The method integrates a CFD model within a finite element system for thermal and structural analysis. The thermal coupling between the CFD and FE models assure continuity of temperature and heat flux. Using a spring analogy method, the mesh for the fluid equations is dynamically modified to account for the boundary deflections predicted by the finite element solver. As an example of the methodology, the cavity flow in a turbine stator well contained within a low-pressure turbine is investigated. The resulting coupled model is run through a realistic flight cycle, during which the relative movements between stator and rotor influence the labyrinth seal leakage and the ingestion of hot gas from the main annulus. The effect of the change in the geometry on the flow dynamics is discussed with special attention given to its impact on the predicted metal temperature.

Key Words: *Stator Well, Thermo-Mechanical Coupling, Spring Analogy.*

1. INTRODUCTION

The optimisation of heat transfer between fluid and metal plays a crucial role in gas turbine design. In order to manage the metal temperatures in the gas turbine, coolant flow is extracted from the compressor and used for cooling and sealing within the turbine. However, this coolant flow corresponds to a loss in the thermodynamic cycle, and needs to be minimised, while keeping the component temperatures within acceptable limits.

Traditionally, in industry fluid and solid simulations are conducted separately. The prediction of metal stresses and temperatures, generally based on finite element analysis, requires the definition of a thermal model whose reliability is largely dependent on the validity of the boundary conditions prescribed on the solid surfaces. These boundary conditions are obtained from empirical correlations matched to engine test data. Modern commercial considerations require more confidence at an earlier stage of a design process, and the development of improved analysis methods is a prerequisite to achieve this goal. In this context, recent studies have demonstrated the benefits of employing coupling techniques, whereby the boundary conditions are obtained from CFD models through an exchange of data between codes for different physics. Due to their relevance to this paper, we mention the work of Sun et al. [1], in which two distinct codes are iteratively coupled under the assumption that the unsteadiness of the flow is negligible on the time scales relative to the metal heat conduction. In this way, steady CFD calculations can be employed to alleviate the computational costs, which otherwise would be prohibitive for a coupled calculation over an entire flight cycle.

This paper represents an extension of the above methodology. The geometrical deformations predicted by the structural analysis are included in the coupling process, allowing the capture of phenomena where the feedback between metal movement and flow is essential. This is important as the geometrical deformation and the air temperature can strongly influence the developing flow dynamics.

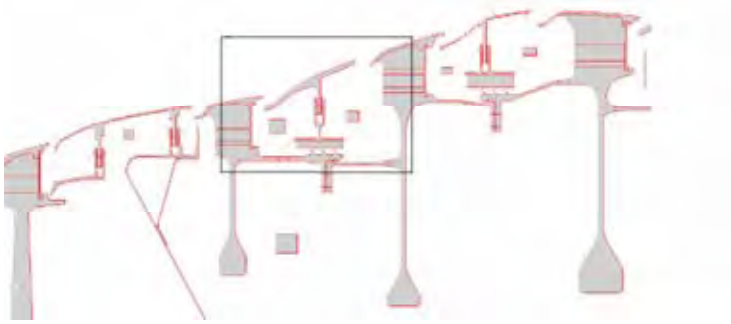

FIGURE 1. Geometry of the turbine. The square encloses the stator well under consideration.

As an example study, the method has been applied to predict the flow in a turbine stator well cavity. The flow in a turbine stator well offers a typical example of a situation where the mechanical effects are important: here the thermo-mechanical distortions govern the labyrinth clearance. This clearance directly affects the amount of flow ingested through the rim seal, which in turns determines the resulting heat flux.

2. COUPLING METHODOLOGY

The work presented is based on the coupling between two proprietary codes, SC03 and HYDRA, developed by Rolls-Royce. SC03 is a finite element code performing transient thermal and mechanical analysis. A description of the SC03 code and its use in engine thermal analysis is given by Armstrong et al. [2] and by Dixon et al. [3]. HYDRA is an unstructured finite volume solver of the compressible Reynolds Averaged Navier-Stokes equations [4].

Within SC03, the user defines a "flight cycle'', i.e. the evolution of a set of parameters through the time span to simulate. These include rotational speed, mass flow rates, operating temperatures and pressures. At each time point during the cycle, the coupling method employs two nested iterative loops. The external one couples the thermal and structural analysis. These are performed in sequence by SC03 until both geometry and temperature are stabilised. The internal loop is called during the thermal analysis: the system invokes the CFD code HYDRA, passing to it the current estimate of boundary temperatures and boundary deflections. HYDRA adapts an initial mesh to conform to the boundary deflections read, and runs a steady state case with the prescribed wall temperatures. The resulting heat fluxes are returned to SC03, which in turns performs a new thermal iteration. When the difference in metal temperature between thermal iterations is below a specified tolerance, the external loop resumes. Typically two external iterations are required for convergence at a time step, after which the analysis moves to the next time step in the cycle.

To conform the mesh to the dynamic geometry, the method adopted is the torsional spring analogy algorithm [5]. A pseudo-structural problem is defined assigning elastic properties to each element of the mesh. Enforcing the static equilibrium on the internal nodes of the mesh results in a nonlinear system of equations in which the unknowns are the nodal displacements. The system is solved using Newton-Raphson iterations, in conjunction with a Preconditioned Conjugate Gradient method for the solution of the linearised equation.

The coupling communications are controlled by a plug-in of the SC03 program. It is within SC03 that the user specifies one or more coupled walls, outlining a fluid domain, which may cover part or the whole of the finite element model. At the moment the interactive use of CFD would be computationally too expensive to be used for all the boundaries of an engine. The method is therefore restricted to the most critical components.

3. EXAMPLE APPLICATION CASE STUDY

The methodology has been applied to a turbine stator well within a low pressure turbine. The geometry of the turbine under investigation is shown in fig.1. The area outlined encloses the stator well to couple. An axisymmetric CFD model of the turbine stator well has been used to limit computational time. This model has been extended into the annulus region with inlet/outlet

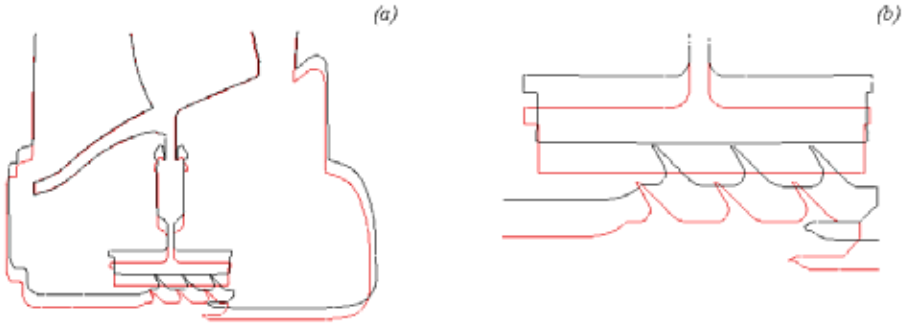

FIGURE 2. Deformation of the fluid domain. Black lines identify the deflected shape. (a): Global view. (b): Close-up view of the labyrinth.

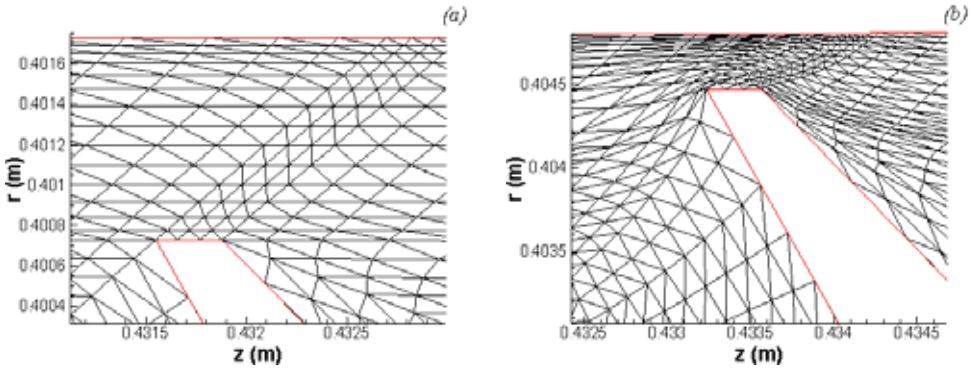

FIGURE 3. Mesh adaptation performed by spring analogy. (a): Original mesh. (b): Modified mesh on the deformed geometry.

boundaries downstream/upstream of the relevant blades. Note that in the axisymmetric finite element model, the blades over the disc are not directly modelled. Their effect on the disk is included in the boundary conditions imposed on the outer disk surface.

The model has been run through a cycle consisting of two distinct regimes, during which the engine operates at low power and high power conditions, respectively. Figure 2-a shows the deformation of the fluid domain caused by the metal deflections predicted during the high power regime. Both cavity and disc are subjected to a radial shift combined with a smaller axial excursion of the cavity. In this movement, the mostly strongly affected region is the labyrinth, with the gap narrowing considerably. Figure 3 shows a close-up view of the labyrinth, with the initial mesh and that obtained by spring analogy on the deformed geometry

Figure 4 highlights the effect of the change in the geometry on the flow. More precisely, figure 4-a refers to a pure “thermal coupling” process, in which the solution is obtained enforcing the continuity of the heat flux on the cold geometry (no movement). Streamlines projected onto the meridional plane are superposed on the contour of the swirl ratio, defined as the ratio between the local angular velocity and the angular velocity of the rotor. For clarity, the positive azimuthal direction comes out of the plane. Note the existence of two large regions of recirculating flow, associated with the ingestion of hot gas from the main annulus. Figure 4-b refers to thermo-mechanical solution, on the deformed geometry. As the labyrinth narrows, the mass flow through it reduces due to the higher losses between the teeth. In the absence of cooling, the mass flow ingested is also reduced to fulfil mass conservation. This ultimately leads to a much smaller level of swirl (in magnitude) within the cavity. The ingested flow starts blowing in the positive azimuthal direction and the mixing plane associated with it drives the fluid below the disc to recirculate counter-clockwise, that is in the opposite direction than that observed in the thermal coupling. The pumping effect associated with the cavity rotation plays a

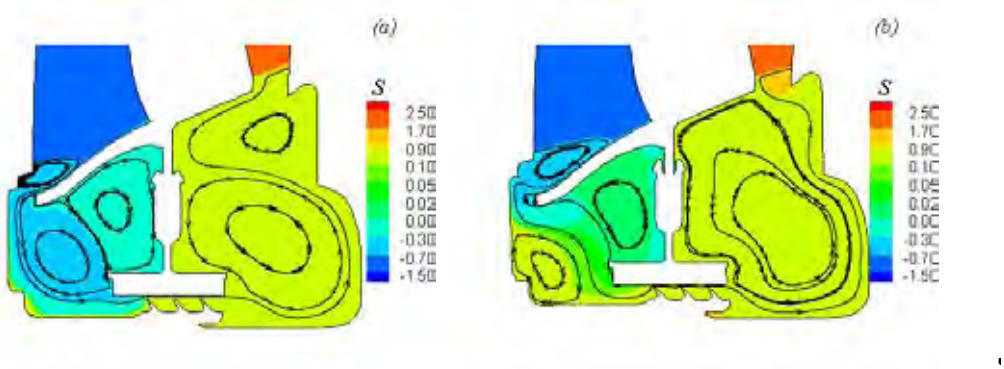

FIGURE 4. Coupled CFD solutions. (a): Thermal coupling. (b): Thermo-mechanical coupling.

similar role at the bottom left corner of the cavity, where the boundary layer of the rotating cavity drives fluid to recirculate clockwise.

4. CONCLUSIONS

A coupling methodology has been developed for coupled fluid/solid modelling accounting for the boundary deflections predicted by the structural analysis. The capability of the method has been demonstrated for a stator well subjected to severe deformations. Despite the assumption of axisymmetry, the results show the importance of a thermo-mechanical coupling procedure to obtain more accurate aerothermal modelling.

5. ACKNOWLEDGEMENTS

The reported work was performed within the European research project "Main Annulus Gas Path Interactions – MAGPI" (RTD-Project 6th FP, Contract No. 30874). The permission for the publication is gratefully acknowledged. The authors also wish to thank colleagues at Rolls-Royce plc, for the engine model provided and the technical support received.

REFERENCES

[1] Z. Sun, J.W. Chew, N.J. Hills, K. Volkov and C.J. Barnes, Efficient FEA/CFD thermal coupling for engineering applications, *Proceedings of ASME Turbo Expo 2008*, GT2008-50638, 2008.

[2] I. Armstrong and T.M. Edmunds, Fully automatic analysis in the industrial environment, *Proceedings of 2nd International Conference on Quality Assurance and Standards*, NAFEMS, 1989.

[3] J. Dixon, J.A. Verdicchio, D. Benito, A. Karl and K.M. Tham, Recent developments in gas turbine component temperature prediction methods, using computational fluid dynamics and optimization tools, in conjunction with more conventional finite element techniques, *J. Power and Energy*, 218, 2004.

[4] P. Moinier, Algorithm developments for an unstructured viscous flow solver, *PhD Thesis*, Oxford University, 1999.

[5] C. Farhat, C. Degand, B. Koobus and M. Lesoinne, Torsional springs for two-dimensional dynamic unstructured fluid meshes, *Comput. Methods App. Mech. Engrg*, 163, 1999.

First International Conference on Computational Methods for Thermal Problems
ThermaComp2009, September 8-10, 2009, Napoli, Italy
N.Massarotti and P.Nithiarasu (Eds.)

BOUNDARY CONDITION EVALUATION AND STABILITY ISSUES IN SWIRLING FLAME GAS COMBUSTION

Jiří Vondál

Institute of process and environmental engineering, Brno University of Technology, Technická 2, 616 69 Brno, Czech Republic, vondal@upei.fme.vutbr.cz

Jiří Hájek

Institute of process and environmental engineering, Brno University of Technology, Technická 2, 616 69 Brno, Czech Republic, hajek@fme.vutbr.cz

ABSTRACT

Prediction of wall heat fluxes in combustion chambers attracts attention of design engineers in process industry due to its implications for the construction of combustors, boilers and similar devices. Furthermore, reliable experimental evaluation of the heat loads in large-scale experiment is rare. This work deals with stability issues observed in simulation of swirling diffusion gas flames and compares them to the real-world experiment and its instability. Steady and unsteady simulations using Reynolds-averaged Navier-Stokes (RANS) equations are discussed. The experimental facility has a sectional water cooled combustion chamber equipped with a staged-gas 745 kW low-NO_x type burner with axial-type swirl generator.

Key Words: *Combustion, CFD, Burner, Swirl, Heat Flux, Stability.*

1. INTRODUCTION

Swirl-stabilised flames are very popular, especially in the so-called power burners [1] that are widely used in power and process industries. However, it has been recognised for long time that the prediction of swirling diffusion flames using moment turbulence closures is extremely problematic [2, 3], in spite of partial successes [4]. Recent progress achieved using large-eddy simulations coupled with advanced chemistry models [5, 6] is on one hand very promising but on the other hand it is still far from being applicable to industrial problems due to excessive computational requirements, tractable only using supercomputing facilities.

Industry primarily requires predictions of wall heat fluxes (typically for membrane walls or tubes). In spite of that, combustion modelling research almost exclusively focuses on the details of flame core structure and wall heat loads are typically disregarded. The present work thus focuses on validation of computationally manageable Reynolds-Averaged Navier-Stokes (RANS) models by accurately measured local wall heat fluxes. The experiments were performed at a new experimental facility described in [1, 7]. The paper extends previous work reported in [8] which dealt with error analysis of the experimental data and reported several heat flux predictions. The target here is to identify some of the sources of deviation from experimental results.

2. EXPERIMENTAL FACILITY

Combustion chamber of the testing facility was designed for maximum firing capacity of 2 MW and consists of 7 water-cooled sections enabling separate heat flux monitoring. The wall material is steel covered with high-temperature black paint for increased emissivity. Industrial-type low-NO_x, natural gas burner with staged gas supply (8 primary and 8 secondary nozzles) and an axial-type swirl generator were employed for the experiment. The firing rate was adjusted to 745 kW.

3. IDENTIFICATION OF BOUNDARY CONDITIONS

Boundary conditions were an all-important factor in model set-up. Most conditions were easy to evaluate thanks to the measuring instrumentation of the facility – e.g. natural gas flow rate and temperature, air flow rate and temperature, etc. Besides these, some boundary conditions were much harder to evaluate accurately and these were deemed to be responsible for a significant part of the observed deviations from measurements [8]. Wall temperature on the water side was one these hard-to-determine parameters.

Heat transfer through the cooled walls depends on one hand on hot-side properties (radiation contributes by about 90%) and on the other hand it is influenced by heat transfer coefficient and surface temperature on the water-side. Local boiling was possible only in places with low water velocity (considering inlet water temperature was 21°C and outlet about 30°C), but water flow in each section was directed by a helical fin for minimization of such dead zones.

Computational model of a single cooling section has been created to study the heat transfer on the water side in detail, assuming no boiling and a uniform heat flux from the flame side. Contours of calculated water-side surface temperature are shown in Fig. 1. The highest temperatures were however incorrect due to the missing boiling model. Therefore temperatures above the boiling point (124.2 °C at 236.4 kPa) [9] served only to identify locations of local boiling. Real values lay in between the boiling point and the displayed value due to increased heat transfer coefficient caused by boiling [10]. Area weighted average from the calculated values over the heat-exchanging surface was 96 °C. Future work is necessary to adjust this value while taking the boiling into account. Currently all simulations presented in this work used an estimated value of 80 °C as the wall boundary condition.

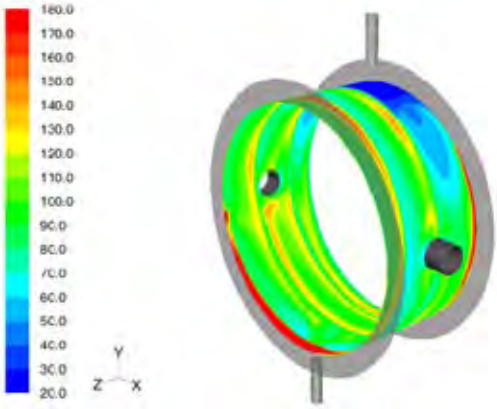

FIGURE 1. Contours of surface temperature [°C]

4. COMPUTATIONAL SET-UP

Modelling of the swirling diffusion flame was performed using several turbulence models and a simple fast chemistry model with one global reaction as implemented in commercial code FLUENT 6.3.26 [11]. Specifically the baseline model included turbulence model SST k-ω, discrete-ordinates radiation model with weighted-sum-of-gray-gases cell-based model for the absorption coefficient, one-step reaction mechanism and pressure-velocity coupling using so-called pressure-staggering option. During the computation, several stability issues were observed that are discussed in the next section. Standard computational procedures were followed, namely start up without radiation and switching to higher-order discretization scheme (QUICK) after the solution almost converged. This was performed firstly for the density and after several iterations also for the velocity. Increasing the order of discretization for velocity caused severe instability in the calculated heat fluxes (see Fig.2) but was crucial for accuracy.

5. STABILITY PHENOMENA

One of the biggest issues of numerical computations is convergence and stability. In the present case of combustion calculation we focus on the stabilization of heat fluxes. Fig. 2 shows convergence history of heat flux for all 7 sections of the combustion chamber. One can see that after application of the QUICK discretization scheme in the momentum equations (at 9000 iterations), the calculation became strongly unstable with the amplitude of heat flux fluctuations up to 6 kW/m^2. This problem prevailed even after modification of relaxation factors and with other higher-order schemes.

The primary reason for the observed instability was found in the physics of the flow. [12] explains that in swirl combustion several types of fluctuations and instabilities, e.g. flame wobble and precessing vortex core are present. Measured instabilities in the heat fluxes (naturally smoothed out by the averaging and damping effect of the steel walls and cooling water) are also displayed in Fig. 3. It is important to note that the RANS modelling approach cannot properly account for these fluctuations but it was not discarded based on the reasoning presented in the Introduction.

Fig. 4 displays instantaneous results from iterations 8900, 13000, 16000 and 19000 as snapshots from the iteration history shown in Fig. 2. The changes in reported heat fluxes are well visible.

A more reliable value (than instantaneous) of the heat fluxes was obtained through simple averaging of the results over certain range of iterations. Rate of fluctuation was taken into account via non-symmetric error bars defined as follows:

$$q' = q - \bar{q} \quad , \quad \text{for } q' > 0: \ \sigma_{up} = \frac{1}{n}\sum_{0}^{n} q' \quad , \quad \text{for } q' < 0: \ \sigma_{down} = \frac{1}{n}\sum_{0}^{n} q' \tag{1}$$

where q is instantaneous heat flux, $\bar{q}$ is the average, q' is fluctuation and σ is mean deviation.

A comparison of measured and average heat fluxes from the histories shown in Fig. 2 (averaged from 9 500 up to 19 000 iterations) is shown in Fig. 5, including non-symmetric error bars defined in

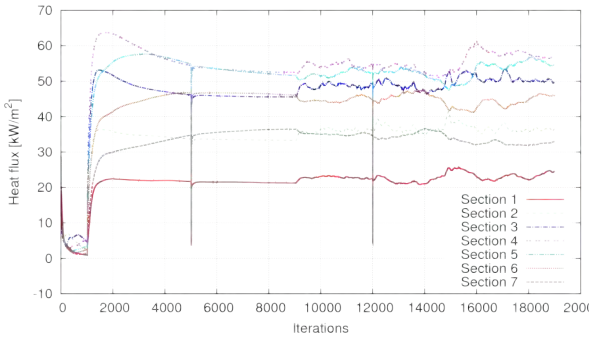

FIGURE 2. Convergence history of heat fluxes

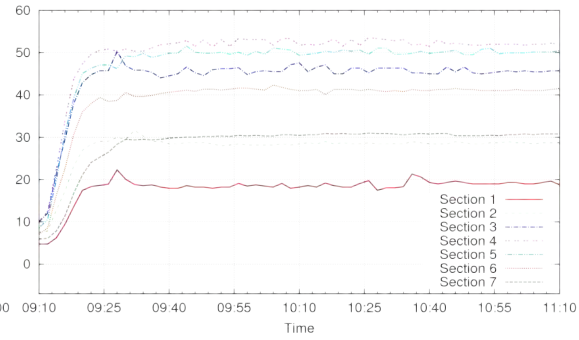

FIGURE 3. Heat flux stabilization in experiment

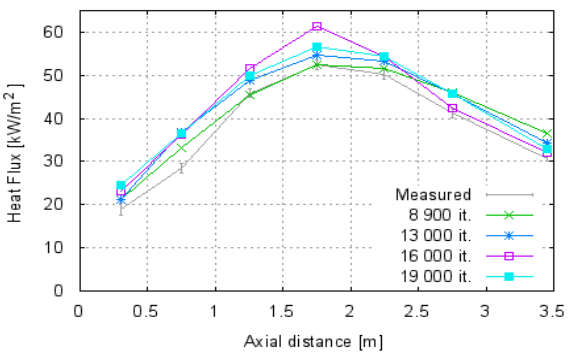

FIGURE 4. Comparison of instantaneous heat fluxes at different iterations (SST *k-ω*)

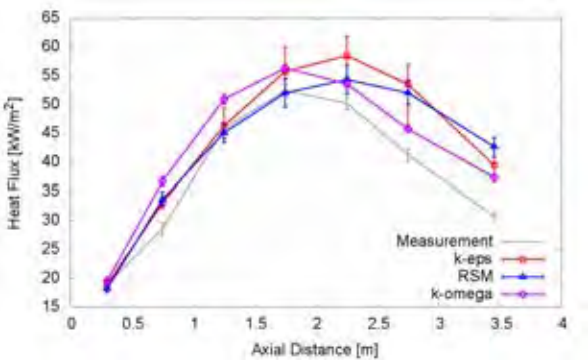

FIGURE 5. Heat fluxes averaged over 9 500 iterations

equation (1). The figure includes also averages obtained using two other RANS models, namely realizable k-ε model and a second-order Reynolds-stress model.

6. CONCLUSION

Measured data from a large-scale industrial-type swirl combustor were used to validate simulations. Thermal boundary condition at the cooled walls was analyzed in detail. The total deviation of the best computed result (SST k-ω) after averaging was 12.6 %, which is considered acceptable thanks to the complexity of the problem. Stability issues in calculated and measured heat transfer were studied and averaging method was described.

REFERENCES

[1] V. Kermes, P. Bělohradský, J. Oral, and P. Stehlík, "Testing of gas and liquid fuel burners for power and process industries," *Energy*, vol. 33, 2008, pp. 1551-1561.

[2] A. Khelil, H. Naji, L. Loukarfi, and G. Mompean, "Prediction of a high swirled natural gas diffusion flame using a PDF model," *Fuel*, vol. 88, 2008, pp. 374-381.

[3] A.E. German, T. Mahmud, "Modelling of non-premixed swirl burner flows using a Reynolds-stress turbulence closure", *Fuel*, vol. 84, 2005, pp. 583-594

[4] A. Frassoldati, S. Frigerio, E. Colombo, F. Inzoli, T. Farevelli, "Determination of NOx emissions from strong swirling confined flames with an integrated CFD-based procedure", *Chemical Engineering Science*, vol. 60, 2005, pp. 2851-2869

[5] C. Fureby, F.F. Grinstein, G. Li, E.J. Gutmark, "An experimental and computational study of a multi-swirl gas turbine combustor", *Proceedings of the Combustion Institute*, vol. 31, 2007, pp. 3107-3114

[6] S. James, J. Zhu, M.S. Anand, "Large eddy simulations of turbulent flames using the filtered density function model", *Proceedings of the Combustion Institute*, vol. 31, 2007, pp. 1737-1745

[7] V. Kermes, P. Skryja, and P. Stehlík, "Up to date experimental facility for testing low-NOx burners," *10th Conference on Process Integration, Modelling and Optimisation for Energy Saving and Pollution Reduction PRES 2007*, Ischia Porto, Italy: 2007, pp. 1-6.

[8] J. Vondál and J. Hájek, "Experimental and numerical analysis of wall heat transfer in non-premixed gas combustor", *Chemical Engineering Transactions*, vol 18, 2009, pp. 587-592

[9] W. Wagner, J. Cooper, A. Dittmann, J. Kijima, H. Kretzschmar, A. Kruse, R. Mareš, K. Oguchi, H. Sato, I. Stöcker, O. Šifner, Y. Takaishi, I. Tanishita, and J. Trübenbach, "The IAPWS Industrial Formulation 1997 for the Thermodynamic Properties of Water and Steam," *Journal of Engineering for Gas Turbines and Power*, vol. 122, 2000, pp. 184, 150.

[10] F.P. Incropera, *Fundamentals of Heat and Mass Transfer*, New York: John Wiley & Sons, 2007.

[11] Fluent, "FLUENT 6.3.26, User`s Guide," 2006.

[12] N. Syred, "A review of oscillation mechanisms and the role of the precessing vortex core (PVC) in swirl combustion systems," *Progress in Energy and Combustion Science*, vol. 32, 2006, pp. 93-161.

First International Conference on Computational Methods for Thermal Problems
ThermaComp2009, September 8-10, 2009, Napoli, Italy
N.Massarotti and P.Nithiarasu (Eds.)

HEAT TRANSFER AND KNOCK MODELING IN A "DOWNSIZED" SPARK-IGNITION TURBOCHARGED ENGINE

Fabio Bozza
Università di Napoli "Federico II", Via Claudio 21 – 80125 Napoli - Italy, fabio.bozza@unina.it

Daniela Siano, Michela Costa
Istituto Motori-CNR, Viale Marconi 8 – 80125 Napoli - Italy, d.siano@im.cnr.it, m.costa@im.cnr.it

ABSTRACT

In the present paper a combined procedure for the quasi-dimensional modeling of both heat transfer, combustion and knock phenomena in a "Downsized" Spark-Ignition Turbocharged Engine is presented. The procedure is extended to include the cycle-by-cycle variations effects, too. Heat transfer is modeled by means of a commercial software procedure (GT-Power) employing a finite element (FE) model of the combustion chamber. Combustion model is based on a fractal description of the flame front area. Cyclic dispersion is characterized through the introduction of a random variation on a number of parameters controlling the rate of heat release (air/fuel ratio, initial flame kernel duration and radius, EGR rate, turbulence intensity). The intensity of the random variation is specified in order to realize an Indicated Mean Effective Pressure (IMEP) Coefficient of Variation (CoV) similar to the experimentally observed one. A kinetic scheme is then solved within the unburned gas zone, characterized by different thermodynamic conditions occurring cycle-by-cycle. In this way, an optimal choice of the "knock-limited" spark advance can be carried out and compared with the experimental data.

Key Words: *Heat Transfer, Finite Elements, ICE modelling, Knock, cyclic dispersion.*

1. INTRODUCTION

Recently, a tendency is consolidating to produce low displacement turbocharged spark-ignition engines. This design philosophy, known as "engine downsizing", allows to reduce mechanical and pumping losses at low load as a consequence of the higher operating Brake Mean Effective Pressure (BMEP). The presence of the turbocharger allows to restore the maximum power output of the larger displacement engine. Additional advantages are a higher low-speed torque and hence a better drivability and fun-to-drive. Of course, at high loads, the spark-advance and heat transfer phenomena through the cylinder walls must be carefully controlled to avoid the knock occurrence. Small variations of the unburned gas temperature, related to variations in heat transfer rate and spark-advance setting, non-linearly affect the knocking onset. For this reason, the knowledge of the heat transfer details allows to carefully compute the so-called "knock-limited spark timing", being a key point for the reduction of the fuel consumption drop at high loads. Under this point of view, the effects exerted by the presence of continuous "cycle-by-cycle variations" inside the internal combustion engines (ICE) may play a fundamental role, too. They mainly cause fluctuations in the heat released by the combustion process and heat loss through the walls, turning in fluctuations in the unburned gas temperature during the combustion process. In addition, since the spark timing is usually set for the "average" operating cycle, faster-than-average cycles are most likely to knock. The optimal "knock-limited" spark advance must therefore be chosen taking into account both heat transfer regime and cycle-to-cycle variations. In the present paper, basing on a previous study [1], a quasi-dimensional combustion model [2,3] is extended to characterize the cyclic dispersion of a turbocharged SI engine. Heat transfer is modeled by means of a procedure which is based on a FE model of the combustion chamber. The inputs to the FE model include combustion chamber geometry, coolant and oil temperatures, together with their convective heat transfer coefficients. Cyclic dispersion is computed by introducing proper random variations on a number of parameters that affect the heat release rate (A/F ratio, flame kernel formation and extension, turbulence and EGR levels, etc.). The combustion model, utilizing a deeply validated approach, is based on a

fractal schematization of the flame front surface. The combustion model is included within a 1D simulation code and is coupled to a chemical kinetic solver (CHEMKIN), for the estimation of knocking onset. The latter is carried out for each individual engine cycle, through the solution of a kinetic scheme inside the "end-gas" unburned zone. This allows to estimate a statistical distribution of a proper knocking index, able to identify the presence of knocking cycles, even in the absence of knocking on the average cycle. The CoV of the IMEP and of the numerical knock indicator are finally compared and discussed.

2. COMBUSTION MODEL RESULTS

A quasi-dimensional turbulent combustion model has been developed since many years at DIME [2,3], applying to the "wrinkled-flamelet" combustion regime. It is based on a two-zone approach and includes a fractal schematization of the flame front surface. The model relates the burning rate to the turbulence flow characteristics inside the combustion chamber. In particular, the fractal dimension of the flame and its wrinkling scales are defined as a function of the mean turbulence intensity inside the combustion chamber (k-K model [1]). Both the combustion and the turbulence submodels have been implemented in the 1D simulation code using the "user model" features of the GT-POWER® commercial product [4]. Pressure cycles computed by the previously described model are compared in figure 1 to the experimental data at different engine speeds, full load conditions. Experimental data are ensemble averaged over 94 consecutive cycles. In order to better appreciate the quality of the predictions, both the combustion period and the whole engine cycle are reported in a p-ϑ and log(p)-log(V) plane, respectively. The angular delay between the spark and the time of first pressure rise is well reproduced by the model. Moreover, the satisfactory agreement along the compression stroke and during the pumping loop suggests that a good matching with the turbocharger and a proper simulation of the 1D flow in the intake and exhaust systems is obtained.

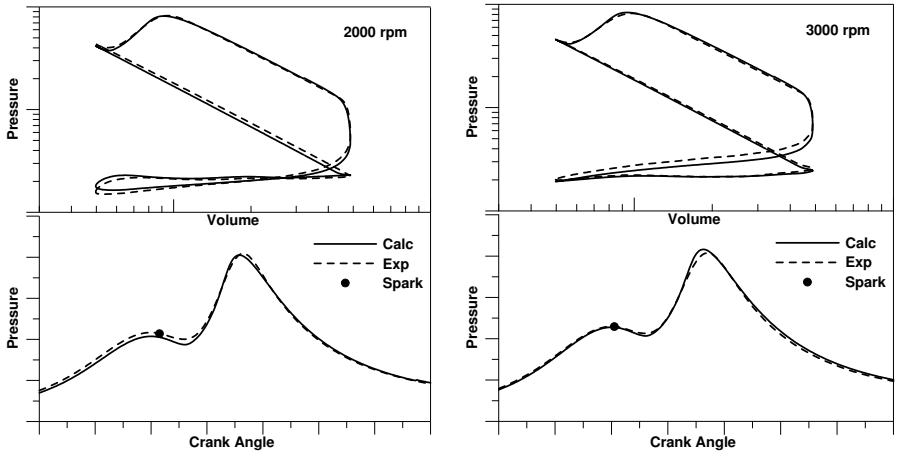

FIGURE 1. Comparisons on the average pressure cycle at two different engine speeds

3. HEAT TRANSFER AND KNOCK MODEL RESULTS

The accuracy of the previous results is also depending on a detailed heat transfer model, included in the G-Power software, which allows to predict the surface temperature in various combustion chamber zones. The calculation of surface temperatures is based on a FE model of the head, valves, cylinder liner, and piston [4]. This model is generated from the supplied geometric attributes and some general assumptions regarding combustion chamber geometry. Figure 2 shows, as an example, the temperature distribution predicted on the piston (a) and on the cylinder head (b). The above values depend on local heat transfer rates (c) computed as a function of materials, geometry, coolant and oil temperatures, and convective heat transfer coefficients. The temperature evolution of particular macro-zones, representing selected groups of elements of the FE mesh, are displayed in fig. 3, at different speeds.

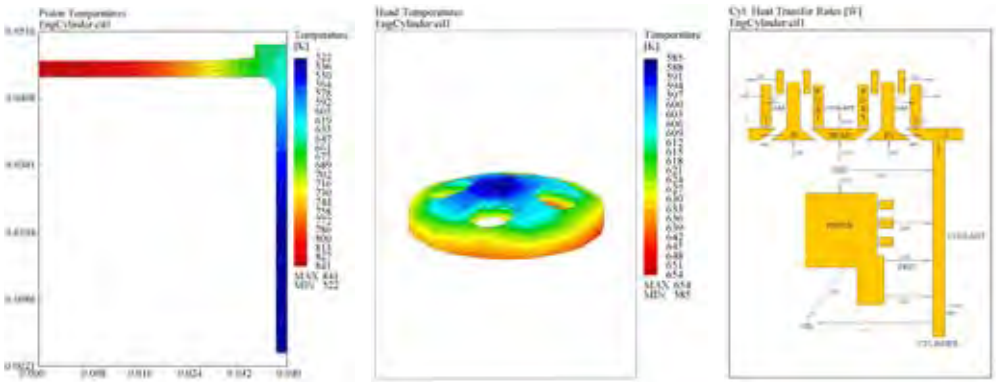

FIGURE 2. Temperature Contour plots on the piston (a) and cylinder head (b). Heat transfer rates in different sections of the combustion chambers (c). Engine speed = 5500 rpm, full load operation.

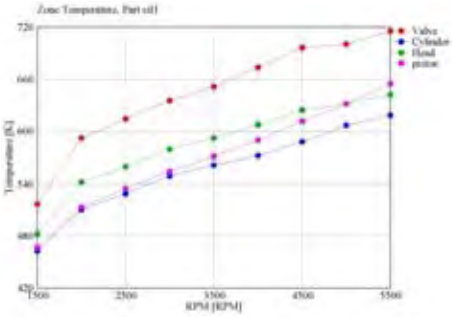

FIGURE 3. Computed wall temperatures inside the combustion chamber

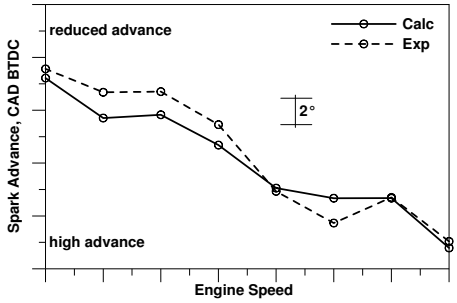

FIGURE 4. Knock-limited Spark Advance

Thanks to the above models, an accurate prediction of the unburned gas temperature and pressure is available, allowing to couple the thermo-dynamic engine model to a kinetic solver for knocking calculations. The kinetic solver (CHEMKIN), basing on a prescribed hydrocarbon oxidation scheme [5,6], is able to compute the eventual presence of heat released by autoignition phenomena (Q_{ub}). The above heat can be normalized with respect to the overall chemical heat available in the injected fuel, so defining a non-dimensional knock index x_{Qub}. Figure 4 displays the spark advance values required to get a prescribed level of the above index. In order to identify the so-called "knock-limited spark advance", a very low x_{Qub} level (about 1%) must be assigned in each case. Computed data are compared to the corresponding experimental values in the fig. 4, and a very good agreement is found at each engine speed.

3. CYCLIC DISPERSION MODEL RESULTS

To the aim of characterizing the cyclic dispersion phenomena, a random perturbation is introduced in the combustion model on a number of parameters usually considered the most important combustion rate controlling factors (kernel radius, turbulence intensity, air/fuel ratio, etc) [1,7,8]. Figure 5 reports the experimental and computed pressure fluctuations at 4000 rpm. Experiments and computations exhibit a similar qualitative behavior in terms of peak pressure and angle of peak pressure fluctuations. The briefly described procedure hence allows to compute a set of instantaneous pressure data statistically equivalent to the experimental one. Starting from this data set, the previous knock analysis can be carried out on a cycle-by-cycle basis. Figure 6 shows the cycle-by-cycle IMEP and x_{Qub} index variations. Despite the IMEP CoV (defined as the ratio between the IMEP standard deviation and the average IMEP level) is reduced (1.5%), a very higher CoV level is found for the x_{Qub} index (61.6%). This demonstrates that even small cycle-by-cycle differences may induce a dramatic effect on knocking occurrence, due to the high non-linearity of

the reactions rates involved in the knocking phenomenon. Moreover, despite the average x_{Qub} level ensures a knock-free operation on the average cycle, the numerical procedure recognizes that 4-6 individual cycles (on a base of 500 consecutive cycles) are characterized by a light knocking.

A 0.8-1.2 percentage of knocking cycles is hence predicted in correspondence to the spark advance levels of fig. 4. As demonstrated, the developed procedure gives the possibility to select the spark advance realizing only a prescribed and controlled percentage of individual knocking cycles.

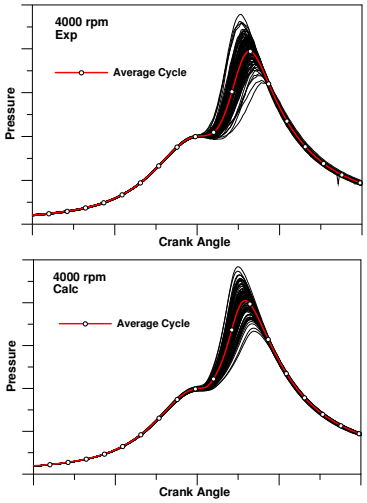

FIGURE 5. Pressure fluctuations

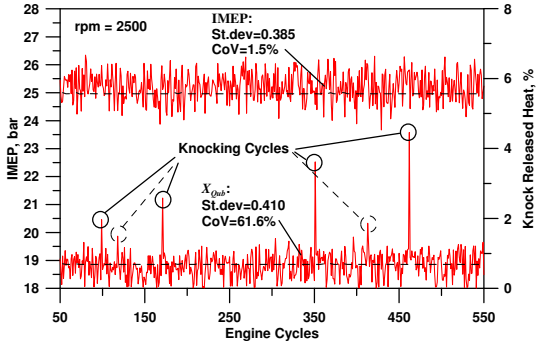

FIGURE 6. IMEP and x_{Qub} fluctuations at 2500 rpm

4. CONCLUSIONS

The heat transfer, combustion development and the knock risk of a "downsized" turbocharged spark-ignition engine have been numerically estimated. An accurate prediction of the combustion process and of the average in-cylinder pressure cycle has been obtained, providing reliable initial conditions for the further modeling of the knocking phenomena. The latter has been realized through the solution of a reduced kinetic scheme within the unburned gas zone. Knock-limited spark advance has been computed with good accuracy in the whole speed range of the investigated engine. The model has been extended to include the effects of the cyclic dispersion. The model allowed to highlight the relation existing between the cyclic variability and knock occurrence. The results presented demonstrate that even small cycle-by-cycle differences may induce a dramatic effect on knocking occurrence. This indicates the need to perform a better choice of the spark advance, accounting for the cyclic dispersion. The numerical analysis carried out put into evidence the possibility to perform an optimal choice of the "knock-limited" spark advance realizing only a prescribed and controlled percentage of individual knocking cycles.

REFERENCES

1. Bozza F., Fontana G., Galloni E., Torella E., "3D-1D Analyses of the Turbulent Flow Field, Burning Speed and Knock Occurrence in a Turbocharged SI Engine", SAE 2007 Transaction, Journal of Engines - section 3, vol. 116, pp. 1495-1507, ISBN 978-0-7680-1982-7, 2008.
2. Bozza F., Gimelli A., Siano D., Torella E. Mastrangelo G., "A Quasi-Dimensional Three-Zone Model for Performance and Combustion Noise Evaluation of a Twin-Spark High-EGR Engine", SAE 2004 Transaction, Journal of Engines - section 3, vol. 113-3, pp. 491-501, ISBN 0-7680-1552-9, 2005.
3. Bozza F., Gimelli A., Merola S. S., Vaglieco B. M., "Validation of A Fractal Combustion Model through Flame Imaging", SAE 2005 Transaction, J. of Engines - section 3, vol. 114-3, pp. 973-987, ISBN 0-7680-1689-4, 2006.
4. GT-Power, User's Manual and Tutorial, GT-SUITE^{T}M Version 6.1, Gamma Technologies.
5. Keck J., Hu H., "Explosions of Adiabatically Compressed Gases in a Constant Volume Bomb", 21st International Symposium on Combustion, The Combustion Institute, 1986, pp. 521-529.
6. Tanaka S., Ayala F., Keck J., "A Reduced Chemical Kinetic Model for HCCI Combustion of Primary Reference Fuels", Combustion & Flame, 132, pp. 219-239, 2003.
7. Litak G., Kaminski T., Czarnigowski J., Grzegorz A K., Wendeker G. M., "Combustion process in a spark ignition engine: analysis of cyclic peak pressure and peak pressure angle oscillations", Meccanica (2009) 44: 1–11, DOI 10.1007/s11012-008-9148-0
8. Galloni E., "Analyses about parameters that affect cyclic variation in a spark ignition engine", Applied Thermal Engineering 29 (2009) 1131–1137

First International Conference on Computational Methods for Thermal Problems
ThermaComp2009, September 8-10, 2009, Napoli, Italy
N.Massarotti and P.Nithiarasu (Eds.)

Thermal profiles of a catalytic micro-burner close to the extinction point

Almerinda Di Benedetto[a], Valeria Di Sarli[a], Raffaele Pirone[a], Gennaro Russo[b]

[a]Istituto di Ricerche sulla Combustione, CNR, Piazzale Tecchio 80, 80125, Naples, Italy

[b]Dipartimento di Ingegneria Chimica, Università degli Studi di Napoli Federico II, Piazzale Tecchio 80, 80125, Naples, Italy

e-mail addresses: dibenede@irc.cnr.it; disarli@irc.cnr.it; pirone@irc.cnr.it; genrusso@unina.it

ABSTRACT

The range of conditions for stable combustion of lean propane/air mixtures in a catalytic micro-reactor is investigated by means of a two-dimensional CFD model. Extinction conditions are determined as functions of inlet gas velocity and temperature. It is found that, on decreasing the inlet gas velocity, reaction extinguishes at higher inlet gas temperatures, owing to the imbalance between heat losses and heat produced by combustion.

Key Words: *Heat Transfer, Reacting flows, Micro-combustors.*

1. INTRODUCTION

The use of micro-burners for heat production via fossil fuel combustion is an interesting option to substitute traditional lithium batteries in micro-electromechanical systems (MEMS). Micro-combustors exhibit a lower weight (thanks to the large energy density of hydrocarbons), an easier recharge procedure and a more environmentally friendly impact than conventional battery systems. They may be succeeding, provided that an efficient system is developed to convert thermal energy into electricity (as, for example, thermo-electric or thermo-photovoltaic devices) and the heat generated during combustion is efficiently transferred to electricity generators. In particular, thermal profiles in micro-burners must be controlled and optimized to enhance the efficiency of the entire system.

In scaling down from macro- to micro-reactors, some phenomena negligible at macro-scales may become relevant at micro-scales. Actually, miniaturizing macro-combustors leads to an increase of the surface area to volume ratio and, thus, thermal quenching may prevail leading to reaction extinction [1-3]. The presence of a catalyst deposited on the reactor walls allows sustaining chemical reaction even in the presence of high heat losses (typical of micro-reactors), thus reducing the impact of thermal quenching. However, in such catalytic micro-combustors, thermal fluxes have to be properly managed in order to get stable operation.

In the present paper, extinction conditions for combustion of lean propane/air mixtures in a catalytic micro-reactor are investigated by running two-dimensional CFD simulations at varying the inlet gas velocity and temperature.

2. MODEL

2.1 Set-up configuration

In Figure 1, the scheme of the micro-combustor is shown which consists of two parallel plates (gap distance, d = 600 m; wall thickness d_w = 200 m; length, L = 0.01 m).

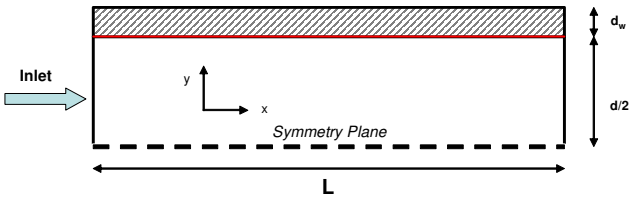

Figure 1 – Scheme of the catalytic micro-combustor (parallel plate reactor). The dashed line is the axis of symmetry.

2.2 The model equations

A two-dimensional CFD model is developed to simulate the coupling of the fluid flow and the chemical processes at the gas/solid interface and in the gas phase. The model solves the mass, momentum, species and energy conservation equations in the fluid, along with the energy equation in the solid wall. Steady-state simulations are carried out.

At the inlet of the micro-combustor, a fixed flat velocity profile is assumed. For species and energy, Danckwerts boundary conditions are used. At the exit, the static pressure is imposed as equal to the atmospheric pressure, and far-field conditions are specified for the remaining variables. At the fluid/wall interface, a no-slip boundary condition is assigned (the fluid has zero velocity relative to the boundary) along with the species balances (the mass flux of each species, J_i, is equal to its rate of production/consumption, $_{y,i}$):

$$J_i = \quad _{y,i} \tag{1}$$

and the energy balance:

$$k\frac{\partial T}{\partial r} = k_w \frac{\partial T_w}{\partial r} + \quad _h \tag{2}$$

where $_h$ is the heat surface production rate.

Heat losses from the ends of the micro-combustor are not considered (insulated ends), while Newton's law of convection is used at the outer surface of the wall:

$$q = h\left(T_{w,ext} - T_{a,ext}\right) \tag{3}$$

where h is the exterior convective heat transfer coefficient, $T_{w,ext}$, is the temperature at the exterior wall surface, and $T_{a,ext}$ is the external temperature.

The reaction rate for homogeneous combustion of propane is calculated according to the single-step reaction rate by Westbrook and Dryer [4]. The catalytic reaction is assumed to be irreversible, first order in fuel concentration and zeroth order in oxygen concentration. Its rate is calculated as in Ref. [3].

The molecular viscosity is approximated through Sutherland's law for air viscosity. The fluid specific heat and thermal conductivity are calculated by a mass fraction weighted average of species properties. The species specific heat is evaluated as a piecewise fifth-power polynomial function of temperature.

The model equations are discretised using a finite volume formulation on a structured mesh built by means of the Gambit pre-processor of the Fluent package (version 6.3.26) [5]. Grid independent solutions are found by using cells with 2.5 E-2 mm dimension.

The spatial discretization of the model equations uses first order schemes for all terms, except for the diffusion terms that are treated with a second order central difference scheme. Computations are performed by means of the segregated solver of the Fluent code [5] adopting the SIMPLE method for treating the pressure-velocity coupling. All residuals are always smaller than 1.0 E-7.

Table 1 summarizes the operating conditions adopted.

Table 1 – Simulation conditions

Parameter	Value
Gas preheating temperature (inlet gas temperature), $T_{preheating}$ [K]	Varies
Inlet gas velocity, v_{in} [m/s]	Varies
Inlet fuel equivalence ratio,	0.6
External temperature, $T_{a,ext}$ [K]	Varies ($T_{a,ext} = T_{preheating}$)
Exterior convective heat transfer coefficient, h [W/(m^2 K)]	20
Solid thermal conductivity, $_w$ [W/(m K)]	2

3. RESULTS

In Fig. 2, the temperature maps in the channel are shown as calculated at three inlet gas velocities (and $T_{preheating} = T_{a,ext} = 600°C$). It is found that reaction occurs very close to the inlet section of the micro-combustor, especially at lower inlet velocities. Downstream, both wall and bulk gas temperatures rapidly decrease, owing to heat losses to the surrounding.

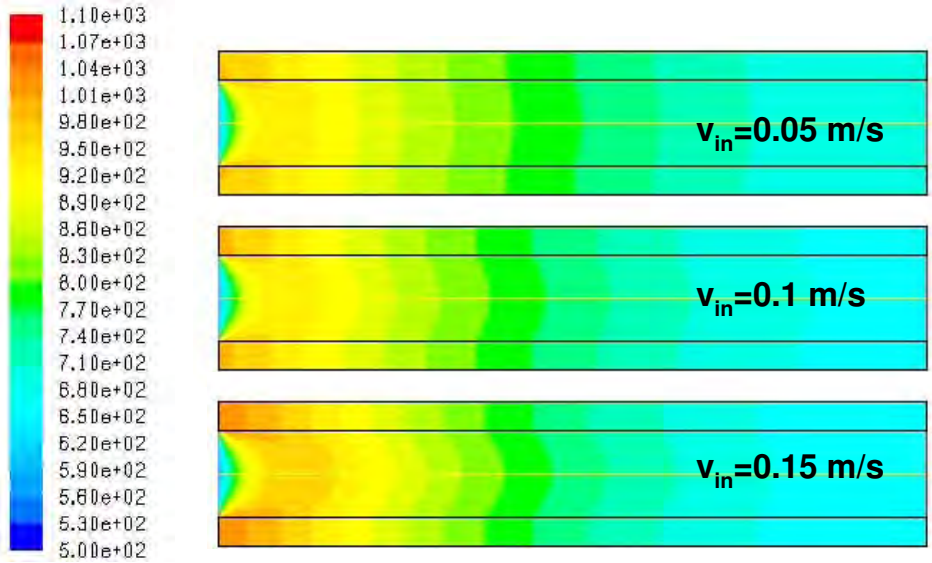

Figure 2 – Temperature [K] maps in the channel at different inlet gas velocities (and $T_{preheating} = T_{a,ext} = 600°C$).

In Fig. 3, the stability maps are shown as obtained at three inlet gas velocities in terms of maximum wall temperature as a function of the gas preheating temperature ($T_{preheating} = T_{a,ext}$). The symbols (circle, square, triangle) represent the extinction points, i.e., the points at which reaction cannot be sustained anymore. Extinction is the result of the imbalance between heat losses and heat produced by reaction.

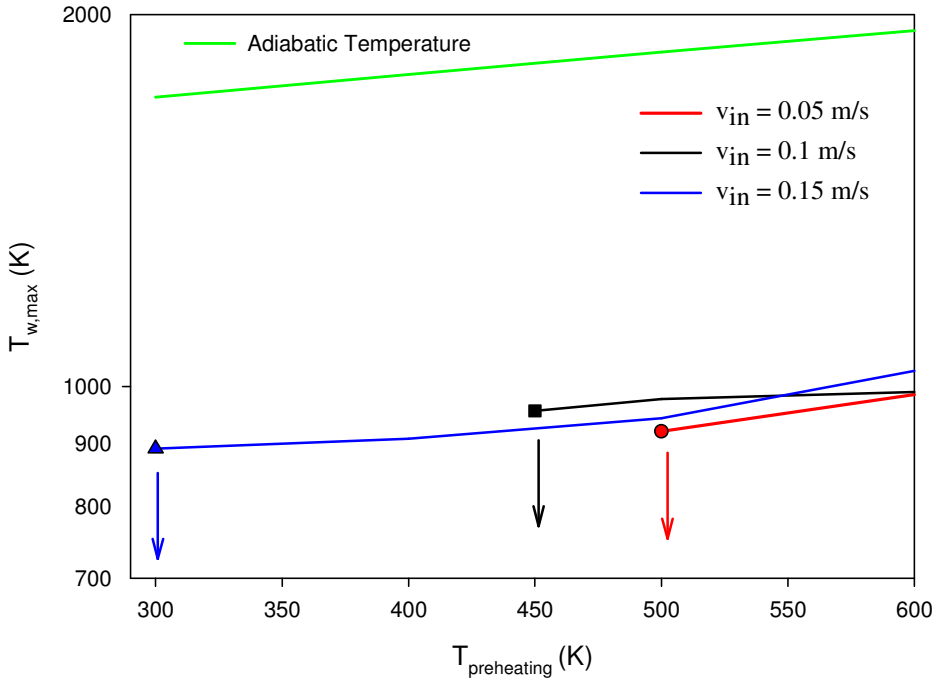

Figure 3 – Maximum wall temperature vs. gas preheating temperature ($T_{preheating} = T_{a,ext}$) at different inlet gas velocities.

It is found that, on decreasing the inlet gas velocity, extinction occurs at higher values of the preheating temperature. At $v_{in} = 0.15$ m/s, stable operation may be obtained even at $T_{preheating} = T_{a,ext} = 300$ K, whilst, to sustain combustion at $v_{in} = 0.05$ m/s, $T_{preheating} = T_{a,ext} \geq 500$ K are needed.

4. CONCLUSIONS

A two-dimensional CFD model has been developed to identify the critical conditions for stable combustion of lean propane/air mixtures in a catalytic micro-reactor. In particular, extinction conditions in terms of inlet gas velocity and inlet gas temperature have been identified. It has been found that, on decreasing the inlet gas velocity, reaction extinguishes at higher inlet gas temperatures, owing to the imbalance between heat losses and heat produced by combustion.

REFERENCES

[1] Fernandez-Pello, A.C., *Proc. Combust. Inst.* 29, 883-899, 2002.
[2] Aghalayam, P., Vlachos, D.G., *AIChE J.* 44, 2025-2034, 1998.
[3] Di Benedetto, A., Di Sarli, V., Russo, G., *Catal. Today*, doi:10.1016/j.cattod.2009.01.048, 2009.
[4] Westbrook, C.K., Dryer, F., *Combust. Sci. Technol.* 27, 31-43, 1981.
[5] Fluent (version 6.3.26), Fluent Inc. www.fluent.com, accessed 08.05.09.

First International Conference on Computational Methods for Thermal Problems
ThermaComp2009, September 8-10, 2009, Naples, Italy
N.Massarotti and P.Nithiarasu (Eds.)

Effects of Turbulence Modeling for Diesel Engine Simulation within the OpenFOAM toolkit

A. Aprovitola, M. Briani, V. Fraioli, M.na Migliaccio
Istituto Motori, Via Marconi, 8-80125 Napoli, a.aprovitola@im.cnr.it

ABSTRACT

In this work the performance of the turbulence models commonly used in diesel engine simulation is analyzed within the OpenFOAM toolkit. In-cylinder simulations have been performed with $k-\epsilon$ and RNG models both in motored configuration and with spray injection. The effects due the compressibility in RNG model have been accounted for in OpenFOAM, defining a variant of RNG turbulence model class. The influence of the models on in-cylinder pressure peak and their impact on turbulent viscosity and fluctuations are investigated.

Key Words: *Engine simulation, turbulence modeling, OpenFOAM.*

1. INTRODUCTION

Turbulence modeling is a fundamental task in engine simulation which influences both fuel spray evolution and the combustion process. Furthermore it is now well known that the level of description of the turbulent field has a non negligible impact on the emissions predictions, due to the high coupling between thermal, compositions and fluid dynamic fields [1]. The large scale structures produced by the intake motion are responsible of the turbulent energy transfer and set up the value of turbulent viscosity at the beginning of the compression stroke. The interaction among the swirl motion induced by the intake flow and the squish during the compression stroke leads to a strongly anisotropic and unsteady velocity field which violates the equilibrium assumption between energy production and dissipation on which $k-\epsilon$ model is based. Furthermore the in-cylinder air motion is influenced by the spray injection which enhances the turbulent fluctuations due to the momentum transfer from the surrounding liquid. A common choice in engine simulations is to use the $k-\epsilon$ model for high Reynolds number with wall functions. Study on flow predictions using such model demonstrated that it provides too large turbulent diffusion [2]. In addition, as the turbulent mixing time imposed by the large scale motion directly influences the reaction rates, it appears clear that the description of the whole combustion process remains altered by high turbulent diffusivity. Such a consideration suggests the use in engine simulation of turbulence models which are not based on equilibrium hyphotesis. In the work of [2] the RNG model proposed by Yakhot and Orszag (1986) has been modified introducing the effect of compressibility. Such modified version of RNG model has then been implemented in KIVA code, massively used for engine simulation. Aim of this work is to assess the behaviour of the turbulence models implemented in the **OpenFOAM** libraries with respect to the engine simulation problems. OpenFOAM is a set of $C++$ libraries, capable of handling a large variety of complex flow problems [3]. In addition, OpenFOAM has the advantage of being an open environment, therefore it provides a complete access to the numerical methods implemented in it [4]. In the OpenFOAM version 1.4 currently used by the authors the RNG model does not account for the dilatation effects during the compression and expansion strokes. Therefore a new class has been added to the existent compressible turbulent ones in order to include such effects . Several simulations are performed in a motored configuration, in order to evaluate the impact of the model on the mean cylinder pressure, in comparison with the measured profile. The turbulent viscosity and the intensity of turbulence are reported in the presence of spray. In addition, the turbulent mixing time is computed, as commonly used in approaches to account for the impact of turbulence on the chemical reaction rates [5],[6].

2. TURBULENCE MODELS SET UP

In order to reproduce the flow conditions at the beginning of the compression stroke a swirl motion is superimposed on initial conditions. Initial value of turbulent kinetic energy and the energy dissipation at the intake valve closure are assumed uniform and are evaluated as reported in [2] thus a turbulent motion inside the cylinder is induced. The in-cylinder flow in such a configuration is described by the set of Favre averaged mass, momentum and energy equations. The nonlinear terms of the conservation laws are discretized with a Total Variation Diminishing (**TVD**) scheme [7]. The use of TVD in engine simulations where large gradients of flow properties and high swirl are involved seems to be adequate. The diffusive fluxes are discretized using a second order accurate central formulation. It is worth stressing that in the OpenFOAM version 1.4 there are no source terms in the turbulence model equation due to the spray. As it was shown the effect of dilatation is taken into account evaluating the constant C_3 in the RNG model with the following relation [2]:

$$C_3 = \frac{-1 + 2C_1 - 3m(n-1) + (-1)^{\delta}\sqrt{6}C_{\mu}C_{\eta}\eta}{3}. \tag{1}$$

where $C_{\mu} = 0.0845, C_1 = 1.42, C_2 = 1.68$ are the model constant. For an ideal gas $\mu \simeq T^m$ with $m = 0.5$ and n is the exponent of the polytropic process, in the present case we refer to an adiabatic process and select n=1.4 [2]. The index $\delta = 1, 0$ accounts for the variations of divergence sign between the compression and the expansion stroke, while $\eta = S\frac{k}{\epsilon}$ is the ratio of the turbulent to mean strain-time scale. Such relation is implemented in OpenFOAM adding a new class to compressible turbulence ones.

3. RESULTS

In this section the results of some simulations for a diesel engine in motored conditions are presented. The engine characteristics are reported in [8], the adopted mesh for a sector of 51° is constituted by 22785 hexahedra at the bottom dead center with a cell width between 0.5 mm and 1mm in the bowl. A grid independent RANS solution is performed using 106920 hexaedra in order to assess the quality of the grid with respect to the choice of selected discretization method. With reference to such resolution the computed pressure and temperature fields are in agreement with the results obtained on the coarser grid. By looking at FIG.1 the computed pressure profiles agree reasonably with the measured pressure evolution. The comparisons are made exploiting the RNG model with different values of C_3 in order to underline the correction due to the dilatation effects with respect to the cases adopting constant values of $C_3 = -0.33$ and $C_3 = -1$. For the sake of completeness the results obtained with $k - \epsilon$ model are also reported. Switching from the value $C_3 = -1$ to the value $C_3 = -0.33$ the RNG model provides a slightly higher pressure peak. Such value is further increased when C_3 =Eq.(1). Once assessed the effect of the models on the mean pressure field, the fuel injection (from -0.8 Crank Angle Before Top Dead Center to 6.4 Crank Angle After Top Dead Center) has then been included in order to evaluate their influence on the spray dynamics. Time behaviour of turbulent viscosity is reported

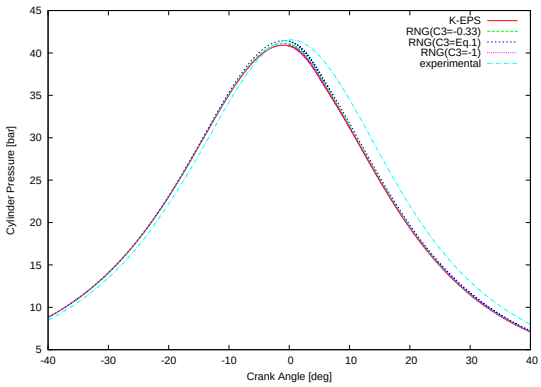

FIGURE 1. Time evolution of in cylinder pressure with $k - \epsilon$ and RNG models

in FIG.2 while turbulent intensities evolution is reported in FIG.3. As expected spray affects both the turbulence viscosity and intensities during the injection. Owing to the piston movement and the radial motion (squish) produced by the reentrant bowl, in the compression stroke turbulence intensities increase until fuel injection strongly enhances the kinetic turbulence energy. The RNG model, with both constant values of C_3 gives lower turbulent viscosity and intensities than the standard $k-\epsilon$ and such trend is further confirmed when using C_3 =Eq.(1). Such an effect, lowering the relative gas velocity, directly influences spray submodels, such as breakup, evaporation and drag models reducing the vapour diffusion as shown in FIG.4 [9]. Anyway negligible differences are observed by varying C_3, also for vapour penetration probably due to the absence of the spray source term in the turbulence equations. FIG.5 reports the temporal evolution of the turbulent mixing time $\tau_{mix} = C_{mix}\frac{k}{\epsilon}$ in the different cases: when the variable C_3 expression is adopted, lower values of the mixing time are attained in the compression stroke. As soon as injection starts, the differences among the cases are reduced, however, at about 6 degrees after top dead center, at the end of the injection, the differences keep amplifying

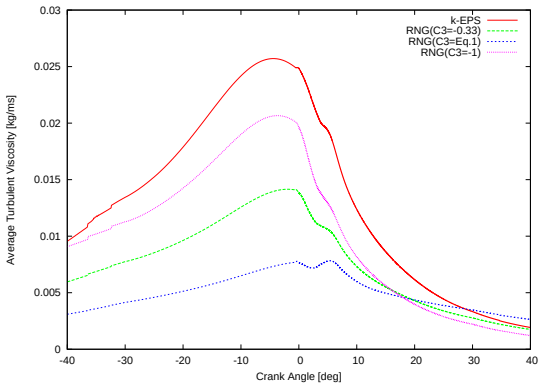

FIGURE 2. Time evolution of turbulent viscosity with $k-\epsilon$ and RNG models

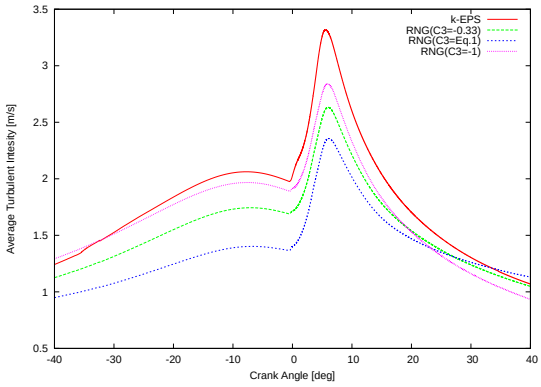

FIGURE 3. Time evolution of turbulent intensity with $k-\epsilon$ and RNG models

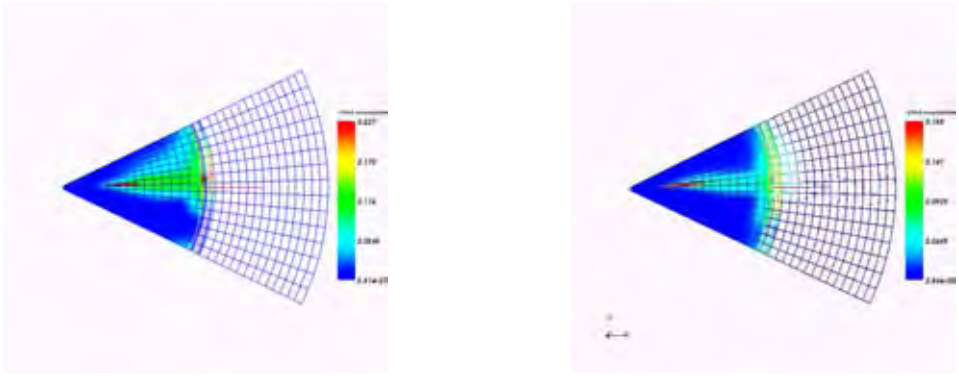

FIGURE 4. Vapour distribution at 7 C.A. ATDC with $k-\epsilon$ (left) and RNG-C_3 =Eq.(1) (right)

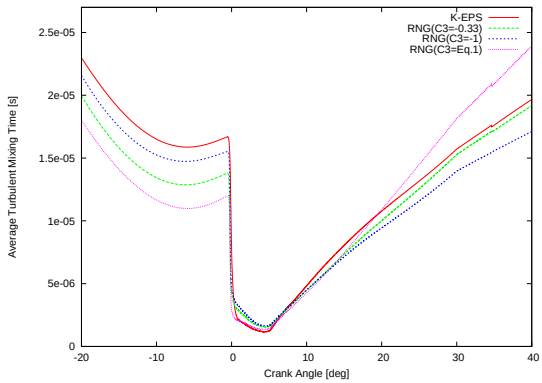

FIGURE 5. Time evolution of turbulent mixing time with $k - \epsilon$ and RNG models

again. Such variations can be significant in the framework of the simulations in fired conditions: in fact several models, widely adopted to account for the effect of turbulence over the reaction rates, perform a comparison between the mixing time and a characteristic chemical time to determine whether combustion rate is kinetically controlled or not.

4. CONCLUSIONS

Object of this work was the analysis of turbulence models implemented in OpenFOAM toolkit with respect to the diesel engine simulation. The RNG model version including the compressibility effects has been added to OpenFOAM version 1.4. The impact of the model on the in-cylinder evolution of the turbulent flow-field and the subsequent effect on the spray have been investigated. Simulations confirmed that although the pressure profiles are slightly influenced by the turbulence model, more important variations are obtained as concern turbulent viscosity and intensities. The influence of such effects can be significant under fired conditions directly affecting the chemical reaction rates. The limited impact of the different values of C_3 on the liquid spray behaviour can be probably justified by the absence of the spray source term in the turbulence model equations, in OpenFOAM version 1.4 which, differently, is present in some other engine simulation codes.

REFERENCES

[1] A. D. Gosman, State of the Art of Multi-Dimensional Modeling of Engine Reacting Flows, *Oil and Gas Science and Technology-Rev. de l'IFP*, Vol. **54** (1999), No.2, pp.149-159

[2] Z.Han, R.D.Reitz, Turbulence Modeling of internal Combustion Engines Using RNG $k - \epsilon$ Models, *Combust.Sci. and Tech.*, Vol. **106**, (1995), pp. 267-295

[3] H.G.Weller, G.Tabor, H.Jasak, C.Fureby, A tensorial approach to computational continuum mechanics using object-oriented techniques, *Computers in Physics*, Vol. **12**, No.6, (1998)

[4] A.Aprovitola, M.Briani, V.Fraioli, M.na Migliaccio, Reliability of In-Cylinder Simulation with OpenFOAM, *Technical Report*, 2009RR, No. 1916, (2009)

[5] J. Gustavsson, V.I.Golovitchev, Spray Combustion Simulation Based on Detailed Chemistry Approach for Diesel Fuel Surrogate Model, *SAE Paper* No. 0137, (2003)

[6] P. A. N. Nordin, *Complex Chemistry Modeling of Diesel Spray Combustion*, Ph.D. thesis, (2001)

[7] H. V. Versteeg, W. Malalasakera, *An Introduction to Computational Fluid Dynamics*, Longman Scientific and Technical, (1995)

[8] G. Avolio, C. Beatrice, C. Bertoli, Development of a Single Cylinder Direct Injection Diesel Engine for advanced combustion system studies, *HTCES2005 PAPER*, (2005)

[9] F.Peng Karrholm, N. Nordin, Numerical Investigation of Mesh/Turbulence/Spray interaction For Diesel Applications, *SAE PAPER*, 2005-01-2115

First International Conference on Computational Methods for Thermal Problems
ThermaComp2009, September 8-10, 2009, Napoli, Italy
N.Massarotti and P.Nithiarasu (Eds.)

ENTROPY GENERATION ANALYSIS FOR THE DESIGN OPTIMIZATION OF SOLID OXIDE FUEL CELLS

Adriano Sciacovelli
Politecnico di Torino Dipartimento di Energetica, c.so Duca degli Abruzzi 24, Torino, Italy,
adriano.sciacovelli@polito.it

Vittorio Verda
Politecnico di Torino Dipartimento di Energetica, c.so Duca degli Abruzzi 24, Torino, Italy,
vittorio.verda@polito.it

ABSTRACT

The aim of this paper is to investigate possible improvements in the geometry of a monolithic solid oxide fuel cells (SOFCs) in order to increase its performance. The analysis is focused on the localization and evaluation of entropy generation rates inside the fuel cell. The use of this technique make it possible to identify and understand the causes provoking main irreversibilities. Entropy generation rates are obtained through 3D numerical calculations, accounting for heat, mass, momentum, species and current transport. The system is then optimized in order to minimize the overall entropy generation and increase the efficiency.

Key Words: *Solid oxide fuel cell, Entropy generation minimization, CFD model, Geometry optimization.*

1. INTRODUCTION

Solid oxide fuel cells have attracted much attention due to their high efficiency and cleanliness, and they are expected to be one of the most favourable electrical power generation technology in the near future. However, in real plants the actual efficiency is still far from theoretical limit. One of the causes is due to internal irreversibilites connected to non-uniform distribution of thermodynamic quantities as temperature, species concentrations, flow velocity, etc. This cause is studied in this paper, together with fuel cell geometry optimization focused on reduction of main sources of irreversibility and increase of efficiency. In particular Second Law study is suitable for these goals and therefore is here adopted. Analysis and optimization are performed at single cell level: CFD approach has been adopted since it may provide a detailed description of the geometry and the transport phenomena.

2. MAIN BODY

A tubular-like fuel cell geometry with an injection tube is considered, as shown in figure 1. The fuel cell is composed of a solid electrolyte layer between a porous cathode and anode. Fuel and air flows in trapezoidal channels, but air is introduced through an injection tube located inside the cathodic channel. The air flows along the cell exchanging heat while it reaches the fuel cell bottom end. Air exiting the tube flows in the trapezoidal channel from the bottom, providing the oxygen necessary for electrochemical reactions. In particular at the anode side hydrogen reacts with oxygen ions generating water

$$H_2 + O^{2-} \rightarrow H_2O + 2e^- \qquad (1)$$

The water produced goes back to the anode channel and exits the cell, together with the other non oxidized gas. At the cathode side the oxygen is reduced and the resulting ions migrate thorough the electrolyte:

$$1/2\,O_2 + 2e^- \rightarrow O^{2-} \quad (2)$$

Thus, a oxygen flux is established from the channel to the electrode-electrolyte interface. The resulting overall reaction is:

$$H_2 + 1/2\,O_2 \rightarrow H_2O \quad (3)$$

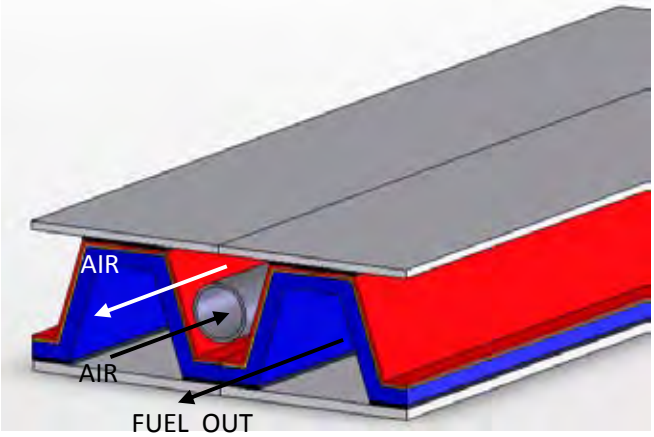

FIGURE 1. Schematic of fuel cell module

The fuel cell is analyzed using CFD technique. A 3D model is adopted, based on elementary balance equations solved for fluids: continuity, momentum, energy, species and current transport. The following assumption are used in this model: steady state conditions, ideal gas mixture, laminar and incompressible fluid flow, porous media proprieties are considered homogeneous and isotropic. The governing equations for the fuel cell model can be given in the following compact form:

$$div\begin{Bmatrix}\rho\vec{v}\\ \rho\vec{v}\otimes\vec{v}\\ \rho e\vec{v}\\ \rho\omega_i\vec{v}\\ 0\end{Bmatrix} + div\begin{Bmatrix}0\\ p\bar{\bar{I}}\\ p\vec{v}\\ 0\\ 0\end{Bmatrix} = div\begin{Bmatrix}0\\ \bar{\bar{\tau}}\\ \vec{q}_c + \sum_k h_k \cdot \vec{J}_k\\ \vec{J}_i\\ \vec{\imath}\end{Bmatrix} + \begin{Bmatrix}0\\ S_v\\ S_h\\ S_i\\ 0\end{Bmatrix} \quad (4)$$

Where ρ – density, $\vec{v}$ – velocity vector, ω_i – mass fraction of gas component i, e – total energy, p – pressure, $\bar{\bar{\tau}}$ – stress tensor, $\vec{q}_c$ – conductive heat flux, $\vec{J}_i$ – diffusive flux of species i, h_k – enthalpy of species k, $\vec{\imath}$ – current density, S_v – momentum source, S_h – energy source, S_i – creation/destruction source of specie i.

The rate of entropy generation is used as a thermodynamic objective to be minimized through fuel cell geometry modification. An expression of the rate of entropy generation can be derived in term of fluxes and gradients of physical quantities. This equation is obtained from entropy balance written for an infinitesimal volume

$$\rho\frac{Ds}{Dt} = -\nabla\cdot\vec{\sigma} + g_p \quad (5)$$

In particular the local entropy generation can be split in different contribution, each strictly correlated to a specific physical phenomena:

$$g_p = \frac{1}{T}\Delta{:}\,\tau + \frac{1}{T^2}\left(-q_c\cdot\nabla T\right) + \frac{1}{T}\left(\sum_j -J_j\cdot\nabla\mu_j\right) + \frac{1}{T}\left(\sum_j -s_j J_j\cdot\nabla T\right) \quad (6)$$

Where Δ is the strain tensor, μ_j is the chemical potential and s_j is the specific entropy. The first term of (6) represents the irreversibilities due to fluid friction, the second term account for the entropy generation due to heat transfer, the third is due to mass transfer (concentration gradient), and the fourth term is due coupling between heat and mass transfer. In the case of a fuel cell, ohmic losses contribute also to entropy generation the correspondent term is

$$g_{ohm} = \frac{1}{T}\sigma\nabla\varphi \cdot \nabla\varphi \qquad (7)$$

The previous term is present only in conductive regions, i.e. electrolyte and electrodes.

3. RESULTS

The partial differential equations presented in the previous sections are discretized using the finite volume method (FVM) to calculate velocity field, temperature, mass fraction and current density. Once convergence is reached entropy generation is calculated and stored. Figure 2 shows the velocity path lines inside the cathode channel. At the closed end of the fuel cell two vortexes take place: a typical feature of tubular fuel cells.

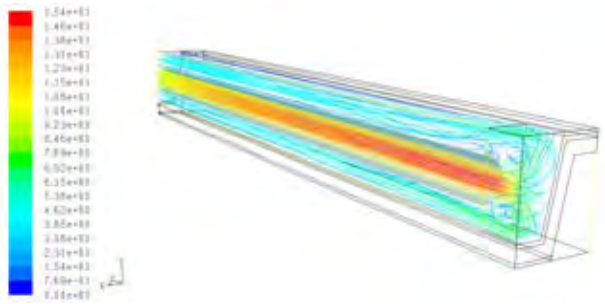

FIGURE 2. Velocity path lines inside cathode channel.

Figure 3 shows hydrogen and oxygen mass fraction along the fuel cell. Hydrogen mass fraction presents strong gradients streamwise and along x-y plane, this profile is characterized by the rate of consumption of hydrogen due to electrochemical reaction. Oxygen concentration is higher at the cell bottom end, since air flows first inside the injection tube. From fig. 3 is clear that oxygen concentration has strong transversal gradients, this occurs because cathode porous matrix represents an obstacle to the air flow.

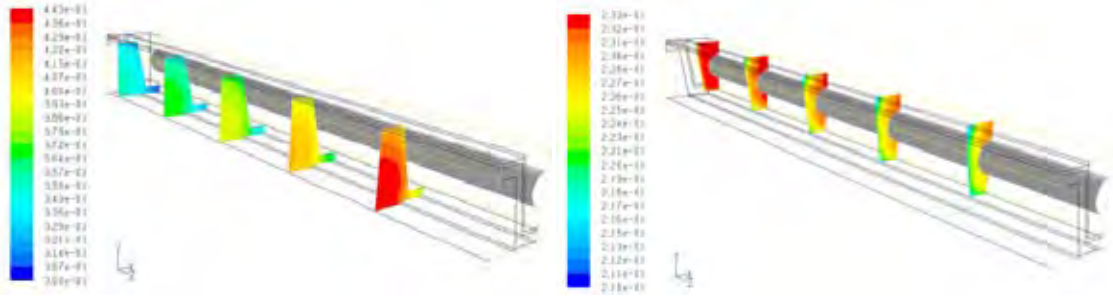

FIGURE 3. Hydrogen (left) and oxygen (right) mass fractions.

Each term of (6) is also post-processed and analyzed. As an example Fig. 4 depicts the entropy generation rate related to mass transfer in four longitudinal cross sections [(a) z=20mm; (b) z=40mm; (c) z=60mm; (d) z=80mm]. The electrochemical reactions cause species consumption and strong mass fraction gradients. These gradients are the source of mass transfer entropy generation. This kind of irreversibilities is particularly strong inside porous media, i.e. inside the electrodes where species are mainly transported by diffusion. Entropy generation distribution correctly captures where losses are predominant, i.e. along the upper plane of the cell and close to the corners.

The fuel cell optimization is performed by considering the global entropy generation as the objective function to be minimized, namely

$$G_p = \int (g_\mu + g_h + g_m + g_c + g_{ohm}) dV \qquad (7)$$

Each term of (7) is considered separately, in order to understand which are the main causes of irreversibilities.

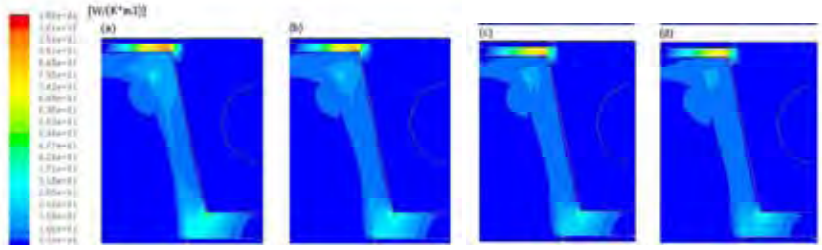

FIGURE 4. Entropy generation due to mass transfer on cross section planes.

Shape optimization of the cell has been performed with a proper parameterized SOFC geometry. In this work the scaling factors along x and y, together with the injection tube diameter. The optimization task follows these steps: the optimization algorithm generates set of design variables, representing the cell geometry. These parameters are sent to mesh generator which creates and passes the computational grid to the CFD solver. This solver computes the conservation equations and the objective function to minimize. Finally, the numerical values of the objective functions are sent back to the optimizer, and so on.

In figure 5, various geometries analyzed during the optimization process are considered. The figure shows that the reduction in the entropy generation, brings an increase in the electric power produced per unit active area.

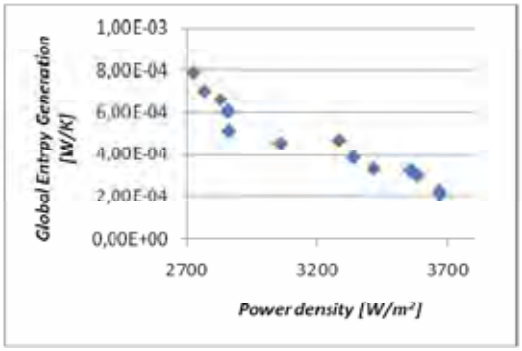

FIGURE 5. Entropy generation vs. Power density.

The optimal configuration is identified by X scale = 1.4 and Y scale = 0.8, therefore turns out to be stretched along x direction and smaller than the initial design in y direction.

4. CONCLUSIONS

In this paper, geometry optimization of a tubular solid oxide fuel cell is performed. A numerical model accounting for mass transfer, heat transfer, current transfer as well as electrochemical reaction is presented. The shape optimization is conducted using the entropy generation as the objective function to be minimized. It is shown that the entropy generation in the optimized geometry is reduced of about 25% while the power density increase of about 10%.

First International Conference on Computational Methods for Thermal Problems
ThermaComp2009, September 8-10, 2009, Napoli, Italy
N.Massarotti and P.Nithiarasu (Eds.)

A STABILIZED FINITE ELEMENT ALGORITHM FOR THE SOLUTION OF SOFC PROBLEMS

Fausto Arpino
Department of Mechanics, Structures and Environment (DiMSAT), University of Cassino, Via G. Di Biasio 43, 03043 Cassino (FR), Italy. E-mail: f.arpino@unicas.it

Nicola Massarotti
Department for Technologies (DiT), University of Napoli "Parthenope", Isola C4, Centro Direzionale di Napoli, 80143 Napoli, Italy. E-mail: nicola.massarotti@uniparthenope.it

Alessandro Mauro
Department for Technologies (DiT), University of Napoli "Parthenope", Isola C4, Centro Direzionale di Napoli, 80143 Napoli, Italy. E-mail: alessandro.mauro@uniparthenope.it

Perumal Nithiarasu
Civil and Computational Engineering Centre, School of Engineering, Swansea University, Swansea SA2 8PP, U.K. E-mail: P.Nithiarasu@swansea.ac.uk

ABSTRACT

In this work, a new stabilized finite element algorithm, using a single domain approach for the solution of mass and energy transport phenomena in solid oxide fuel cells is presented. The proposed numerical procedure is based on the Artificial Compressibility (AC) Characteristic Based Split (CBS) scheme. The stability analysis carried out by the authors for the first time is based on the order of magnitude analysis of all the terms present in the conservation equations. The stability limits speed up the simulation process enormously. Furthermore, the single domain approach allows the application of the present method to the simulation of a whole cells stack.

Key Words: *SOFC, Finite Elements, Stability analysis, Explicit CBS, Matrix inversion free.*

1. INTRODUCTION

The ever increasing energy consumption, the rising public awareness for environmental protection and the existing nature of fossil fuels, convey much of the research work to focus on alternative and renewable energy sources. The fuel cell technology for energy generation is one of the most promising technologies with a much reduced impact on the environment. SOFCs are very promising since the high operating temperature brings several advantages (inexpensive catalyst materials, direct use of different fuels, possibility of cogeneration) and makes the SOFCs technology suitable for stationary power generation. However, the slow start up, high cost and intolerance to sulphur content are some of SOFCs drawbacks. Planar and tubular configurations are the two most commonly employed shapes in the construction of SOFCs. Among these two types, planar configuration has recently received a great deal of attention due to its potential to offer higher power density. Despite the intensive research and significant progress, SOFCs are still not ready for commercial use due to high manufacturing costs, low reliability and high operating costs. Therefore, much more effort has to be done in the research stage, to optimize the design process and make them commercially competitive. In the authors opinion, the development of efficient models for the solution of SOFCs thermo fluid dynamic, chemical and electrochemical internal complex processes is absolutely essential to bring the design of these systems to a commercial stage. However at present, not many robust and sound numerical solution procedures are available.

In the present work, a numerical simulation procedure for SOFCs, based on the Artificial Compressibility (AC) Characteristic Based Split (CBS) scheme [1, 2], is presented. The present scheme has been successfully used by the authors for the solution of incompressible flows [1] and flow through saturated porous media [2]. The authors have been carried out a stability analysis of the present algorithm in presence of high source terms (i.e. due to the presence of a porous medium with a very low permeability), in order to apply it successfully to high temperature fuel cells simulation. The stability analysis is based on the order of magnitude of all the terms present in the governing equations [3]. The stabilization limits, together with the local time stepping procedure, speed up the process enormously. Based on the general and detailed mathematical model recently presented by the authors for high temperature fuel cells simulation [4], this work investigates for the first time the performances of the AC-CBS algorithm for the simulation of energy and mass transport phenomena, occurring in high temperature fuel cells operation, by using a single domain approach. Recently, the phenomena evolving inside the SOFCs have been successfully simulated by the authors by employing the semi-implicit (SI) version of the CBS algorithm with a separate domain approach [4]. While the SI version of the CBS algorithm shows great computational demand, because of the simultaneous solution of algebraic equations, the AC version of the CBS scheme does not require a matrix inversion procedure and offers the possibility of an efficient parallelization. The present stabilized AC-CBS scheme converges firmly faster than the SI version of the CBS. Furthermore, the single domain approach allows the application of the present method to the simulation of a whole cells stack, resulting very promising for 3-D simulations. The results show that the present algorithm compares very well with numerical and experimental data available in the literature.

2. GOVERNING EQUATIONS

A general approach to the solution of coupled porous media and free fluid flow problems consists in the use of the generalized model [2, 3]. The quantities of interest in the flow channels, in the porous electrodes and in the electrolyte are described by the following advection-diffusion type equation:

$$\frac{\partial \mathbf{W}}{\partial \vartheta} + \frac{\partial \mathbf{F}_j}{\partial x_j} + \frac{\partial \mathbf{G}_j}{\partial x_j} = \mathbf{S} \tag{1}$$

Whose terms are presented in:

$$\mathbf{W} = \begin{pmatrix} u_i \\ \left[\left(c_p \right)_f + (1- \,) \left(c_p \right)_s \right] T \\ {}_e y_k \end{pmatrix}; \quad \mathbf{F_j} = \begin{pmatrix} u_j \\ \dfrac{u_i u_j}{} + p_{\;ij} \\ \left(c_p \right)_f u_j T \\ u_j \;\; {}_e y_k \end{pmatrix};$$

$$\mathbf{G_j} = \begin{pmatrix} 0 \\ - \;{}_e \dfrac{\partial u_i}{\partial x_j} \\ -k_e \dfrac{\partial T}{\partial x_i} \\ - \;{}_e D^e_{km} \dfrac{\partial y_k}{\partial x_j} \end{pmatrix}; \quad \mathbf{S} = \begin{pmatrix} 0 \\ \dfrac{u_i}{K} + \dfrac{F_o{}^2 |\mathbf{u}|}{\sqrt{K}} \\ S^e \\ S^m_k \end{pmatrix} \tag{2}$$

The subscript *e* for density and viscosity in Equation (2) indicates the effective quantity in the porous domain [2]. The same set of equations can then be used for the calculation of the quantities of interest in both the free fluid region $(= 1; K \to \infty)$ and in the porous domain

$(0< <1; 0<K<\infty)$ by just changing the properties of the medium considered (effective property → fluid property) [2, 4]. The Right Hand Side (RHS) includes the source/sink terms S_k^m and S^e in the species and energy conservation equations, that are derived from chemical and electrochemical reactions.

3. RESULTS

The stabilization procedure for the AC-CBS scheme developed by the authors has been previously tested on a benchmark case of forced convection in a channel horizontally divided in low permeability porous medium and free fluid [3]. Then, the proposed algorithm is here applied to the simulation of the energy and mass transport phenomena in a planar anode-supported fuel cell, for which some experimental data are available in the literature. The computational domain and the boundary conditions employed are shown in Figure 1. The reactants consumption and production are calculated by using the faraday equation and are applied at the interface between electrode and catalyst layer. In an equivalent way the heat production due to fuel cell operation is applied at the catalyst layer as a linear source term. The H_2 concentration at the catalyst layer moving from inlet section to outlet section is constant for larger values of mean current density (Figure 2). The stabilized AC-CBS scheme is validated against the experimental data presented by Yakabe et al [5]. Figure 3(a) shows the concentration polarization difference between a mixture containing argon and a mixture with no argon. The present numerical solution agrees excellently with the experimental data. Compared to the values predicted with the present procedure, the numerical results of Yakabe et al. [5] present a larger deviation from the experimental data at almost all fuel concentration values considered. Figure 3(b) shows the cell operative voltage and the power density as a function of the average cell current density. The quick drop in the cell operative voltage at high values of the average cell current density is followed accordingly by a drop in the cell power density.

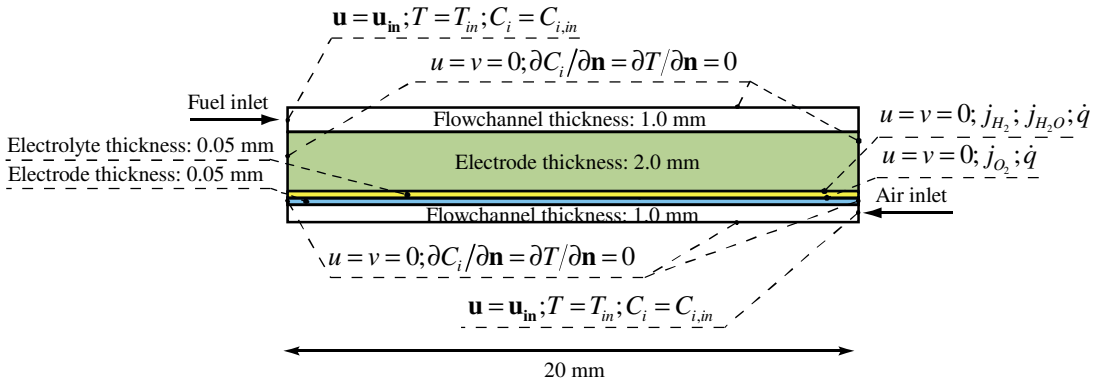

Figure 1. Domain definitions and boundary conditions employed.

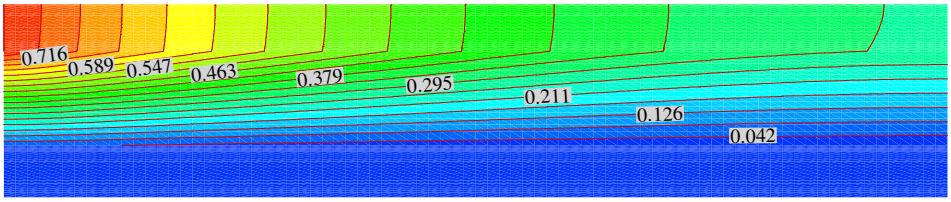

Figure 2. H_2 mass fraction distribution. Average current density: 0.90 A/cm^2.

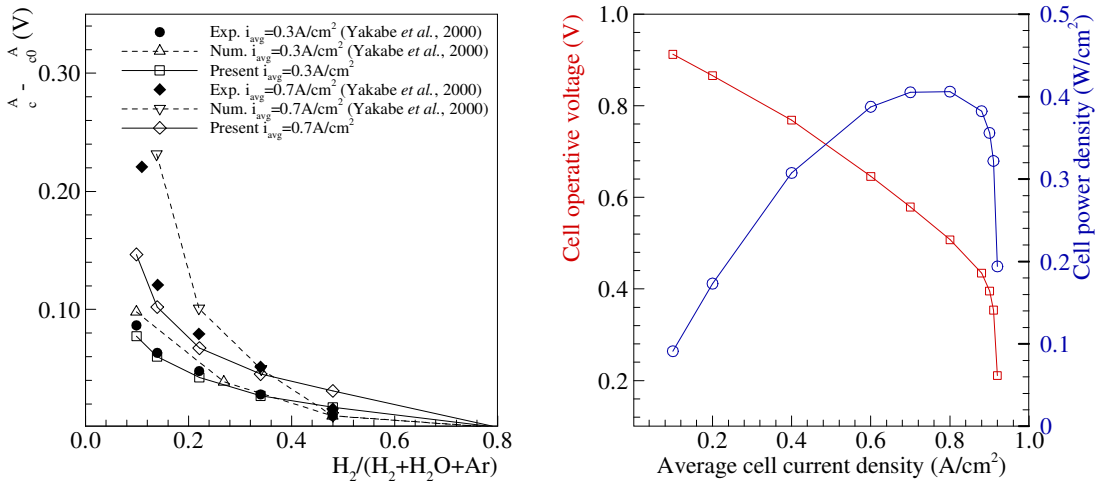

(a) (b)

Figure 3. (a) Concentration overpotentials at iavg=0.3 A/cm^2 and i_{avg}=0.7 A/cm^2 for an Argon diluted fuel; (b) Cell operative voltage and power density as a function of the average cell current density.

4. CONCLUSIONS

The local time step procedure and the stabilization limits imposed for the presence of the porous domain allows to obtain a very stable and fast AC-CBS algorithm, even in presence of very large source terms. The results obtained also showed a very good agreement with the experimental data available in the literature. Finally, the use of a matrix-free inversion algorithm offers promising expectations for the 3D solution of both single cell and multiple cells arranged in stack, also thanks to an easy and efficient parallelization.

REFERENCES

[1] P. Nithiarasu, An efficient artificial compressibility (AC) scheme based on split (CBS) method for incompressible flows. International Journal for Numerical Methods in Engineering;. 56: 1815-1845, 2003.

[2] F. Arpino, N. Massarotti, A. Mauro and P. Nithiarasu, Artificial Compressibility Based CBS Scheme for the Solution of the Generalized Porous Medium Model. Numerical Heat Transfer, Part B; 55: 196-218, 2009.

[3] F. Arpino, N. Massarotti, A. Mauro, A stability analysis for the AC-CBS algorithm for the solution of interface problems in presence of large source terms, Proceedings of the First International Conference on Computational Methods for Thermal Problems, ThermaComp2009, Napoli, Italy, September 8-10, 2009.

[4] F. Arpino, A. Carotenuto, N. Massarotti, P. Nithiarasu. A robust model and numerical approach for solving solid oxide fuel cell (SOFC) problems. International Journal of Numerical Methods for Heat and Fluid Flow; 18: 811-834, 2008.

[5] H. Yakabe, M. Hishinuma, M. Uratani, Y. Matsuzaki, and I. Yasuda, Evaluation and modeling of performance of anode-supported solid oxide fuel cell, Journal of Power Sources, Vol. 86 No. pp. 423-431, 2000.

First International Conference on Computational Methods for Thermal Problems
ThermaComp2009, September 8-10, 2009, Naples, Italy
N.Massarotti and P.Nithiarasu (Eds.)

Modeling and optimization of heat exchangers.

T. Koponen
Departement of Physics, University of Kuopio, P.O.B. 1627, FI-70211 Kuopio, Finland,
Tarmo.Koponen@uku.fi

T. Hämäläinen
Danfoss LPM Finland, P.O.B. 19, FI-79101 Leppävirta, Finland, Taija.Hamalainen@danfoss.com

J. Hämäläinen
Departement of Physics, University of Kuopio, P.O.B. 1627, FI-70211 Kuopio, Finland,
Jari.Hamalainen@uku.fi

ABSTRACT

Keywords: *Plate heat exchanger, CFD, Optimization, Innovative optimization.*

1. INTRODUCTION

In this paper an analysis of results obtained from a recently developed fast method to simulate and optimize chevron-type plate heat exchangers is presented. In this type of heat exchanger, corrugated plates are used to separate hot and cold fluids that flow in channels formed by layered plates and thus the design of the plate surfaces is a key issue. Previously Bobbili et al. [1] have been conducting experimental work with this type of exchanger and their results suggest that the pressure distributions are uneven. These results agree with previous analytically derived results [2]. In this study, we modeled a single heat exchanger channel in such manner that the end effects can be neglected and the efficiency can be extrapolated to simulate the efficiency of a whole heat exchanger (Fig. 1) which in this case consists of 30 plates. In this model, the flowing water was cold with initial temperature of 323K and the plates were at constant temperature of 335K. The results indicate that the model is

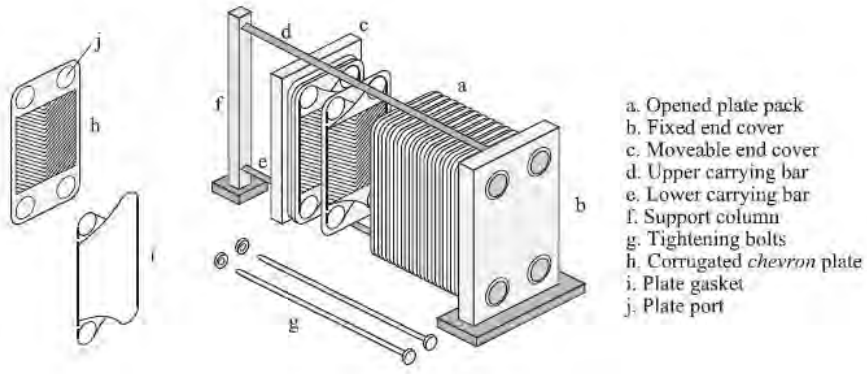

FIGURE 1. Structure of a typical chevron-type plate heat exchanger. [3]

2. Setup and methods

This work consists of over 1000 samples of simulated heat exchanger geometries which were simulated using Fluent CFD software and optimized using a custom genetic algorithm code. The CFD model applied was a depth-averaged model presented more thoroughly articles by Lyytikäinen et al. [2] The depth-averaging allows reducing the complexity of the heat and flow equations to 2D, but is still capable of taking into account the heat transfer to and from the plates so that the CFD simulations are reasonably accurate and can be ran much faster than full 3D-simulations. Our main focus in simulating and optimizing the heat exchangers has been in actively varying the corrugation angle, since its variation interval was greatest and in preliminary test runs it proved to have the most uniform parameter in sense of optimization. Therefore, our results are best illustrated when plotted as a temperature-pressure - diagrams, and the data points being colored by angle. Such a representation makes it is easy to see, how the pressure drop and temperature difference change with angle and how the deviation of the other two design variables, corrugation depth and length, affect the result. Corrugation angle is defined as zero when it is parallel to fluid flow. Corrugation lengths used varied from 6,5mm to 15mm and corrugation depths used were between 18mm and 32mm.

3. Results

In previous section we discussed that the corrugation angle is the best way to categorize our results. The figure 2 clearly shows that corrugation angle has a strong effect in pressure loss and heat transfer. The distribution of data points shows a clear correlation between pressure loss and corrugation angle since the flow encounters more resistance when the angle is bigger. Also, the distribution of data points in each set of angles demonstrates that outcome of the simulation is very sensitive to changes in the other two variables. The sensitivity can be seen from descriptive statistics as the data range increases with corrugation angle while the minimum values do not seem to change in any significant way even though the main data mass of the largest angle dataset is in the 3th and 4th quartile. In the other two sets there is significantly less dispersion.

The corrugation angle has an adverse effect on the stability of CFD simulations at values greater than 40°. This may lead to non-feasible results such as a temperature difference greater than 12K or a negative difference in pressure and such simulation outcomes need to be eliminated. The stability was determined by simulation convergence, since we had set the maximum number of iterations at 1000 to limit computation time.

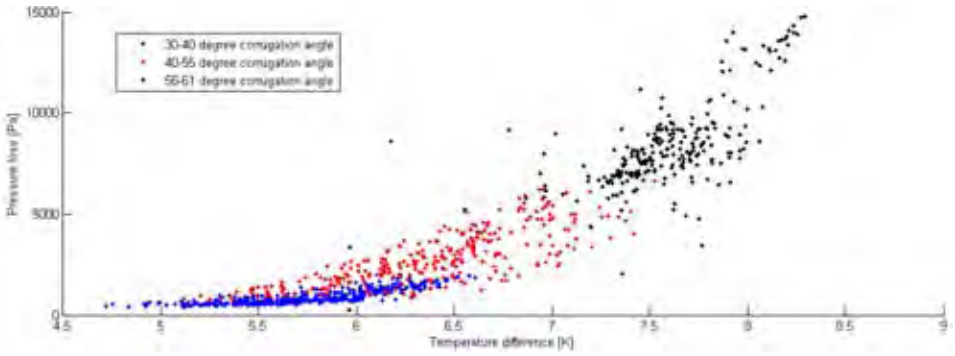

FIGURE 2. The results of our simulation data color-coded by corrugation angle.

4. Conclusions

A great amount of data has been aquired from CFD optimization on chevron-type heat exchangers. The results provided show that the model is working properly and it is producing feasible results with reasonable accuracy and will prove useful in future development of heat exchangers. It also agrees with previous experimental and theoretical results in such extent that it can be considered a reliable study that can provide consistent data for engineering purposes.

REFERENCES

[1] P.R. Bobbili, B. Sunden, S.K. Das, An experimental investigation of the port flow maldistribution in small and large plate package heat exchangers, *Applied Thermal Engineering*, 26, 1919-26, 2006.

[2] M. Lyytikäinen, T. Hämäläinen and J. Hämäläinen, A fast modelling tool for plate heat exchangers based on depth-averaged equations, *International Journal of Heat and Mass Transfer*, 2008.

[3] J.A.W. Gut, R. Fernandes, J.M. Pingo, C.C. Tadini, Thermal model validation of plate heat exchangers with generalized configurations, *Chemical Engineering Science*, 59, 4591-4600, 2004.

First International Conference on Computational Methods for Thermal Problems
ThermaComp2009, September 8-10, 2009, Naples, Italy
N.Massarotti and P.Nithiarasu (Eds.)

Optimization of two phase heat exchangers

Julio Pacio
Norwegian University of Science and Technology, Kolbjorn Hejes vei 1b, 7034, Trondheim,
julio.pacio@ntnu.no

Carlos Dorao
Norwegian University of Science and Technology, Kolbjorn Hejes vei 1b, 7034, Trondheim,
carlos.dorao@ntnu.no

ABSTRACT

Two phase hat exchangers are main components of large Liquefied Natural Gas (LNG) and air liquefaction plants. Therefore, an optimal design of the heat exchanger may determine the overall performance of the plant. The traditional approach for optimization of single phase heat exchangers is based on lumped parameters models (such as ϵ-NTU), avoiding solving for the temperature distribution, but this is not valid for the two phase case. A constant heat transfer coefficient (HTC) and pressure gradient are usually assumed over wide ranges, even though that it is well known this is not valid for two phase flow. In this work, the governing equations (mass, momentum and energy balances) are solved using the least squares method. Different correlations for HTC and pressure drop are studied along with different figures of merit for establishing optimization criteria.

Key Words: *Optimization, Heat Exchanger, Two Phase flow, Least Squares.*

1. INTRODUCTION

Liquefied Natural Gas (LNG), natural gas processing and CO_2 capture industries are rapidly growing worldwide. Since heat exchangers (HX) are main components in these industries, both in terms of capital costs and technical challenges, the development of energy efficient and environmentally friendly processes turn the attention focus on the HX modeling and design problem.

The mathematical modeling of a HX is based on mass, momentum and energy balances, and these governing differential equations are solved numerically. The traditional numerical approach for this problem is based on Finite Difference Method (FDM) or Finite Volume Method (FVM) formulations. Each stream is divided into nodes and the solution is approximated by a first order polynomial between the nodes. These methods are very simple to implement and are widely used for HX simulation [1,2]. Commercial FDM and FVM codes are available for computation fluid dynamics (CFD) analysis. However, generally hundreds of discretization points are required for a suitable solution, resulting in a high computational cost. Many times, the high computational costs typical of FDM and FVM cannot be avoided, even assuming the lost in accuracy, because the unconverged solution may present numerical oscillations and instabilities, and for this reason a large number of points are usually required [1,2,3].

The design, optimization and scaling up of new processes requires to take into account the most favorable and most disfavorable conditions in order to guaranty optimal performance and production under specifications. This means that lots of simulations are required for an optimal design. On this basis, as an effort for reducing the computational costs, a high order least squares (LS) formulation is presented in this work as a numerical alternative for this problem.

The LS method consists in a minimization problem approach, i.e. the best approximation available for the solution is searched within certain constraints. This approach has several advantages. It's very versatile and can be applied to lots of problems. It always leads to symmetric problems which result in positive definite systems that can be solved by traditional iterative solvers. And the convergence

rate of high order methods is much faster than FDM. This way, the computational time can be reduced considerably, while increasing the accuracy.

Heat transfer and pressure drop are modeled on the base of experimental data, i.e. they rely on different correlations. For two phase flow, these correlations can increase significantly the complexity of the governing equations. For this reason, heat transfer coefficient (HTC) and frictional pressure gradient are assumed to be constant over wide ranges. But now, with a more effective numerical solver available, more complex problems can be tackled. In this work, a complete model for heat transfer and pressure drop is performed on the base of the correlations available on literature [4].

The structure of this work is as follows. In section 2 the mathematical model and numerical method are introduced. A numerical examples is presented in section 3. Finally in section 4 the main conclusions of this work are discussed.

2. DESCRIPTION OF THE MODEL

The scope of this work is limited to the one–dimensional, steady–state and constant cross section case. With these assumptions, one dimensional mass, momentum and energy balance equations can be written for every stream i in the HX as follows:

$$\frac{\partial \dot{m}_i}{\partial z_i} = 0 \tag{1}$$

$$\frac{\partial p_i}{\partial z_i} = -\rho_i V_i \frac{\partial V_i}{\partial z_i} - \rho_i g - \frac{4\tau_{w_i}}{D_{h_i}} \tag{2}$$

$$\frac{\partial h_i}{\partial z_i} = -V_i \frac{\partial V_i}{\partial z_i} - g + \frac{4\tau_{w_i}}{\rho_i D_{h_i}} + \frac{1}{\dot{m}_i} \sum_{j=1}^{N_s} (UP)_{ij}(T_j - T_i) \tag{3}$$

where z_i is the flow direction of the stream i. The mass balance (eq. 1) simply means that the mass flow rate ($\dot{m}_i[kg/s]$) is constant along the stream. And this means that $\rho_i V_i = G_i$ is also constant.

The pressure gradient in the momentum equation (2) has three contributions: acceleration, gravity and friction, where p_i is the pressure $[Pa]$, ρ_i the density $[kg/m^3]$, V_i the velocity $[m/s]$, τ_w the shear stress $[Pa]$ and D_{h_i} the hydraulic diameter of the channel $[m]$. The frictional term is expected to be dominant and special attention in modeling the shear stress τ_w. Comparing different two–phase flow friction models (homogeneous, separated flow, drift flux) [5], and homogeneous models based on Moody friction factors was chosen, since it's simple to implement numerically.

The general formulation of the energy balance (eq. 3) in terms of specific enthalpy ($h_i[J/kg]$) allows us to work with either single or two–phase flow. The last terms on the right hand side represent the heat transfer between streams i and j at local temperatures $T_i$and T_j $[K]$, with N_s the total number of streams. UP is the overall heat transfer coefficient per unit length $[W/(mK)]$, and for steady–state analysis is computed on the base of thermal resistances.

In general, HX may have complex geometries, with multiple inlet and outlets for every stream. In this work, a two–streams tube–in–tube HX as shown in the scheme of figure 1 was studied.

For this configuration, the overall HTC can be computed as:

$$\frac{1}{UP} = \frac{1}{\pi d_o \alpha_h} + \frac{1}{\pi d_i \alpha_c} + \frac{log(d_o/d_i)}{2\pi\lambda_w} \tag{4}$$

where α_c and α_h are the *local* HTC on the cold and hot streams, and the last term represents the thermal resistance of the wall, being λ_w the wall thermal conductivity. A general three regions model was chosen for α_c and α_h: single phase–liquid, two phase and single phase–gas. For both single phase regions, a proper Dittus-Bolter correlation [6] was implemented. For two phase flow heat transfer, different models were used for the hot and cold streams. For condensation heat transfer a Shah correlation was used, while Chen model was chosen for boiling flow [4].

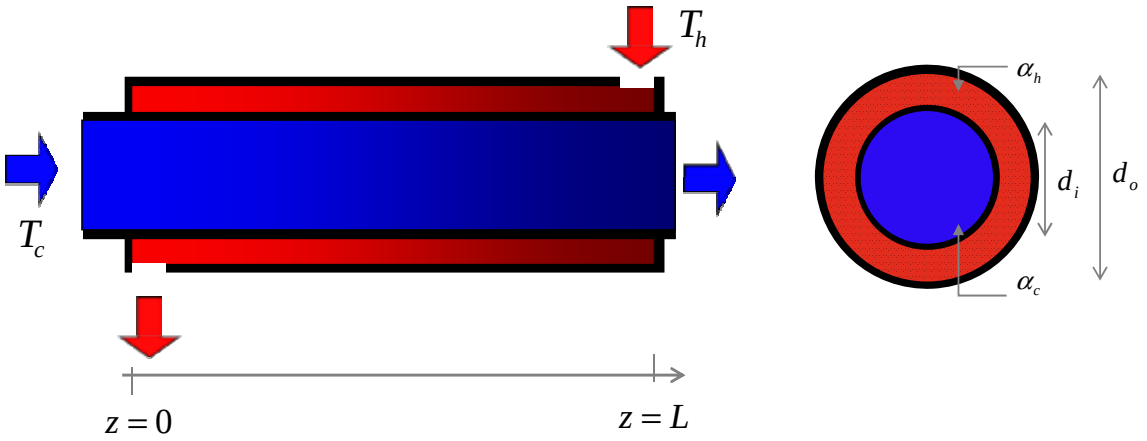

FIGURE 1. Schematic representation of a tube-in-tube heat exchanger

With all these considerations, eqs. 1 to 3 were solved numerically by a high order LS method for both streams , with proper inlet boundary conditions. The main advantage of LS is the spectral convergence that allows to improve the accuracy and the computational cost [7].

Several figure of merit can be defined for a two phase heat exchanger, depending on the application, such as capital cost, total weight, etc. In this work integral responses like total heat duty, pressure drop or pumping power will be studied.

3. RESULTS

Figure 2 shows the temperature distribution for parallel and counter flow HX. The hot fluid is butane at 2.4 bar, and the cold fluid is R134a at 6.2 bar (inlet pressures).

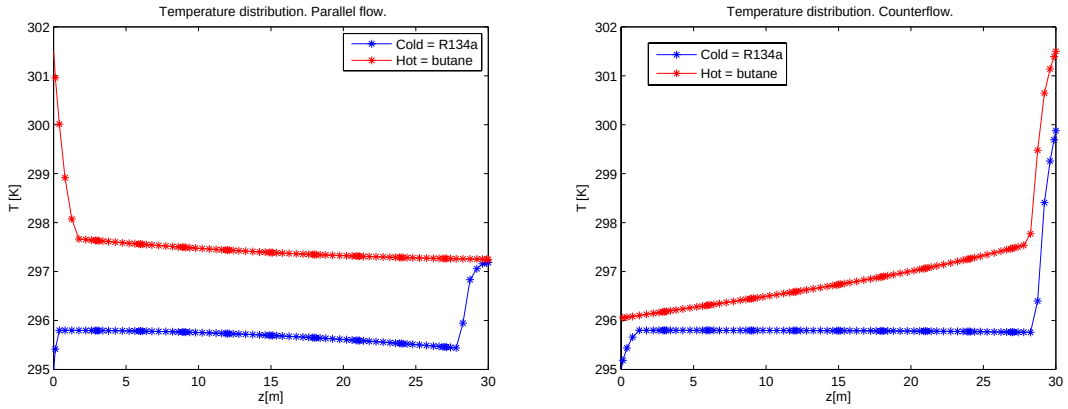

FIGURE 2. Temperature distribution for parallel and counter flow case

In figure 2 it can be seen that, for the counterflow there is a point in the core of the HX where the temperature difference is the smallest. This is known as the *pinch point*, and there are some optimization criteria related to this ΔT_{min}. But this escapes the scope of this work, which is limited to integral responses, like the ones mentioned above

This problem is influenced by lots of parameters. For given working fluid, all the physical properties are only dependent on the inlet pressures ($p_{c_{IN}}$ and $p_{h_{IN}}$) and temperatures ($T_{c_{IN}}$ and $T_{h_{IN}}$). The geometrical parameters involved are the diameters (d_i and d_o) and the length L. Finally, the mass flow

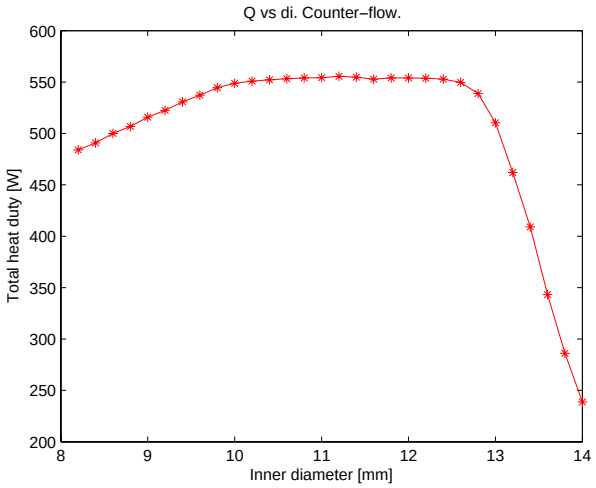

FIGURE 3. Schematic representation of a tube-in-tube heat exchanger

rates ($\dot{m}_c$ and $\dot{m}_h$) and the wall thickness t and thermal conductivity λ_w. This means that for a simple case like the tube–in–tube there are more than 10 relevant parameters.

The optimization process consists in searching the set of parameters that maximize or minimize some objective function. One objective function can be, for example, the total heat duty. The dependence of this objective function on some parameters is clear: it increases with the length L and decreases with the wall thickness t. With other parameters the analysis is not so straightforward. Figure 3 shows the evolution of the heat Q with the inner diameter d_i, showing a wide optimum.

4. CONCLUSIONS

The dependence of the objective functions on two phase HX (e.g. the total heat duty) on some parameters can be quite intricate. This is the motivation for solving the governing equation in stead of using simplified lumped–parameters models that disregard some effects. The use of a high order LS method allows us to do that with acceptable accuracy and at reasonable computational cost. Different integral responses (heat duty, pressure drop, pumping power) are studied in this work as objective functions.

5. REFERENCES

[1] Z. Li and M. Zheng, Development of a numerical model for the simulation of vertical U-tube ground heat exchangers, *Applied Thermal Engineering*, 29(5-6), 920-924, 2009.

[2] K.D.P. Nigam, M. Mridha, B. Faizee and V. Kumar, Numerical studies of a tube-in-tube helically coiled heat exchanger, *Chemical Engineering and Processing: Process Intensification*, 47 (12), 2287-2295, 2008

[3] J.B. Jensen and S. Skogestad, Optimal operation of a simple LNG process, *International Symposium on Advanced Control of Chemical Processes*, 2006

[4] K. Stephan, Heat transfer in Condensation and Boiling, Springer-Verlag, 1992

[5] P. B. Whalley, Boiling, Condensation and gas–liquid flow, Oxford Science Publications, Clarendon Press – Oxford, 1987

[6] F. P. Incropera and D.P. Dewitt, Fundamentals of Heat and Mass Transfer Fourth Edition, John Wiley & Sons, Inc. 1996

[7] B. De Maerschalc and M.I. Gerritsma, Least-squares spectral element method for non-linear hyperbolic differential equations, *CJournal of Computational and Applied Mathematics*, 215 (2), 357-367, 2008

First International Conference on Computational Methods for Thermal Problems
ThermaComp2009, September 8-10, 2009, Napoli, Italy
N.Massarotti and P.Nithiarasu (Eds.)

NUMERICAL ANALYSIS OF THE DYNAMIC THERMAL BEHAVIOR OF RF BIPOLAR TRANSISTORS

Salvatore Russo, Vincenzo d'Alessandro, Niccolò Rinaldi
Department of Biomedics, Electronics and Telecommunications Engineering, University of Naples Federico II, via Claudio 21, 80125 Naples, Italy, email: salvatore.russo3@unina.it

Massimiliano de Magistris
Department of Electrical Engineering, University of Naples Federico II, via Claudio 21, 80125 Naples, Italy, email: m.demagistris@unina.it

Luigi La Spina, Lis K. Nanver
Laboratory of Electronic Components, Technology & Materials (ECTM), Delft Institute of Microsystems and Nanoelectronics (DIMES), Delft University of Technology, P.O. Box 5053, Feldmannweg 17, 2600 GB Delft, The Netherlands, email: l.laspina@tudelft.nl

ABSTRACT

A 3-D FEM simulator is calibrated to accurately predict the transient thermal behavior of RF transistors. Besides, an *in-house* code is developed to extract an optimized Foster network for the description of the thermal impedance of the devices, thus allowing the analysis of the thermal response in the frequency domain. Both tools are successfully employed to study the thermal dynamics of silicon-on-glass BJTs.

Key Words: *Bipolar Junction Transistors (BJTs), Finite-Element Method (FEM), Heat Transfer, Silicon-On-Glass (SOG), Thermal Impedance, Thermal Networks, Thermal Resistance.*

1. INTRODUCTION

The semiconductor industry is constantly aiming to improve the performance of high-speed radio-frequency (RF) devices. Aggressive isolation schemes, which rely on oxide- or even air-filled trenches, often combined with silicon-on-insulator substrates, are increasingly exploited to reduce parasitics and minimize electrical interactions with neighboring devices/circuits and cross-talk via substrate. In this scenario, the silicon-on-glass (SOG) technology represents the ultimate solution in terms of dielectric isolation: the active area is located in a small silicon island entirely enclosed by insulating layers, and a high-resistivity glass substrate is employed to annihilate cross-talk effects [1]. Unfortunately, due to the dramatically low thermal conductivities of the insulating materials, even low-power RF transistors are often affected by considerably high operating temperatures that lead to performance degradation and hamper the realization of reliable integrated circuits (e.g., [2]). As a consequence, thermally optimizing electronic devices/circuit at the design stage has become of utmost importance, and predicting the temperature of the transistors for an assigned dissipated power under both steady-state and dynamic conditions is essential. Analytical approaches to accomplish this task would lead to computationally inexpensive formulations; however, they are viable only for oversimplified device geometries as e.g., devices embedded in conventional bulk substrates. Thus, effective numerical strategies are to be sought.

The contribution of this work is twofold. First, a tuning strategy is applied to enable the finite-element-method (FEM) Comsol package [3] to perform reliable – yet not highly onerous from the computational standpoint – 3-D thermal transient simulations of state-of-the-art bipolar transistors, which are massively employed in communication systems. As a result, the software can be exploited to provide an in-depth insight into the heat propagation process, as well as to predict – prior to fabrication – the influence of technological solutions devised to counteract the electrothermal feedback. Second, an *in-house* routine is developed to extract the equivalent (thermal) resistances and capacitances of a Foster network to describe the thermal behavior of the devices in the frequency domain. The tools are adopted to quantify the influence of design parameters and the cooling action of on-wafer heatspreaders on the dynamic behavior of SOG bipolar junction transistors (BJTs), although they can be in principle exploited for any device category.

2. FEM SIMULATION STRATEGY

The simulation strategy can be described as follows.

In-house routines were conceived and developed to automatically (and precisely) build the mesh representing the SOG BJTs to be thermally analyzed within the software environment starting from the layout file and information concerning the thicknesses of the layers. A suitable optimization of the mesh-building parameters (i.e., the so-called *scaling factors*) allowed overcoming the meshing issues due to the concurrent presence of extremely thin layers with different material properties.

The measurements of SOG BJTs were performed on wafers of 10 cm in diameter, where the heat can spread over a volume much larger than that corresponding to a single transistor; several simulations were therefore carried out in order to identify the minimum area to achieve an acceptable degree of accuracy without accounting for a considerably high number of mesh elements. It was found that an area of 1000×1000 μm^2 is enough to guarantee satisfactory results (see Figure 1). Further area enlargements only increase the CPU/memory requirements without sensibly modifying the calculated temperature field over the BJTs under analysis.

Due to the inherent symmetry of the SOG devices, only one quarter of each domain was simulated (see Figures 1 and 2) and the missing portions were virtually recreated by imposing adiabatic conditions (i.e., zero outgoing heat flux) over the planes of symmetry, thereby reducing the number of elements to be considered.

Further minimization of the required computational resources was achieved by suitably employing automated grid refinement strategies, which allow obtaining finely-meshed regions only where high temperature gradients are more likely to occur (see Figure 3).

Note that the base and emitter lines were accurately defined within the simulator environment (see the zoom-in of Figure 2) to correctly predict the thermal behavior under transient conditions for devices provided with an aluminum nitride layer deposited on the front-wafer, which operates as a heatspreader. The metal tracks of emitter and base represent indeed a fundamental path for the heat to be quickly transferred from the active region to the AlN layer.

A boundary condition (b.c.) of the 3rd kind was imposed over the top surface of the bondpads to account for the heat flow through the probes contacted to the device during experiments. This b.c. relates the outgoing heat flux to the temperature field on the pads by a parameter known as *heat transfer coefficient*, the value of which was set to 5 W/cm^2K.

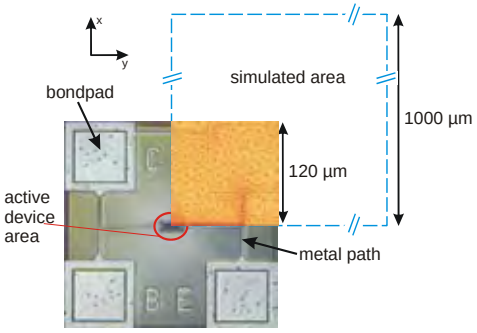

FIGURE 1. Top-view (microscope image) of an SOG BJT along with the representation (not to scale) of the domain actually simulated.

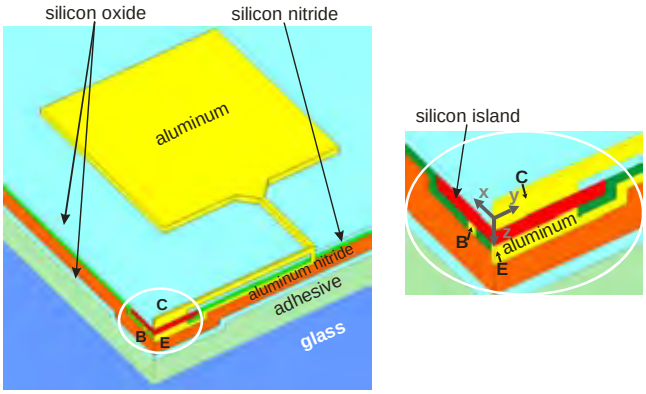

FIGURE 2. Details of the structure of an SOG BJT provided with an AlN heatspreader and zoom-in of the silicon island (not to scale).

A typical 3-D mesh comprises 2×10^5 elements. A steady-state solution (i.e., the static temperature field in any point of the overall domain) is evaluated in about 1 minute. The calculation of the whole transient response to a unitary power step requires slightly more than 1 hour by using a computer equipped with a quad-core processor at 2.9 GHz and an 8 GB RAM.

As concerns the proper setting of the material parameters (i.e., thermal conductivity and specific heat) involved, a calibration procedure was adopted that can be explained as follows.

First, a reference structure without any heatspreaders was numerically simulated by tuning the – rather uncertain – specific heats of silicon nitride, glue, and glass so as to guarantee the best fit with the experimental thermal impedance (namely, the transient temperature increase over ambient normalized to the dissipated power) over the whole time range considered. By converse, all other parameters were taken from the literature (further details can be found in [4]).

Subsequently, an SOG BJT provided with a 2-µm-thick polycrystalline AlN layer on the front-wafer was simulated, and the thermal conductivity and specific heat of AlN was adjusted so as to favorably match the thermal impedance measured on the same AlN-cooled transistor. As concerns the thermal conductivity, the best fitting was achieved with a value of 17 W/mK.

As can be observed in Figure 4, the simulated and measured thermal impedances versus time excellently match for devices with and without heatspreaders.

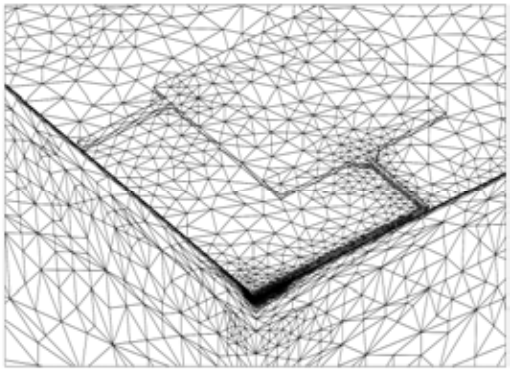

FIGURE 3. Details of the optimized mesh adopted for a typical SOG BJT.

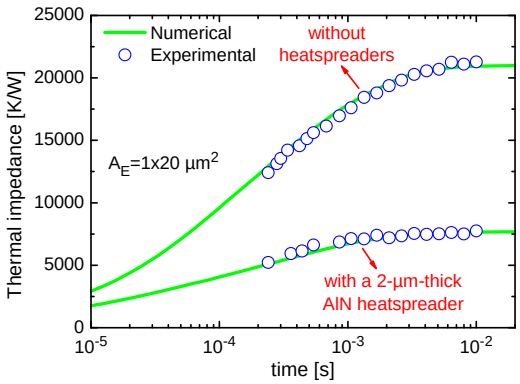

FIGURE 4. Thermal impedance versus time for devices with and without heatspreaders as evaluated both experimentally (symbols) and numerically (solid lines). The emitter area A_E of the devices under analysis amounts to 1×20 µm^2.

3. NETWORK OPIMIZATION

As mentioned earlier in this work, an *in-house* routine was developed to obtain the minimum number of RC-ports (i.e., the poles of an equivalent transfer function) so as to describe an either measured or numerical thermal impedance versus time with a prescribed degree of accuracy. The code operates as follows. First, some Foster networks employing a given number of elementary RC-ports are determined via various approaches (e.g., [5]). Afterward, the curve associated with the minimum error is identified. The attained values of the equivalent resistances and capacitances are then further optimized through a custom code relying on a *least-square* algorithm. Throughout this work, the maximum error allowed for the identification process was set to 3%. It was found that 5-pole Foster networks guarantee errors sensibly smaller than 3% for any of the SOG devices under analysis. The optimized Foster network was employed to extend the analysis of the SOG BJTs in the frequency domain.

4. RESULTS AND DISCUSSION

Let us first recall that the rise time is defined as the time period separating 10% and 90% of the steady-state value of the thermal impedance (i.e., the self-heating thermal resistance), thereby describing the speed of the system to (thermally) respond to a power step.

Figure 5 shows the effect of varying the area of the emitter stripe for a prescribed aspect ratio (i.e., an assigned shape) for devices with and without a 2-µm-thick AlN layer integrated on the front-wafer. The analysis was carried out through the approach described in Section 2 by keeping constant the spacing between the edges of the emitter stripe and the trench sidewalls. An inspection of the figure

reveals that the thermal resistance exhibits a 35% reduction when enlarging the emitter area from 20 μm^2 to 180 μm^2 (i.e., increasing the area of the silicon island from 300 μm^2 to 910 μm^2); as far as the rise time is concerned, an increase of 27% is obtained meaning that the system is slower from a thermal point of view.

It is noteworthy that the calibrated numerical tool can be also adopted to detect temperature maps over chosen device regions. This can be particularly useful to effortlessly explore the influence of alternative materials on the thermal behavior of the transistors, and quantify the thermal coupling between elementary devices integrated in the same chip, which might play a decisive role in the electrothermal behavior of devices and circuits.

The magnitude of the thermal impedance versus frequency, as evaluated through the approach described in Section 3, is reported in Figure 6 by varying the emitter area for devices with and without an AlN heatspreader. It is shown that the thermal cut-off frequency (i.e., the frequency at which the magnitude reduces by 30% with respect to the maximum value) decreases with enlarging the emitter area (and therefore the area of the silicon island), while slightly increasing by employing an AlN heatspreader for the same area. Lastly, it is to be underlined that the thermal cut-off frequencies are in the order of hundreds of Hz, while the electrical ones are equal to a few tens of GHz; as a consequence, thermal issues are not critical for small signal operation of SOG BJTs.

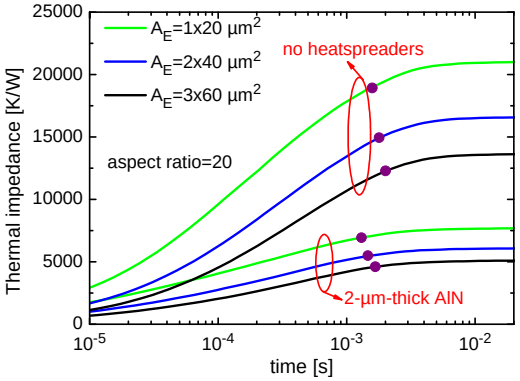

FIGURE 5. Simulated thermal impedance versus time by varying the emitter area and keeping the aspect ratio equal to 20. The points where the thermal impedance reaches the 90% of the steady-state value are identified with dots.

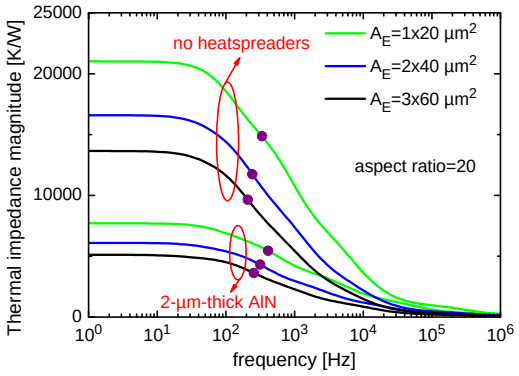

FIGURE 6. Thermal impedance magnitude versus frequency as evaluated through the approach described in Section 3 by varying emitter area for devices with and without an AlN layer acting as a heatspreader. Also identified are the magnitudes corresponding to the cut-off frequencies.

REFERENCES

[1] L. K. Nanver *et al.*, "A back-wafer contacted silicon-on-glass integrated bipolar process – Part I: The conflict electrical versus thermal isolation," *IEEE Transactions on Electron Devices*, vol. 51, no. 1, pp. 42-50, 2004.

[2] N. Rinaldi *et al.*, "Analysis of the bipolar current mirror including electrothermal and avalanche effects," *IEEE Transactions on Electron Devices*, vol. 56, no. 6, pp. 1309-1321, 2009.

[3] Comsol Multiphysics 3.5, *User's Guide*, Comsol AB, 2008.

[4] S. Russo *et al.*, "Thermal transient behavior of silicon-on-glass BJTs," *Proc. IEEE EuroSime*, 2009, pp. 93-100.

[5] Z. Jakopović *et al.*, "Identification of thermal equivalent – Circuit parameters for semiconductors," *Proc. IEEE Workshop on Computers in Power Electronics*, 1990, pp. 251-260.

First International Conference on Computational Methods for Thermal Problems
ThermaComp2009, September 8-10, 2009, Napoli, Italy
N.Massarotti and P.Nithiarasu (Eds.)

FEM SIMULATION OF THERMAL BEHAVIOR OF A POLY-Si PV CELL AND DEFECTS CHARACTERIZATION

G. Acciani **O. Falcone** **S. Vergura**

POLITECNICO DI BARI, st. E.Orabona 4, 70125, Bari, Italy

acciani@poliba.it falcone@deemail.poliba.it vergura@deemail.poliba.it

ABSTRACT

The paper introduces the issue of the numerical simulation of the thermal behaviour of a poly-silicon PV cell and the typical defects that can affect the device. These defects are modelled by means of Finite Element Method (FEM) and implemented in Comsol Multiphysics environment in order to analyze the temperature distribution in the whole defected PV cell, because abnormal temperatures reduce the PV cell efficiency. The attention is focused on two specific defects: linear edge shunt and hole. Both defects can be classified as process induced. Simulation results are compared with the thermo-grams of real cases and the goodness of the models is confirmed.

Key Words: *Heat Transfer, Finite Elements, PV cell, Typical Defects.*

1. INTRODUCTION

The study in depth of the dependence on temperature of the performances of PV devices is to be considered of critical importance as the abnormal increasing of the temperature of the whole cell as well as of some area strongly reduces the cell performances. Electrical parameters, such as voltage and current, of solar devices are strongly influenced by temperature increasing (Figure 1 a). Also the efficiency and the output power of the PV cell are strongly influenced by temperature variations as well as the fill factor FF (Figure 1 b) [1].

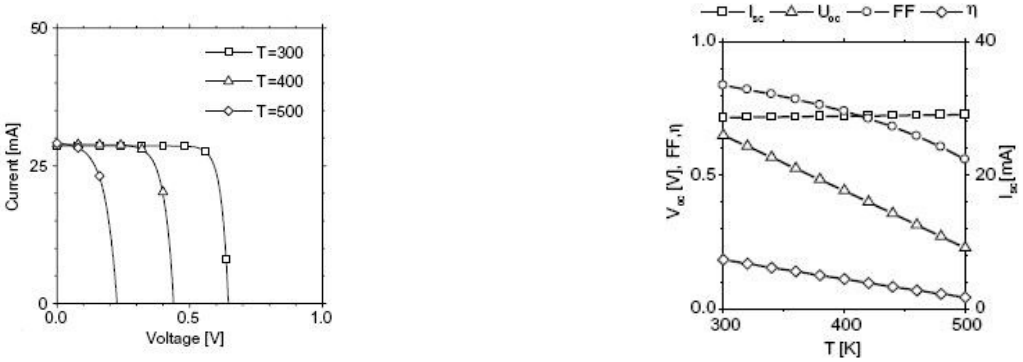

a) b)

Figure 1. Dependence of current – voltage curves a) and parameters of solar cell upon the temperature.

From Figure 1 it is possible to note as while the V_{OC} strongly decreases when the temperature increases, the I_{SC} current shows only slightly variation [2].
This aspect highlights the critical influence of the defects on the cell performances. Defects can be considered as parasitical resistances connected to the photovoltaic cell; their presence causes an abnormal increasing of the cell temperature with a clear degradation of the device performances.

At the state of the art possible shunts in PV cells are classified in nine different typologies. Shunts are defined resistive like if they explain a current – voltage characteristic resistive-like or linear. In this case they are available in both polarization conditions during the lock-in thermography. If they appear only under one polarization condition (forward or reverse), they will show a nonlinear I-V curve: in this case the shunt is said to be diode-like.
From a physical point of view, shunts can be grouped in two categories: process induced and material induced. As this paper proposes the models of two process induced shunts (linear edge shunt and hole), a brief description of them follows. The former one is due to an incorrect edge insulation of PV device and is localizable in monocrystalline as well as in polycristalline cells. The presence of such a shunt allows a low resistivity path develops between top and bottom side of the cell acting as short circuit on the lateral side of the cell. The latter one can be produced by laser cutting. During screen printing, some metal paste may penetrate the hole and, after firing, strong linear shunts can occur [3]. Figure 2 reports the lock-in thermogram in both forward and reverse bias: the shunts generating the hot areas, available in both polarization conditions, are resistive-like.

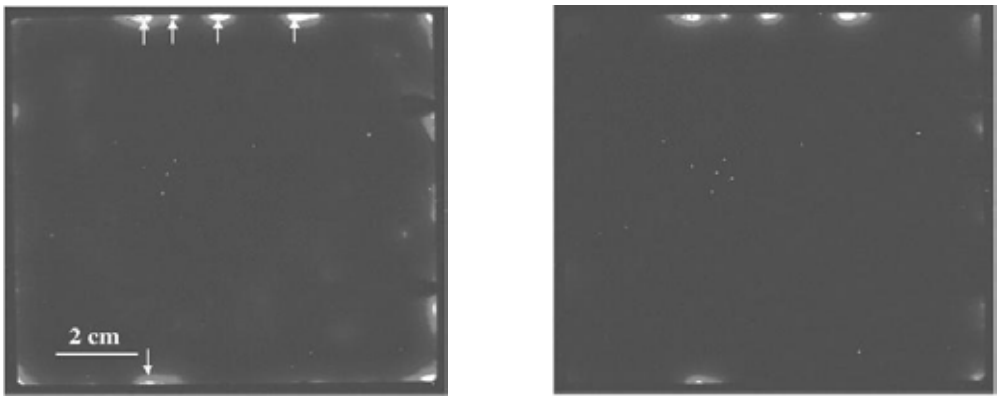

(a) (b)

FIGURE 2. Figure 2: (a) lock-in thermo-gram at +0.5 V, (b) lock-in thermo-gram at -0.5 V. Hot spots focused with arrows, visible in both figures, are linear edge shunt.

The paper proposes a simulated analysis of the described shunts for a poly-Silicon cell to highlight the thermal behavior of the defected area with respect to the remaining cell. The shunts can be classified as negligible, light or strong depending from the maximum value of the temperature.
The paper is organized as follows: Section 2 introduces the features of the modelled defects, while Section 3 proposes the simulation results for all considered cases. Section 4 reports conclusions and future works.

2. PROPOSED MODEL

As told, shunts can be grouped in two categories according to their I-V characteristic: the shunt is said resistive-like if it is present independently from the polarity of the supply voltage, otherwise it is said diode-like [4]. The FEM model of the Poly-Si PV cell has been implemented trough CAD tools available in Comsol's environment, according to the geometrical features characterizing the well operating model of a commercial monocrystalline PV cell explained in [5]. From a physical point of view the monocrystalline layer has been substituted by a Poly-Si layer while the other layers have been modelled as in [5], i.e. top and bottom electrodes modelled as silver and support oxide layer composed by TiO_2. All thermal and/electrical features of the mentioned materials are available in Comsol's Material Library (Table 1).

Material	Ag	Poly-Si	TiO_2
k	429	34	k(T[1/K])[W/(m*K)]
	10500	2320	rho(T[1/K])[kg/m^3]
C_P	235	678	C(T[1/K])[J/(kg*K)]

Table 1. Thermal parameters of each layer.

Note that in the case of the oxide layer all parameters are expressed by an equation available in Comsol's material libraries as a temperature function.
The linear edge shunt has been modelled as a short circuit on one side of the cell; geometrical dimensions of the short-circuit are 1cm×250 m (length×height), while the electrical conductivity $_{el}$ has been set to different values. This aspect allows simulating the behaviour of different hot spots corresponding to the implemented defect. Figure 3 shows the short-circuit (in blue colour) superimposed on a well operating PV cell model.

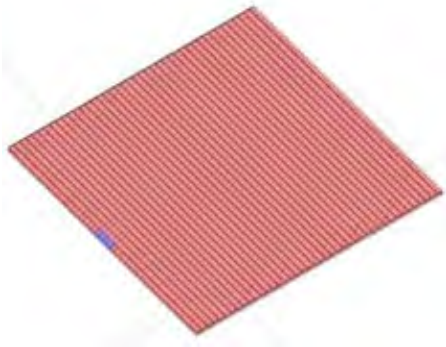

FIGURE 3. Model of a linear edge shunt applied on a well operating PV cell.

Instead, the hole has been modelled as a 2 mm-diameter cylinder constituted by metal paste and inserted into a well-operating PV cell structure [5] with the poly-Si layer. Figure 4 shows the defect implemented into the well operating cell structure. The conductivity value $_{el}$, for the low resistivity path due to the hole filled of metal paste, has been set to 10^3 S/m.

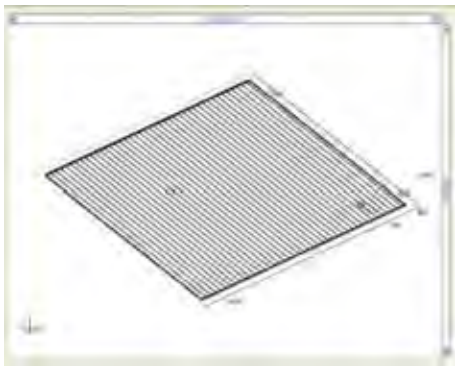

FIGURE 4. Structure of a PV cell with hole.

3. RESULTS

All simulations have been run using multiphysics simulation tools available in Comsol's environment. The complexity of the developed model arises from the high number of degrees of freedom to be solved. The solution of a FEM model requires the subdivision of the continuous system into a finite number of sub domains. This aspect is possible through the mesh generation step. In the proposed model the mesh size has been set up to *very coarse*. The resulting mesh is composed by 356.982 elements. Reducing the mesh elements size, memory overflow happens. Two different typologies of solvers can be used, all available in Comsol Multiphysics environment: direct and iterative ones. The choice depends on the available computational power: if a great computational power is available direct solvers are preferred. As a multiprocessor architecture has been used, PARDISO (sPARse DIrect Solver) solver, that improves factoring process using Level-3 BLAS supernode technique, has been chosen, becaues it results the most efficient solver for these applications [6]. Using other solvers, such as UMFPACK (Unsymmetric multifrontal sparse LU factorization package) based on LU factoring, or SPOOLES (SParse Object Oriented Linear Equation Solver) used to solve both symmetric and asymmetric systems, very long simulation times are needed. The TAUCS solver algorithm that is based on Cholesky factoring cannot be used as it needs the coefficients matrix of the system to be symmetric. For the proposed poly-Si PV cell model the number of degrees of freedom is 570.578. To complete the model definition the set up of the boundary conditions is required. According to the analysis to be developed, different boundary conditions can be set up. In the case of the thermal analysis, which has been conducted using the Comsol's Heat Transfer Module, a Neuman's boundary condition, has been set up: so the value of the incoming flux is fixed. According to NOCT (Nominal Operative Cell Temperature) this value has been fixed to 800 W/m^2. The model of total flux on the cell implemented in Comsol Multhiphysics is the following:

$$-n \bullet q = q_0 + h(T_{inf} - T) + \sigma\varepsilon(T_{env}^4 - T^4) \qquad (1)$$

where q_0 is the incoming flux, while h is the heat transfer coefficient, whose value depends on geometrical features of the model and has been evaluatedt equal to 11 W/ (m^{2}K) for this application. Temperatures values T_{inf} e T_{env} are set equal to 20 °C, is the Stefan-Boltzmann constant, while the correct value of the emissivity is to be set up for each material used into the model. The emissivity values are reported in Table 2.

Material	Ag	Poly-Si	TiO_2
	0.01	0.85	0.9

Table 2. Emissivity value of each layer.

Simulations have been run using steady state analysis. Table 3 reports simulation times depending on the used solver.

Solver	Simulation time (s)
UMFPACK	442
SPOOLES	1807
PARDISO	240
TAUCS	-

Table 3. Simulation time.

As expected TAUCS cannot solve the simulation. This is the reason of the empty field in the table. Figure 5 shows the simulation results for the well operating poly-Si PV cell.

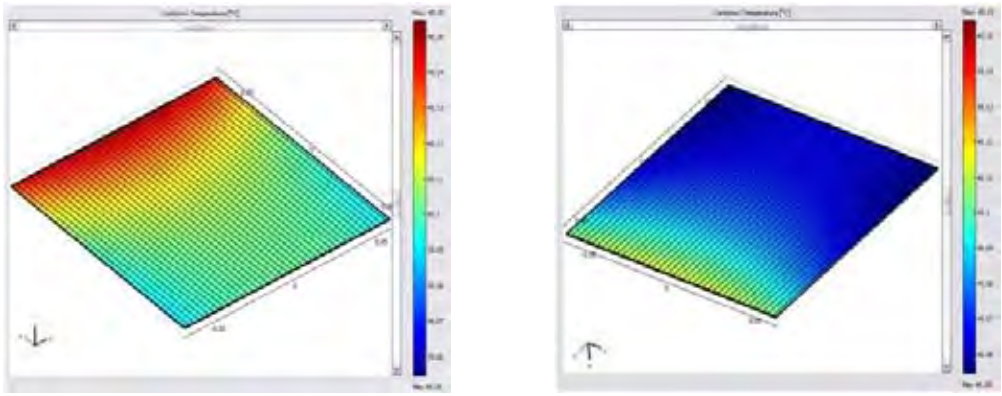

(a) (b)

FIGURE 5. Temperature distribution on the poly-Si PV cell. (a) upper surface, (b) lower face.

The value of the temperature reaches 45.15°C and it agrees with NOCT of commercial PV cell. In fact the NOCT specifications of a commercial Poly-Si photovoltaic cell with an incoming flux of 800 W/m^2, a wind speed of 1 m/s and an environment starting temperature of 20 °C, the cell has to reaches a temperature of 45 °C with a tolerance of 2°C. The temperature difference, even if small, across upper and lower faces of the cell depends on the value of incoming flux q_0 that has been set on both faces. To simulate a real operating situation the incoming flux of the lower has been set up to 0 W/m^2. Figure 6 (a) (b) and (c) shows the temperature distribution of a PV cell, when different linear edge shunts occur. From a numerical point of view the number of mesh elements that have been generated using a very coarse mesh size is of 365.181 that correspond to 1.163.498 degrees of freedom to be solved. The reason of this large number of degrees of freedom to be solved comes from the multiphysical analysis that has been conducted on this model. To develop such a simulation two Comsol's modules are to be used at the same time: Heat Transfer and AC/DC. In this way there are two groups of equations to be solved. All the simulations have been run using PARDISO solver and have been solved in about 850 seconds. To simulate different hot spots, different values of the electrical conductivity of the modelled low resistivity walk across cell electrodes have been considered. Hot spots connected with possible shunts can be defined as negligible, light or strong according to the temperature increasing of the defected area with respect to the remaining cell. Setting the value of $_{el}$ equal to 2 x 10^4 S/m a strong hot spot is simulated (Figure 6 (a)), while the behaviour simulated in the figures 6 (b) and (c) corresponds to electrical conductivity values set to 6 x 10^3 S/m and 4 x 10^3 S/m, respectively.

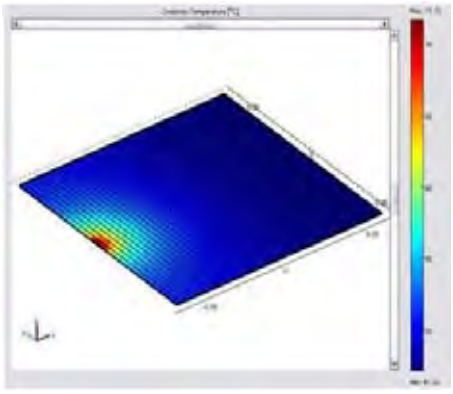

(a)

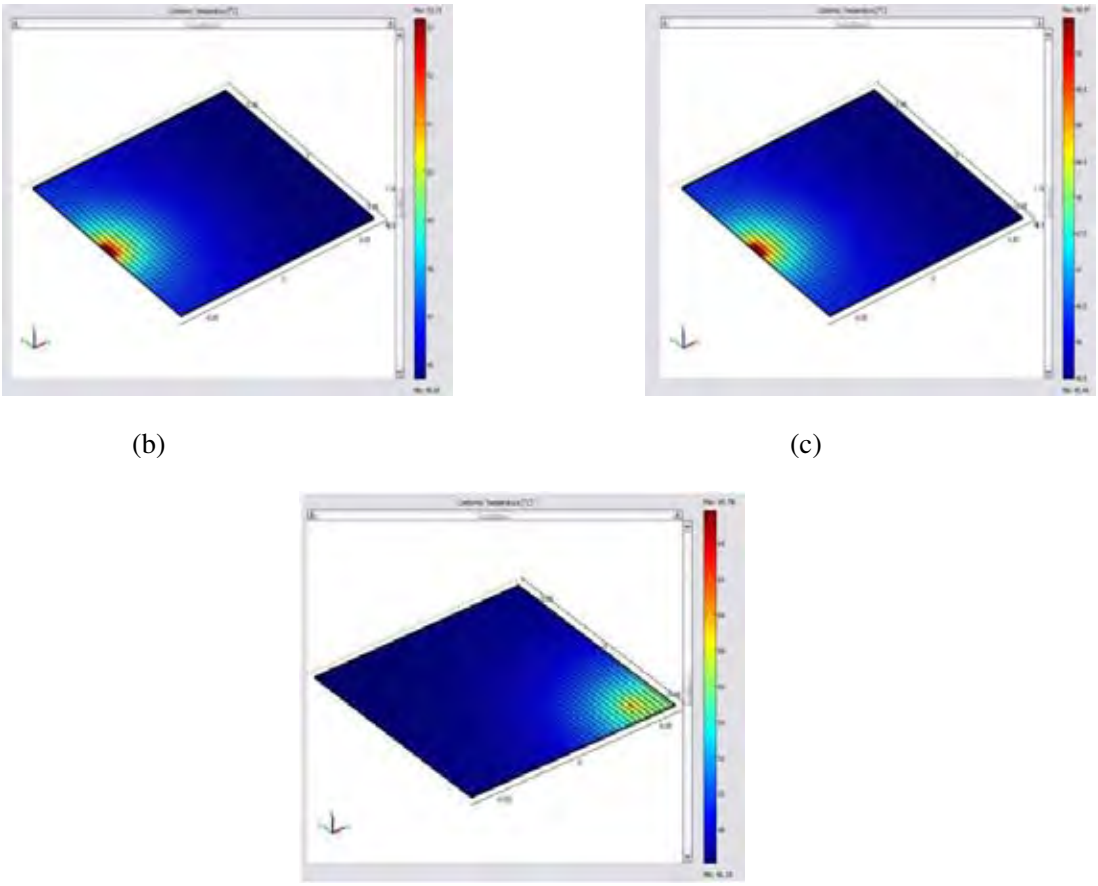

(b) (c)

(d)

FIGURE 6. Temperature distribution for defected cell: (a) strong hot spot connected to the linear edge shunt, (b) light hot spot, (c) negligible hot spot, (d) hot spot connected with the hole presence.

Figure 6 (d) shows thermal diagram for a PV cell with a hole-type defect. In this case the degrees of freedom to be solved is 1.199.274. This simulation has been completed, using PARDISO solver, in about 900 seconds. Observing the temperature distribution of the defected cells (Figure 6), some considerations can be done:

a) the temperature of the hot spot for the linear edge shunt is 71.71 °C, while the remaining part of the cell shows a temperature of 47.16 °C. As the temperature difference between the two regions is over than 18°C, this hot spot is classified as strong and the power loss is about 8%.

b) the temperature of the defected area reaches the value of 53.15 °C. In this case the hot spot is said light and the power loss concerning a defect like this is of about 4%

c) the hot spot shows a temperature difference with respect to the whole cell of about 5 °C. In fact the temperature of the defected area in this case is of 50.47 °C while the remaining cell reaches the temperature of 45.48 °C This hot spot can be considered negligible and the power loss is less than 2%.

d) the temperature of the hot spot for the hole is 65.786 °C, respect to the 46.109 °C of the remaining cell. This typology of hot spot is always strong [4].

The following Table 4 summarizes the comparison between the temperature increasing of some area of the cell and the power decreasing when abnormal heating occurs.

ΔT(increase)	ΔP(decrease)
< 5°C	< 2%
10°C	4%
18°C	8%

Table 4. Power decreasing vs. temperature increasing in a solar cell.

The temperature difference between defected and sound areas of poly-Si PV cell, for both the defect typologies, is higher than the temperature difference for monocrystalline PV cell [7]. Simulation results agree with the temperature values of hot spots revealable through infrared analysis, as explained in [8]. Then, the goodness of the model is confirmed and it can be used for an in-depth investigation of other typologies of PV cell defects.

4. CONCLUSIONS

The proposed model of poly-Si PV-cell has allowed to highlight that the same specific defects (linear edge shunt and hole) produce different thermal behaviour for poly-Si PV-cell with respect to the monocrystalline one. Future works will be oriented to the implementation in Comsol of other typologies of defects in order to evaluate the thermal behaviour of poly-Si PV-cell as well as of monocrystalline one.

REFERENCES

[1] D. Menes-Rodrìguez, P.P. Horley, J. Gonzàlez-Hernàndez, Y.V. Vorobiev, P.N. Gorley, Photovoltaic solar cell performance at elevated temperatures, *Solar Energy*, 78, 243-250, 2005.

[2] E. Skoplaki, J.A. Palyvos, On the temperature dependence of photovoltaic module electrical performances: A review of efficiency/power correlations, *Solar Energy*, 83, 614-624, 2009.

[3] O. Breitenstein, M. Langenkamp, O. Lang, A. Schirrmacher, Shunts due to laser scribing of solar cell evaluated by highly sensitive lock-in thermography, *Solar Energy and Solar Cells*, 55-62, 2001.

[4] O. Breitenstein, JP Rakotoniaina, M.H. Al Rifai, M. Werner, Shunt type in crystalline solar cells, *Progress in photovoltaics research and application*, 12, 532, 2004.

[5] S. Vergura, G. Acciani, O. Falcone, "*3-D PV-cell Model by means of FEM*", IEEE-ICCEP, 35-40, Capri, Italy, 9th -11th June 2009.

[6] O. Schenk, K. Gärtner, and W. Fichtner, *"Efficient sparse LU factorization with left – right looking strategy on shared memory multiprocessors"*, BIT, 40(1), 158 – 176, 2000.

[7] S. Vergura, G. Acciani, O. Falcone, "*Modeling defects of PV-cells by means of FEM*", IEEE-ICCEP, 52-56, Capri, Italy, 9th -11th June 2009.

[8] O. Breitenstein, JP Rakotoniaina, M.H. Al Rifai, Quantitative evaluation of shunts in solarcells by lock-in thermography, *Progress in photovoltaics research and application*, 11, 515-526, 2003.

First International Conference on Computational Methods for Thermal Problems
ThermaComp2009, September 8-10, 2009, Napoli, Italy
N.Massarotti and P.Nithiarasu (Eds.)

RADIATIVE HEATING AND JOULE'S EFFECT HEATING OF A SCALED PV-CELL MODEL

G. Acciani **O. Falcone** **S. Vergura**

POLITECNICO DI BARI, st. E.Orabona 4, 70125, Bari, Italy

acciani@poliba.it falcone@deemail.poliba.it vergura@deemail.poliba.it

ABSTRACT

The paper introduces the issue of simulating the thermal behaviour of a monocrystalline PV-cell under different heating sources. The models have been developed by means of Finite Element Method (FEM) and implemented in Comsol Multiphysics environment. The attention has been focused on three specific situations: cell under solar radiation, cell in conduction state (the only heat source is the current flowing between the electrodes), cell exposed to both the effects. Simulations confirm the goodness of the implemented model for simulating a real well operating PV cell.

Key Words: *PV-cell, Solar Radiation, Joule's Effect, FEM.*

1. INTRODUCTION

The temperature distribution of a photovoltaic cell depends on two factors: the solar radiation and the Joule's effect. The thermal and thermo-electrical simulations for the PV device in different operating conditions let to show the lower heating due to the Joule's effect with respect to the heating due to the solar radiation. In this paper the thermal behaviour of a well operating PV cell under different heating sources is studied by means of FEM in Comsol Multiphysics environment. Formerly, heating due to the solar radiation is presented, according to real operative conditions of a PV cell. Then, the thermal behaviour of the cell due to the current flowing through the external circuit between the cell electrodes is analyzed. Finally simulation results taking into account both the effects are evaluated. In the following the three simulations are named as case a), case b), and case c). The coupling analysis has been possible using the multhiphysical features available in Comsol environment and the simulation results have shown the goodness of the proposed model. It can be used to evaluate abnormal heating deriving by defects of the cell [1], highlighted and evaluated by means of thermography [2] that is the most performing method to localize shunting path within solar cells. These problems are often encountered during cell manufacturing or due to the field aging [3]. The paper is organized as follows: Section 2 introduces the proposed model, Section 3 proposes the simulation results, while Section 4 reports conclusions and future works.

2. PROPOSED MODEL

The FEM model of a commercial PV cell (Figure 1 and 2) has been implemented by means of CAD tools available in Comsol's environment [4]. To solve such a multiphysical model an extreme computation power is required and also PCs with very high computational performances reveal strong difficulties to complete the simulation. This paper proposes a scaled model of the PV cell in [4] that can be solved on PC with large computational power. The side of the structure described in [4] has been scaled of a factor 2, while the thickness of each layer has the original value as well as all physical features. Only one parameter, depending on geometrical features of the developed model, has been re-determined to find the correct value to be set up. In fact the *heat transfer*

coefficient, *h*, depends on geometrical dimensions of the structure; its value is function of length, width and thickness of the model. Length and width have the same value because a square structure is considered. So *h* value has been computed considering the same thickness of the original model reducing length and width of a factor 2. Then, the new value for the heat transfer coefficient results equal to 15.6 W/m^{2}K. Thermal analysis has been developed using the *Heat transfer* module available among Comsol's modules.
Incoming flux for the simulations related to the case a) and c) has been set equal to the value of 800 W/m^2. This condition has been set up only on the upper face of the structure, which is directly run over by the solar radiation. The value of the incoming flux for the lower face has been set equal to 0 W/m^2 as it happens in real photovoltaic modules during the normal operation. These thermal boundary conditions are defined by NOCT (Nominal Operative Cell Temperature) specifications. This conditions imposes the value of incoming flux to be set equal to 800 W/m^2, wind speed equal to 1m/s and environment temperature of 20 °C[1]. All these values can be set up on the model using the Boundary conditions setting mask available in Comsol's interface. When the value of the incoming flux is fixed a Neumann's boundary condition, that imposes the value of solution derivative on boundaries, is set up. Moreover, on the cell sides a thermal insulation condition has been imposed. It allows reproducing the same real operative conditions of a PV cell into a PV module. For the simulations related to the case b) and c) the AC/DC module has been used together with the Heat Transfer one to study the thermo-electrical behaviour of the modelled PV cell: a voltage of 0.6 V has been applied across the cell electrodes. All the other parameters to be imposed in Comsol's Sub domain setting mask (materials emissivity, conductivity, environmental temperature, etc.) have been set as in [4]. From a numerical point of view, the development of a multiphysical analysis increases strongly the complexity of the developed model in terms of discrete domains.

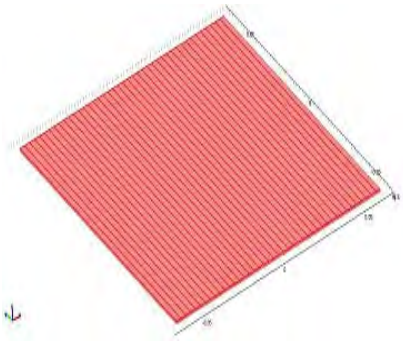

FIGURE 1. Proposed model.

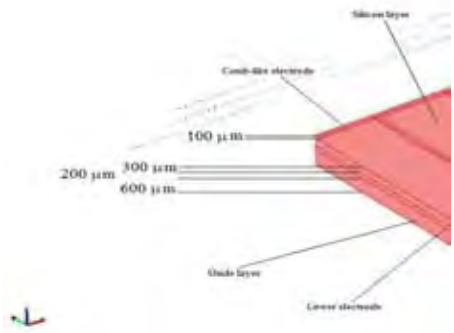

FIGURE 2. Zoom on the thickness.

3. RESULTS

The simulations have been run under a Dell workstation with the following features: dual core INTEL XEON 5130, clock frequency 2 GHz, RAM 16 GB. According to the FEM theory, a linear equations system coming from a PDE system has to be solved. To obtain the resolving linear system, it has to be divided in a lot of elements, finite in number and dimension. This can be obtained during the mesh creation step. The software allows to use a pre-defined mesh size. In the proposed model the mesh size has been set up to extra coarse size. The number of the mesh elements is 493.073 corresponding to 1.495.150 degrees of freedom. It is important to highlight that the number of degrees of freedom is valid for all the three cases. The model complexity is strongly

[1] Often in experimental analysis the reference condition considered is the STC (Standard Test Condition). It imposes that the solar flux is to be set equal to 100 mW/cm^2 (=1000 W/m^2) conforming to the standard reference AM 1.5 spectrum and temperature of 298.16 K that corresponds to 25 °C. The use of this value for the incoming flux can be really useful as the efficiency in percent is numerically equal to the power output expressed in mW/cm^2 [5].

dependent on grid element size: reducing the elements size, the number of degrees of freedom to be solved increases and the calculator memory becomes saturated yet when a *dense* size of the mesh elements is set. Table 1 reports the *grid dependence analysis* developed on the original model explained in [4] to highlight this aspect.

Mesh element size	Number of mesh elements	Degrees of freedom
Extra coarse	140893	3512306
Very coarse	352449	570578
Medium coarse	700404	1112541
Coarse	1130921	1772226
Normal	1765066	2735076
Dense	2490426	3842953
Medium dense	3512306	5340937
Very dense	-	-
Extra dense	-	-

Table 1. Global mesh characteristics.

The presence of empty fields is due to overflow of the PC memory.
The high number of degrees of freedom to be solved is connected to the multiphysical analysis that has to be run. The use of two modules at the same time allows considering the model like a double model: an electrical one and a thermal one. This increases the number of resulting degrees of freedom. For this reason it is not possible to simulate the thermal behaviour of a 36 PV-cells module in spite of the computational performances of the utilized PC power.
The software offers two typologies of solvers: direct and iterative ones. The large computational power available allows using direct solvers for the simulations. Simulation issues have shown that the most performing solver is PARDISO (SParse Object Oriented Linear Equation Solver) solver. It happens because it uses the Level-3 BLAS supernode technique of matrix factorization [6]. Each one of the three simulations with this solver has required about 8 minutes. The other direct solvers available in Comsol are UMFPACK (Unsymmetric multifrontal sparse LU factorization package), SPOOLES (SParse Object Oriented Linear Equation Solver) and TAUCS. The last one needs that the coefficient matrix is symmetric; then it cannot be used for the cases under study. Iterative solvers available may be used if simulations are to be run on calculators with lower calculation power respect to the used one. Those available in Comsol environment are the GMRES (Generalized Minimal RESidual), Conjugate Gradient and Geometric multigrid. The first one and the second one concern the solution methods of Krylov's subspace and consist in the product of a matrix with a vector or else in the internal product between two vectors. The last methods can be considered the most performing among the iterative ones available in Comsol even if complex linear problems come from the linearization of PDE's problems. Their complexity comes from the need to solve finite element models with variable mesh element size [7].
All the simulations have been run in steady state. Simulation results of case a) can be observed in Figures 3 (a) and (b). The comparison among the figures allows revealing the different temperatures between the lower and the upper surfaces. In fact the upper face reaches a temperature of 39.72 °C while the temperature of the lower one is of 39.67 °C. Even if it is small, the temperature difference represents a real operating situation, highlighting that the model well simulates a well operating PV cell. It is important to highlight that to simulate such a real behaviour of the modelled cell a good setting of boundary conditions is to be done: according to NOCT condition the incoming flux value has been fixed equal to 800 W/m^2. This is true only for the upper face of the cell that receives the direct sun irradiation. In the case of the lower face, the value of the incoming flux has to be set up equal to 0 W/m^2. To analyze the influence of the only Joule's effect on the heating of the device (case b)), the cell has been closed on a resistive load, modelled as a thin resistive layer.

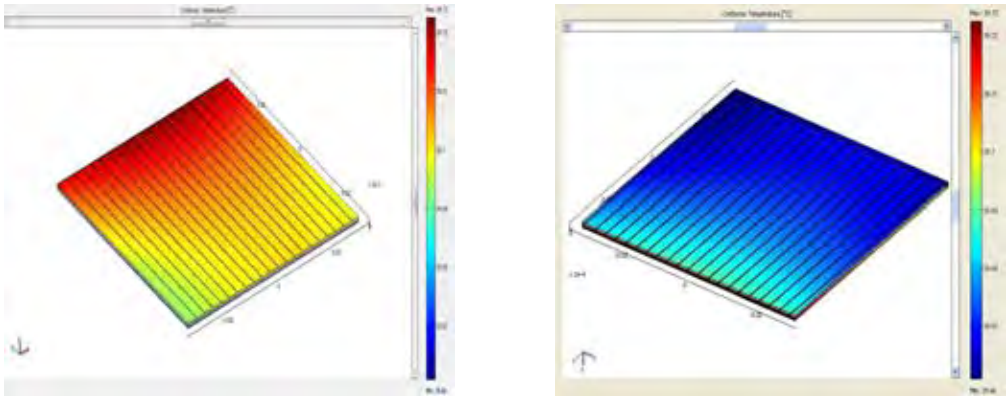

(a) (b)

FIGURE 3. (a) Upper surface of the cell under direct solar radiation; (b) lower surface of the cell.

A voltage of 0.6 V has been applied across cell pins while on the other surfaces a boundary condition of electrical insulation has been set up. At the contact surfaces between the cell and the thin layer a condition of continuity has been set up, whose mathematical model is shown in equation (1).

$$n \bullet \left(J_1 - J_2 \right) = 0 \qquad (1)$$

where J_i (i = 1,2) is the density of the current flowing from the cell inside the connected load.
This case-study needs the incoming flux value to be set to zero for both faces of the cell: the simulation result shows the temperature distribution on the system due to the only Joule's effect. The cell temperature is 28.76 °C, as reported in Figure 4. The temperature value is about 11 °C lower than the temperature reached by the cell under the solar radiation, (Figure 3 (a) and (b)).

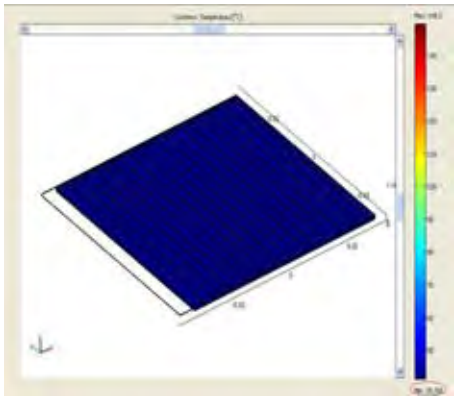

FIGURE 4. Temperature distribution of the cell under heating for Joule's effect.

Finally the thermal behaviour of the cell has been analyzed considering the device exposed to both the effects simultaneously using multiphysical utilities available in Comsol environment that allow to use more than one single module at the same time. In this case the boundary conditions applied on the model are the same of thermal analysis (case a)), while from the electrical point of view conditions on voltage across cell electrodes, electrical insulation and continuity are the same of the case b).
In this case the maximum temperature of the cell is 48.01 °C, as shown in Figure 5.

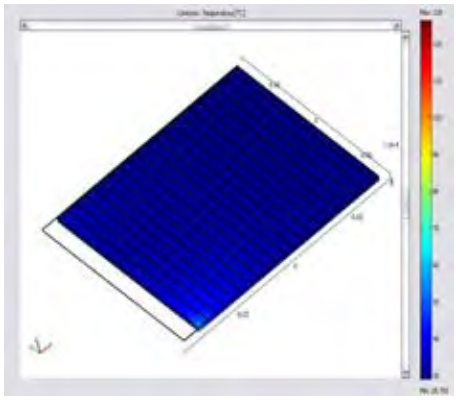

FIGURE 5. Temperature distribution of the cell with both heating sources.

Table 2 summarizes all the results: T_0 is the environmental temperature, while T_f is the final temperature reached by the cell. The first row of the table is referred to the cell under the only solar radiation. It is possible to observe how the temperature increase is about 20 °C. The second row refers to the Joule's effect on the device heating and it highlights the low influence; in this case the temperature goes from 20 °C to 28.76 °C. The last row refers to the real case in which both the effects are present simultaneously: the cell conducts and is exposed to the solar radiation. In this case there is a strong increase of the cell temperature, about 29 °C. From table 2 it is possible to observe as the ΔT of the case c) is almost equal to the sum of the corresponding values of the other two cases. This shows that the system can be considered quasi - linear.

	T_0	T_f	ΔT
Radiative flux	20°C	39.72°C	19.72°C
Joule's effect	20°C	28.76°C	8.76°C
Radiative flux and Joule's effect	20°C	48.01°C	28.01°C

TABLE 2. Temperature comparison among the three cases.

4. CONCLUSIONS

The simulation results have allowed to highlight the goodness of the proposed 3-D model for a PV-cell utilizing FEM. Simulation results are presented for the heating due to Joule's effect, heating due to the radiative flux, and heating due to both of them. Results agree with measures on real PV-cells. Specific issues related to the numerical implementation of a PV-cell in Comsol environment are introduced. The strategy to implement a scaled model of the PV-cell in order to avoid the problems related to computational burden has been effective. This approach will be used in future works to model typical defects of PV-cells.

The grid dependence analysis highlights the computational costs for the proposed 3-D PV-cell model. It is worth noting that even if a great computational power has been used, a higher mesh definition cannot be used to avid memory overflow.

REFERENCES

[1] O. Breitenstein, JP Rakotoniaina, M.H. Al Rifai, M.Werner, Shunt type in crystalline solar cells, *Progress in photovoltaics research and application*, 12, 532, 2004.

[2] O. Breitenstein, JP Rakotoniaina , M.H. Al Rifai , Quantitative evaluation of shunts in solar cells by lock-in thermography, *Progress in photovoltaics research and application*, 11, 515-526, 2003

[3] D. L. King, J. A. Kratochvil, M. A. Quintana and T. J. McMahon, Applications for infrared imaging equipment in Photovoltaic cell, module, and system testing, *Photovoltaic Specialists Conference*, 1487-1490, 2000.

[4] S. Vergura, G. Acciani, O. Falcone, "*3-D PV-cell Model by means of FEM*", IEEE-ICCEP, 35-40, Capri, Italy, 9th – 11th June 2009.

[5] T. Markvart, *"Solar electricity"*, 2nd. Edition Wiley, p.37, 2000.

[6] O. Schenk, K. Gärtner, and W. Fichtner, *"Efficient sparse LU factorization with left – right looking strategy on shared memory multiprocessors"*, BIT, 40(1), 158 – 176, 2000.

[7] A.Greenbaum, *Iterative Methods for Solving Linear Systems*, SIAM, 1997.

First International Conference on Computational Methods for Thermal Problems
ThermaComp2009, September 8-10, 2009, Napoli, Italy
N.Massarotti and P.Nithiarasu (Eds.)

TRANSIENT PHONON HEAT TRANSPORT IN QUASI-1D NANOSTRUCTURES

Stefano di Stasio
Istituto Motori C.N.R., *Aerosol & Nanostructures* Lab, Via Marconi 8 – 80125 Napoli - s.distasio@im.cnr.it

Aniello Iazzetta
Istituto Motori C.N.R., *Aerosol & Nanostructures* Lab, Via Marconi 8 – 80125 Napoli

ABSTRACT

The Debye model for heat capacity of crystals is used to study the phonon heat transfer properties of quasi-1D structures such as nanowires and nanorods. According to the results reported in previous literature, we schematize a nanowire by a stack of 40 cells, total length 400 nm, with z-direction for heat flux coincident with the axis of nanowire and initial temperature 300 K. Transient temperature (time step 2 ps) field is studied after that at t=0 the wall of the first cell is set at 500 K. The nanostructure dimensions considered in the plane perpendicular to the z-axis are 2-50 nm. Calculations are performed by Monte Carlo simulation for the phonon drift movements and scattering process. The main result is the following: the smaller sizes L_x, L_y, of the simulation cell in the plane perpendicular to the heat flux (x-, y-axis) does influences the rate of temperature transient response in the neighbouring of hot boundary (~50 nm) at short times (200 ps). Moreover, smaller L_x, L_y, yield to predicted longer times (~10 ns) for settling of linear temperature regime and to smaller heat conductivity within 10% at parity of heat flux.

Key Words: *Phonons, Transient Heat Transfer, Debye Model, Crystalline Solids*

1. INTRODUCTION

Quasi-1D nanostructures, namely those nanomaterials with all but one dimension below 100 nm, are very interesting media to study quantum confinement effects in physics and chemistry.
Nanoscale heat transfer deal with the mechanisms of transferring heat energy flux through domains with dimensions too small to allow the application of macroscopic thermophysical properties. In the case of crystal nanostructure the lattice vibrations can significantly contribute to the global heat transfer balance and the carrier of quantum vibrational energy are called phonons. Fourier law loose its applicability for two reasons. The first one is the size effect which accounts for the interactions between heat carrier (electrons, phonons) and the physical boundaries of nanostructures. The second one concerns with the interactions and anomalous effects at sub-molecular level. Nanoscale thermal phenomena occur not only for crystalline solid state but also in the case of nanometer-sized particles embedded in a liquid matrix. In the materials in which phonon heat transport is expected to be significant, one of the possible approach is the Debye model. The related theory is dated 1912 and was conceived to describe the phonon contribution to heat capacity at low temperature in solids. One of the striking feature of this approach is the fact that Einstein's approach based on non interacting quantum harmonic oscillators fails when Debye, who represents the vibrations of atomic lattice as phonons in a box, does predict correctly the dependence on T^3 of the heat capacity observed at low temperatures by experiments.
The aim of this communication is to present the preliminary results by Debye modelling of phonon heat transfer in nanowires and nanoclubs. Such structures are object of our previous work [1].

2. THEORETICAL FRAMEWORK

For a crystal with N number of atoms the normal modes of vibration are $3N$-6 where the subtracting term accounts for the rotational and translational degree of freedom. The vibrational energy of the nanosystem is written in terms of sum of normal mode quanta. The total energy of the crystal is evaluated as:

$$E(n_j) = \sum_{j=1}^{3N} h \quad _j\left(n_j + \tfrac{1}{2}\right) = \sum_{j=1}^{3N} h \quad _j n_j + E_0 \tag{1}$$

where E_0 is the zero point energy.
From statistical thermodynamics, the energy can be expressed in terms of vibration frequencies of harmonic oscillators at temperature T. The result is:

$$E = \int_0^{\infty} \left[\frac{h}{e^{h \ /kT} - 1} + \frac{h}{2} \right] g(\ )\, d \tag{2}$$

where $g(\ )$ is the density of states which is normalized with the condition $\int g(\ )\, d \ = 3N$. The 1D nanostructure is modelled as a stack of cells with axis coincident with the propagation of heat flux. The transverse dimensions of each cells are L_x, L_y. The dimension along the axis is L_z. The elastic waves are supposed to be characterized by two transverse modes and one longitudinal mode. The number of vibrational modes with frequencies between and +d can be written as:

$$g(\ )d \ = \frac{12 \ V}{c_S^{\ 3}} \ ^2 d \tag{3}$$

where c_S is the speed of sound, V is the system volume. According to Debye, it is possible to write the specific internal energy and the heat capacity of the solid system in terms of Debye's temperature and frequency which are written as the following:

$$T_D \equiv \left[hc_S / (2k) \right] \sqrt[3]{6N/(\ \ V)} \qquad _D \equiv c_S \sqrt[3]{3\,N/(4 \ \ V)} \ . \tag{4}$$

Then the specific energy is subtracted of the so-called zero point energy and it can be expressed as:

$$\frac{E_{phon}}{V} = \frac{E}{V} - \frac{E_0}{V} = \int_0^{D} \frac{9nh}{\ _D^{\ 3}} \frac{^3}{e^{h \ /kT} - 1} d \tag{5}$$

where n is the atom concentration, h and k the Planck and Boltzmann constants. The phonon energy spectrum has upper-bound $_D$ which is the cutoff due to the constraint that the normal mode wavelength can not to be shorter that the atomic spacing in the crystal lattice. The definition of quantum energy can be put in differential form $dE_{phon} / V = h \quad dN_{phon}(\ ) / V$ where dN_{phon} is the number of vibrational quanta with frequencies in the range to $+d$. The Eq. (5) above for specific energy is then written in terms of normal modes as following:

$$\frac{N_{phon}}{V} = \int_0^{D} \frac{9n}{\ _D^{\ 3}} \frac{^2}{e^{h \ /kT} - 1} d \tag{6}$$

To evaluate the phonon distribution we use the equation

$$_S(\ ) = \frac{9n}{\ _D^{\ 3}} \frac{^2}{e^{h \ /kT} - 1} \ . \tag{7}$$

All the equations written hitherto are based on the assumption that the 1D crystal is in thermodynamic equilibrium. In condition of non-equilibrium, owing to the very short transient times (~100 ps), the Eqs.(5), (6) do not apply strictly for the meaningless interpretation of temperature. We will use at place of temperature a fictitious *pseudo-temperature* T* such that it returns the value of energy E_{phon} according to the following:

$$\frac{E_{phon}}{V} = \frac{9nkT^*}{\left(T_D/T^*\right)^3}\int_0^{T_D/T^*}\frac{\left(h\ /kT^*\right)^3}{e^{T_D/T^*}-1}\,d\left(h\ /kT^*\right) = \frac{9nkT^*}{\left(T_D/T^*\right)^3}\int_0^{D}\frac{^{*3}}{e^{\ *}-1}\,d\ ^* \qquad (8)$$

where $^*=T_D / T^*$.

3. ALGORITHM OF SIMULATION

The nanowire is modelled as a stack of 40 cells with heat flux flowing along the nanowire axis (z-axis) and transversal dimension in the range 2-50 nm (x-,y- axes). The Eq. (6) is used to establish the initial number of phonons in each cells. Dimensions of each cell are L_x, L_y, L_z. The initial position and velocity of each phonon are set by random generator according to the procedure described elsewhere [2]. Thus the phonon velocity components are $c_x = c_S\ C$, $c_y = c_S\ S\cos\ $, $c_z = c_S\ S\sin$ where c_S is the phonon speed. The same procedure will be used to select a new velocity after the occurring of a scattering event. The assignment of frequencies is made by Eq (7) by a technique of acceptance-rejection [2]. The algorithm is initiated by using Eq(1) to write down the initial energy in each cell. Then the *target* energy is evaluated from the real initial temperature by Eq. (5). At each phonon is assigned a velocity vector with constant magnitude and random direction as described above. Phonons are allowed to move with a drift velocity for one time interval Δt. This last should be shorter with respect to the time necessary to the phonon to travel the cell length without collision [3]. In our case time step is Δt = 2 ps. At step one we consider the drift movements. The particles are allowed to propagate along the z axis. Vice versa they collide with x or y cell faces and are reflected specularly. Each phonons has possibility to enter the previous or the next cell. In this case the total number of phonons in the cell is modified and so it is the *actual* cell energy E_c, which is then recalculated with Eq.(1). At this point the pseudo-temperature T* is evaluated for the step one by numerical inversion of Eq.(8) and the algorithm starts the scattering simulation. A numerical technique is used to introduce the collisions events by mean free path. As a consequence of collisions, each phonon can change its momentum and energy. Scattering processes arise from phonon-phonon interactions (*Normal* and *Umklapp*) and phonon-crystal lattice interactions. The simplest scheme is one in which the probability of phonon scattering does not depend on the cell pseudo-temperature and phonon frequency. The distance travelled by a phonon during the drift period is $d = c_S\ \Delta t$. A Poisson probability distribution is introduced for collision assessment written in the form $P(d) = 1 - e^{-d/l_{phonF}}$ where l_{phon} is the phonon mean free path, supposed independent from T, $d = c_S\ \Delta t$ and Δt =2 ps. A random number is selected in (0,1) to indicate the presence of collision. If the random number is less than $P(d)$ we decide that a collision takes place. In this case the direction of phonon velocity vector and the phonon frequency are changed by random selection. Acceptance-rejection of phonon frequency number is made by substituting in Eq(7) for $_S$ the current cell pseudo-temperature T^*. The phonon position is not changed during the scattering event. The cell *actual* energy E_c is then recalculated according to Eq(1) and compared with the cell *target* energy E^*_c computed by Eq.(5) with substitution of T* used in the drift procedure from numerical inversion of Eq(7). If E_c and E^*_c are equal, according to a pre-defined criterion of approximation, we consider the next cell along z. If E^*_c is smaller of E_c some phonons are destructed one at a time by random selection till the two energies are comparable. If E^*_c is larger with respect to E_c it is necessary to create new phonons, one at a time. The frequency is selected by new random number in (0, $_D$) and we use Eq. (7) with the cell pseudo-temperature T* just immediately evaluated at place of temperature T. Position and velocity is chosen at random as before. When E^*_c becomes comparable to E_c, the phonon creation is suspended. This procedure at step one is repeated for each cell. The boundary cells are subjected to the initial

temperatures T_1=500 K, T_2 = 300 K and each cell energy is evaluated by Eq.(5) substituting T_1 and T_2. Also in the boundary cells some phonons can enter or outgo as well, and the process of photon creation-destruction is implemented according to the procedure above.

4. RESULTS AND CONCLUSIONS

In order to compare with other authors [2] the model was preliminarily operated with the following physical parameters: T_D=115 K, M=30, $_D$=2.4 × 10^{12} Hz, C_D=824.7 J/(kg K), $_T$=16.5 W(mK), $_T$=6.67×10^{-6} m^2/s, =3000 kg/m3, l_f = 20 nm, c_S=1000 m/s, L_x=L_y=L_z=10 nm.
At the decreasing of the transversal dimensions L_x=L_y=L, the derivative of temperature with respect to z, $\partial T/\partial z$, after 6 ns exibits oscillatory behaviour. Thus, when L=20 nm is compared with L=10 nm a slight decrease is observed, then with L=5 nm an increase of $|\partial T/\partial z|$ is observed. This last yields to a diminishing of thermal conductivity of 8.5 % at parity of heat flux. On the other hand, at the decreasing of L the ratio of the phonon mean free path to the transverse distance increases and from the kinetic theory the thermal conductivity is expected to increase coherently with the equation $_T = \frac{1}{3} c \ c_S \ l_{phon}$ where c is the constant volume lattice specific heat, J/(m^3 K), c_S is the sound velocity (m/s) and l_{phon} is the phonon mean free path (m). Thus, the phonon simulation leads to a result apparently in contrast with respect to the kinetic theory. However, the pecentage variations of $_T$ are in absolute value below 10 % when sides L=L_x=L_y is changed from 20 to 5 nm. Moreover, with small transverse size of the 1D nanostructure, oscillations of the temperature vs. z-axis are significantly wider about the linear temperature regime relative to Fourier bulk conduction, which is normally settled in the structure after 6 ns.

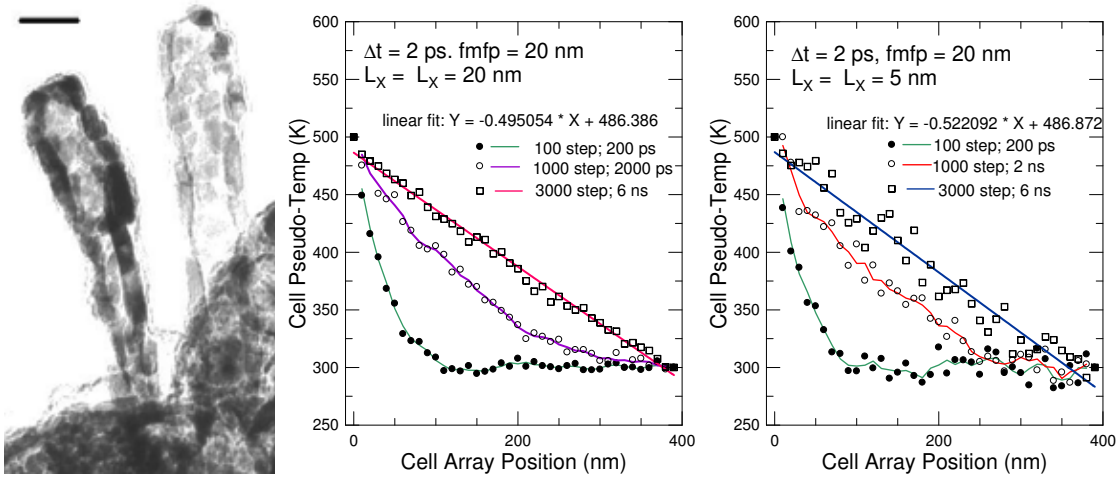

FIGURE 1. *left*) TEM Zinc 1D nanocrystal elsewhere called *nanoclubs* [1]. Transverse size at base about 50 nm, length about 340 nm. Bar scale 66 nm; *middle*) simulations: stack length 400 nm, L_x=L_y=20 nm, L_z=10 nm; *right*) simulations: L_x=L_y=5 nm, . L_z=10 nm Average of results over 5 random processes.

REFERENCES

[1] S. di Stasio S, Growth of Zinc Hollow Nanofibers and Nanotubes by Thermal Evaporation-Condensation-Deposition Route, *Chemical Physics Letters* 393, 498-503, 2004.

[2] R.B. Peterson, Direct Simulation of Phonon-Mediated Heat Transfer in a Debye Crystal, *Journal of Heat Transfer* 116, 815-822, 1994.

First International Conference on Computational Methods for Thermal Problems
ThermaComp2009, September 8-10, 2009, Napoli, Italy
N.Massarotti and P.Nithiarasu (Eds.)

Numerical study of laminar forced convection of a nanofluid in a horizontal annulus with uniform wall temperature

Mohsen. Izadi
Mechanical Engineering Department, Sahand University of Technology, Tabriz, Iran.
m.izadi.mec@gmail.com

Amin Behzadmehr*
Mechanical Engineering Department, University of Sistan and Baluchestan, Zahedan, Iran
amin.behzadmehr@eng.usb.ac.ir

Davood Jalai-Vahid
Mechanical Engineering Department, Sahand University of Technology, Tabriz, Iran

Hossian Shahraki
Iran Petrochemical research & technology company, h.shahraki@npc-rt.ir

ABSTRACT

Laminar forced convection of a nanofluid consisting of water and Al_2O_3 in a horizontal concentric annulus has been studied numerically. Single-phase model has been used to investigate thermal behaviours of the nanofluid over wide range of Reynolds numbers and nanoparticle volume fraction. Comparisons with previously published experimental and analytical works in horizontal annulus show good agreements between the results. For a given Reynolds number and particle mean diameter axial evolution of convective heat transfer coefficient for different nanoparticles concentration as well as the axial variation of wall heat flux are presented and discussed.

Key Words: *nanofluid, laminar forced convection, horizontal concentric annulus*.

1. INTRODUCTION

Heat transfer through new class of fluids is named nanofluids [1] that show special heat transfer characteristics compared with common fluids as water, mineral oil and ethylene glycol which play a vital role in many industrial processes, including power generation, chemical processes, heating or cooling processes, and microelectronics. These fluids enable to solve some problems that arise from the poor heat transfer properties of common fluids. Heat transfer to a nanofluid flowing in a horizontal concentric annulus is a particularly interesting problem. Its considerable technical importance is due to its capability of heat transfer from both inner and outer surfaces which can transfer heat independently. The present paper investigates laminar forced convection of a nanofluid in horizontal concentric annulus with using single phase method with axial uniform constant temperature. An effective thermal conductivity model, for which the Brownian motion of the nanoparticles and also their mean diameter is brought into account, is used. Also an effective viscosity for nanoparticles is used which is a function of Brownian velocity, mean diameter of nanoparticles and temperature. For a given mean diameter of nanoparticles effects of particle volume fraction on thermal parameters have been presented.

2. MATHEMATICAL FORMULATION AND NUMERICAL PROCEEDURE

Laminar forced convection of a nanofluid consisting of water and Al_2O_3 in horizontal concentric annulus with uniform wall temperature has been studied by developing a computational code.

Dissipation and pressure work are neglected. Single phase model is used for the study thus the dimensional conservation equations for steady state mean conditions are as follows:

$$\nabla.(\ _{eff} V_m) = 0 \tag{1}$$

$$\nabla.(\ _{eff} V_m V_m) = -\nabla p + \nabla.(\ _{eff} \nabla V_m) \tag{2}$$

$$\nabla.(\ _{eff} C V_m T) = \nabla.(k_{eff} \nabla T) \tag{3}$$

The physical properties of above equation are:

Effective density: $_{eff}=(1-\ )\ _f + \ _p$ (4)

Effective specific heat: $C_{eff} =(1-\ )C_f + C_p$ (5)

Chon et al.[2] correlation which considers the Brownian motion and nanoparticles mean diameter has been used for calculation the effective thermal conductivity

$$\frac{K_{eff}}{K_f} = 1 + 64.7 \times \ ^{0.7460}\left(\frac{d_f}{d_p}\right)^{0.3690}\left(\frac{K_s}{K_f}\right)^{0.7476} \times \mathrm{Pr}^{0.9955} \times \mathrm{Re}^{1.2321} \tag{6}$$

Recently Masoumi et al. [3] develops a new equation for prediction of the nanofluids effective viscosity which is a function of temperature, mean nanoparticle diameter, nanoparticle volume fraction, nanoparticle density and the based fluid physical properties. This equation is adopted for calculating nanofluid effective viscosity. This set of nonlinear elliptical transport equations has been solved subject to following boundary conditions:

-At the inlet of annulus (X=0): $V_{mx}=V_i$, $V_{mr}=0$ and $T=T_i$ (7)

-At the walls: $V_{mx}= V_{mr}=0$, at $r=r_i$ $T=T_{wi}$, and at $r=r_o$ $T=T_{wo}$ (8)

-At the annulus outlet(X=L):the diffusion flux in the direction normal to the exit plane is assumed to be zero for all variables except for the temperature that fully developed condition is considered.

This set of coupled non-linear partial differential equations was discretized with the finite volume technique. For the convective term a first order upwind method is used while the SIMPLE algorithm is introduced for the velocity-pressure coupling. Cells of Grid are non-uniform in two directions of axisymmetric geometry. It is finer near the wall and annulus entrance because the variables gradient is higher than other positions. Several different grid size have been tested to ensure that variation of grid numbers have no effect on the results. The selected grids consist of 25 and 250 cells, respectively in the radial and axial directions. Increasing the grid numbers in the radial and also axial directions does not significantly affect the results. Some axial and radial profiles have been tested to be sure the results are grid independent. In order to demonstrate validity and also precision of code, comparisons with available analytical and experimental data have been done. The concordance between the results is good. Therefore the numerical code is reliable and can predict forced convection flow in a horizontal annulus.

3. RESULTS

Numerical simulation of forced convection has been performed with uniform wall temperature. For two given Reynolds number R=100 and 900, four nanoparticle volume fractions (0%, 1%, 3% and 5%) with 25nm mean diameter hydrodynamics parameter of laminar nanofluid flow have been studied numerically. Axial evolutions of the convective heat transfer coefficient at the inner wall for different T_{wi} and T_{wo} are shown in figures 2. For same temperature at walls, in general increasing the temperature does not have any effect on the heat transfer coefficient. But for different inner and outer wall temperature the behaviour is complicated. Since the outer wall temperature is higher than the inner wall temperature. Therefore the bulk temperature is affected by the higher temperature of

the outer wall. As seen in figure 2c for the case of inner wall temperature 305k (T_{wi}=305K) the bulk temperature become higher than the inner wall temperature (T_b>305 K) at X/L≈0.13.

Thus at that region first the heat transfer coefficient increases significantly (T_b approach T_{wi}) and then decreases suddenly to a negative value and goes to its negative asymptotic value ($T_b > T_{wi}$). This means that instead of heating the fluid flow by the wall temperature. Energy transfers from the fluid flow to the wall. The same behaviour is also seen in other cases as well. In general the same behaviour is seen for the convective heat transfer coefficient at the outer wall. Increasing nanoparticle concentration augments the outer heat transfer coefficient (It is not shown because of lack of space). Evolution of heat fluxes along the annulus length is presented in figure 3. It shows that at both the inner and outer wall, for given walls temperatures the corresponding wall heat flux augments with nanoparticle concentration. Which means using nanoparticle concentration enhances heat transfer through the annulus.

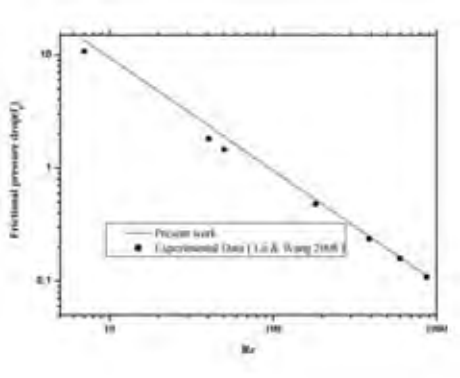

FIGURE 1: Comparison of the predicted frictional pressure with the experimental results

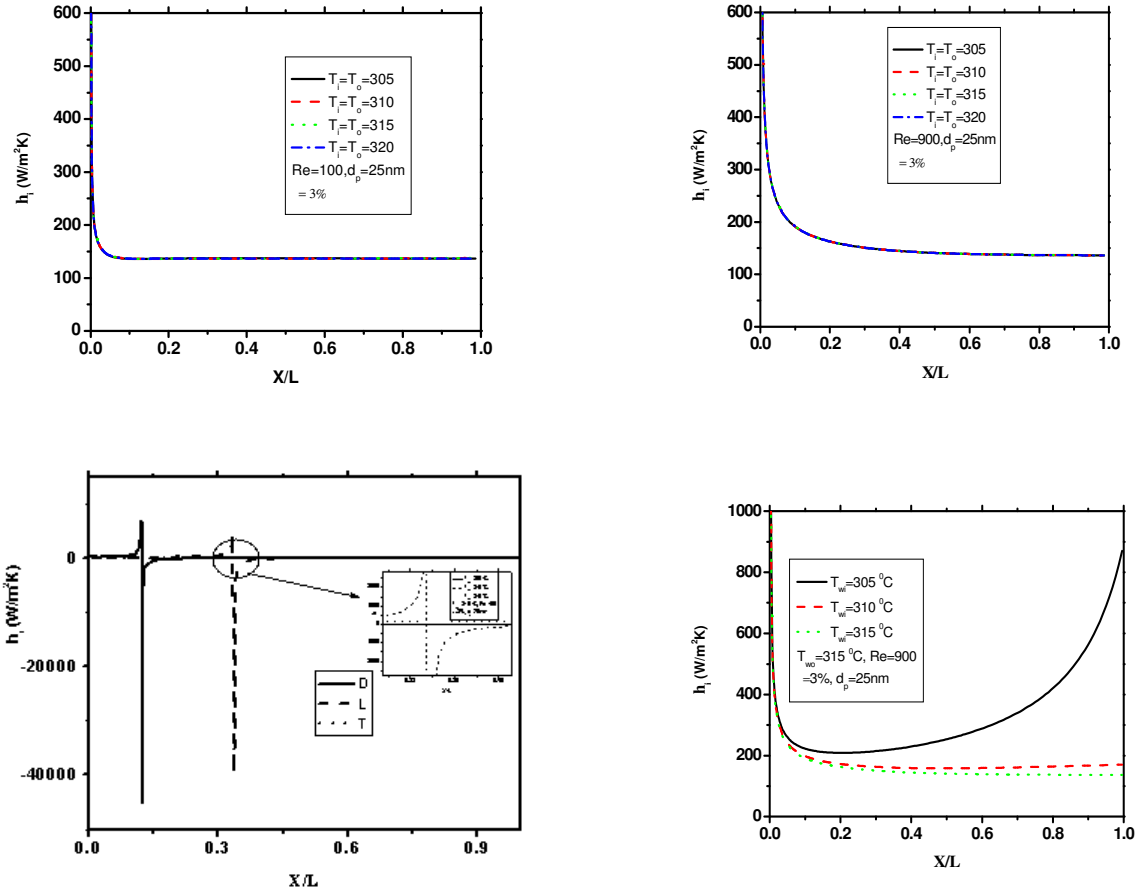

FIGURE. 2: Axial evolutions of convective heat transfer coefficient at the inner wall along the annulus length

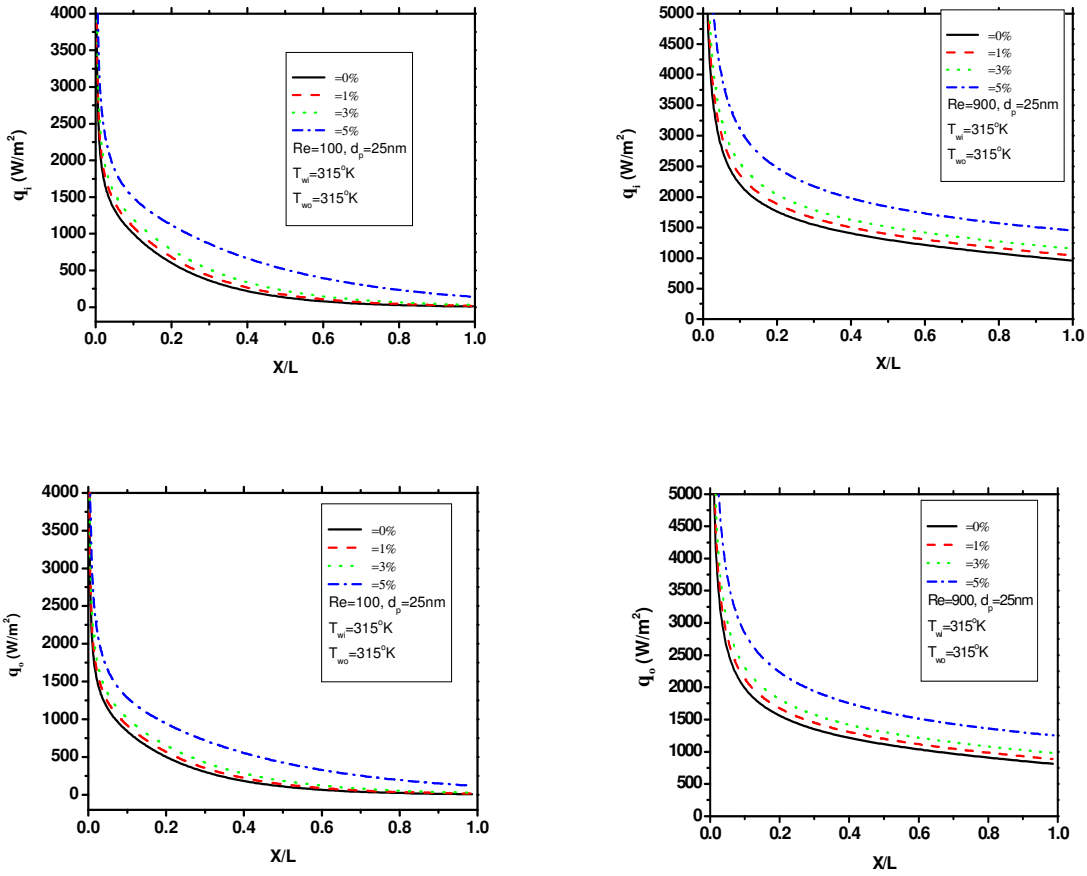

FIGURE. 3: Axial evolutions of heat flux at the inner and outer wall along the annulus length

4. CONCLUSIONS

Single-phase approach has been used to investigate numerically thermal behaviours of a nanofluid consisting of water and Al_2O over wide range of Reynolds numbers and nanoparticle volume fractions. Comparisons with previously published experimental and analytical works in horizontal annulus show good agreements between the results. It is shown that increasing the nanoparticle concentration augment the heat transfer coefficient at the inner and outer wall. However, when the inner wall temperature is much lower than the outer wall temperature a negative heat transfer is appeared. Energy transfers from the fluid flow to the inner wall.

REFERENCES

[1] S.U.S. Choi, Enhancing thermal conductivity of fluid with nanoparticles, Developments and Applications of Non-Newtonian Flow, ASME, FED 231/MD 66 (1995) 99–105.

[2] Chon, C.H., Kihm, K.D., Lee, S.P., Choi, S.U.S., 2005. Empirical correlation finding the role of temperature and particle size for nanofluid (Al_2O_3) thermal conductivity enhancement, Applied Physics Letters 87, 1-3.

[3] Masoumi N., Sohrabi N. and Behzadmehr A., A new model for calculating the effective viscosity of nanofluids, J. Physics. D: Applied Physics 42 (2009) 055501.

[4] Lu G., Wang J., Experimental investigation on heat transfer characteristics of water flow in a narrow annulus, Applied Thermal Engineering 28 , (2008) 8–13.

First International Conference on Computational Methods for Thermal Problems
ThermaComp2009, September 8-10, 2009, Napoli, Italy
N.Massarotti and P.Nithiarasu (Eds.)

NUMERICAL STUDY OF TURBULENT CONVECTION IN Al_2O_3/WATER NANOFLUID WITH VARIABLE PROPERTIES

Vincenzo Bianco

DIAM-SUN, Via Roma, 29 – 81031 Aversa (CE) – Italy, vincenzo.bianco@unina2.it

Oronzio Manca

DIAM-SUN, Via Roma, 29 – 81031 Aversa (CE) – Italy, oronzio.manca@unina2.it

Sergio Nardini

DIAM-SUN, Via Roma, 29 – 81031 Aversa (CE) – Italy, sergio.nardini@unina2.it

ABSTRACT

In this paper turbulent forced convection flow of a water–Al_2O_3 nanofluid in a circular tube subjected to a constant and uniform heat flux at the wall is numerically analyzed. Two different approach are taken into account: single and two-phase models, with Particle dimension equal to 38 nm. Temperature dependant thermophysical properties are considered. It is found that convective heat transfer coefficient for nanofluids is greater than that of the base liquid. Heat transfer enhancement is increasing with the particle volume concentration and Reynolds number. A good agreement is found with the correlation of Xuan and Li [1].

Key Words: *Nanofluids, Numerical Simulations, Forced Convection.*

1. INTRODUCTION

Maxwell [2] was the first to show the possibility to increase thermal conductivity of a solid-liquid mixture by more volume fraction of solid particles. These fluids containing colloidal suspended nanoparticles have been called nanofluids. Several investigations revealed that the thermal conductivity of the nanoparticles suspension could be increased more than 20% for the case of very low nanoparticles concentrations.

Nowadays a fast growth of research activities in this heat transfer area is present [3, 4]. It is demonstrated that solid nanoparticle colloids are extremely stable and exhibit no significant settling under static conditions, even after weeks or months [5]. However, the development of nanofluids is still hindered by several factor such as the lack of agreement among experimental results from different research groups, poor characterization of suspensions and the lack of theoretical understanding of the heat transfer mechanisms [7].

Relatively few theoretical and experimental investigations have been reported on convective heat transfer in confined flows, as also reviewed in [8, 9]. Experimental results are provided for convective heat transfer of nanofluids laminar and turbulent flow inside a tube in [1, 10-12].

Very recently Buongiorno et al. [11-12] performed two interesting experimental studies on laminar and turbulent nanofluids convection. They used water/zirconia and water Al_2O_3 nanofluids and for both of them they concluded that the heat transfer enhancement is simply due to the improved thermophysical properties and the classical correlations can be used to predict Nusselt number, if temperature dependant properties are used.

More numerous papers, instead, focus on the investigation of laminar and turbulent convection by means of numerical analysis. Basically there are two approach to simulate nanofluids convection, the single phase model where the fluid with the suspended nanoparticles is assumed to be continuous and the two phase model with a better description of the mixture, taking into account the interactions between the liquid and the nanoparticles.

The two phase approach seems a better model to describe the nanofluid flow. In fact, the slip velocity between the fluid and particles may not be zero [4] due to several factors such as gravity, friction between the fluid and solid particles, Brownian forces, the phenomena of Brownian diffusion, thermophoresis and dispersion. The two phase approach provides a field description of the dynamics of each phase or, alternatively, the Lagrangian trajectories of individual particles coupled with the Eulerian description of the fluid flow field [4, 13-15].

In the present paper developing turbulent forced convection flow of Al_2O_3/water nanofluid in a circular tube is numerically investigated. The finite volume method is employed to solve the problem and two modelling concepts are considered: the two phase mixture model and single phase model.

Temperature dependant thermophysical properties are considered for both the models. Average steady state of a turbulent two dimensional symmetric flow is considered, with uniform heat flux on the tube wall. The study is carried out for water with alumina particles with a spherical size of 38 nm diameter.

A comparison among results obtained by the different models is accomplished in terms Nusselt number is accomplished with the Xuan and Li [1] correlation.

2. MATHEMATICAL MODELLING

The geometrical configuration under consideration is presented in Fig. 1. It consists in a channel with a circular section. The forced convection flow is steady and turbulent and a nanofluid flows inside the channel. The base fluid is water and the particles are of alumina (Al_2O_3). The channel is L=1.0 m long and has a diameter D=$1.0\cdot10^{-2}$ m. The fluid enters with uniform temperature and uniform velocity profiles at the inlet section. The condition of the uniform wall heat flux has been considered in this study. Moreover, the flow and the thermal field are symmetrical with respect to the longitudinal middle plane vertical, so half channel has been considered.

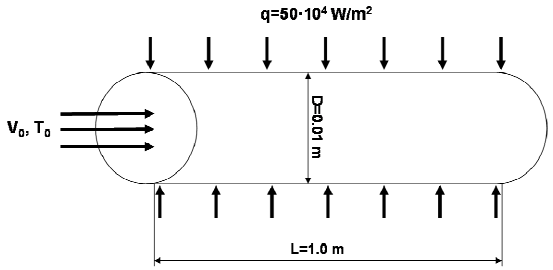

FIGURE 1. Schematic of the configuration under investigation

The equations used to calculate the themophysical properties are the following [4, 13, 15]:

$$_{nf} = (-1.1 + 9.7\cdot10^{-3}T - 1.3\cdot10^{-5}T^{2})\cdot(4.97\quad^{2} + 2.72\quad + 1) \tag{1}$$

$$_{nf} = 2.4\cdot10^{-5}\cdot10^{\frac{247.8}{T-140}}\cdot\left(123\cdot\quad^{2} + 7.3\cdot\quad + 1\right) \tag{2}$$

3. RESULTS

Results were carried out employing the single phase model and mixture model, for φ= 1%, 4% and 6%, Re= $20\cdot10^{3}$-$40\cdot10^{3}$ and q= $50\cdot10^{4}$ W/m^2. In all cases the particles size is considered equal to 38 nm.

In Fig. 2 wall and bulk temperature profiles for Re=$40 \cdot 10^3$ and φ=6% are reported. The figure clearly shows that temperature dependence of thermophysical properties has a relevant influence on wall and bulk temperature. In fact, for the single phase model wall temperature results to be about 2 K lower, whereas for the mixture model wall temperature is about 7-8 K lower. As for the bulk temperature, they remain substantially equal.

Fig. 2b shows that, in terms of wall temperature, mixture and single phase model lead to quite different results, instead the bulk temperature is, practically, the same for the two models.

Nusselt number, for all the cases considered, is reported in Table 1. It is possible to notice that in the case of a concentration of 1%, Nusselt numbers calculated with single phase and mixture model are quite similar, with an average deviation of about 10% respect to Xuan and Li correlation [1].

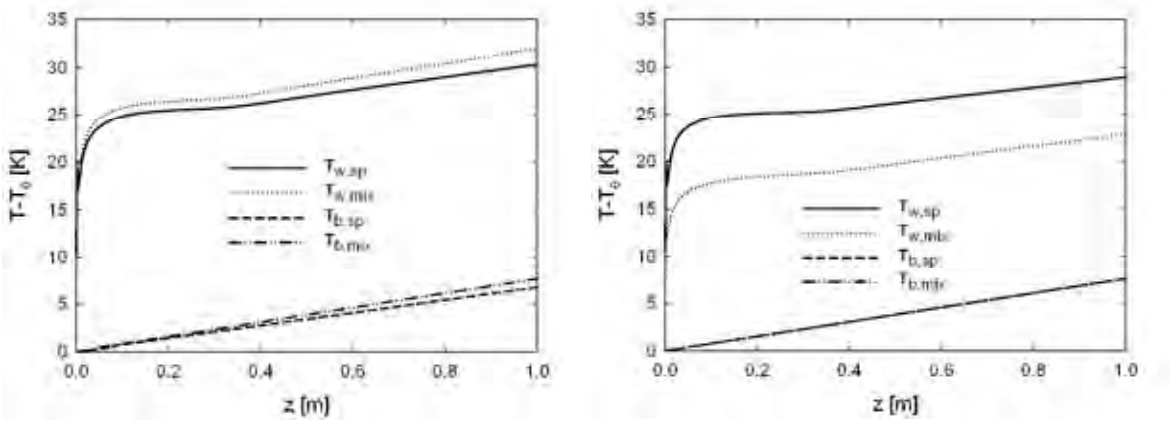

FIGURE 2. Wall and bulk temperature profile for constant properties (a) and temperature variable properties (b)

At the increase of the concentration, the deviation between the two models becomes more important, leading to quite different Nusselt number. For φ=4% , Nusselt number values calculated with mixture model present a maximum deviation from Xuan and Li correlation [1] of 13% at Re=$4.0 \cdot 10^4$, whereas the single phase model leads to a more consistent deviation, averagely equal to 24%. A similar behaviour is detected also for φ=6%, which shows that the single phase model produces underestimated results respect to Xuan and Li correlation, while mixture model results to have a much better approximation.

Re	Nu_{sp} φ=1%	Nu_{mix} φ=1%	Xuan-Li φ=1%	Nu_{sp} φ=4%	Nu_{mix} φ=4%	Xuan-Li φ=4%	Nu_{sp} φ=6%	Nu_{mix} φ=6%	Xuan-Li φ=6%
$2.0 \cdot 10^4$	180	187	147	184	224	220	188	258	268
$3.0 \cdot 10^4$	237	248	219	244	301	327	250	350	397
$4.0 \cdot 10^4$	293	307	291	303	375	433	312	438	524

TABLE 1. Comparison between Nusselt number obtained by means of numerical simulation and the correlation of Xuan and Li

4. CONCLUSIONS

In the present paper steady turbulent convection of water-Al2O3 nanofluid inside a circular tube was numerically investigated by means of finite volume method.

Single phase and mixture models with temperature dependent thermophysical properties were taken into account in order to simulate the water-Al_2O_3 nanofluid. Results showed the benefic contribution to the heat transfer provided by the inclusion of nanoparticles. In fact, Nusselt number increases at the increase of both Reynolds number and particle concentration.

The mixture model results to guarantee a better agreement with the experimental correlation of Xuan and Li [1], especially at the increase of particles concentration. This should be due to the fact that in the mixture model the concentration equation is solved in addition to mass conservation, energy and momentum equations. In this way, a better description of the two phases interaction is obtained, ensuring a better agreement among numerical and experimental results.

REFERENCES

[1] Y. Xuan, Q. Li, Investigation on Convective Heat Transfer and Flow Features of Nanofluids, *Journal of Heat Transfer*, 125, 151-155, 2003.

[2] J.C. Maxwell, *A Treatise on Electricity and Magnetism*, 2nd. Edition, Oxford University Press, 1881.

[3] K. Khanafer, K. Vafai and M. Lightstone, Buoyancy-driven heat transfer enhancement in a two-dimensional enclosure utilizing nanofluids, *International Journal of Heat and Mass Transfer*, 46, 3639-3653, 2003.

[4] S. K. Das, S. U. S. Choi, W. You and T. Pradeep, *Nanofluids science and technology*, John Wiley & Sons, 2008.

[5] J. A. Eastman, S. U. S. Choi, S. Li, G. Soyez, L. J. Thompson and R. J. Di Melfi, Novel thermal properties of nanostructured materials, *Material Science Forum*, 312-314, 629-634, 1999.

[7] G. Polidori, S. Fohanno and C.T. Nguyen, A note on heat transfer modelling of Newtonian nanofluids in laminar free convection, *Int. J. of Thermal Sciences*, 46, 739-744, 2007.

[8] X. Q. Wang and A. S. Mujumdar, Heat transfer characteristics of nanofluids: a review, *International Journal of Thermal Sciences*, 46, 1–19, 2007.

[9] J. Buongiorno, Convective transport in nanofluids, *Journal of Heat Transfer*, 128, 240–250, 2006.

[10] B.C. Pak and Y.I. Cho, Hydrodynamic and heat transfer study of dispersed fluids with submicron metallic oxide particles, *Experimental Heat Transfer*, 11, 151–170, 1998.

[11] W. Williams, J. Buongiorno, L.W. Hu, Experimental investigations of turbulent convection heat transfer and pressure loss of alumina/water and zirconia/water nanoparticles colloids (nanofluids) in horizontal tube, Journal of Heat Transfer, 130, 042412, 2008

[12] U. Rea, T. McKrell, L.W. Hu, J. Buongiorno, Laminar convective heat transfer and viscous pressure loss of alumina/water and zirconia/water nanofluids, International Journal of Heat and Mass Transfer, 52, 2042-2048, 2008.

[13] V. Bianco, F. Chiacchio, O. Manca and S. Nardini, Numerical investigation of nanofluids forced convection in circular tubes, *Submitted to Applied Thermal Engineering*.

[14] A. Behzadmehr, M. Saffar-Avval and N. Galanis, Prediction of turbulent forced convection of a nanofluid in a tube with uniform heat flux using a two phase approach, *International Journal of Heat and Fluid Flow*, 28, 211–219, 2007.

[15] V. Bianco, O. Manca and S. Nardini, Numerical Investigation on Nanofluids Turbulent Convection Heat Transfer Inside a Circular Tube, *Submitted to Numerical Heat Transfer*.

First International Conference on Computational Methods for Thermal Problems
ThermaComp2009, September 8-10, 2009, Napoli, Italy
N.Massarotti and P.Nithiarasu (Eds.)

GROWING NUMERICAL CRYSTALS

Vaughan R. Voller and Man Liang
Civil Engineering, University of Minnesota, Minneapolis, MN 55455, volle001@umn.edu

ABSTRACT

A simple two-dimensional model for the solidification of a "warm" solid seed placed in an under-cooled liquid melt is presented. Under the physically restrictive assumptions of no surface anisotropy or curvature and kinetic under-cooling a closed form similarity solution can be constructed for this problem. A fixed grid enthalpy "like" solution can also be constructed. When this enthalpy solution is implemented in a one-dimensional cylindrical geometry it produces excellent agreement with the analytical solution. When implemented in a two-dimensional geometry, however, due to the lack of front stability provided by the surface under-cooling, dendritic crystals are predicted. Theses crystals are referred to as "numerical crystals" to highlight the fact that they are a pure artefact of the anisotropies introduced by the grid, and the initialization and operation of the proposed numerical method. The paper closes by suggesting that the proposed analytical solution, although not physically complete, is a rigorous and hard test for the quality of a given crystal growth algorithm, since an "ideal" two-dimensional numerical method should be able to recover the cylindrical growth of the seed without forming dendrites.

Key Words: *Crystal Growth, Similarity Solution, Enthalpy Method.*

1. INTRODUCTION

The modelling of crystal growth processes is an active field in numerical heat transfer research. An often used test problem is the solidification of an initially circular solid seed in an under-cooled liquid melt. This problem is investigated in the current paper. The particular interest is the case where crystal anisotropy and under-cooling of the solid-liquid interface are neglected; a case that admits an analytical solution. Against this analytical solution the predictive performance of a current fixed grid enthalpy method [1-3] is tested. The question asked is; how well does this method recover the analytical solution for the growth of the solid seed?

2. A CRYSTAL GROWTH PROBLEM

The problem of interest involves a solid circular seed at the equilibrium phase change temperature ($T = 0$ say) placed in a two-dimensional under-cooled liquid melt, with insulated far field boundaries and at uniform temperature $T_i < 0$. The placement of seed sets up a temperature gradient pointing from the solid into the liquid. Under this gradient, the latent heat of the liquid in contact with the solid leaks away, results in solidification and the growth of the solid. In the absence of crystal anisotropy this growth will maintain the circular shape of the seed. Further, if curvature and kinetic under-cooling of the solid-liquid interface is neglected a closed form similarity solution is obtained. Following Carslaw and Jaeger [4] this solution sets the growth of the crystal as $R = 2\lambda\sqrt{t}$ where the parameter λ is given by solving the equation $L\lambda^2 E_1(\lambda^2) + T_i e^{-\lambda^2} = 0$; L is the dimensionless latent heat and $E_1(x) = \int_x^\infty \frac{e^{-t}}{t} dt$ is the exponential integral.

The above stated problem can also be solved numerically using the recently proposed fixed grid enthalpy like method for equiaxed crystal growth [3]. This approach closely follow that of a time explicit enthalpy scheme with modifications that allow for the advance of the front from fully solid to liquid computational cells and procedures to calculate interface curvature and under-cooling from the nodal liquid fraction field. When applied to problems that involve anisotropy and interface under-cooling this method predicts dendritic crystals grown from an initial seed that match the correct asymptotic physical behaviours and are relatively free of artificial anisotropy introduced by the numerical grid. In the current problem, however, since physical anisotropy is removed and the stabilizing effects of under-cooling are not included it is not clear how well this simple enthalpy model will work.

3. RESULTS

Figure 1 compares the seed growth predictions $R(t)$ of the enthalpy method, implemented in a cylindrical coordinate geometry, with the analytical solution, for the case where $L = 1, T_i = -0.5$. The agreement between the numerical and analytical model is very satisfactory. Figure 2, however, shows predictions for the crystal shape in a case where the enthalpy methods is applied in a two-dimensional Cartesian geometry (a mesh of square control volumes); the distinct difference seen in the crystal shapes a result of the choice of the initial seed and the methodology used to advance the solidification between computational cells. Clearly these results are far from the correct form of a circular crystal shape; what is happening? Essentially, due to the chosen initial seed (achieved by setting some cells to solid) and the non-circular anisotropy imposed by the grid and interface advance scheme, as the seed grows, parts of the interface find themselves in regions more favourable for growth. In the absence of interface under-cooling to control this growth, the interface advances further into favourable growth regions leading to a "run away" process and the formation of the dendritic crystals shown in Figure 2. Hence, although the resulting images are pleasing in appearance and have the morphology of realistic crystals they can not be regarded as physically meaningful and should be correctly referred to as "numerical crystals."

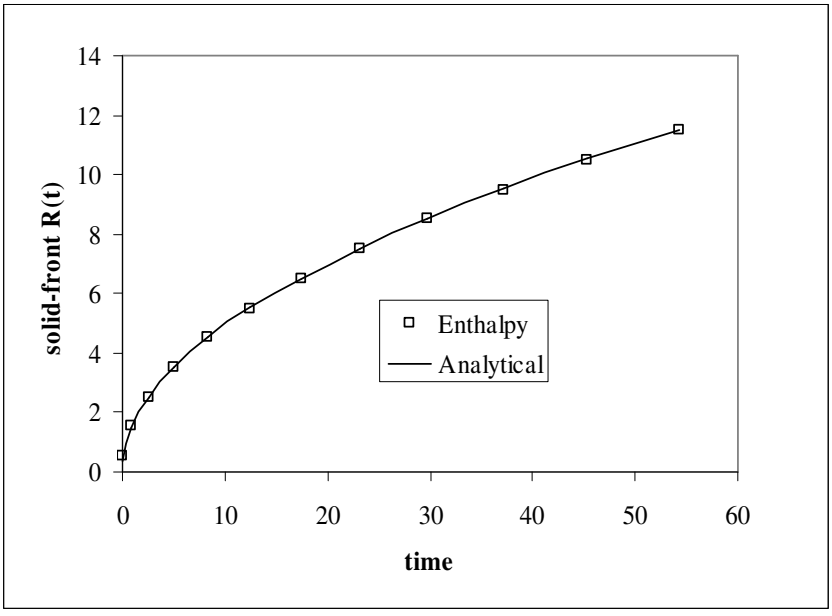

FIGURE 1. Enthalpy method predictions for seed growth *R(t)* compared with analytical solution

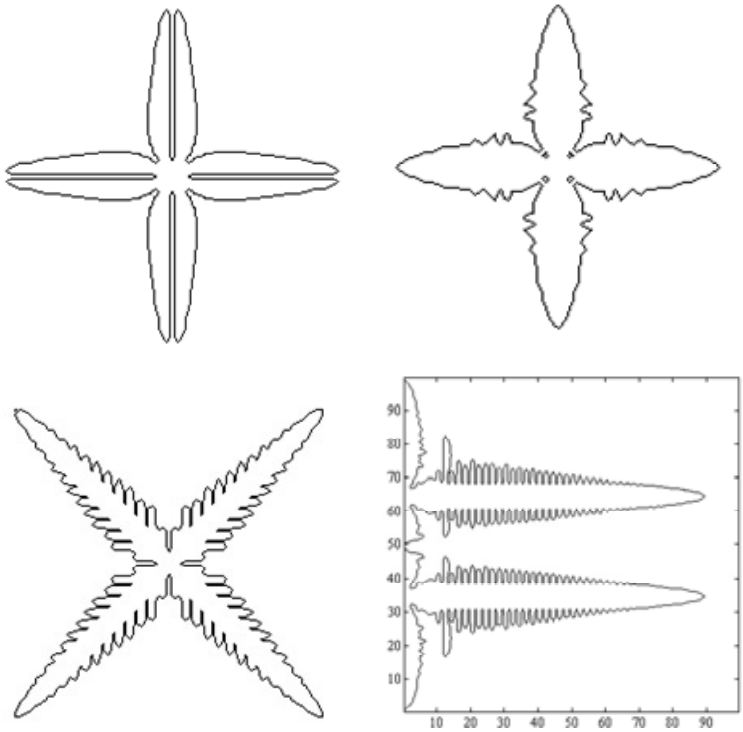

FIGURE 2. Examples of numerical crystals predicted by enthalpy model with different seeds and front advance algorithms

4. CONCLUSIONS

The crystal growth problem used in this work poses a rigorous and difficult test problem for heat transfer solidification codes. Not only does this test problem have a closed form analytical solution, due to the lack of controlling (anisotropy) or stabilising (interface under-cooling) features, it also offers a stringent test of a given methods level of induced grid anisotropy. As demonstrated in this paper, when this numerically artificial feature is not controlled, attractive but physically meaningless numerical crystals will form.

REFERENCES

[1] K-H. Tacke , Application of finite difference enthalpy methods to dendritic growth, Free Boundary Problems: Theory and Applications (eds. K-H Hofmann, J. Sprekels) Longman Sci. Tech. , Essex, 1990.

[2] D. Pal, J. Bhattacharya, P. Dutta, and S. Chakraborty, An enthalpy model for simulation of dendritic growth, *Num. Heat Transfer B*, 50, 59-78, 2006.

[3] V.R. Voller, An enthalpy method modeling dendritic growth in a binary alloy, *Int. J. Heat Mass Transfer*, 51, 823-834, 2008.

[4] H. Carslaw, and J. Jaeger, *Conduction of Heat in Solids*, 2nd Edition, Clarendon Press, Oxford, 1959.

First International Conference on Computational Methods for Thermal Problems
ThermaComp2009, September 8-10, 2009, Naples, Italy
N.Massarotti and P.Nithiarasu (Eds.)

Free Convection in a Non-Newtonian Fluid Saturated Square porous Enclosure with an Isothermal Corrugated Wall

S. V. S. S. N. V. G. K. Murthy
Department of Mathematics and Statistics, Indian Institute of Technology, Kanpur -208016, India,
sgkmurthy@gmail.com,skmurthy@iitk.ac.in

B. V. Rathish Kumar
Department of Mathematics and Statistics, Indian Institute of Technology, Kanpur-208016, India,
bvrk@iitk.ac.in

ABSTRACT

In this paper the Darcy natural convection process induced by an isothermal vertical wavy wall in a porous enclosure saturated with power-law type Non-Newtonian fluid is considered. The coupled non-linear partial differential equations modeling such a free convection process are then solved by Finite Element Method (FEM). Numerical results illustrating the effects of the governing parameters such as Rayleigh number (Ra), power-law index (n), number of waves per unit length (N), amplitude of the wavy curve modeling the wall (a), phase of the wavy curve (ϕ), on the convection process are presented. The flow and temperature fields are analyzed through streamlines, isotherms and Local / Cumulative heat flux plots.

Key Words: *Free convection, Non-Newtonian fluid, Porous Media, Finite Element Method.*

1. INTRODUCTION

Study of Natural convection of non-Newtonian fluids in porous media is very important in many engineering applications such as oil recovery, food processing, mineral processing, filtration, ceramic processing, liquid composite molding etc. So far not much work has been reported on Darcy natural convection in a wavy vertical square porous enclosure with a non-Newtonian power law type fluid. This study is focused in this direction. Detailed numerical simulations are carried out by Galerkin finite element method for a wide range of parameters such as Rayleigh number (Ra), wave amplitude (a), power-law index(n), no of waves(N), wave phase(ϕ).Flow and temperature distribution is analyzed by tracing Streamlines, Isotherms, local / cumulative heat fluxes.

2. MAIN BODY

We consider a two dimensional enclosure filled with a non-Newtonian power law fluid saturated porous medium with the left vertical wavy wall at the constant temperature 'T_w' and the other three walls are adiabatic. The porous medium is assumed to be isotropic with permeability 'K' and Boussinesq approximation is valid in the momentum equation for the density term. Under the above mentioned assumptions, non-dimensional equations [4] governing the Darcy flow through a homogeneous porous medium near the left wavy vertical surface can be written as follows.

$$V^{n-1}\left[\frac{\partial^2\Psi}{\partial X^2}+\frac{\partial^2\Psi}{\partial Y^2}\right]+(n-1)V^{n-3}\left[\left(\frac{\partial\Psi}{\partial X}\right)^2\frac{\partial^2\Psi}{\partial X^2}+2\frac{\partial\Psi}{\partial X}\frac{\partial\Psi}{\partial Y}\frac{\partial^2\Psi}{\partial X\partial Y}+\left(\frac{\partial\Psi}{\partial Y}\right)^2\frac{\partial^2\Psi}{\partial Y^2}\right]=\left(\frac{\partial\theta}{\partial Y}\right)$$

where, $V = \sqrt{\left(\frac{\partial \Psi}{\partial X}\right)^2 + \left(\frac{\partial \Psi}{\partial Y}\right)^2}$ is the dimensionless velocity.

$$\frac{\partial \Psi}{\partial Y}\frac{\partial \theta}{\partial X} - \frac{\partial \Psi}{\partial X}\frac{\partial \theta}{\partial Y} = \frac{1}{Ra^{\frac{1}{n}}}\left(\frac{\partial^2 \theta}{\partial X^2} + \frac{\partial^2 \theta}{\partial Y^2}\right)$$

The appropriate boundary conditions in non-dimensional form are:

Left wall : $\Psi = 0,\ \theta = 1 \quad on \quad Y = aSin(\pi X)$

Right wall : $\Psi = 0,\ \theta = 0, \quad on \quad Y = 1$

Bottom and Top Wall : $\Psi = 0, \quad \frac{\partial \theta}{\partial X} = 0 \ \ on \ \ X = 0 \ \ and \ \ X = 1$

3. RESULTS

The above non-dimensional governing equations with boundary conditions have been solved using Galerkin Finite Element method. To begin with code has been validated by comparing the results for Newtonian case with reported in literature. To ensure grid independency of the results grid selection test has been carried out on four different mesh systems consisting of 40×40, 50×50, 60×60 elements. It is observed that as one moves from 50×50 grid system to 60×60 grid system there is only a marginal variation (less than 1%) in Nu values. Hence 50×50 grid system has been chosen for extensive numerical simulations for various values of the parameters.

In Table 1 global Nusselt number (Nu_g) corresponding to total heat flux along the wavy vertical wall for $0.5 \leq n \leq 1.5$, $Ra = 100$, $N = 1$, $a = 0.2$, $\phi = 0^0$ are presented. From the data in Table 1 one can clearly see that the Nu_g decreases with increasing values of the power-law index. There is a drastic fall in Nu_g as power law index is increased from 0.5 to 0.75. Cumulative heat flux (CHFLXs) plots in Figure 1 along the wavy wall for the above set of parameters depict a steep raise in CHFLXs along the lower part of the wavy wall especially for smaller values of power-law of index. The corresponding isotherm plots have shown the presence of steep thermal boundary layers (TBLs) along the lower portion of the wavy wall which is protruding into the domain. It may be noted that the tangent to the lower segment of the wavy wall till the cusp region gets increasingly aligned to convection favoring buoyancy forces. Heat fluxes all along the trough are relatively small at all values of 'n'.

Data in Table 2 corresponds to the influence of wave amplitude on heat fluxes for n=0.75, 1.5, Ra=100, $\phi = 0^0$, N=1, $0 \leq a \leq 0.4$. Nu_g increases with increasing values of wave amplitude. At all values of 'a' Nu_g decreases with increasing values of power-law index. Simulations are also carried out to analyze the influence of N, Ra, and ϕ on flow and temperature fields. At all values of 'n' while Nu_g is seen to decrease with 'N' it increases with 'Ra'. Nu_g is found to be a maximum when $300^0 \leq \phi \leq 360^0$. i.e when the lower portion of the wavy wall is nearly aligned to the convection favoring buoyancy forces. Streamlines and isotherms corresponding to the set of parameters (n=1.5, Ra=100, $\phi = 0$, N=1, a=0.4) and (n=0.75, Ra=100, $\phi = 0$, a=0.2, N=2) are presented in Fig 2(a-b) and Fig 3(c-d) respectively.

Power-law index(n)	Global Nusselt Number(Nu_g)
0.5	15.3081846
0.75	4.6706233
1.0	2.55069661
1.25	2.33359241
1.5	2.43161297

TABLE 1. Global Nusselt number values along the wavy vertical wall for $0.5 \leq n \leq 1.5$, $Ra = 100$, $N = 1$, $a = 0.2$, $\phi = 0^0$

Amplitude effect(a)	Global Nusselt Number(Nu_g) when n=0.75	Global Nusselt Number(Nu_g) when n=1.5
0.0	6.81224871	3.68495607
0.1	6.11269045	3.24001741
0.2	4.6706233	2.43161297
0.4	3.07622814	1.47171974

TABLE 2. Global Nusselt number values for n=0.75, 1.5, when Ra=100, $\phi = 0^0$, N=1, $0 \leq a \leq 0.4$

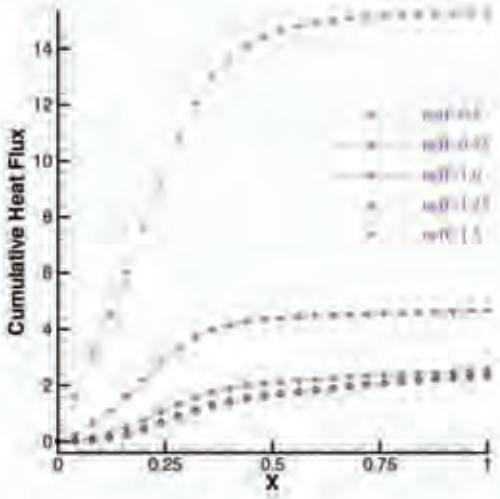

FIGURE 1. Cumulative heat fluxes for Ra=100, (D / H)=0.1 and $0.5 \leq n \leq 1.5$

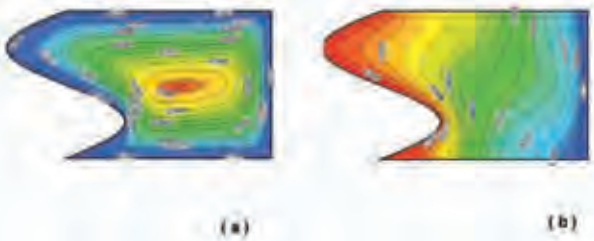

FIGURE 2. Stream line and isotherm plots when n=1.5, Ra=100, $\phi = 0^0$, N=1, for Amplitude eff(a=0.4) respectively

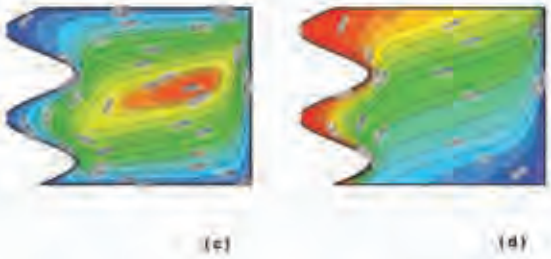

FIGURE 3. Stream line and isotherm plots when n=0.75, Ra=100, $\phi = 0^0$, a=0.2 for wave eff(N=2) respectively

4. CONCLUSIONS

Flow and temperature fields are highly sensitive to flow governing parameters such as power law index (n), Rayleigh number (Ra), and on the extent and frequency of the corrugation in isothermal vertical wall modeled by sinusoidal waves i.e wave amplitude (a) and wave number (N). While global heat fluxes from the isothermal corrugated vertical wall are enhanced by increasing 'Ra', and 'a' they are decreased by increasing 'n' and 'N'.

REFERENCES

[1] B.V. Rathish Kumar, P.V.S.N. Murthy, P. Singh, Free convection heat transfer from an isothermal wavy surface in a porous enclosure, *nternational Journal for Numerical Methods in Fluids*, 28(4), 633-61, 1998.

[2] M.A. Hossain, D.A.S Rees, Combined heat and mass transfer in natural convection flow from a vertical wavy surface, *Acta Mechanica*, 136, 133-41, 1999.

[3] Gi Bin Kim, Jae Min Hyun, Buoyant Convection of a power-law Fluid in an enclosure filled with heat generating Porous Media, *Numerical Heat Transfer, Part A:Applications An International Journal of Computation and Methodology*, 45(6), 569-82, 2004.

[4] B. V. R. Kumar, Shalini, Mohit Nigam, Vivek Sangwan, and S. S. N. G. K. Murthy, A Numerical Study of Pulsatile Power Law Fluid Flow in a Porous Channel, *(To appear in Journal of Mechanics in Medicine and Biology-2009)*.

[5] Ching-Yang Cheng, Combined heat and mass transfer in natural convection flow from a vertical wavy surface in a power-law fluid saturated porous medium with thermal and mass stratification, *International Communications in Heat and Mass Transfer*, 36, 351-356, 2009.

First International Conference on Computational Methods for Thermal Problems
ThermaComp2009, September 8-10, 2009, Napoli, Italy
N.Massarotti and P.Nithiarasu (Eds.)

Modelling of ice melting in horizontal annulus using enthalpy method

Esad Tombarević
University of Montenegro, Cetinjski put bb, esadt@ac.me

Igor Vušanović
University of Montenegro, Cetinjski put bb, igorvus@ac.me

ABSTRACT

Phase change ice-water and vice versa in the geometry of horizontal cylindrical annulus with constant inner wall temperature and adiabatic outer wall is modelled with enthalpy based mixture model. Melting phenomenon is analyzed through a sequence of numerical calculations. Inner pipe wall temperature has a strong influence on the shape of ice-water interface, the flow and temperature fields in the liquid, the heat transfer coefficients and the rate of melting. Results of numerical calculations show good qualitative agreement with available experimental and other numerical results.

Key Words: *isothermal phase change, melting, enthalpy model, fixed grid, annulus.*

1. INTRODUCTION

Modelling of solid-liquid phase change has received a lot of attention since it often appears in practice. One of the key challenges that has been in focus of research in past is tracking of transient phase change interface which is usually treated either with moving or fixed grid methods. Moving grid method [1] assumes fixing of solid-liquid interface in each time step, solving of conservation equations separately for solid and liquid phase and applying of classical Stefan formulation to find interface position in the next time step. With fixed grid method [2] the same set of equations is solved for the whole domain and phase change is taken into account with appropriate source terms, without explicit tracking of interface. The configuration of horizontal annulus is studied theoretically and experimentally and extensive review is given in Yao and Prusa [3]. Recent review of research on cold thermal energy storage is given in the paper of Saito [4].

2. PHYSICAL AND MATHEMATICAL MODEL

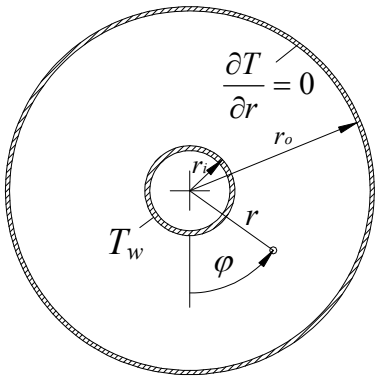

FIGURE 1. Physical model

Physical model considered is a horizontal circular annulus with the inner pipe radius r_i and the outer pipe radius r_o (Figure 1). The no-slip conditions regarding the velocities are applied on both walls, while temperature of inner pipe is constant and uniform along the pipe. The outer pipe is assumed to be thermally insulated. Ice in the annular space is initially on temperature T_i and the melting starts when the inner pipe temperature is suddenly risen above the phase change temperature. Due to its simplicity, fixed grid enthalpy-based method is used for modeling of phase change. The same set of conservation equations is used for the whole domain and the need for explicit tracking of solid-liquid interface is excluded. Flow field is considered two dimensional, laminar and incompressible. The physical properties of water and ice are temperature invariant, except the water density whose nonlinear variation with temperature is included in buoyancy term in the momentum equation. Based on the enthalpy method, governing equations, written out in form suitable for numerical integration with CV method [5] are:

$$\frac{\partial \rho}{\partial t}+\nabla\left(\rho\vec{V}\right)=0 \tag{1}$$

$$\frac{\partial}{\partial t}(\rho v_r)+\nabla\left(\rho\vec{V}v_r\right)-\frac{\rho v_\varphi^2}{r}=-\frac{\partial p}{\partial r}+\nabla(\mu\nabla v_r)-\mu\frac{v_r}{r^2}-\frac{2\mu}{r^2}\frac{\partial v_\varphi}{\partial\varphi}-\rho g\beta(T-T_{ref})sin\varphi+S_r \tag{2}$$

$$\frac{\partial}{\partial t}(\rho v_\varphi)+\nabla\left(\rho\vec{V}v_\varphi\right)+\frac{\rho v_r v_\varphi}{r}=-\frac{1}{r}\frac{\partial p}{\partial\varphi}+\nabla(\mu\nabla v_\varphi)-\mu\frac{v_\varphi}{r^2}+\frac{2\mu}{r^2}\frac{\partial v_r}{\partial\varphi}+\rho g\beta(T-T_{ref})cos\varphi+S_\varphi \tag{3}$$

$$\frac{\partial}{\partial t}(\rho h)+\nabla\left(\rho\vec{V}h\right)=\nabla(\lambda\nabla T)-\left[\frac{\partial}{\partial t}(\rho\Delta H)+\nabla\left(\rho\vec{V}L\right)\right],\ H=h+\Delta H \tag{4}$$

where S_r and S_φ are Darcy like source terms that nullify velocities in the solid phase. The jump of total enthalpy H on the phase change temperature is converted to linear function ΔH in the narrow temperature interval. Details on numerical integration of equations (1)-(4) are given in [2].

3. RESULTS AND DISCUSSIONS

A number of numerical calculations are performed in order to estimate the influence of inner pipe temperature on the shape of ice-water interface, the temperature and flow fields in the liquid phase, local and average heat transfer coefficients. Annulus dimensions are r_i=12.7 mm and r_o=50.8 mm and ice in the annulus is initially on the phase change temperature in all calculations.

The temperature and flow fields in several time instances for the case of melting with T_w=4°C are given on Figure 2. At the beginning, conduction is dominant heat transfer mechanism and ice-water interface has the shape of circle with the center on the axis of annulus. As melting continues, convection in the liquid phase intensifies which results in isotherms deformations. In this case, water in the vicinity of inner pipe has the highest density and therefore flows downwards along the inner pipe, while the water in the vicinity of ice surface flows upwards.

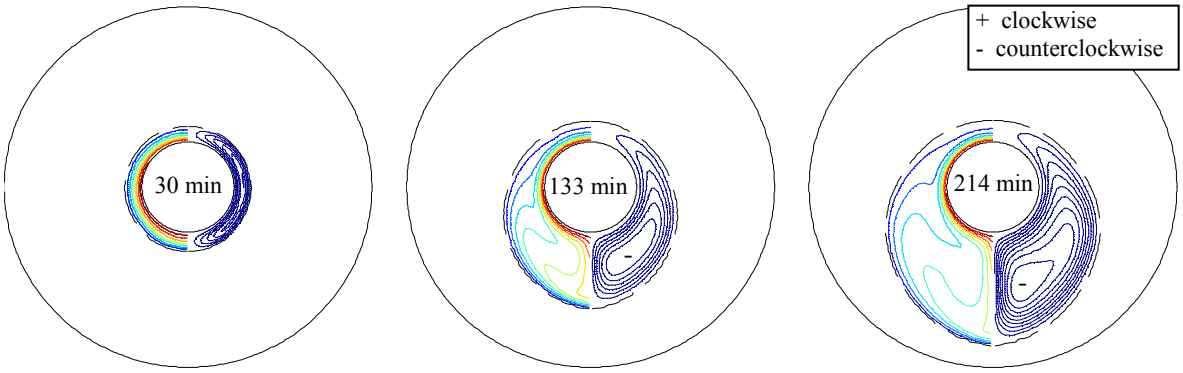

FIGURE 2. Temperature field (left) and flow field (right) for T_w=4°C

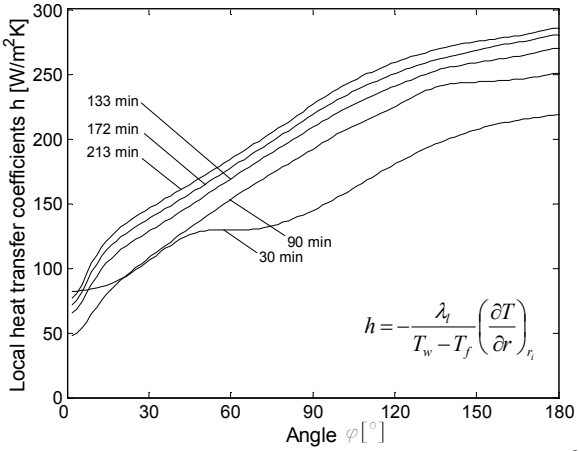

FIGURE 3. Local heat transfer coefficients for T_w=4°C

Local heat transfer coefficients as a function of angle φ are given on Figure 3. It is evident that heat transfer is more intense on the top of the heat source (higher φ values) since relatively cold water, previously cooled down during the flow along the ice surface comes into contact with heat source. On the ice surface there is an opposite situation-relatively warmer water comes in contact with ice surface below heat source and consequence is pear shaped melted region facing downwards.

In all cases when T_w>4°C, isotherm T=4°C, i.e. density extreme is somewhere between the surface of inner pipe and ice surface, and two distinct type of flow cells appears in the melted region. The temperature and flow fields in several time instances for T_w=8°C are given on Figure 4. Ice-water interface retains circular shape over a relatively longer period of time. As melting continues, flow in the outer vortex, next to the ice-water interface intensifies and occupies most of the melted region and as a result moving of interface is determined by the flow in the outer vortex and melting is more intense under the heat source.

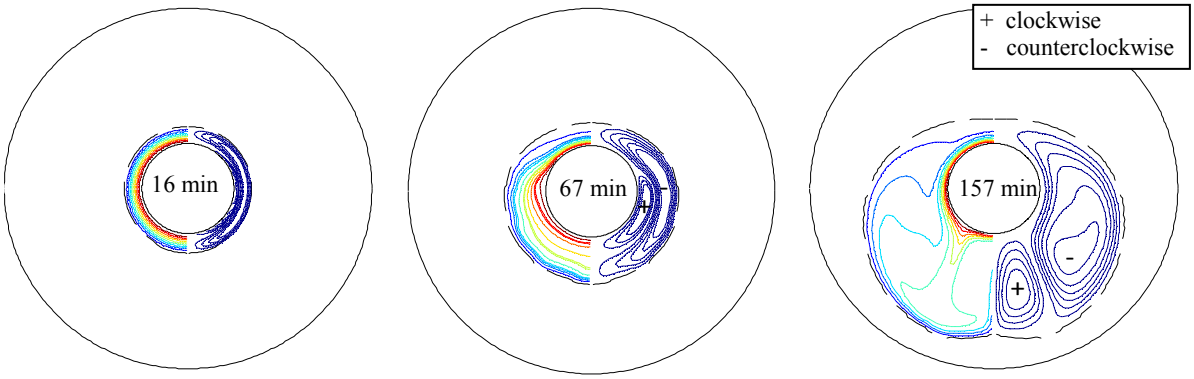

FIGURE 4. Temperature field (left) and flow field (right) for T_w=8°C

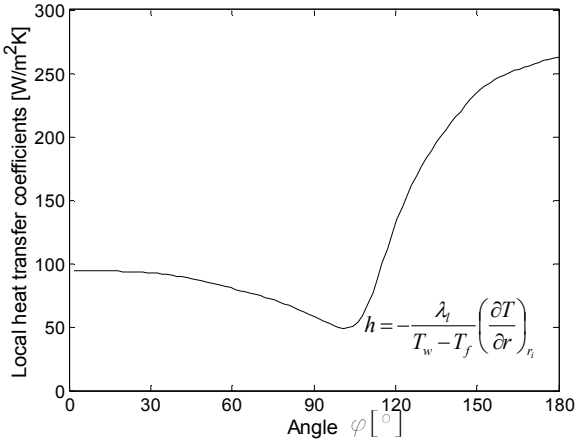

FIGURE 5. Local heat transfer coefficients for T_w=8°C

Local heat transfer coefficients from the pipe surface to the water for t=67 min (Figure 5) have minimum values for $\varphi \approx 100^o$, i.e. on the contact of inner and outer vortex where temperature gradients have minimum. For $\varphi<100^o$ local heat transfer coefficients are relatively smaller since there is a clockwise circulation in inner vortex down the isotherm T=4°C and then along the surface of cylinder T_w=8°C. For $\varphi>100^o$C local heat transfer coefficients are relatively higher since there is a counterclockwise circulation of water in outer vortex, along the ice surface T_f=0°C and then down the warm surface of cylinder T_w=8°C.

For T_w=13.6°C (Figure 6) at the very beginning of process, melted region takes pear shape facing upward. Melting is more intense above heat source, and retarded over a quite long period under the cylinder where heat transfer is conduction dominated.

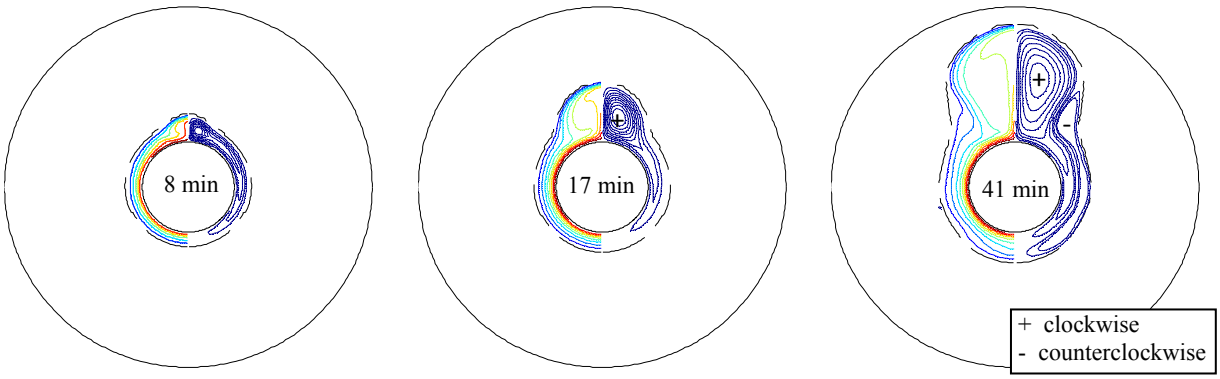

FIGURE 6. Temperature field (left) and flow field (right) for T_w=13.6°C

Average values of heat transfer coefficients from inner pipe surface to the water for T_w 4, 6 and 8°C are given on Figure 7. Initial high values are characteristic for transient conduction dominated heat

transfer. After 16000 s for T_w=4°C and 12000 s for T_w=8°C water comes into contact with outer insulated pipe of annulus and therefore there is a drop of average heat transfer coefficients. Variation of molten volume ratio V/V_o (V-volume of molten region, V_o volume of heat source) with time is given on Figure 8, together with experimental data of White et al. [6] for T_w 4, 8 and 10 °C.

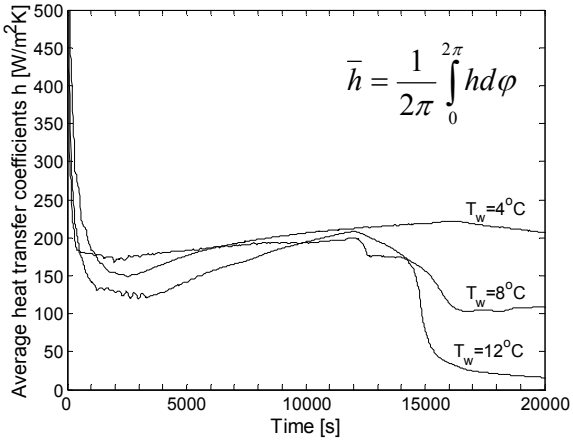

FIGURE 7. Average heat transfer coefficients

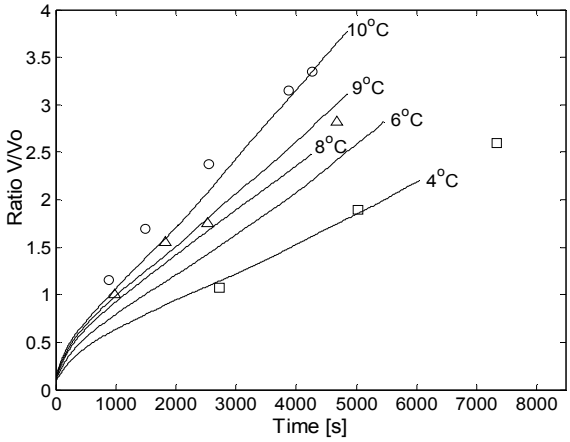

FIGURE 8. Variation of molten volume with time

4. CONCLUSIONS

Isothermal phase change, such as ice melting, can be successfully simulated with proposed single domain enthalpy based model. Performed calculations exhibit qualitatively good agreement with available experimental [6] and numerical results [1] where moving grid temperature based method is used. Temperature of inner cylinder wall strongly affects the flow in liquid and shape of solid – liquid interface unlike the freezing process [7] where convection influence is less pronounced. For inner pipe temperatures under or equal 4°C water with the highest density is next to the inner wall, and flow is directed to the bottom of annulus causing the pear shape melted region on the bottom of annulus, and highest heat transfer coefficient on the top of annulus. With inner wall temperature T_w above 4°C, isotherm with highest water density moves in the liquid region, and separates two distinct cells with opposite flow directions. Higher wall temperatures move maximum density isotherm closer to the phase change interface and causes supremacy of clockwise flow in liquid and forming of pear shape on the top side of annulus. Average heat transfer coefficients on the inner pipe wall change during the melting process and can be obtained by integrating local values around the circumference of inner pipe.

REFERENCES

[1] C.J Ho, S. Chen, Numerical simulation of melting of ice around a horizontal cylinder, *International Journal of Heat and Mass Transfer*, 29/9, 1359-1369, 1986.

[2] V.R. Voller, C. Prakash, A fixed grid numerical methodology for convection diffusion mushy region phase change problems, *International Journal of Heat and Mass Transfer*, 30/8, 1709-1719, 1987.

[3] L.S. Yao, J. Prusa, Melting and freezing, *Advances in Heat Transfer*, 19, 1-95, 1989.

[4] A. Saito, Recent advances in research on cold thermal energy storage, *Journal of refrigeration*, 25, 177-189, 2002.

[5] S.V. Patankar, *Numerical Heat Transfer and Fluid Flow*, Hemisphere, New York, 1980.

[6] D. White, R. Viskanta, W. Leidenfrost, Heat transfer during melting of ice around a horizontal, isothermal cylinder, *Experiments in Fluids*, 4, 171-179, 1986.

[7] E. Tombarević, I. Vušanović, Influence of inner pipe wall temperature on freezing of water in a horizontal cylindrical annulus, *Proceedings of EUROTHERM Seminar Nr.84-Thermodynamics of phase change*, Namur, Belgium, 2009.

First International Conference on Computational Methods for Thermal Problems
ThermaComp2009, September 8-10, 2009, Napoli, Italy
N.Massarotti and P.Nithiarasu (Eds.)

NUMERICAL METHODS OF MINICHANNEL FLOW BOILING HEAT TRANSFER COEFFICIENT CALCULATION AND THEIR MODIFICATIONS

S. Hozejowska
Kielce University of Technology, Al. 1000-lecia PP 7, 25-314 Kielce, Poland,
e-mail: ztpsf@tu.kielce.pl

L. Hozejowski
Kielce University of Technology, Al. 1000-lecia PP 7, 25-314 Kielce, Poland,
e-mail: hozej@tu.kielce.pl

M.E. Poniewski
Warsaw University of Technology, ul. Lukasiewicza 17, 09-400 Plock, Poland, e-mail: meponiewski@pw.plock.pl

ABSTRACT

The paper deals with methods of numerical determination of heat flux and heat transfer coefficient between the boiling liquid that is flowing through a vertical, rectangular and asymmetrically heated minichannel and the heating foil. Two approaches were determined: one- and two-dimensional, both based on experimental results of thermosensitive liquid crystal technique application. One-dimensional approach takes into account the temperature foil change only along the flow direction, whereas two-dimensional approach includes also the direction perpendicular to the flow. The two-dimensional approach uses heat polynomials which satisfy Laplace equation. Provided the mesaurement errors are known it is allowed to apply equalizing calculus in both approaches. Basing on the equalizing calculus, the criterion for the correctness of numerical method selection is presented.

Key Words: *Minichannel Flow Boiling Heat Transfer, Heat Polynomials, Equalizing Calculus.*

1. INTRODUCTION

Proposed models for heat flow through foil and glass, see Figure 1, deal with a system composed of the liquid (R11) which flows into a minichannel and has the lower temperature than the temperature of boiling, and of two partitions: quasiadiabatic partition on the one side and the heating foil covered with thick glass pane on the other, which separate the liquid from the environment. The foil acts as a source of heat, and the liquid crystal layer on its surface at the contact with the glass allows measuring the temperature distribution on the exterior heating surface. Increasing electrical power supply to the foil during the flow of the liquid through the minichannel causes the increase in the heat flux supplied to the liquid, which leads to bubble boiling incipience. The quantities to be found are both the heat flux and the heat transfer coefficient on the contact surface of the heating foil and the boiling liquid.

2. ONE- AND TWO - DIMENSIONAL APPROACHES

In one-dimensional approach the investigations took into account the dimension along the flow direction (x), but the dimension perpendicular to it (y) was related only to the foil thickness, see Figure 1. The glass pane, owing to its very low conductivity (λ_G = 0.71 $Wm^{-1}K^{-1}$), quite large

thickness (δ_G = 5mm) and a low heat transfer coefficient on its exterior surface, may be treated as a perfect insulator. Consequently, it may be assumed that the entire volumetric heat flux generated inside the foil, is transferred by heat conduction across the foil thickness to the flowing liquid, and the heat flux on the surface contacting the liquid is given by the equations:

$$- \frac{\partial T_F(x, \ )}{\partial y} = q_V \ = q_w \quad \text{(a)} \qquad \text{where} \qquad q_V = (U\,I)(\ W_F\ L_F\ )^{-1} \quad \text{(b)} \tag{1}$$

At the boundary surface $y = \ + \ $ heat is dissipated by convection, therefore

$$- \frac{\partial T_F(x, \ + \ )}{\partial y} = \ (x)\left(T_F(x, \ + \ ) - T_l(x)\right) \tag{2}$$

where $T_l(x)$ changes, for simplicity, linearly from $T_{l,inlet}$ to $T_{l,outlet}$. Since $\ $ is very small, it is possible to replace the partial derivative in equation (1a) with a finite difference, and after taking condition (2) into account we get a simple formula for the heat transfer coefficient:

$$_{1D}(x) = (q_V \ \ )(\ \left(T_F(x, \ ) - T_l(x)\right) - q_V \cdot \ )^{-1} \tag{3}$$

The temperature $T_F(x, \ )$ is measured at discrete points and then approximated with a polynomial. In two-dimensional approach we assume a stationary heat transfer process in the foil and glass, expressed with the equations:

$$\text{• in glass: } \nabla^2 T_G = 0 \text{ (a)} \qquad \text{and} \qquad \text{• in foil: } \nabla^2 T_F = -q_V \ \ ^{-1} \text{ (b)} \tag{4}$$

At the glass – foil contact the equality of both temperatures and their gradients is found:

$$T_F(x_k, \ ) = T_G(x_k, \ ) = T_k \quad \text{(a)} \qquad - \ \frac{\partial T_F}{\partial y} = - \ \frac{\partial T_G}{\partial y}, \ \text{y} = \ , 0 \le x \le \text{L} \ \text{(b)} \tag{5}$$

It is assumed that the remaining boundaries are isolated, see Figure 1. The unknown glass temperature $T_G(x,y)$ and foil temperature $T_F(x,y)$ are approximated with a linear combination of the heat polynomials $u_n(x,y)$ which satisfy the equation (4a) [3]

$$T_G(x,y) \approx \sum_{i=0}^{N} a_i u_i(x,y) \ \text{(a)} \qquad T_F(x,y) \approx \tilde{u}(x,y) + \sum_{j=0}^{M} b_j u_j(x,y) \ \text{(b)} \tag{6}$$

where $\tilde{u}(x,y)$ is any specific solution to equation (4b). Unknown coefficients a_i and b_j are calculated by the least squares method which leads to the minimization of error functionals.

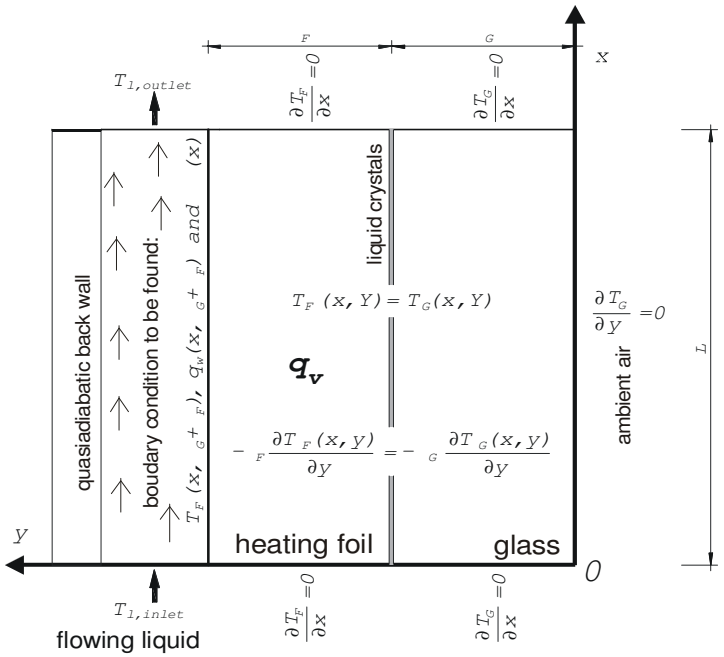

FIGURE 1. Diagram of flow boiling process in the investigated minichannel

and boundary conditions

Those functionals describe the mean square errors between approximates and prescribed boundary conditions in Figure 1. The measurements T_k contain local temperature measurement errors ε_k which we use to construct weights in the error functional J_G [1]:

$$J_G = \int_0^L \left(\frac{\partial T_G(x,0)}{\partial y} \right)^2 dx + \int_0^{\delta} \left[\left(\frac{\partial T_G(0,y)}{\partial x} \right)^2 + \left(\frac{\partial T_G(L,y)}{\partial x} \right)^2 \right] dy + \sum_{k=1}^{K} \left(\frac{T_G(x_k,\delta_G) - T_k}{\varepsilon_k} \right)^2 \tag{7}$$

They are the errors in estimating values of the foil temperature, based on the hue indicated by liquid crystals [2,3,4]. When in (7) $T_G(x,y)$ is substituted with dependence (6a), the minimum of functional J_G is determined from the solution for the system of equations:

$$\frac{\partial J_G}{\partial a_i} = 0, \quad i = 0, 1, ..., N \tag{8}$$

Coefficients b_j are determined in the same manner as in equation (8). For function $T_F(x,y)$, the minimized functional J_F has a similar form to the functional (7). If we know the function $T_F(x,y)$ on the boundary $y = \delta_G + \delta_F$, we can compute the heat flux and the heat transfer coefficient from the condition (2). In the equalizing calculus we are looking for such corrections ε_k for measurements T_k, that for the corrected foil temperature $\tilde{T}_k$ the following condition is satisfied

$$\tilde{T}_k = T_k + \varepsilon_k \tag{9}$$

Corrections ε_k are assumed to feature normal distribution with mean value equal to zero and finite variance equal to σ_k^2 [1]. Correction ε_k is determined so as to minimize the Lagrange function

$$\Omega = \sum_{k=1}^{K} \varepsilon_k \sigma_k^{-2} \varepsilon_k + 2\sum_{k=0}^{K} \Omega_k \left(\tilde{T}_F(x_k, \delta_G) - \tilde{T}_k \right) \to \min \tag{10}$$

where: Ω_k are Lagrange multipliers**.** Additionally, we assume equality between the corrected temperature $\tilde{T}_F$, and the corrected measurement of temperature $\tilde{T}_k$, that is

$$\tilde{T}_F(x_k, \delta_G) - \tilde{T}_k = 0 \tag{11}$$

The equalizing calculus is employed in an analogical manner for the one–dimensional approach [5].

3. RESULTS

In the one-dimensional approach the measurements of temperature T_k were approximated using a 5-degree polynomial, i.e. n=5; in the two-dimensional approach it was assumed that $\tilde{u}(x,y) = -0.5 q_v \lambda_F^{-1} y^2$ and $N = M = 5$. Heat transfer coefficients calculated on the basis of both approaches have similar values.

According to the assumed corrections ε_k, function W given by equation

$$W = \sum_{k=1}^{K} \varepsilon_k \sigma_k^{-2} \varepsilon_k \tag{12}$$

has a distribution χ^2 with K-n-1 degrees of freedom in the one-dimensional approach, and K-N-1 in two-dimensional approach. The calculations confirm that the value of function W in each run is lower than the number of degrees of freedom. Function W helps test the fitting of measurement data by means of an n-degree polynomial (one-dimensional approach) or a combination of N+1 heat polynomials (two-dimensional approach). With the use of χ^2 we can verify the correct fitting hypothesis for measurement data T_k using a 5th -degree polynomial (one-dimensional approach) or a combination of six heat polynomials (two-dimensional approach) [1]. The calculations did not

confirm only one case of the reviewed hypothesis. Additionally, the corrections $_k$ should fulfill condition [1]:

$$\left| _k \right| < 3 \ _k \tag{13}$$

In one-dimensional approach there is one case (experimental run) when not all corrections fulfill condition (13). In all other cases the condition is fulfilled by all corrections $_k$. The results are similar for the two-dimensional approach. The assessment of measurement accuracy errors in experimental studies was carried out for both approaches. The square mean error was used as a measure for error values. They were calculated as roots of sum of function partial derivatives products in relation to a given exterior parameter in direct measurement, by the mean error of the given parameter measurement. Heat transfer coefficient mean errors, calculated before and after the equalizing calculus, were determined for both approaches. The use of the equalizing calculus helped reduce the heat transfer coefficient error.

4. CONCLUSIONS

• The calculated heat transfer coefficients α, based on two the presented approaches, have similar values. The results verify one another, which confirms the correctness of the assumed approaches and the used numerical procedures.

• Test ^{2} verifies the hypothesis of measurement data fitting using an *n*-degree polynomial (for the one-dimensional approach) or a linear combination *N*+1 of heat polynomials. For the two – dimensional approach, the measurement data fitting is fulfilled for nearly all the runs.

REFERENCES

[1] S. Brandt, *Data analysis, statistical and computational methods for scientists and engineers*, Springer Verlag, New York, 1999.

[2] S. Hozejowska, M. Piasecka, M.E. Poniewski, 2009, Boiling heat transfer in vertical minichannels. Liquid crystal experiments and numerical investigations, *Int. J. of Thermal Sciences*, **48**, 1049-1059

[3] M. Piasecka, S. Hozejowska, M.E. Poniewski, 2004, Experimental evaluation of flow boiling incipience of subcooled fluid in a narrow channel, *Int. J. Heat & Fluid Flow*, **25**, 159-172

[4] M. Piasecka, S.Hozejowska and M.E. Poniewski, Experimental error analysis and heat polynomial method improvement for boiling heat transfer numerical calculations in minichannels, *Proc. 3rd Int. Conf. on Microchannels and Minichannels*, Toronto , 2005, paper # ICMM2005-75142.

[5] M. Piasecka, M.E. Poniewski, S. Hozejowska, L. Hozejowski, Various models and numerical procedures of boiling heat transfer calculations in minichannels, *Proc. Euromech Colloquium #472 on Microfluidics and Transfer*, Grenoble, 2005, p.4.

First International Conference on Computational Methods for Thermal Problems
ThermaComp2009, September 8-10, 2009, Naples, Italy
N.Massarotti and P.Nithiarasu (Eds.)

SIMULATION OF TWO-PHASE FLOW UNDER CONSTANT HEAT FLUX USING HIGH ORDER METHODS

Manavela Chiapero, E.
Department of Energy and Process Engineering, Norwegian University of Science and Technology, Trondheim, Norway, ezequiel.m.chiapero@ntnu.no

Dorao, C. A.
Department of Energy and Process Engineering, Norwegian University of Science and Technology, Trondheim, Norway, carlos.dorao@ntnu.no

Fernandino, M.
Department of Energy and Process Engineering, Norwegian University of Science and Technology, Trondheim, Norway, maria.fernandino@ntnu.no

ABSTRACT

In this work a two-phase separated flow model is presented for studying two phase flow, pressure drop and heat transfer during evaporation in a horizontal tube for several refrigerants under constant heat flux. The numerical model is solved using a least squares spectral element method (LSSEM). The results are validated with experimental data.

Key Words: *Heat Transfer, Least Squares Spectral Element Method, Horizontal Tubes.*

1. INTRODUCTION

The heat transfer coefficient during evaporation in horizontal tubes is a very important parameter for the design of heat exchangers. Several refrigerants are available at present with different characteristics. A validated simulation tool for the computing of the heat transfer coefficient is necessary in order to avoid the need of performing experiments each time an analysis of the performance of a different fluid is needed.

In this work the numerical model is solved based on the least squares formulation. The least squares formulation is an interesting alternative to Galerkin and Petrov–Galerkin weak formulations for the discretization of partial differential equations. The least squares method (LSM) consists in finding the solution which minimizes the integral of the square of the residual over the computational domain. The LSM presents the characteristic of converting a well–posed partial differential equations into symmetric positive definite algebraic equations irrespective of the type of the underlying problem operator.

2. MATHEMATICAL MODEL

The model describes the evaporation of a given refrigerant along a heated horizontal tube under constant heat flux. The model is a steady state 1-D model, based on a separated flow model, assuming the existance of a liquid film at the wall and a single-phase gas flow at the core. The main assumptions for the modelling are that the liquid and vapour are at the same pressure and in thermodynamic equilibrium. The conservation of mass and momentum equations are solved for the control volume showed in Fig. 1. For the friction pressure drop, the single phase friction factor is calculated with the Haaland's equation [1], and for the two phase frictional pressure drop the Friedel two-phase multiplier is used [2]. The heat transfer coefficient for the liquid film is calculated with the correlation of Chaddock [3].

The one-dimensional domain is splitted into several slabs, in which the LSSEM is used for the resolution of the differential equations. The boundary conditions for the slab n+1 are the solutions of the slab n.

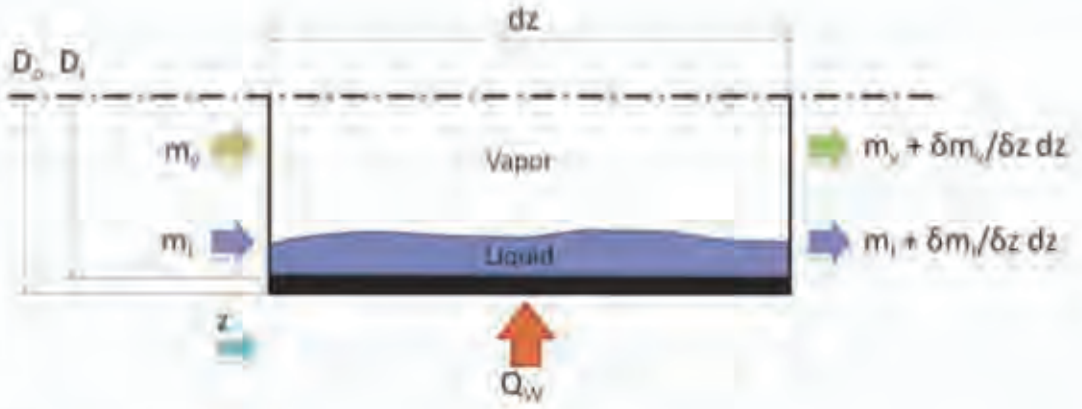

FIGURE 1. Control volume used for the model

3. THE LEAST SQUARES METHOD

In the last decade, finite element models based on the least–squares variational principles have gained considerable attention [4].

The least–squares method presents the characteristic that independent of the underlying equation or set of equations the final problem is defined as a convex, unconstrained minimization problem. In this way, the finite element problem belongs again to a variational setting.

For a particular problem we can define the norm–equivalent functional

$$\mathcal{J}(f;g) \equiv \frac{1}{2} \parallel \mathcal{L}f + g \parallel^2_{Y(\Omega)} \tag{1}$$

with the norm $\parallel \bullet \parallel^2_{Y(\Omega)}$ defined as

$$\parallel \bullet \parallel^2_{Y(\Omega)} = \langle \bullet, \bullet \rangle_{Y(\Omega)} = \int_\Omega \bullet \bullet \, d\Omega \tag{2}$$

So, the least–squares formulation consists in finding the minimizer of the norm–equivalent functional $\mathcal{J}(f;g)$. Based on variational analysis, the necessary condition for the minimization of $\mathcal{J}$ is equivalent to:

Find $f \in X(\Omega)$ such that

$$\mathcal{A}(f,v) = \mathcal{F}(v) \qquad \forall v \in X(\Omega) \tag{3}$$

with

$$\mathcal{A}(f,v) = \langle \mathcal{L}f, \mathcal{L}v \rangle_{Y(\Omega)} \tag{4}$$

$$\mathcal{F}(v) = \langle g, \mathcal{L}v \rangle_{Y(\Omega)} \tag{5}$$

where $\mathcal{A} : X \times X \to \mathbb{R}$ is a symmetric, continuous bilinear form, and $\mathcal{F} : X \to \mathbb{R}$ a continuous linear form.

Finally, the searching space is restricted to a finite dimensional space such that $f_N \in X_N(\Omega) \subset X(\Omega)$.

3.1. **Spectral element approximation.** The spectral element method consists in sub–dividing the computational domain Ω into K non–overlapping sub–domains Ω_k of diameter h_k, called spectral elements, such that

$$\Omega = \bigcup_{k=1}^{K} \Omega_k, \qquad \Omega_k \cap \Omega_l = \emptyset, \quad k \neq l \tag{6}$$

Within each element Ω_k the unknown function is approximated by $\mathbb{P}_{N_k}$, i.e. the set of all polynomials of degree $\leq N_k$. Hence, each spectral element can be characterized by the discretization pair (h_k, N_k). A

particular efficient approximation of the unknown is given in terms of the Lagrange polynomials $\Phi(\xi)$ using nodal point at the zeros of the Gauss–Legendre–Lobatto integration rule.

4. RESULTS

The results are validated with the available experimental data of Wattelet and Chato [5]. The experimental data corresponds to a 2.44 m long tube, with an inner diameter of 10.21 mm and a tube roughness of 0.0015 mm. The test fluid used is R12. In Fig. 2 the pressure drop along the tube for the model and for the experimental test are shown. The refrigerant and wall temperature profiles for the model and the experimental data are shown in Fig. 3.

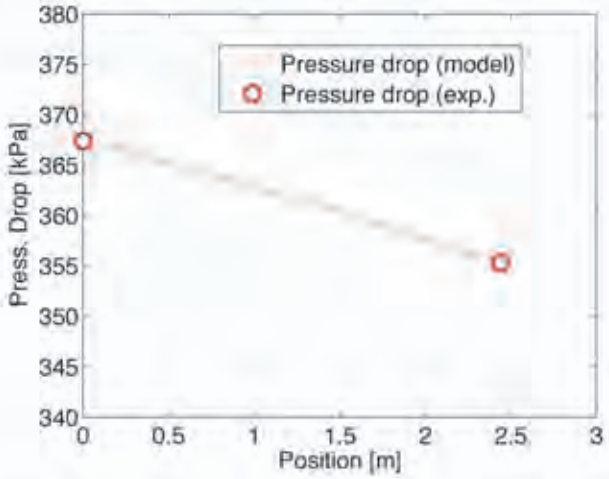

FIGURE 2. Comparison between model and experimental data. Refrigerant mass flux of 540 kg/m^2s, heat flux of 10.2 kW/m^2 and inlet quality of 0.197 [5].

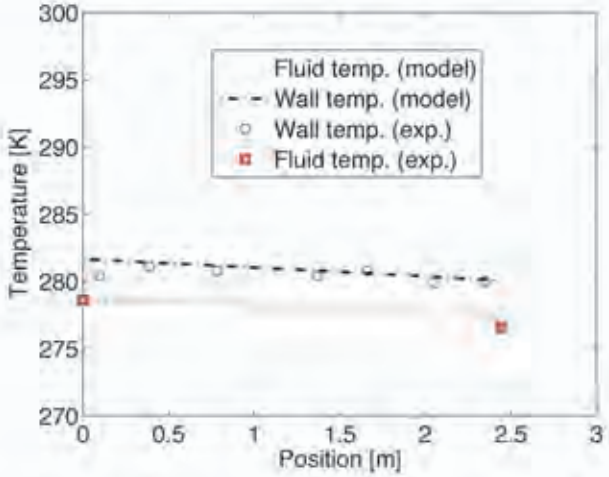

FIGURE 3. Comparison between model and experimental data. Refrigerant mass flux of 540 kg/m^2s, heat flux of 10.2 kW/m^2 and inlet quality of 0.197 [5].

5. CONCLUSIONS

A simple separated flow model for two phase flow systems was developed for the calculation of heat transfer coefficient and pressure drop along a horizontal tube. The results for R12 evaporation under constant heat flux were validated with experimental data.

REFERENCES

[1] S.E. Haaland, Simple and explicit formulas for the skin friction in turbulent pipe flow, *Journal of Fluids Engineering*, 105 (1983) 89-90.

[2] P. B. Whalley, *Boiling, Condensation and Gas-Liquid Flow*, Clarendon Press. Oxford. 1987.

[3] K. Stephan, *Heat Transfer in Condensation and Boiling*, Springer-Verlag. 1992.

[4] B. Jiang, *The Least-Square Finite Element Method: Theory and Applications in Computational Fluid Dynamics and Electromagnetics*, Springer. 1998.

[5] W. Stripattrapan, S. Wongwises, Two-phase flow of refrigernats during evaporation under constant heat flux in a horizontal tube, *Intenational Communications in Heat and Mass Transfer*, 32 (2005) 386-402).